Title
Experimental and Analytical Investigation of Reinforced Concrete Columns Subjected to Horizontal and Vertical Ground Motions

Author
Lee, Hyerin

Publication Date
2011

Experimental and Analytical Investigation of Reinforced Concrete Columns Subjected to Horizontal and Vertical Ground Motions

By

Hyerin Lee

A dissertation submitted in partial satisfaction of the

requirements for the degree of

Doctor of Philosophy

in

Civil and Environmental Engineering

in the

Graduate Division

of the

University of California, Berkeley

Committee in charge:

Professor Khalid M. Mosalam, Chair
Professor Stephen A. Mahin
Professor David R. Brillinger

Fall 2011

Experimental and Analytical Investigation of Reinforced Concrete Columns
Subjected to Horizontal and Vertical Ground Motions

by

Hyerin Lee

Abstract

Experimental and Analytical Investigation of Reinforced Concrete Columns
Subjected to Horizontal and Vertical Ground Motions

by

Hyerin Lee

Doctor of Philosophy in Engineering – Civil Engineering

University of California, Berkeley

Professor Khalid M. Mosalam, Chair

The effect of vertical excitation on shear strength of reinforced concrete (RC) columns has been investigated by various researchers. Field evidences, analytical studies and static or hybrid simulations suggested that excessive tension or tensile strain of the column may lead to shear degradation, and that vertical excitation can be one of the causes of shear failure. The published literature lacks dynamic experiments to investigate the effect of vertical excitation on the shear strength of RC columns due to limitations of testing facility. Considering that current seismic codes do not have a consensus on the effect of vertical acceleration on the shear demand and capacity, the presented dynamic tests and accompanying analytical investigation contribute to better understanding of the effect of vertical excitation on shear failure, one of the most critical brittle failure mechanisms.

This dissertation provides the experimental and computational results, which confirm that the vertical acceleration can induce shear strength degradation of RC columns. Dynamic tests of two reduced geometrical scale specimens were conducted on the UC-Berkeley shaking table at Richmond Field Station. The two specimens had different transverse reinforcement ratio. As a result of an analytical investigation and preliminary fidelity tests, 1994 Northridge earthquake acceleration recorded at the Pacoima Dam was selected as an input motion among the 3,551 earthquake acceleration records in the PEER NGA database. The chosen ground motion was applied to the test specimens at various levels ranging from 5% to 125%. The specimens were subjected to combinations of the vertical component and the larger of the two horizontal components of the selected ground motion record. For the 125%-scale, not only combined vertical and horizontal motion was applied but also a single horizontal component was considered for direct evaluation of the effect of the vertical excitation.

The experimental results imply that vertical acceleration has the potential to degrade the shear capacity of RC columns. The peak shear force in the 125%-scale run with only the horizontal component was larger than that in the 125%-scale runs with the horizontal and vertical components for each specimen, where the peak force was determined by the shear strength at these high-level tests. For these runs, considerable tensile forces were induced on the tested columns due to the vertical excitation. Tension in the columns resulted in degradation of the

shear strength, which is mainly due to the degradation of the concrete contribution to the shear strength. Flexural damage at the top of the column took place before the flexural damage at the base since the bending moment at the top was larger. This was a result of the large mass moment of inertia and rigid body rotation of the mass blocks at the top of the column. In addition, comparison of the bending moment histories at the base and top of the two test specimens indicated that they were opposite in sign during the strong part of the excitation of all the intensity levels suggesting that the columns were in double-curvature. As a result of flexural yielding at the top and base of the column when bending in double curvature, the shear force reached the shear capacity which would not take place if yielding occurred only at the base. Consequently, shear cracks took place and extended over the entire column height as the intensity increased especially under the presence of significant axial tension.

The analytical investigation also revealed that considerable axial tension forces can be induced in RC columns which resulted in degradation in the shear strength. Two types of computational models were utilized in the computational platform, OpenSees. Models A and B had a beam with hinges element and a nonlinear beam-column element, respectively. In addition, a new shear spring element was implemented in the same computational platform to employ code-based shear strength estimation. The element incorporates the shear strength estimations based on ACI or Caltrans SDC equations addressing the effect of column axial load and displacement ductility. Each of the models A and B was developed both without and with the newly-developed shear spring element. Upon improved modeling, results from the analysis of the tested specimens were examined in terms of shear strength variation. Accordingly, current code equations and the corresponding computational models were evaluated. The models without the shear springs did not capture the shear strength degradation accurately, whereas those including the ACI and Caltrans SDC shear springs captured the shear strength degradation due to the axial tension. Both of the ACI and Caltrans SDC springs provided results on the conservative side, where the ACI shear spring predictions were closer to the experimental results than those of the Caltrans SDC shear spring. Elimination of the concrete contribution to the shear strength under any tension was the main reason for the highly conservative predictions of the Caltrans SDC shear strength equation where the strength reduction caused by ductility was not as significant as that by the axial tension force.

Khalid Mosalam 12/14/2011

Professor Khalid M. Mosalam, Chair
Dissertation Committee Chair

Table of Contents

List of Figures

List of Tables

Acknowledgements

Several people have sincerely guided and supported my research. I would like to begin by appreciating all of their kind help.

I could not write this page without expressing my deepest thanks to my advisor, Professor Khalid M. Mosalam. He has always been cordial, attentive, available and supportive throughout all the peaks and valleys of my Ph.D. course. In all research meeting, he never failed to advise me with his inspiring perspective, amazing engineering-intuition, tireless enthusiasm, and firm and solid knowledge.

I am grateful for all the support and advice of Professor Stephen A. Mahin, chairing my qualifying examination and serving as a member of my dissertation committee. His keen perspective on dynamic experiments was exceptionally helpful, and his sincere advice on leading my research opportunities toward a meaningful contribution to examining the effect of vertical excitation on RC columns was tremendously valuable.

I also thank Professor David R. Brillinger for serving on both my qualifying examination committee and my dissertation committee, and thank Professor James M. Kelly and Professor Bozidar Stojadinovic for serving on my qualifying examination committee.

Professor Sashi K. Kunnath at the University of California, Davis, provided invaluable guidance on this research, for which I am grateful. His firm and rigorous knowledge was very helpful in understanding RC structures under seismic excitation.

Without Dr. Frank McKenna, the analysis presented herein would not have been possible. The help provided by staff at the Pacific Earthquake Engineering Research Center (PEER), University of California, Berkeley, is gratefully appreciated. In particular, the experimental phase of this research, conducted in the research laboratories of PEER, benefited considerably from the advice and hard work of Mr. Don Clyde, Dr. Shakhzod Takhirov, and Mr. Wesley Neighbour.

Dr. Selim Günay greatly profited this research by his immeasurable kindness and intellectually stimulating exchanges. I hope to be as informative and impactful with my future colleagues as he is with his. Pardeep Kumar, Hans Christian, and Maura Torres Acevedo provided indispensable help in constructing and testing the specimens. I am thankful to have a chance to work with them.

My former advisor, Hong-Gun Park, encouraged me to study at the University of California, Berkeley. He gave me cordial advice to do my best.

Last but not least, I would like to thank my friends and family. I would not be here today without their love. I cannot thank my parents and my younger brother enough for their unbounded love, patience and sacrifice.

This work was supported by the California Department of Transportation (Caltrans) under Master Agreement No. 22A0486 (Award Number 07-003895-UCB) for the project entitled “Effect of Vertical Ground Motions on Shear Demand and Capacity in Bridge Columns.” It is gratefully acknowledged.

Chapter 1

Introduction

1.1 Motivation

1.1.1 Statement of the Problem

Bridges constitute a major component of the transportation network. Partial or total collapse of bridges after earthquakes may lead to considerable interruption of emergency and recovery services. Reinforced concrete (RC) and prestressed concrete (PC) bridges, which are vital in this stated manner, were observed to have substandard performance during earthquakes, due to the inherent lack of redundancy of the structural system [1]. Bridges and other parts of the transportation network have been constructed prior to the recent advances in earthquake engineering in many parts of the world. In addition, bridges designed according to the modern codes have been severely damaged or collapsed in the earthquakes which occurred within the last two decades in various parts of the world, including the United States, Japan, Taiwan, and others. Since bridge structures do not have enough redundancy and columns are the most critical part of the bridge structural system, their brittle failure should be prevented.

Shear failure is one of the most critical brittle failure mechanisms and involves rapid strength degradation due to a complex shear mechanism related to increasing flexure-shear crack width. It is known that axial force or strain affects the shear capacity. As an example, near fault vertical ground motions may lead to tensile forces on the bridge columns during short time intervals leading to negligible contribution of concrete to shear capacity after cracking. Although the effect of axial force on shear capacity is an accepted fact, current seismic codes do not have a consensus on this effect and different code equations might lead to different shear capacity estimations. On the demand side, axial forces which are not taken into consideration, such as those due to vertical excitation may lead to an increase in the moment capacities, which result in greater shear forces than expected.

1.1.2 Objectives and Scope of the Research

The main objective of this study is to investigate the effect of axial force, produced by the vertical component of the ground motion, on the behavior of bridge columns, especially on shear strength degradation. Outline of the research activities is presented in Fig. 1.1.

This study consists of three parts. In the first part, a bridge prototype is described and it is stated that its shear demand changes under the existence of vertical acceleration. Also, a parametric study is conducted on a single column model which is based on a representative bridge prototype. Using a sub-set of ground motions from the Pacific Earthquake Engineering Research (PEER) Center's Next Generation Attenuation (NGA) ground motion database[1], with strong influence of the vertical acceleration, shear demand is compared to capacity suggested in current codes. The outline of specimen design and input candidates are determined based on the parametric study results.

The main objective of the second part is to design dynamic tests and describe the test results. The specimens, which are ¼-scale models of the prototype columns, are designed based on the Caltrans[2] SDC[3]. Corresponding mass and mass moment of inertia are determined from the prototype. Fidelity tests are used to choose the most suitable motion which can be replicated by the shaking table at the Richmond Field Station, University of California, Berkeley. Dynamic tests of two specimens are conducted and the results imply that vertical acceleration has the potential to degrade the shear capacity of an RC bridge column.

In the third part, a new OpenSees[4] shear spring element is developed because existing elements do not reflect the ductility-axial-shear coupled behavior. Upon improved modeling, results from the specimen analysis are examined scrupulously, especially in terms of shear strength variation. Current code equations are evaluated and compared to the analysis results.

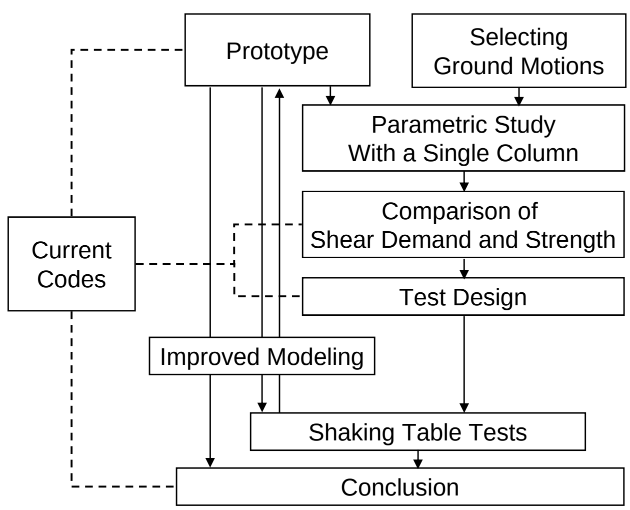

Fig. 1.1 Outline of the research

[1]PEER NGA is an update and extension to PEER Strong Motion Database, http://peer.berkeley.edu/nga/.

[2] Caltrans is California Department of Transportation.

3 Seismic Design Criteria, http://www.dot.ca.gov/hq/esc/earthquake_engineering/SDC_site/.

4 OpenSees is the Open System for Earthquake Engineering Simulation, http://opensees.berkeley.edu/.

1.2 Overview of Shear Strength Assessment

Estimating the shear strength of RC members is still controversial and there is a wide divergence of opinions, design approaches, and code equations. In particular, the influences of axial load, flexural ductility, and size of members and aggregates are not well agreed upon within different codes. The following code equations and an analytical approach are widely used methods to estimate the shear strength of RC members, e.g. columns.

1.2.1 ACI 318-08

According to ACI[5] 318-08 [2], the nominal shear strength is computed by:

$$V_n = V_c + V_s \tag{1.1}$$

where V_c and V_s are the nominal shear strength provided by concrete and shear reinforcement, respectively. When shear reinforcement perpendicular to the axis of the member is used, one can use

$$V_s = \frac{A_v f_y d}{s} = \frac{A_v f_y (0.8D)}{s} \tag{1.2}$$

where A_v is the cross-sectional area of the spiral reinforcement within spacing s and D is the diameter of the concrete section. For circular members with circular ties, hoops or spirals used as shear reinforcement, it is permitted to take the effective depth, d, as 0.80 times the diameter of the concrete section and A_v can be taken as two times the area of the bar cross-section used as the spiral. Finally, f_y is the specified yield strength of the spiral reinforcement.

For members subjected to axial compression,

$$V_c = 2\left(1 + \frac{N_u}{2000 A_g}\right)\sqrt{f_c'}\, b_w d \tag{1.3}$$

and for members subjected to significant axial tension,

$$V_c = 2\left(1 + \frac{N_u}{500 A_g}\right)\sqrt{f_c'}\, b_w d \tag{1.4}$$

but not less than zero, where N_u is positive for compression and negative for tension. In the above two equations, N_u/A_g and the concrete compressive strength of the standard specimen f_c' have psi units, and A_g is the gross cross-sectional area with web width b_w and effective depth d.

For circular members, the area used to compute V_c can be taken as the product of the diameter and effective depth of the concrete section. Hence, the following V_c can be used,

---

[5]ACI is American Concrete Institute.

$$V_c = 2\left(1+\frac{N_u}{2000A_g}\right)\sqrt{f_c^{'}}\left(0.8D^2\right) \text{ for members subjected to axial compression} \quad (1.5)$$

$$V_c = 2\left(1+\frac{N_u}{500A_g}\right)\sqrt{f_c^{'}}\left(0.8D^2\right) \text{ for members subjected to axial tension} \quad (1.6)$$

where $A_g = \dfrac{\pi D^2}{4}$.

1.2.2 A Note about Size Effect

Unfortunately, 'size effect' is not considered in Eqs. (1.3) to (1.6) for V_c. Size effect is the phenomenon that the failure shear stress for members without web reinforcement decreases as the member depth increases. Eqs. (1.3) to (1.6) were obtained from specimens with average height of 340 mm (13.4 in) and as a result, the ACI expressions offer a continuous and linear increase in the contribution of concrete to shear capacity as the member depth increases. This means that these expressions are not suitable for deeper members without web reinforcement.

The Modified Compression Field Theory (MCFT) [3] provides analytical model which is capable of predicting the load-deformation response of RC elements subjected to in-plane shear and normal stresses. It is developed from the compression-field theory for RC members subjected to torsion and shear. While the compression-field theory did not take into account tension in the cracked concrete, the MCFT reflects tensile stresses between cracks. Also, in the MCFT, the size effect is related to the crack spacing in the web and the crack width.

Cracking usually occurs along the interface between the cement paste and the aggregate particles and the rough cracks can transfer shear by aggregate interlocking. Based on Walraven's experimental study [4], the relationship between the shear transfer across the crack and the crack width was derived. Roughly, the larger crack width which occurs in a larger member reduces aggregate interlocking and accordingly reduces the shear transfer. In other words, the shear stress decreases as the crack width increases and as the relative maximum aggregate size (compared to the member size) decreases. Therefore, the shear stress limit of a large member is lower than that of a small member. The crack width is the average crack width over the crack surface and it can be taken as the product of the principal tensile strain and the crack spacing. It means that crack widths increase linearly with both the tensile strain in the reinforcement and the spacing between cracks.

The AASHTO[6] LRFD[7] [6] and the 2004 CSA[8] Standards [7] are based on the Simplified Modified Compression Field Theory (SMCFT) [8], but has been considerably simplified. Simple expressions have been developed for the factor determining the ability of diagonally-cracked concrete to transmit tension, β, the crack angle, θ, and the longitudinal strain in the web, ε_x, thereby eliminating the need to iterate to solve for these values.

---

[6]AASHTO is the American Association of State Highway and Transportation Officials.

[7]LRFD is the Load and Resistance Factor design.

[8]CSA is the Canadian Standards Association.

1.2.3 AASHTO (2010)

AASHTO LRFD Bridge Design Specification [6] defines the shear resistance of a concrete member as the sum of resistance due to shear stress of concrete, V_c, tensile stress in the transverse reinforcement, V_s, and the vertical component of prestressing force, if any, V_p, as follows,

$$V_n = V_c + V_s + V_p \tag{1.7}$$

The contribution of concrete is determined in N-mm units as follows:

$$V_c = 0.083\beta\sqrt{f_c^{'}}b_v d_v \tag{1.8}$$

where b_v is the effective web width taken as the minimum web width with the depth d_v. For a circular section, $b_v = D$, $d_v = 0.9d_e$ can be used, where $d_e = \frac{D}{2} + \frac{D_r}{\pi}$ as shown in Fig. 1.2. The value of β, factor to determine the ability of diagonally-cracked concrete to transmit tension, is defined as follows:

$$\beta = \frac{4.8}{1+750\varepsilon_s} \tag{1.9a}$$

$$\beta = \left(\frac{4.8}{1+750\varepsilon_s}\right)\left(\frac{51}{39+s_{xe}}\right) \tag{1.9b}$$

Eq. (1.9a) is for sections containing at least the minimum amount of transverse reinforcement and Eq. (1.9b) is for the rest. The minimum amount of transverse reinforcement is defined as $A_v \geq 0.05 b_w s/f_y$, where b_w is the width of web. In addition, the crack spacing parameter is calculated as follows:

$$s_{xe} = s_x \frac{1.38}{a_g + 0.63} \tag{1.10}$$

where a_g is the maximum aggregate size in mm, and s_x is the lesser of either d_v or the maximum distance between layers of longitudinal crack control reinforcement. s_{xe} should be between 12 in (305 mm) and 80 in (2032 mm). If there is no prestressing tendon, the net longitudinal tensile strain in the section at the centroid of the tension reinforcement, ε_s, is defined as follows:

$$\varepsilon_s = \frac{\left(\frac{|M_u|}{d_v} + 0.5N_u + |V_u|\right)}{E_s A_s} \tag{1.11}$$

where N_u, M_u, and V_u are the factored axial force, bending moment, and shear force, respectively, and A_s and E_s are the cross-sectional area and modulus of elasticity for the longitudinal tension reinforcement.

The contribution of transverse reinforcement is determined as follows:

$$V_s = \frac{A_v f_y d_v \left(\cot\theta + \cot\alpha\right)\sin\alpha}{s} \tag{1.12}$$

$$\theta = 29^o + 3500\varepsilon_s \tag{1.13}$$

The parameter α is the angle of inclination of transverse reinforcement (with cross-sectional area, A_v, yield stress, f_y, and spacing, s) to the longitudinal axis of the member, and θ is the angle of inclination of the diagonal compressive stress. The factors β (Eq. (1.9)) and θ (Eq. (1.13)) depend on the applied loading and the properties of the cross-section.

Prior to the 2008 interim revisions, AASHTO provided the procedure for shear design, which was iterative and required the use of tables for the evaluation of β and θ. With the 2008 revisions, this design procedure was modified to be non-iterative and algebraic equations were introduced for the evaluation of β and θ. These equations are functionally equivalent to those used in the Canadian code (CSA 2004), which were also derived from the SMCFT [8]. Since Eq. (1.8) and Eq. (1.16) are equivalent, only CSA equations will be used in Chapter 2.

The longitudinal strain, ε_s, is affected by diagonal compressive stresses. After diagonal cracks have formed in the web, the shear force applied to the web concrete, V_u, is primarily carried by diagonal compressive stresses in the web concrete. These stresses result in a longitudinal compressive force in the web concrete of $V_u \cot\theta$, refer to Fig. 1.3 Equilibrium requires that this longitudinal compressive force in the web needs to be balanced by tensile forces in the two flanges, with half the force, that is $0.5V_u \cot\theta$, being taken by each flange. For simplicity, the longitudinal demand due to shear in the longitudinal tension reinforcement may be taken as V_u without significant loss of accuracy. After the required axial forces in the two flanges are calculated, the resulting axial strains in the steel reinforcement and concrete, ε_s and ε_c, respectively, can be calculated based on the axial force-axial strain relationships.

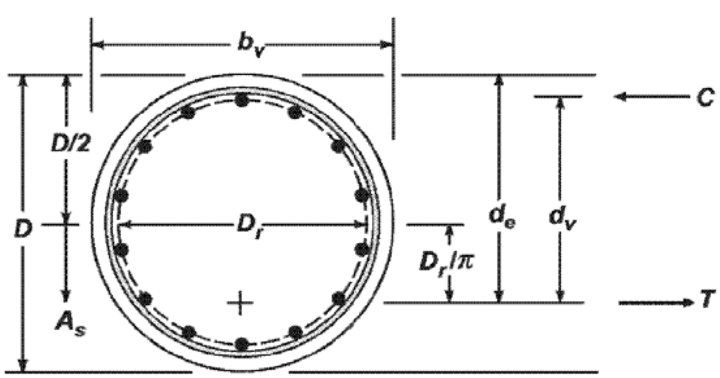

Fig. 1.2 Parameters b_v, d_v and d_e for a circular column, AASHTO (2010) [6]

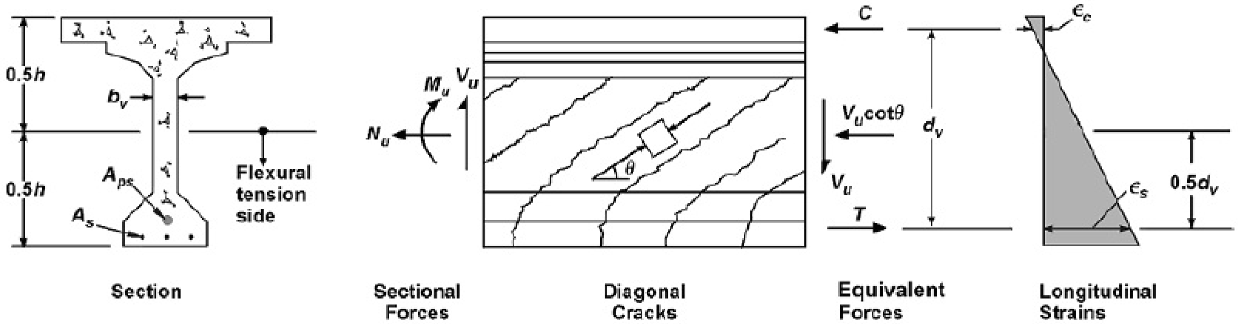

Fig. 1.3 Shear parameters, AASHTO (2010) [6]

1.2.4 Canadian Code (2004)

2004 CSA A23.3 [7] shear provisions for RC are based on the MCFT like the AASHTO [6]. In CSA, the shear strength in assumed to be the sum of V_c, V_s, and V_p (Eq. (1.7)) as in other codes where V_c is the shear resistance from concrete, which is due to the shear stress transfer across the crack itself, usually called aggregate interlocking stresses, V_s is from the transverse reinforcement, specifically due to the yielding stirrup legs that cross the diagonal crack, and V_p is the vertical component of the prestressing force, if any. Since the vertical force from dowel action is ignored in the MCFT, it is ignored in the CSA as well.

The aggregate interlocking resistance of the complex crack geometry may be estimated at only one depth in the member, e.g. mid-height, and this can represent the entire crack surface. The shear stress resistance of the flexural compression region is larger than that of the cracked region, and thus the ability of the cracks to resist shear stresses controls the member strength for members without stirrups.

The shear resistance from transverse reinforcement is defined as follows:

$$V_s = \frac{A_v f_y d_v \cot\theta}{s} \tag{1.14}$$

$$\theta = 29^o + 7000\varepsilon_x \tag{1.15}$$

$$V_c = \beta\sqrt{f_c^{'}}b_v d_v \tag{1.16}$$

$$\beta = \left(\frac{0.4}{1+1500\varepsilon_x}\right)\left(\frac{1300}{1000+s_{ze}}\right) \tag{1.17}$$

where A_v is the cross-sectional area of the spiral reinforcement, f_y is the yield strength of the spiral reinforcement material, s is the spacing of the spiral reinforcement, and $f_c^{'}$ is the compressive strength of concrete and its unit is MPa. The parameters which define β and θ for the determination of V_c and V_s, respectively, are similar to the case of AASHTO, except the longitudinal strain. In CSA, the longitudinal strain at the centroid, ε_x, is used rather than the longitudinal strain at the centroid of the tension reinforcement, ε_s.

Since the aggregate interlocking relationship directly depends on the crack width, the calculation of such crack width is needed to determine V_c. Approximately, the crack width can be estimated as the product of average crack strain perpendicular to the crack and the average crack spacing in this direction. Previous studies demonstrated that the crack patterns are consistent from one size to another, and the crack spacing increases as the RC member (without shear reinforcement) is scaled to a larger size. Since wider cracks carry less shear stresses, larger member's shear stress related to V_c cannot exceed that of a smaller member. However, members with transverse reinforcement do not follow this trend because transverse reinforcement controls the crack spacing. Therefore, such RC members (with shear reinforcement) do not show a significant size effect. Hence, the basic crack spacing s_z is taken as 300 mm (11.8 in) for the members with stirrups or transverse reinforcement, rather than $s_z = d_v = 0.9D$ (where D is the diameter of the column) which is used by CSA 2004 for the members without stirrups.

The effective crack spacing parameter, s_{ze}, reflects the effect of different coarse aggregate sizes in mm, a_g, and it is calculated as follows:

$$s_{ze} = \frac{35 s_z}{15 + a_g} \geq 0.85 s_z \tag{1.18}$$

In case of a member with transverse reinforcement and 19 mm (0.75 in) coarse aggregate, $s_{ze} = 308.8$ mm (12.2 in). For a circular section, $d_v = 0.72D$ in CSA 2004. Also, nominal shear strength should not be taken larger than the following:

$$V_{n,\max} = 0.25 f_c^{'} b_v d_v \tag{1.19}$$

1.2.5 Eurocode (2004)

Eurocode 2 [9] suggests the use of Eq. (1.1) with following definitions:

$$V_s = \min\left(\frac{A_v z f_y \cot\theta}{s}, \frac{\alpha_c b_w z \nu f_c^{'}}{\cot\theta + \tan\theta} \right) \tag{1.20}$$

$$V_s = \frac{A_v z f_y \cot\theta}{s} = \frac{A_v f_y \left(0.72D\right)}{s} \tag{1.21}$$

where z is the lever arm and θ is the angle of the inclined struts. The recommended limiting values are: $1 \leq \cot\theta \leq 2.5$, i.e. $22° \leq \theta \leq 45°$. In this study, $\cot\theta = 1$, i.e. $\theta = 45°$, is used unless otherwise noted. The parameter α_c is a coefficient which takes into account the effect of normal stresses on the shear strength and its recommended value is as follows:

$$\left(\begin{array}{l} \text{non-prestressed} : \alpha_c = 1 \\ 0 < \sigma_c \leq 0.25 f_c^{'} : \alpha_c = 1 + \sigma_c / f_c^{'} \\ 0.25 < \sigma_c \leq 0.50 f_c^{'} : \alpha_c = 1.25 \\ 0.50 < \sigma_c \leq 1.0 f_c^{'} : \alpha_c = 2.5\left(1 - \sigma_c / f_c^{'}\right) \end{array} \right) \tag{1.22}$$

where σ_c is the compressive stress in concrete from axial load or prestressing. The parameter ν is a coefficient that takes into account the increase of fragility and the reduction of shear transfer by aggregate interlocking with the increase of the compressive concrete strength. It may be taken to be 0.6 for $f_c^{'} \leq 60\text{MPa}$, and $0.9 - f_c^{'}/200 > 0.5$ for high-strength RC members.

$$V_c = \frac{\pi D_c^2}{4}\left[\tau_{rd} k\left(1.2 + 40\rho_l\right) + 0.15\sigma_{cp}\right] \tag{1.23}$$

$$D_c = D - 2c_c - 2d_{bw} \tag{1.24}$$

where d_{bw} is the diameter of the spiral reinforcement and c_c is the concrete cover outside the spiral.

$$\tau_{rd} = 0.25\left(0.7\sqrt{f_c^{'}}\right) \tag{1.25}$$

$$k = 1 \tag{1.26}$$

$$\sigma_{cp} = \frac{N}{A_c} \tag{1.27}$$

where N is the axial load and $A_c = \frac{\pi D_c^2}{4}$.

1.2.6 Priestley et al. (1996)

Priestley et al. (1996) [1] suggested the following equations to calculate the nominal shear strength of RC columns. In this approach, V_c is calculated for the plastic hinge zone considering the effect of displacement ductility and V_s is calculated based on the truss model for circular columns. The shear strength enhancement resulting from axial compression, V_p, is considered as an independent compression strut. Accordingly, Eq. (1.7) is used in this model.

The contribution of transverse reinforcement to the shear strength is based on the truss mechanism using θ as the angle of inclination between the shear cracks and the vertical column axis. Accordingly, one obtains,

$$V_s = \frac{\pi}{2}\frac{A_v f_y D^{'}}{s}\cot\theta \tag{1.28}$$

where A_v is the total transverse reinforcement cross-sectional area and $D^{'}$ is the distance between centers of the peripheral hoop in the direction parallel to the applied shear force. The angle of the critical inclined flexure shear cracking to the column axis is taken as $\theta = 30°$ unless limited to larger angles by the potential corner-to-corner crack. The contribution of concrete is given as follows:

$$V_c = k\sqrt{f_c^{'}}A_e \tag{1.29}$$

where $A_e = 0.8A_g$ is the effective shear area and k depends on the instantaneous displacement or ductility. In case of displacement ductility and when subjected to biaxial ductility demand, μ_Δ,

k is defined as follows when the concrete strength and the effective shear area are respectively in MPa and mm^2 units:

$$\begin{pmatrix} \mu_\Delta \le 1 : k = 0.29 \\ 1 < \mu_\Delta \le 3 : k = 0.10 + 0.19(3 - \mu_\Delta)/2 \\ 3 < \mu_\Delta \le 7 : k = 0.05 + 0.05(7 - \mu_\Delta)/4 \\ 7 < \mu_\Delta : k = 0.05 \end{pmatrix} \tag{1.30}$$

The shear strength increase by axial force is calculated as a result of an inclined compression strut given as follows:

$$V_p = P \tan\alpha = \frac{D - c}{2a} P \tag{1.31}$$

where D is cross-section height or diameter, c is the compression zone depth and it is determined from flexural analysis. The parameter a is the shear span which is $L/2$ for a column in double curvature and L for a column in single curvature, Fig. 1.4.

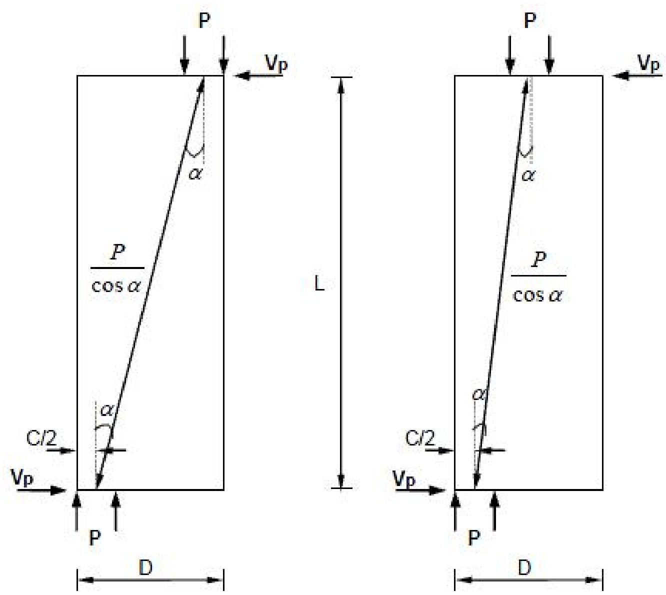

Fig. 1.4 Contribution of axial forces to shear strength, Priestley et al. (1996) [1]

1.2.7 Caltrans SDC (2010)

Caltrans SDC (2010) [13] suggests the use of Eq. (1.1) with following definitions for the shear strength of ductile concrete circular members.

$$V_s = \frac{A_v f_y D'}{s} \tag{1.32}$$

$$A_v = n\left(\frac{\pi}{2}\right) A_b \tag{1.33}$$

$$V_c = v_c A_e \tag{1.34}$$

where n is the number of branches of the transverse reinforcement crossed by the diagonal shear cracks, A_b is the cross-sectional area of the bar used as transverse reinforcement, $A_e = 0.8A_g$ is the effective shear area and v_c is determined by the location of the cross-section, transverse reinforcement, and ductility demand ratio as follows:

Inside the plastic hinge zone, 'Factor1' is included in calculating v_c.

$$v_c = \text{Factor1} \times \text{Factor2} \times \sqrt{f_c^{'}} \le 0.33\sqrt{f_c^{'}} \tag{1.35}$$

Outside the plastic hinge zone, the constant, 0.25, is used instead of 'Factor1'.

$$v_c = 0.25 \times \text{Factor2} \times \sqrt{f_c^{'}} \le 0.33\sqrt{f_c^{'}} \tag{1.36}$$

It should be noted that $f_c^{'}$ is the concrete strength in MPa.

The factors in the above equations are defined as follows:

$$0.025 \le \text{Factor1} = \frac{\rho_s f_{yh}}{12.5} + 0.305 - 0.083\mu_d \le 0.25 \tag{1.37}$$

where f_{yh} is transverse reinforcement (e.g. hoop) yield strength in MPa units and $\rho_s f_{yh}$ (where ρ_s is the volumetric ratio of the transverse reinforcement) is limited to 0.35 ksi (2.413 MPa).

$$\text{Factor2} = 1 + \frac{P_c}{13.8A_g} < 1.5 \tag{1.38}$$

where P_c is the axial load in N and A_g is in mm^2. As defined above, 'Factor1' is affected by the transverse reinforcement and lateral displacement ductility, μ_d, and 'Factor2' is affected by the axial pressure. It should be noted that $v_c = 0$ for members whose net axial load is in tension.

Except that it takes account of displacement ductility instead of curvature ductility in the estimation of the shear strength, Caltrans SDC (2010) [13] adopts the approach of Priestley et al. (Section 1.2.6) [1] for ductility and combines it with the approach of ACI [2] and Eurocode [9] for axial pressure. Another unique feature of the SDC approach is that it provides different estimation along the member. 'Factor1', which is determined by the transverse reinforcement and displacement ductility, is only effective inside the plastic hinge zone and it ranges from 0.025 to 0.25. Since 0.25 is applied instead of 'Factor1', V_c of the cross-section outside the plastic hinge zone is equal or larger than that inside the plastic hinge zone.

1.3 Studies on V/H

One of the sources of axial load on bridge columns is attributed to the effect of the vertical component of the earthquake acceleration. Vertical excitation has been neglected in most design provisions for several decades. However, as confirmed in [10] and other field observations, the effect of vertical ground motion can be destructive. In addition, the ratio of peak vertical-to-horizontal ground accelerations (V/H) may exceed 2/3, which is the value usually considered in current design codes, in the near-source region. For the 1994 Northridge earthquake in California, the vertical peak ground acceleration at Rinaldi receiving station was 0.83g and the horizontal one was 0.63g according to PEER NGA database [11], for which the ratio of vertical peak ground acceleration to the horizontal peak ground acceleration (V/H) is 1.31. In Table 1.1, V/H ratios from various earthquakes which are greater than 2/3 are presented.

In many codes, vertical earthquake motion is represented by scaling a single design spectrum which is derived for horizontal components. This procedure was devised by Newmark et al. (1973) [12] and has been widely used. Generally, the scaling factor, i.e. the vertical-to-horizontal ratio, has been taken as 2/3. The weakness of this procedure is that horizontal and vertical components have the same frequency content and this does not reflect the actual structural responses of bridge systems.

Current provisions in Caltrans SDC (2010) [13] specifies the requirements on demand due to vertical ground motion. As specified in Section 2.1.3 of [13], the current provisions in SDC do not provide guidelines considering the adverse consequences of vertical accelerations in seismic design of ordinary bridges where the site peak rock acceleration is smaller than 0.6g. Also, when this acceleration is 0.6g or greater, only equivalent static methods are required. In other words, current provisions in SDC do not provide adequate guidelines for the effect of vertical accelerations in ordinary bridges and this deficiency is demonstrated by the following review of previously published research.

Table 1.1 V/H ratios from several earthquakes

Earthquake	Station	PGA [g]		V/H
		Horizontal	Vertical	
Nahanni 1985	Site 1	1.06	2.09	1.98
Gazli 1976	Karakyr	0.644	1.26	1.96
Kobe 1995	Port Island	0.315	0.562	1.78
Kobe 1995	Kobe University	0.310	0.380	1.23
Landers 1992	Lucerne	0.721	0.819	1.14
Loma Prieta 1989	LGPC	0.784	0.886	1.13
Northridge 1994	Jensen Filter Plant	0.764	0.825	1.08

1.3.1 Vertical Component of Ground Motion

As widely known, the vertical component of ground motion is associated with the P-waves while the horizontal components are mainly caused by the S-waves. The wavelength of the P-waves is shorter than that of the S-waves, which means that the former is associated with higher frequencies. In the near-source region, ground motion is characterized mainly by source spectra. The P-wave spectrum has a higher corner frequency than that of the S-wave. P and S corner frequencies gradually move to lower frequencies as waves propagate away from the source and, as a result, the vertical motion is modified at a faster rate. The relative characteristics of these two components of ground motion are often represented by the V/H (vertical to horizontal) peak ground acceleration ratio.

The dependence of V/H on distance and local site conditions is explained from a seismological point of view and it is related to S-to-P conversion. Silva (1997) [14] explains the S-to-P conversion mechanism at near-source soil and rock sites. At near-source soil sites, as the waves propagate through rock/soil boundary, the large contrast in S-waves at the interface induces inclined SV-waves to be converted to P-waves. These are amplified and refracted into a more vertical angle of incident by a shallow P-wave velocity gradient. This has the effect of significantly increasing the amplitude of the vertical component of ground motion over that caused by direct P-waves only. This effect is diminished at near-source rock sites because of less S-to-P converted energy due to the smaller S-wave and P-wave velocity gradients and a subsequently smaller value of V/H. In case of larger distances, the SV-wave is beyond its critical angle of incidence and does not propagate to the surface effectively, according to [14], [15]. Hence, the lower amplitude direct P-waves will be dominant in the vertical component and cause relatively smaller values of V/H. Similarly, Amirbekian and Bolt (1998) [16] concluded that the high-amplitude, and high frequency vertical accelerations that are observed on near-source accelerograms are most likely generated by the S-to-P conversion within the transition zone between the underlying bedrock and the overlying softer sedimentary layers.

1.3.2 Vertical Design Spectra

To consider the effect of vertical ground motion appropriately, some recent studies have focused on constructing vertical design spectra. In particular, references [17] to [19] proposed a vertical design acceleration spectrum which consists of a flat portion at short periods (0.05 to 0.15 sec) and a decaying spectral acceleration for $T \geq 0.15\,\text{sec}$. In reference [19], procedures were suggested for assessing the significance of vertical ground motion, indicating when it should be included in the determination of seismic actions on buildings. These procedures included the calculation of elastic and inelastic vertical periods of vibration incorporating the effects of vertical and horizontal motion amplitude and the cross-coupling between the two vibration periods. Also, a procedure was suggested for combining vertical and horizontal seismic action effects which accounts for the likelihood of coincidence, or otherwise, of peak responses in the two directions.

Elgamal and He (2003) [20] studied the characteristics of vertical ground motion with 111 free field records and down-hole array records. They found that significant high frequency (about 8 Hz or higher) prevailed in all vertical records and site distance from source affects the spectral shape. They also discovered that the spectra of Elnashai and Papazoglou proposed in [18] with corner periods of 0.05 sec and 0.15 sec are quite representative for near-field sites. From the scarce available down-hole array records, they found little variation with depth in spectral shape and concluded that using the surface spectral shape for a spectrum at any depth may be acceptable, but the values should be gradually reduced by 1/2 to 2/3 as the depth reaches the range of 20 m.

Bozorgnia and Campbell (2004) [21] studied the characteristics of vertical ground motion extensively and proposed a ground motion model for the vertical-to-horizontal ratio (V/H) of the peak ground accelerations. From over 400 near-source accelerations with large M_w (i.e. $4.7 \leq M_w \leq 7.7$), they found no bias in the V/H estimates from independent analyses of vertical and horizontal response spectra.

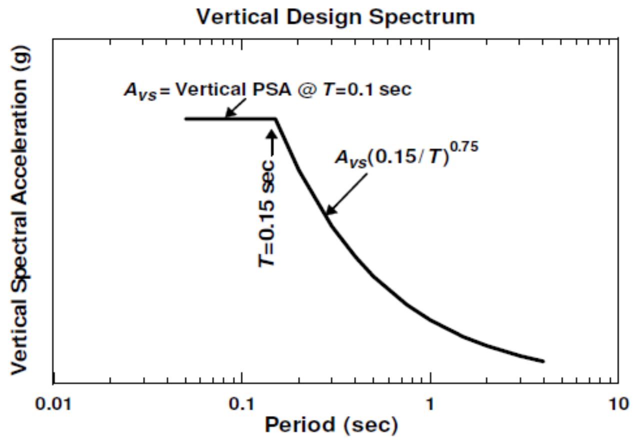

Fig. 1.5 Suggested vertical design spectrum by Bozorgnia and Campbell (2004) [21]

In addition, V/H was found to be a strong function of natural period, local site conditions, and source-to-site distance and a relatively weaker function of magnitude, faulting mechanism, and sediment depth. V/H exhibits its greatest differences at long periods on firm rock (NEHRP: BC), where it has relatively low amplitudes, and at short periods on firm soil (NEHRP: D), where it has amplitudes that approach 1.8 at large magnitudes and short distances. Bozorgnia and Campbell suggested in [21] a 5%-damped acceleration design spectrum as shown in Fig. 1.5. Even if the vertical spectral ordinate at $T = 0.1\text{sec}$ is not available, the design spectrum can be obtained using their V/H model [21].

1.3.3 Arrival Time Interval

As discussed in [19], [22], the arrival time interval is an important parameter which affects the interaction between horizontal and vertical responses. In these studies, the interval between the peak acceleration of horizontal component and that of vertical one is utilized as the arrival time interval. According to the results, arrival time interval was shown to be zero, i.e. coincident, within a radius of 5 km of an earthquake source and the interaction was significant within a radius of 25 km. Also, this turned out to be magnitude-dependent similar to the V/H ratio.

Collier and Elnashai (2001) [19] pointed out that a maximum interaction effect between the horizontal and vertical motions occurs when the arrival time interval is less than 0.5 sec. They also showed that there is no interaction effect when the arrival time is longer than 4.0 sec.

1.4 Studies on Bridge Columns Subjected to Combined Vertical and Horizontal Excitation

1.4.1 PWRI Study

Sakai and Unjoh (2007) [23] conducted shaking table experiments with combined horizontal and vertical excitations. The specimen was a 1/4-scale circular column which had 3 m height and 600 mm diameter, corresponding to an effective aspect ratio of 5 (Fig. 1.6). The inertia mass was 27000 kg and the axial force and stress were 280 kN and 0.99 MPa at the bottom cross-section. The longitudinal reinforcement ratio was 1.01% (40-D10 bars) and the hoop reinforcement ratio was 0.31% (D6 bars at 75 mm spacing). Yield strengths of the D6 and D10 bars were 340 MPa and 351 MPa, respectively. Ultimate strengths were 514 MPa and 496 MPa for the D6 and D10 bars, respectively. The standard cylinder strength of concrete was 41.7 MPa.

The test had two phases, one for dynamic response in elastic range and the other for nonlinear response. The amplitudes in all the three directions were scaled by 20% and 400% for each phase. The lateral period was 0.3 sec and the vertical period was 0.08 sec. Note that the vertical period was much smaller than those of real bridge systems and this implies that the experiment may not represent the real behavior of bridge columns. Fig. 1.7 shows the displacements at the center of gravity (C.G. in Fig. 1.6) in 20% and 400% tests. After 4 times repetition of 40% to 75% larger displacements than the ultimate displacement based on the design code of Japan, slight spalling of cover concrete was observed. As the displacement increased up to twice of the ultimate displacement, cover concrete spalled and the longitudinal bars buckled.

Because the predominant natural period in the vertical direction was 25% of that in the lateral directions, the lateral response and axial force rarely reached their maximum values simultaneously. Hence, the lateral response was not significantly affected by the fluctuation of the axial force.

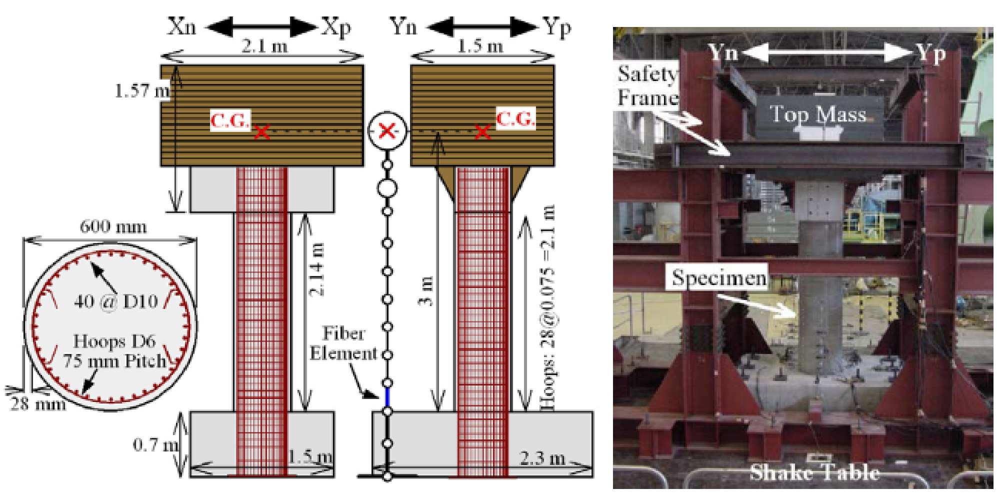

Fig. 1.6 Specimen and shaking table setup of Sakai and Unjoh (2007) [23]

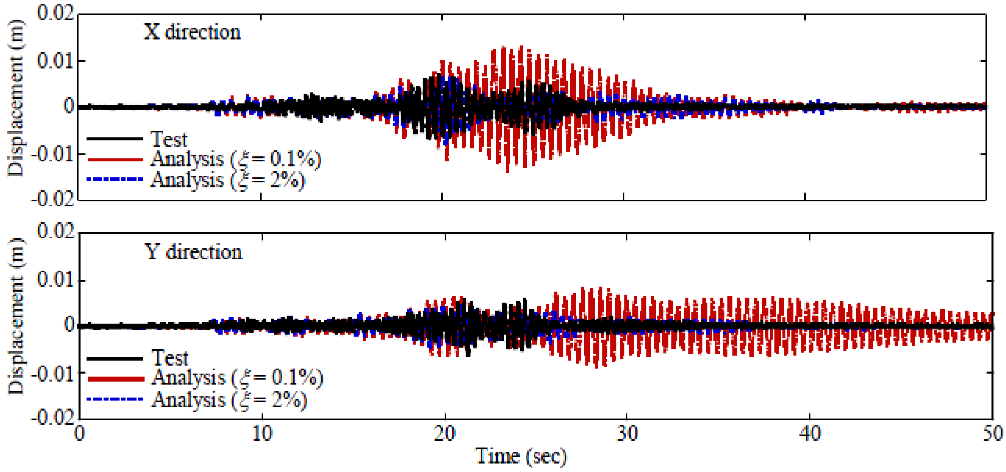

(a) 20% of 1983 Nihonkai Chubu earthquake (Tsugaru bridge record) [23]

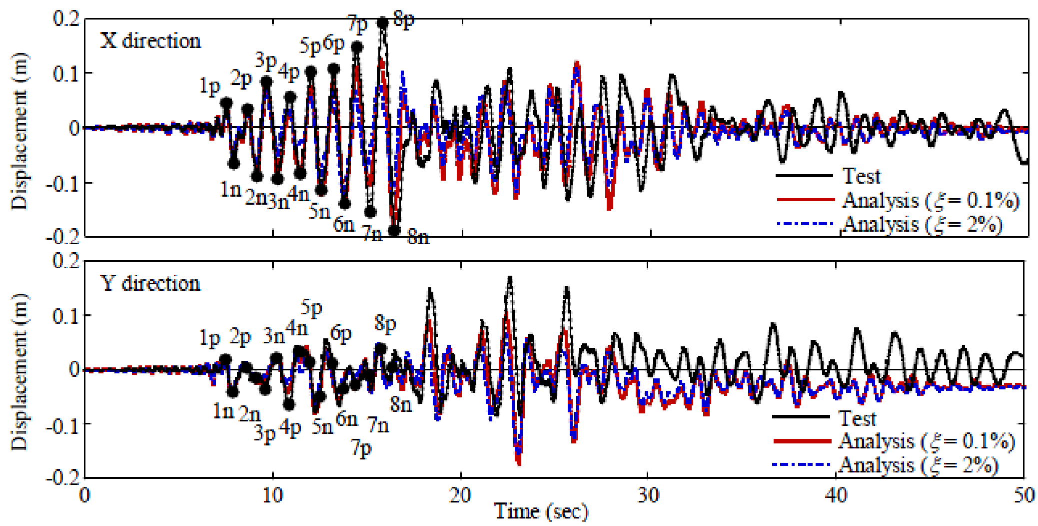

(b) 400% of 1983 Nihonkai Chubu earthquake (Tsugaru bridge record)

Fig. 1.7 Displacement at the C.G. [23]

Fig. 1.8 compares the responses for 3D excitation (XYZ), 2D excitations (XY and XZ) and 1D excitation in X obtained from analytical simulations. Two horizontal motions (XY) produce 15% larger displacement than the 1D ground motion due to the bidirectional bending effects. But, the vertical ground motion does not have a significant effect on the lateral displacement response.

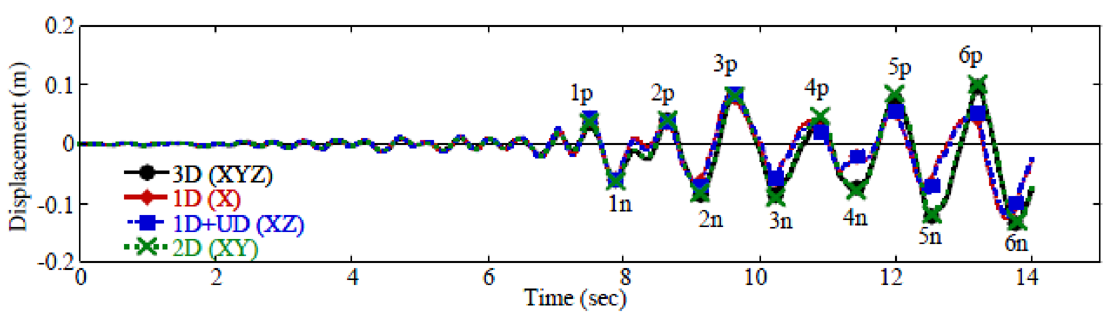

Fig. 1.8 Analytical study on the effect of multidirectional loading ($\xi = 0.1\%$) [23]

1.4.2 Multi-axial Full-scale Substructure Testing and Simulation Study

To investigate the effect of vertical ground motion on RC bridges and buildings, Kim and Elnashai (2008) [22] performed extensive analytical and experimental investigations. For RC bridges, they assessed the effect of various peak vertical-to-horizontal acceleration ratios and studied the effect of time intervals between the arrival of vertical and horizontal peaks of given earthquake records. Also, they investigated the effect of vertical ground motion on RC bridge piers by employing sub-structured pseudo-dynamic (SPSD) tests with combined horizontal and vertical excitations of earthquake ground motion. They evaluated the effect of axial load on bridge piers by employing cyclic static tests with different constant axial load levels.

1.4.2.1 Analytical Investigation

In this investigation, Kim and Elnashai [22] evaluated the effect of vertical ground motion on RC bridge columns with two prototypes, Santa Monica Bridge (Fig. 1.9) and FHWA Bridge #4 (Fig. 1.10). Some observations from their analytical study are as follows:

- The ratio of vertical seismic force to gravity load of pier was higher for the bridge with shorter span because the fundamental period of short span bridge was close to the dominant period of vertical motion.
- The shear capacity decreased due to vertical excitation.
- The contribution of vertical ground motion to axial force variation increased as the span ratio (i.e. the ratio between the two adjacent span lengths) increased since increased span ratio was associated with shorter vertical period. Therefore, shear capacity was reduced as well, but the effect of vertical ground motion on shear demand varied irregularly.
- The shear capacity of shorter column height was significantly reduced with vertical excitation while shear demand decreased as the height increased.

They also assessed the effect of vertical-horizontal interaction on the inelastic periods of RC columns and on axial force amplitude and direction. They concluded that lateral inelastic periods were significantly affected by vertical ground motion in case of Santa Monica Bridge, but not significantly in case of FHWA Bridge #4. The vertical period increased in both cases. As vertical amplitude increased, the lateral displacement increased or decreased in both bridges. The ranges were -34% to 24% (Santa Monica Bridge) and -7% to 11% (FHWA Bridge #4). Including vertical ground motion significantly affected the moment demand as well as the axial force variation of the pier when V/H ratio increased. They mentioned that the increased axial force variation lead to significant reduction of shear capacity which may cause brittle shear failure. In the analysis of Santa Monica Bridge and FHWA Bridge #4 , it is observed that reduction of shear capacity occurred up to 30% and 24%, respectively.

It was concluded in [22] that the effect of arrival time was minimal on the periods of vibration, axial force variation, and moment and shear demands. On the other hand, it was shown that the time interval had an effect on the shear capacity, which changed by -18% to 23% (Santa Monica Bridge) and -7% to 22% (FHWA Bridge #4) compared to the response with coincident horizontal and vertical peaks. In summary, reference [22] stated that vertical ground motion should be considered in assessing the shear capacity and in the demand assessment when V/H is likely to be high and the arrival time interval is near zero or very short.

1.4.2.2 Experimental Study

In this investigation, Kim and Elnashai [22] conducted SPSD tests and cyclic static tests with different axial loads using the Multi-Axial Full-Scale Sub-Structured Testing and Simulation (MUST-SIM) facility at University of Illinois at Urbana-Champaign. The prototype was the FHWA Bridge #4 (Fig. 1.10) and the sub-structure was selected as an experiment module. Note that the pinned connection at the base was modified to fixed connection and this increased the shear demand on the column. Due to the capacity limitations of the MUST-SIM facility, a ½-scale model was constructed. Two SPSD tests were conducted to investigate the effect of vertical ground motion, one under horizontal ground motion only (IPH) and the other under horizontal and vertical ground motions (IPV). To investigate the effect of axial force, two specimens were used for static cyclic tests, one subjected to tension (ICT) and the other subjected to compression (ICC). Their properties are listed in Table 1.2 and the axial forces were based on the analytical predictions of the bridge system.

In specimen IPH, significant flexural, vertical and inclined shear cracks were observed at the top and bottom of the pier. Spalling of the concrete cover was observed on the left face at the top and on the right face at the bottom of the pier.

In specimen IPV, significant diagonal cracks occurred in the middle of the pier while the simulation was approaching the second peak. Inclined cracks on the front of the pier along the height as well as significant flexural and vertical cracks at the top and bottom of the pier were observed. Spalling of concrete cover was observed at the top left and bottom right of the pier.

Table 1.2 Aspect ratios and expected axial levels of test specimens [22]

Specimen	Height [mm]	Aspect ratio	Axial load [kN]	$P/A_g f_c'$ [%]
IPH	3048	2.5	-1348 to -613	-10.63 to -4.84
IPV	3048	2.5	-2652 to 450	-20.92 to 3.55
ICT	2590.8	2.125	222	1.75
ICC	2590.8	2.125	-1112	-8.77

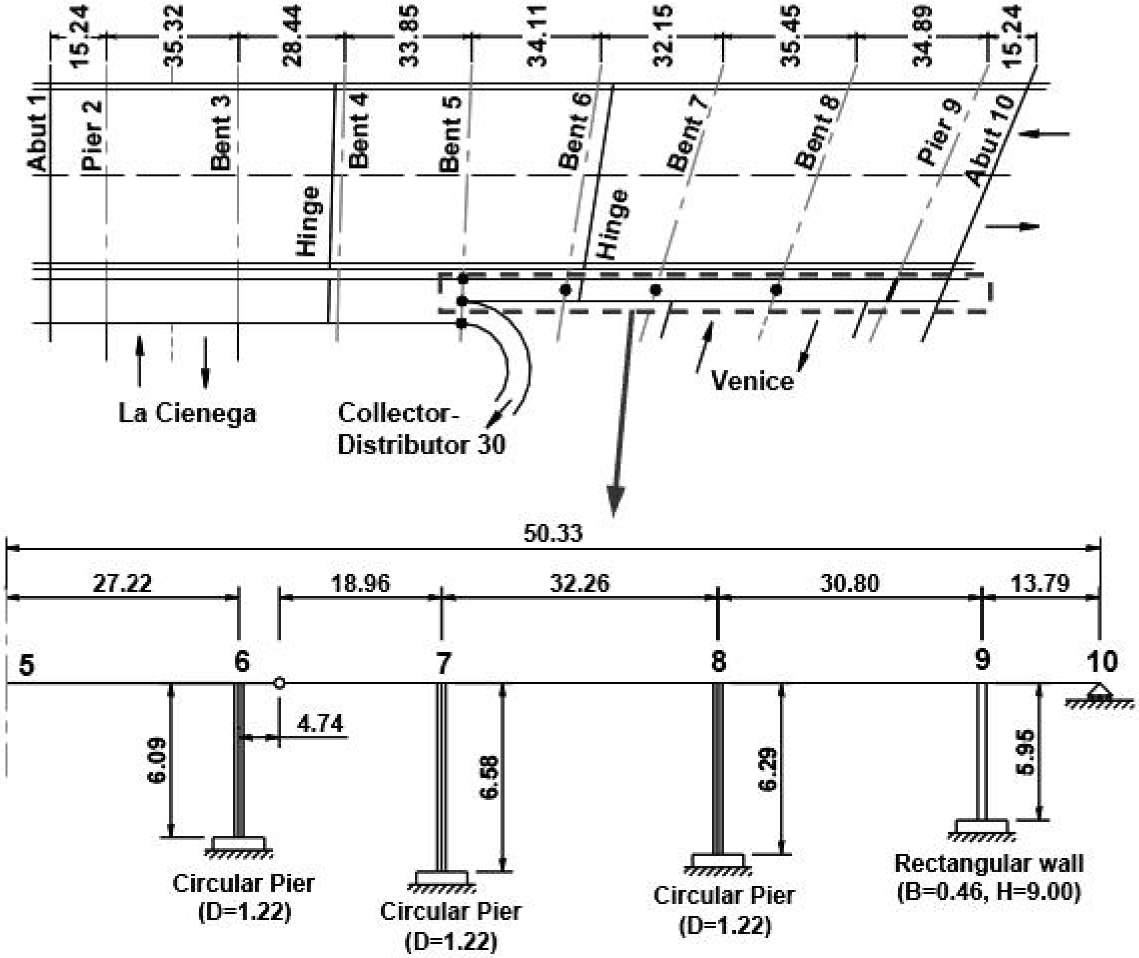

(a) Layout (unit: m)

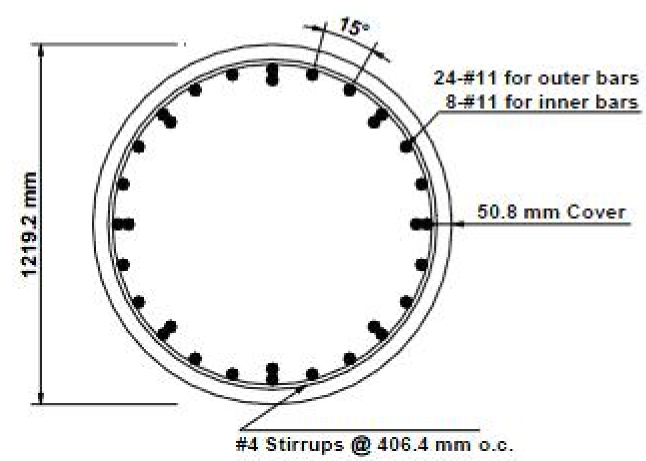

(b) Pier reinforcement

Fig. 1.9 Santa Monica Bridge [22]

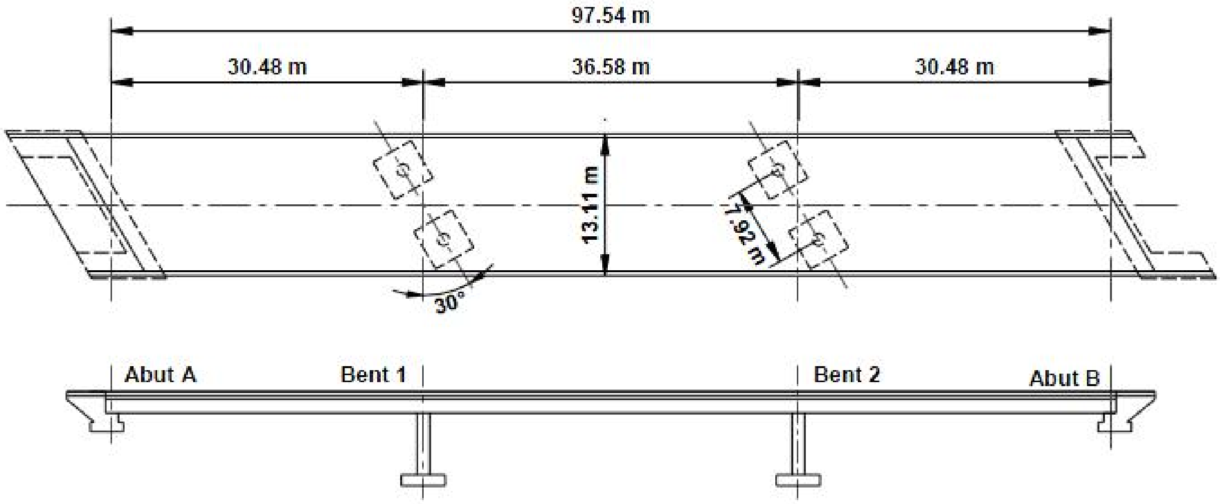

(a) Plan view and elevation

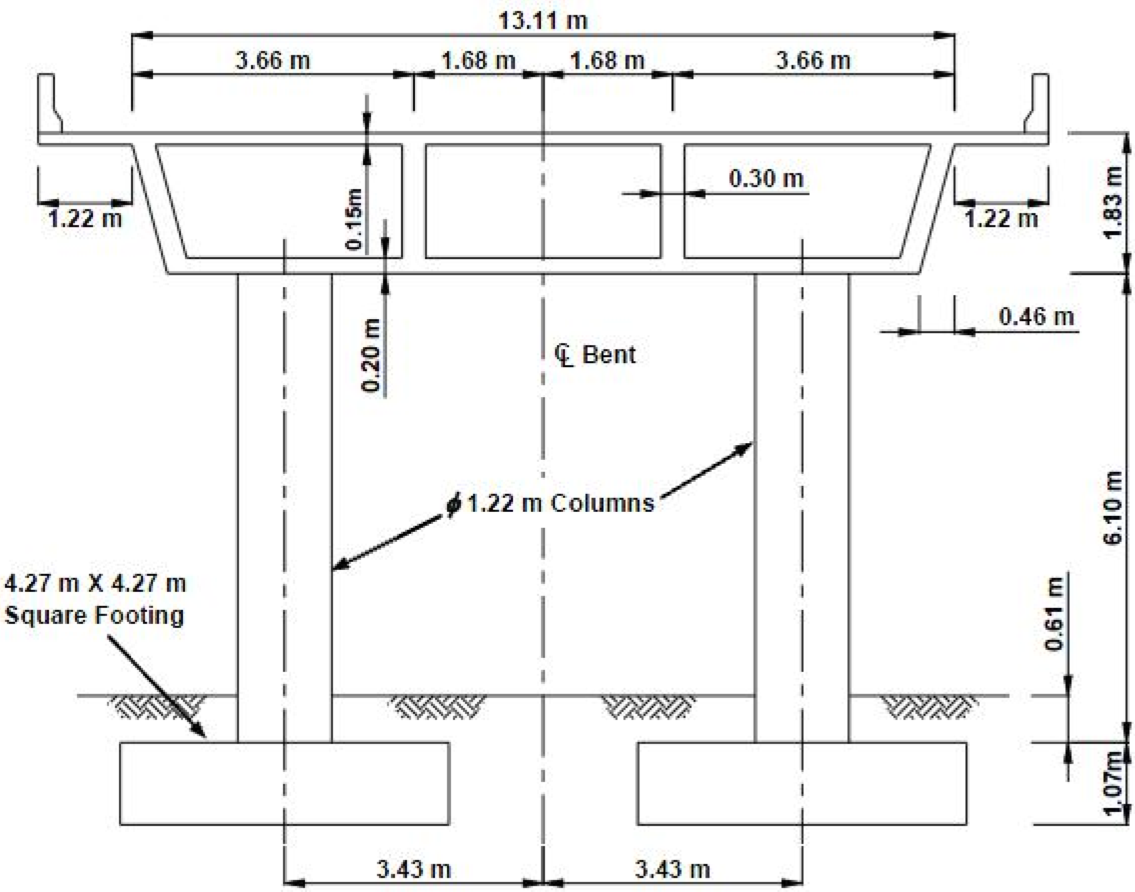

(b) Cross-section

Fig. 1.10 FHWA Bridge #4 [22]

In these tests, it was observed that the vertical ground motion significantly affected the axial displacement and force more than the lateral displacement and rotation. The axial force variation increased by up to 100% and the tensile force was detected only with vertical ground motion. The fluctuation in the lateral force due to axial force variation was clearly shown by observing the relationship between the lateral force and displacement. The lateral force of specimen IPH increased smoothly as displacement increased, but that of IPV showed rise and fall corresponding to fluctuations in the axial force.

The damage in IPV was more severe than that of IPH. At mid height of IPV, severe shear damage was observed. Although the effect of vertical ground motion on the longitudinal strain distribution was not significant, that on the spiral strain was significant. The maximum spiral strain in IPH and IPV was detected at 20% and 55% of the pier height, respectively, and the spiral strain at the same level increased by 160% due to the vertical ground motion. Considering trends of the strain distribution and the maximum spiral strains measured from both piers, it was estimated that the spiral strain increased up to about 200% when the vertical ground motion was included. In summary, it was concluded that including the vertical ground motion reduced the shear capacity of the pier.

In specimen ICT, a flexure-dominated behavior was clearly observed. There was no significant strength degradation until the loading reached the lateral displacement where the maximum lateral force, 700 kN, was recorded. As the loading approached this displacement level, significant diagonal crack opening was observed in the bottom front of the specimen.

In specimen ICC, during the third cycle of displacement amplitude of 101.6 mm, significant diagonal cracking occurred on the front and back of the pier. During the first cycle of displacement amplitude of 127 mm, the lateral force dropped by 37.4% and most of the strain gauges on the spirals were damaged at this stage. After this stage, large pinching effects were observed. During the first application of the displacement limit of 152.4 mm, drastic shear failure occurred at the bottom third of the pier with the rupture of spirals located at about 19% of the pier height. The lateral force was recorded to be 159.4 kN which was 18.6% lower than the maximum force measured during the simulation.

ICC experienced brittle shear failure with rupture of the spiral. On the other hand, ICT subjected to moderate tension was severely damaged with significant flexural and inclined cracks as well as large opening of diagonal cracks near the bottom of the pier. However, there was no strength degradation in ICT. The measured longitudinal strains were similar for ICC and ICT up to the first peak of the first cycle. However, after that, strains measured in specimen ICT were increasing due to axial tension, while those of ICC were slightly decreasing. An overall tendency for the spiral strains of specimen ICC to be much larger than those of ICT was observed. Accordingly, it can be mentioned that different axial load levels, especially switching from compression to tension or vice versa, can affect the pier behavior and change the failure mode. After the first peak, the lateral forces and moments of ICC reduced rapidly as the number of cycles increased, while those of ICT increased slightly. Compared to the strength at the first peak, the strength of ICT increased by 3% and that of ICC decreased by 56%. According to the experimental observations, ICT experienced a ductile behavior and ICC experienced a shear dominant behavior with significant strength degradation. This implies that ignoring the vertical ground motion in design may cause underestimation of shear demand and overestimation of shear capacity.

Kim and Elnashai [22] compared the shear strength evaluated by employing the design code methods and a predictive approach, with the observed values from the experiments. ACI 318-05 [24] and AASHTO LRFD (2005) [5] were used as conventional design code methods and Priestley et al. (1994) [25] as the predictive approach. They concluded that the approaches except that in [25] were conservative for IPH, IPV, and ICC considering the observed spiral strain histories and damage state of the specimens. ICT showed higher shear strength than that predicted by all approaches.

1.4.3 E-Defense Tests

In most dynamic tests, substantially reduced scale specimens were used. Considering many critical behavior issues which are sensitive to scale, trying to reach full-scale is a task worth the effort. Also, the test methods, such as quasi-static and pseudo-dynamic tests, affect the measured behavior due to changing the strain rate. Hence, the full-scale shaking table test can be considered as the most ideal approach in earthquake engineering and the E-Defense shaking table in Japan permits this unique approach. Based on the NEES and E-Defense collaboration, large-scale shaking table tests on bridge structures have been conducted on E-Defense, the world's largest shaking table in Miki City, Japan, based on the testing plan agreed by Japanese and US researchers in August 2005 [26].

C1 tests, tests on component models, had the following objectives: 1) clarifying the failure mechanism of RC columns which failed during the Kobe Earthquake, 2) determining the effectiveness of the current standard seismic retrofit methods for existing RC columns, 3) estimating the seismic performance of RC columns based on the current design codes in Japan and US, and 4) evaluating the effect of damper technology. The US C1 model was designed in accordance with the Caltrans SDC [13]. C1 models were large-scale RC columns and they were designed to have as large cross-sections as possible. C2 tests, tests on system models, had the following objectives: 1) clarifying progressive failure mechanisms of a bridge system under various loading conditions, and 2) determining the effectiveness of advanced technology such as damper and unseating prevention devices.

The test of the first specimen of the Japanese C1 column was conducted in December, 2007. It was a full-scale bridge column connected to horizontal members. Seven full-scale RC bridge columns which represent past and current Japanese design and construction practices (Fig. 1.11) were planned to be conducted in 2008 and 2009. The US full-scale column specimen was designed after testing the first specimen of the Japanese C1 column on E-Defense, but it has not been tested. C2 tests were planned to be conducted in 2009, but they are postponed indefinitely. A unique feature of the test setup is its mass support conditions. Each girder is supported by the top of the specimen at one end and by a steel pier at the other end as shown in Fig. 1.12. Fig. 1.13 shows the configuration of the support bearings under the 10 m long steel girders. As shown, three different types of bearings were used on the column: pin, movable pin, and sliding bearings. All bearings were free to rotate. Pin bearings were fixed in the longitudinal, transverse, and vertical directions. Movable pin bearings were fixed in the transverse and vertical directions only. Thus, the girder could move in the longitudinal direction. Sliding bearings were fixed only in compression in the vertical direction. As a result, the bending moment at the top of the specimen was negligible.

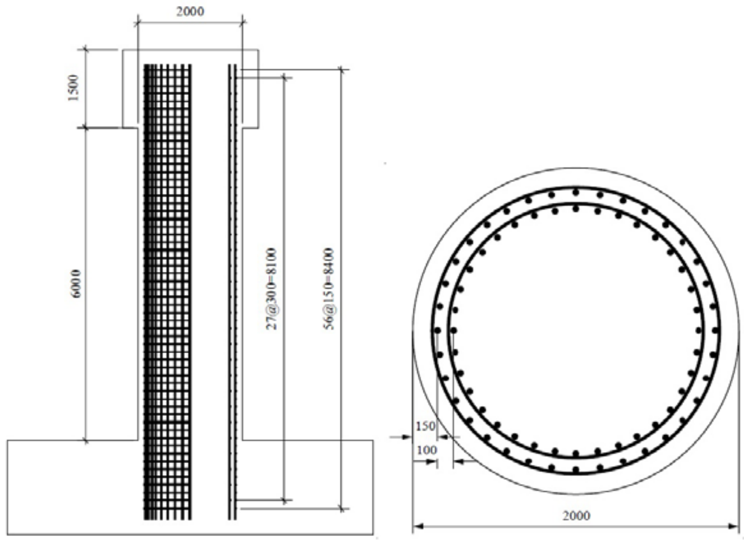

Fig. 1.11 E-Defense C1 model designed based on Japanese current design criteria (unit: mm) [1]

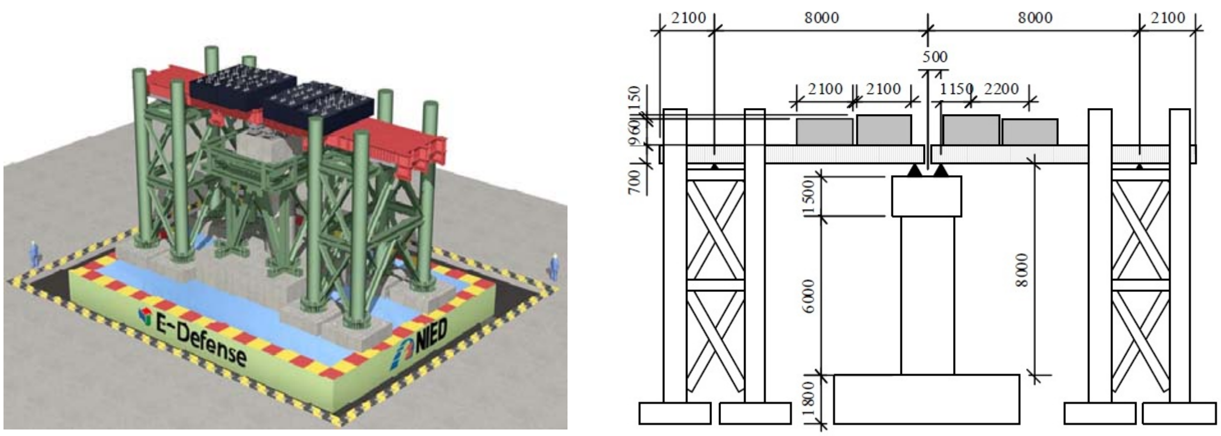

Fig. 1.12 E-Defense C1 test setup (unit: mm) [1]

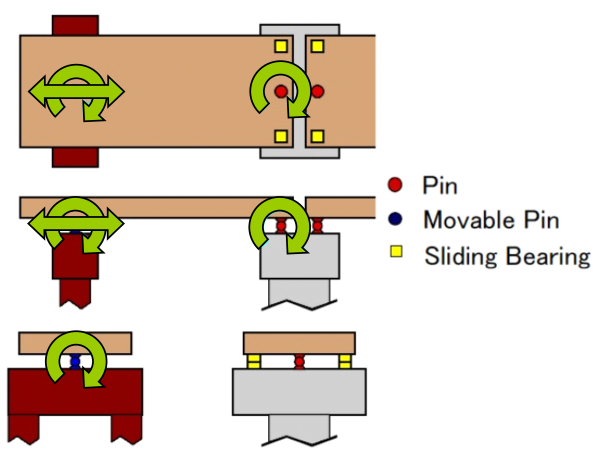

Fig. 1.13 Conditions of support bearings [1]

1.5 Organization of the Dissertation

In **Chapter 2**, the development of dynamic tests is presented. First, the number of ground motion candidates is narrowed down from 3,551 in PEER NGA database. Based on three criteria, the ground motions with high shear demand and noticeable vertical acceleration are selected. Second, a parametric study is performed to choose the aspect ratio, test setup, number of components, and ground motions with significant shear strength degradation by current codes.

In **Chapter 3**, the design of dynamic tests is discussed. Based on the fidelity test result, the input motion and the geometric scale of the specimen are determined. The specimens corresponding to the ¼-scale prototype are designed. Subsequently, the test setup, instrumentation, and test sequence are finalized.

In **Chapter 4**, the global responses of dynamic tests are presented. From the stiffness tests, free vibration tests, and low-level tests, the period and the damping values of each specimen are estimated. As the scale of input becomes larger, the inelastic behavior is observed more clearly. In addition, the shear cracks spread over the east and west sides of the columns. Based on the test data, the responses under the existence of vertical acceleration are examined thoroughly and are compared to those without vertical excitation. Force and displacement histories are presented.

In **Chapter 5**, the local responses of dynamic tests are presented. Curvature and strain histories are presented. In particular, the responses under the strongest excitation with and without the vertical component are compared.

In **Chapter 6**, the development and evaluation of a new analytical model is described. OpenSees, a computational platform for developing applications to simulate the performance of structural systems, provides several material models and beam-column elements for various analyses. However, existing material models and elements in OpenSees do not represent the shear strength change due to axial force or ductility variation. A shear spring material is developed to reflect code-based shear strength estimation. The responses of column models with and without this new shear spring are compared to each other, and the validity of each analytical model is discussed.

In **Chapter 7**, the conclusions of this research are made. In addition, the suggestions for future research are proposed.

Chapter 2

Development of Dynamic Tests

This chapter presents the analyses conducted prior to the planned shaking table tests on the PEER earthquake simulator of University of California, Berkeley. Results of these analyses were utilized as a guidance to select the ground motions, column geometry and reinforcement, and the setup of the shaking table tests. First, the method used for selecting a smaller number of critical ground motions from a larger set is presented. Subsequently, the possible representative bridge prototypes are described. Finally, a parametric study conducted for a single column based on one of the prototypes is described and the results of this parametric study are presented.

2.1 Selection of Ground Motion

PEER NGA database [11] provides 3,551 earthquake acceleration records and their meta-data. Among them, 3,466 ground motions, with all three components available, are selected from the database. Three criteria are utilized to select the ground motions from these 3,466 recorded motions to be used in the parametric study. According to the first criterion, ground motions with peak ground acceleration (PGA) of one or two horizontal components less than 0.25g are eliminated. After this elimination, the ground motion set is reduced from 3,466 to only 293 ground motions. The second criterion is based on the ratio of the pseudo-spectral acceleration corresponding to the vertical component (PSa_v) to those corresponding to the horizontal components (PSa_{h1}, PSa_{h2}). For each of the 293 ground motions, pseudo-spectral accelerations of the vertical component are calculated corresponding to the vertical periods (T_v) of 0.05, 0.1, 0.15, and 0.2 seconds and pseudo-spectral accelerations of the horizontal components are calculated corresponding to the horizontal periods (T_h) of 0.4, 0.5, 0.6, 0.7, and 0.8 seconds. The chosen T_v and T_h values result in 20 T_v, T_h pairs. Since each ground motion has two horizontal components, there are two spectral ratios, namely PSa_v/PSa_{h1} and PSa_v/PSa_{h2}, for each pair. Fig. 2.1 and Fig. 2.2 present the relationships of the ratios PSa_v/PSa_{h1} versus the ratios PGA_v/PGA_{h1}, PGA_{h1}, and PGA_v for T_h=0.4 sec and T_h=0.7 sec, respectively, for different values of T_v.

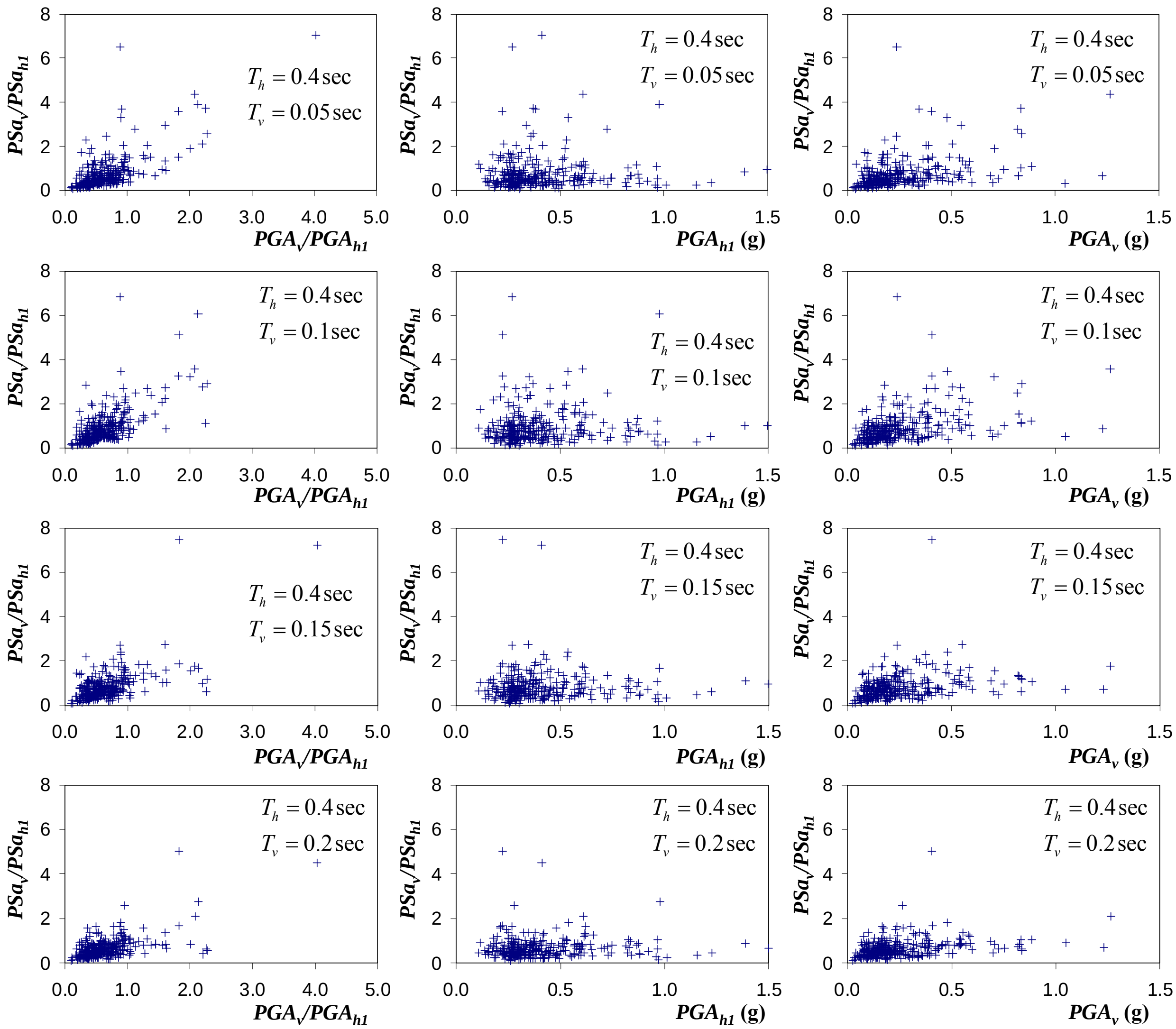

Fig. 2.1 Variation of PSa_v/PSa_{h1} with peak ground accelerations and their ratio for T_h=0.4 sec

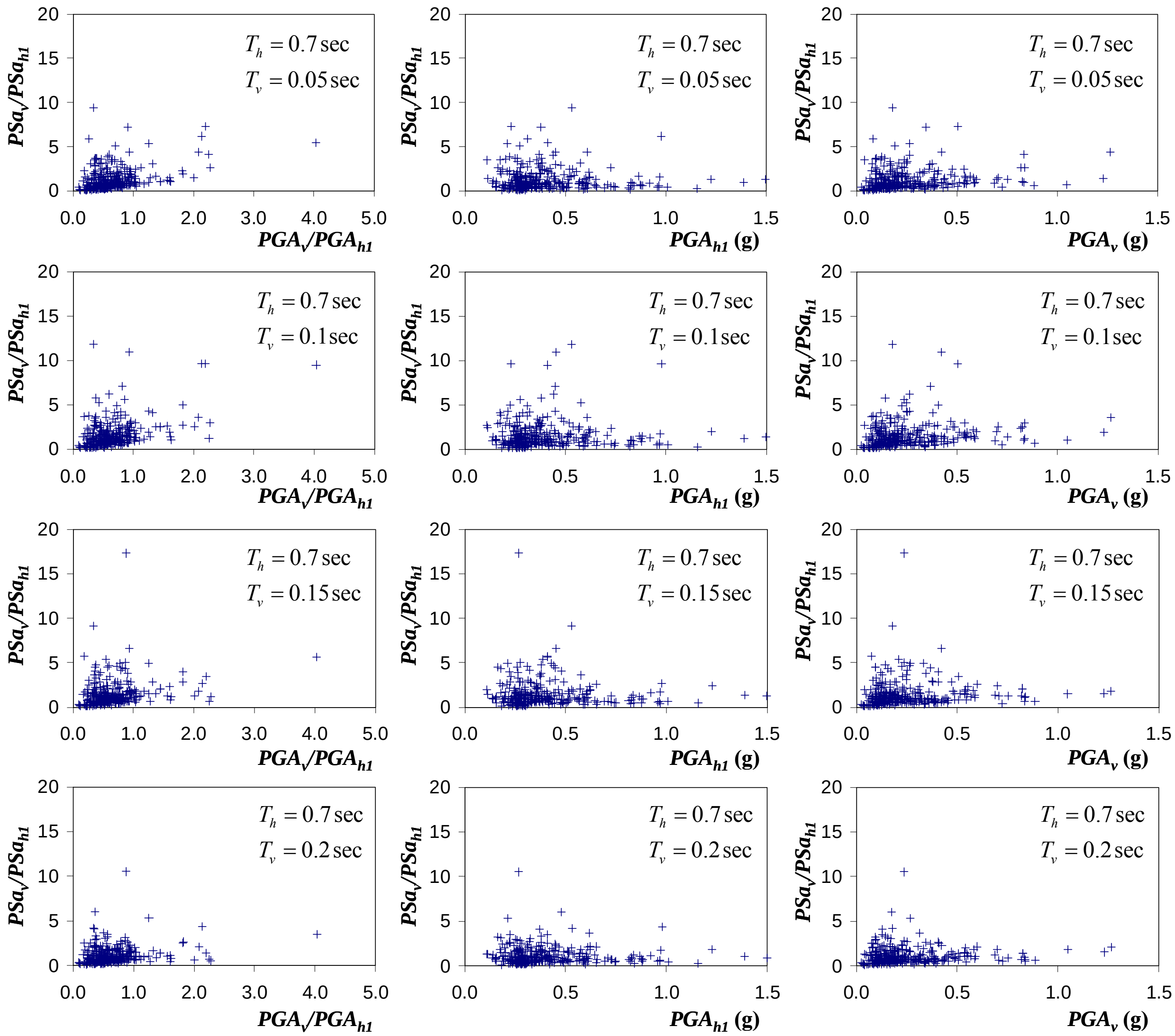

Fig. 2.2 Variation of PSa_v/PSa_{h1} with peak ground accelerations and their ratio for T_h=0.7 sec

The followingobservations are deducted from Fig. 2.1 and Fig. 2.2:

- As T_v increases, the ratio PSa_v/PSa_{h1} tends to decrease.
- As T_h increases, the ratio PSa_v/PSa_{h1} tends to increase.
- There are many ground motions which have small PGA_{h1}, PGA_v, and PGA_v/PGA_{h1}, but large ratios of PSa_v/PSa_{h1}. Among them, ground motions with small PGA_{h1} are not useful since they will not lead to inelastic behavior.
- In the plots of PSa_v/PSa_{h1} versus PGA_v/PGA_{h1}, the dispersion angle around the origin becomes narrower as T_v increases.

If PSa_v/PSa_{h1} or PSa_v/PSa_{h2} is larger than 1.0 in at least 15 pairs among the 20 pairs defined above, it is selected as one of the ground motions to be applied in the parametric study. The number of the considered ground motions is reduced from 293 to 80 according to this second criterion.

Arrival time is utilized as the third criterion. As discussed in [19], [22], the interval between the horizontal and the vertical peak accelerations affects the interaction of the horizontal and the vertical responses and accordingly can be considered as an indicator. Among the 80 chosen ground motions after application of the second criterion, there were some motions which have significant arrival time interval. Anza-02 earthquake recorded at Idyllwild-Kenworthy Fire Station (Record sequence number (RSN) 1944 in [11]) is shown in Fig. 2.3 as an example. The interval between the peaks is longer than 3 sec, i.e. 3.160 sec for H1 versus V and 3.345 sec for H2 versus V. In this case, the PGA of the vertical component took place more than 3 seconds before the horizontal components reach their PGA values. With this perspective, 14 ground motions are also eliminated from the 80 ground motions. In addition, 4 ground motions are removed since they have only low frequency content. One ground motion was removed because it was almost identical to another ground motion. Finally, based on the above three criteria and after removing the ground motions with only low frequency content, 61 ground motions are selected from the existing 3,551 ground motions in [11], which are listed in Appendix A.

Selection of ground motions based on the ratio PSa_v/PSa_h being greater than 1.0 discussed above might lead to the exclusion of some important ground motions in the cases where PSa_h is large and PSa_v is large enough to produce a significant difference between the two cases with and without vertical excitation even if PSa_v/PSa_h is not larger than 1.0. This observation is discussed further at the end of the chapter.

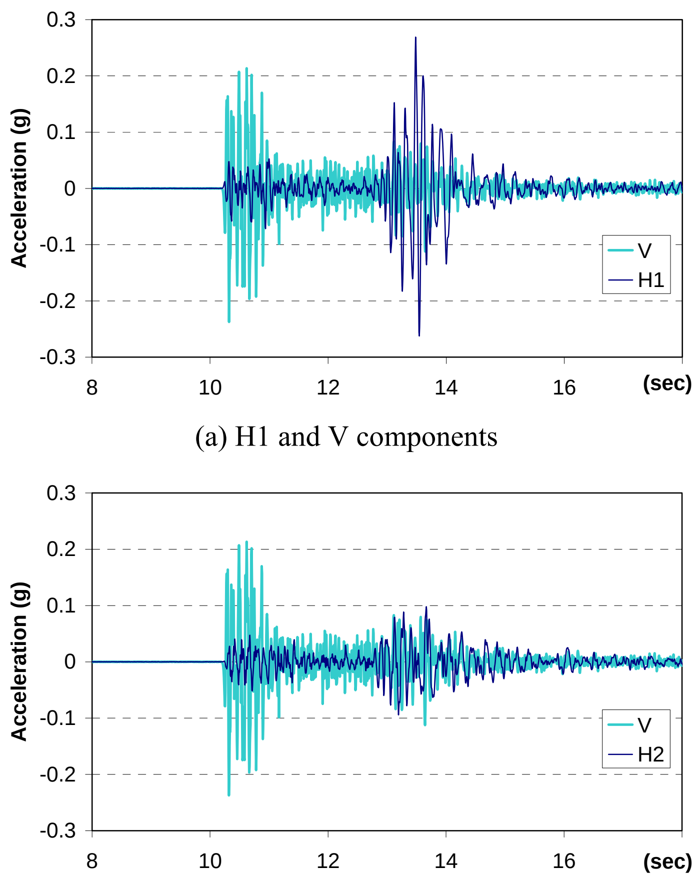

(a) H1 and V components

(b) H2 and V components

Fig. 2.3 Horizontal and vertical components of Anza-02 Earthquake at Idyllwild-Kenworthy Fire Station

2.2 Prototype

Kunnath et al. (2008) [27] considered two types of bridges: single bent, two span overpass and single-column bent, multi-span bridge. For the overpass system, a segment of El Camino Del Norte Bridge was selected as the prototype bridge whereas the Amador Creek Bridge was used as the prototype bridge for the multi-span system. The selected overpass represents short-span RC bridges whereas the multi-span system represents long-span PC bridges.

According to the analyses in [27], the effect of the vertical acceleration was more significant in El Camino Del Norte Bridge, which has a multi-column bridge bent. However, even though the effect of axial force might be more significant in multi-column bridge bents, it is not practical to represent this effect in shaking table testing. Moreover, the complexity of the behavior of multi-column bridge bents due to other factors beyond the effect of vertical acceleration makes shaking table testing of single-column bridge bents for understanding the effect of vertical acceleration more realistic. Hence, the columns of single-column bridge bents are investigated in this study. It should be noted that only ACB is used as the prototype for the parametric study in Section 2.3.

2.2.1 Prototype 1: Amador Creek Bridge

The Amador Creek Bridge (ACB) is a three-bent, four-span RC bridge and its total length is 685 ft (207.6 m). The spans are 133.0 ft (40.5 m), 177.1 ft (53.7 m), 177.1 ft (53.7 m), and 133.0 ft (40.5 m). The bents of the bridge consist of single double-spiral columns. Fig. 2.4 shows the elevation view and cross-sectional details of the columns of this bridge. The column heights are 64.8 ft (19.75 m), 91.9 ft (28.0 m), and 83.7 ft (25.25 m). Based on the height of the third bent, H3 in Fig. 2.5(a), the column aspect ratios (ratio of height to cross-section dimension in the loading direction) considering the weak (X) and strong (Y) axes are 13.95 and 9.30, respectively.

The bridge is modeled as an elastic superstructure supported on nonlinear columns founded on elastic foundation using OpenSees[28]. The assumption of elastic superstructure is based on the capacity design approach employed by Caltrans via SDC-2010 [13]. Area, A, moment of inertia, I_x, I_y, and polar moment of inertia, J, properties of the superstructure cross-section of the ACB are presented in Table 2.1.

The compressive strength of unconfined concrete and the yield strength of longitudinal reinforcement are specified to be 4 ksi (27.6 MPa) and 60 ksi (413.7 MPa), respectively, as designated on the design drawings. The compressive strength and ultimate strain of confined concrete were computed as 5.83 kips (25.9 kN) and 0.0157 using Mander's model [29]. "Concrete01" material in OpenSees is used for both confined and unconfined concrete. A bilinear model with a post-yield stiffness of 1% of the initial stiffness is used to model the reinforcing steel. The columns of the bridge rest on shallow foundations. Therefore, six elastic springs in 3 translational and 3 rotational directions are used to model the soil-foundation system for each column. The approximate expressions in FEMA-356 (FEMA 2000) [30] are used to compute the properties of the corresponding springs. Table 2.2 lists the values of the spring stiffness representing the foundation system resting on a soil with a shear wave velocity of 1181 ft/s (360.0 m/s).

Table 2.1 Section properties of the Amador Creek Bridge superstructure

Parameter	Value
A	6.73 m^2
I_x	4.56 m^4
I_y	73.75 m^4
J	78.31 m^4

Table 2.2 Elastic properties of springs used to model the soil-foundation system for the Amador Creek Bridge

Parameter	Value
Translation, X	5.18×10^6 kN/m
Translation, Y	6.01×10^6 kN/m
Translation, Z	4.99×10^6 kN/m
Rotation, X	1.05×10^8 kN-m/rad
Rotation, Y	1.16×10^8 kN-m/rad
Rotation, Z	5.30×10^7 kN-m/rad

Seat type abutments are used at both ends of the bridge. Spring systems are used to model the stiffness of the abutments. In the transverse direction, shear keys are designed to break off during a strong ground motion. Hence, seat type abutments do not possess stiffness in the transverse direction. In the vertical direction, the movement of the bridge is prevented at the abutments in both upward and downward directions. Thus, the abutments are modeled as restraining supports in the vertical direction. In the longitudinal direction, the bridge is free to move in the opposite direction of the abutment at each end. Towards the abutment, there is a certain amount of gap before the deck makes contact with the abutment. When the deck and the abutment are in contact, the stiffness of the abutment is computed as $K_{abut} = K_i w(h/5.5)$ [13], where K_i is the initial stiffness of the abutment and is taken as 20.0 k/in per ft of abutment width (11.49 kN/mm per m) and w and h are the projected width and height (in feet) of the abutment taken as 22.8 ft and 82.0 ft, respectively. Accordingly, a spring which has no stiffness in tension and elastic in compression with spring stiffness of 6785 kip/ft (99,019.6 kN/m) and with a 4 in (101.6 mm) gap is used to model the abutment behavior in the longitudinal direction.

In single-column bridge bents, the superstructure is expected to be more vulnerable to torsional effects (rotation about X axis defined in Fig. 2.5(a)) than multi-column bridge bents. To ensure the proper modeling of the torsional properties of the deck, a three dimensional (3D) shell model of the bridge was created in SAP2000 (Fig. 2.5(b)) [32]. Inertia properties of the OpenSees model, Table 2.1, are adjusted later to match the periods of vibration of the SAP2000 model.

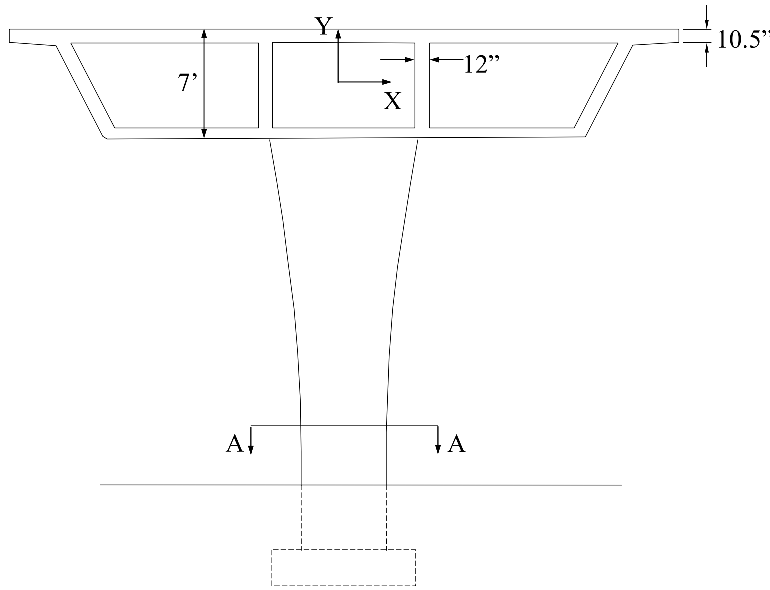

(a) Elevation

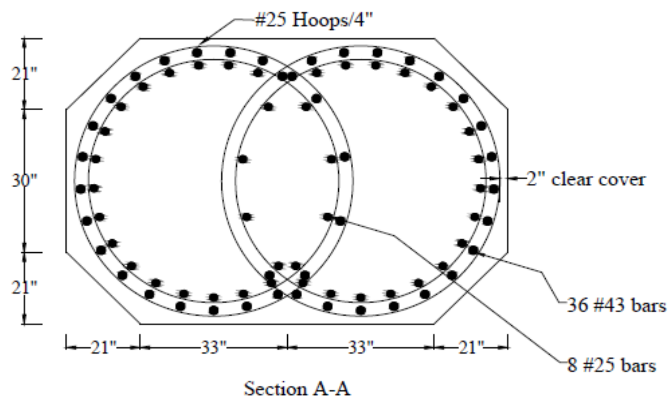

(b) Interlocking spiral section (original section, units: in)

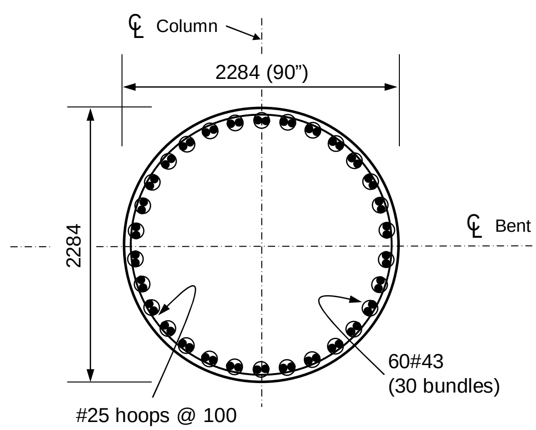

(c) Effective circular section (units: mm)

Fig. 2.4 Bent elevation and column cross-section of the Amador Creek Bridge

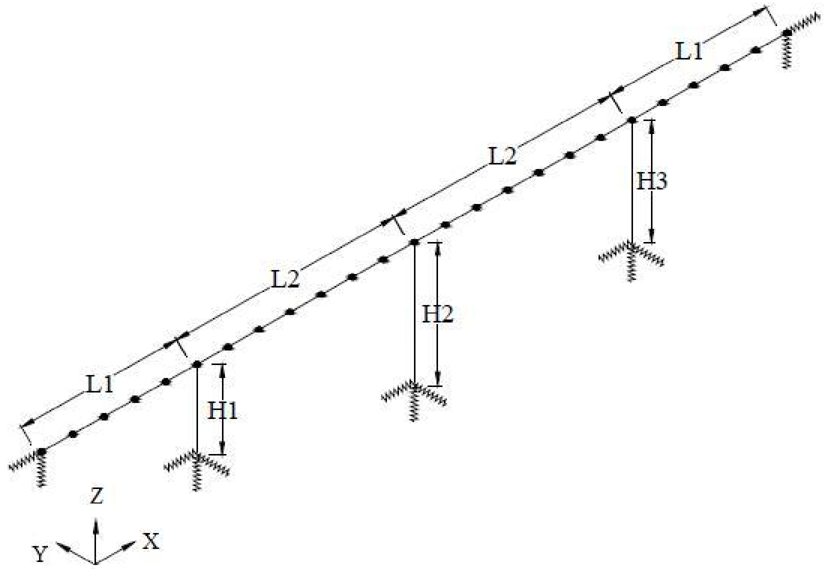

(a) Line model in OpenSees

(b) 3D shell model in SAP2000

Fig. 2.5 OpenSees and SAP2000 models of the Amador Creek Bridge

2.2.1.1 Interlocking Spiral Section and Effective Circular Section

As mentioned previously, the objective of the parametric study is to provide guidance about the ground motion, column geometry and reinforcement, and setup of the shaking table tests. Since the objective of the tests is to observe the effect of vertical excitation, a symmetric circular cross-section is more suitable than an asymmetric interlocking spiral cross-section. In this way, the effect of the difference of the cross-section moment of inertia and capacity in the two main orthogonal directions, an unnecessary complication affecting the results, is avoided. In addition, a circular section is more suitable from a practical point of view for test specimen detailing and construction. Due to the shaking table limitations, the test specimen should at most be a 1/4-scale of the prototype dimensions. Under these conditions, the interlocking spiral reinforcement should be installed in a small cross-section with unknown influence of this reduced scale on the role of the interlocking spiral. Considering these reasons, the interlocking spiral section which has different properties in each direction is replaced by an effective circular cross-section.

To determine the size and number of longitudinal reinforcing bars and size (i.e. radius) of the effective circular column, flexural and axial capacities are considered. Since the original (interlocking spiral) cross-section has different moment capacities in each direction, the weak axis properties are chosen as the properties to be matched. Resulting area and moment of inertia values for the effective cross-section in comparison with the original interlocking spiral cross-section are listed in Table 2.3. The spacing and diameter of the spiral reinforcement used in the interlocking spiral column are directly employed for the effective circular cross-section.

A series of elastic modal analyses were carried out on both systems (with interlocking spiral and with effective circular cross-sections) to calibrate the inertial properties of the superstructure of the OpenSees model. Fig. 2.6 presents the fundamental elastic mode shapes in longitudinal, transverse, vertical, and torsional directions along with the corresponding periods for OpenSees models. Also, Table 2.4 clearly shows that the line model created in OpenSees is capable of reasonably capturing the eigenvalues of the ACB in all directions as compared to the more detailed finite element shell model developed in SAP2000.

Table 2.3 Column cross-section properties of the Amador Creek Bridge

Parameter	Interlocking spiral section	Effective circular section
A	5.03 m^2	4.10 m^2
I_x	1.40 m^4	1.40 m^4
I_y	3.13 m^4	1.40 m^4
J	4.53 m^4	2.80 m^4

Table 2.4 Modal properties of the Amador Creek Bridge

Cross-Section	Mode number	SAP2000 (Fig. 2.5(b)) period [sec]	OpenSees (Fig. 2.5(a)) period [sec]
Interlocking spiral	1	2.12 (X)	2.29 (X)
	2	1.81 (Y)	1.85 (Y)
	3	1.28 (mixed)	1.35 (mixed)
	4	1.04 (mixed)	0.80 (mixed)
	5	0.52 (Z)	0.53 (Z)
	6	0.41 (mixed)	0.40 (mixed)
Circular	1	2.51 (Y)	2.76 (Y)
	2	2.15 (X)	2.21 (X)
	3	1.78 (mixed)	1.86 (mixed)
	4	1.08 (mixed)	0.83 (mixed)
	5	0.53 (Z)	0.68 (mixed)
	6	0.42 (mixed)	0.52 (Z)

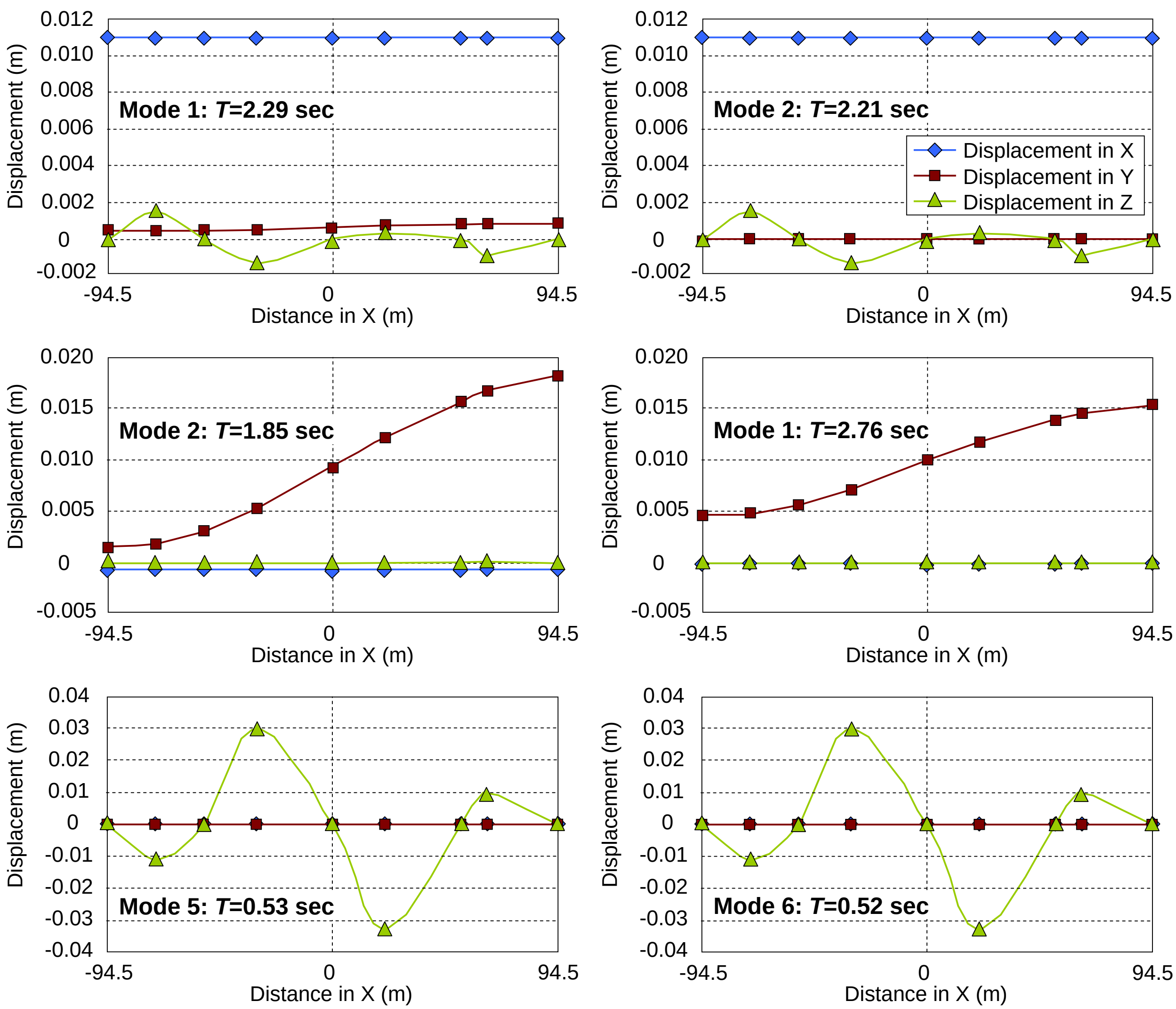

(a) Interlocking spiral column **(b) Effective circular column**

Fig. 2.6 Eigenvectors of the Amador Creek Bridge

2.2.1.2 Comparison of Responses of the Bridge Systems with the Interlocking and the Effective Circular Cross-Sections

Fig. 2.7 compares responses at the second column of the ACB (Column H2 in Fig. 2.5(a)) with the interlocking cross-section and the corresponding effective circular cross-section as described above. These results are provided for the bridge response under the three components of the ground motion #40 in Appendix A (RSN 1063 in PEER NGA database [11], Rinaldi receiving station, Northridge earthquake).

Fig. 2.7(a), (b), and (c) show comparisons of moment at the base, M_x, base shear force, F_y, and axial force, F_z, respectively, for column H2 (Fig. 2.5(a)) of the ACB using OpenSees line model shown in Fig. 2.5(a). Although the interlocking spiral and the circular cross-sections do not have the same response, the discrepancy is less than 20% when considering the maximum values. Therefore, using the effective circular cross-section instead of the interlocking spiral cross-section is an efficient option to reduce complexity of this study and the planned shaking table experiments.

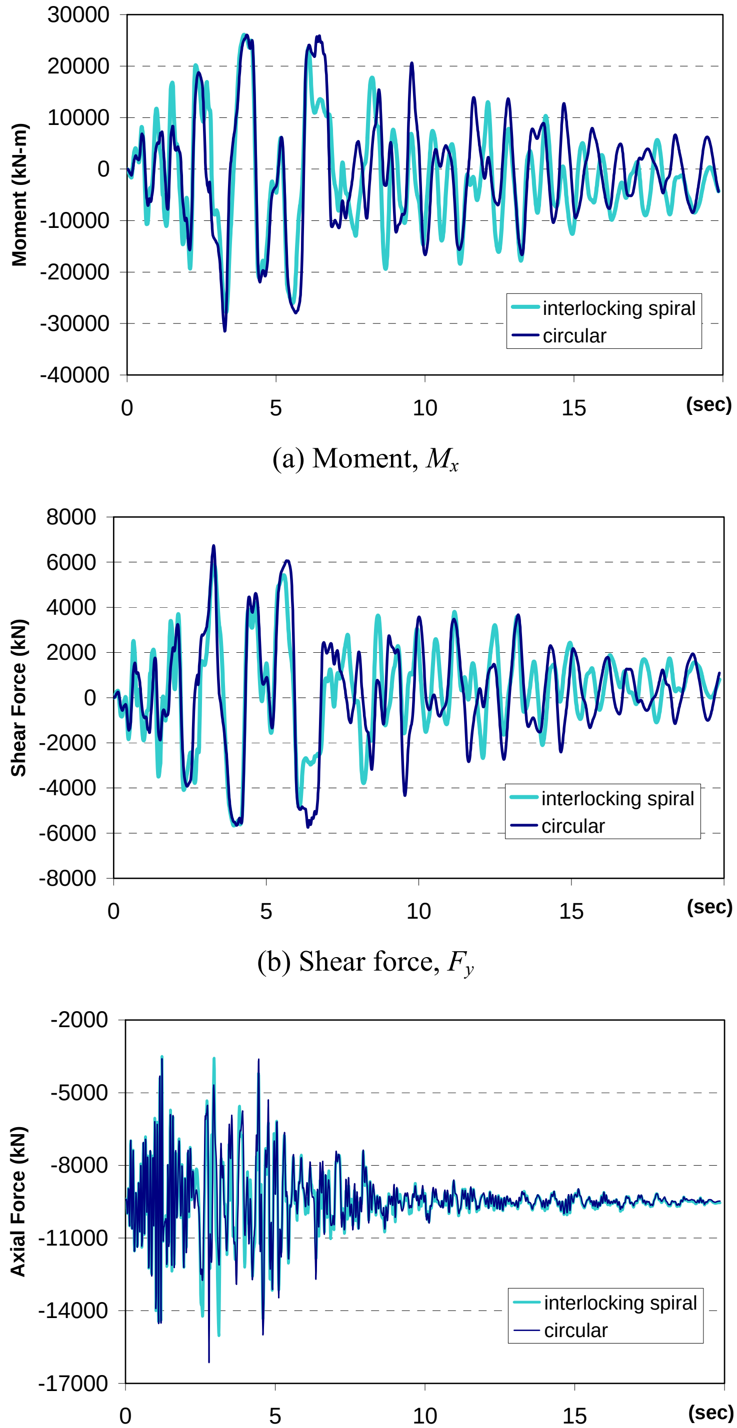

(a) Moment, M_x

(b) Shear force, F_y

(c) Axial force, F_z

Fig. 2.7 Responses of the Amador Creek Bridge at column H2 (Fig. 2.5(a)) with interlocking spiral and effective circular cross-sections

2.2.2 Prototype 2: Plumas-Arboga Overhead Bridge

The Plumas-Arboga Overhead Bridge (PAOB) is a two-bent, three-span RC bridge. It is designed by Caltrans according to post-Northridge design practice as the ACB. Its total length is 456 ft (139 m) and the spans connected to abutments are about 133 ft (40.5 m) each and the span between columns is about 190 ft (58.0 m). The heights of the two bents shown in Fig. 2.8(a) were modeled as 29.7 ft (9.0 m). The aspect ratio along the 'Bent center line' (weak axis) is 3.58 and that along the 'Bridge center line' (strong axis) is 5.37. Table 2.5 presents area and moment of inertia properties of the elastic superstructure of the PAOB and Table 2.6 lists properties of its original interlocking spiral column cross-section and the modified effective circular cross-section. This latter cross-section is used for the design of the shaking table test specimens and column properties related to mass and mass moment of inertia are discussed in Chapter 3, since its aspect ratio is closer to the desired value than that of ACB.

Table 2.5 Cross-section properties of the Plumas-Arboga Overhead Bridge superstructure

Parameter	Value
A	6.73 m^2
I_x	5.28 m^4
I_y	70.09 m^4
J	75.37 m^4

Table 2.6 Column cross-section properties of the Plumas-Arboga Overhead Bridge

Parameter	Interlocking spiral cross-section	Modified effective circular cross-section
A	3.61 m^2	3.14 m^2
I_x	0.715 m^4	0.788 m^4
I_y	1.247 m^4	0.788 m^4
J	1.962 m^4	1.575 m^4

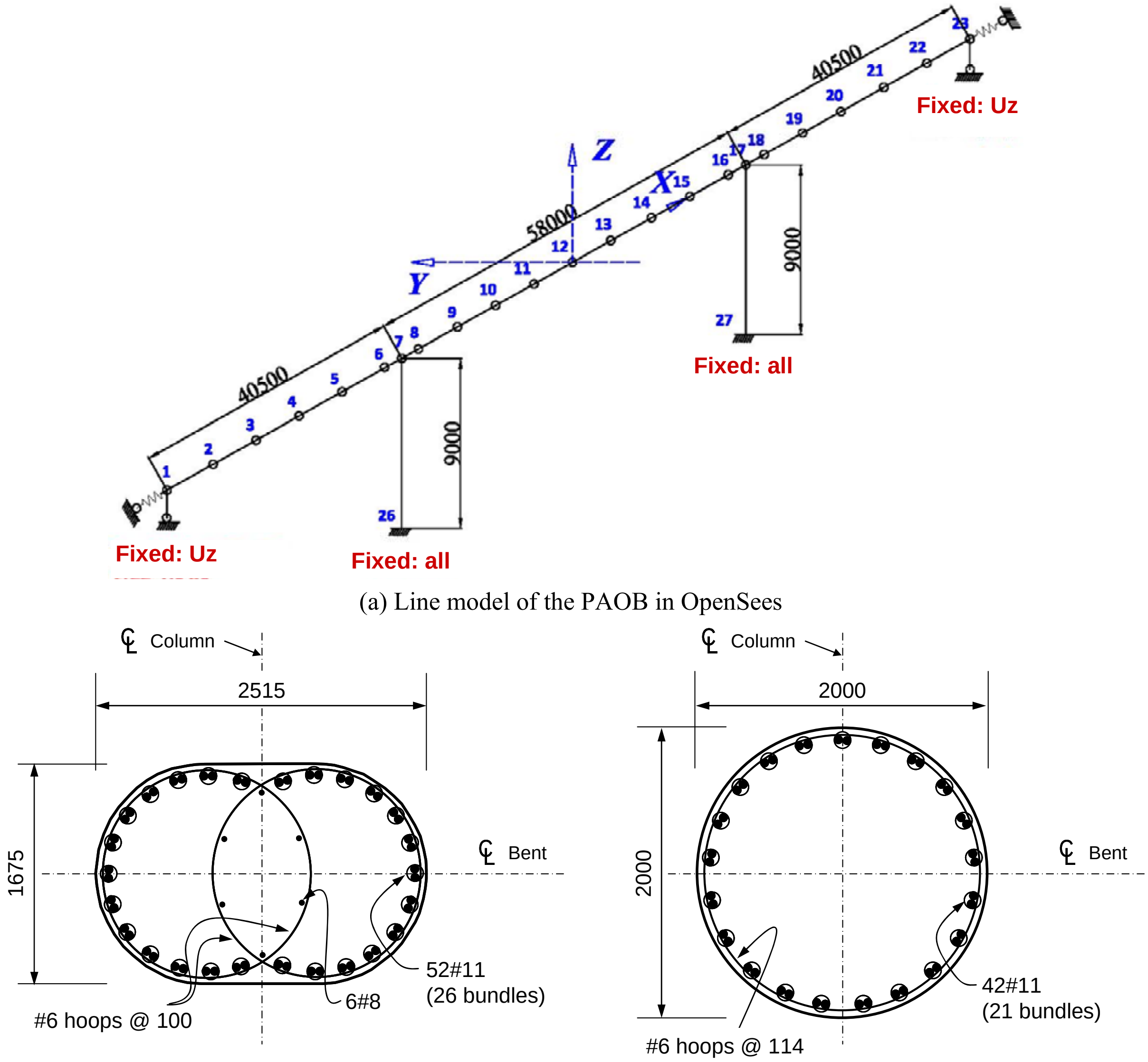

(a) Line model of the PAOB in OpenSees

(b) Interlocking spiral cross-section (original)

(c) Modified effective circular cross-section

Fig. 2.8 OpenSees line model and column cross-sections of the Plumas-Arboga Overhead Bridge (unit: mm)

2.3 Description of Parametric Study

Using a single column model with effective circular cross-section from the ACB, the following parametric study is conducted. Considered parameters are ground motions, number of components of ground motions, aspect ratios, and existence of mass moment of inertia. The chosen values of these parameters are described in the following sub-section.

2.3.1 Parameters

2.3.1.1 Ground Motions

As stated in Section 2.1, 61 ground motions are selected in this study from the PEER NGA database [11]. To confirm the effectiveness of the selected ground motions, 293 ground motions with PGA larger than 0.25g are applied in this parametric study and the results are compared.

2.3.1.2 Ground Motion Components

To study the effect of vertical motions, the responses with and without vertical ground motion are compared. In this comparison, three cases are utilized, which are stated below.

- X, Y, and Z components versus X and Y components (effect of vertical excitation when both horizontal components are present)
- X and Z components versus X component (effect of vertical excitation when one of the horizontal components only is present)
- Y and Z components versus Y component (effect of vertical excitation when the other horizontal component is present only)

2.3.1.3 Mass Moment of Inertia

To represent a bridge system which is idealized with free rotation at the connection between the column and the bridge deck, a model with no mass moment of inertia on top of the column is adopted. However, mass moment of inertia can be added on top of the column corresponding to the more realistic connection in the bridge system. Note that the value of the mass moment of inertia was calibrated to obtain the same periods, mainly the period in the bridge transverse direction, T_T, for both the bridge system (with the bridge deck modeled) and the single column cases.

2.3.1.4 Aspect Ratio

As the aspect ratio (AR), i.e. height to diameter ratio, of a column, i.e. H/D, gets large, the column becomes less likely to observe shear failure. To study this important parameter, 6 aspect ratios of values 2.5, 3.0, 3.5, 4.0, 4.5, 5.0, were considered in the parametric study. Note that H is taken as the height of the column itself, which does not include the rigid end zone lengths due to the physical size of the added mass on top of the column as discussed in the following section or due to the footing size.

2.3.2 Computational Models

To represent the full-scale single column, the following models are used. Type 1 and Type 2 represent the cases without and with mass moment of inertia, respectively (Fig. 2.9). For both Types, the suggested equivalent circular cross-section is considered and the column is modeled using ‘beam with hinges’ (BWH) element in OpenSees. For Type 1, mass blocks are installed below the column top to lower the center of mass to the pin location. Since the system can become unstable during shaking, a catching system needs to be utilized for safety purposes but it is not included in the analytical model. For Type 2, regular mass blocks are employed as shown in Fig. 2.9. In addition, a third type, designated as Type 2-1 is utilized which is derived from Type 2 model by employing the mass blocks of the Type 1 model to lower the center of mass. Line representations of the three types are presented in Fig. 2.10.

Mass was determined from the gravity load of the full-scale prototype bridge system and mass moment of inertia was determined to match the periods of the bridge system.. However, it is not possible to match the vertical period of the single column to that of the bridge system, mainly because of the lack of the additional flexibility introduced by the bridge deck in the single-column model. Instead, it is reasonable and practical to match the vertical response of the single column model to that of the corresponding column which is a part of the whole bridge system model. The horizontal and vertical periods of the two models Types 1 and 2 are shown in Table 2.7. The periods of Type 2 are larger than those of Type 1 which is due to the added mass moment of inertia and the difference in height. The differences between the periods of models Type 2-1 and Type 1 are smaller than the differences between the periods of models Type 2 and Type 1 since models Type 1 and Type 2-1 have the same heights, as shown in Fig. 2.10.

Table 2.8 presents the vertical periods of the bridge system, which can be compared to those of Type 2 or Type 2-1 single column model listed in Table 2.7. Vertical periods of the bridge system can be as high as 8.5 times of those of the single column model. The difference is basically due to the effect of the flexibility of the deck in the bridge system, which is not considered in the single column model, as mentioned above. Note that the vertical periods do not significantly change due to the properties of the springs at the column base, representing flexible foundation. Since the vertical response is expected to have an influence on the shear strength and is closely related to the vertical period, these differences cannot be neglected.

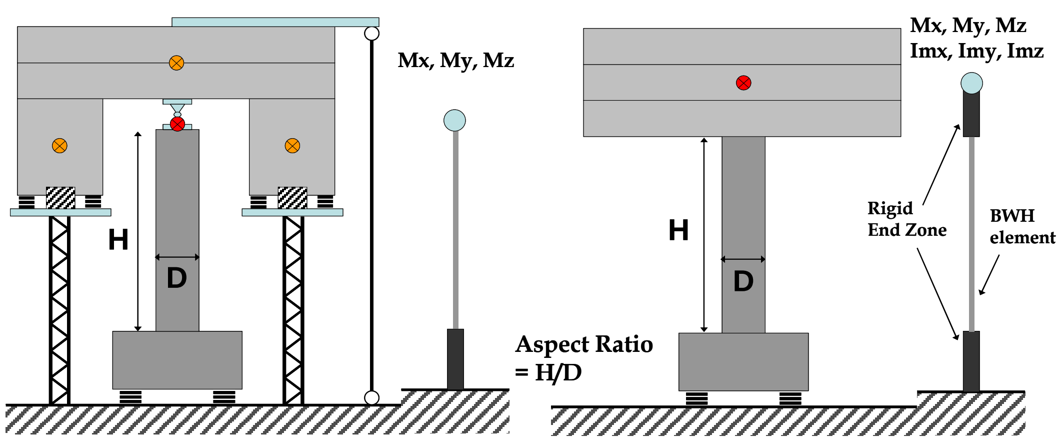

(a) Type 1 (b) Type 2

Fig. 2.9 Models for the parametric study

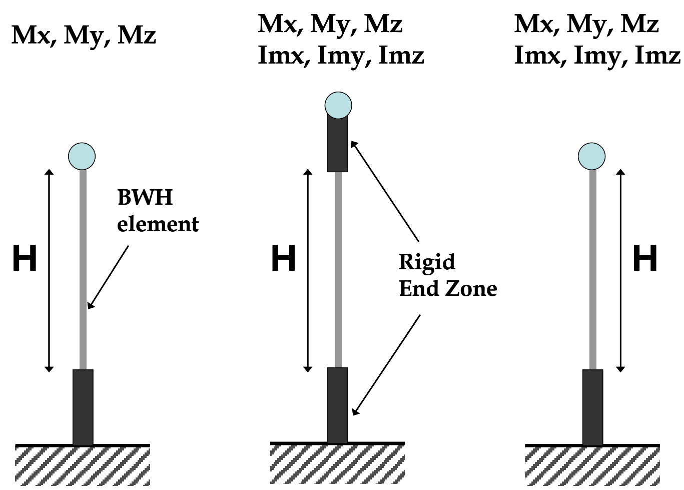

(a) Type 1 (b) Type 2 (c) Type 2-1

Fig. 2.10 Line representations of the considered models

Table 2.7 Modal properties of the single column models

AR	Type 1		Type 2		Type 2-1	
	T_h [sec]	T_v [sec]	T_h [sec]	T_v [sec]	T_h [sec]	T_v [sec]
2.5	0.320	0.046	0.469	0.054	0.372	0.046
3.0	0.429	0.051	0.584	0.058	0.475	0.051
3.5	0.549	0.055	0.716	0.062	0.597	0.055
4.0	0.687	0.059	0.860	0.066	0.731	0.059
4.5	0.835	0.063	1.014	0.069	0.876	0.063
5.0	0.993	0.067	1.179	0.073	1.032	0.067

Table 2.8 Vertical periods of the bridge system model with the effective circular cross-section

AR	T_v [sec]	
	Fixed	With springs at the base
2.5	0.385	0.392
3.0	0.386	0.393
3.5	0.389	0.395
4.0	0.392	0.397
4.5	0.395	0.400
5.0	0.397	0.402

2.3.3 Comparison of Responses of the Bridge System and the Single Column Models

Ideally, responses of the single column model are preferred to be identical to those of the bridge system, but for practical purposes, differences within ±20% are considered to be acceptable. Fig. 2.11 presents the bending moment and axial force of the single column model, specifically Type 2 with AR = 4.0, and those of the corresponding system model using all three components of ground motions #60 (Whittier Narrows earthquake record at LA Obregon Park) and #7 (Northridge earthquake record at Rinaldi Receiving Station) (refer to Appendix A for further details about these records). In case of ground motion #60, the bending moment history is similar in the two models and the amplitude of axial force is also similar, even though the frequency is quite different from each other, which is due to the fact that the vertical period of the bridge system is longer than that of the single column. However, ground motion #7 produces very different results. Although the bending moment history is similar in the two models for ground motion #7 as in the case of ground motion #60, the amplitude of the axial force of the bridge system is less than 40% of that of the single column. This means that in this case, the axial response of the single column which may be used in the shaking table tests cannot represent the real axial response of the bridge system. Since the axial force and accordingly the axial strain are considered as main parameters in estimating the shear strength (refer to Section 1.2), this situation can cause underestimation of the shear strength and as a result overestimation of the effect of the vertical component of the ground motion.

Due to the limitations of the shaking table, it is not possible to construct the complete bridge system. Even though the discrepancy is related to the properties of ground motion, demonstrated by comparing responses of ground motions #60 and #7 as discussed above, modifying input excitations may not be an effective way to resolve this discrepancy within the shaking table limitations. In that regard, the experimental effort on a single column model, even with this discrepancy in comparison with the bridge system model, can be viewed as a means to generate benchmark experimental data sets for developing and calibrating accurate analytical shear strength models for further use in computational modeling of the full bridge system. Finally, it is expected that the effect of the vertical excitation on the seismic response of the bridge system can be computationally assessed using these accurate analytical shear strength models of the RC bridge columns.

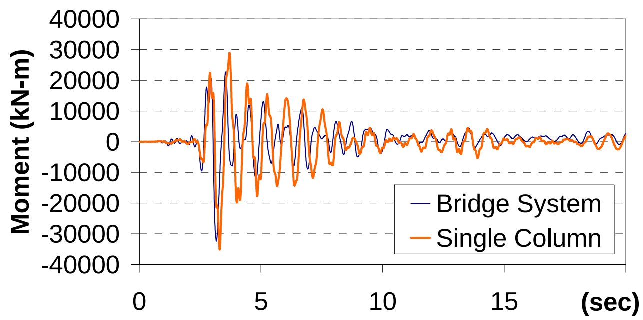

(a) Bending moments at the base due to #60 ground motion

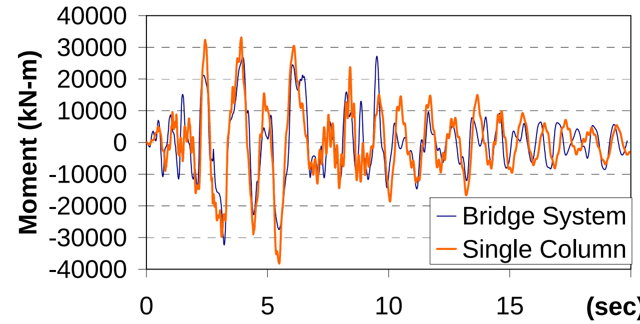

(b) Bending moments at the base due to #7 ground motion

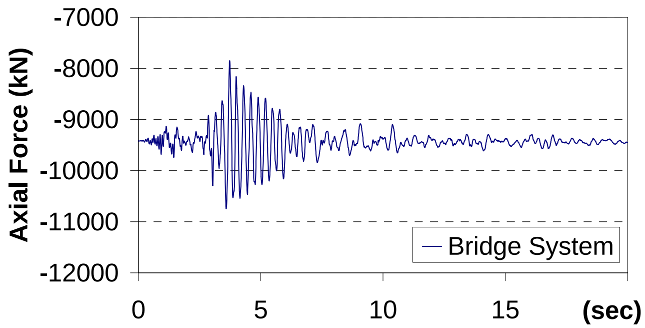

(c) Axial force in the bridge system due to #60 ground motion

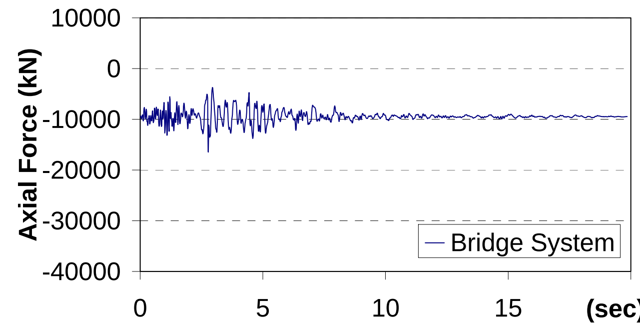

(d) Axial force in the bridge system due to #7 ground motion

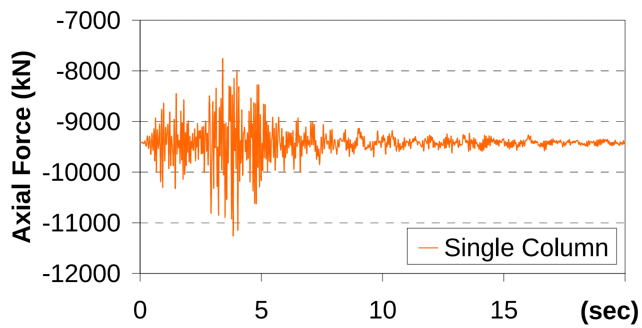

(e) Axial force in the single column due to #60 ground motion

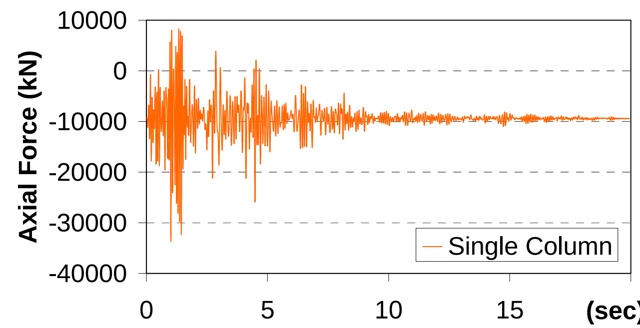

(f) Axial force in the single column due to #7 ground motion

Fig. 2.11 Responses of the bridge system and the single column models

2.4 Results of the Parametric Study

Since there are 3 cases of ground motion components (Section 2.3.1.2), 2 models (Types 1 and 2 only) and 6 aspect ratios, a total of 36 cases are analyzed. For each case, 61 ground motions are applied and maximum values of translational displacements at the top of the column, and maximum forces and bending moments at the bottom of the column are calculated. The difference ratio due to the vertical component (*VDR*) is computed using Eq. (2.1).

$$VDR = \frac{\max(\text{response with vertical component})}{\max(\text{response without vertical component})} - 1 \qquad (2.1)$$

The ratios using the X+Y+Z and X+Y (effect of vertical excitation when both horizontal components are present) which are applied to Type 2 model are shown in Fig. 2.12. Values on the horizontal axis are ground motion numbers and those on the vertical axis are the difference ratios (*VDR*) as defined in Eq. (2.1). Although the ratios are not narrowly-distributed, most of them are concentrated near zero and mostly located in the range of -0.1 to 0.1 except for the case of the maximum displacement in the Z-direction, D_z, and the maximum force in the Z-direction, F_z. Note that the ratios (*VDR*) for D_z and F_z are all positive. It should be noted that the ground motion numbers on the horizontal axis of Fig. 2.12 are sorted in a descending order of the peak vertical acceleration (PGA_v). Therefore, it can be concluded that the motions with relatively larger vertical acceleration result in larger *VDR* in most responses.

The average values of the absolute difference ratios (*VDR*) for a constant AR are shown in Fig. 2.13. The values on the horizontal axis are aspect ratios and those on the vertical axis are absolute difference ratios (*VDR*). Since X+Z versus X and Y+Z versus Y do not have significant responses in the Y-direction and X-direction, respectively, the values corresponding to these cases are not presented in the corresponding figures.

Except the maximum displacement and force in the Z-direction, D_z and F_z, respectively, the effect of the vertical ground motion is not significant. The averages for the maximum displacement in the X-direction, D_x, are less than 1.5% for all cases and those for the maximum displacement in the Y-direction, D_y, are less than 1.4%. In case of forces in the X- and Y-directions, F_x and F_y, respectively, average values are less than 3% and they are less than 2.5% for moments about the X- and Y-directions, M_x and M_y, respectively. However, the average values for D_z are between 28% and 75% and those for F_z are between 50% and 85%. As the AR becomes larger, the different ratios tend to increase. This means that in general the effect of vertical motion becomes more significant as the column becomes taller.

From Fig. 2.12 and Fig. 2.13, it can be observed that the change in the response quantities other than the axial force and axial displacement is not important. Accordingly, it can be stated that the shear demand change due to the vertical ground motion has a minor importance compared to the change in shear capacity. However, the change in the axial force due to vertical ground motion is noteworthy resultjng in decrease of the shear strength when axial tensile forces occur. Since the plots in Fig. 2.12 and Fig. 2.13 are for maximum responses, the effect of the occurrence of the axial tensile forces or the decrease in the axial compressive forces is not explicitly identifiable from these figures. However, the drastic change in the axial forces due to the vertical excitation can be clearly observed. The effect of axial force in the reduction of shear force capacity is examined in more details in the following section. The difference due to the number of applied horizontal components is not significant on the effect of the vertical excitation on the axial force F_z. In Fig. 2.13(f), it can be observed that the difference between the average difference ratios (*VDR*) in the presence of two and one horizontal component is less than 10%.

The difference ratio due to the employed model (Type 1 versus Type 2) is calculated using Eq. (2.2) which defines the type difference ratio. The results using this ratio are presented in Fig. 2.14 and Fig. 2.15.

$$TDR = \frac{\max(\text{response in Type 1})}{\max(\text{response in Type 2 or Type 2 - 1})} - 1 \qquad (2.2)$$

Fig. 2.14 presents the *TDR* values under the presence of all three components of ground motion. As before, the ground motions were sorted in a descending order of the peak vertical acceleration. The motions with large peak vertical acceleration tend to have smaller *TDR* values except for D_z and F_z. The ratios are more widely distributed than the *VDR* values obtained by Eq. (2.1), mainly due to the different dynamic properties of the two types and the presence of the top moment in Type 2 model Most of these values are in the range of -1.0 to 1.0. However, having observed that the axial force is one of the response parameters that is affected by the vertical ground motion from Fig. 2.12 and Fig. 2.13, it can be concluded that the effect of the model type is not important considering that the *TDR* values are within the range -0.2 and 0.2, mainly concentrated around zero, for the axial force F_z. Same observation can be deducted from Fig. 2.15 which presents the average for the absolute values of the type difference ratios (*TDR*) for different aspect ratios with and without vertical excitation cases. In this figure, average absolute values are mostly below 10% for the axial force and they are between 15% and 38% for the other response parameters. For all the response parameters, the ratios *TDR* tend to be larger as the aspect ratio becomes smaller.

Fig. 2.16 presents the average absolute *TDR* values for different response parameters for comparison of Type 1 and Type 2-1 models, i.e. average of the absolute type difference ratios between Type 1 and Type 2-1, instead of Type 1 and Type 2 shown in Fig. 2.15. The mean of *TDR* between Type 1 and Type 2-1 decreases compared to that between Type 1 and Type 2. This can be explained by the reduced discrepancy of periods which are shown in Table 2.7. This is especially true for the average values of *TDR* for D_y, D_z, F_y, and M_x, which are reduced significantly when comparing results in Fig. 2.16 Average absolute *TDR* values for different response parameters for comparison of Type 1 and Type 2-1 models to those in Fig. 2.15. In addition, the average absolute values of *TDR* for D_z and F_z have different patterns. Comparing Fig. 2.15(c) to Fig. 2.16(c) and Fig. 2.15(f) to Fig. 2.16(f), it can be observed that the values under the presence of vertical excitation (designated as 'With Z') decrease noticeably when Type 2-1 is used instead of Type 2. It is due to the fact that Type 1 and Type 2-1 have smaller differences in T_h and the same T_v. When vertical excitation is applied, the vertical responses depend more on the vertical periods compared to the horizontal periods. Hence, compared to Type 2, Type 2-1 is closer to Type 1 considering the responses D_z and F_z.

The main observations for the results discussed above can be summarized as follows:

- The presence of one or both of the horizontal components does not produce significant differences.
- Except for the axial displacement and force (D_z and F_z), the difference in other response quantities due to vertical excitation is not significant, less than 5%, in general.
- For both setups, Types 1 and 2, the effect of vertical excitation is significant in F_z with a potential to affect their shear strength.
- The difference in D_z or F_z of Type 1 and Type 2 is relatively small. For other response parameters, the difference between Type 1 and Type 2 cannot be ignored and becomes larger as the column has a smaller aspect ratio. However, since the axial force is the only important (from the point of view of the present study) parameter that is significantly affected from the vertical excitation, it can be concluded that the differences between Types 1 and 2 are not important for the purposes of this study. These differences are even less important between Types 1 and 2-1.

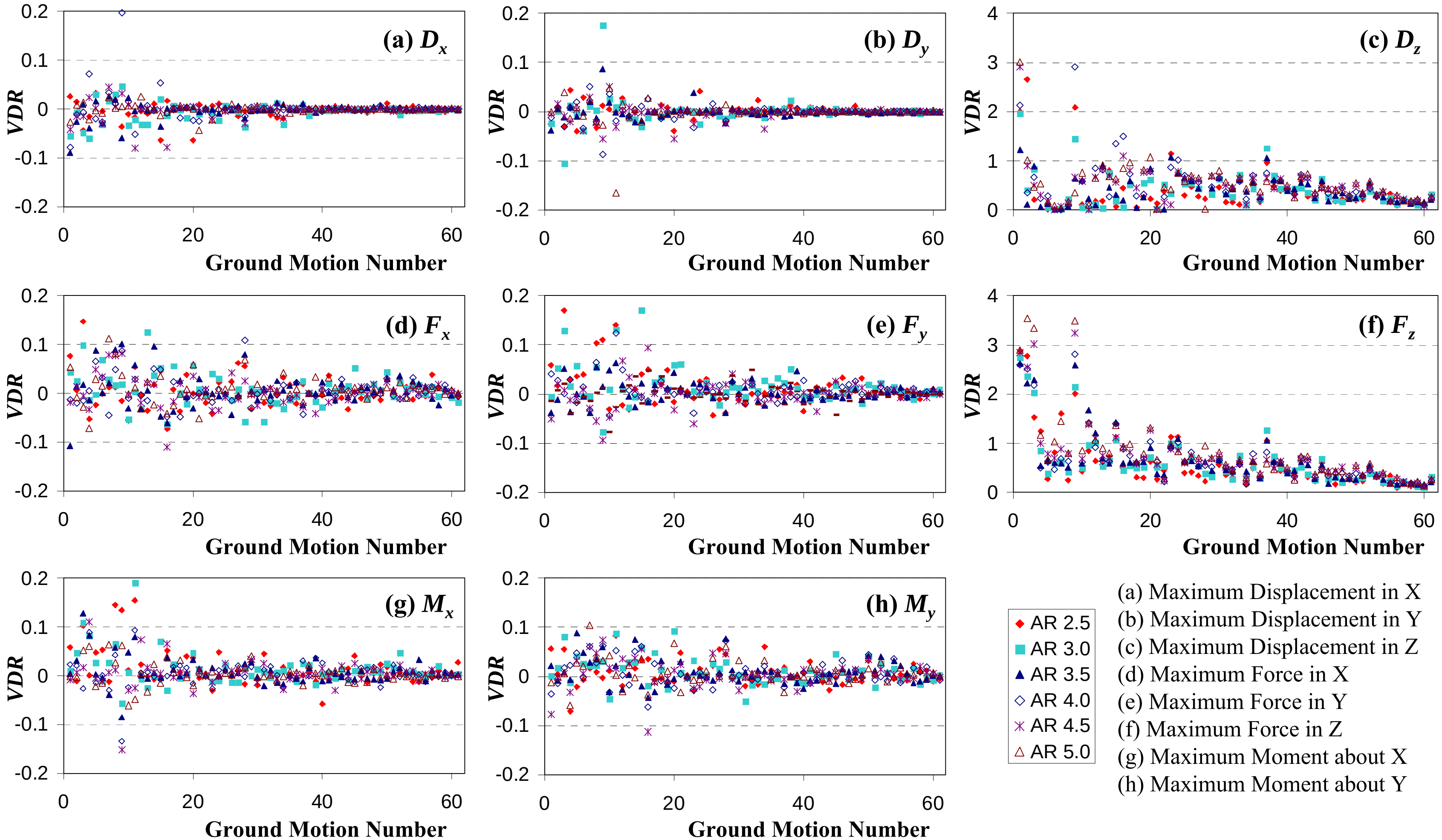

Fig. 2.12 *VDR* values for different response parameters for Type 2 model for the case of both horizontal components present

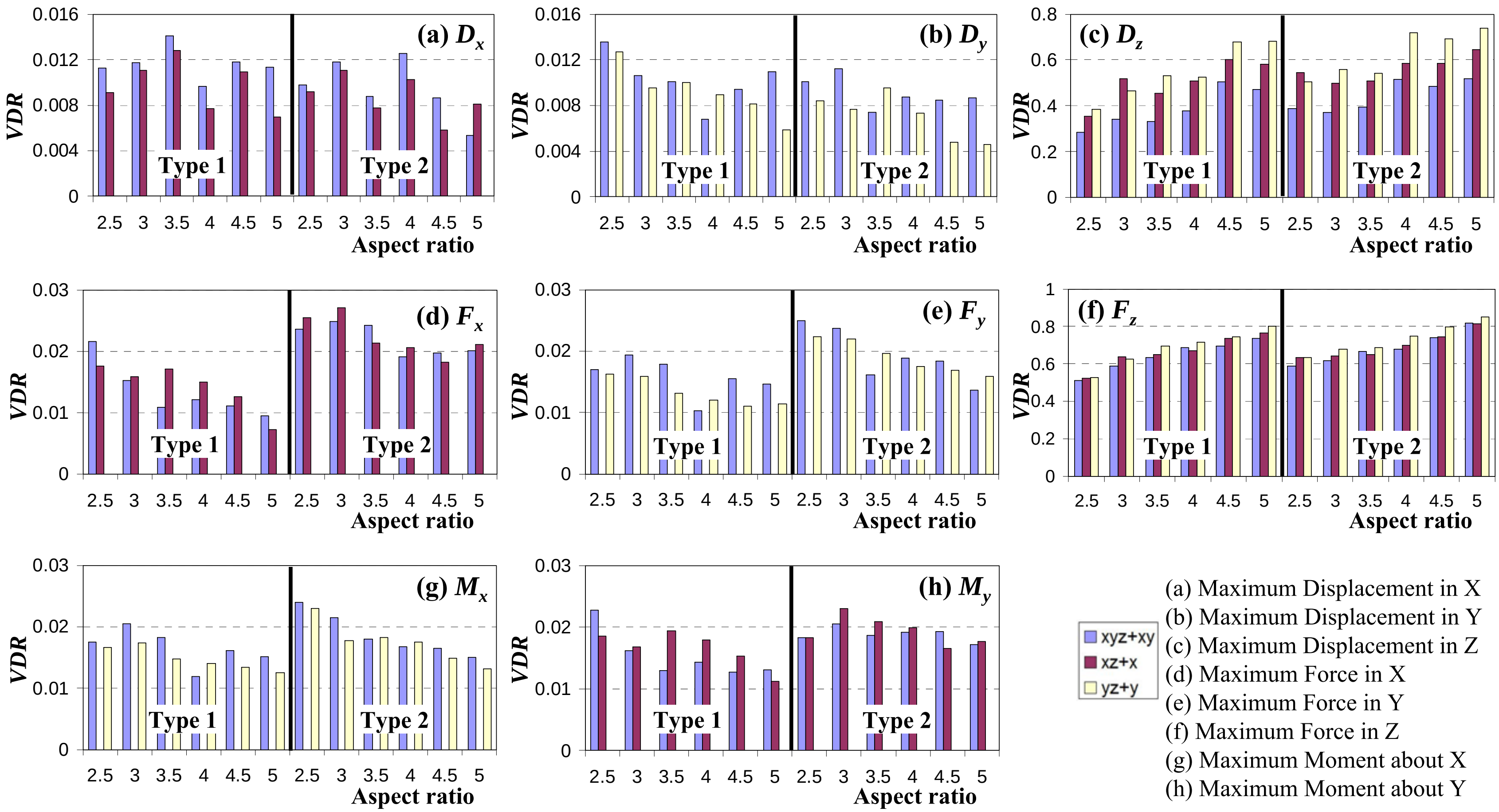

Fig. 2.13 Average absolute *VDR* values for different response parameters

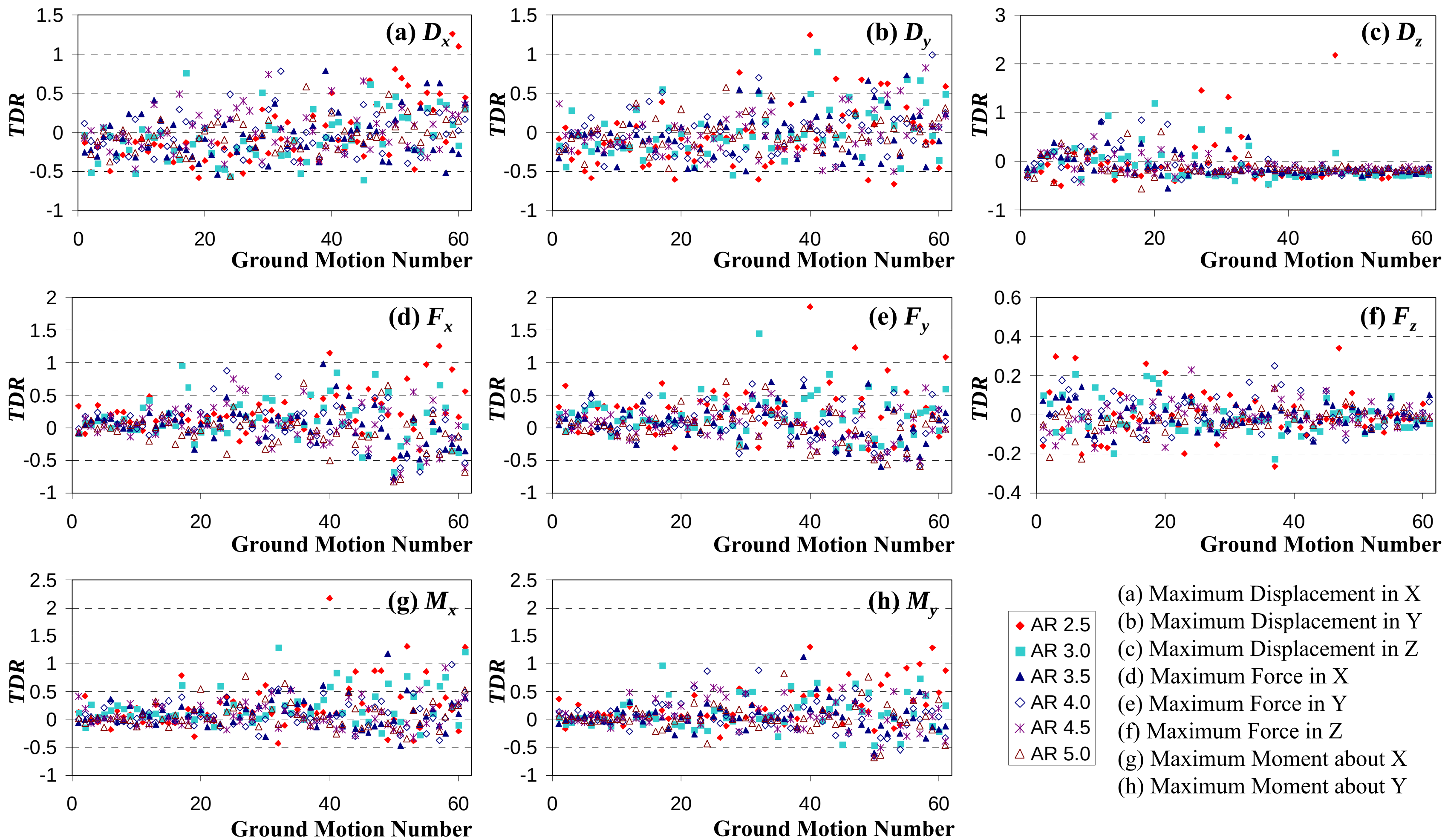

Fig. 2.14 *TDR* values for different response parameters for comparison of Type 1 and Type 2 models for the case of both horizontal components present

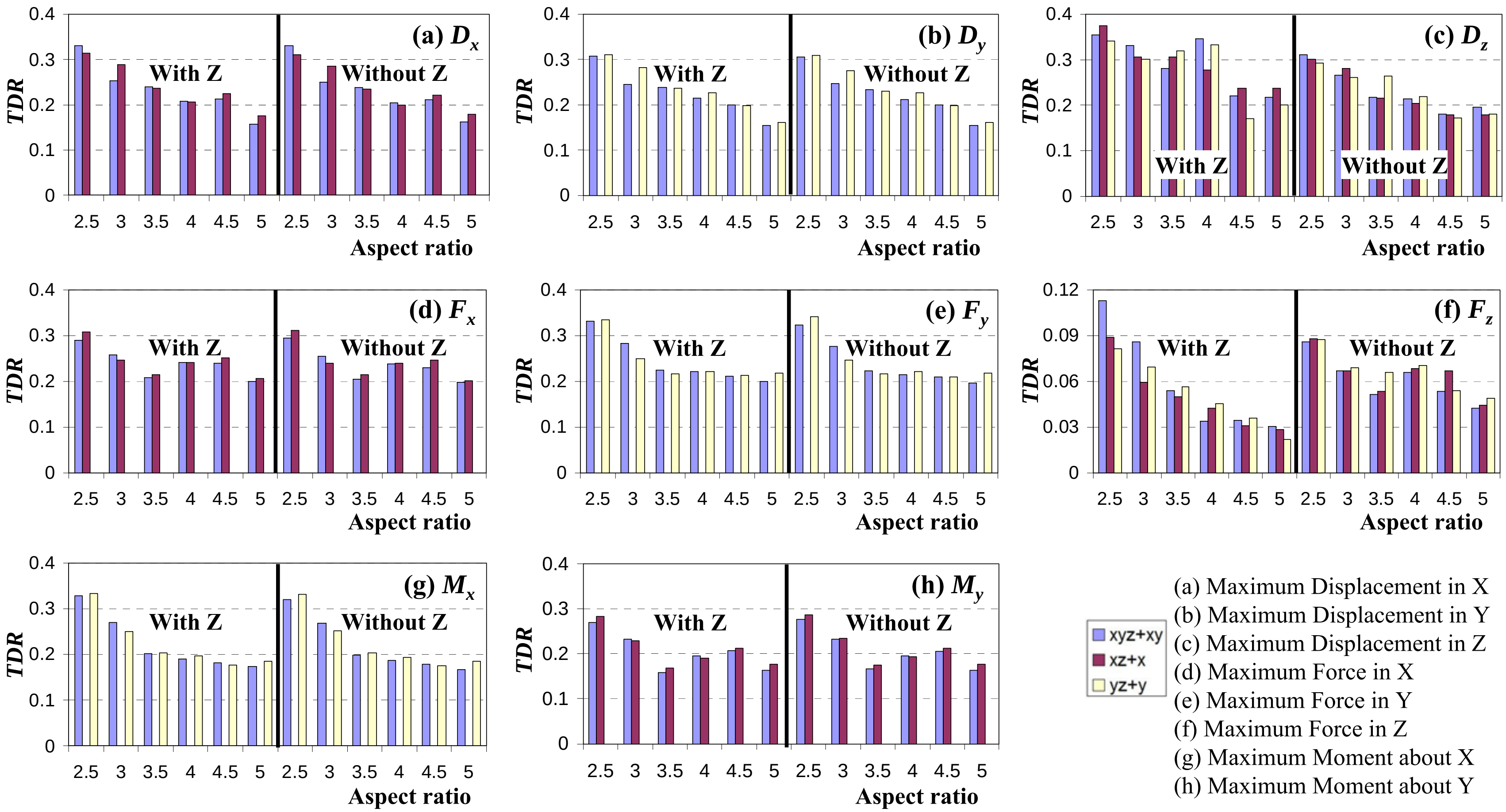

Fig. 2.15 Average absolute *TDR* values for different response parameters for comparison of Type 1 and Type 2 models

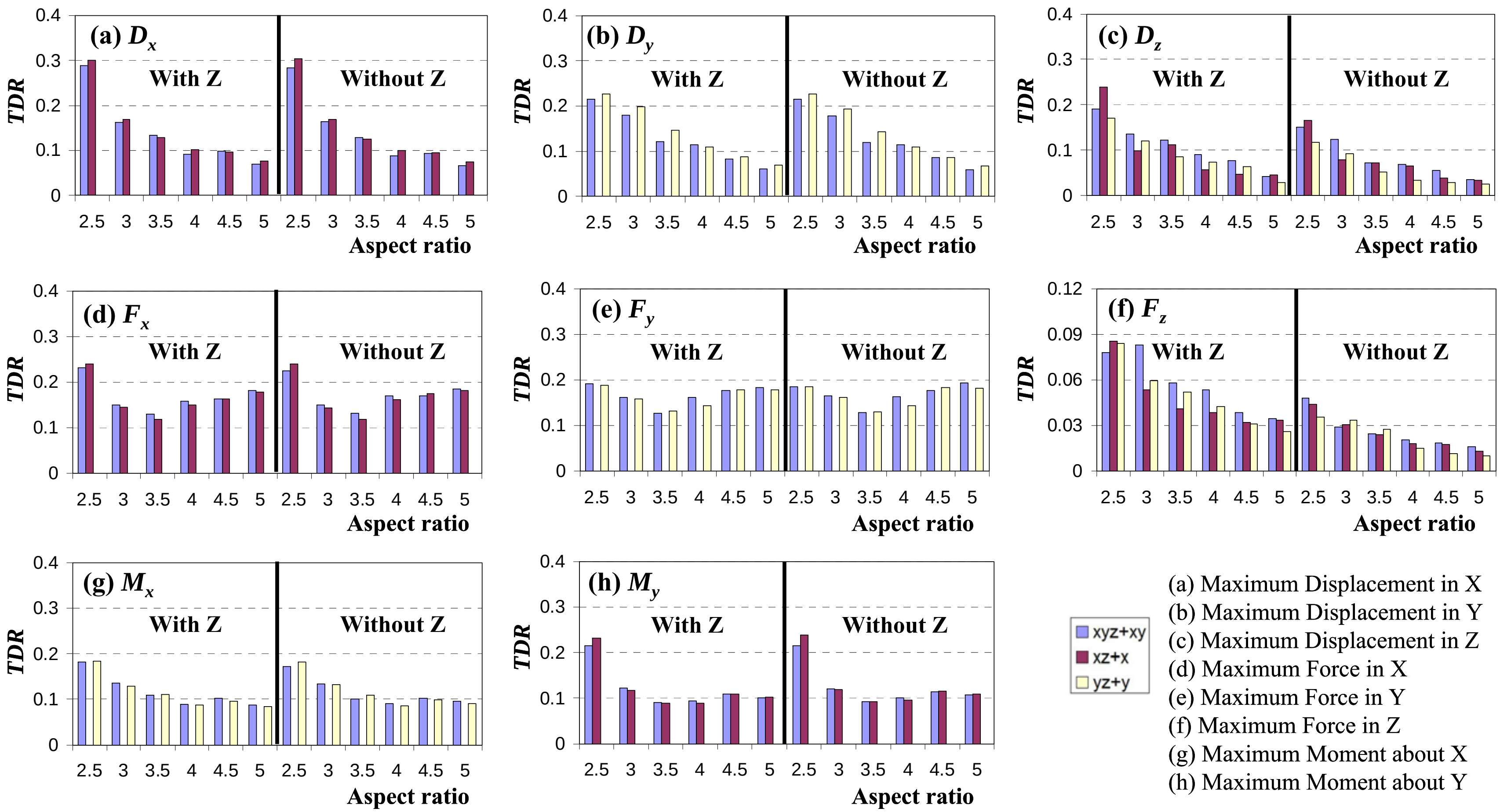

Fig. 2.16 Average absolute *TDR* values for different response parameters for comparison of Type 1 and Type 2-1 models

2.5 Detailed Investigation of the Effect of Axial Force on the Shear Capacity

2.5.1 Comparison of Shear Demand and Capacity

In Section 2.4, the change of demand due to vertical excitation is discussed using three different modeling types, several aspect ratios, and various ground motions. It is observed that axial force is the only force parameter that is affected by the presence of vertical excitation. In this section, effect of axial force on the shear strength is investigated in details using different shear strength equations presented in Chapter 1. Moreover, the shear demand is compared with the shear capacity.

Fig. 2.17 presents comparison of the shear strength calculated using equations given in ACI (Section 1.2.1), CSA (Section 1.2.4), Eurocode (Section 1.2.5) and Caltrans SDC (Section 1.2.7) and the shear demand using ground motion #9 (Landers earthquake recorded at Lucerne station) (refer to Appendix A for further details about the record) with one of the horizontal components and with and without the vertical component (designated as 'xz' and 'x', respectively) for Fig. 2.17(c) and (d) are for Type 2. It can be observed that ACI, CSA, Eurocode, and SDC do not provide consistent results in estimating the shear strength. Before the ground motion is applied (i.e. under the presence of only gravity loading), ACI offers the most conservative estimation, but once the dynamic excitation is included, the estimates change significantly for all the methods. In general, the prediction of CSA changes more dramatically than ACI, Eurocode, or SDC during dynamic excitation. Another observation from Fig. 2.17 is that the possibility of shear failure increases when vertical excitation is present. For example, including the Z-component produces shear strength which is much closer to the shear demand compared to the shear strength without the Z-component. It should be noted that the SDC has the minimum value of 5681.9 kips whenever tensile axial force is applied, as shown in Fig. 2.17(b) and (d).

The maximum ratio of the shear demand and shear strength, *Maxdcr*, and the reduction of the shear strength due to the earthquake excitation, *Red*, are calculated using Eq. (2.3) and Eq. (2.4), respectively. *Maxdcr* and *Red* using ACI are shown in Fig. 2.18. All the aspect ratios are considered for all the 61 ground motions. Only the results of the case, 'X+Y+Z and X+Y' (effect of vertical excitation when both horizontal components are present) applied to Type 2, are shown. Almost all of the *Maxdcr* values are between 0.1 and 0.6 and as expected, small aspect ratios have large values of *Maxdcr*. Although *Maxdcr* values do not significantly change by adding the vertical earthquake component, there are differences in some of the ground motions. For example, *Maxdcr* for AR = 2.5 increases from 0.564 to 0.617 under ground motion #3 (Appendix A). Another observation is that *Red* values change significantly with relatively large vertical acceleration (ground motions #1 to approximately #20), as expected. Also, *Maxdcr* values decrease as the number of the ground motion increases, in general. It is noted that, as before, the ground motion numbers on the horizontal axis of Fig. 2.18 are sorted in a descending order of the peak vertical acceleration (PGA_v).

$$Maxdcr = \max\left(\frac{\text{shear demand at each time step}}{\text{shear strength at each time step}}\right) \tag{2.3}$$

$$Red = \frac{\min\left(\text{shear strength}\right)}{\text{shear strength before excitation}} \tag{2.4}$$

ACI and SDC provide similar *Maxdcr* and *Red* values with relatively small vertical acceleration (ground motions #20 or above). However, with the ground motions below #20, there is a great disparity between *Maxdcr* and *Red* of SDC and those of ACI. In Fig. 2.19(a) and (b), *Maxdcr* values based on SDC without and with Z-component, respectively, are shown. Both cases have the values between 0.1 and 1.0 with the ground motions below #20, but it is noticeable that more points are between 0.6 and 1.0 in Fig. 2.19(b) than those in Fig. 2.19(a). In Fig. 2.19(c) and (d), *Red* values based on SDC without and with Z-component, respectively, are shown. There are 4 ground motions which have significant reduction caused by lateral displacement ductility even without Z-component. It is important to note that there are more than 20 ground motions causing the same *Red* around 0.53 with Z-component included. Since the shear strength contribution of concrete, V_c, from SDC is zero under tension, only the shear strength of transverse reinforcement remains. It should be noted that V_c is zero using SDC, regardless of how large the tension is.That is why for all the ground motions that result in tension, *red* becomes equal to V_c divided by the sum of V_c and V_s, which is equal to 0.53. Zeroing the concrete continuation to shear strength under tension in SDC makes a significant difference between ACI and SDC estimates. *Maxdcr* and the minimum of shear strength may not occur simultaneously in case of ACI estimate. Therefore, *Maxdcr* using ACI may not increase significantly even if there is noticeable reduction in *Red* using ACI. On the contrary, *Red* using SDC may occur several times during the excitation and in general *Maxdcr* may occur during one of these times. Consequently, *Maxdcr* based on SDC equations increases significantly with the inclusion of the Z-component.

The average values of *Maxdcr* and *Red* for the two Types 1 and 2 and all the aspect ratios are shown in Fig. 2.20 for the ACI approach, in Fig. 2.21 for the SDC approach, in Fig. 2.22 for the Eurocode approach, and in Fig. 2.23 for the CSA approach. As shown, *Maxdcr* decreases as the AR increases and *Red* increases as the AR increases even though it is a very small increase (almost constant) in the case of the ACI and also the Eurocode approaches. Moreover, the difference due to the number of horizontal components (one versus two) is less than 10% in *Maxdcr* for ACI, Eurocode, and SDC. On the contrary, this difference is sometimes more than 10% in *Maxdcr* for CSA and this difference tends to increase as the AR decreases. However, all approaches are similar in producing larger *Maxdcr* with two horizontal components compared to only one horizontal component. Finally, the effect of the vertical component is much more noticeable in *Red* where, for some ground motions, it decreases to 0.6.

For all four codes, *Red* decreases when the vertical component is included. This means that the capacity decreases with the inclusion of the vertical excitation. This is expected because ACI, SDC, and Eurocode have an axial force term and CSA has an axial strain term. With vertical excitation, these terms fluctuate significantly and the shear strength also goes up and down. Due to the discrepancy of the variation of the axial force of the cross-section and that of the axial strain at the centroid (which is affected not only by the cross-section axial force but also by the cross-section bending moment), the shear strength estimate by CSA is quite different from those by ACI, SDC, and Eurocode. Fig. 2.24 present *Maxdcr* and *Red* for the whole 293 ground motions whose horizontal PGA's are larger than 0.25g. Similar to Fig. 2.18, in Fig. 2.24, shows the results for Type 2 model with the application of X+Y+Z and X+Y components. To avoid excluding ground motions which may have significant effect of its vertical excitation, all 293 motions (discussed in Section 2.1) were applied and analyzed. As observed in Fig. 2.18, ground motions #1, #2, #3, #4, #7, and #10 in Appendix A have significant decrease in *Red* with the inclusions of the vertical (Z) excitation.

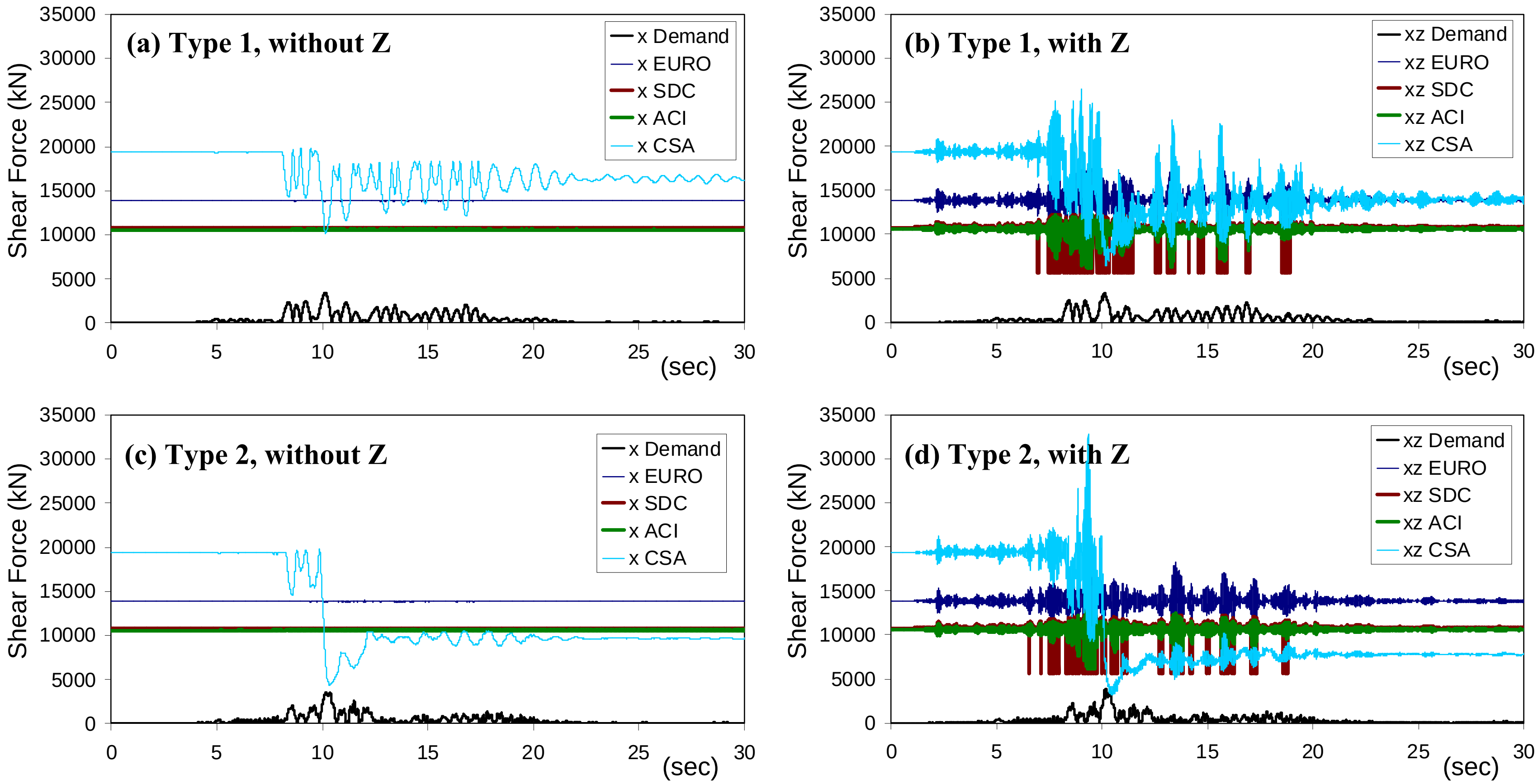

Fig. 2.17 Shear demand and capacity with ground motion #9

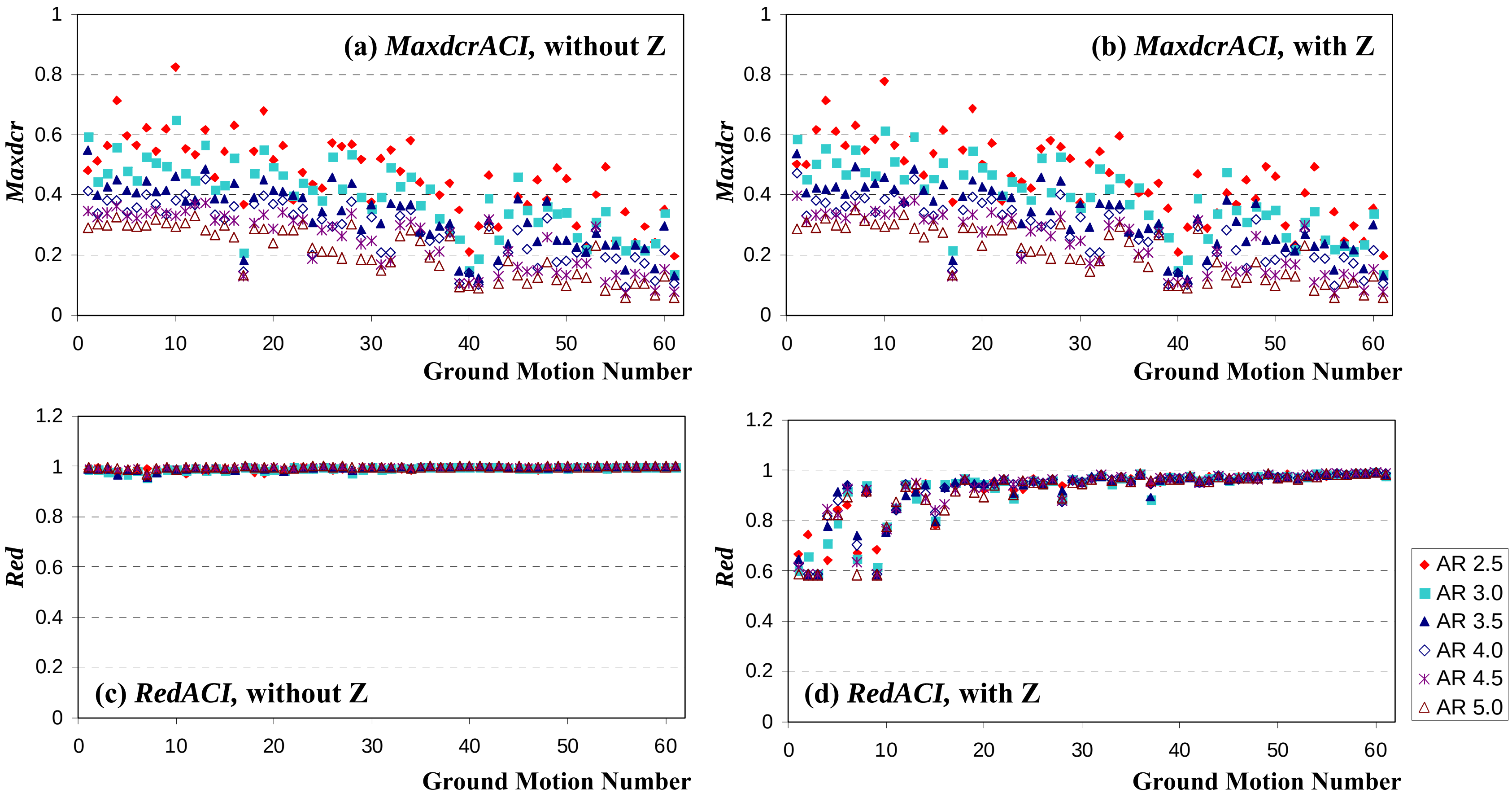

Fig. 2.18 Demand to capacity ratio (*Maxdcr*) and reduction in shear strength (*Red*) considering ACI equation for Type 2 and the selected 61 ground motions

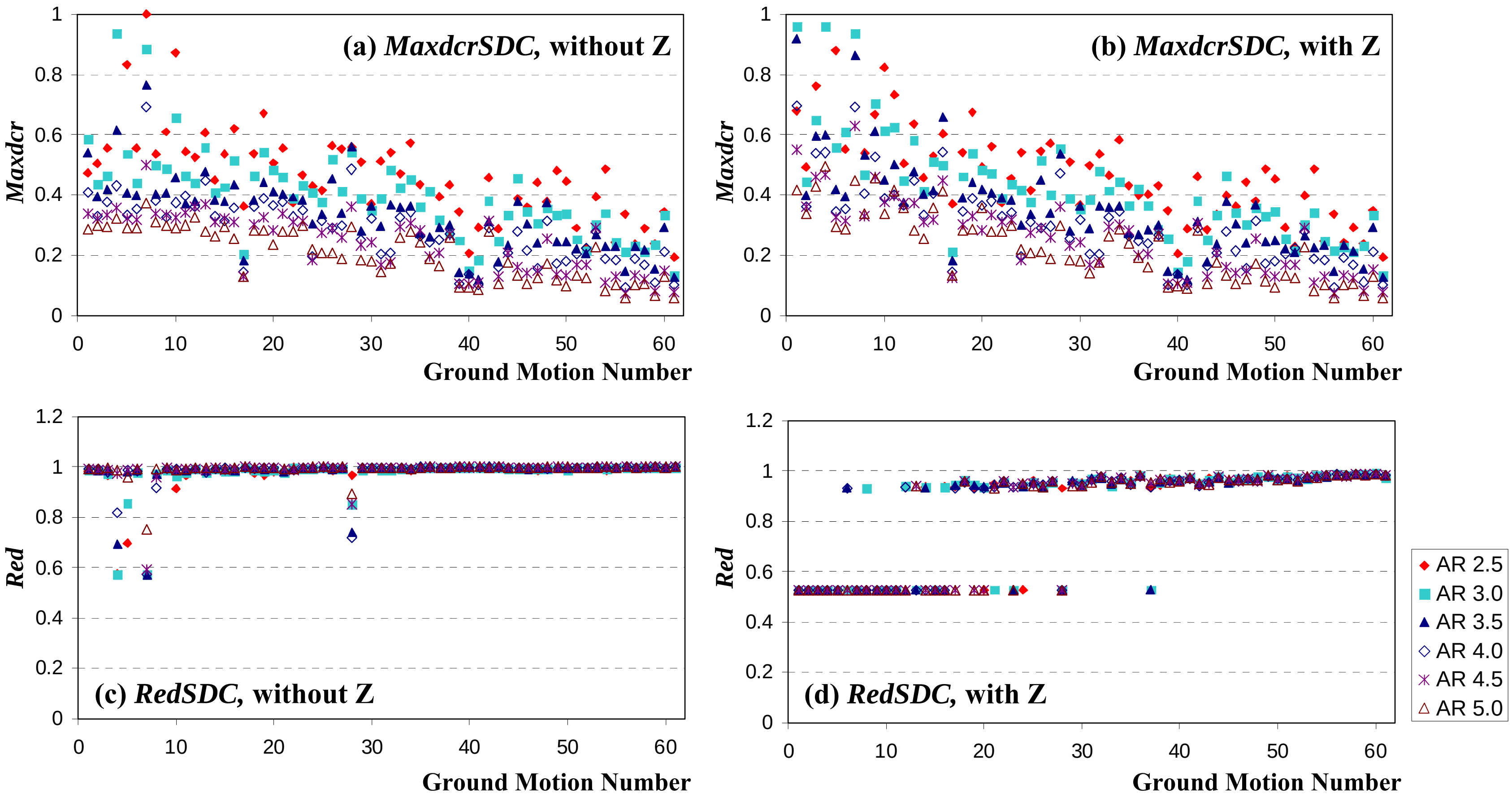

Fig. 2.19 Demand to capacity ratio (*Maxdcr*) and reduction in shear strength (*Red*) considering SDC equation for Type 2 and the selected 61 ground motions

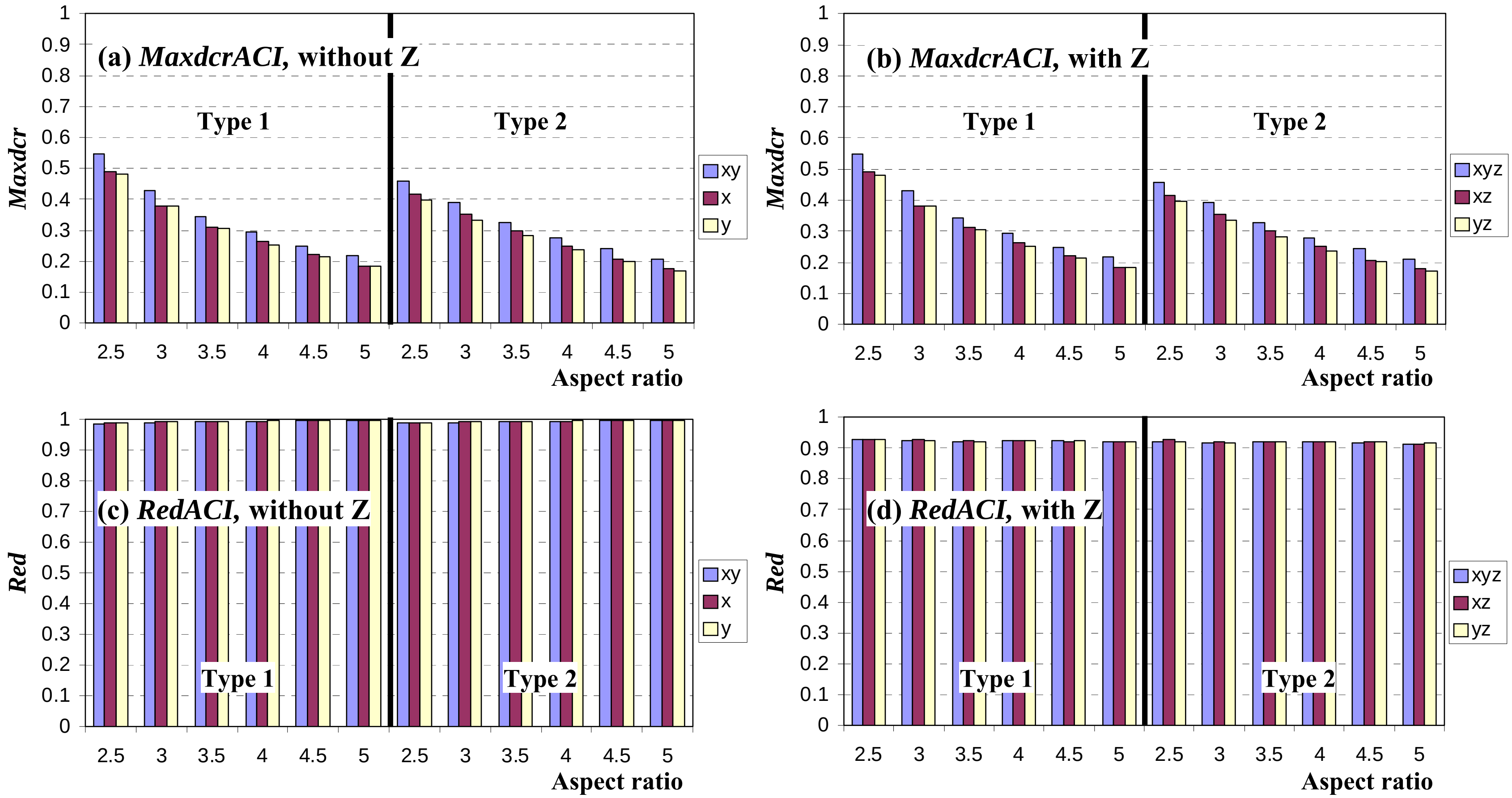

Fig. 2.20 Mean of demand to capacity ratios (*Maxdcr*) and mean of reduction in shear strength (*Red*) considering ACI apprach

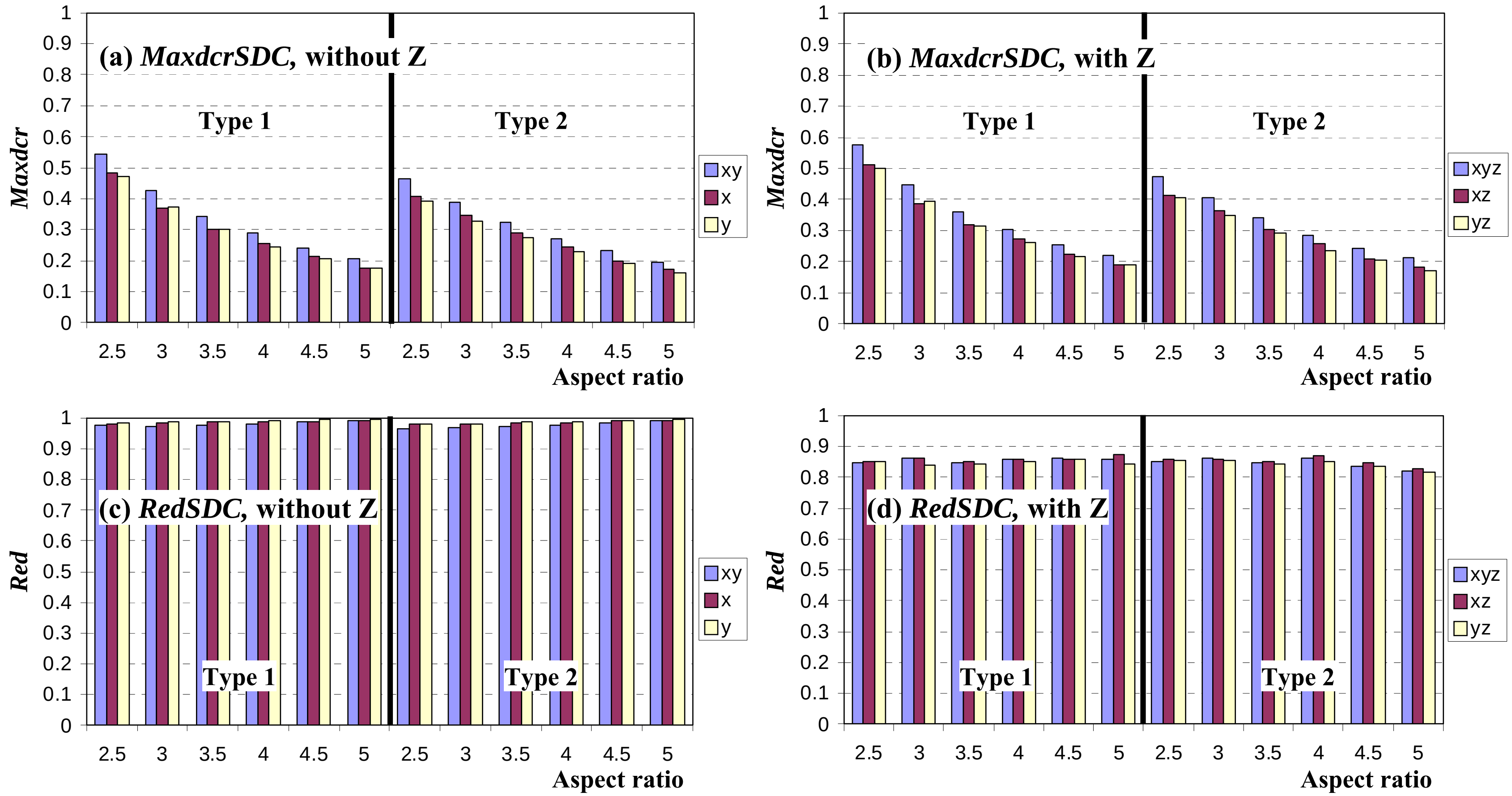

Fig. 2.21 Mean of demand to capacity ratios (*Maxdcr*) and mean of reduction in shear strength (*Red*) considering SDC approach

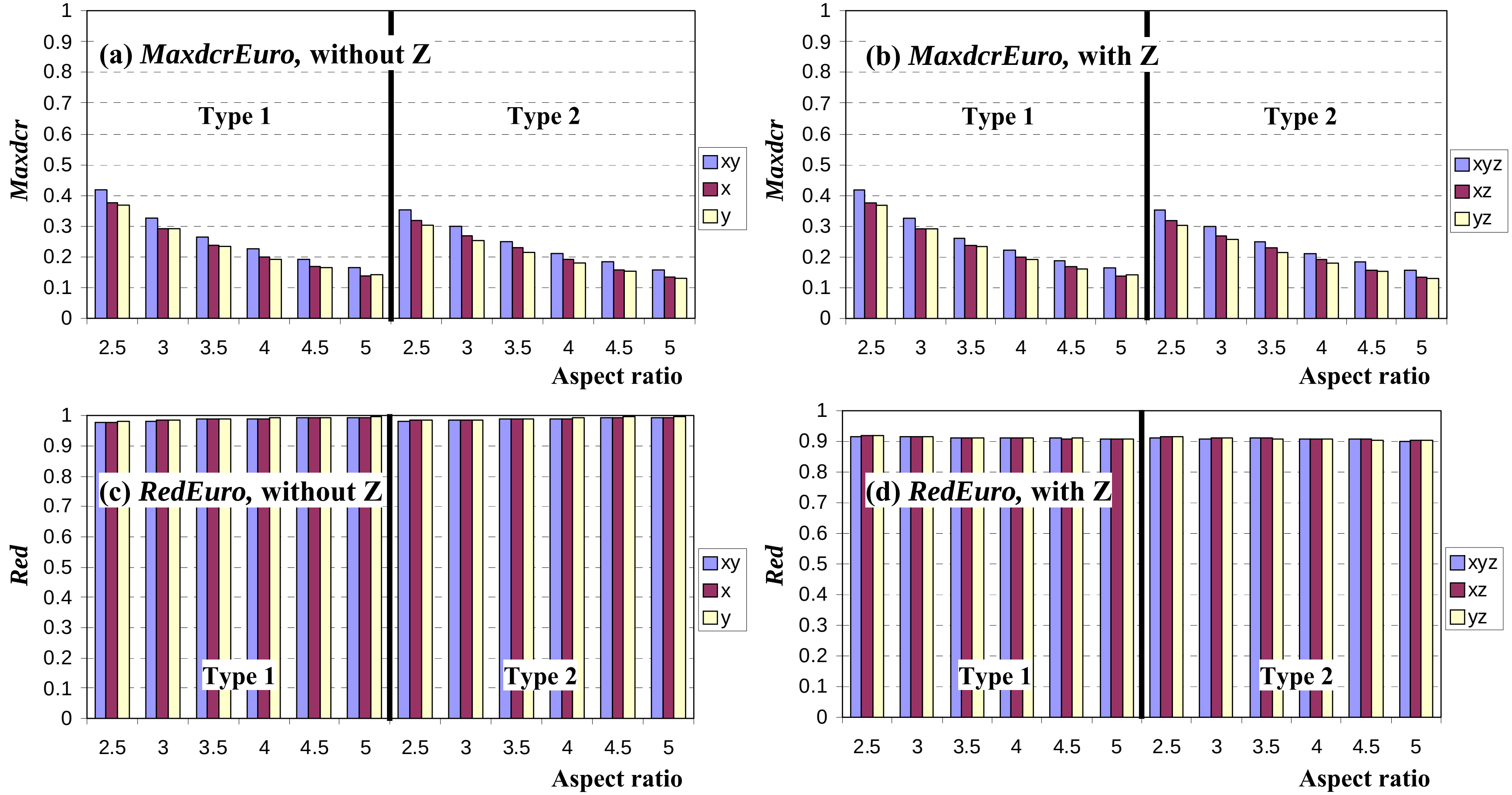

Fig. 2.22 Mean of demand to capacity ratios (*Maxdcr*) and mean of reduction in shear strength (*Red*) considering Eurocode approach

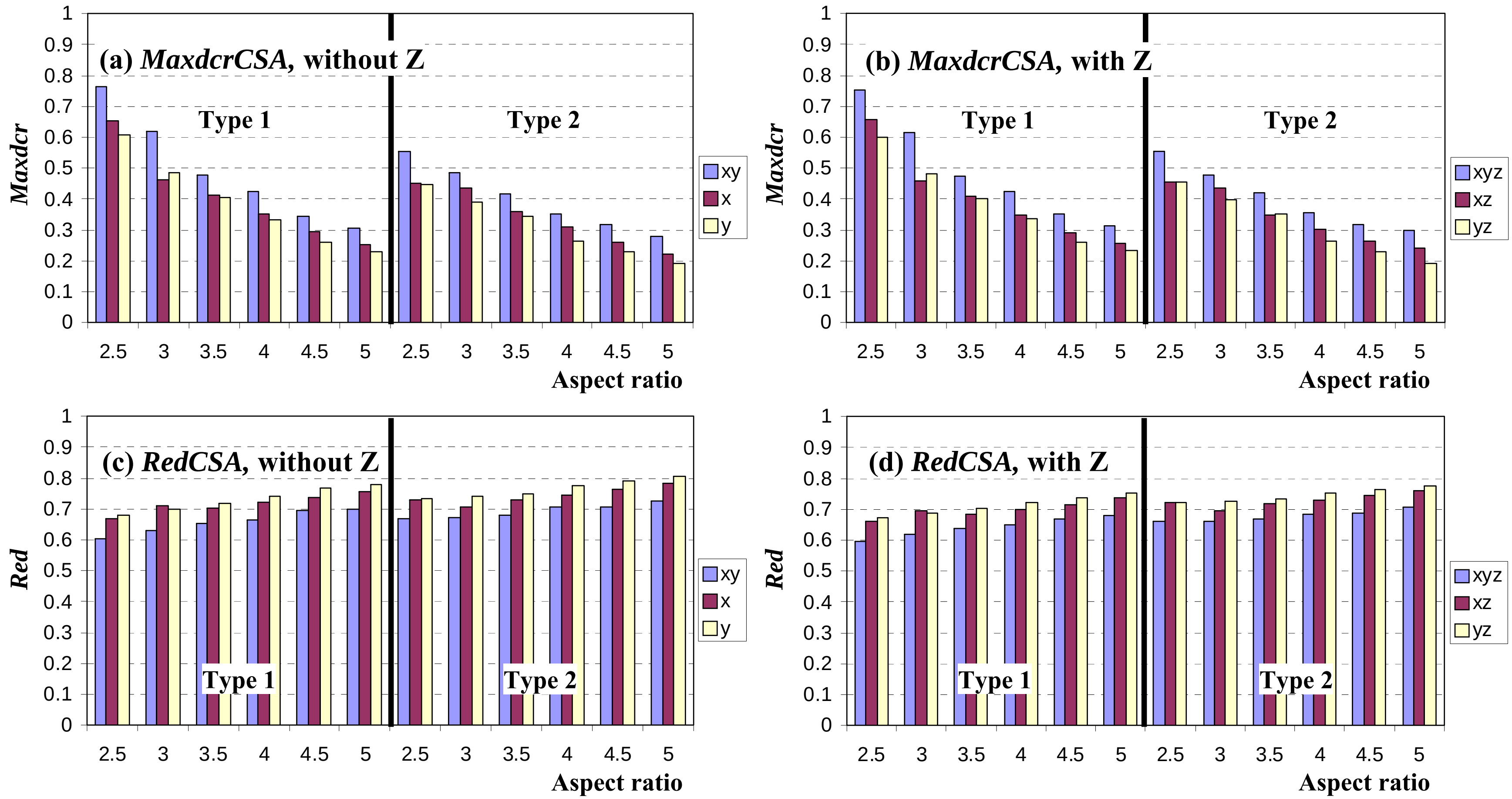

Fig. 2.23 Mean of demand to capacity ratios (*Maxdcr*) and mean of reduction in shear strength (*Red*) considering CSA approach

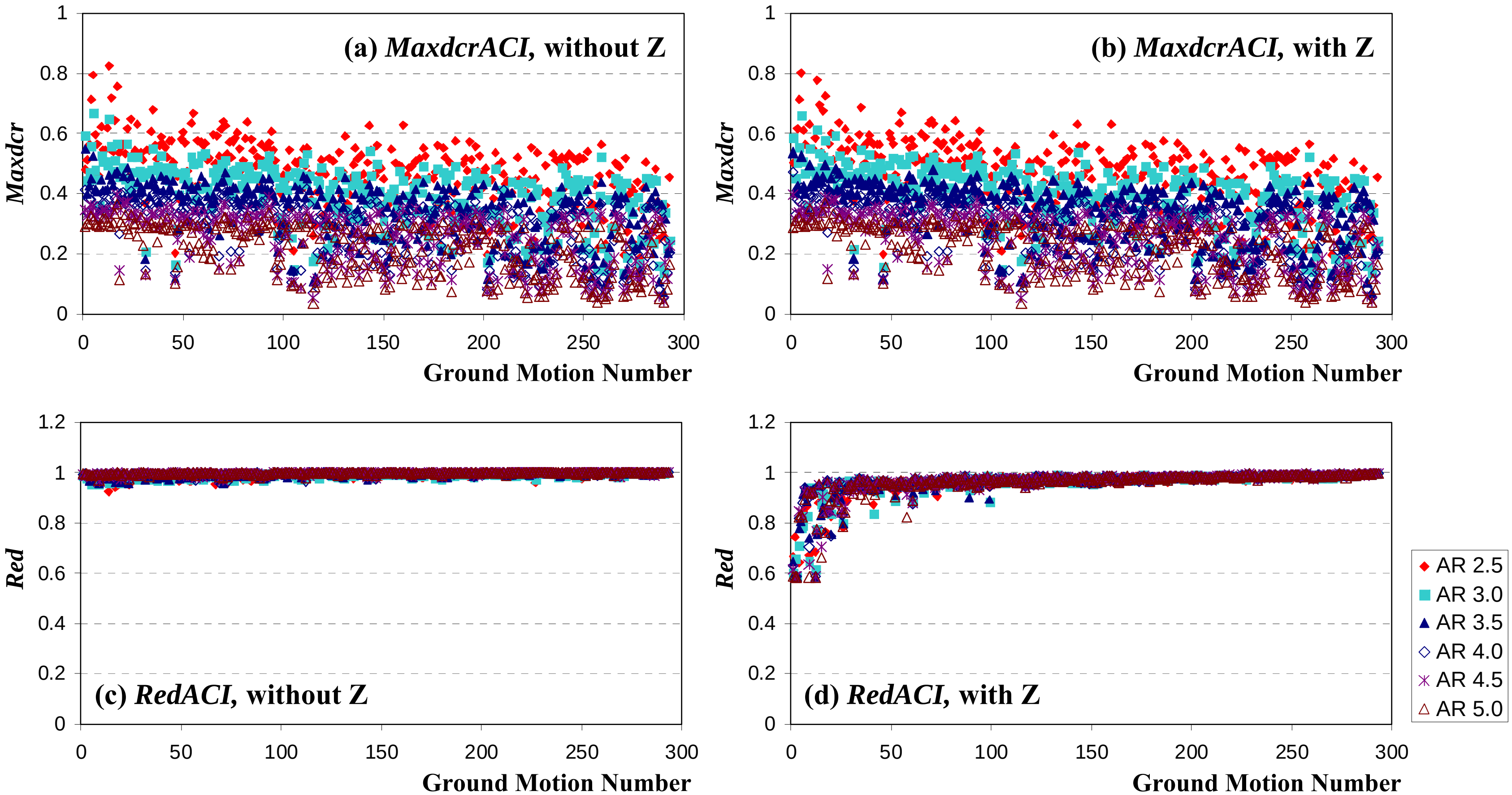

Fig. 2.24 Demand to capacity ratio (*Maxdcr*) and reduction in shear strength (*Red*) considering ACI equation for Type 2 and the 293 ground motions with $PGA_h > 0.25$g

2.5.2 Concluding Remarks

Based on the results and discussions above, one can summarize the main observations from the parametric study as follows:

- Due to considering both horizontal components, *Maxdcr* of the column subjected to X+Y+Z (or X+Y) is larger than that subjected to X+Z, Y+Z (or X, or Y).
- Reduction of shear strength (*red*) due to application of X+Y+Z (or X+Y) is smaller than that due to application of X+Z, Y+Z (or X, Y).
- For shear strength demand to capacity ratio (*Maxdcr*) values, the sequence from different codes is Eurocode < ACI ≤ SDC < CSA, on average. The inequality between ACI and SDC holds when tension is present.
- For shear strength reduction (*Red*) values, the sequence from different codes is CSA < SDC < ACI ≈ Eurocode, on average.
- A smaller aspect ratio tends to have a larger *Maxdcr* and a larger aspect ratio tends to have a slightly larger *Red* factor (i.e. it is reduced less).
- The pattern of reduction factors of ACI, SDC, and Eurocode depends moderately on the vertical excitation. In cases of ACI and Eurocode, the reduction factors of several ground motions are less than 0.85. The ground motions which make noticeable changes are #1, #2, #3, #4, #7, and #10 (descending order of PGA_v) in Appendix A. SDC has a unique pattern because its V_c is zero, under tension regardless of the value of the tension.
- The reduction factors of CSA do not depend on the vertical excitation as much as the ACI, SDC and Eurocode. Their reduction pattern does not change significantly, with or without the vertical component.
- ACI, SDC, and Eurocode explicitly consider the axial force. Therefore, in the case without vertical excitation, their capacity predictions do not differ from ground motion to ground motion or from aspect ratio to aspect ratio, compared to those from CSA.
- CSA takes the effect of axial force into consideration by using axial strain at the centroid of the section, which results in differences in the shear capacity predictions for different ground motions and different aspect ratios in the case without vertical excitation, since the axial strain at the centroid of the section is not only affected by the axial force but also by the bending moment.

2.6 Summary

Among 3,551 earthquake acceleration records in the PEER NGA database, 61 ground motions are selected as input candidates based on three criteria. The 1st is the horizontal peak ground acceleration where at least one of the horizontal components should have the peak ground acceleration larger than 0.25g. The 2nd criterion is based on the ratio of the pseudo-spectral acceleration corresponding to the vertical component (PSa_v) to those corresponding to the horizontal components (PSa_{h1}, PSa_{h2}) where for the 20 pairs of periods T_h-T_v (T_v=0.05, 0.1, 0.15, and 0.2 seconds and T_h=0.4, 0.5, 0.6, 0.7, and 0.8 seconds), PSa_v/PSa_{h1} or PSa_v/PSa_{h2} were calculated. If one of these two ratios is larger than 1.0 in at least 15 pairs, the ground motion is selected as one of candidates. The 3rd criterion is the arrival time interval between horizontal and vertical peak accelerations which affects the interaction of the horizontal and the vertical responses. The interval should be shorter than the cut-off of 1 sec. Finally, based on the criteria and after removing the motions with only low frequency content, 61 ground motions are selected.

A parametric study was conducted to identify the most influential ground motions on the columns with the modified effective circular section of Prototype 1 (ACB) from the perspective of the effect of vertical excitation. The following parameters were varied: ground motion, number of components, mass moment of inertia, and aspect ratio. First, 61 motions were applied. Second, three cases were considered, all three components versus two horizontal components, X and Z components versus X component, Y and Z components versus Y component. Third, the existence of the mass moment of inertia was considered and its effect on the responses was examined. The mass moment of inertia of Prototype 1 (ACB) was implemented to Type 2 model. Since Type 2-1 has no rigid end zone, it is identical to Type 1 except for the inclusion of the mass moment inertia, obtained lateral and rotational periods. Fourth, six aspect ratios from 2.5 to 5.0 were taken into account.

The following remarks can be made form the findings of the parametric study. First, the presence of two or one of the horizontal components does not produce significant differences. Second, except the D_z and F_z, the difference in other responses due to vertical excitation is not significant. Third, the effect of vertical excitation is significant in F_z and this might affect the shear strength for both setups Types 1 and 2. Fourth, the difference in D_z or F_z between Types 1 and 2 is relatively small. For other response parameters, the discrepancy between Types 1 and 2 cannot be ignored and becomes larger as the aspect ratio decreases. However, since the axial force is the only parameter that is significantly affected from the vertical excitation (the focus of this study), it can be concluded that the differences between Types 1 and 2 (especially Type 2-1) may not be important for the purpose of this study.

The effect of axial force on the shear strength is investigated using different shear strength code approaches. Comparing the shear demand to the shear strength, the maximum ratio of shear demand and shear strength, *Maxdcr*, and the reduction of the shear strength due to the earthquake vertical excitation, *Red*, are calculated. *Maxdcr* of the column subjected to X+Y+Z (or X+Y) is larger than that subjected to X+Z, Y+Z (or X, or Y). For *Maxdcr*, Eurocode < ACI ≤ SDC < CSA, on average. *Red* due to application of X+Y+Z (or X+Y) is smaller than that due to application of X+Z, Y+Z (or X, or Y). For *Red*, CSA < SDC < ACI ≈ Eurocode, on average. Moreover, a smaller aspect ratio tends to have a larger *Maxdcr* and a larger aspect ratio tends to have a slightly larger *Red*, i.e. it is reduced less. It should be noted that ACI, SDC, and Eurocode explicitly consider the axial force. On the other hand, CSA takes the effect of axial force into consideration by using axial strain at the centroid of the cross-section, which results in differences in the shear capacity predictions for different ground motions and different aspect ratios even in the case without vertical excitation. This is because the axial strain at the centroid of the cross-section is not only affected by the axial force but also by the bending moment.

Chapter 3

Design of Dynamic Tests

3.1 Introduction

Dynamic testing is the most ideal method to replicate earthquake input motions. Due to limitation of facilities, only a few shaking table tests have been conducted to examine the effect of vertical acceleration on bridge columns, up to this date. To perform tests on the UC-Berkeley shaking table at the Richmond Field Station (RFS), ¼-scale bridge column specimens, instrumentation and input sequence were prepared to investigate the response of a bridge column subjected to the horizontal and vertical dynamic excitations.

3.2 Description of the Shaking Table

In 1969, Professor J. Penzien (together with Professor R. Clough) led the design of the world's first shaking table at RFS, which went through several upgrades to eventually become a shaking table with six degrees of freedom (6 DOFs), three translational and three rotational components of motions. It is operated by the Pacific Earthquake Engineering Research (PEER) Center and is now the largest 6 DOFs table in the United States.

The shaking table is stiffened by heavy transverse ribs and the eight horizontal hydraulic actuators (four in each direction) are attached to the ribs. The four vertical actuators are attached to the table by post tensioning rods at points located 1.5 ft × 1.5 ft (305 mm × 305 mm) from each corner. All 12 actuators are 75 kips (334 kN) capacity hydraulic actuators and connected to 1580 kips (7028 kN) reaction block. As a result, about 3*g* can be achieved with the empty table which weighs about 100 kips (445 kN). Decoupling of components is accomplished by the length of the actuators and the control system. A unique feature of the UC-Berkeley shaking table is that a 1.5 psi air pressure supports the total weight of the table and specimen while the table is in operation. This feature allows the hydraulic actuators to operate more efficiently during dynamic loading. Table 3.1 summarizes the characteristics of the UC-Berkeley shaking table. Fidelity tests, as discussed in the next section, were performed before the actual RC bridge column tests to confirm the performance of the shaking table.

Table 3.1 UC-Berkeley shaking table characteristics

Property	Value
Table dimensions	20 ft × 20 ft (6.1 m × 6.1 m)
Table weight	About 100 kips (445 kN)
Components of motion	6 DOFs
Displacement limits	horizontal limits are ±5 in (±127 mm) vertical limit is ±2 in (±50.8 mm)
Velocity limits	30 in/s (0.76 m/s) in all axes with an unloaded table
Acceleration limits	About 3*g* in all axes with an unloaded table

3.3 Selection of Input Motion: Fidelity Tests

In the presence of a vertical excitation, the shaking table is governed by its own frequency and it is not possible to reproduce all frequencies of the input motion exactly. Therefore, some motions may not be possible to be reproduced. Performing fidelity tests is the considered approach to select suitable motions for the intended dynamic tests.

On March 19, 29, and April 2, 2010, a total of 30 trials were conducted to check the table performance and feasibility of 4 different ground motions from the PEER NGA database [11]. These ground motions were selected from the motions discussed in Section 2.1.

3.3.1 Fidelity Test Setup

To verify the shaking table performance, it is important to have the fidelity test setup similar to the intended dynamic test specimen. Even though it is practically not feasible to achieve the horizontal and vertical periods comparable to those of the real specimen, the over-turning moment due to the height of the center of gravity (C.G.) which is one of the main factors that affect the table performance under vertical and horizontal excitation inputs can be controlled by stacking mass blocks and supporting steel beams.

The geometrical scale of the setup corresponds to the ¼-scaled prototype. The total weight is 118 kips (525 kN) and the C.G. is 9 ft (2.74 m) above the table (Fig. 3.1 and Fig. 3.2). Locations of the instruments placed on the shaking table and the mass blocks are shown in Fig. 3.3. Since the specimen is a ¼-scale specimen (length scale= S_L = prototype length/model length= 4), each ground motion is compressed in time using a factor of $\sqrt{S_L}$ =2.

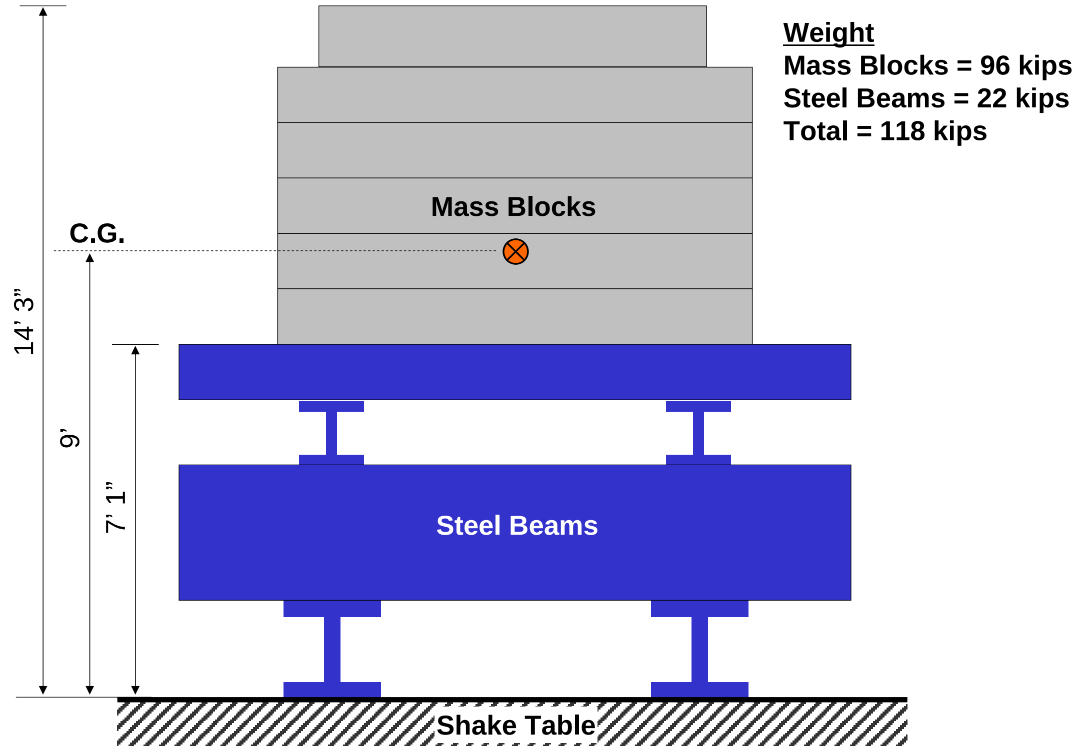

Fig. 3.1 Schematic of the fidelity test setup (1′=305 mm, 1″=25.4 mm)

Fig. 3.2 Photograph of the fidelity test setup

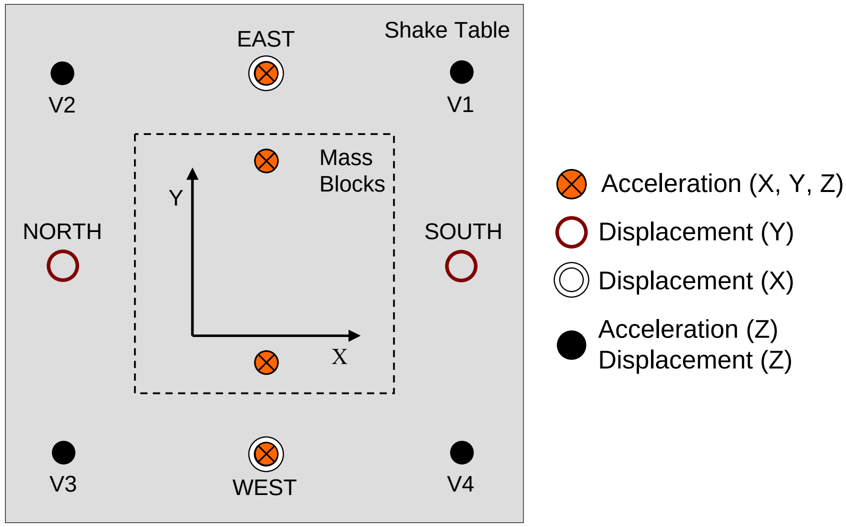

Fig. 3.3 Shaking table plan, axes, and instrumentation for the fidelity tests

3.3.2 Input Ground Motion Candidates and Scale Factors

The ground motions listed in Table 3.2 are selected based on the analysis using a full-scale single-column model with the aspect ratio of 3.5 (refer to Chapter 2). GM 1, 2, 3, 5, 7, and 9 (earthquake records #3, 1, 15, 9, 4, and 7, respectively, in Table A.1) are selected from the 80 ground motions, which satisfy the 1st and 2nd criteria in Section 2.1, based on the capacity reduction calculated using the ACI equation (*RedACI*<0.8), and based on comparison of demand and capacity history. GM 4, 6, 8, and 10 (earthquake records #10, 8, N/A (because it belongs to the 80 records not the 61 records listed), and 28 in Table A.1) are added since the ductility demand is high even though they are not selected based on the *Red* and *Maxdcr* values. It should be noted that X-component produces more significant effect on *Red, Maxdcr* and displacement ductility, rather than Y-component. Therefore, only *PGA* for X-component is specified in Table 3.2.

Table 3.2 10 Selected ground motions for the fidelity tests

GM	RSN	EQ Name	YYMMDD	Station	*PGA* [g] (unfiltered)	
					X	Z
1	126	Gazli, USSR	760517	Karakyr	0.61	1.26
2	495	Nahanni, Canada	851223	Site 1	0.98	2.09
3	752	Loma Prieta	891018	Capitola	0.53	0.54
4	825	Cape Mendocino	920425	Cape Mendocino	1.50	0.75
5	879	Landers	920628	Lucerne	0.73	0.82
6	982	Northridge-01	940117	Jensen Filter Plant	0.57	0.82
7	1051	Northridge-01	940117	Pacoima Dam (upper left)	1.58	1.23
8	1054	Northridge-01	940117	Pardee-SCE	0.66	0.38
9	1063	Northridge-01	940117	Rinaldi Receiving Station	0.83	0.83
10	1085	Northridge-01	940117	Sylmar-Converter Sta. East	0.83	0.38

Since the performance of the shaking table needs to be verified for the entire intensity level range which will be applied in the dynamic tests, magnitude scales for different intensity levels should be determined. These scales are calculated as follows based on the analyses results from the parametric study in Chapter 2:

1. Nonlinear time history analyses of the full-scale single-column are conducted using the full scale ground motions with the larger of the two horizontal components (referred to as X component) and the vertical (Z) component. The force reduction factor (R) is calculated from the obtained ductility values, μ, based on the equal energy assumption by Newmark and Hall [33], i.e. $R = \sqrt{2\mu - 1}$. The scale factor for 'Yield Level' is subsequently calculated as $1/R$.
2. Since significant strain hardening is expected, the maximum considered earthquake (MCE) level is assumed to correspond to ductility=2, hence the force reduction factor corresponding to MCE level (R_{MCE}) is calculated as $\sqrt{2 \times 2 - 1} = 1.73$.
3. The scale factor for MCE is calculated as R_{MCE} multiplied by the scale of the yield level which is equal to 1.73/R.
4. For simplicity and to preserve the basis of the selection criteria mentioned in Section 2.1, the scale factors determined for the horizontal components using the above procedure are utilized for the vertical components as well.

It should be noted that the MCE level was not determined using the typical method of site-specific pseudo-acceleration, S_a, from the USGS maps at low and high periods and then finding S_a at the specific period, because the site of the prototype bridge resulted in small S_a values. Instead of choosing another site, the MCE level was determined based on the response. In addition, although the maximum ductility achieved in the real tests were about 5 in the dynamic tests with the actual specimen as presented in Table 4.1, the scales determined using the assumption of ductility=2 (as mentioned in item 2 above) was sufficient to evaluate the table performance, since the scales determined in this manner resulted in accelerations close to the table limits.

After further elimination based on the demand and capacity histories, GM 1, 5, 7, and 9 were utilized in the fidelity tests with the determined scales (in terms of the target PGA after filtering, as mentioned below) listed in Table 3.3. As mentioned before, all ground motions are compressed in time using a factor of 2. The ground motions are filtered using a filter range of 0.6~30 Hz for the X components and 2~60 Hz for Z components to accommodate the displacement limits of the shaking table.

Table 3.3 Properties of the finally selected four ground motions for the fidelity tests

GM	RSN	EQ Name	Station	Target PGA [g] (filtered)			
				Yield Level		MCE Level	
				X	Z	X	Z
1	126	Gazli, USSR	Karakyr	0.48	0.96	0.83	1.66
5	879	Landers	Lucerne	0.41	0.64	0.71	1.11
7	1051	Northridge-01	Pacoima Dam (upper left)	0.98	0.78	1.70	1.35
9	1063	Northridge-01	Rinaldi Receiving Station	0.25	0.26	0.44	0.44

3.3.3 Fidelity Test Results

Among the four ground motions shown in Fig. 3.4 to Fig. 3.14, GM7 seems to be the most suitable input given the shaking table performance. In these figures, the expected natural period range of the test specimens and its elongation due to damage is identified in terms of the important frequency range (in this study) using double headed horizontal arrows. In addition, In addition, the legend “f-measured” in these figures stands for the filtered measured data. As discussed, the shaking table does not reproduce frequencies over the entire range in the vertical direction. For example, for each ground motion, the response spectrum of the measured vertical acceleration has a sharp peak at 5~15 Hz and a valley at 15~30 Hz and another peak around 45 Hz. Therefore, ground motions with spectra like GM1 (Fig. 3.4 and Fig. 3.5), GM5 (Fig. 3.6 and Fig. 3.7), or to a lesser extent GM9 (Fig. 3.11 to Fig. 3.14) is not suitable to be replicated on the UC-Berkeley shaking table. In most cases, the measured horizontal acceleration spectra are much more similar to the target spectra, compared to the case of the vertical spectra.

Results of GM7 0.5-yield, yield, and MCE levels are shown in Fig. 3.8, Fig. 3.9, and Fig. 3.10, respectively. The corresponding scale factors are 0.33, 0.66, and 1.14 compared to the originally recorded motion. In the important frequency range defined by the horizontal double headed arrow, the shaking table has an acceptable performance in matching the target spectra for yield and MCE levels of GM7 for both of the horizontal and vertical components.. The basic information on GM7 is in PEER NGA database [11] and Table 3.4 shows the record and station information. The Northridge earthquake occurred on January 17, 1994 in the city of Los Angeles, California. The epicenter was in Reseda and the hypocenter latitude and longitude were 34.2057 and -118.554, respectively.

The strong motion response of Pacoima Dam was recorded by a network of California Division of Mines and Geology (CDMG) accelerometers. Pacoima Dam is a concrete arch dam which is 365 ft (111.25 m) high and has a thickness at the crown cross-section that varies from 10.4 ft (3.17 m) at the crest to 99 ft (30.18 m) at the base. GM7 was recorded at the station on the left abutment and its peak acceleration was 1.5g. Considering the peak acceleration at a downstream location was 0.44*g* and that at 80% of the height was 2.3*g*, frequency-dependent topological amplification affected the ground motion significantly as mentioned in Fenves and Mojtahedi [34] and Alves [35]. The motion of the dam has higher frequency components than those at the base or downstream. Moreover, Alves [35] points out that the ground motion delays are consistent with the seismic waves traveling upward along the canyon, and that the waves appear to be dispersive because the delays are frequency-dependent. Fenves and Mojtahedi [34] presumed that higher frequency components were possibly caused by higher mode contributions of the dam or impact due to pounding of contraction joints.

One cannot state that the GM7 obtained from the PEER NGA database [11] has higher frequency content compared to the other ground motions, i.e. GM1, GM5, or GM9, as shown in Fig. 3.4 to Fig. 3.14. In particular, the frequency content of the vertical component of GM7 mostly leans towards lower frequency range compared to the other three ground motions (refer to Fig. 3.8 to Fig. 3.10).

Table 3.4 GM7 Information

Earthquake	Northridge-01 19940117 12:31
Moment magnitude	6.69
Seismic moment	1.2162+E26 dyne-cm
Mechanism	Reverse Fault Rupture
Hypocenter depth	17.5 km
Fault rupture length/width	18.0 km / 24.0 km
Average fault displacement	78.6 cm
Fault name	Northridge Blind Thrust
Slip rate	1.5 mm/yr
Station	CDMG 24207 Pacoima Dam (upper left abutment)
Instrument housing	Earth dam (abutment)
Mapped local geology	Granitic
Geotechnical subsurface characteristics	Rock
Preferred Vs30	2016.10 m/s
Epicentral distance	20.36 km
Hypocentral distance	26.85 km
Joyner-Boore distance	4.92 km
Campbell R distance	7.01 km
RMS distance	18.60 km
Closest distance	7.01 km

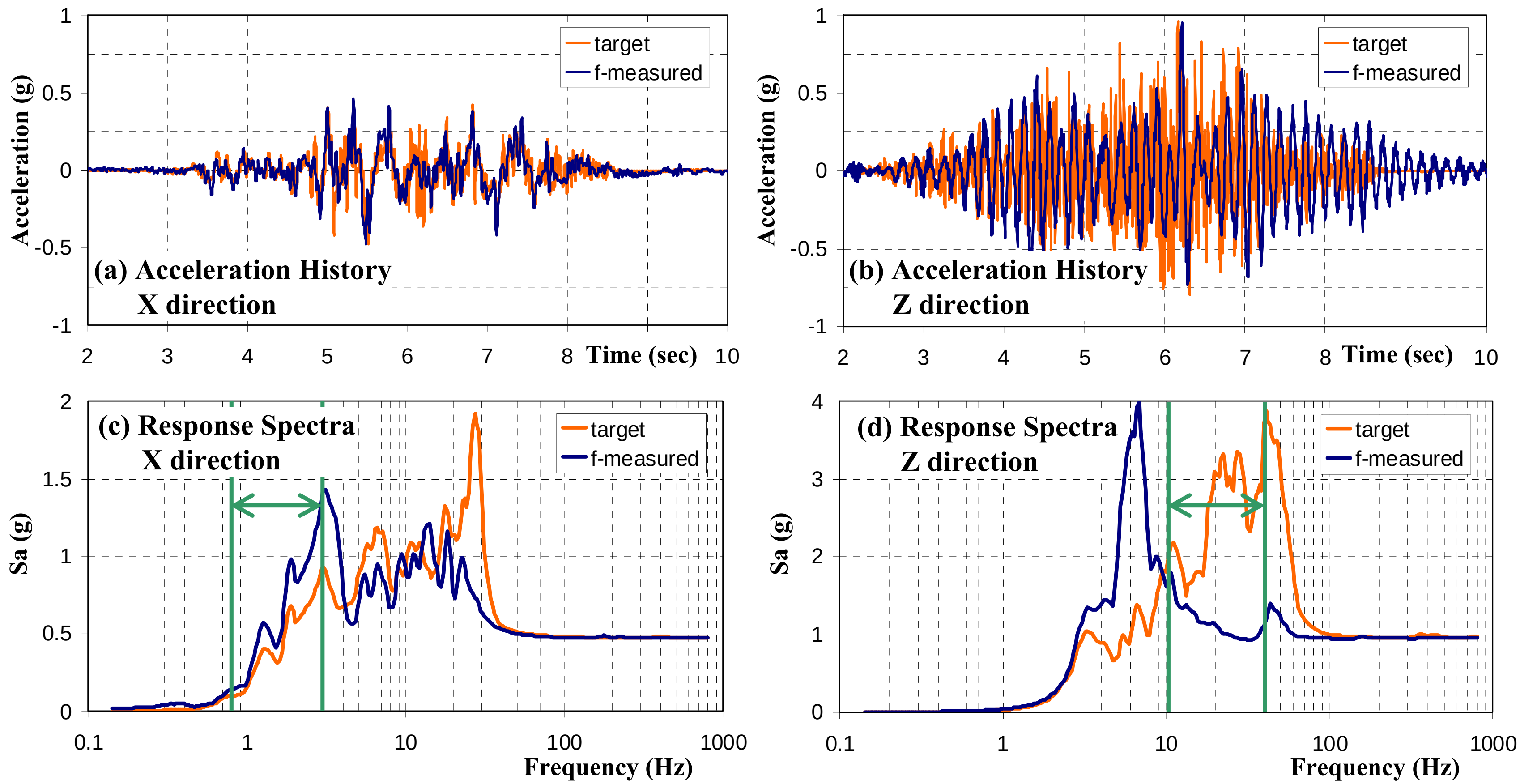

Fig. 3.4 GM1 yield level

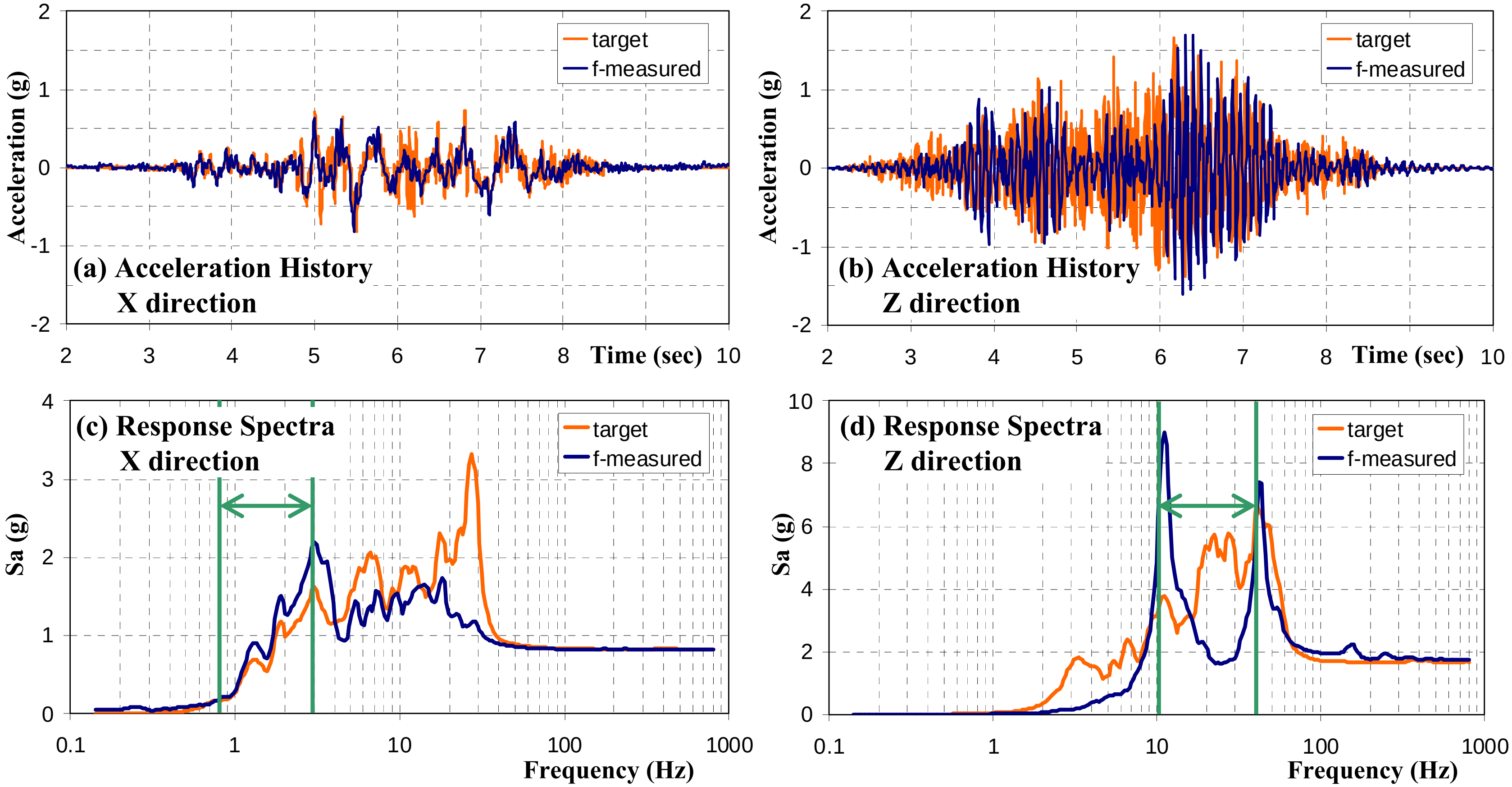

Fig. 3.5 GM1 MCE level

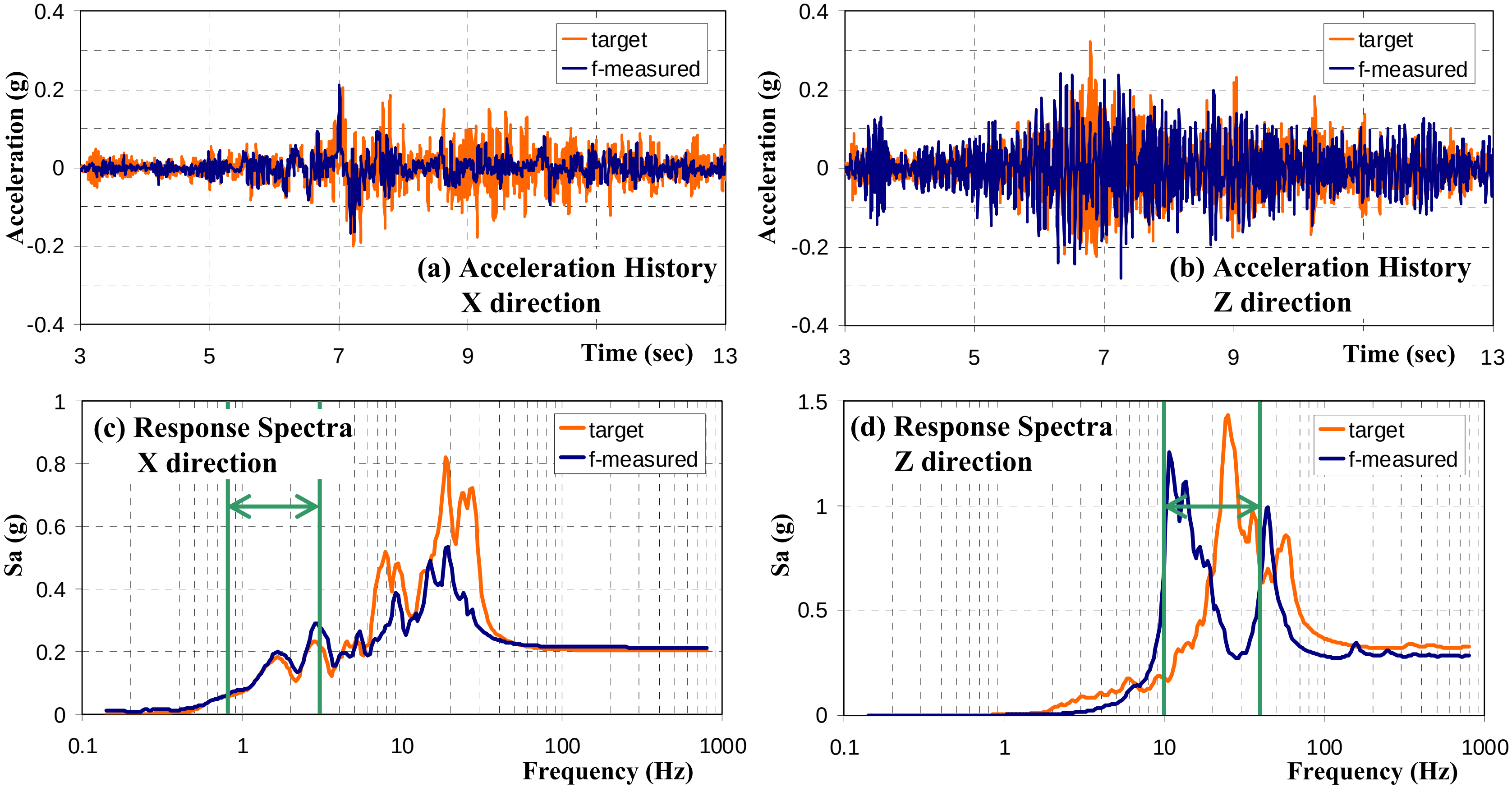

Fig. 3.6 GM5 0.5-yield level

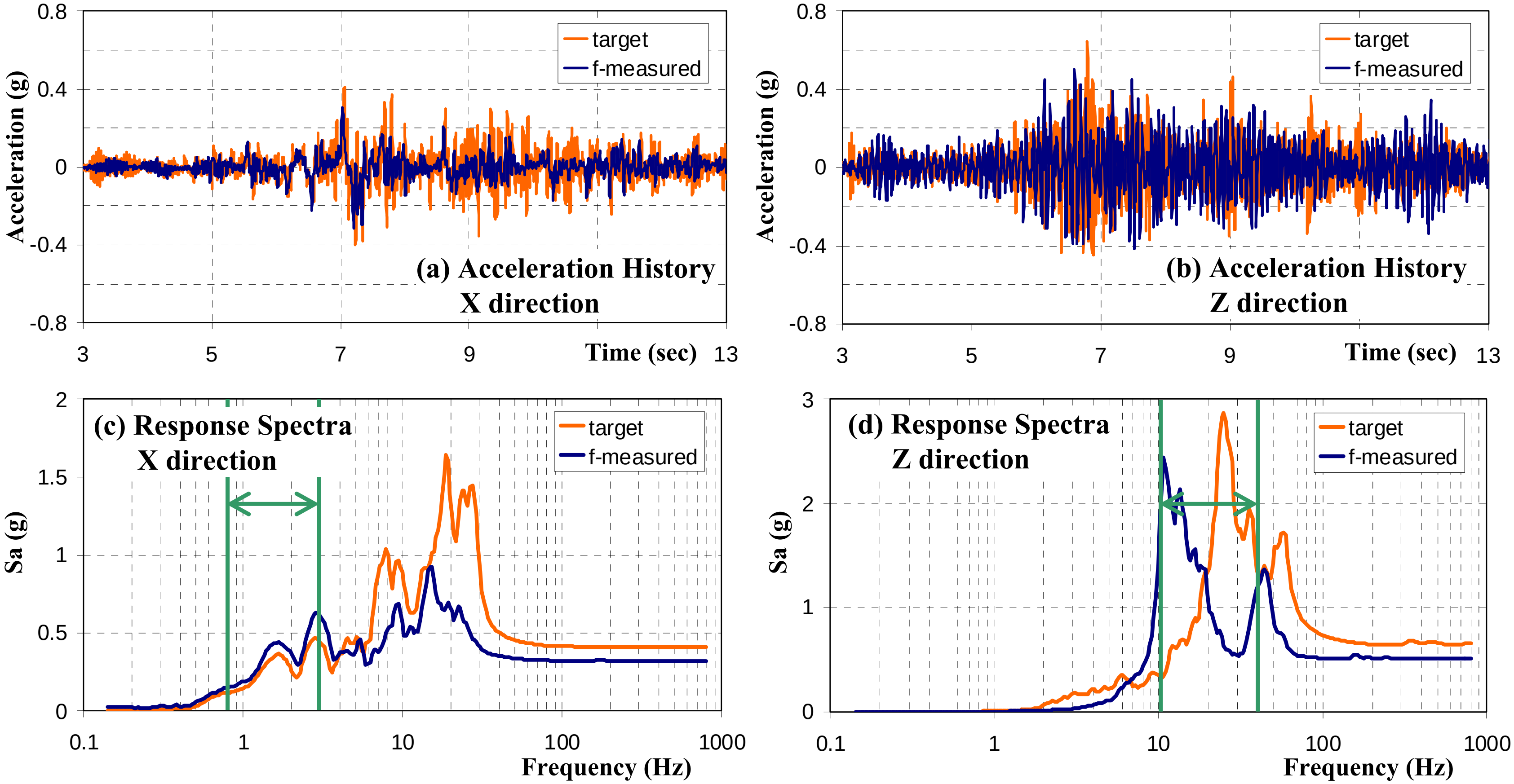

Fig. 3.7 GM5 yield level

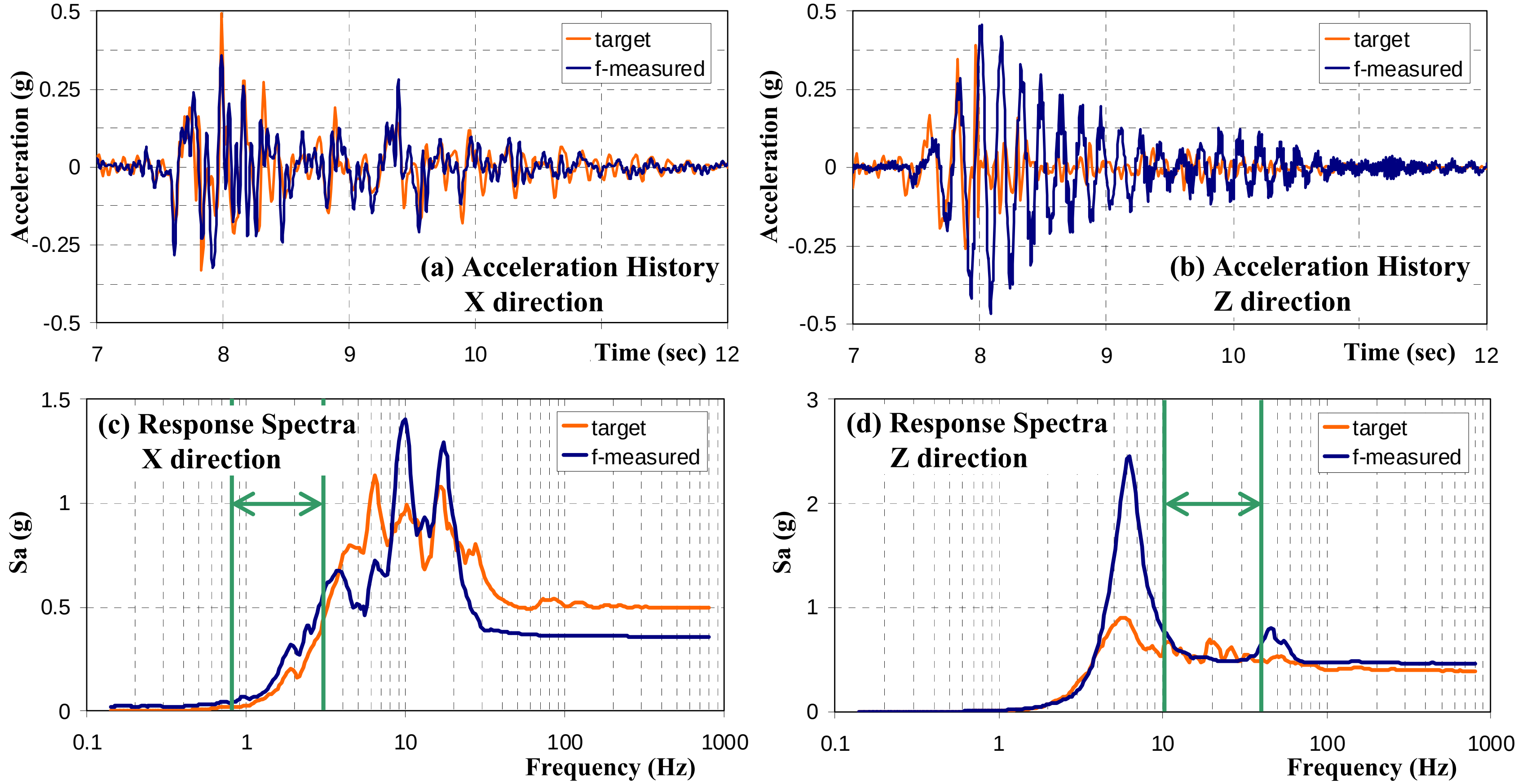

Fig. 3.8 GM7 0.5-yield level

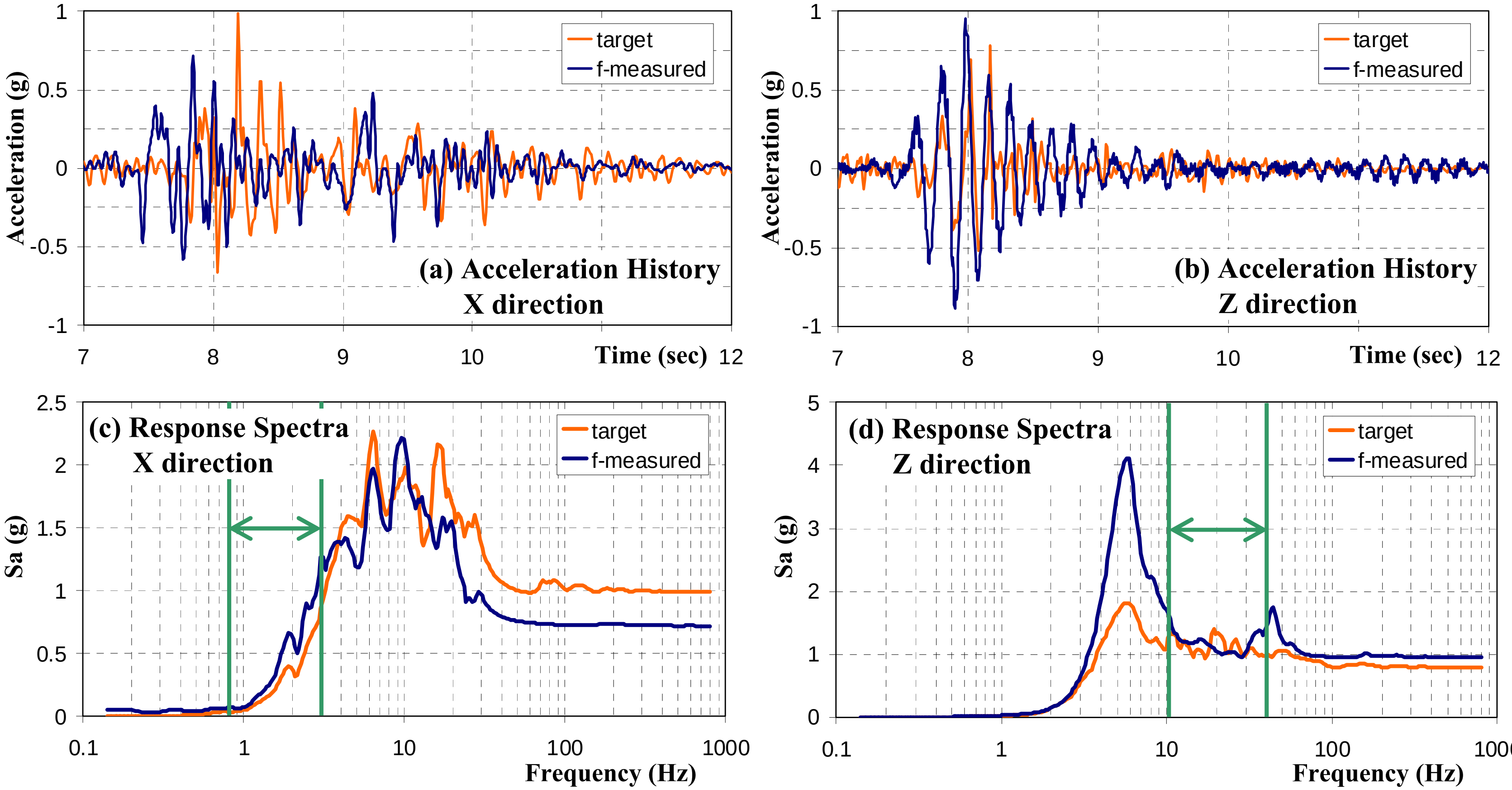

Fig. 3.9 GM7 yield level

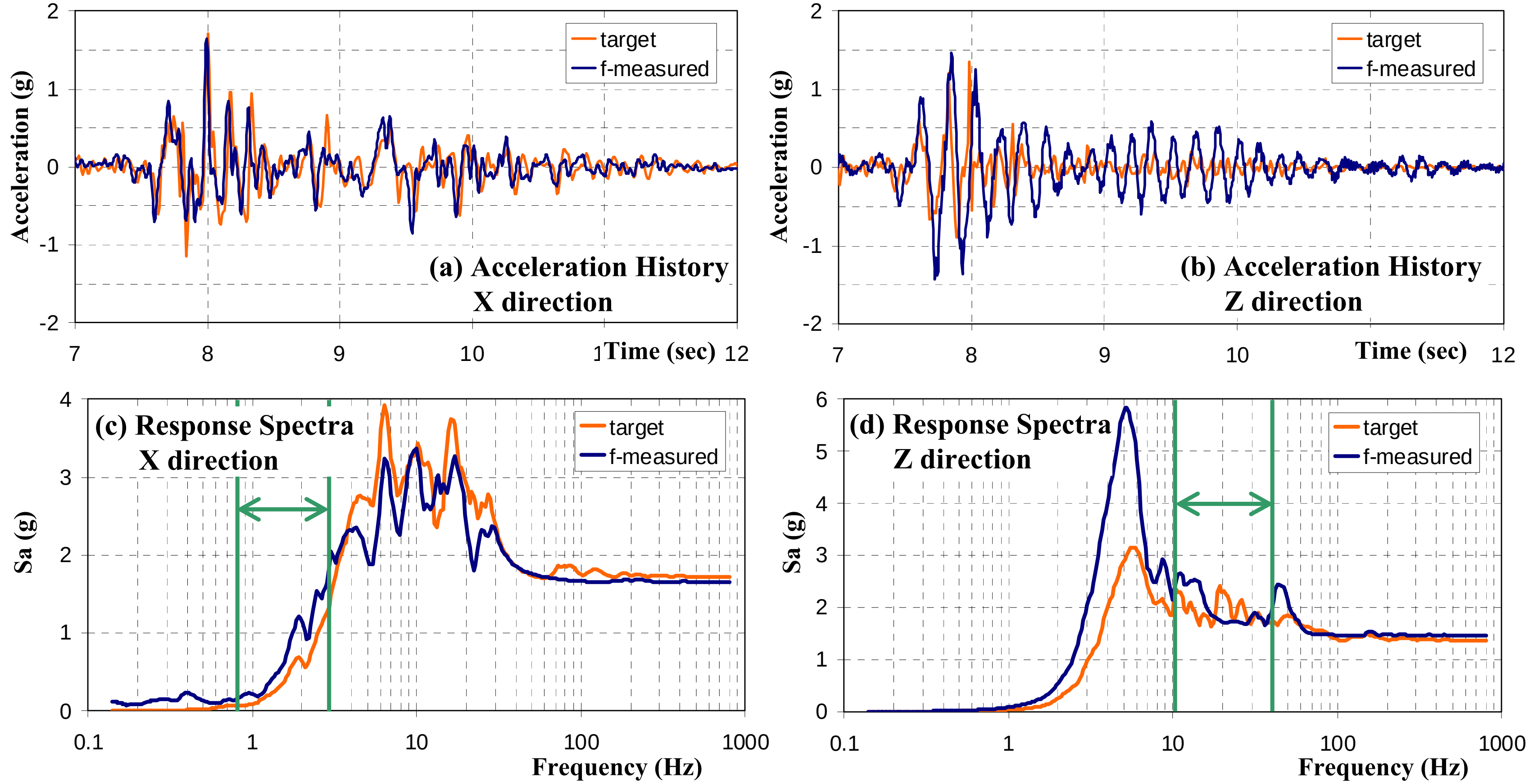

Fig. 3.10 GM7 MCE level

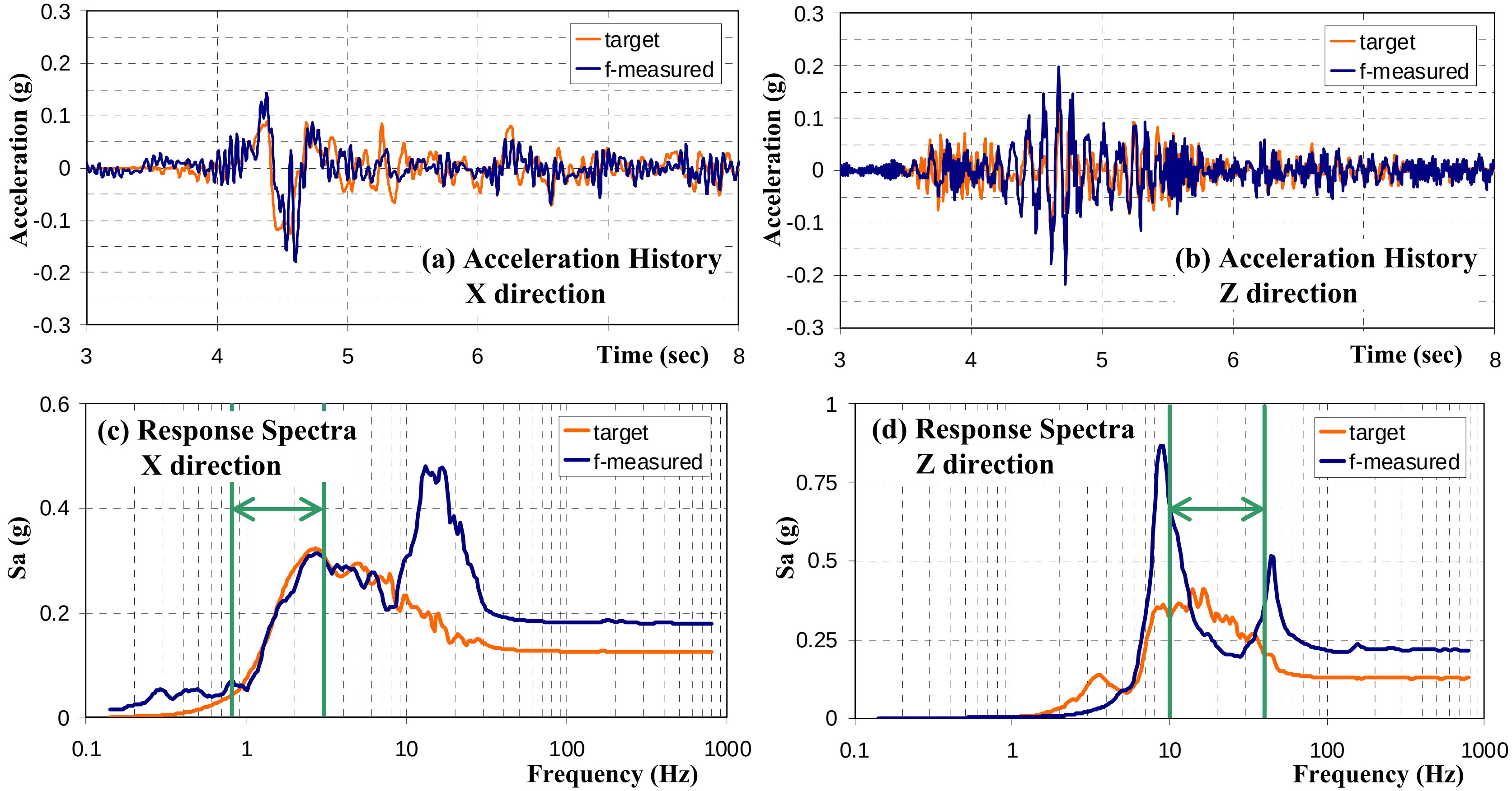

Fig. 3.11 GM9 0.5-yield level

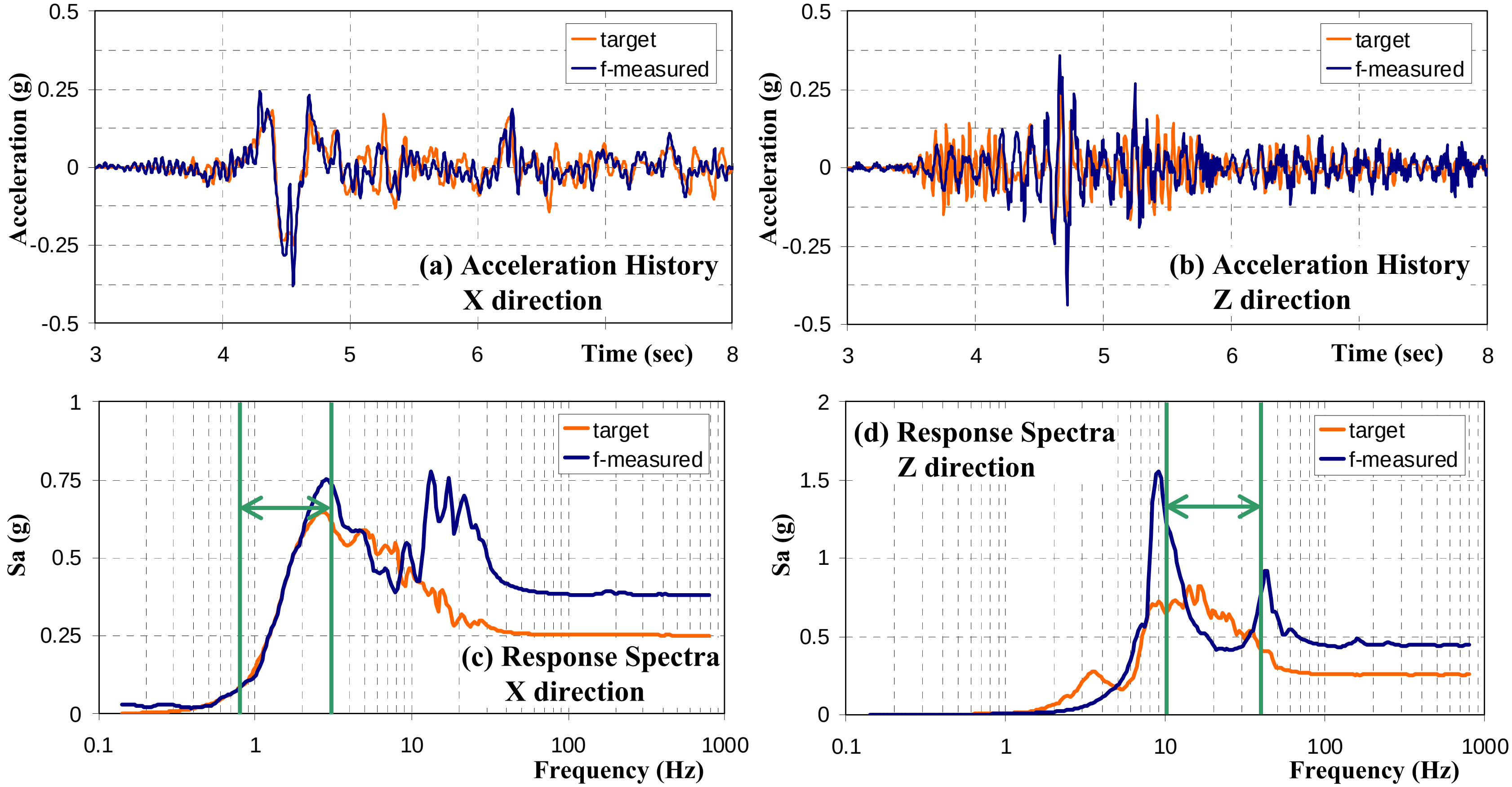

Fig. 3.12 GM9 yield level

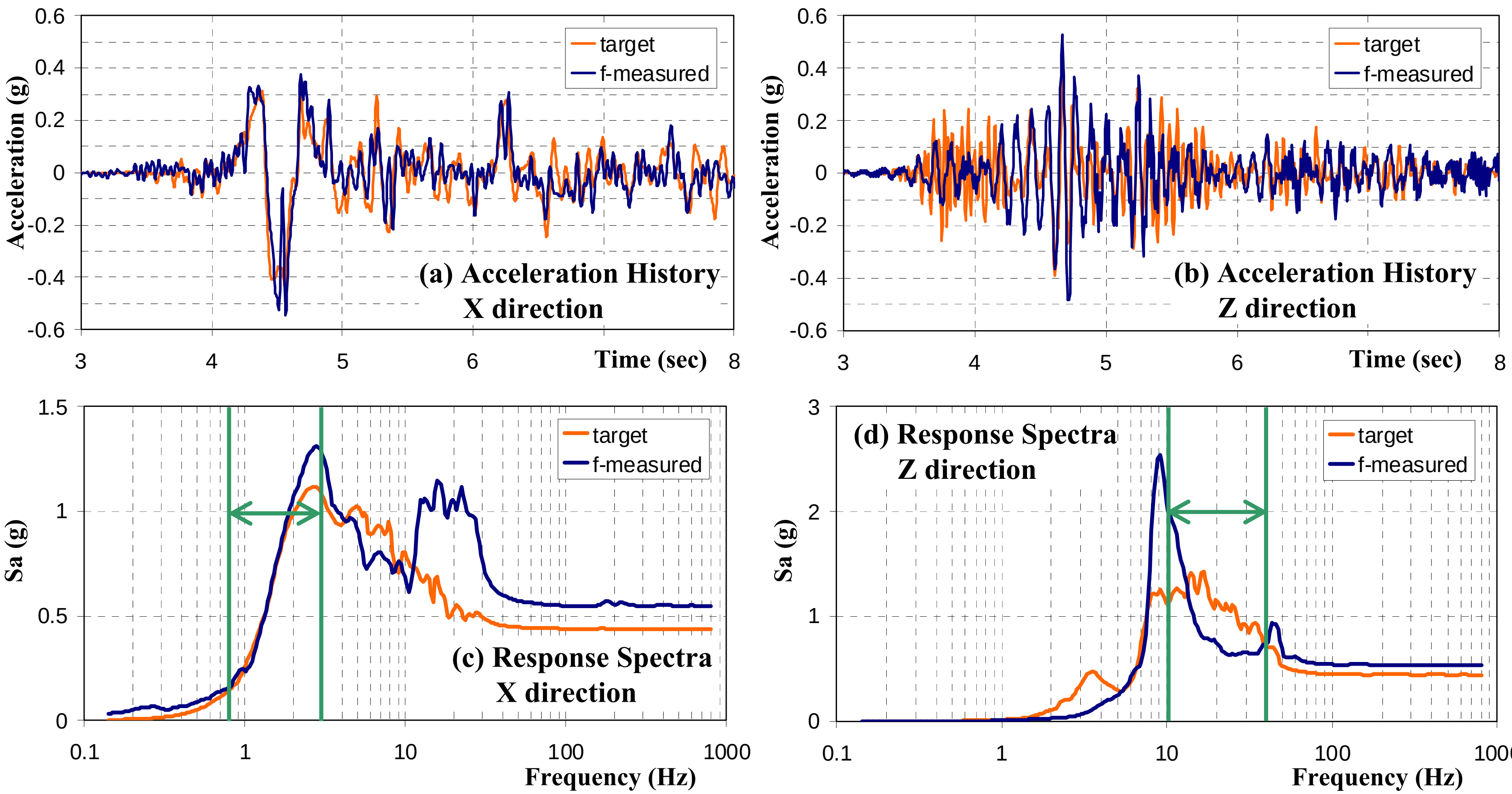

Fig. 3.13 GM9 MCE level

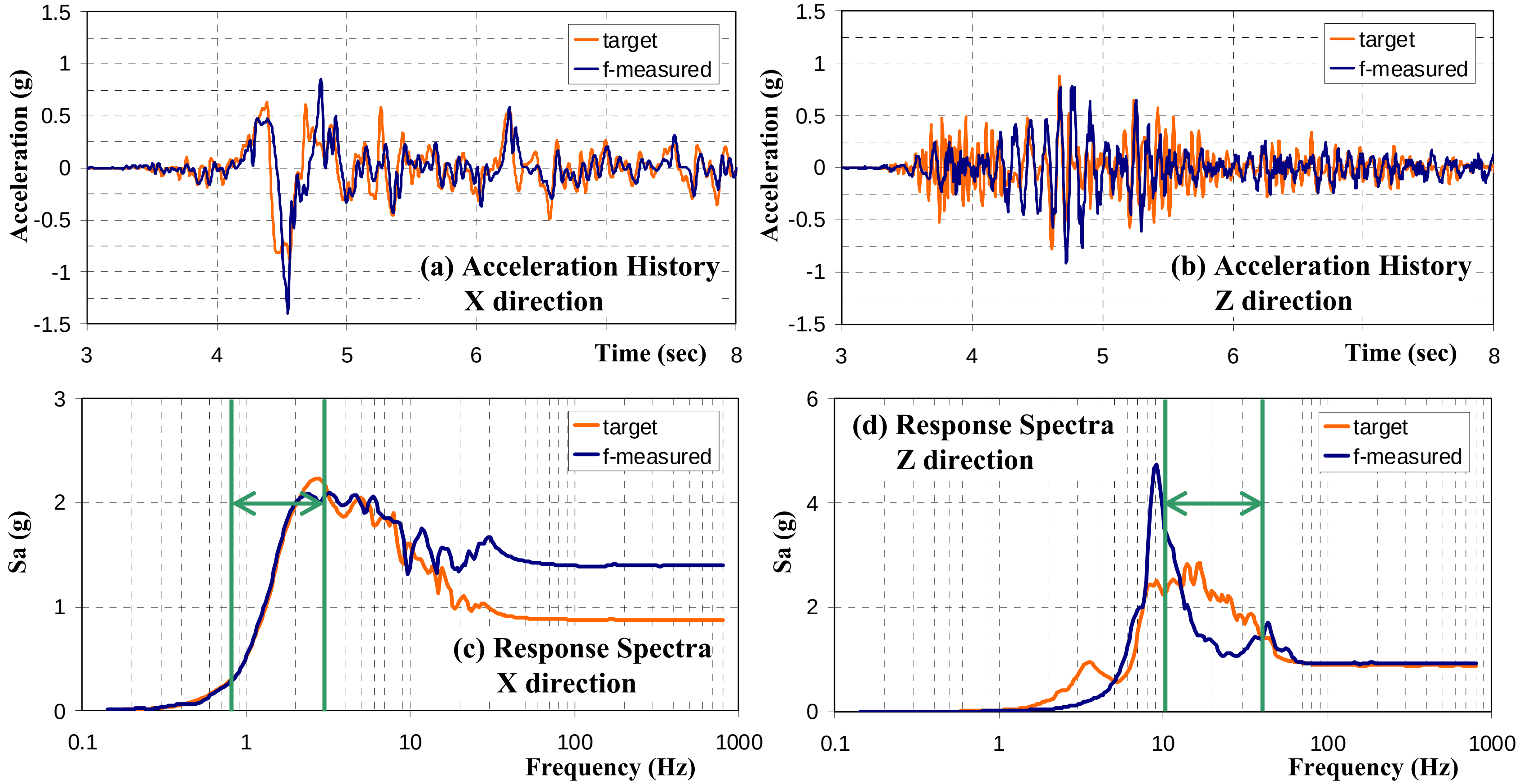

Fig. 3.14 GM9 2-MCE level

3.3.4 Further Discussion about GM7

After the completion of the fidelity tests, MCE level is determined to be the highest intensity level that can be applied with acceptable shaking table performance. This determination is based on the following calculations as explained in the next few paragraphs.

The capacity of a vertical actuator is given as 77 kips (342.5 kN). There are 4 vertical actuators and they should resist (a) the vertical force due to vertical acceleration applied on the shaking table and test setup and (b) that due to horizontal acceleration of the test setup, ignoring the damping force for simplicity. The vertical force mentioned in (a) above is expressed as $(m_t a_t + m_s a_s)$ where m_t, m_s, a_t, and a_s are the shaking table mass, test setup mass, vertical acceleration measured on the shaking table, and vertical acceleration measured on the mass blocks, respectively. This vertical force in (a) can be approximately expressed as $(m_t + m_s)a_t$ for all four vertical actuators because $a_t \approx a_s$ in most cases. On the other hand the vertical force mentioned in (b) above is expressed as $\pm m_s a_s h/2l$ where h and l are the height of the C.G. (9 ft (2.74 m)) and the arm length between the opposite two pairs of the vertical actuators (17 ft (5.18 m)). Therefore, two different equations can be defined, Eqs. (3.1a) and (3.1b), determining the axial force demand of each vertical actuator. Fig. 3.15 shows the history of the axial forces calculated by using these equations and it can be observed that they both exceed the actuator force limit of 77 kips (342.5 kN) during short durations.

$$P = (m_t + m_s)a_t/4 + m_s a_s h/2l \tag{3.1a}$$

$$P = (m_t + m_s)a_t/4 - m_s a_s h/2l \tag{3.1b}$$

Since the forces are not obtained as a result of direct measurements but through calculation using Eqs. (3.1a) and (3.1b), the exceedance of the actuator force limits is further validated through an alternative calculation. Considering the shaking table weight is about 100 kips (445 kN), it is reasonable to accept that the acceleration limit of the empty shaking table (i.e. without any test specimen) is about 3g (precisely, $77 \times 4/100 = 3.08g$). The total fidelity test setup and shaking table weight is 218 kips (970 kN). Therefore, the maximum achievable vertical acceleration is $77 \times 4/218 = 1.41g$. Fig. 3.16 shows this limit and the acceleration history of each vertical actuator. It can be observed that the actuators on the north side (V2 and V3) tend to have larger acceleration values than those on the south (V1 and V4), but both pairs exceed the average limit of 1.41g.

Although the calculated forces and measured accelerations of the individual actuators are slightly higher than the indicated limits for very short durations of time, the average measured accelerations of all four vertical actuators are below the limit. Fig. 3.17 compares the average vertical acceleration history of the four actuators below the table and that measured on the east and west sides on the shaking table (accelerometers in Fig. 3.3). The plotted time histories are slightly below the shaking table limits with a small margin. Hence, for good performance of the shaking table in this study, MCE of GM7 for the specified mass and C.G. height of the test specimen is considered as the maximum excitation level that can be applied. It should be noted that all the vertical acceleration data used in Fig. 3.15 to Fig. 3.17 were filtered and the filter range was [0.01, 40] Hz.

The fidelity tests revealed the following remarks:

- The performance of the UC-Berkeley shaking table is acceptable with the proposed mass and C.G. height of the ¼-scale test specimen. Therefore, the proposed ¼-scale specimen is feasible unless bigger mass or higher C.G is utilized.
- Among the four ground motions which were selected based on the analytical study, GM7 is the most suitable for the dynamic tests with vertical excitation considering the shaking table characteristics.
- GM7 MCE level is the highest level that is applied in the fidelity tests and the response spectra suggest that the shaking table performance is still acceptable. However, this intensity level is found to be near the limits of the shaking table based on the measured vertical accelerations. Hence, sufficient performance is not expected if a stronger excitation is applied, or if a bigger mass or higher C.G is utilized. Therefore, GM7 MCE level and the fidelity setup mass and C.G height are considered as defining the upper limit for the excitation and specimen configuration in this study.

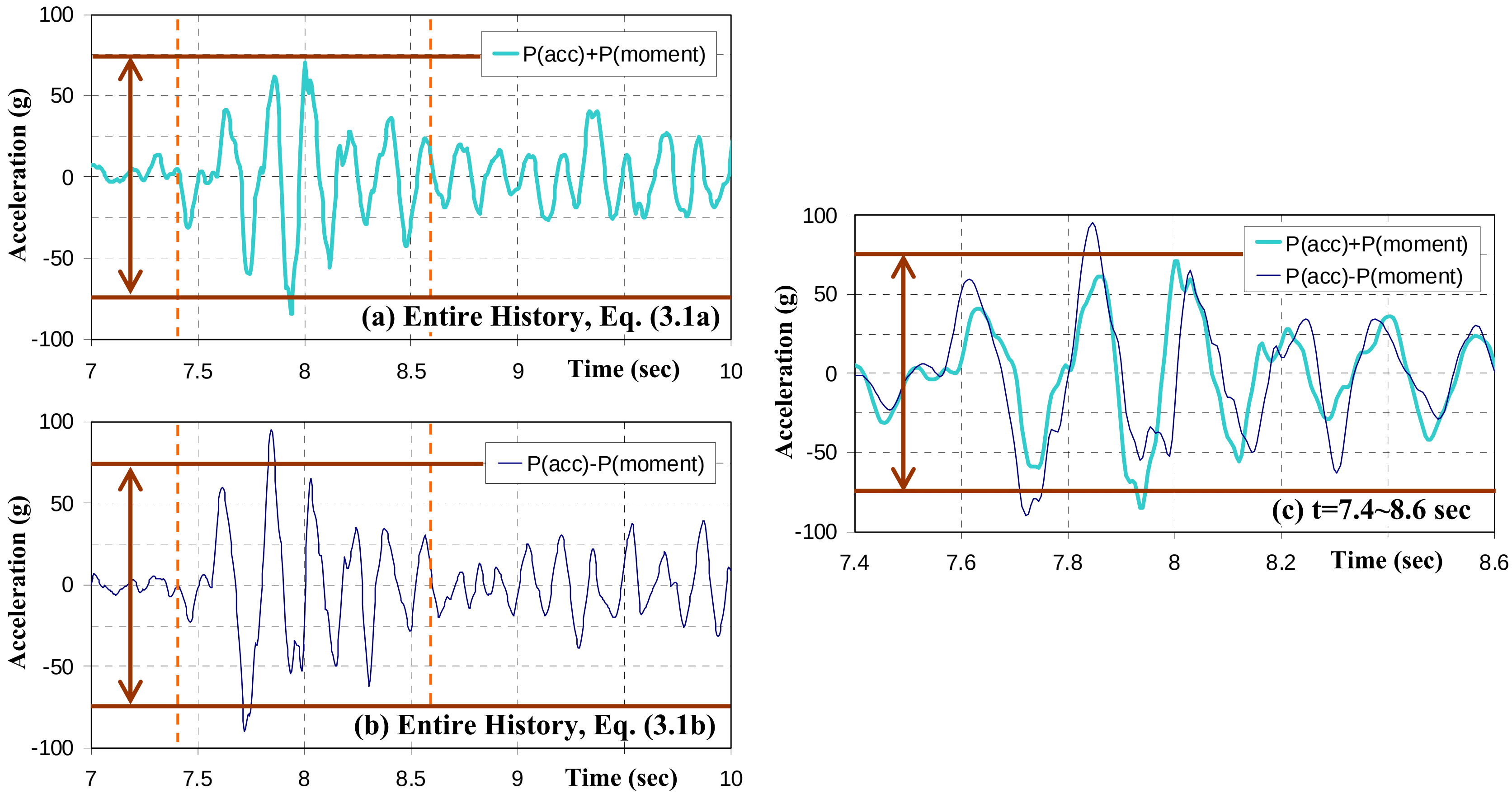

Fig. 3.15 Axial force of a vertical actuator (GM7 MCE level)

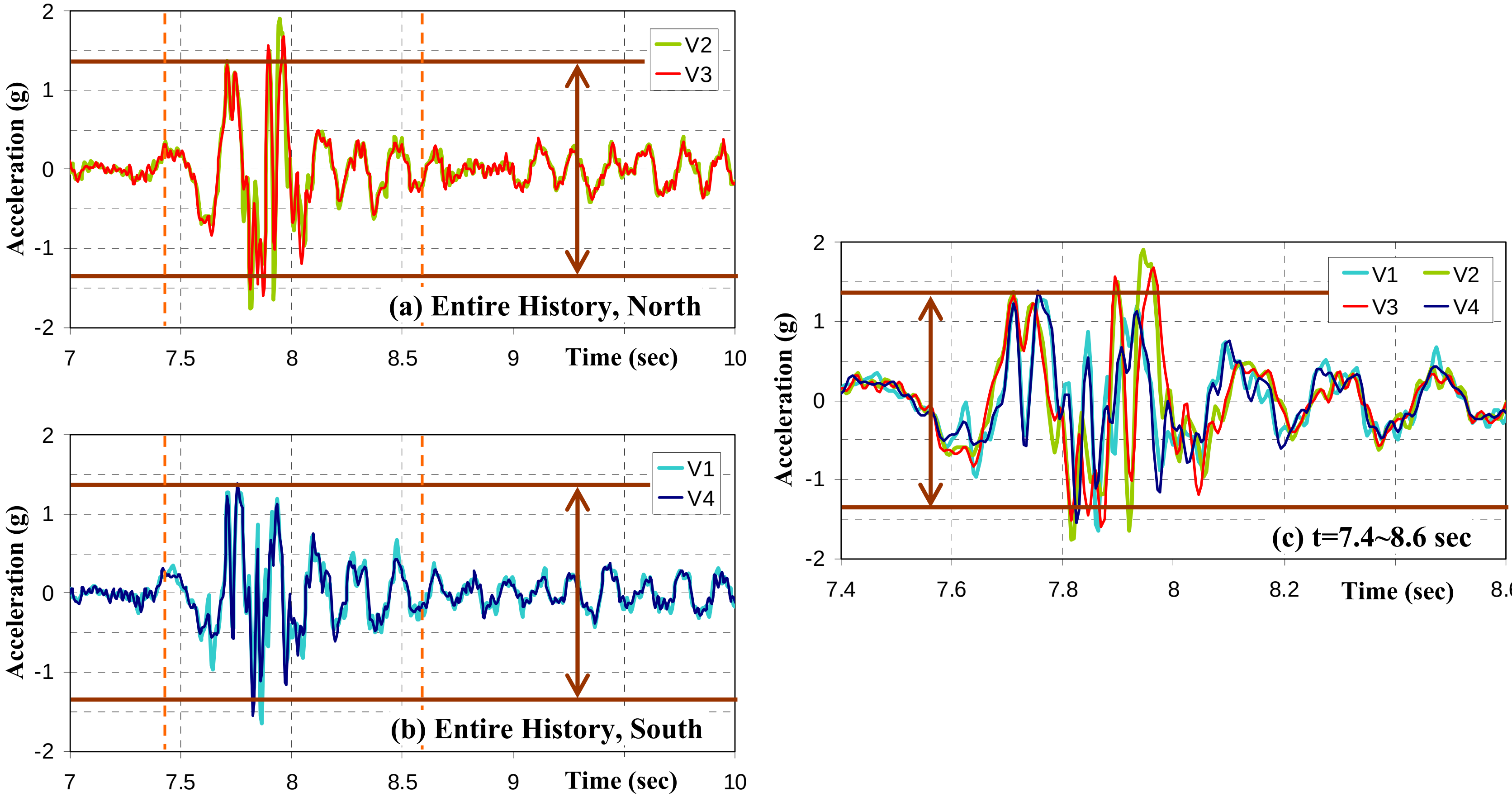

Fig. 3.16 Vertical acceleration of all vertical actuators (GM7 MCE level)

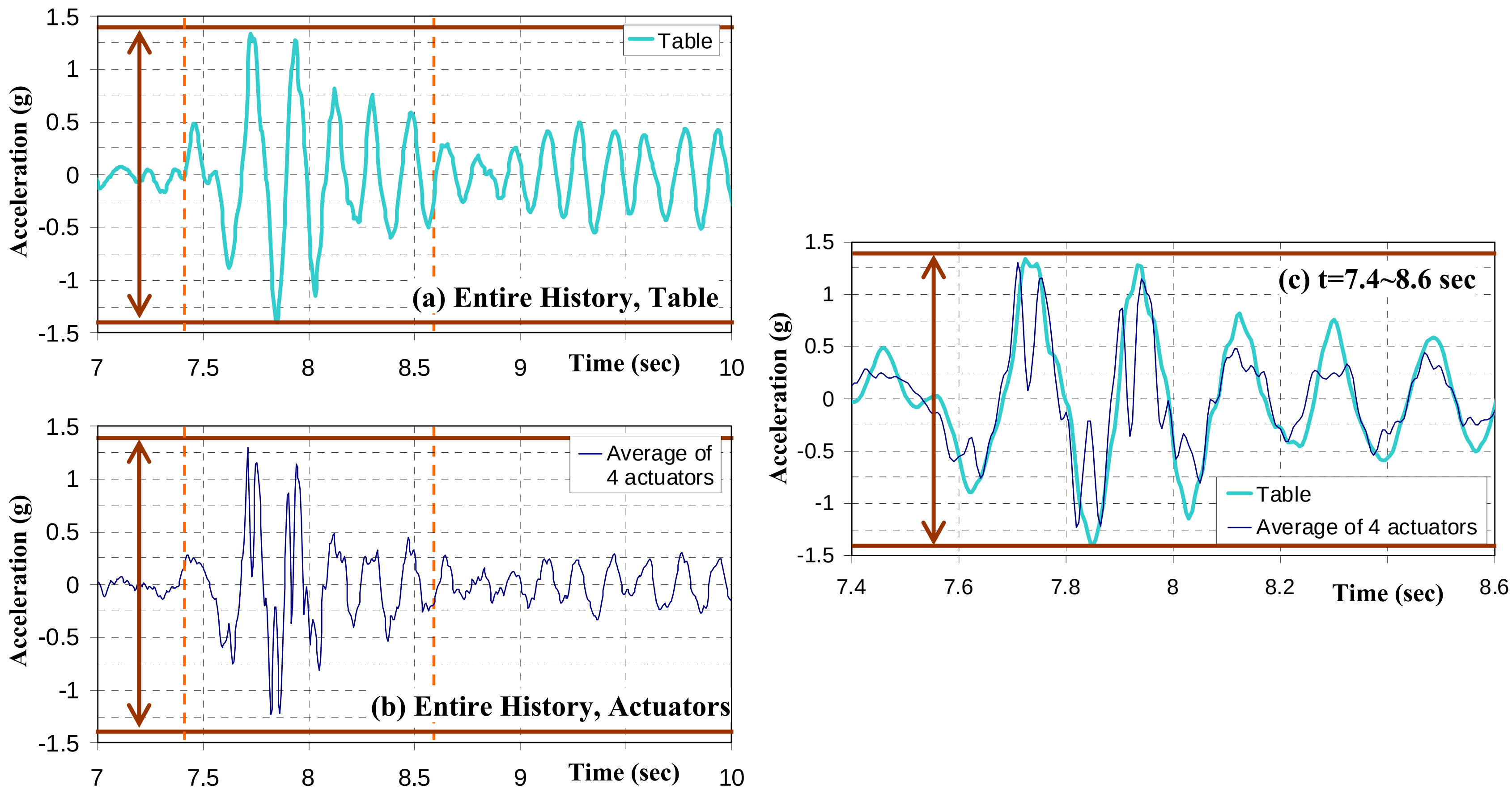

Fig. 3.17 Average vertical acceleration measured (GM7 MCE level)

3.4. Specimen Design and Construction

3.4.1 Design of Specimens

The Plumas-Arboga Overhead Bridge (PAOB) is the selected prototype for designing the test specimens, since its aspect ratio is closer to the desired value than that of ACB. It should be noted that ACB is the prototype for the parametric study in Chapter 2, not for the test specimen. In Section 2.2.2, the superstructure, original column cross-section and modified effective circular column cross-section of the prototype were described. The circular cross-section is scaled down using a scale of ¼ for the test specimen.

A column with a low aspect ratio (H/D) is expected to show shear or flexure-shear behavior. As discussed in Section 2.5.1, *Maxdcr* tends to increase as the aspect ratio decreases. To represent real bridge columns constructed in California, an aspect ratio of 3.5 is used in the test specimen for the dynamic tests.

3.4.1.1 Cross-Section Properties

Two specimens were designed and the design properties are identical except for the transverse reinforcement ratio. The comparisons of cross-section properties are summarized in Table 3.5. Section A is the cross-section of the PAOB. Sections B and C are the cross-sections of the 1st and 2nd specimens (SP1 and SP2), respectively. These cross-sections are illustrated in Fig. 3.18.

Confined concrete properties (peak stress and strain, $f'_{cc}, \varepsilon_{cco}$, respectively, and ultimate stress and strain, $f'_{ccu}, \varepsilon_{ccu}$, respectively) for each cross-section are calculated based on Mander's model [29]. M_{max} of each cross-section was calculated assuming the yield strength of the longitudinal and transverse reinforcing bars f_y, f_{yt}, respectively, of 60 ksi (413.7 MPa) and the aspect ratio (AR) of 3.5. V_s and V_c were calculated based on the ACI equations as defined in Chapter 2.

In Table 3.5, the concrete contribution to the shear capacity, V_c, for the 'maximum tension' and 'gravity only' are specified. Assuming the pseudo-acceleration of GM7 MCE level (corresponding to 114% of the original record) at 0.03 sec with 2% damping as 1.98*g*, the maximum tension was estimated. The vertical period, 0.03 sec, was calculated from the mass configuration in Section 3.4.1.2 and from axial stiffness *EA/L*.

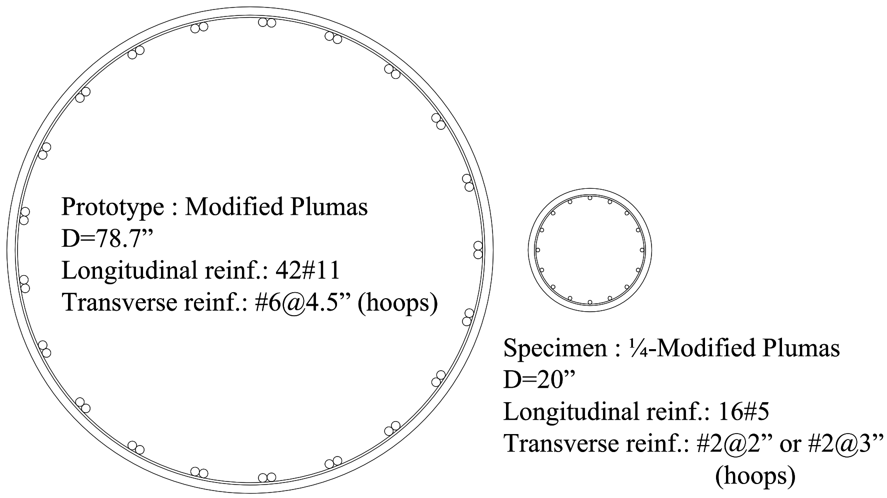

Fig. 3.18 Prototype and test specimen column cross-sections (1″=25.4 mm)

3.4.1.2 Mass and Mass Moment of Inertia

Mass at the top of the test specimen was determined to match 6.5% axial load ratio (ALR) as listed in Table 3.6. Mass moment of inertia (MMI) is calculated as 64.0 -m^2 (47.2×10^3 slug-ft^2) by scaling MMI of the prototype column using similitude relationships as explained in Section 3.5.1.1. MMI of the prototype column is determined such that the lateral period of the column matches the lateral period of the full scale bridge system. Mass corresponding to 6.5% ALR is used in both of the single column and bridge system models. By using the same mass and matching the modal properties, the best resemblance between the prototype column in the bridge system model and that in the single-column model was achieved. Finally, the calculated MMI for the prototype column and the test specimen are 12.084×10^6 slug-ft^2 (16384 t-m^2) and 47.2×10^3 slug-ft^2 (64.0 t-m^2), respectively. By a proper combination of concrete blocks, lead blocks, and steel beams on the test specimen, the desired weight for the intended ALR, MMI, and height of C.G. are achieved.

Table 3.5 Cross-section properties

Parameter	Unit	A. PAOB	B. SP1	C. SP2	A/B	A/C
Diameter, D	[in] ([m])	78.7 (2.0)	20 (0.508)	20 (0.508)	3.94	
Area, A	[in^2] ([m^2])	4869.5 (3.14)	314.2 (0.203)	314.2 (0.203)	15.50	
Height, H	[in] ([m])	275.6 (7.0)	70 (1.778)	70 (1.778)	3.94	
Longitudinal reinforcing bars		42#11	16#5	16#5	-	
Diameter, d_{sl}	[in] ([mm])	1.41 (35.8)	0.625 (15.875)	0.625 (15.875)	2.26	
Bar Area, A_{sl}	[in^2] ([mm^2])	1.56 (1007)	0.307 (197.9)	0.307 (197.9)	5.09	
Total Area, A_s	[in^2] ([mm^2])	65.52 (42310)	4.909 (3166.9)	4.909 (3166.9)	13.36	
Reinf. Ratio	[%]	1.348	1.563	1.563	0.862	
Transverse reinforcing bars		#6@4.5″	#2@2″	#2@3″	-	
Diameter, d_{sh}	[in] ([mm])	0.75 (19)	0.25 (6.35)	0.25 (6.35)	3.0	
Bar Area, A_{sh}	[in^2] ([mm^2])	0.44 (283.5)	0.0491 (31.68)	0.0491 (31.68)	9.0	
Spacing, s	[in] ([mm])	4.5 (114.3)	2 (50.8)	3 (76.2)	2.25	1.5
Vol. Reinf. Ratio	[%]	0.543	0.545	0.363	0.996	1.496
$A_v D/s$, $A_v = 2A_{sh}$	[in^2] ([mm^2])	15.39 (9929.2)	0.982 (623.4)	0.655 (415.6)	15.7	23.5
Confinement: f'_c = 4 ksi (27.58 MPa)						
f'_{cc}	[ksi]	4.98	5.02	4.68	0.992	1.064
f'_{ccu}	[ksi]	4.31	4.33	3.97	0.995	1.086
ε_{cco}	-	0.00446	0.00456	0.00371	0.978	1.202
ε_{ccu}	-	0.01187	0.01241	0.00961	0.956	1.235
Capacity (6.5% axial load)						
M_{max}	[k-ft] ([kN-m])	15047.2 (20404)	233.0 (316.0)	230.3 (312.3)	64.57	65.33
V_s	[kip] ([kN])	756.5 (3364.8)	46.5 (206.8)	31.0 (137.8)	16.27	24.42
$V_{c,\min}$ (max tension)	[kip] ([kN])	307.7 (1368.8)	19.85 (88.29)	19.85 (88.29)	15.50	
$V_{c,\max}$ (gravity)	[kip] ([kN])	709.0 (3153.4)	45.74 (203.45)	45.74 (203.45)	15.50	
$V_{n,\min} = V_s + V_{c,\min}$, $V_{n,\max} = V_s + V_{c,\max}$	[kip]	1064.2, 1465.5	66.35, 92.24	50.85, 76.74	16.04, 15.89	20.93, 19.10

Table 3.6 Mass of the ¼-scale test specimen

Item	Unit	SP1 and SP2		
Diameter	[in] ([m])	20 (0.508)		
Area	[in^2] ([m^2])	314.2 (0.203)		
f_c'	[ksi] ([MPa])	4.0 (27.58)		
$A_g f_c'$	[kip] ([kN])	1256.8 (5590.0)		
Axial Load Ratio (ALR)	[%]	4.5	5.0	6.5
ALR× $A_g f_c'$	[kip] ([kN])	56.6 (251.5)	62.8 (279.5)	81.7 (363.3)

3.4.2 Construction of Specimens

Two specimens were constructed from July 8 to July 28, 2010. The construction procedure includes installing strain gages on the reinforcing steel bars, form-work, making reinforcing bar cages, placing the desired concrete mix, curing the cast concrete, stripping the forms, and finally transporting the specimen and attaching it to the shaking table. Detailed construction procedure and construction photographs are presented in Appendix B.

3.4.3 Material Properties

For reliable estimation of the capacity of test specimens, material properties were obtained by conducting material tests for the standard concrete cylinders and samples of the reinforcing steel bars. These material tests were conducted in the material and structure laboratory, Davis Hall, UC-Berkeley.

3.4.3.1 Concrete

The concrete mix was specified as normal weight concrete with the 28th-day design strength of 4 ksi (27.58 MPa). Detailed concrete mix design specifications are presented in Table 3.7. A total of 48 6″×12″ concrete cylinders were prepared at the time of column casting. Three cylinders were tested on the 7th, 14th, 20th, 28th days, the day of preliminary stiffness tests (72nd day), the days of tests (93rd and 111th days), and the 406th day, as specified in Table 3.8 where μ and σ represent the mean and standard deviation, respectively. Fig. 3.19 presents the strength maturity curve based on these cylinder tests. The strength gradually increases until the 28th day, and the mean strength reaches 85% of the design strength. However, the 2nd and 3rd cylinders on the 72nd day and all the cylinders on the 93rd days had relatively lower strength. The strength from these cylinders is significantly low even compared to expected values based on the linear interpolation between the mean values on the 28th and 111th days. Possible errors in concrete sampling and testing these cylinders are suspected to cause this discrepancy.

American Society for Testing and Materials (ASTM) specifies the procedure for concrete cylinder making and testing. Cylinder making procedure is stated in ASTM C31 [36] and was followed in this study. It is also important to obtain a sample of concrete that is representative of the concrete in the truck mixer. According to ASTM C172 [37], concrete should be sampled from the middle of the truck load. At least three portions of discharge are necessary to obtain a representative sample since the first or last discharge portions from the load will not provide a representative sample. Using the last discharge might have caused the large deviations shown in Table 3.8 and Fig. 3.19. In addition, the strength values on the 93rd day are clustered between 2.9 and 3.5 ksi. Their standard deviation is not as large as those on the 28th and 72nd days. This implies that there is a high probability there was a mistake in testing the cylinders on the 93rd day. Of course, the possibility of choosing three low-strength cylinders cannot be ignored.

Table 3.7 Concrete mix specifications

28th day strength [psi]	4.0 (27.58 MPa)
Cement	ASTM C-150 TYPE II
Fly ash	ASTM C-618 CLASS F 15%
Admixture (water reducer)	ASTM C-494 TYPE A
Cementitious sacks/yd^3	5.00
Maximum size aggregate [in]	¾ (19 mm)
Slump [in]	4 (102 mm)
Water/cement ratio	0.602

Table 3.8 Strength properties of concrete

Day	Compression strength [psi]	Tensile strength [psi]
7th (Aug. 4, 2010)	1429, 1471, 1712	180, 154, 195
	μ =1537, σ =152.6	μ =177, σ =20.7
14th (Aug. 11, 2010)	2009, 2447, 2104	258, 238, 242
	μ =2187, σ =230.6	μ =246, σ =10.3
20th (Aug. 17, 2010)	2985, 3063, 2943	265, 265, 257
	μ =2997, σ =61.0	μ =262, σ =4.5
28th (Aug. 25, 2010)	3572, 2978, 3657	361, 326, 347
	μ =3402, σ =370.0	μ =345, σ =17.3
72nd (Oct. 8, 2010)	3897, 3057, 3196	N/A
	μ =3383, σ =450.6	
93rd (Oct. 29, 2010)	2909, 3365, 3435	278, 307, 263
	μ =3236, σ =285.6	μ =283, σ =22.4
111th (Nov. 16, 2010)	4108, 4144, 3759	336, 356, 368
	μ =4004, σ =212.5	μ =353, σ =16.1
406th (Sep. 7, 2011)	4669, 4750, 4693	N/A
	μ =4704, σ =41.7	

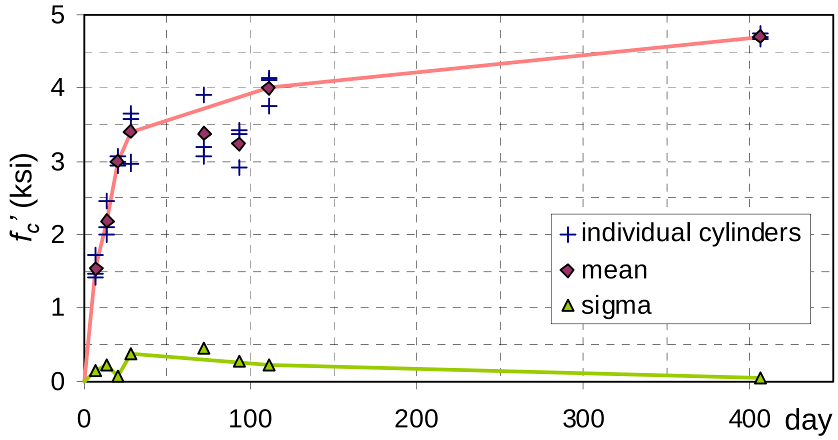

Fig. 3.19 Concrete strength maturity curve

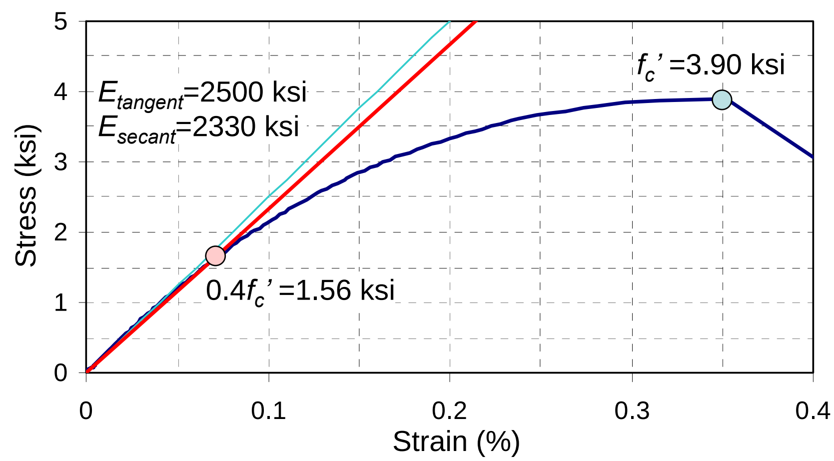

Fig. 3.20 Example concrete stress-strain relationship on the 72nd day (1st cylinder)

A sample stress-strain relationship that is obtained from one of the tested cylinders is shown in Fig. 3.20. From this figure, the obtained compressive strength is 3.9 ksi (26.89 MPa), the corresponding peak strain is 0.35%, and the initial tangent modulus is 2500 ksi (17.24 GPa). The secant modulus which connects the origin and $0.4 f_c'$ is 2330 ksi (16.06 GPa), as specified in Fig. 3.20.

3.4.3.2 Steel Reinforcing Bars

The strength and elastic modulus of reinforcing bars need to be tested to subsequently use in estimating the response of the test specimen. Both longitudinal and transverse (i.e. hoops) steel reinforcing bars of the columns are tested. #5 bars were used as longitudinal reinforcement. To check their properties, these bars were sampled from the test specimens after testing. Since the middle of the test specimen was not damaged, the portions of the longitudinal bars in the middle of the test specimen remained elastic allowing them to be tested. Total of four tensile tests were conducted on September 28, 2011. In addition, four tensile tests were conducted to confirm the properties of the #2 reinforcing bars used as hoops on May 27, 2010, as shown in the photograph of Fig. 3.21(d). Fig. 3.21(a) and (b) show the obtained stress-strain relationships of the longitudinal and transverse reinforcement, respectively. One linear variable differential transformer (LVDT) is used to measure the displacement between two points with 2 in (51 mm) spacing. For #2 bar, a strain gage is placed to measure strain at one point in the middle of the LVDT gage length. As shown in Fig. 3.21(b), both stress-strain relationships are very similar. However, as shown in Fig. 3.21(c), the strain from the LVDT has a slightly steeper slope and smaller strain after 5%-strain which corresponds to 87 ksi (599.84 MPa) in stress. This is due to the difference in measuring the strain, i.e. the strain from the strain gage near the necking point is larger than that obtained by the LVDT averaging over its 2 in (51 mm) gage length. Table 3.9 summarizes the properties of both reinforcing bars. The yield stress is calculated based on the 0.1% offset method [38].

Table 3.9 Average properties of the reinforcing bars

Property	Longitudinal bars #5, from LVDT	Transverse bars #2, from LVDT
Yield stress, f_y [ksi]	77.54	63.13
Ultimate stress, f_u [ksi]	105.06	90.25
Yield strain, ε_y [%]	0.27	0.22
Ultimate strain, ε_u [%]	12.04	11.64

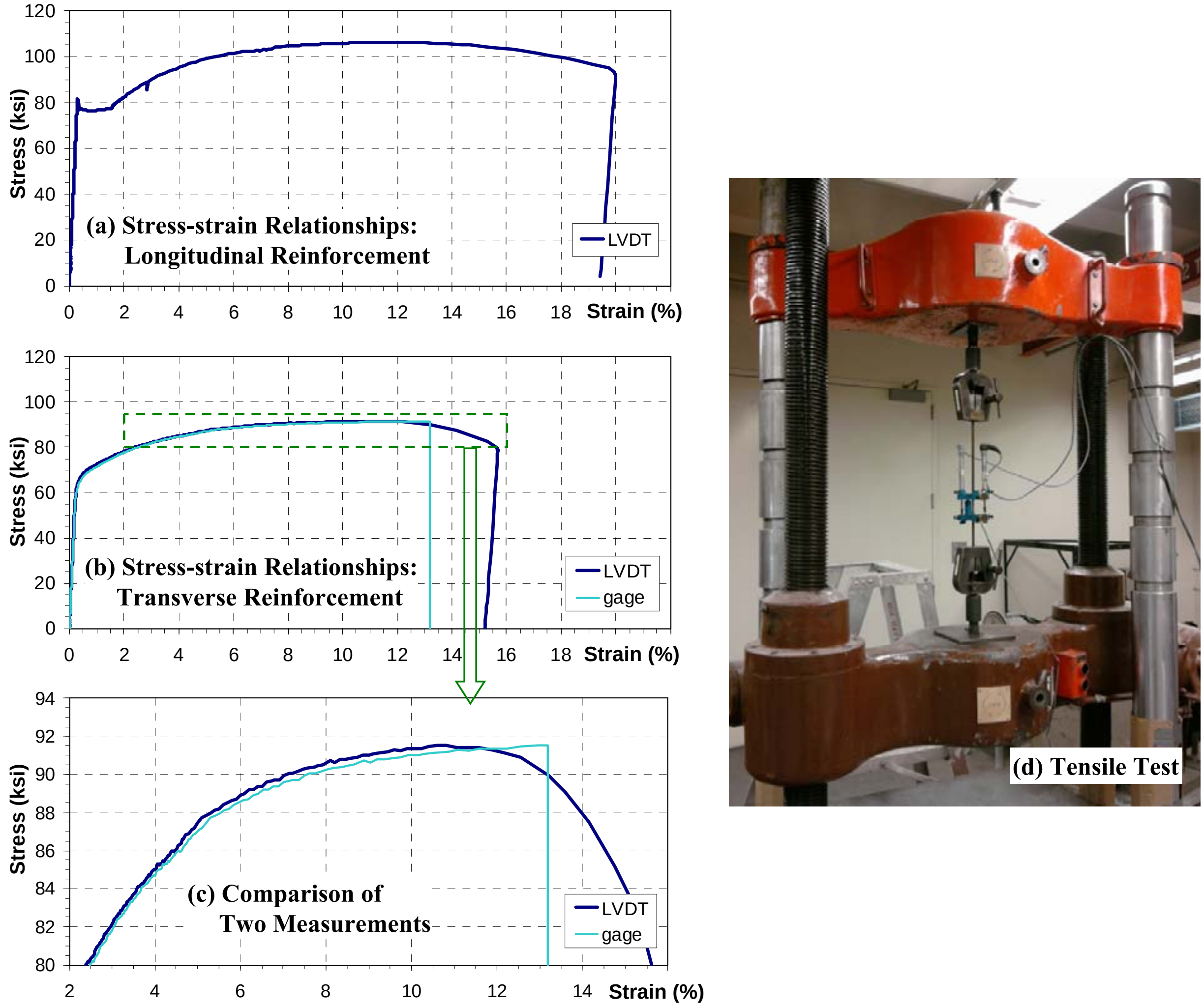

Fig. 3.21 Testing longitudinal and transverse reinforcing bars (sample results and setup)

3.5 Experimental Setup and Test Program

3.5.1 Test Setup

Two shaking table tests were conducted at the Richmond Field Station Earthquake Simulator, at Richmond Field Station of UC-Berkeley. As shown in Fig. 3.22(a), the specimen is placed at the center of the shaking table using a thick large transition steel plate, $8' \times 8' \times 3.35''$ (2.44 m × 2.44 m × 85 mm), for better shaking table performance and control purposes which would otherwise be critical due to the large specimen weight. Steel chains shown in this figure are connected to the prestressing rods for the top concrete blocks to prevent collapse of the test specimen. The prestressing rods connect the steel beams and concrete blocks to achieve the stability and avoid any sliding of the mass system during the shaking tests.

3.5.1.1 Dimensional Analysis

As mentioned previously, the test specimens are scaled from the prototype column by using a length scale of 4. Keeping the accelerations and stresses same for the prototype and the scaled columns lead to the following scale factors for time, mass and MMI.

Length: $L = 1/4$

Acceleration: $LT^{-2} = 1$, therefore, $T = 1/2$

Stress: $ML^{-1}T^{-2} = 1$, therefore, $M = 1/16$

MMI: $I = ML^2$, therefore, $I = 1/256$

where T and M are the scale factors for time and mass, respectively.

3.5.1.2 Column

The test columns are 20 in (508 mm) in diameter and 70 in (1778 mm) in height. For longitudinal reinforcement, 16#5 bars are used for both specimens and the longitudinal reinforcement ratio is 1.563%. For transverse reinforcement, #2 hoops are used where the first specimen (SP1) has 2 in (51 mm) spacing and the second specimen (SP2) has 3 in (76 mm) spacing. For both specimens, the spacing is uniform over the entire column height. The volumetric ratio of the transverse reinforcement is 0.545% for SP1 and 0.363% for SP2 as listed in Table 3.5. Bridge Design Specifications (BDS) [39] by Caltrans provide the required minimum volumetric ratio as 0.468%. Therefore, SP1 satisfies the BDS while SP2 does not satisfy the BDS in terms of the transverse reinforcement. Finally, the weight of the column, except for the footing, is about 3.9 kips (17.35 kN). Complete set of drawings of the test specimens can be found in Appendix C.

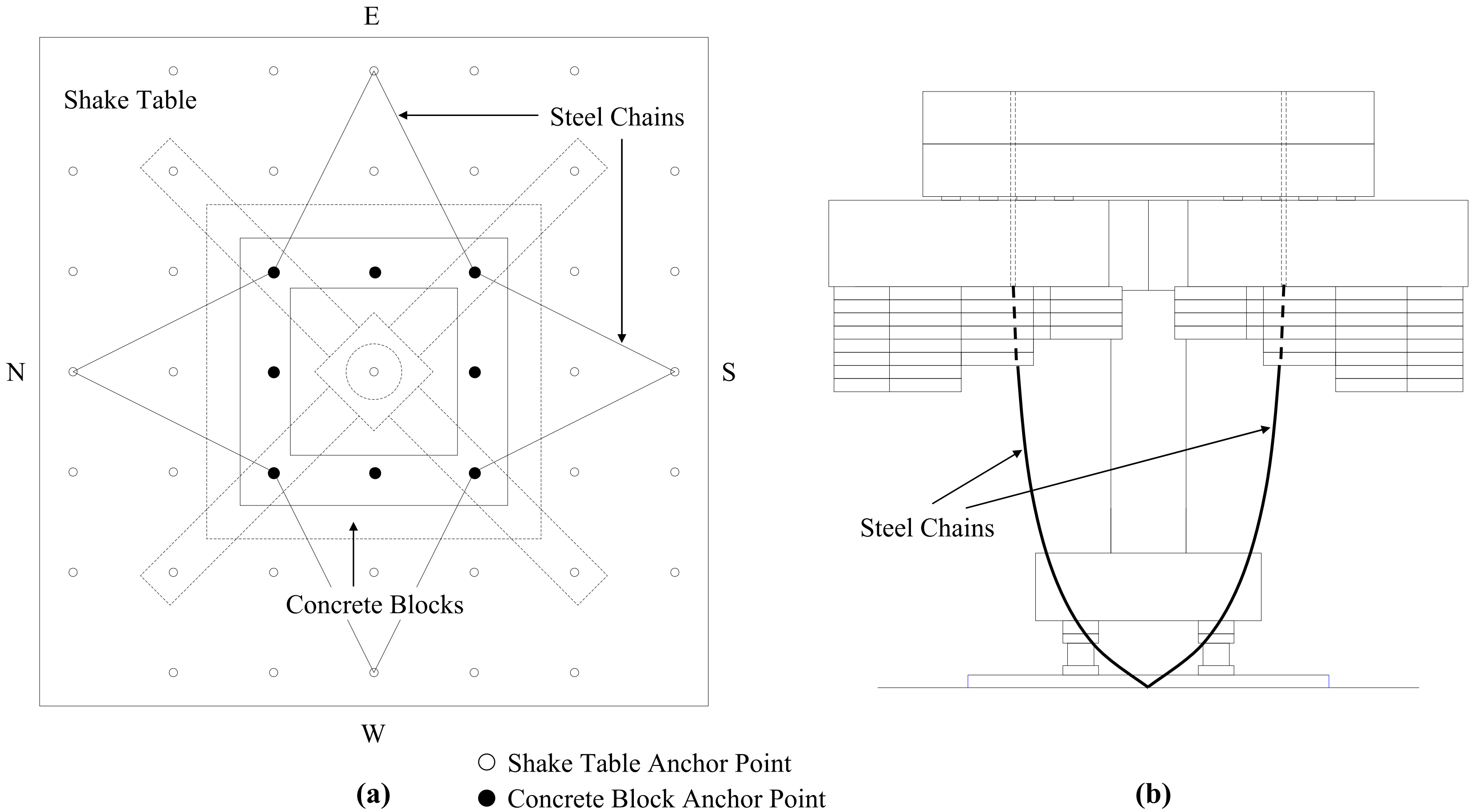

Fig. 3.22 Specimen location on the shaking table and the catching safety system (a) Plan view, (b) Elevation view

3.5.1.3 Base Plate, Footing, and Top Steel Beams

The base steel plate is designed to place the test specimen at the center of the shaking table. Nine 2.5″ (64 mm) holes, to connect the plate to the shaking table, and 16 7/8″ (22 mm) tap (threaded) holes, to connect the load cells to the plate, were drilled on the $8' \times 8' \times 3.35''$ (2.44 m × 2.44 m × 85 mm) base steel plate. Design details of the base plate are given in Appendix C.

The footing is designed to fix the column to the shaking table and it is 60 in × 60 in × 18 in (1524 mm × 1524 mm × 457 mm) in dimensions. It is reinforced with #6 deformed bars in both longitudinal directions and with #3 ties in the transverse direction. The footing is set on four load cells, one at each corner. The footing weight is about 5.7 kips (25.35 kN). Footing details can be found in Appendix C.

The top steel beams are designed to resist prestressing forces and to support inertia forces of the mass blocks which consist of two concrete blocks and 72 lead blocks. The four beam cross sections, HSS 20×12, are designed to have small deflection and enough flexural capacity. Fig. 3.23 shows a plan view showing the layout of these four beams and the number of attached lead blocks. For more information, the design of steel beams is explained in details in Appendix C. The lead blocks are hung by four prestressing rods fixed at the tip of smaller HSS pipes as shown in the photograph of Fig. 3.24. These HSS pipes were welded to the top of the four steel beams.

3.5.1.4 Mass Blocks

As explained in Section 3.4.1.2, the target ALR was 6.5%, but the additional weight of steel beams and miscellaneous items caused slightly heavier gravity load on the column. Finally, 6.8% ALR, i.e. about 85.6 kips, is achieved by two concrete blocks, 72 lead blocks on the column (Fig. 3.23), monolithically case top block with the column, and the tie assembly. The concrete blocks are identical in dimensions and weight. Each block is 10 ft×10 ft×14 in (3045 mm × 3048 mm × 356 mm) in dimensions and about 16.5 kips (73.4 kN) in weight, i.e. a total of concrete blocks weight of 33 kips (146.8 kN). The lead blocks are also identical. Each lead block is 27 in×21 in×3.5 in (686 mm × 533 mm × 89 mm) in dimensions and 0.5 kips (2.22 kN) in weight, i.e. a total of lead blocks weight of 36 kips (160.1 kN). As a result, the center of gravity (C.G.) is about 8.5 ft (2591 mm) above the shaking table as dictated by the test setup shown in Fig. 3.24.

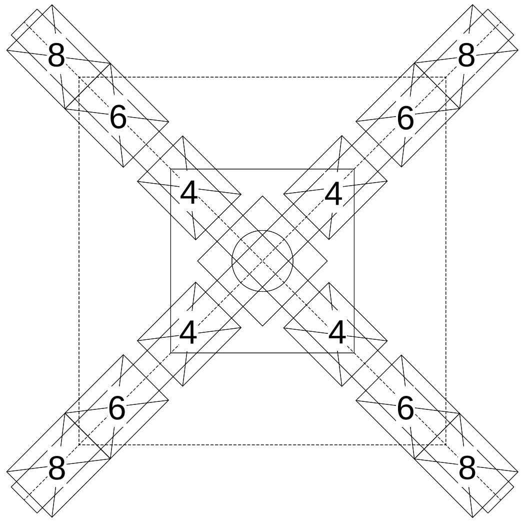

Fig. 3.23 Final mass configuration

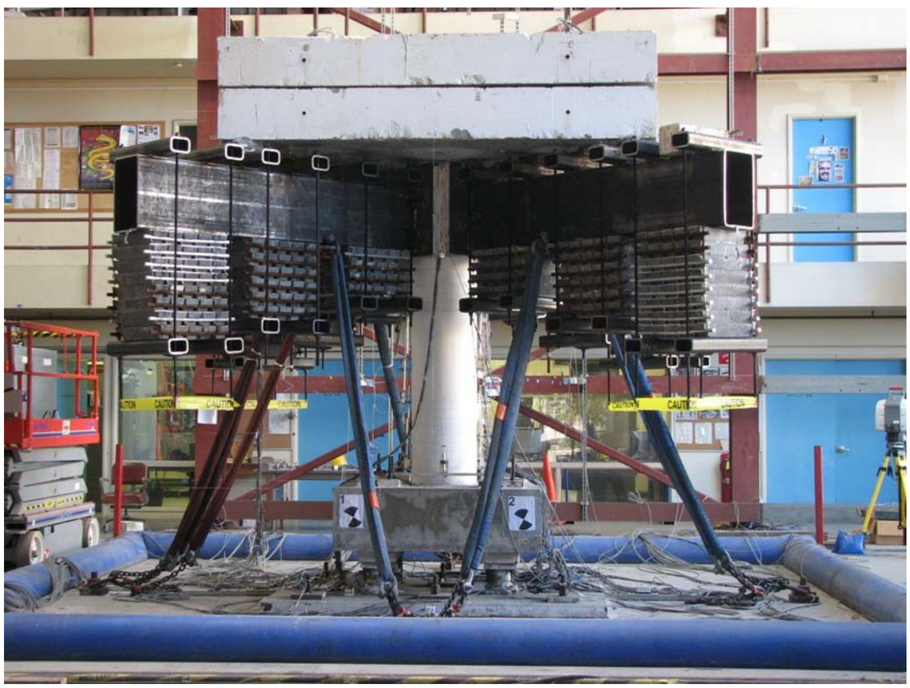
Fig. 3.24 Final test setup

3.5.2 Instrumentation

Total of 137 channels are used for each shaking table test and they are distributed as follows:

- 16 channels for monitoring accelerations and displacements of actuators under the table;
- 12 channels for tri-axial load cells monitoring restoring force of the specimen;
- 27 channels for nine 3D accelerometers and 9 channels for nine 1D accelerometers, monitoring the vertical acceleration at specific points of the test specimen;

- 38 channels for strain gages on the longitudinal and transverse reinforcing bars;
- 14 channels for Novotechniks (after the name of the manufacturer) and 2 channels for direct current differential transformers (DCDTs) monitoring local deformation of the test specimen; and
- 19 channels for wire potentiometers monitoring displacement at specific points of the test specimen.

The channel list and instrumentation drawings are presented in Appendix D.

3.5.2.1 Internal Instrumentation

Total of 38 strain gages were installed on the reinforcing bars for each test specimen. 18 gages were installed on longitudinal bars (L) and 20 gages on transverse bars (H) at the following locations (defined by the column diameter, D, and the column height, H):

- At 3D/2 and 2D from the bottom and D/2 from the top as shown in Appendix D: 2 gages (L) and 2 gages (H);
- At D/2 from the bottom as shown in Appendix D: 2 gages (L) and 6 gages (H);
- At D from the bottom and also from the top as shown in Appendix D: 4 gages (L) and 2 gages (H); and
- At mid-height (i.e. H/2) as shown in Appendix D: 2 gages (L) and 4 gages (H).

3.5.2.2 External Instrumentation

As shown in Appendix D, linear position transducers (Novotechnik), DCDTs, wire potentiometers, accelerometers, and load cells were installed to obtain local deformation, global displacement, acceleration, and restoring force, respectively. These instruments are installed in the following locations:

- **Novotechniks and DCDTs**

  Total of 14 Novotechniks were installed to measure local deformation on the north and south sides of the column. They were mounted on threaded rods penetrating through the column in the horizontal loading direction, as shown in Appendix D. Total of six rods were kept unbonded from the surrounding concrete by the gap of 1/16″ (1.6 mm) around the rod except at the center of the column. The bonded length is roughly 14″ (356 mm). Each rod has a brace on each side to fix the Novotechnik and its wire. Locations of these measurements are given in appendix D. From the Novotechnik data, one can calculate the strain at D/2, D, 3D/2, and 2D from the bottom and at D/2 from the top. These strains from the displacement measurements can be compared to the strains obtained directly from the reinforcing bar strain gages. In addition, section curvatures can also be obtained by using these computed strains on the north and south sides of the column. Moreover, two DCDTs were installed to capture the vertical displacement of the top concrete block. They were located 7″ (178 mm) off from the east and west sides of the column.

- **Wire Potentiometers**

  Total of 19 wire potentiometers were installed to measure displacement of the test specimen. They captured the displacement in the longitudinal (X), transverse (Y) and vertical (Z) directions. These measurements were arranged as follows:
  - Column – 4 wire potentiometers in X and 4 wire potentiometers in Y direction;
  - Footing – 2 wire potentiometers in X and 1 wire potentiometer in Y direction; and
  - Mass – 2 wire potentiometers in X, 2 wire potentiometers in Y and 4 wire potentiometers in Z direction.
- **Accelerometers**

  Total of 18 accelerometers were installed to measure acceleration at the following points. Four 3D accelerometers were located at each corner of the base plate, one below the top block, and four at each corner of the top of the concrete blocks. Eight 1D accelerometers to measure the vertical acceleration were attached along the height on the north side of the column, and one at the center on the top concrete block.
- **Load Cells**

  Four tri-axial load cells support the specimen at the four corners below its footing. They measure axial load, and shear forces in the X and Y directions.

3.5.3 Test Sequence

Two specimens are planned to follow identical test sequence. All excitations are scaled from 5% to 125% of the 1994 Northridge earthquake recorded at Pacoima Dam, and the upper limit is determined by the shaking table limits, as previously discussed. Since each specimen is subjected to irreversible inelasticity in medium or high-level tests, the intensity of excitation is increased gradually. The maximum curvature at the top of the column observed in the analysis is used as the basis for determining each intensity level. While conducting tests of SP1, the longitudinal strain near the base and the top of the column is checked. For SP2, the sequence of testing is almost the same as that for SP1. As a result, the test sequence discussed in Chapter 4 is obtained and followed for SP1 and SP2.

3.6 Summary

The dynamic tests to examine the effect of vertical excitation on shear strength of RC bridge columns were designed within capacity of the UC-Berkeley shaking table in the Richmond Field Station. The geometric scale of the test specimens is selected as ¼. To confirm the shaking table performance, fidelity tests were conducted with steel beams and concrete blocks stacked on the shaking table. Even though the periods were not comparable to those of the scaled prototype, the mass which weighs 118 kips, and the center of gravity, 9 ft from the shaking table, were comparable to those of the test specimens. Four ground motions were selected from 80 ground motions which satisfied the 1st and 2nd criteria in Section 2.1. They were chosen based on capacity reduction (parameter *red* defined in Chapter 2) calculated using the ACI equation, and based on comparison of demand and capacity history. Total of 30 trials were conducted and the input motion was finalized. Also, the intensity limit of the applied motion was identified.

Each RC column was designed as a ¼-scaled prototype. Both of SP1 and SP2 have the longitudinal reinforcement ratio of 1.563% which is close to the prototype value. The transverse reinforcement ratio of SP1 is close to that of the prototype, but SP2 has 2/3 of that of SP1, achieved by adjustment the hoop spacing. The mass on the column was identical in both specimens. Assuming f_c' =4 ksi (27.58 MPa) and 6.5% axial load ratio and including miscellaneous weight, 85.6 kip-weight (38.83 ton) was placed on each column. Total weight on the table is slightly over 100 kips (45.36 ton). The center of gravity of the specimen was about 8.5 ft (2591 mm) above the table. A base plate and prestressing rods were placed to hold the specimen at the center of the shaking table. Steel chains hold the mass blocks to avoid unexpected movement which might cause safety concerns.

Total of 38 strain gages were installed on the reinforcing bars of each specimen. 18 gages were attached to the longitudinal bars and 20 gages were attached to the hoops. For external instrumentation, 9 3D accelerometers, 9 1D accelerometers, 4 loadcells, 14 Novotechniks, 2 DCDT, and 19 wire potentiometers were used.

The input motion, the Northridge earthquake (1994) recorded at the upper abutment of Pacoima Dam, is selected to be applied to the test specimens with increasing intensity, from 5% to 125%-scale. The 2D excitation in X and Z is planned in most cases, but 1D excitation in X is also planned to be applied in some cases as these 1D runs are helpful to observe the difference in responses due to the effect of the vertical excitation.

Chapter 4

Results of Dynamic Tests: Global Responses

4.1 Introduction

A series of tests was conducted on the UC-Berkeley shaking table at Richmond Field Station (RFS) from October 22 to November 2, 2010 for the first specimen (SP1) and on November 16 and November 18, 2010 for the second specimen (SP2) as specified in Table 4.1. The ground motion recorded at the Pacoima Dam station of 1994 Northridge earthquake (RSN 1051) was applied. One of the horizontal (X, Fig. 4.1(a)) and vertical (Z, Fig. 4.1(b)) components were utilized in most cases. X component is selected because it produces bigger shear strength reduction than the other component does. Since the geometrical scale of the specimen corresponds to the ¼-scale modified Plumas-Arboga Overhead Bridge (PAOB), each component of the ground motion was time-compressed by a factor of 2 as shown in Fig. 4.1. It should be noted that the acceleration history in Fig. 4.1 is 100% unfiltered input ground motion obtained from the PEER NGA database [11].

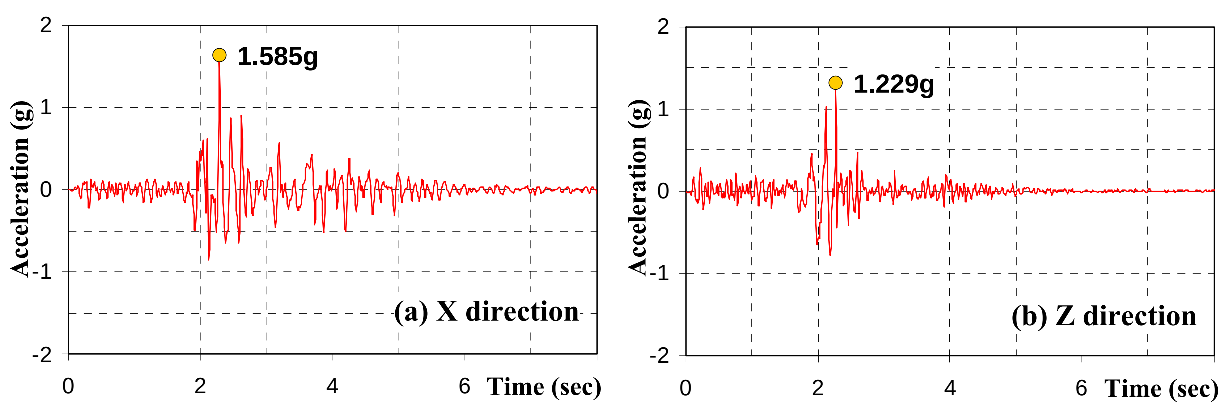

Fig. 4.1 Horizontal (X) and vertical components (Z) of 100% Northridge earthquake

The ground motion was applied in increasing intensity levels and each intensity level was related to the curvature ductility at the top of the column as shown in Table 4.1. All tests are conducted with one of the horizontal and vertical components except the ones noted with 'X only' in Table 4.1. The low-level tests, from 5% to 25%-scale excitations, did not result in yielding of the cross-section at height *h*=60″ (1524 mm) above the top of the footing, which corresponds to the mid-point of the plastic hinge at the top of the column, assuming a plastic hinge length equal to the diameter of the column, $L_p = D = 20''$ (508 mm). The yielding at *h*=60″ (1524 mm) occurs when 50%-scale motion is applied. Even though the maximum curvature of SP1 is larger than that of SP2 during the 50%-scale run, this can be considered as 'yield-level' for both specimens. After this yield-level, 70%, 95%, and 125%-scale motions are applied.

Table 4.1 Test sequence

SP	Run	Scale [%]	Ductility			Date	Notes
			Curvature		Displacement		
			φ/φ_{ys} @60″	φ/φ_y @60″	Δ/Δ_y @70″		
1	1-1	5.0	-	-	-	Oct. 22	-
	1-2	12.5	-	-	-	Oct. 22	-
	1-3	12.5	-	-	-	Oct. 26	50% increased Z
	1-4	12.5	-	-	-	Oct. 26	Repetition of 1-2
	1-5	25.0	0.41	0.35	0.93	Oct. 26	Half-yield
	1-6	50.0	1.11	0.96	1.73	Oct. 27	Yield
	1-7	70.0	1.57	1.36	1.93	Nov. 1	Onset of shear cracks
	1-8	95.0	4.62	4.00	2.33	Nov. 1	Onset of cover spalling
	1-9	125.0	6.15	5.33	4.27	Nov. 1	-
	1-10	125.0	6.54	5.67	4.77	Nov. 2	X only
	1-11	125.0	7.31	6.33	5.47	Nov. 2	Repetition of 1-9
2	2-1	5.0	-	-	-	Nov. 16	-
	2-2	12.5	-	-	-	Nov. 16	-
	2-3	25.0	0.40	0.35	1.05	Nov. 16	Half-yield
	2-4	25.0	0.41	0.36	0.84	Nov. 16	Half-yield, X only
	2-5	50.0	0.92	0.80	1.43	Nov. 16	Yield
	2-6	50.0	0.99	0.86	1.27	Nov. 16	Yield, X only
	2-7	70.0	1.23	1.07	1.97	Nov. 18	Onset of shear cracks
	2-8	95.0	5.00	4.33	2.47	Nov. 18	Onset of cover spalling
	2-9	125.0	5.38	4.67	4.60	Nov. 18	-
	2-10	125.0	5.00	4.33	4.50	Nov. 18	X only
	2-11	125.0	4.23	3.67	4.77	Nov. 18	Repetition of 2-9

As can be identified from Table 4.1, tests without the vertical component are conducted for 125%-scale (run 1-10) for SP1 and 25%, 50%, and 125%-scales (runs 2-4, 2-6, and 2-10, respectively) for SP2 to examine the effect of vertical excitation. In Table 4.1, the curvature ductility, $\varphi_y = 3.0\times10^{-4}$ in^{-1} (1.2×10^{-5} mm^{-1}), is from the test data and $\varphi_{ys} = 2.6\times10^{-4}$ in^{-1} (1.0×10^{-5} mm^{-1}) is from the cross-section analysis. The curvature ductility at *h*=60″ (1524 mm) can be considered as an adequate global response parameter. At *h*=70″ (1778 mm), the yield displacement, Δ_y = 0.3 in (7.62 mm) for both SP1 and SP2, is estimated based on the shear force-lateral displacement relation in Fig. 4.23. It should be noted that only Imperial units (United States customary units) are used from this chapter.

4.2 Stiffness, Natural Frequency, and Viscous Damping

Before the main runs specified in Table 4.1, pullback and free vibration tests were conducted to obtain the stiffness and lateral and rotational vibration periods of each specimen. Obtained period and damping values were confirmed in part with the low-level tests, i.e. up to 12.5%-scale tests.

4.2.1 Pullback Tests

For SP1, total of five pullback tests were conducted as shown in Fig. 4.2. Relative lateral displacement between the top of the footing and the column top (just below the monolithically cast RC block above the column) was measured in three tests and absolute displacement (i.e. displacement between the column top and the top of the table) was measured in two tests. The difference between the absolute and relative displacements results from the rotation of the footing due to the axial flexibility of the load cells. For SP2, three pullback tests were conducted. Relative displacement and absolute displacement were measured in one and two tests, respectively. The lateral stiffness obtained in each case is shown in Table 4.2. As specified, SP1 and SP2 have different stiffness values and the stiffness of SP2 is almost 0.7 that of SP1, regardless of the displacement measurements. Lateral force-absolute displacement relationship in one case for each specimen is shown in Fig. 4.3.

Fig. 4.2 Photographs of the pullback tests without (left) and with (right) total mass

Table 4.2 Stiffness from pullback tests

Displacement measurements	Stiffness of SP1 [k/in]	Stiffness of SP2 [k/in]	Stiffness Ratio (SP2/SP1)
Relative	148.0, 150.0, 148.2	102.1	0.687
	Mean: 148.7		
Absolute	121.8, 116.3	82.1, 82.8	0.693
	Mean: 119.0	Mean: 82.5	

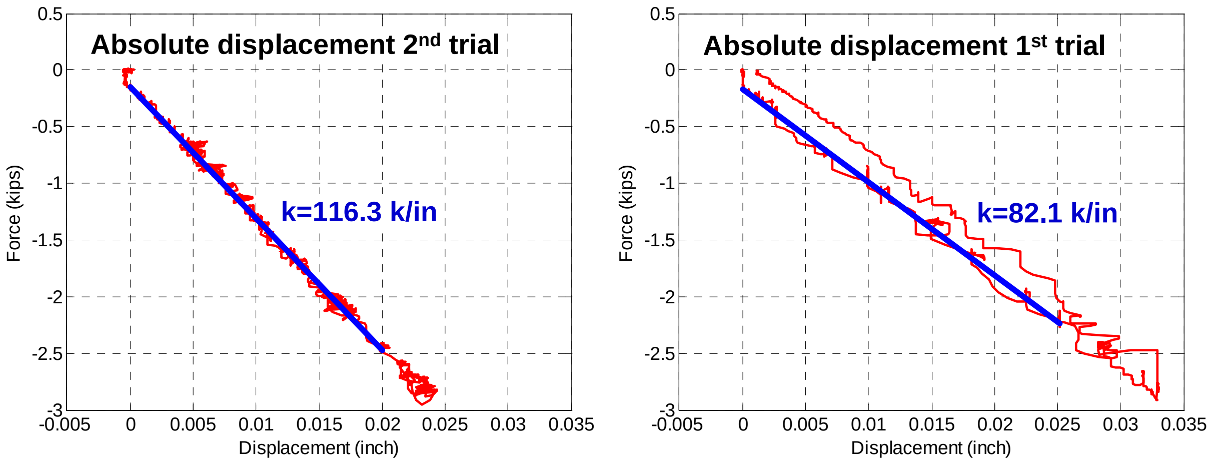

(a) Specimen 1 **(b) Specimen 2**

Fig. 4.3 Estimation of lateral stiffness

4.2.2 Free Vibration Tests

After pullback tests, the lateral and rotational vibration periods of each specimen were estimated based on free vibration tests. Two tests were conducted for SP1 and three tests for SP2. Lateral periods of SP1 and SP2 were 0.43 and 0.47 sec, respectively. It should be noted that if mass moment of inertia provided by the mass assembly did not exist, the ratio of lateral periods would be expected to be the square root of the lateral stiffness, namely 0.83. However for the investigated columns, this ratio is 0.91 which is due to the coupling of the lateral and rotational modes. Lateral periods of the two specimens got close to each other in 12.5% scale runs (Table 4.3). Considering that cracks started to open and close during these excitations, it can be speculated that SP2 had some cracking before the tests. During the 12.5% scale run, cracks initiated for SP1 and increased slightly for SP2 bringing the periods of the two specimens closer. The lateral damping of SP1 and SP2 were calculated as 1.9% and 2.9%, using Eq. (4.1). Fig. 4.4 shows the absolute lateral displacement measured at the top of the column and the theoretical displacement calculated by using the mentioned vibration period and damping values using an equivalent single degree of freedom (SDOF) system.

$$\zeta = \left(\ln\left(u_1/u_{j+1}\right)\right)/\left(2j\pi\right) \tag{4.1}$$

In Eq. (4.1), u_1 is the displacement at the first cycle peak and u_{j+1} is the displacement peak after a number of cycles equals j.

From the Fast Fourier Transform (FFT) amplitudes, damping values were calculated as 2.2~2.5% (SP1) and 2.5~3.0% (SP2), respectively, using half-power bandwidth method [40]. In addition, the two specimens had the same rotational period of vibration, namely 0.096 sec as shown in Fig. 4.5. This value was obtained from FFT amplitudes of the vertical acceleration at the top of the mass blocks and from the response spectra using the vertical acceleration measured on the shaking table with 3% damping. As specified in Fig. 4.5, FFT and response spectra point to the same period. Another peak observed in the response spectra of the shaking table, namely 0.027 sec, was the vertical period of vibration of the test specimen, as discussed in the next section.

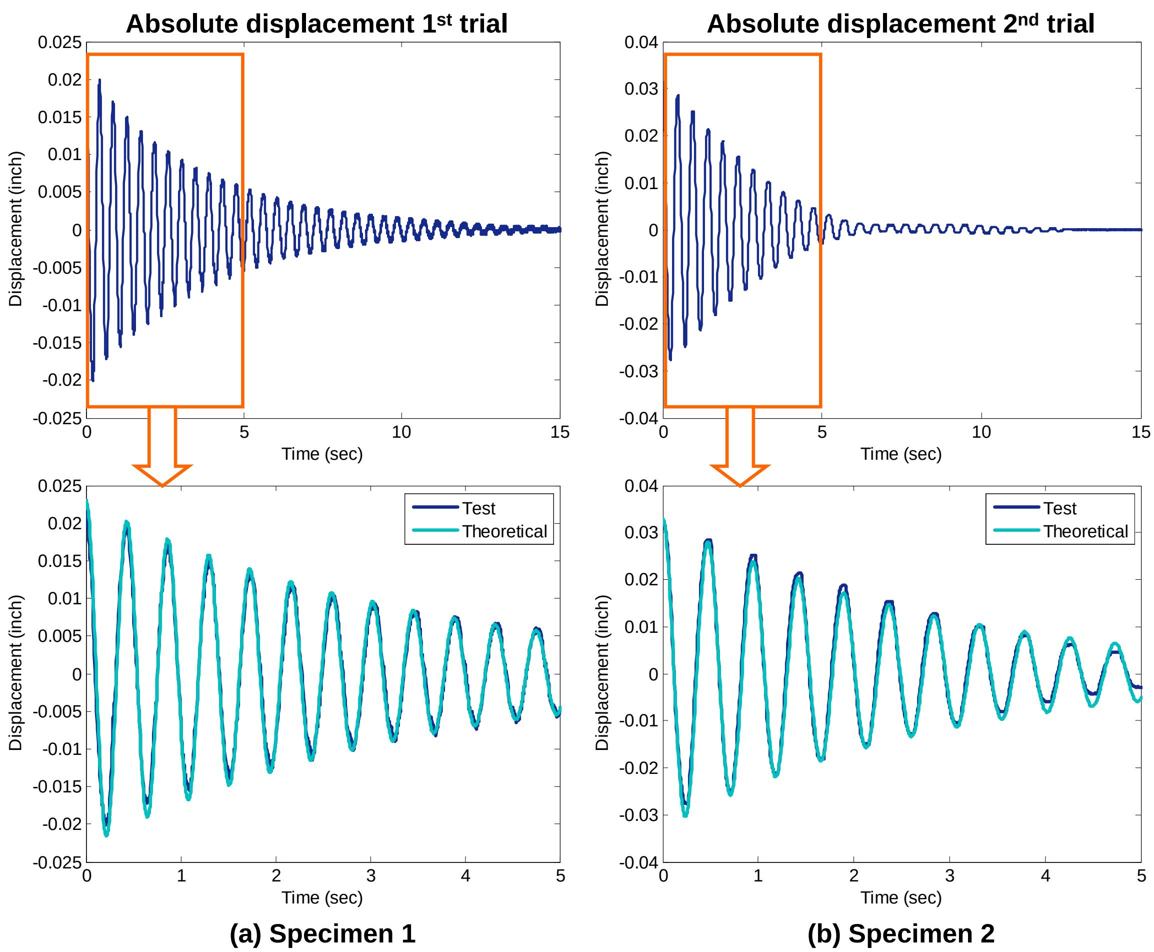

Fig. 4.4 Absolute displacement measured in the free vibration tests

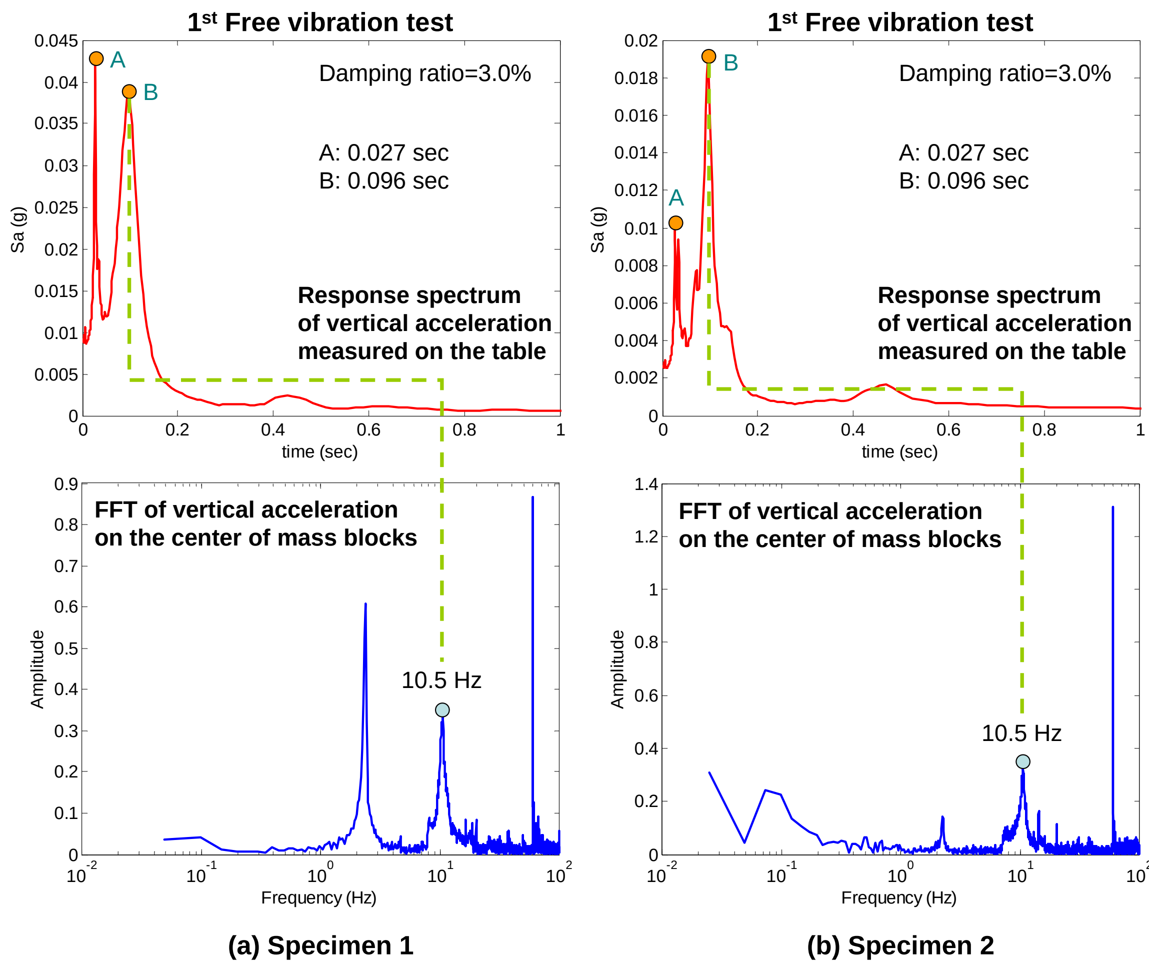

Fig. 4.5 Dominant frequencies of vertical acceleration measurements in the free vibration tests

4.2.3 Estimation of the Vertical Period

Up to the 12.5%-scale runs, vibration periods did not change significantly. Hence, the periods obtained from FFT of the specimen response can be considered as reasonable estimation of the initial periods of vibration. It should be noted that the FFT peaks come from the response of the whole system including the shaking table. This is clearly observed in Fig. 4.6, which shows the FFT of the measured vertical accelerations at various locations where the main peaks are at 6.0~6.6 Hz, i.e. 0.15~0.17 sec. The same peaks are obtained from the vertical accelerometers placed along the heights of the columns for SP1 and SP2. Since the shaking table was flexing due to the interaction of the vertical actuators with each other and the table itself resulting in a vertical degree of freedom at the table level with large mass, a peak consistently appeared at the frequency of 6.47 Hz which does not reflect the vertical period of the test specimen.

Fig. 4.6 shows the peaks for the vertical frequency of the test specimens, which are between 30 and 38 Hz. They are not clearly identified in the FFT plots, but the response spectra are more effective in distinguishing these high vertical frequencies. Fig. 4.7 shows the response spectra using the vertical acceleration obtained with 4.8% damping at different locations of SP1 under 5%- and 12.5%-scale motions. Except for the vibration period corresponding to peak A in

Fig. 4.7(a-2), which is 20% shorter than the others, the observed vertical period values are similar along the column under various intensity levels. The vibration period at peak B is the bending period of the shaking table which corresponds to the dominant frequency in Fig. 4.6. It should be noted that similar periods are observed for SP2.

The shaking table effect appears in the case of the rotational period of vibration of the test specimen. When the table is flexing, it results in a rotational degree of freedom with relatively large mass moment of inertia, which increases the rotational period of the test specimen. In case of applying table motion, the vertical actuators are bending the table when they are trying to hold the table in the commanded vertical displacement. Therefore, the mass moment of inertia of the shaking table affects the rotational period of vibration. This does not occur in the free vibration test since the table is not flexing because the actuators are inactive and vertical restraint is provided by the large damping coefficient of the actuators. In this case, the boundary conditions of the test specimen are almost like four simple supports at the used four load cells. Therefore, the rotational periods obtained from free vibration tests shown in Fig. 4.5 and listed in Table 4.3 can be considered as the rotational period of the specimen itself excluding the shaking table effect. For both specimens, the rotational period was approximately 0.1 sec.

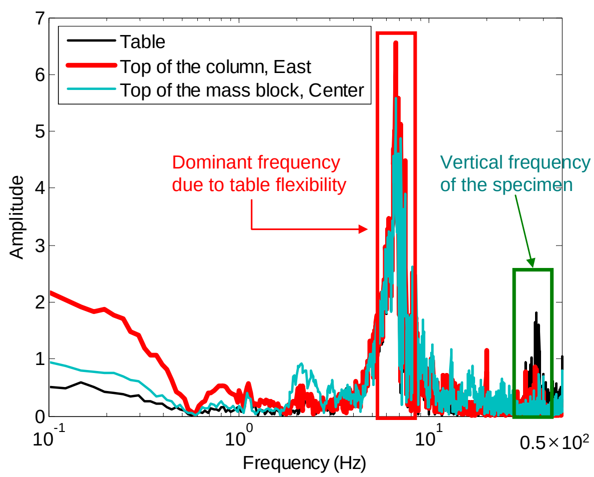

(a) SP1 12.5%

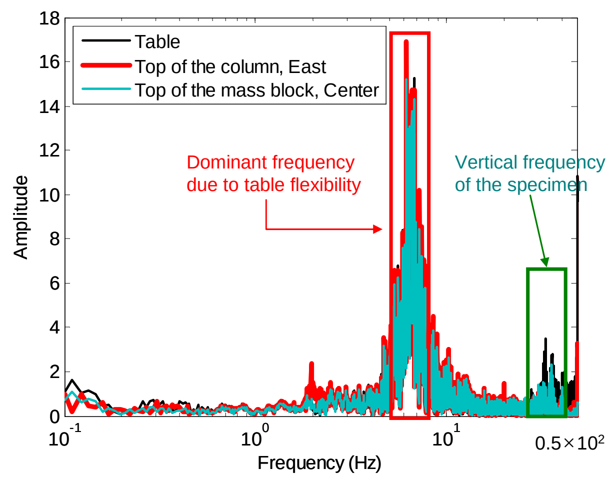

(b) SP2 12.5%

Fig. 4.6 FFT of vertical accelerations measured at various locations

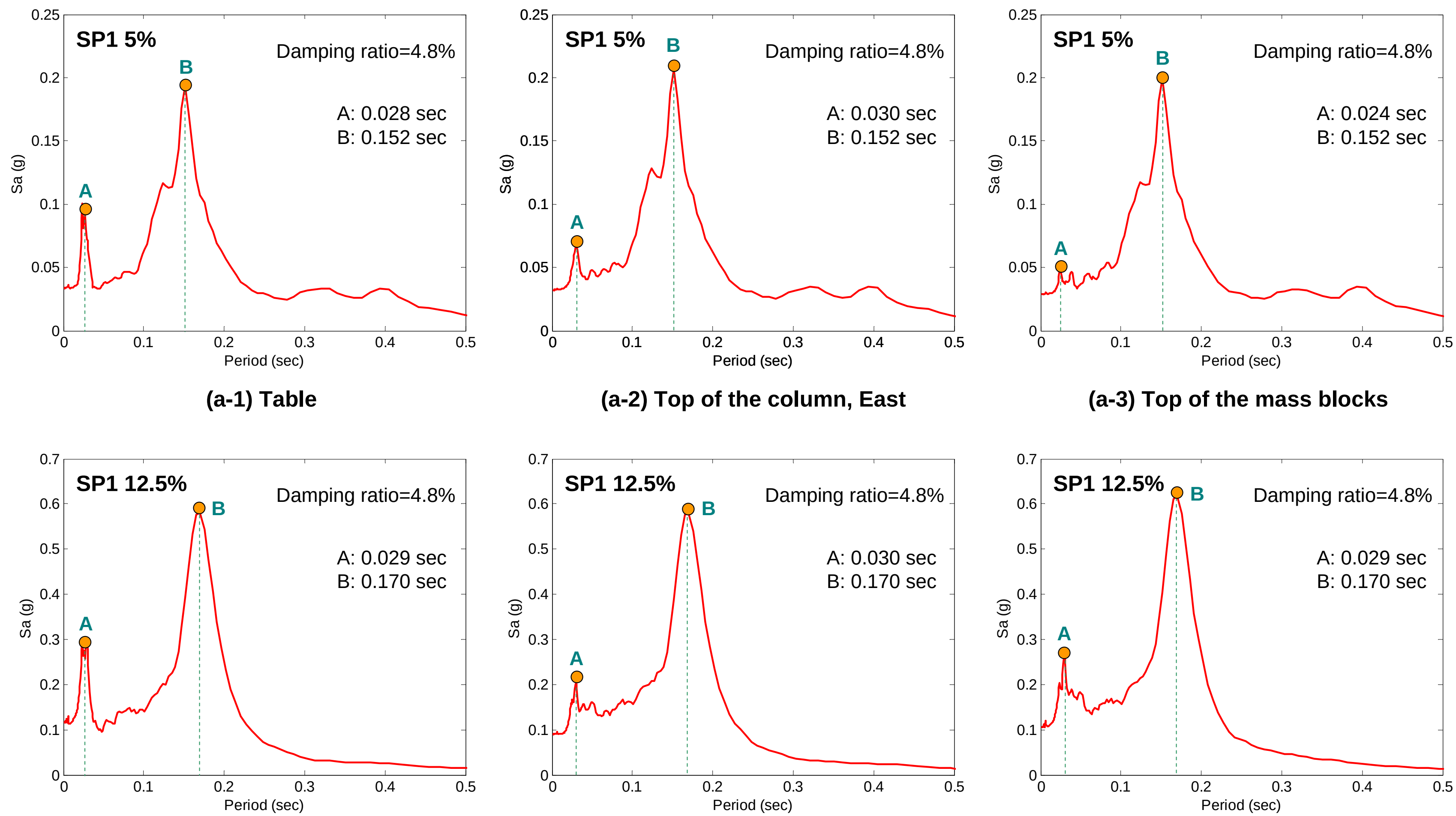

(a-1) Table **(a-2) Top of the column, East** **(a-3) Top of the mass blocks**

(b-1) Table **(b-2) Top of the column, East** **(b-3) Top of the mass blocks**

Fig. 4.7 Response spectra using the measured vertical accelerations

Table 4.3 Estimation of the periods of vibration of the test specimens

SP	Test type	Horizontal [sec]	Rotation [sec]	Vertical [sec]
1	Free Vibration 1	0.43	0.10	0.027
	Free Vibration 2	0.43	0.10	0.027
	5% scale GM	0.43	0.15	0.028
	12.5% scale GM	0.49	0.15	0.029
2	Free Vibration 1	0.47	0.09	0.027
	Free Vibration 2	0.47	0.09	0.027
	Free Vibration 3	0.47	0.10	0.028
	5% scale GM	0.49	0.15	0.028
	12.5% scale GM	0.51	0.16	0.029

4.3 Accelerations

The acceleration response of the test specimen is closely related to the eigenvalues and inertia force of the system. The acceleration history is obtained directly from the accelerometers placed on the shaking table, specimen and concrete blocks. First, the shaking table acceleration is discussed and compared to the target acceleration. Second, the acceleration responses at the top of the column and on the concrete blocks are compared to the shaking table acceleration. Finally, a discussion about the acceleration differences at each location is presented.

4.3.1 Shaking Table Acceleration

Fig. 4.8 and Fig. 4.9 show the comparison of the time histories of thr measured shaking table acceleration and the target acceleration, i.e. the original motion that is required to be reproduced using the shaking table. The table acceleration is the mean of acceleration values obtained from four accelerometers, one at each corner.

In Fig. 4.8(a), (b), and (c), horizontal and vertical components of the shaking table motion in 50%-, 70%-, 95%-scale tests for SP1 are respectively presented. The table replicates the horizontal (X) component with high precision in all three runs. Compared to the X-component, time history of the vertical (Z) component has discrepancies. Although the obtained peak acceleration is similar to that of the target, acceleration history after the peak does not resemble the target acceleration. This is observed in all three runs in Fig. 4.8(a), (b), and (c). In spite of these differences after the peak in the acceleration history, the response spectra of both components obtained from the shaking table are comparable to those of the target, as already discussed in Section 3.3.3.

Another observation is the delayed excitation in the Z direction. In particular, 70%- and 95%-scale Z-components were delayed about 0.2 sec and 0.3 sec, respectively. This is also observed in the 1st 125%-scale test shown in Fig. 4.8(d) where the time lag was about 0.4 sec.

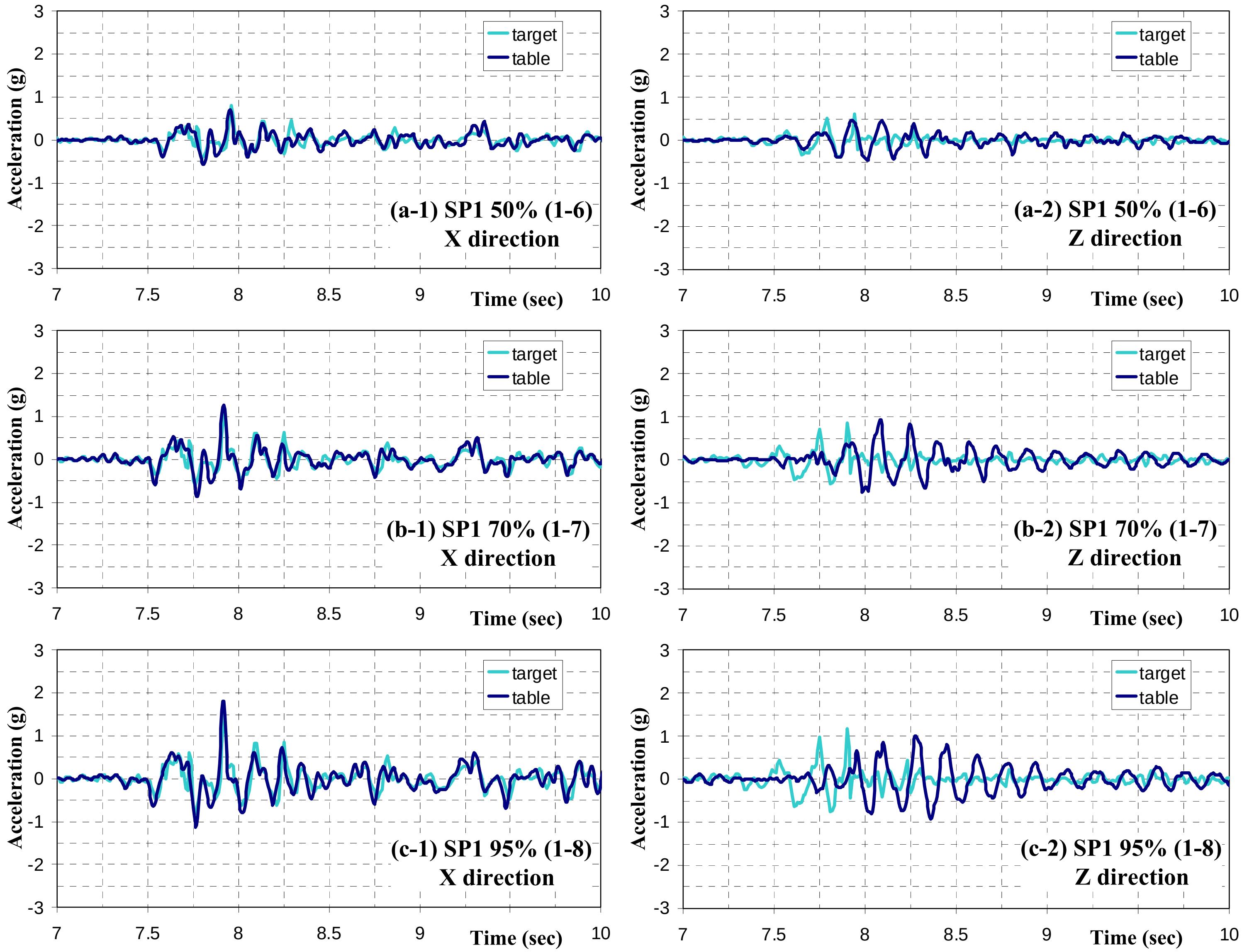

Fig. 4.8 Shaking table acceleration history in SP1 tests

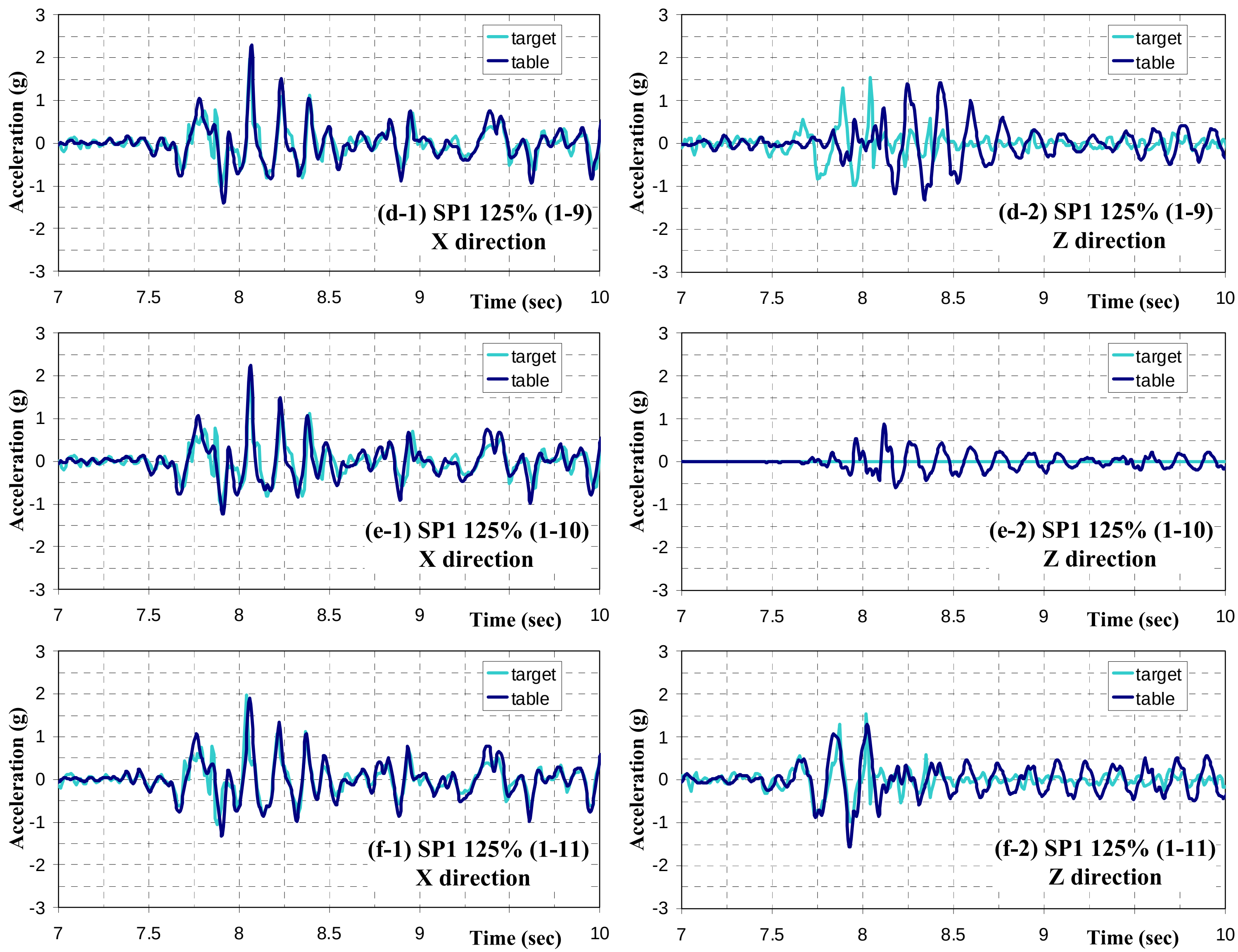

Fig. 4.8 Shaking table acceleration history in SP1 tests (continued)

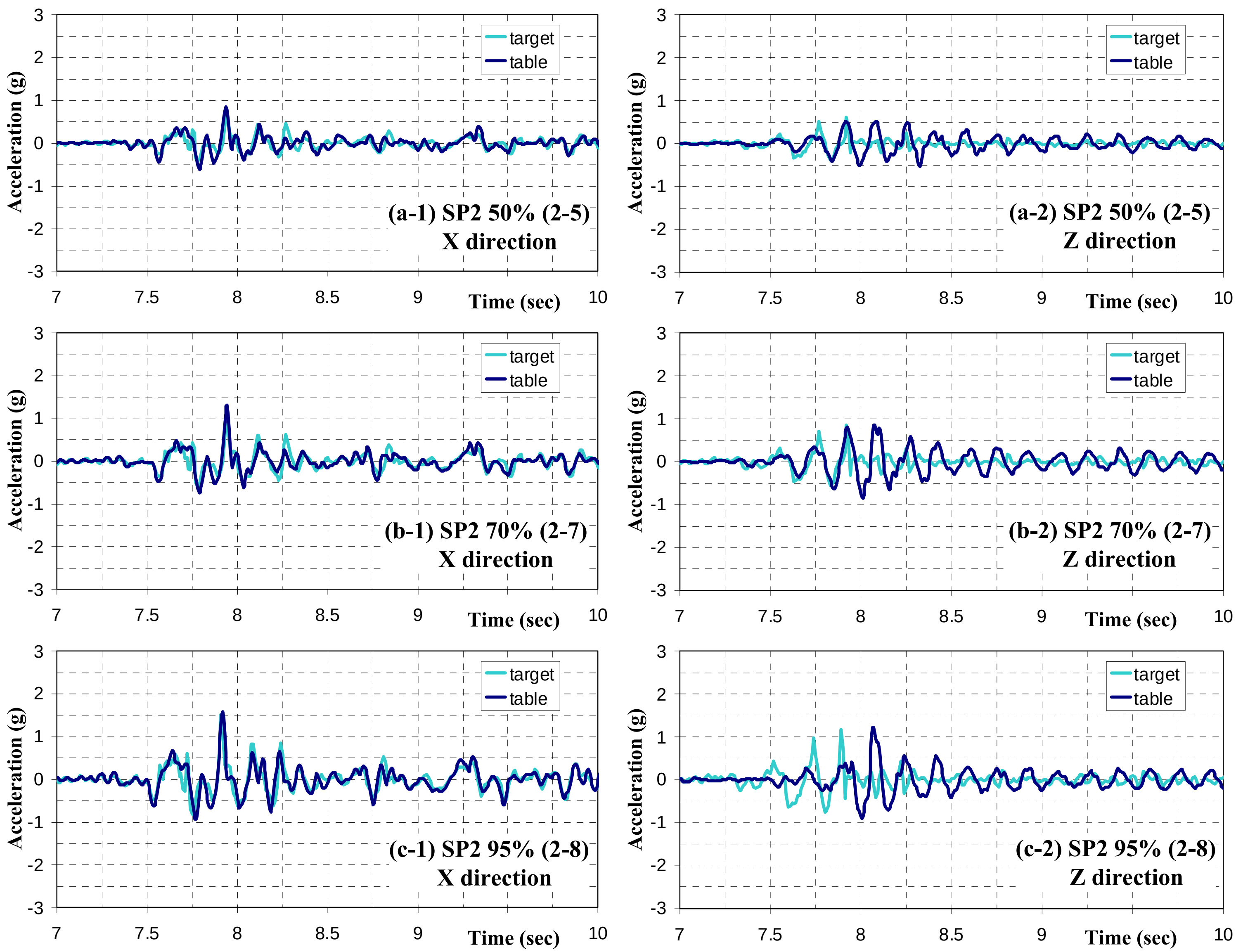

Fig. 4.9 Shaking table acceleration history in SP2 tests

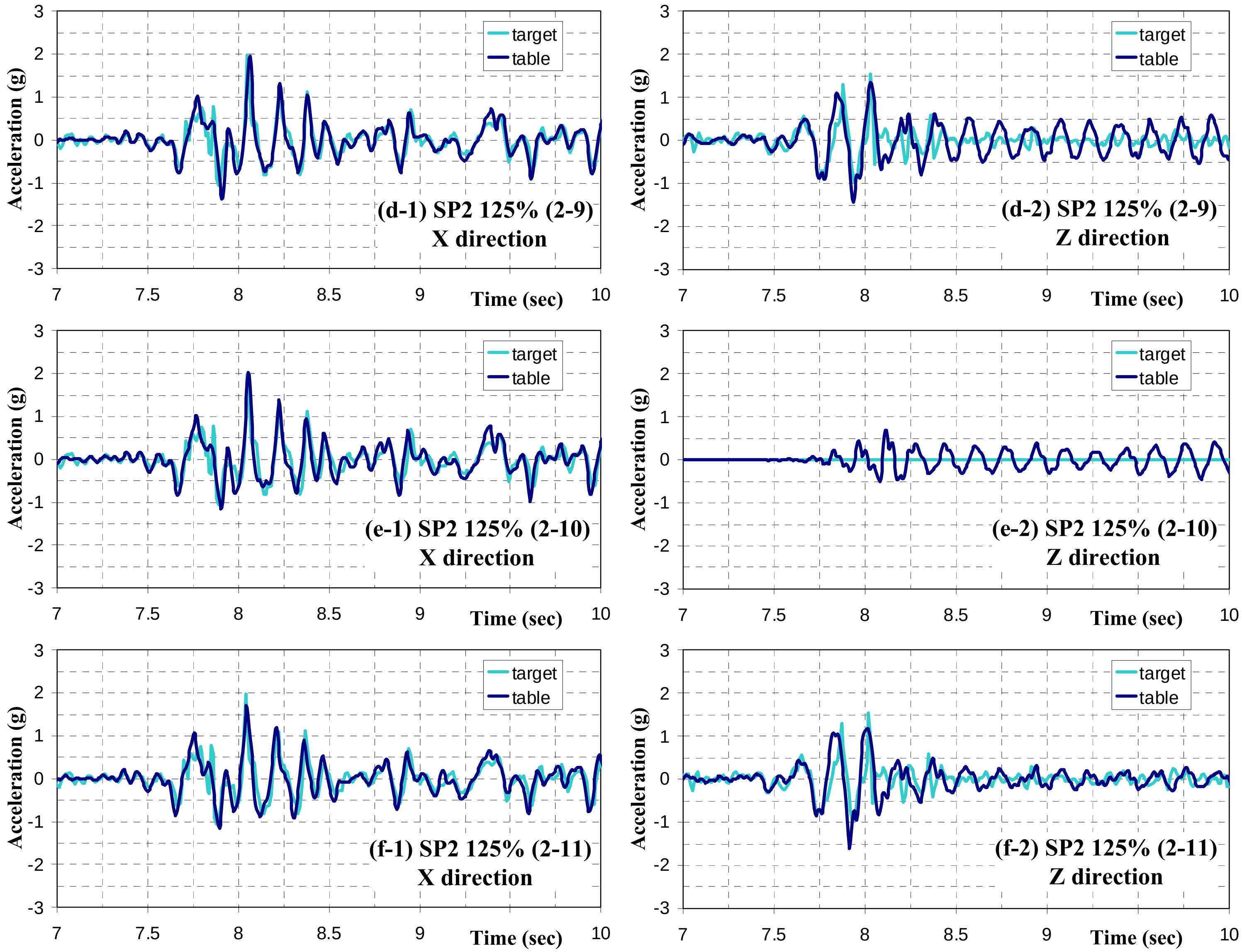

Fig. 4.9 Shaking table acceleration history in SP2 tests (continued)

In Fig. 4.8(d), (e), and (f), horizontal and vertical components of the shaking table motion in 125%-scale tests for SP1 are presented. As mentioned in Table 4.1, the 2nd 125%-scale run was for X-component only. Therefore, Z-component in the 125%-scale 'X only' test is supposed to remain zero, but this is not the case as observed in Fig. 4.8(e-2). The shaking table is controlled by vertical displacement at four points where the vertical actuators are connected. As a result, the vertical acceleration in the middle of the shaking table may not be zero during the horizontal excitation only because of the interaction of the vertical actuators which hold the vertical displacement at zero while balancing the forces due to the overturning moments caused by the horizontal acceleration. The observations mentioned in the above paragraphs for specimen SP1 were also observed for specimen SP2 (Fig. 4.9).

4.3.2 Acceleration at the Top of the Column and Mass Blocks

Total of five 3D accelerometers and nine 1D (in the Z direction) accelerometers were attached to the column and the mass blocks. Except for eight 1D accelerometers, they measured the acceleration time history at the top of the column and that at the top of the mass blocks. These are presented and compared to the shaking table acceleration in Fig. 4.10 and Fig. 4.11. On the left side, X-components are presented. As discussed above, the shaking table acceleration ('table') is the mean of accelerations measured at the four corners of the table. 'column-top' denotes the acceleration measured on the top of the column. More precisely, it is obtained below the monolithically RC top block on the east side. 'mass' denotes the mean of acceleration measured at the four corners on the added concrete blocks. On the right side, Z-components are presented. 'table' and 'column-top' were obtained at the same locations as the X-components, but 'mass' was obtained at the center of the top surface of the added concrete blocks.

In Fig. 4.10(a), (b), and (c), X- and Z-components in 50%-, 70%-, and 95%-scale tests of SP1 are respectively shown. Comparing the acceleration time histories to each other, one can make several remarks. First, measured X-component had a bigger difference from one location to another than that of the Z-component. For example, in case of the 70%-scale test, the PGA_h (i.e. maximum horizontal acceleration) on the shaking table, at the top of the column, and on the mass blocks were 1.28g, 0.94g, and 0.30g, respectively. Moreover, the dominant frequency of 'mass' was not similar to that of the shaking table acceleration. On the contrary, PGA_v (i.e. maximum vertical acceleration) values were similar to each other and so is the frequency content. Since the column was very stiff axially and more flexible laterally, these differences between PGA_h and PGA_v and their corresponding acceleration time histories were expected. The amplitude of the mass acceleration is discussed further in Section 4.3.3. Another observation is that 'column-top' and 'mass' accelerations in the X-direction did not increase as much as the shaking table acceleration. As the intensity of the input motion increased from 50%- to 95%-scale, the peak acceleration on the shaking table increased from 0.72g to 1.82g (ratio of 2.53). On the contrary, the peak values of 'column-top' and 'mass' changed respectively from 0.72g to 1.26g (only ratio of 1.75) and from 0.26g to 0.33g (only ratio of 1.27). This trend continued for the higher intensity level tests, i.e. 125%-scale tests (Fig. 4.10(d), (e), and (f)) where the peak acceleration on the mass blocks did not increase higher than 0.38g (only ratio of 1.46 compared with the 0.26g for the 50%-scale).

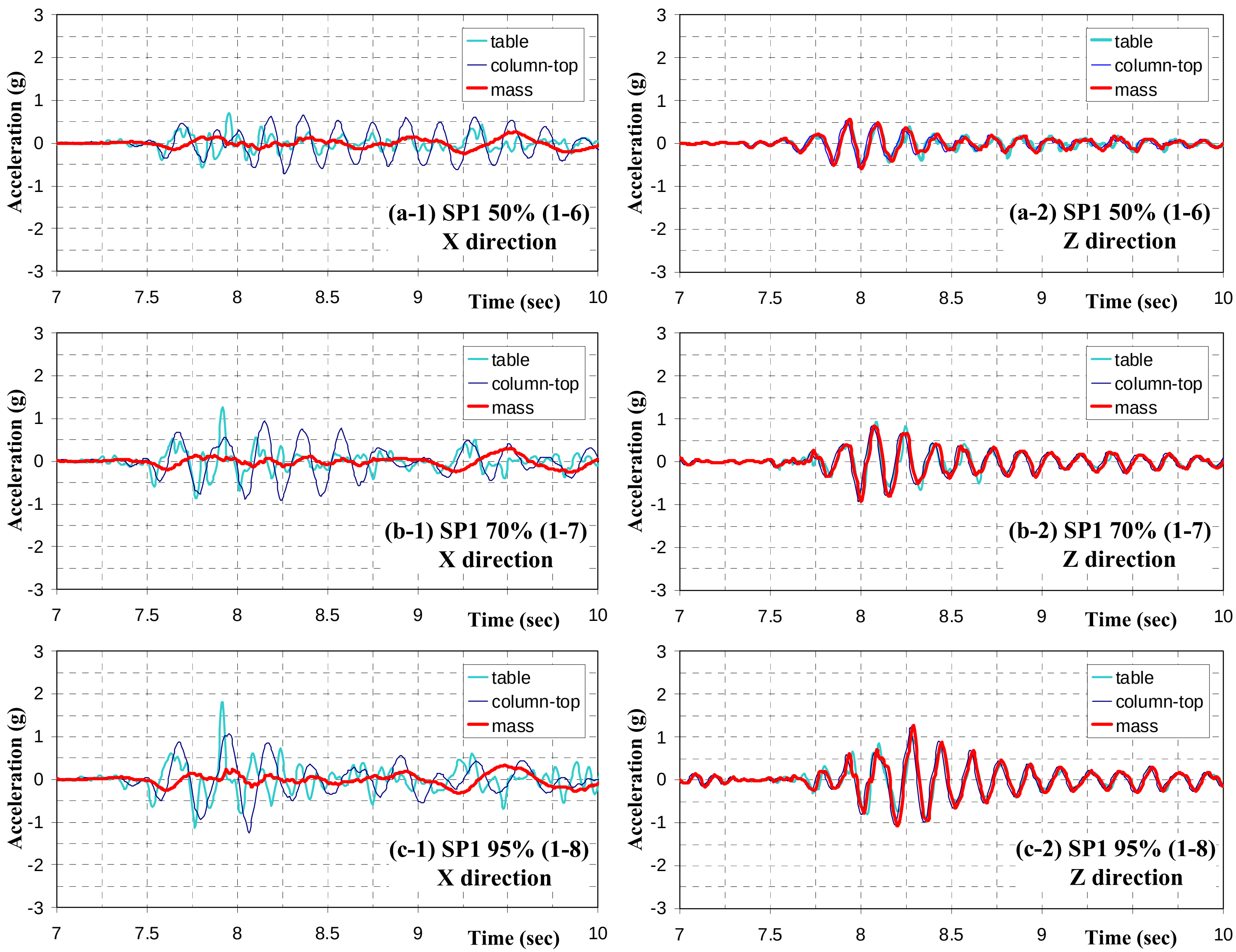

Fig. 4.10 Accelerations at the shaking table, top of the column, and top of the mass blocks in SP1 tests

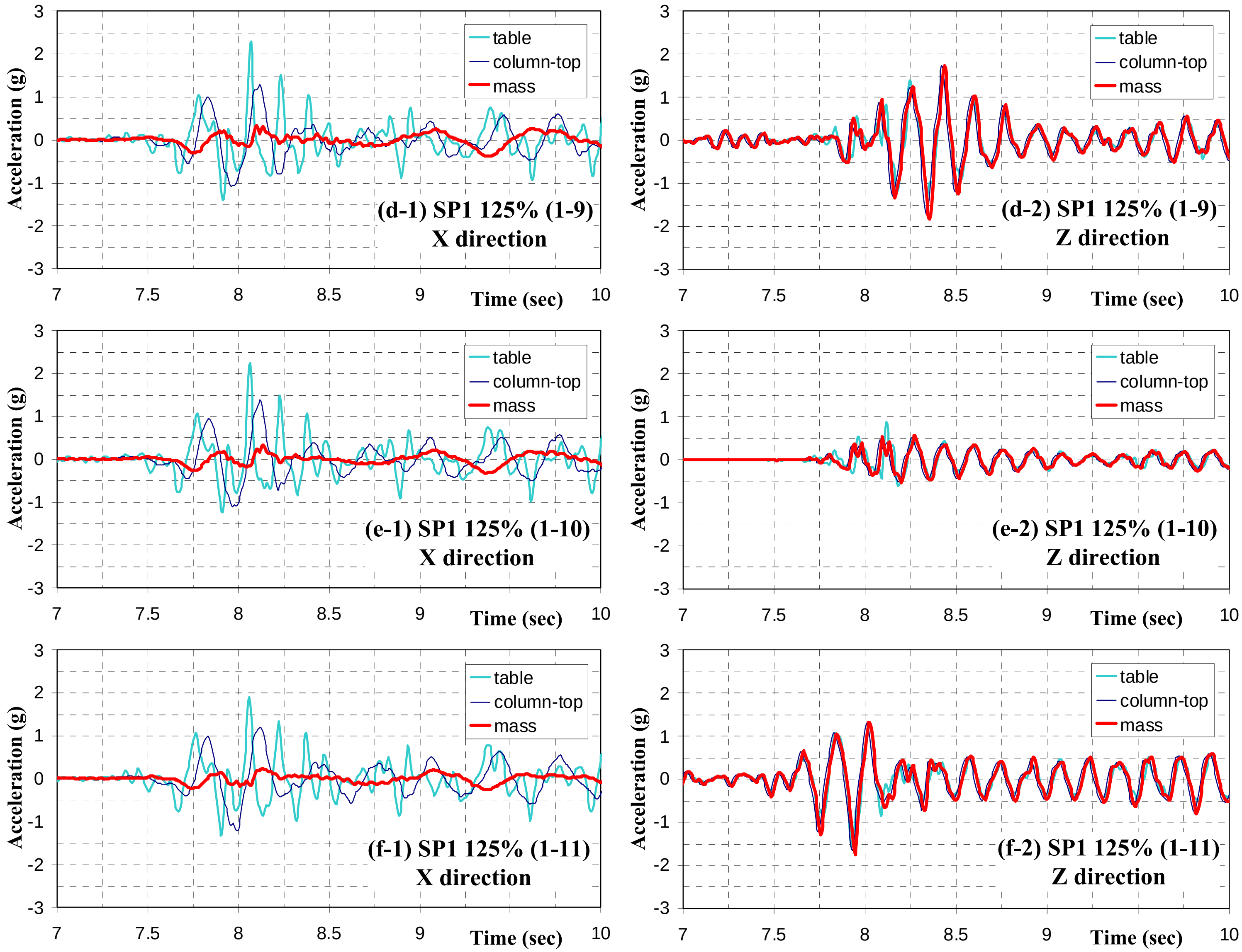

Fig. 4.10 Accelerations at the shaking table, top of the column, and top of the mass blocks in SP1 tests (continued)

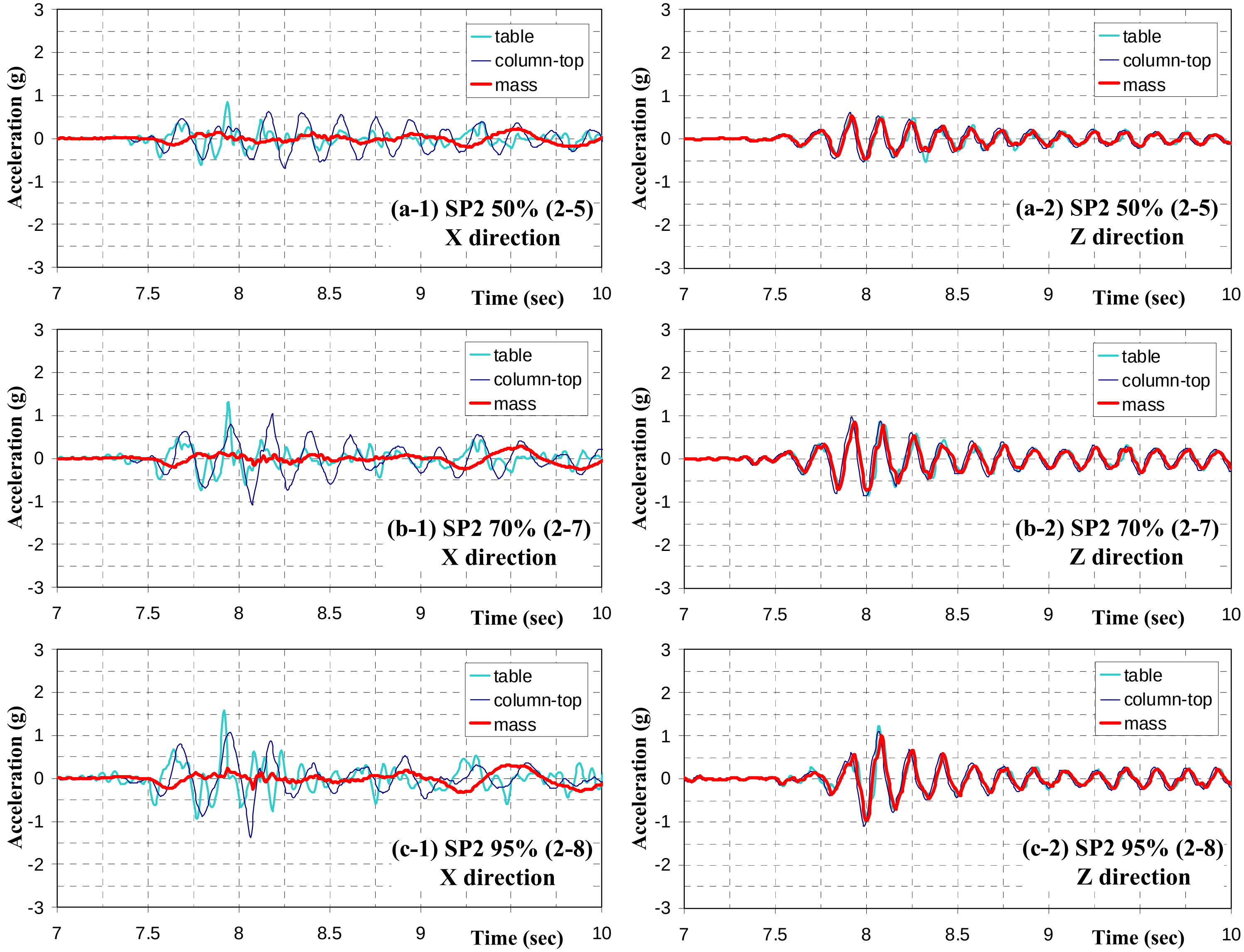

Fig. 4.11 Accelerations at the shaking table, top of the column, and top of the mass blocks in SP2 tests

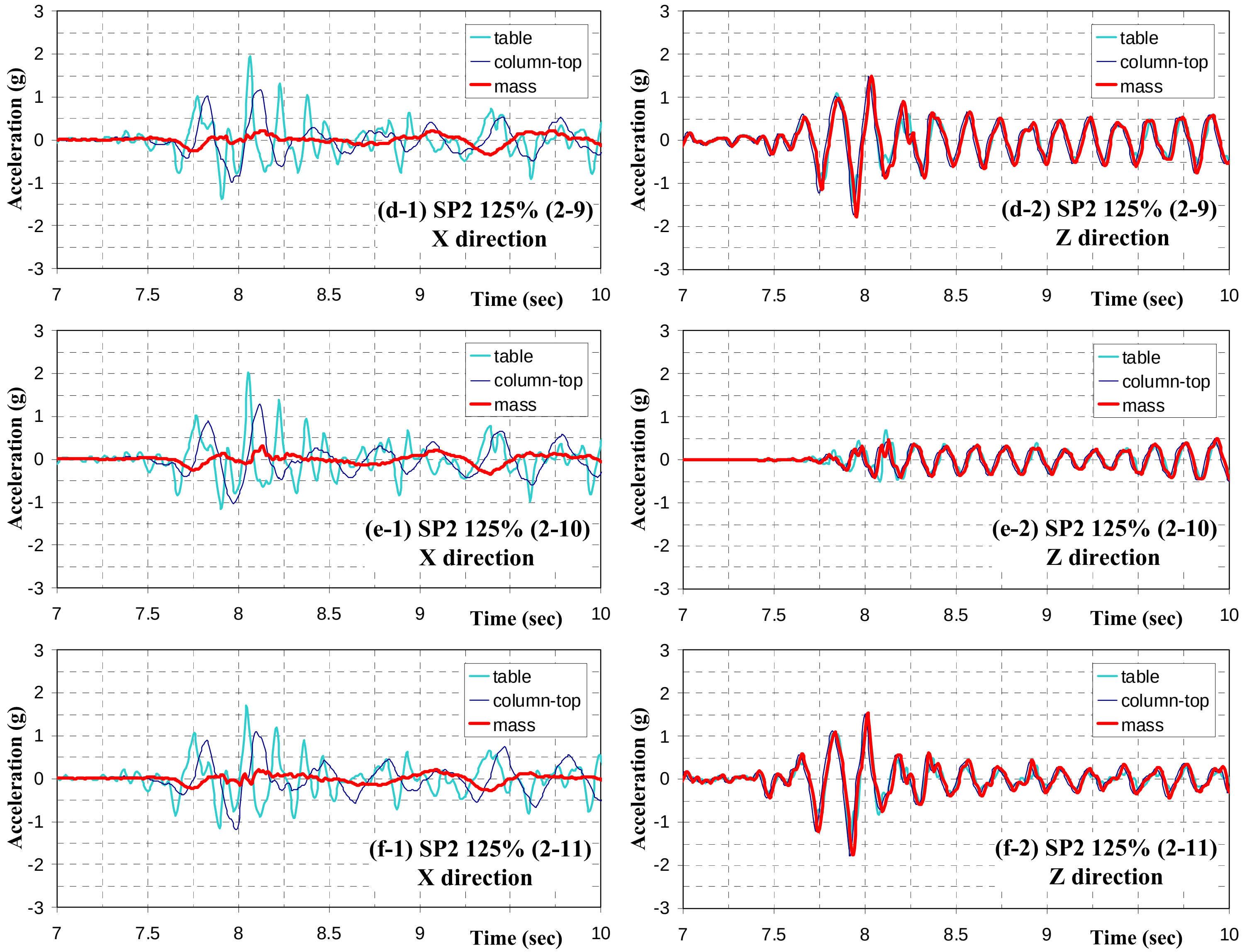

Fig. 4.11 Accelerations at the shaking table, top of the column, and top of the mass blocks in SP2 tests (continued)

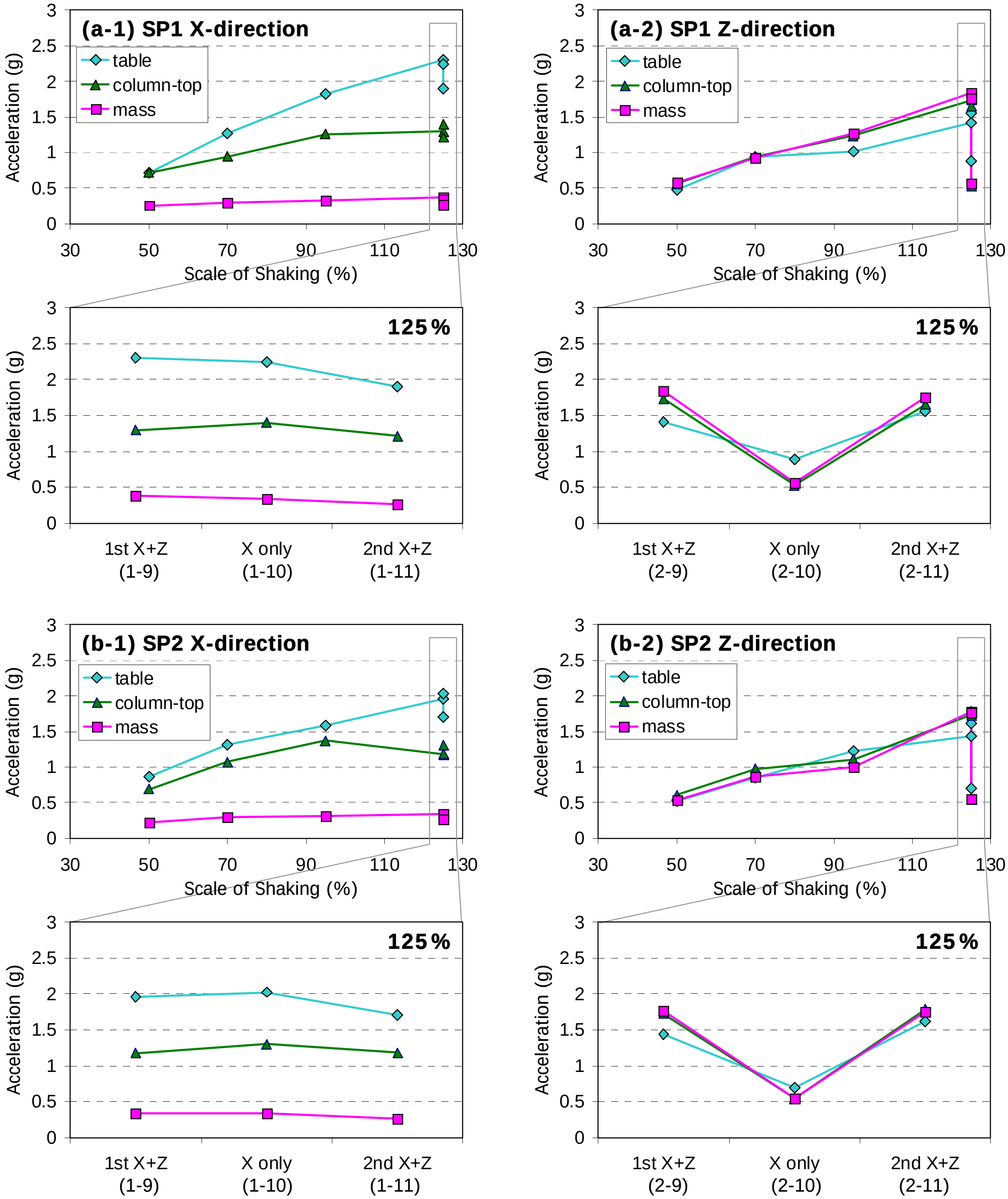

Fig. 4.12 Comparison of peak acceleration values

This trend and the capping of the peak acceleration on the mass blocks were expected results since the stiffness of the column decreased with increasing the level of intensity of shaking and because the base shear capacity of the column was reached (Fig. 4.12(a-1)). This capping was not detected in the Z-components, as shown in Fig. 4.12(a-2). The same trends as discussed above for SP1 were observed in 50%- to 125%-scale tests of SP2, as shown in Fig. 4.11, Fig. 4.12(b-1), and (b-2).

4.3.3 Rotation of the Mass Blocks

The X-component of the acceleration on the mass blocks was significantly lower than that at the top of the column. This difference was due to the additional translational acceleration due to the rotation of the mass blocks. A quantitative explanation is presented in the following paragraphs.

The rotational acceleration is calculated by using the displacement measurements from the wire potentiometers connected to the south side of the mass blocks and the top of the column in X-direction (i.e. direction of the horizontal (north-south) acceleration component). Two wire potentiometers were connected to the south east and south west sides of the top concrete blocks. Hence, the mean of these two displacement measurements is calculated to obtain the displacement at point B in Fig. 4.13(d). Acceleration at point B is obtained through the double differentiation of the displacement time history at point B. On the other hand, acceleration at the top of the column (point A in Fig. 4.13(d)) was obtained from accelerometer measurements. It can be observed in Fig. 4.13(c) that the measured accelerations at the top of the column are very similar to the accelerations calculated from the measured displacements by double differentiation, validating the determination of accelerations at point B from the displacements where accelerometers were not present.

The acceleration difference between points B and A divided by the distance between these points (h_{AB} in Fig. 4.13(d)) resulted in the rotational accelerations on the mass blocks. Additional acceleration on the mass block due to the rotation is equal to the obtained rotational acceleration multiplied by the distance h_{AT}. Then, acceleration at the top of the mass blocks is calculated with Eq. (4.2) by adding the additional acceleration to the measured acceleration at the top of the column.

$$\begin{aligned} a_{derived} &= a_{col-top} + a_{rotation} \\ &= a_{col-top} + \left(\frac{a_{displ(B)} - a_{col-top}}{h_{AB}} \right) \times h_{AT} \\ &= a_{col-top} + \left(a_{displ(B)} - a_{col-top} \right) \times r_h \end{aligned} \tag{4.2}$$

where $a_{col-top}$ is measured acceleration at the top of the column, $a_{displ(B)}$ is the acceleration calculated by differentiation of the mean displacement measured on the south side of the mass blocks, h_{AT} is the vertical distance from the column top to the accelerometers on the mass blocks, and h_{AB} is the vertical distance from the column top to the wire potentiometer targets.

It can be observed from Fig. 4.13(a) and (b) that the derived accelerations calculated with Eq. (4.2) matches well the measured accelerations. This good matching was also observed for the other runs and other test specimen (SP2). This explains the difference observed in Fig. 4.10 and Fig. 4.11 being related to the rotation of the mass blocks. In summary, the lateral acceleration was remarkably changed due to the rotation of the added mass. It should be noted that the shear force on the column was accordingly affected by the acceleration of this mass that depended on the rotation mentioned above. This is discussed further in the following section.

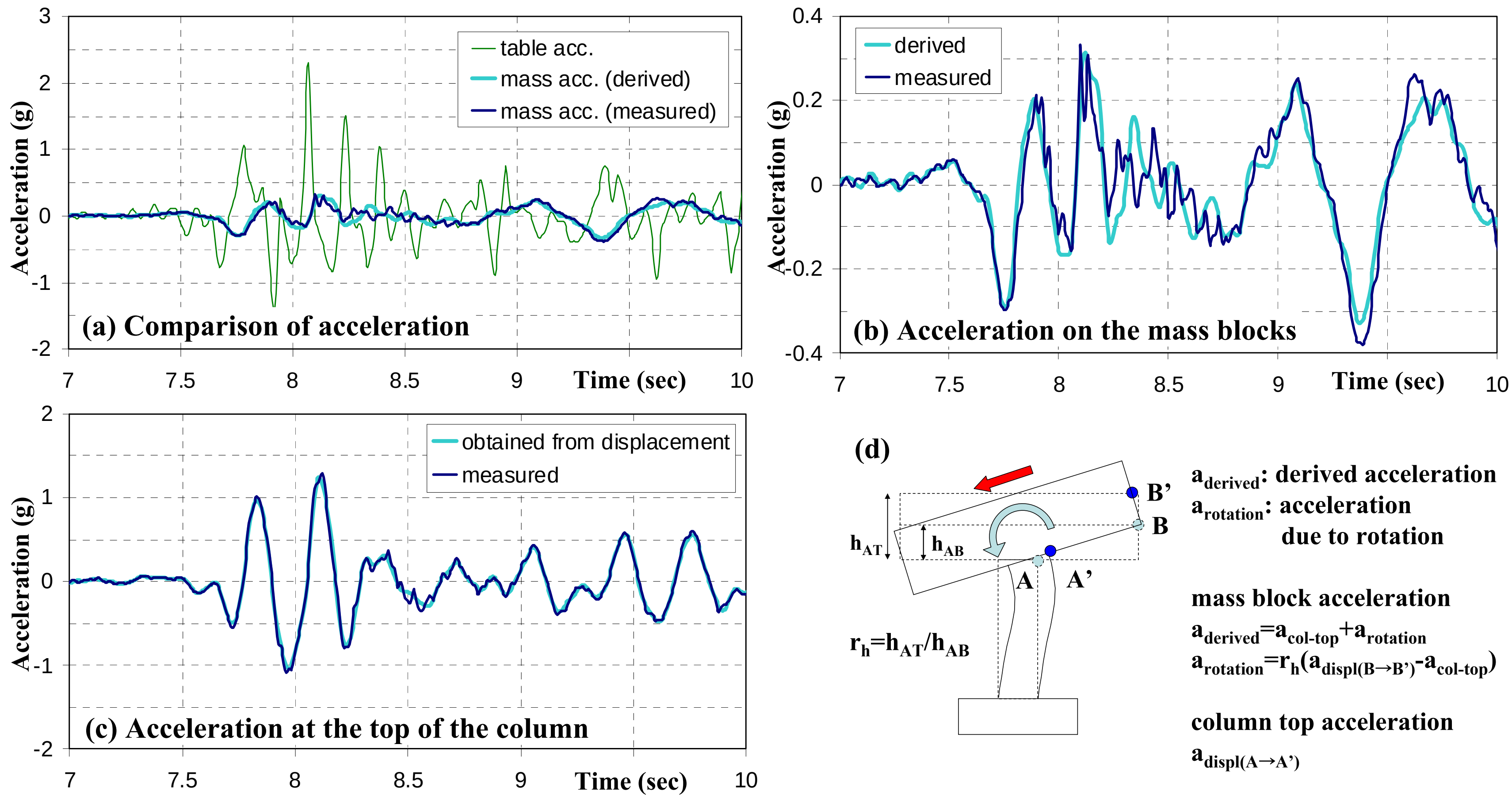

Fig. 4.13 Comparison of measured and derived accelerations (specimen SP1, run 1-9)

4.4 Forces

4.4.1 Shear and Axial Forces

Fig. 4.14 presents the time histories for the axial and shear forces obtained from the load cells for specimens SP1 and SP2 subjected to 50%, 70%, and 95%-scale Northridge earthquake. The runs for these three levels are respectively denoted as 1-6, 1-7, and 1-8 for SP1 and 2-5, 2-7, and 2-8 for SP2 in Table 4.1, Fig. 4.14(a), (b), and (c). For the levels of 125%-scale of Northridge earthquake, the corresponding runs are denoted 1-9, 1-10, and 1-11 for SP1 and 2-9, 2-10, and 2-11 for SP2 in Table 4.1, Fig. 4.14(d), (e), and (f), respectively.

For levels below 125%-scale motion, the axial force is not tension in most cases. SP2 with 95%-scale motion (run 2-8, Fig. 4.14(c-2)) experienced very small peak axial tension, only 1.4 kips. As the intensity increased, the peak-to-peak amplitude of the axial force increased significantly. SP1 had peak-to-peak amplitude of 100.3 kips for axial force under 50%-scale motion, and it became 157.6 kips and 205.0 kips as the scale increased to 70% and 95%, respectively. Hence, under 95%-scale motion, the axial force amplitude was almost twice as large as that under 50%-scale. However, the increase in the shear force was not as large as that in axial force. The peak-to-peak amplitude of the shear force for SP1 increased from 100.4 kips for 50%-scale to 130.3 kips and 165.1 kips for 70%- and 95%-scales, respectively. Similarly, the peak-to-peak amplitude of SP2 changed as follows: 101.8→162.5→198.9 kips (axial force) and 96.8→133.1→149.6 kips (shear force) for scales of 50%→70%→95%, respectively. This is attributed to the fact that the shear forces in these scales were no longer in the linear range, approaching the shear strength of the test specimens. It was also observed that the minimum axial force, i.e. minimum compression (positive) or maximum tension (negative), took place before the maximum shear force except for the cases of SP1 with 95%-scale and the first 125%-scale motions (runs 1-8, Fig. 4.14(c-1) and 1-9, Fig. 4.14(d-1), respectively). This observation for the 95%-scale and the first 125%-scale of SP1 is attributed to the somewhat large time lag of the vertical motion between the target and the shaking table, as shown in Fig. 4.8(c-2) and (d-2).

Total of three 125%-scale tests were conducted for each specimen. As mentioned, the vertical component was not applied in the second of these three runs for each specimen (runs 1-10, Fig. 4.14(e-1), and 2-10, Fig. 4.14(e-2)). It was mentioned previously that vertical acceleration was measured on the shaking table even if the vertical component was not applied due to the interaction between the horizontal and vertical actuators. However, the axial force due to such inevitable vertical acceleration had relatively small compression values with limited effect on the RC column shear capacity. The peak axial and shear forces for the three runs on 125%-scale changed as follows: 252.8→144.5→208.4 kips (axial force, dark line with triangles in Fig. 4.15) and 91.4→92.6→88.3 (shear force) for the respective runs 1-9→1-10→1-11 of SP1 and 227.2→142.8→231.6 kips (axial force) and 77.4→80.9→77.2 kips (shear force) for the respective runs 2-9→2-10→2-11 of SP2. It was observed that the peak shear force increased in the 'X only' runs by 1.29% and 4.47% for SP1 and SP2, respectively, which had the smallest peak axial force. For both specimens, the positive and negative shear force peaks changed in the '2nd X+Z' runs, i.e. 1-11, Fig. 4.14(f-1) and 2-11, Fig. 4.14(f-2), compared to the 'X only' runs, i.e. 1-10, Fig. 4.14(e-1), and 2-10, Fig. 4.14(e-2), especially the positive peak noticeably decreased after significant tension of approximately 60 kips (57.9 kips for SP1 and 63.3 kips for

SP2). The positive shear peak (Fig. 4.15, line with squares), i.e. the 3rd shear peak which is denoted as '3' in Fig. 4.14(d-1), decreased from 92.6 kips to 80.5 kips in SP1 and from 80.9 kips to 67.0 kips in SP2. Considering that the shear forces were similar prior to significant tension for the 'X only' run, where for SP1, this force was 91.4 kips for run 1-9 and 92.6 kips for run 1-10 and for SP2, it was 77.4 kips for run 2-9 and 80.9 kips for run 2-10, the decrease of the positive peak shear force can be explained partly as a result of the vertical excitation, causing axial tension in the column. It was noticed that the decrease of the positive peak shear force was similar in both specimens (12.1 kips for SP1 and 13.8 kips for SP2), which is an indication of the reduction in the contribution of the concrete to the shear force capacity as it was similar for both specimens, while the transverse reinforcement contribution was different in the two test specimens. In addition, it can be stated that the reduction in the shear force capacity is not asymmetric, considering that the decrease in the absolute shear peak and that in the positive shear peak are not the same.

The positive peak shear force was higher for the 1st X+Z test than the 2nd X+Z test (91.4 kips versus 80.5 kips) since the significant axial tension force (-65.8 kips) took place after this shear peak for SP1. However, for SP2, the positive peak shear force was also higher for the 1st X+Z test than the 2nd X+Z test (77.4 kips versus 67.0 kips) although the significant axial tension force (-61.6 kips) took place before this shear peak. Considering the three tests together as a continuous test, it can be speculated that the reduction in the shear peak was due to degradation caused by the occurrence of two successive large axial tensile forces. For SP1, the positive peak shear forces after the first axial tensile peak (-65.8 kips in run 1-9) were 91.4 kips (run 1-9) and 92.6 kips (run 1-10) and they were reduced to 80.5 kips (run 1-11) after the second axial tensile peak (-57.9 kips in run 1-11). For SP2, the positive peak shear forces after the first axial tensile peak (-61.6 kips in run 2-9) were 77.4 kips (run 2-9) and 80.9 kips (run 2-10) and they were reduced to 67.0 kips (run 2-11) after the second axial tensile peak (-63.3 kips in run 2-11). Hence, the positive peak shear force reduced after the second axial tensile peak for both specimens. On the other hand, the peak axial tensile force in the 2nd X+Z tests did not affect the negative peak shear force (88.3 kips in SP1 and 77.2 kips in SP2). This can be explained by the duration of wave propagation in the vertical direction considering that the time between the peak axial tensile force and the negative peak shear force was about 0.04 sec only.

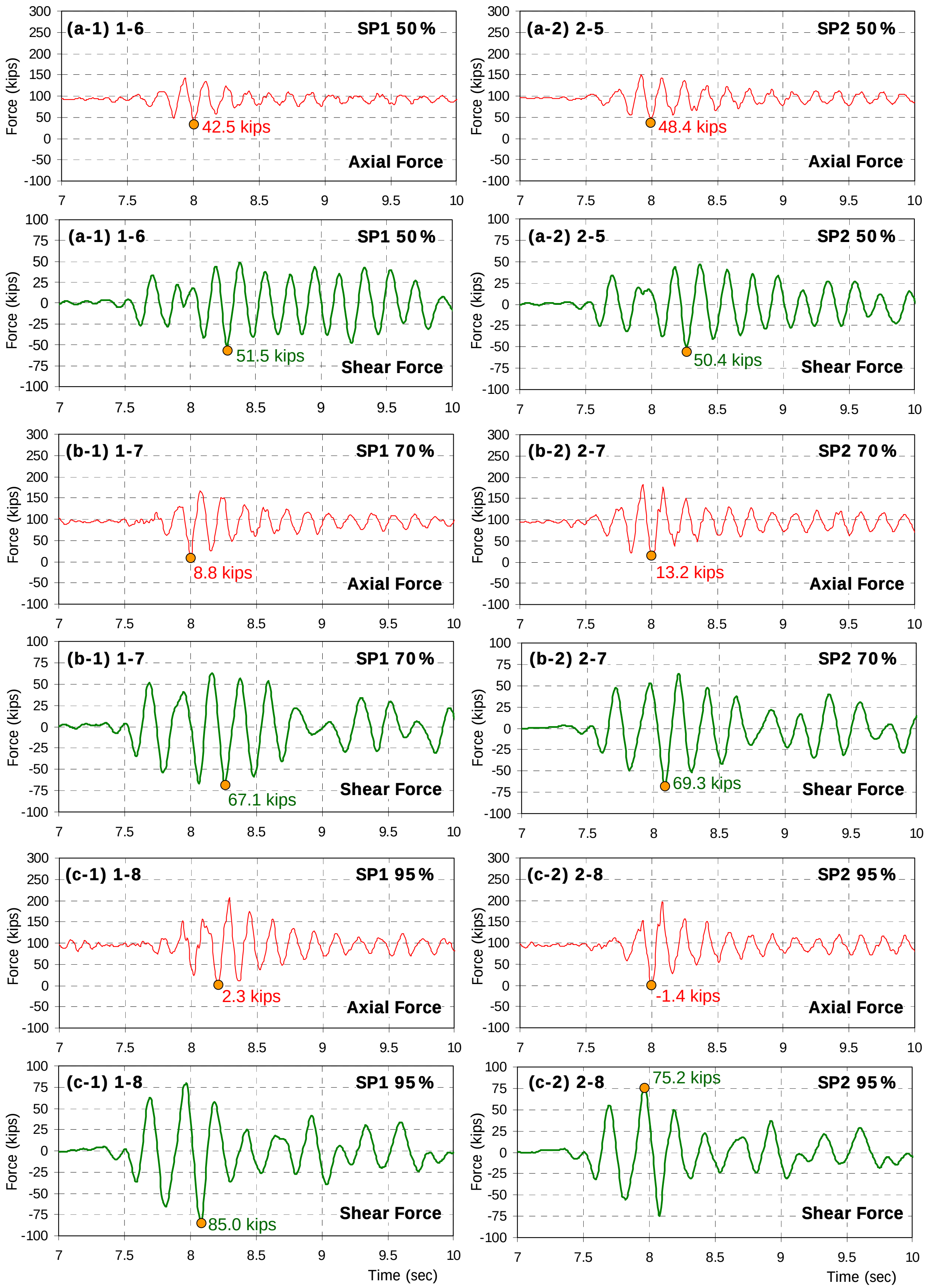

Fig. 4.14 Axial force and shear force history

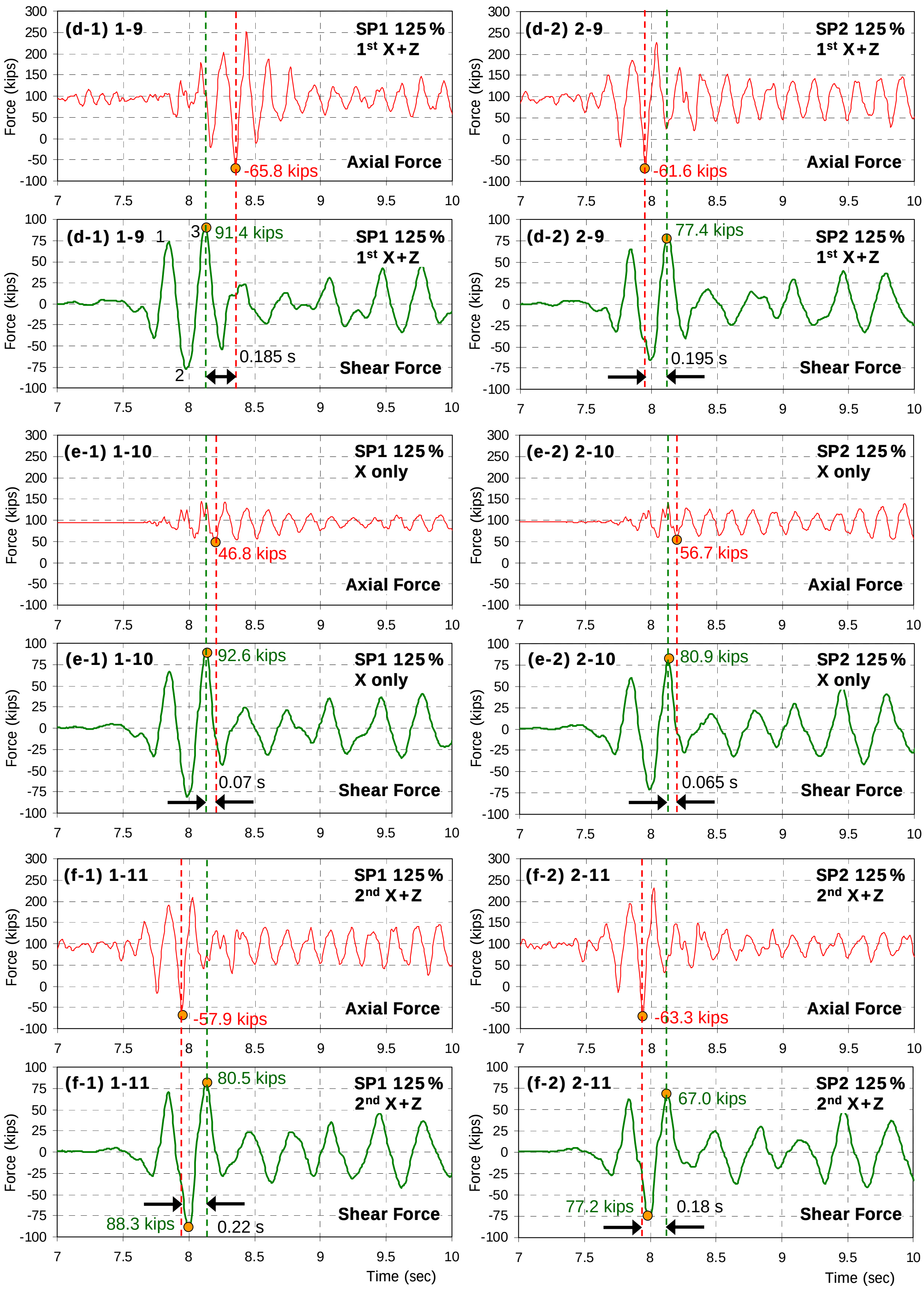

Fig. 4.14 Axial force and shear force history (continued)

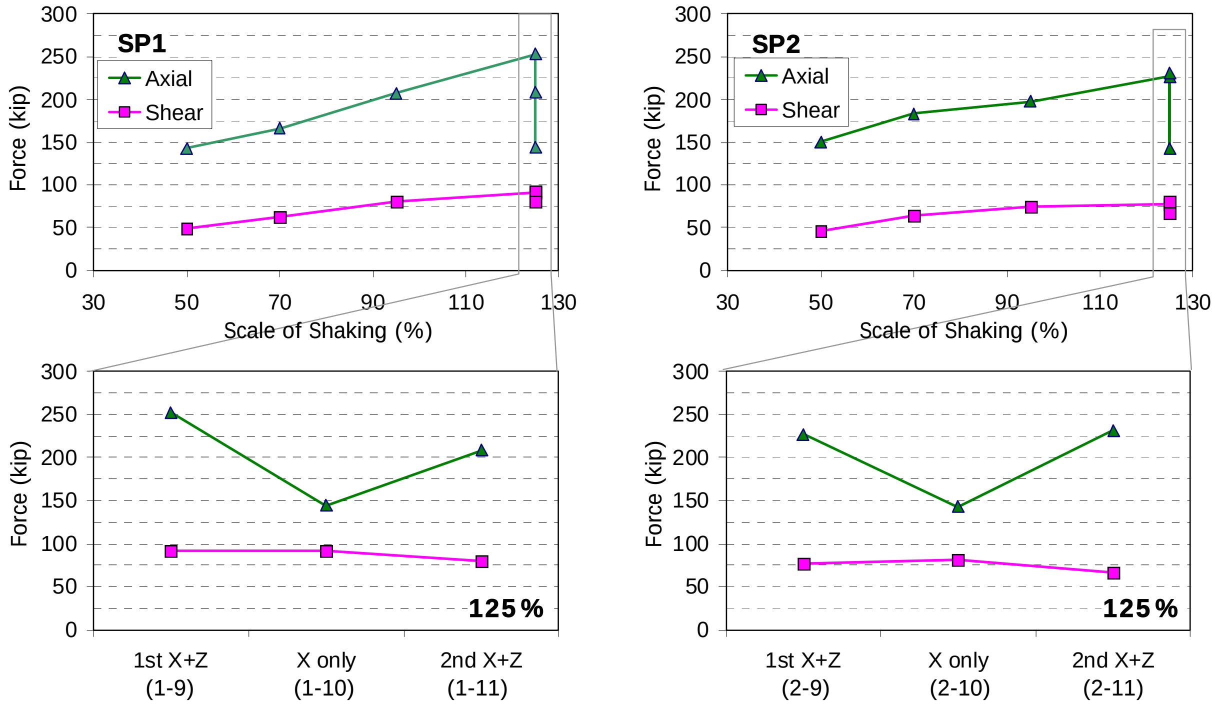

Fig. 4.15 Positive peak axial and shear forces with scale of applied shaking table motion

Table 4.4 compares the axial force at the maximum positive shear force in each test. Even though the decrease of the maximum positive shear force may have partly resulted from the decrease in axial compression, this cannot explain the difference between 'X only' and '2nd X+Z' compared to the difference between 'X only' and '1st X+Z'. In particular, comparing runs 2-9 and 2-10, it was observed that the large difference in the axial force at the maximum positive shear force did not affect the magnitude of the shear force significantly. On the other hand, the maximum tension force and corresponding degradation, as discussed in the previous paragraphs, were more appropriate causes for the shear force difference between 'X only' and 'X+Z' runs.

Table 4.4 Comparison of axial force at the maximum positive shear force

SP	Run	(a) Axial [kips]	(b) Shear [kips]	(c) Axial ratio compared to 'X only' [%]	(d) Shear ratio compared to 'X only' [%]
1	1st X+Z (1-9)	108.4	91.4	77.7	98.7
	X only (1-10)	139.5	92.6	100.0	100.0
	2nd X+Z (1-11)	71.4	80.9	51.2	87.4
2	1st X+Z (2-9)	43.8	78.0	30.7	96.4
	X only (2-10)	142.8	80.9	100.0	100.0
	2nd X+Z (2-11)	73.5	67.1	51.5	82.9

4.4.2 Bending Moments

Bending moment can be calculated from the axial and shear forces recorded using the load cells installed between the footing and the shaking table. The bending moment at any location of the column can be calculated by using a simple free-body calculation. Fig. 4.16(a), (b), and (c) show the bending moment at the base of the column, h=0″ and at the top, h=70″, subjected to the 50%, 70%, and 95%-scale motions, respectively. Before 10 sec, shear and axial forces were significant. Subsequently, the axial force variation almost ceased after 10 sec, and only the shear force governed the bending moment history. In every case, the peak bending moment at the top was larger than that at the base. Moreover, the bending moment at the top and that at the base were out of phase before 9 sec (double curvature). After 10 sec, when the strong part of the horizontal motion ceased, they became in phase (single curvature) and the peak bending moment at the base exceeded that at the top. Therefore, it can be stated that the bending moments at the top and at the base were dominated by the rotational mode before 9 sec, whereas they were dominated by the translational mode after 9 sec. Fig. 4.16(d), (e), and (f) compare the bending moments at the base, h=0″, and at the top, h=70″, subjected to the 125%-scale motions. Similar to the lower level tests, the bending moment was larger at the top and the two bending moments were out of phase during the main excitation of the high level tests.

Table 4.5 compares the maximum values obtained in all the test runs. The absolute values are shown in columns (a) and (b) and the relative values compared to M_{max} (3327.5 kip-in for SP and 3300.1 kip-in), which is modified from the value in Table 3.5 due to higher f_y, are shown in columns (c) and (d). The bending moment at the top relative to its M_{max} was at least 30% larger than that at the base in all test runs. The bending moment values for SP1 and SP2 exceeded M_{max} at the top in the 125%-scale. However, the bending moment at the base never exceeded M_{max} for the all runs of SP1 and SP2. It should be noted that the base bending moment increased by more than 10% in the 125%-scale 'X only' test compared to the 125%-scale 'X+Z' tests while there was little difference in the bending moment at the top, refer to Fig. 4.17.

Table 4.5 Comparison of the maximum bending moment at the base and top of the column

SP	Run	(a) Base [kip-in]	(b) Top [kip-in]	(c) Base [%]	(d) Top [%]
1	50% (1-6)	2029.62	2712.92	61.00	81.53
	70% (1-7)	1899.07	3531.06	57.07	106.12
	95% (1-8)	2459.33	3551.27	73.91	106.72
	125% '1st X+Z' (1-9)	2910.17	3916.73	87.46	117.71
	125% 'X only' (1-10)	3153.47	4110.33	94.77	123.53
	125% '2nd X+Z' (1-11)	2747.91	4046.68	82.58	121.61
2	50% (2-5)	1499.59	2431.99	45.44	73.69
	70% (2-7)	1854.07	3151.16	56.18	95.49
	95% (2-8)	2127.74	3199.51	64.48	96.95
	125% '1st X+Z' (2-9)	2442.27	3627.92	74.01	109.93
	125% 'X only' (2-10)	2736.16	3669.18	82.91	111.18
	125% '2nd X+Z' (2-11)	2343.11	3691.44	71.00	111.86

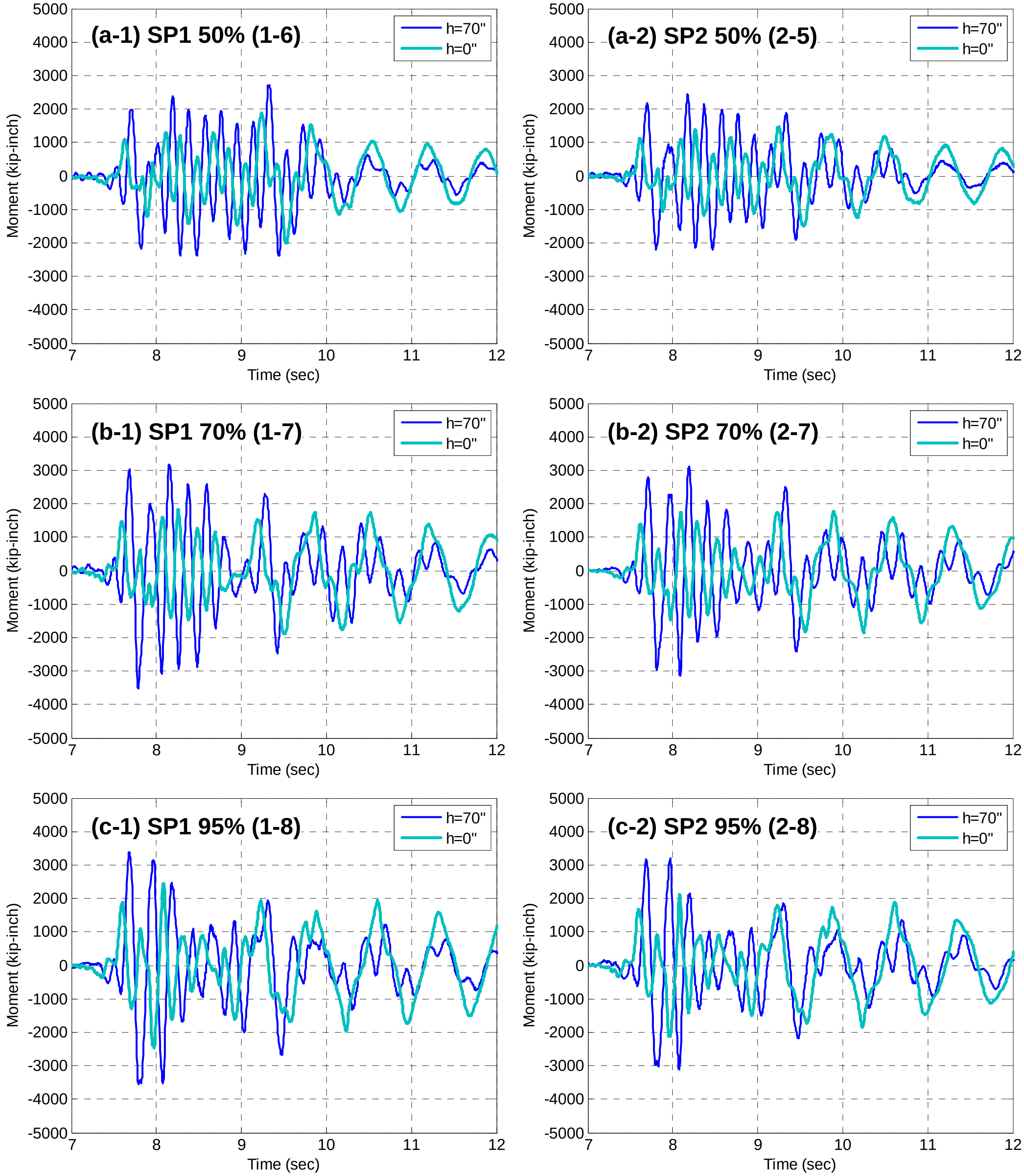

Fig. 4.16 Bending moment history at the top and base of the test specimens

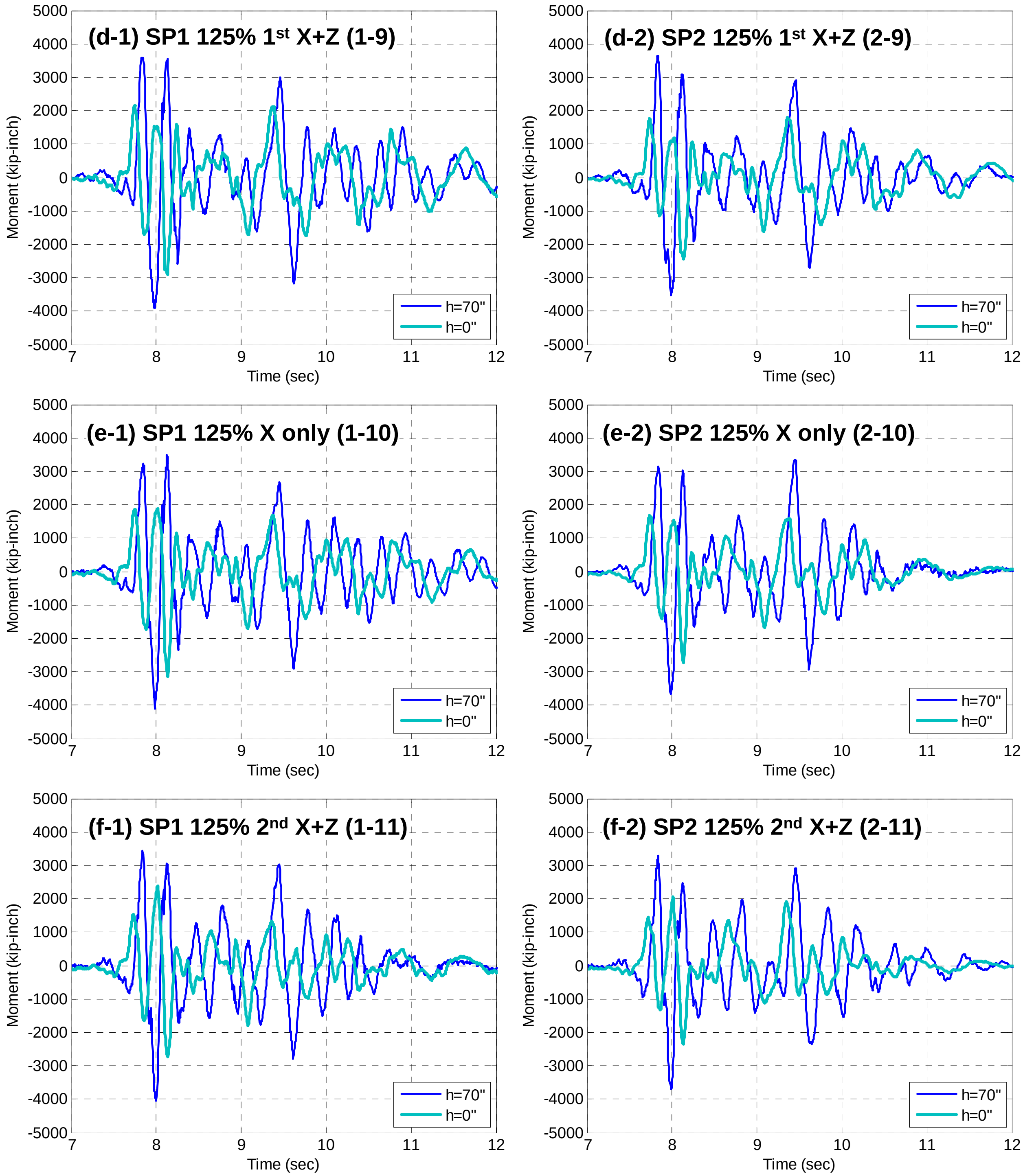

Fig. 4.16 Bending moment history at the top and base of the test specimens (continued)

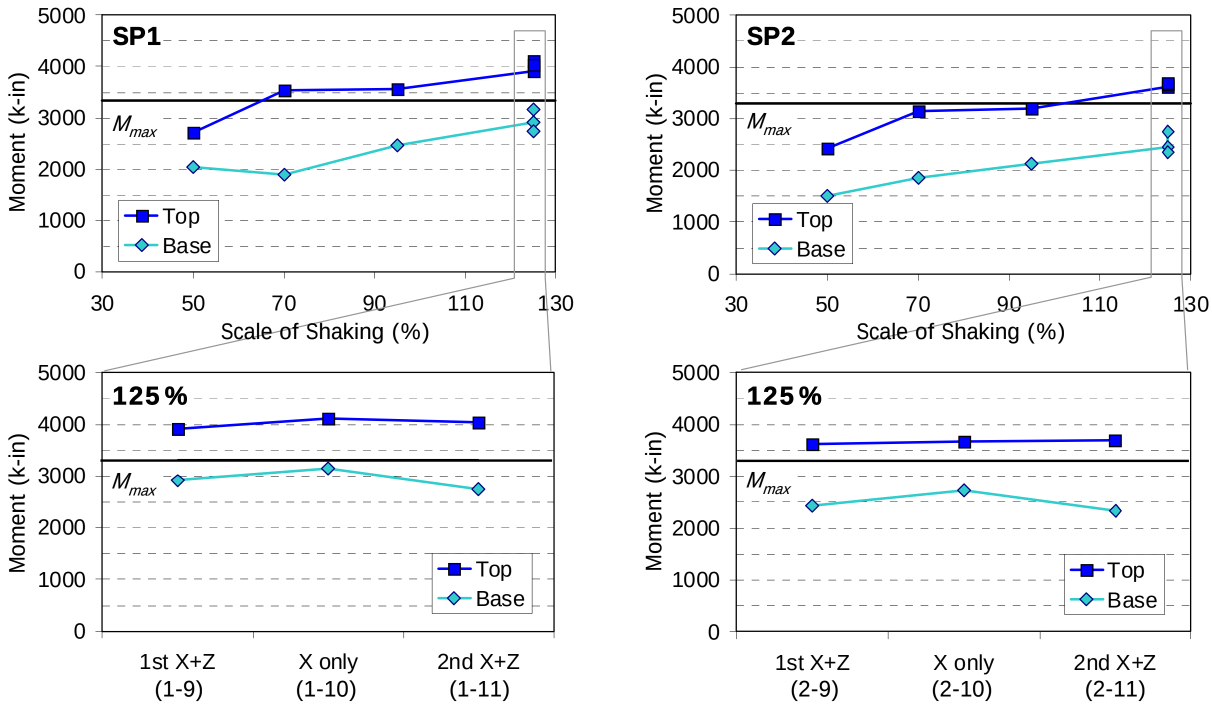

Fig. 4.17 Peak bending moments at the top and base of the test specimens

4.5 Displacements

The lateral and vertical displacement histories were obtained from the wire potentiometers and the DCDTs. The locations are presented in Appendix D.

4.5.1 Lateral Displacement

In this section, relative lateral displacement in the X direction is investigated. Since absolute displacement was obtained from the wire potentiometers, each history was modified by subtracting the displacement at the footing to calculate the relative values. All the displacement histories in Fig. 4.18 are in the X direction, in which the horizontal excitation was applied. Total of four wire potentiometers were connected to the south side of the column and the locations were at h=15″, 35″, 55″, and 70″ above the footing top. Hence, the lateral displacement variation along the column height can be examined.

The relative lateral displacement histories subjected to 50%-, 70%-, and 95%-scale motions are shown in Fig. 4.18(a), (b), and (c), respectively. In general, the top displacement was the largest, as expected. In 50%- and 70%-scale tests, both specimens have the peak lateral displacement after 9 sec, i.e. after the main excitation. However, in the 95%-scale test, both specimens have the peak lateral displacement very slightly before 8 sec.

In Fig. 4.18(d), (e), and (f), the displacement histories for the 125%-scale tests are shown. The top displacement was still the largest in the three runs ‘1st X+Z’, ‘X only’, and ‘2nd X+Z’ tests of both specimens. The peak displacement occurred around 8.14 sec, at which there was a clear 3rd peak of the shear force, refer to Fig. 4.14(d), (e), and (f). It is to be noted that the displacement was centered to the positive side, which means the column deflected more toward the north side, where there was residual displacement.

Fig. 4.19 compares positive (North) and negative (South) peaks before and after 9 sec. This classification was made since the main excitation ended roughly at 9 sec. Positive and negative values mean the top of the column was deflected to the north and south sides, respectively. The positive peak was larger than the absolute value of the negative peak in most cases, and this difference increased as the intensity of the excitation increased. Except for the case of the 125%-scale ‘2nd X+Z’ test of SP2, the positive peak increased or almost did not change for all the 125%-scale runs. The second-order approximation clearly fits well the ‘North’ peaks in Fig. 4.19(a) and (b), but the first-order (linear) approximation is reasonable for the other cases.

The residual displacement increased at the end of every subsequent run. The residual displacement of specimen SP1 was 0.330 in and of specimen SP2 was 0.220 in at the top after the 125%-scale ‘2nd X+Z’ test. At the other locations, the residual displacement was less than at the top of the column. In SP1, after the 3rd 125%-scale test, the residual displacement values were 0.044, 0.110, and 0.180 in at h=15″, 35″, and 55″, respectively. In SP2, the corresponding values were -0.005, 0.030, and 0.079 in, respectively.

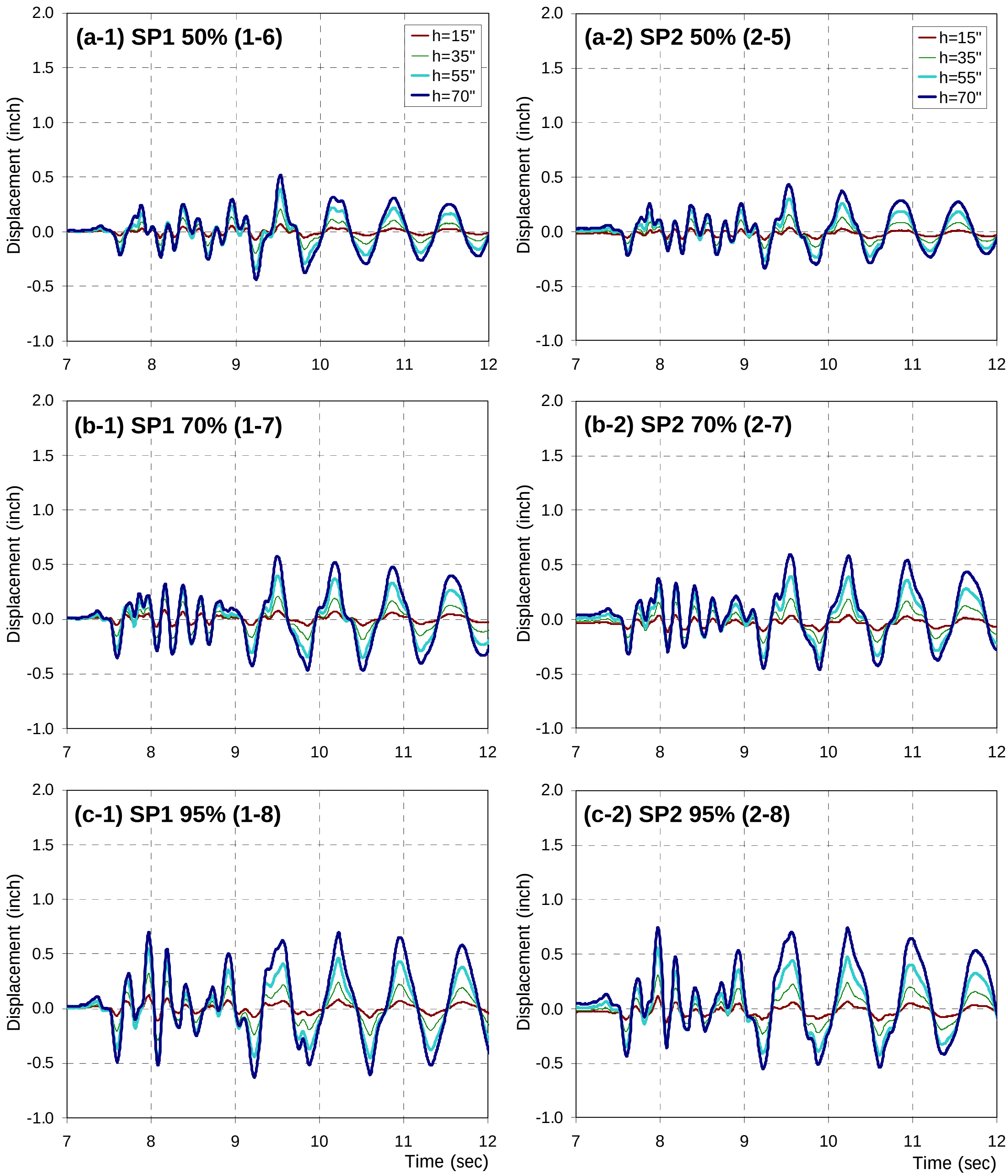

Fig. 4.18 Relative lateral displacement history

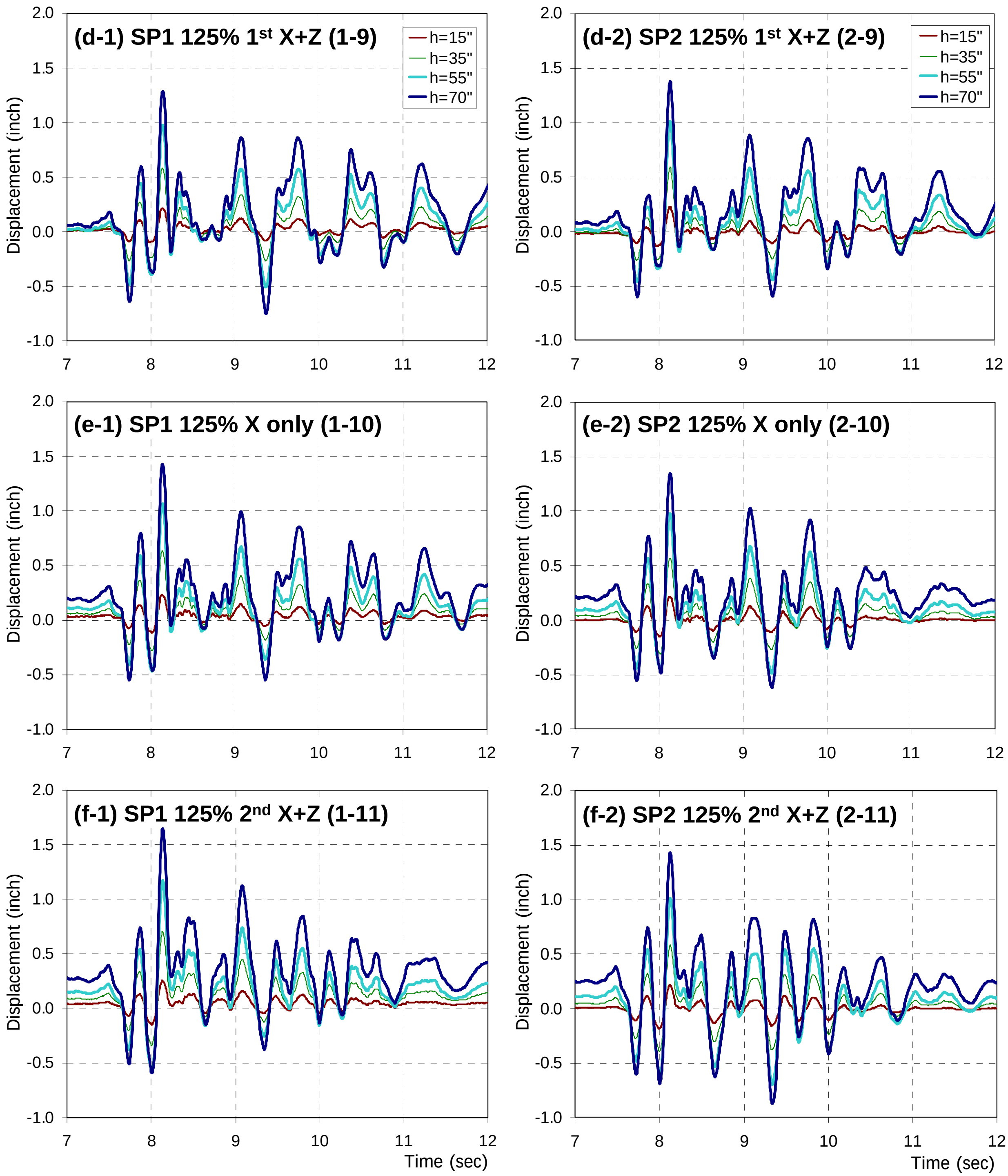

Fig. 4.18 Relative lateral displacement history (continued)

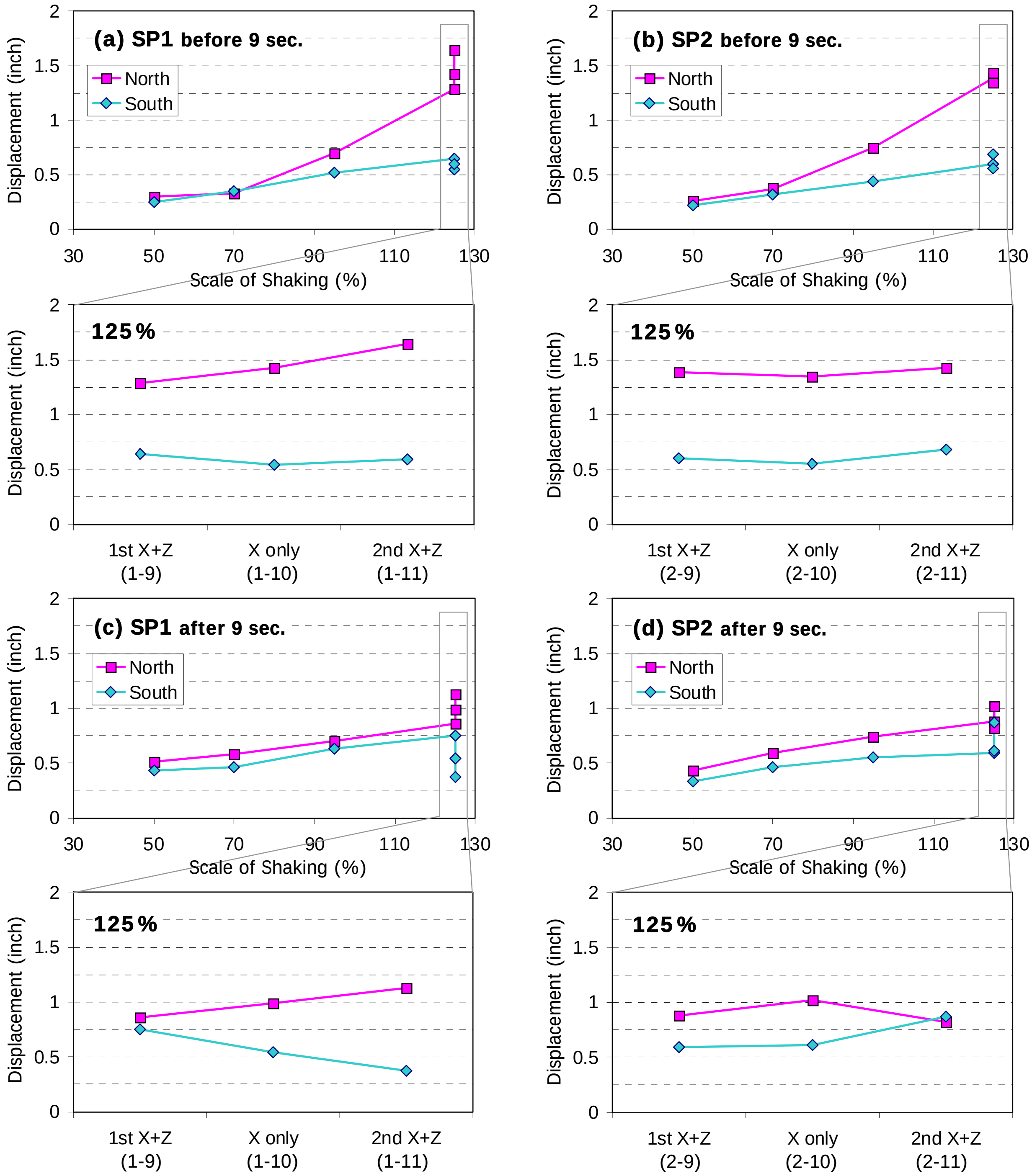

Fig. 4.19 Peak relative lateral displacement at the top of the test specimens

4.5.2 Vertical Displacement

Vertical displacement was measured by wire potentiometers and DCDTs. Total of four wire potentiometers were connected to the bottom of the top concrete blocks. The mean value of the four wire potentiometer measurements is investigated. In addition, two DCDTs were connected to the bottom of the top of the monolithically-cast block on the west and east sides of the column. Similar to the case of wire potentiometers, the mean of the two DCDTs is discussed in this section.

Fig. 4.20(a), (b), and (c) compare the means of the vertical displacement histories from the wire potentiometers and the DCDTs when the specimens were subjected to 50%-, 70%-, and 95%-scale motions, respectively. It is noticeable that the vertical displacement was rarely negative. Since positive displacement was elongation, this observation implies that the centroid of the column cross-section had tensile strains most of the time, which is an expected result considering the cross-sectional analysis of a RC column subjected to eccentric axial forces less than the balanced force. Second observation is that the displacement measured by the wire potentiometers was larger than that measured by the DCDT's (up to 17% for the peak positive peaks). Because the wire potentiometers measured displacements of the concrete blocks, it is expected that the displacement history included more oscillations and errors due to the concrete block mass rotations.

Fig. 4.20(d), (e), and (f) present vertical displacement histories of the specimens subjected to the 125%-scale motions. The two observations in the above paragraph are still valid. In addition, residual displacement, about 0.05 in, was larger than previous cases. Another observation is that the absence of the vertical excitation did not result in a remarkable difference in the vertical displacement. Regarding the peak displacement, there was a decrease in the 125%-scale 'X only' test compared to the '1st X+Z' test. The DCDT measurement of SP1 and SP2 decreased by 3.4% and by 17.7%, respectively (Fig. 4.21). In the case of the peak-to-peak amplitude, it decreased by 14.5% and 29.6% for SP1 and SP2, respectively (Fig. 4.22). The residual vertical displacement increased similar to the case of the residual lateral displacement. Finally, SP1 and SP2 elongated by 0.068 in and 0.040 in after the 125%-scale '2nd X+Z' test, respectively.

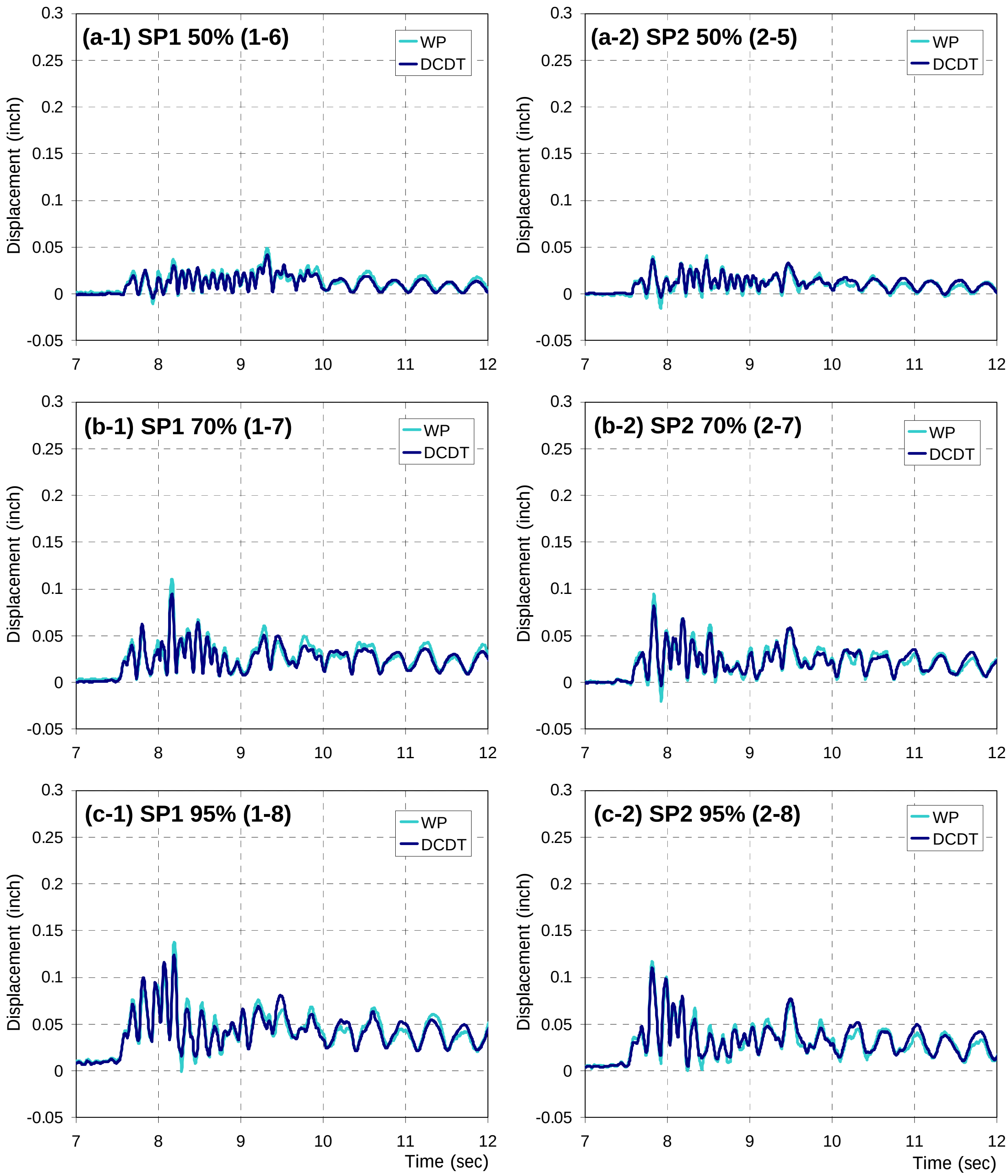

Fig. 4.20 Relative vertical displacement history of the top block and the concrete additional mass blocks

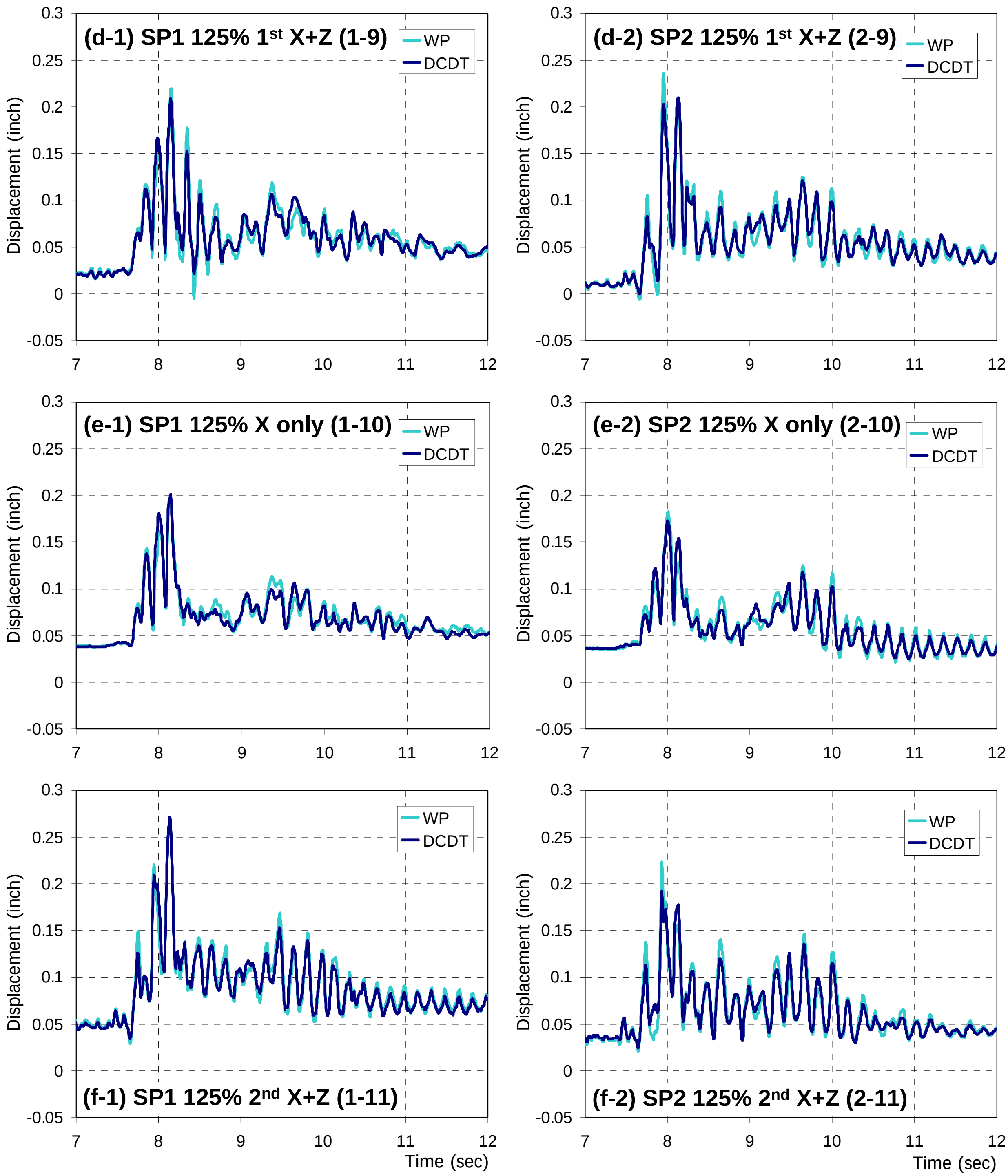

Fig. 4.20 Relative vertical displacement history of the top block and the concrete additional mass blocks (continued)

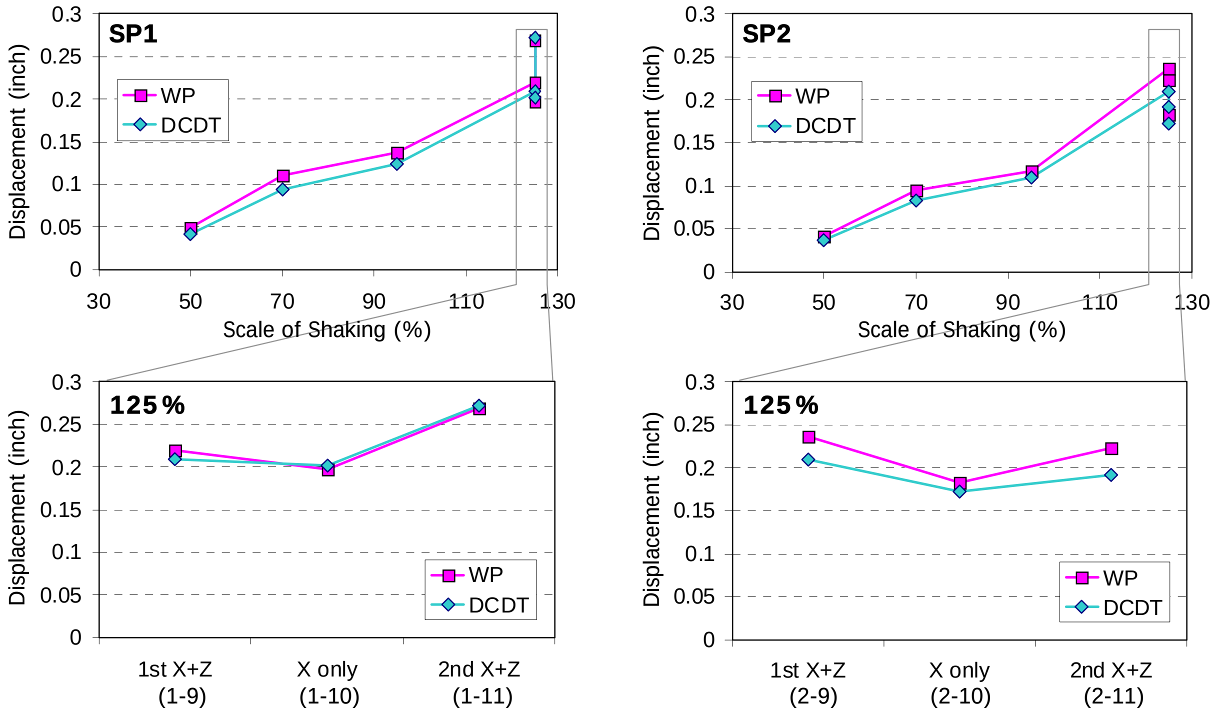

Fig. 4.21 Peak vertical displacement of the test specimens

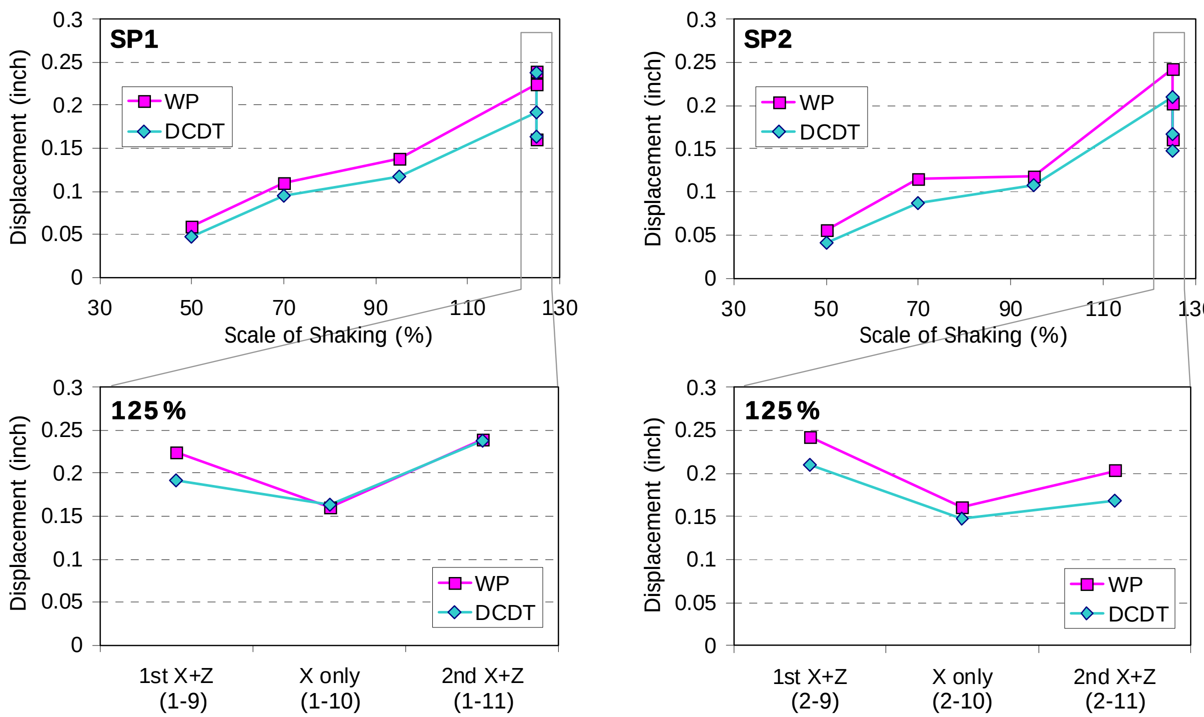

Fig. 4.22 Peak-to-peak vertical displacement of the test specimens

4.6 Force-Displacement Relationships

The relationship of the base shear and lateral displacement is shown in Fig. 4.23, and the relationship of the axial force and axial deformation is shown in Fig. 4.24. Note that the axial force is positive in compression and negative in tension and the axial displacement is positive in elongation and negative in shortening.

Fig. 4.23(a), (b), and (c) present the shear force-lateral displacement relationships of SP1 and SP2 subjected to the respective 50%-, 70%-, and 95%-scale motions (runs 1-7, 1-8, and 1-9 for SP1 and 2-7, 2-8, and 2-9 for SP2). The decrease in the lateral stiffness with increasing damage was observed as the intensity of the ground motion increased. Fig. 4.23(d), (e), and (f) are for the 125%-scale motions (runs 1-10, 1-11, and 1-12 for SP1 and 2-10, 2-11, and 2-12 for SP2). The lateral stiffness slightly decreased with the increase of runs since the damage in the column increased. In addition, the stiffness in the positive force and displacement side was smaller than that in the negative side, which was a consequence of the pulse in the ground motion resulting in asymmetric displacements and accordingly asymmetric damage distribution. As mentioned previously, the decrease in the maximum positive force in the 125% '2nd X+Z' test with respect to the 125% 'X only' test can be partly attributed to the decrease in shear force capacity due to the presence of axial tension. In addition, it should be noted that the maximum positive and negative shear forces of SP2 (95%- and 125%-scales, respectively, in Fig. 4.23) were smaller than those of SP1 since SP2 had lower shear capacity provided by the transverse reinforcement with wider spacing.

Fig. 4.24(a), (b), and (c) present axial force-vertical displacement relationships of SP1 and SP2 subjected to the respective 50%-, 70%-, and 95%-scale motions (runs 1-7, 1-8, and 1-9 for SP1 and 2-7, 2-8, and 2-9 for SP2). It can be confirmed that the column was not under significant tension before the 125%-scale motion was applied. It should be noted that the gravity load was about 100 kips from the load cells measurements, which represents the origin of the force in the axial force-deformation relationships. It was observed that the axial elongation was almost eight times the axial shortening due to the opening of the cracks. From Fig. 4.24(d), (e) and (f), it can be confirmed that the vertical component of the 125%-scale motion caused tension and significant compression in the column as already discussed in Fig. 4.14. The axial force subjected to the excitation with horizontal component only was between 50 and 150 kips (the presence of axial force under only horizontal component was due to the presence of vertical acceleration on the shaking table resulting from the interaction of the vertical and horizontal actuators to balance the overturning moment), but that subjected to both horizontal and vertical components was between -70 and 250 kips. It can be observed that the axial elongation continued to increase for the 125% 'X only' test due to the presence of the cracks.

The straight lines in Fig. 4.23 show the lateral stiffness of each test. The stiffness was calculated based on the maximum shear force on the positive and negative sides and the corresponding lateral displacement. Up to 70%-scale test, the stiffness value on the positive side was identical to that on the negative side. However, as the intensity level increased, the stiffness decrease in the positive side was more significant. From 70%- to 95%-scale and from 95%- to the 1st 125%-scale tests, the lateral stiffness on the positive side decreased by about 40%, while that on the negative side decreased by 25% or less. From the 125% '1st X+Z' to the 'X only' and the subsequent tests, the stiffness change was not remarkable on the positive side but the decrease continued on the negative side. This trend implied that the south side of the column was damaged more first causing less stiffness on the positive side (positive was defined as the direction from south to north). Subsequently, the damage extended to the north side of the column, which caused the following stiffness decrease on the negative side. These observations were consistent with the crack propagation patterns presented in the following section. It should be noted that the stiffness values were different from those obtained from the pullback tests where the column was predominantly deflecting in the 1st mode, which was the translational mode representing a cantilever column. However, during the ground excitations, the column deflected in a shape which was a combination of translational and rotational modes as presented later in Fig. 5.8. Hence, stiffness values calculated from the force-displacement relationships up to 95%-scale tests were on average larger than the lateral stiffness from the pullback test discussed in Section 4.2.1.

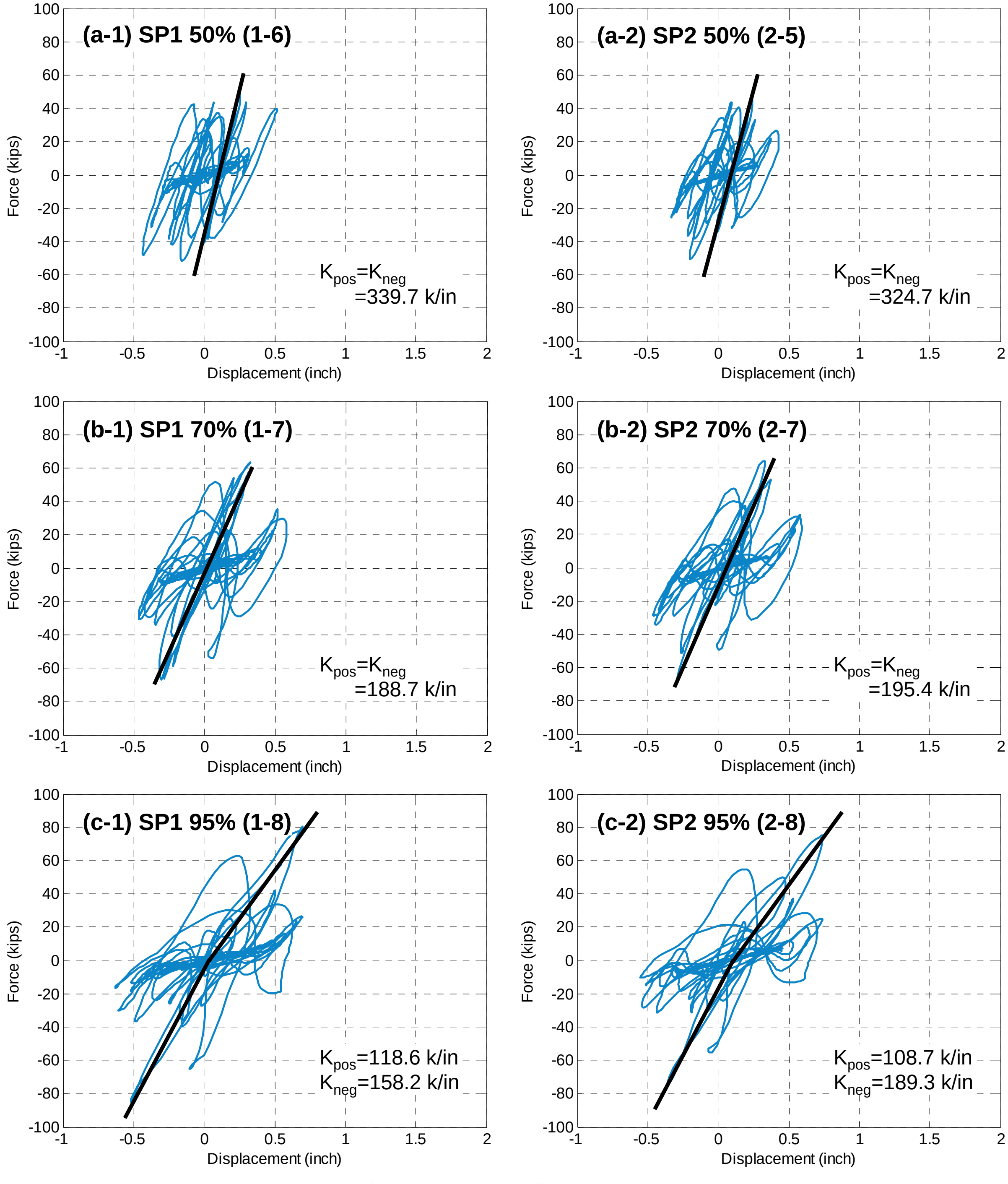

Fig. 4.23 Shear force-lateral displacement relationships

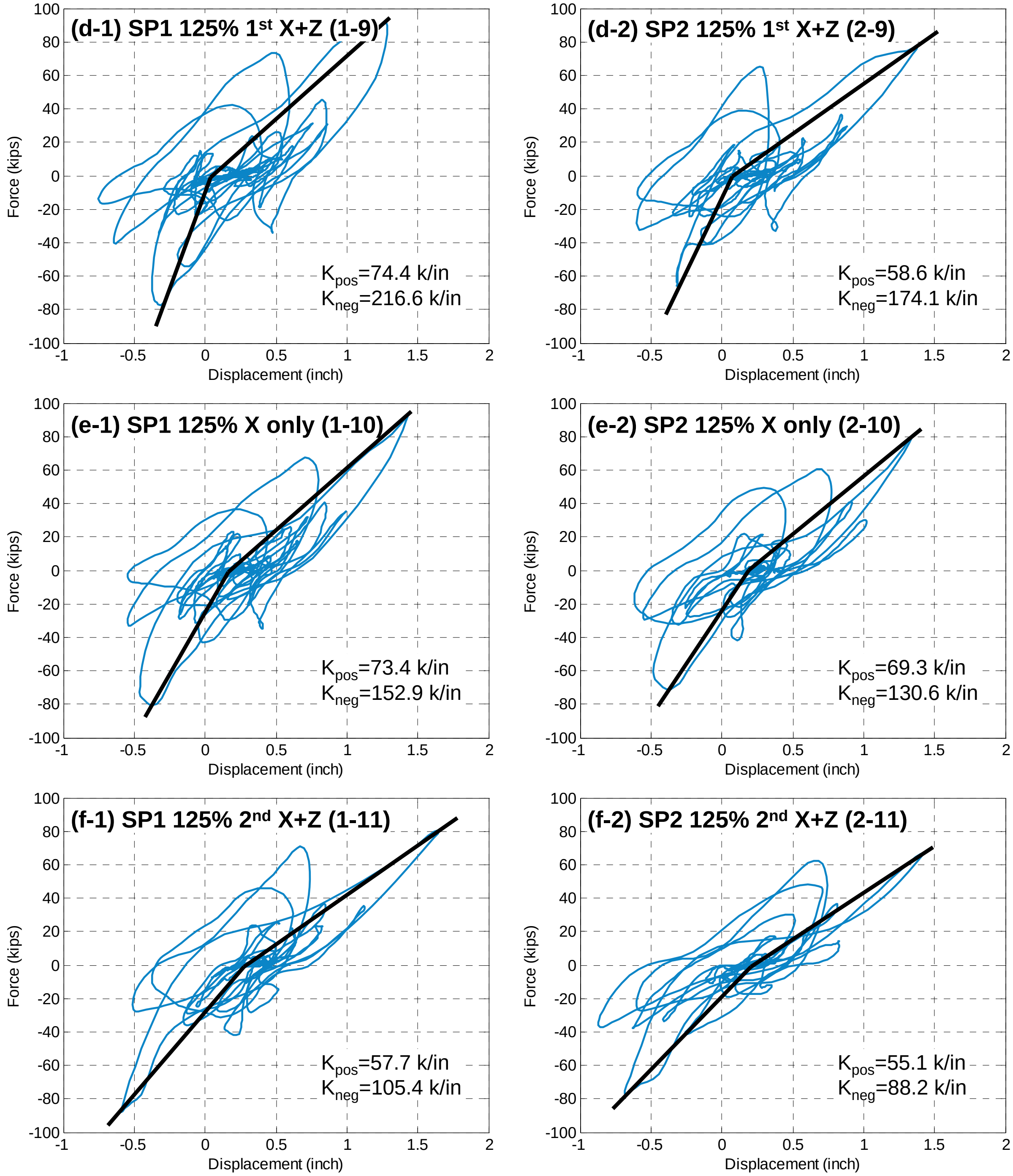

Fig. 4.23 Shear force-lateral displacement relationships (continued)

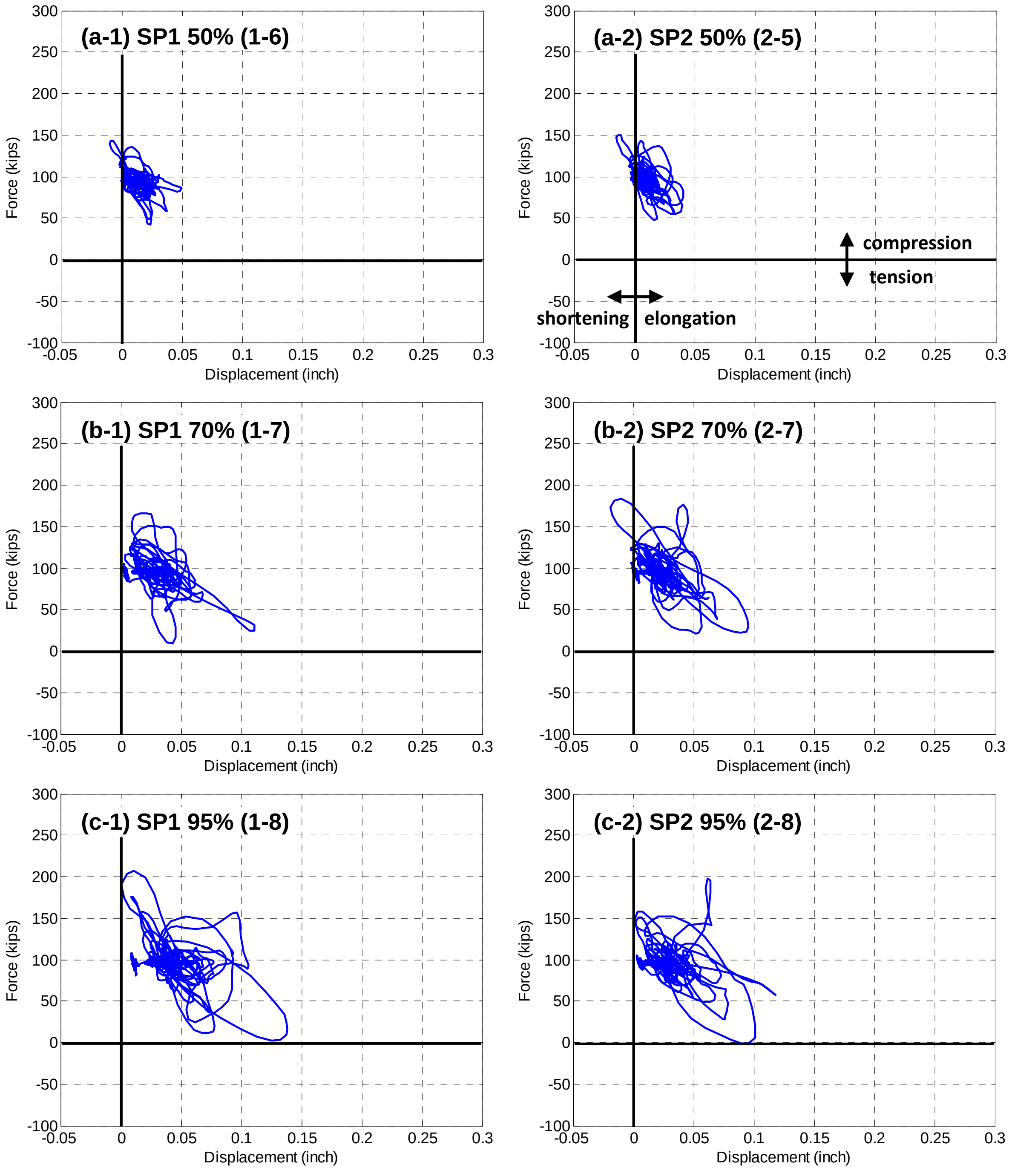

Fig. 4.24 Axial force-vertical displacement relationships

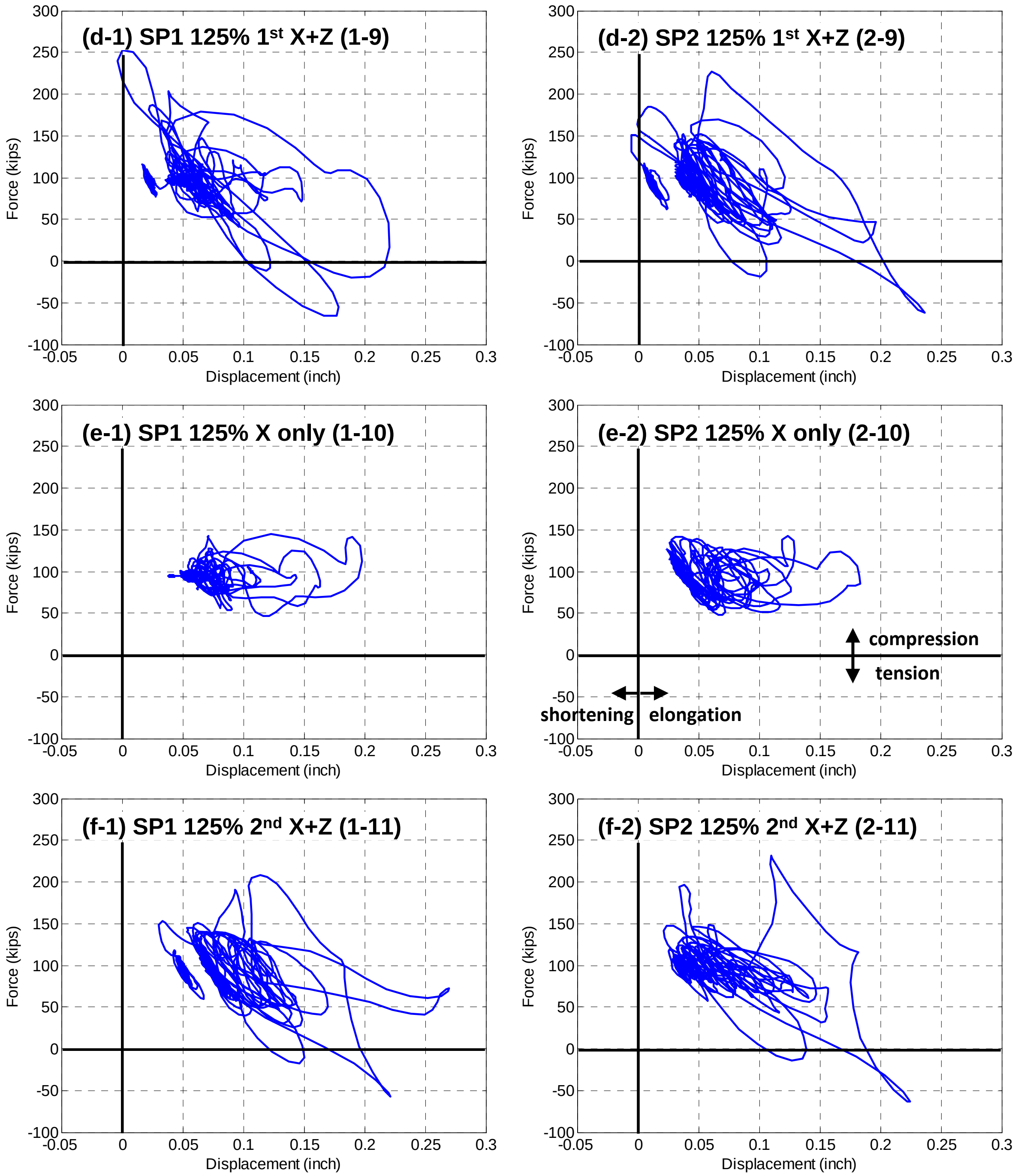

Fig. 4.24 Axial force-vertical displacement relationships (continued)

4.7 Crack Propagation

Crack initiation and propagation of specimens SP1 and SP2 are shown in Fig. 4.25 and Fig. 4.26, respectively. The photographs of the damaged specimens SP1 and SP2 are shown in Appendix E. It should be noted that thicker lines represent new cracks which did not exist in the previous runs.

After the 50%-scale test (Fig. 4.25(a) for SP1 and Fig. 4.26(a) for SP2), only three or four cracks appeared near the top on the south and north sides of SP1 while SP2 had more cracks in the upper part and the first shear crack appeared near *h*=60″. The lower part of each test specimen experienced less cracks than the upper part. Finally, SP2 had the first vertical crack near *h*=40″ on the north side.

After the 70%-scale test (Fig. 4.25(b) for SP1 and Fig. 4.26(b) for SP2), several shear cracks appeared near the top on the east and west sides of the column. They were near or above *h*=50″ in SP1 and some shear cracks appeared even between *h*=35″ and 50″ in SP2. In addition, SP2 had a significant number of vertical cracks above *h*=20″ on the north side.

As shown in Fig. 4.25(c) for SP1 and Fig. 4.26(c) for SP2, cover spalling started at the top on the north and south sides and shear cracks appeared near the bottom on the east and west sides after 95%-scale test (runs 1-8 for SP1 and 2-8 for SP2). As a result, there were several shear cracks along the height of the columns except the regions between *h*=25″ and 35″ on the east and west sides of SP1 and between *h*=20″ and 35″ of SP2. SP1 had vertical cracks above *h*=30″ on the north and above *h*=20″ on the south. SP2 had similar cracks above *h*=10″ on the north and between 10″ and 30″ on the south.

As the intensity increased, cracks extended over the column. In particular, the shear cracks were shown clearly after 125%-scale motions except for the middle of SP1 (*h*=30″ to 40″, i.e. 1.5D to 2.0D). Compared to the 125%-scale 'X+Z' tests, the 'X only' test produced significantly less shear and vertical cracks (Fig. 4.25(e) for SP1 and Fig. 4.26(e) for SP2). This observation is consistent with the reduction of shear strength at '2^{nd} X+Z' test with respect to the 'X only' test (around 12 and 14 kips reduction for SP1 and SP2 respectively) as mentioned in Section 4.4.1. After the 125%-scale '2^{nd} X+Z' test, the vertical cracks extended over the column, except for the region between *h*=10″ and 20″ of SP1. In addition, it is observed that the crack distribution of SP2 was denser than that of SP1 subjected to the same intensity level due to lower shear capacity of SP2 compared to SP1.

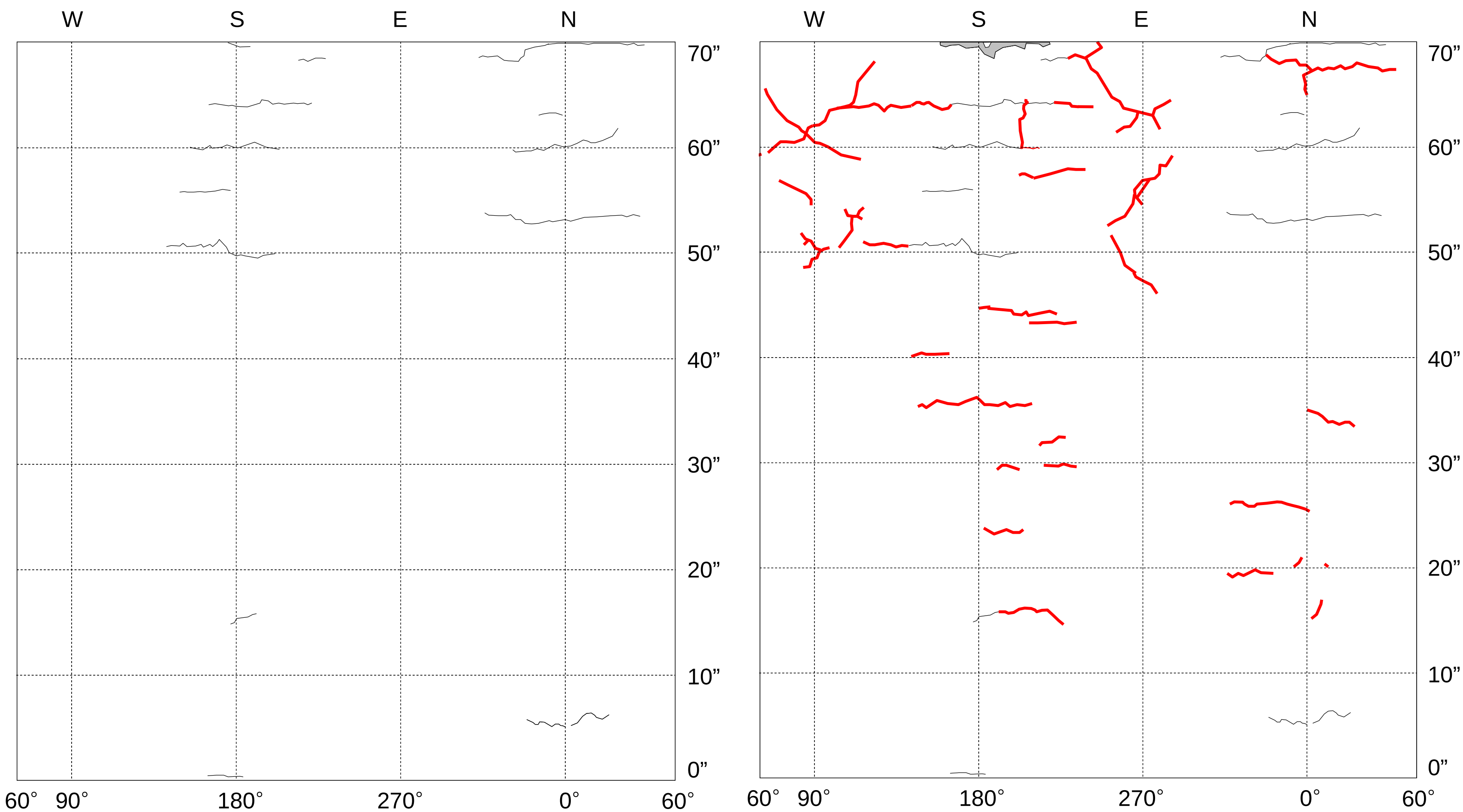

(a) After the 50%-scale run (run 1-6)

(b) After the 70%-scale run (run 1-7)

Fig. 4.25 Crack propagation of SP1

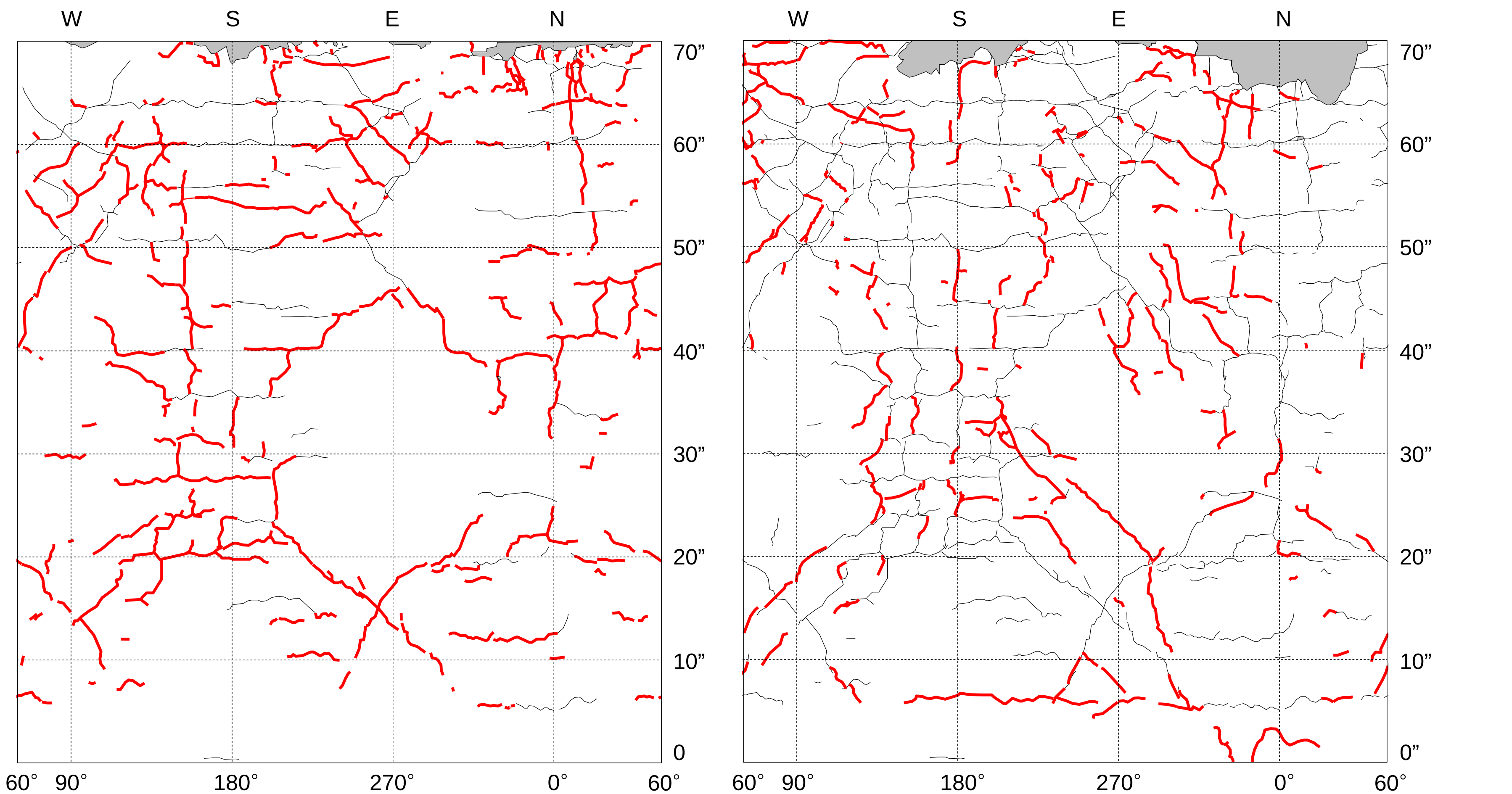

(c) After the 95%-scale run (run 1-8)

(d) After the 125%-scale ‘1st X+Z’ run (run 1-9)

Fig. 4.25 Crack propagation of SP1 (continued)

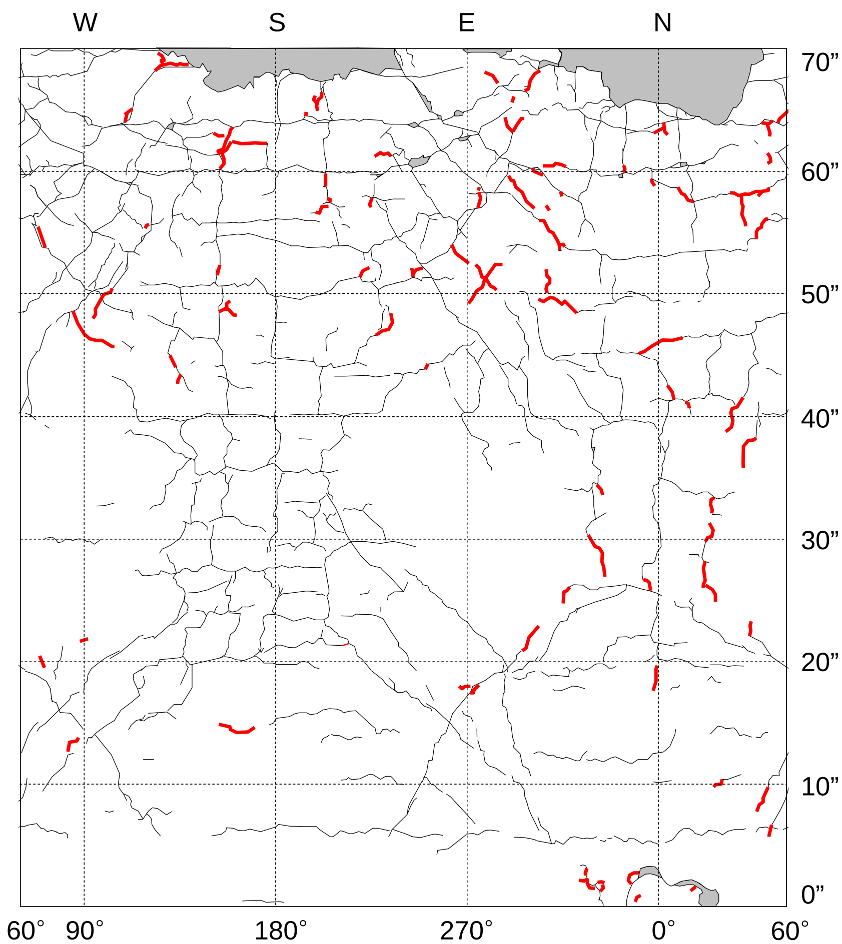

(e) After the 125%-scale ‘X only’ run (run 1-10)

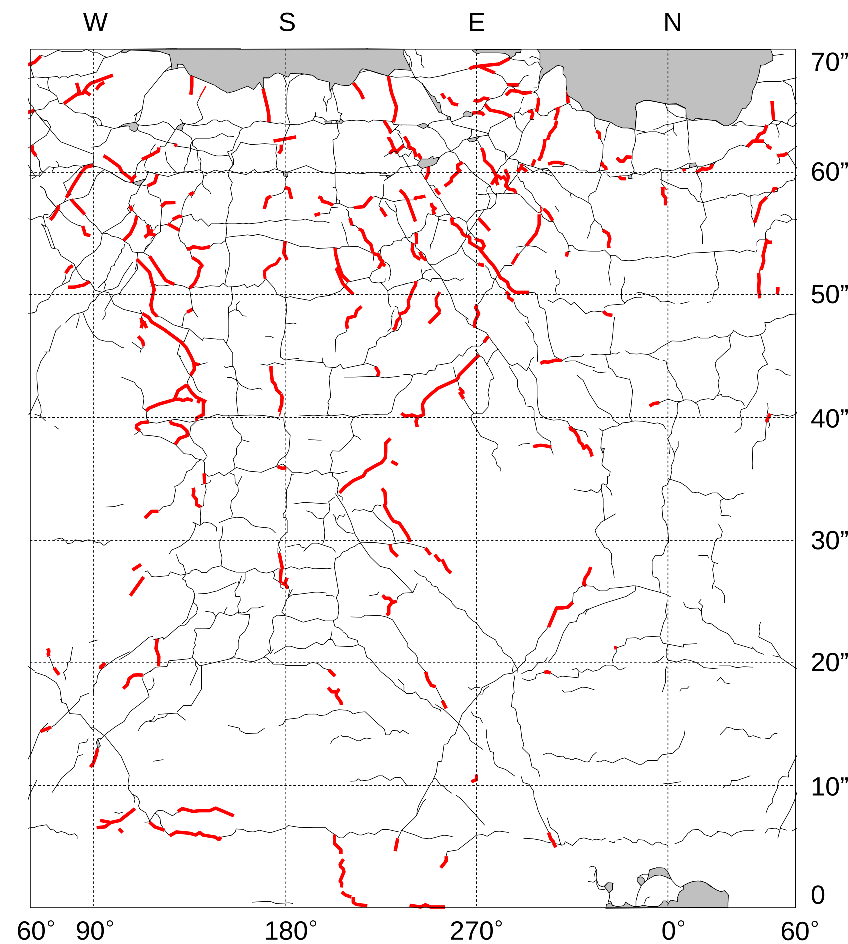

(f) After the 125%-scale ‘2nd X+Z’ run (run 1-11)

Fig. 4.25 Crack propagation of SP1 (continued)

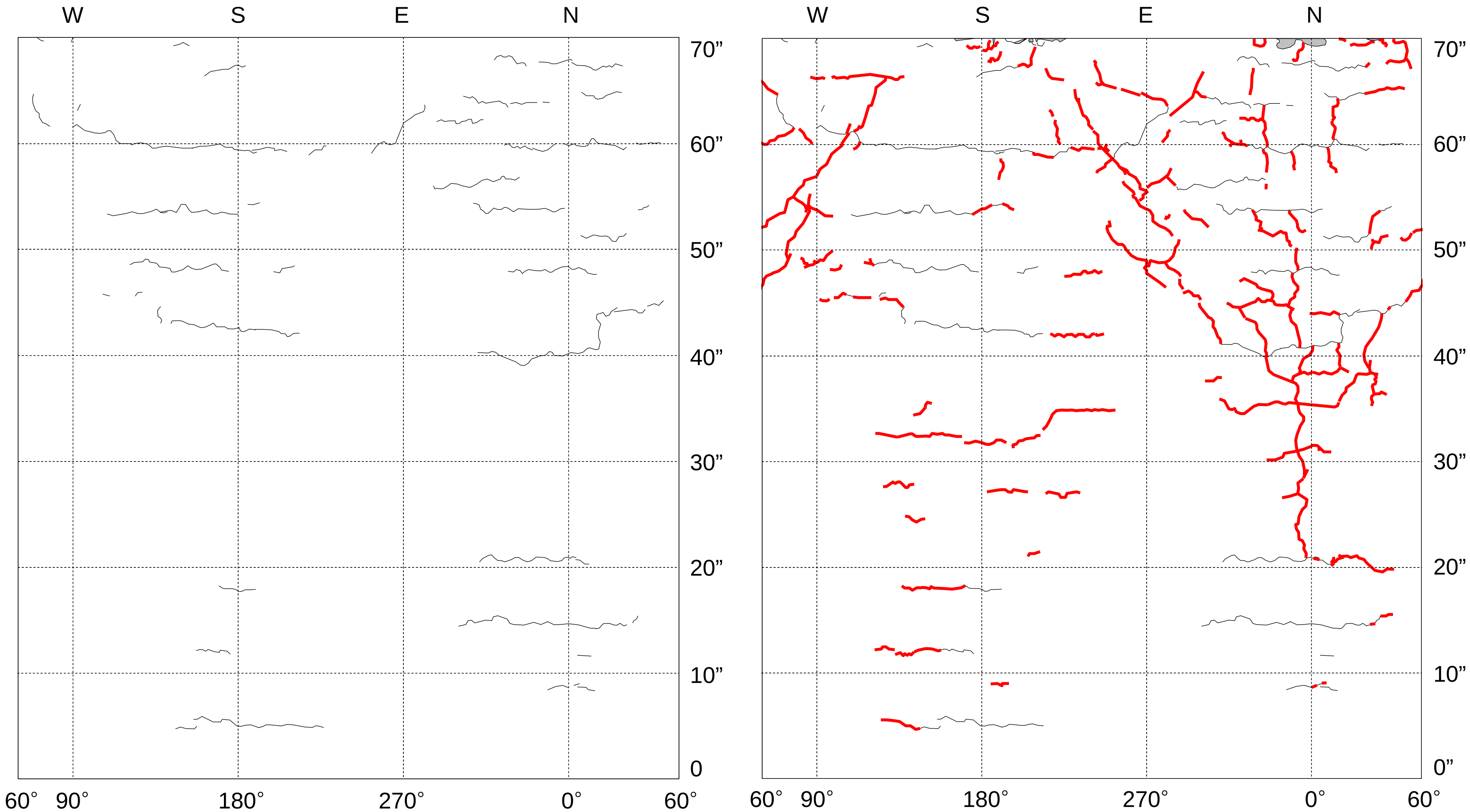

(a) After the 50%-scale run (run 1-6)   (b) After the 70%-scale run (run 1-7)

Fig. 4.26 Crack propagation of SP2

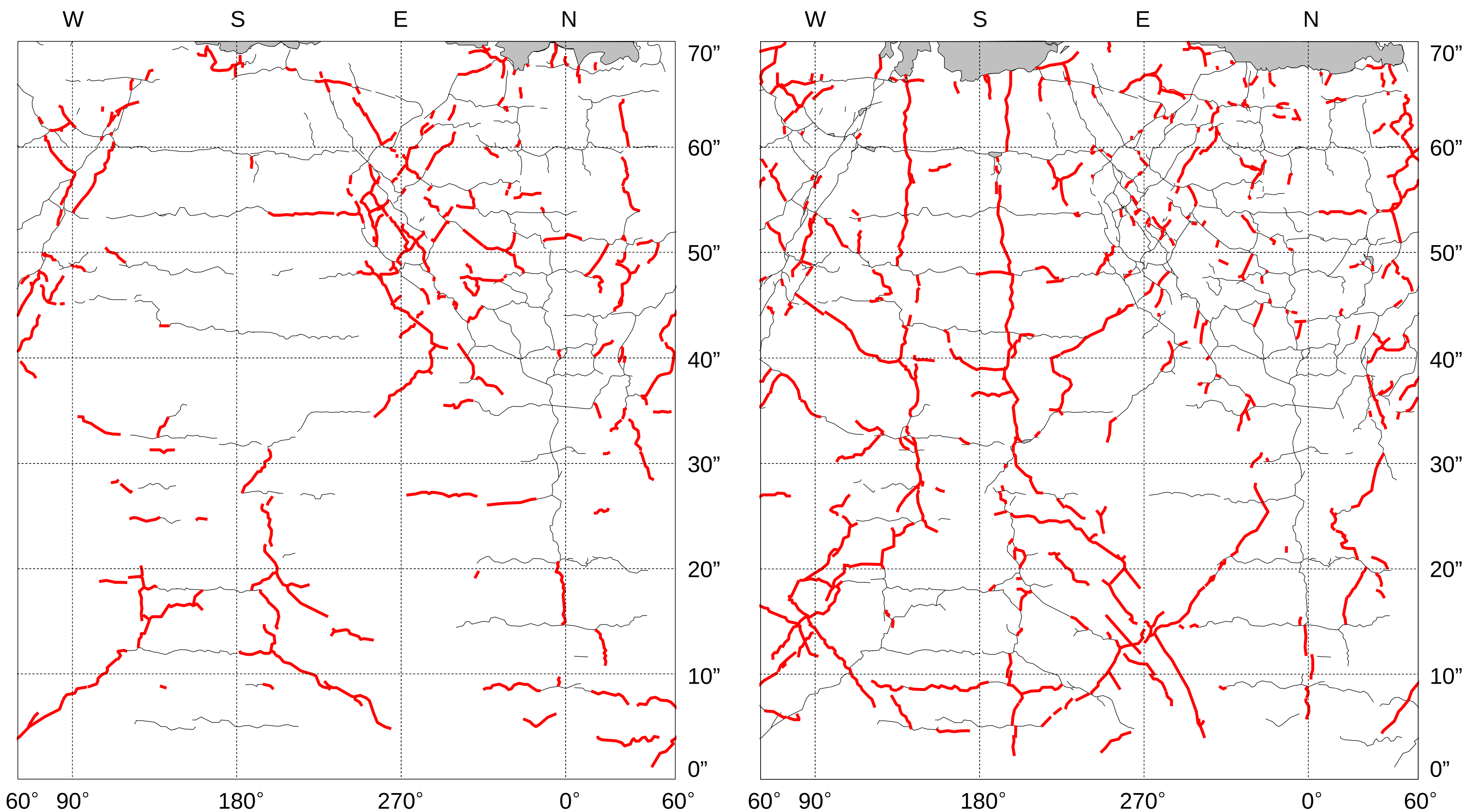

(c) After the 95%-scale run (run 2-8)

(d) After the 125%-scale ‘1st X+Z’ run (run 2-9)

Fig. 4.26 Crack propagation of SP2 (continued)

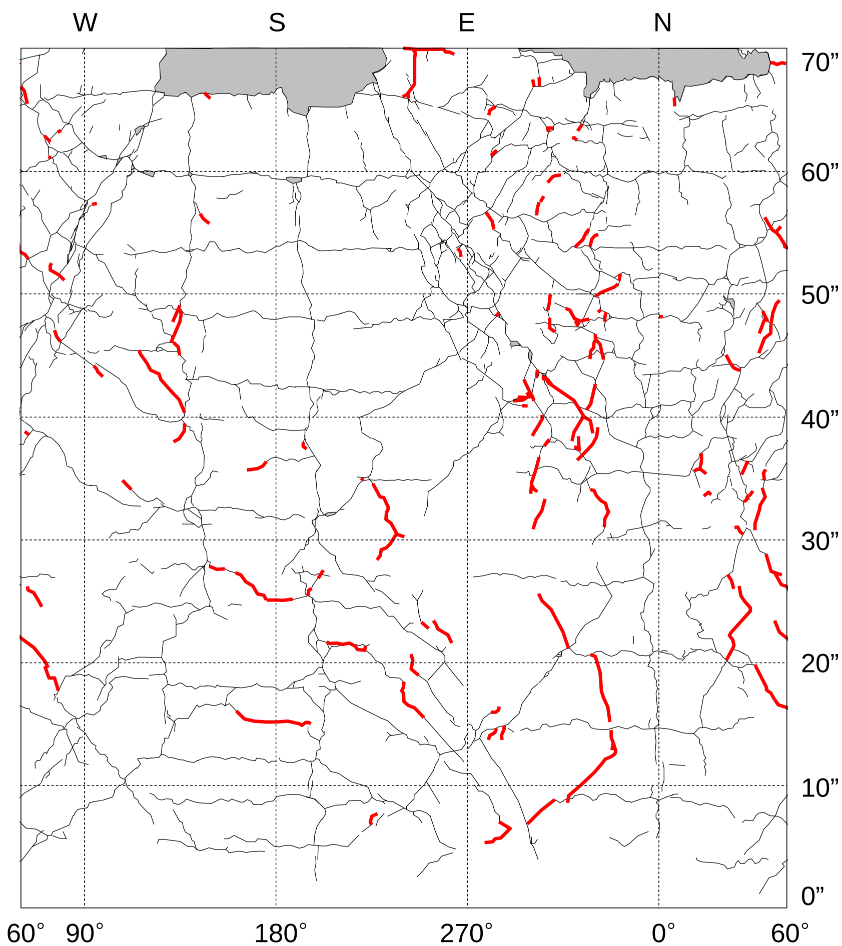

(e) After the 125%-scale ‘X only’ run (run 2-10)

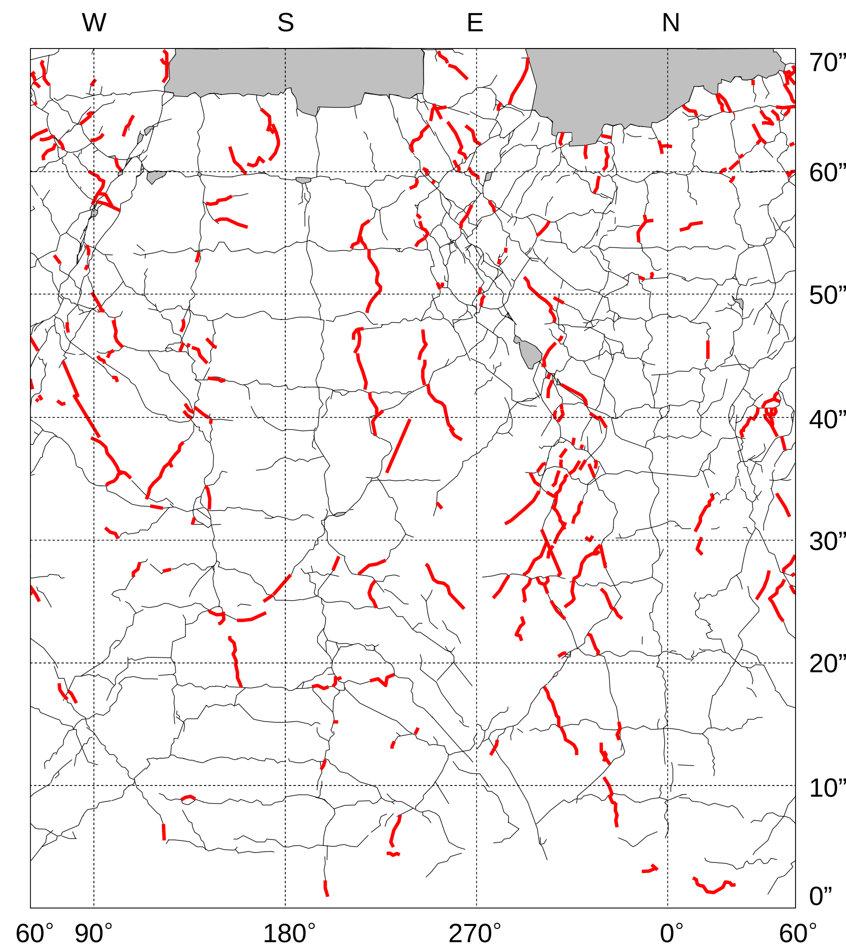

(f) After the 125%-scale ‘2nd X+Z’ run (run 2-11)

Fig. 4.26 Crack propagation of SP2 (continued)

4.8 Summary

The test results regarding global responses were investigated in this chapter. Before the main tests, the pullback and free vibration tests were conducted to determine the initial lateral stiffness and period of each specimen. SP1 was stiffer than SP2 by about 50%, and had a shorter lateral period than SP2 by 8.5%. Reason of not having the ratio of stiffness not equal to the square of the ratio of period was due to the fact that the tested column represented a two degree of freedom system in the lateral direction, with coupling between the translational and rotational modes. During the low-intensity excitations, the periods of both specimens became close to each other. Based on this observation, it is speculated that SP2 had some cracking before the tests.

Shaking table flexibility had a pronounced effect on the vertical response. Dynamic mode that was introduced by the table stiffness (in the vertical direction) and table mass governed the response in the vertical direction; therefore, response due to the column's dynamic mode was pronounced much less compared to the case of a rigid shake table.

In the X direction, the acceleration recorded on the mass had a low frequency content and low amplitude compared to that at the top of the column or on the table which was due to the rigid body rotation of mass blocks.

The maximum acceleration at the top of the column or on the mass blocks did not increase linearly with that on the table or the input intensity due to two reasons First, the lateral stiffness of the column decreased with increasing level of intensity and secondly, base shear capacity of the column was reached at the higher intensity levels. On the contrary, the acceleration histories in the Z direction were almost the same on the table, along the column height and on top of the mass blocks. The maximum values linearly increased with the input intensity, since axial forces were in the linear range and therefore axial stiffness variation was minor.

The force response is essential to the study, since it is closely related to shear strength of the column. Similar to the accelerations, the maximum shear force did not increase linearly with the input intensity, but the maximum axial force did. The peak shear force in 125%-scale 'X only' test was larger than 125%-scale 1st or 2nd 'X+Z' test for each specimen, where the peak force was determined by the shear strength at this intensity. Considerable tensile force was induced on the test column due to vertical excitation. Tension in the columns is believed to result in degradation of shear strength, which is mainly due to the degradation of concrete contribution to shear strength.

Comparison of bending moment histories at the base and top of both of the specimens indicated that they were opposite in sign during the strong part of the excitation of all the intensity levels suggesting that the columns were in double-curvature. Moments at the base and top were similar in sign after the strong part of the excitation ceased for all the tests. It is also be noted that three 125%-scale resulted in similar maximum moment values suggesting that the axial force variation did not affect the bending moment noticeably.

The relative displacement histories captured the horizontal and vertical movement of each specimen. In the X direction, displacement at the top is the largest, and it is less than 2.0 inches. The residual lateral displacement increased with the increased intensity of ground motions.. The vertical displacement rarely went to the shortening side, and the residual vertical displacement kept increasing on the elongation side which implies that the column was elongated by the presence of horizontal and diagonal cracks. Damage detection after the tests indicated the presence of cracks consistent with the residual axial displacements. Also, it is observed that 125%-scale 'X only' motion did not increase the residual vertical displacement.

The change of lateral stiffness is clearly shown in the shear force-lateral displacement relationship. From 95%-scale tests, the decrease in lateral stiffness had a directional difference. It implies that the damage was not symmetric on the north and south. In the last 125%-scale test, stiffness in the positive direction was about 17% of that in 50%-scale test. In the axial force-vertical displacement relation, no significant decrease in stiffness was observed.

Flexural damage took place both at the top and base of the column as the scale of the ground motion increased, and the flexural damage at the top of the column took place before that at the base since the moment at the top was larger. This was a result of the large mass moment of inertia at the top of the column. Reduction of the acceleration on the mass block due to the rotations contributed to this situation as well. As a result of flexural yielding both at the top and bottom of the column in double curvature, shear force reached the shear capacity which would not take place if yielding was happening at the bottom and the moment at the top was smaller than the yield moment. Shear cracks took place as a result of this situation.

The progress of shear failure was visible in crack patterns. Both specimens started to have diagonal cracks near h=50″~65″ on the east and west sides during 70%-scale tests. They spread over the over the east and west sides except h=25″~35″. Also, there were vertical cracks as well as horizontal cracks on the north and south sides. SP2 had more cracks than SP1, since SP2 had wider hoop spacing. It should be noted that the diagonal cracks did not appear during 125% 'X only' test as many as those in 125% 'X+Z' tests supporting the observation that the concrete contribution to shear strength was reduced due to the presence of axial tension.

Chapter 5

Results of Dynamic Tests: Local Responses

5.1 Introduction

Local responses gathered during the tests by 38 strain gages in each specimen. Locations of these gages are specified in Appendix D. They provide information on the response of each section during the test. The curvatures, longitudinal and transverse strains are presented in this chapter. In addition, the relationships of each response quantity and the force histories discussed in Chapter 4 are investigated.

5.2 Curvatures

To measure the curvature at certain points on the north and south sides of the column, LVDTs were installed on the instrumentation rods and the locations of these LVDTs are shown in Appendix D. As an alternative to the calculation of the curvatures using the LVDTs, the longitudinal reinforcement strain data obtained from the strain gages can be used. Theoretically, the curvatures from the LVDTs and from the strain gages should be the same if they were installed at the same height. However, differences exist because of the averaging effect of the LVDTs measurements compared to the point-wise strain gages measurements. Since the strains obtained from the gages were less noisy, and were not affected by averaging, the curvatures in this section were computed using the strain measurements along the longitudinal reinforcing bars. Sign convention for curvature is such that it is positive when $\left(\varepsilon_{SL} - \varepsilon_{NL}\right)$ is positive, where ε_{NL} and ε_{SL} are the longitudinal strain on the north and south bars, respectively. This convention results in consistent signs for displacements and curvatures, i.e. when displacement is positive, curvature is also positive.

In Fig. 5.1, the curvature histories at h=10″ and 60″ are shown. Up to 70%-scale motion (Fig. 5.1(a) and (b)), both specimens had similar curvature time histories. Also, the curvatures of both specimens remained within $\pm 0.5\times10^{-3}$ in^{-1}, and no residual curvature was detected. The curvature histories at h=10″ had opposite sign to that at h=60″ between 8~9 sec (double curvature), during the strong motion part of the excitation applied in X and Z directions. However, both cross-sections had the same curvature sign and consistent lateral displacements, i.e. single-curvature, after 9.5 sec. The first noticeable difference of the magnitude of curvatures for the two cross-sections (top and bottom) appeared during the 95%-scale motion. Between 7.5 and 8.5 sec, the curvature at h=60″ had two negative peaks and it implied that the north side elongated more than the south side. After these two peaks, the curvature at h=60″ had residual curvatures of -0.41×10^{-3} and -0.28×10^{-3} in^{-1} for SP1 and SP2, respectively. Under the same motion, there was no residual curvature at the cross-section at h=10″. Due to the residual curvature at h=60″, the column was in double-curvature even after the strong motion part of the excitation. It should be noted that the curvature of the cross-section near the top of the column was influenced more by the higher modes of vibration than that of the cross-section near the bottom of the column. This was manifested in the form of superposed small amplitude high frequency oscillations in the curvature time history of the cross-section near the top of the column due to the effect of the rotational mode of vibration.

In the 125%-scale tests, Fig. 5.1(d), (e) and (f), SP1 and SP2 experienced different curvature results. In these figures, three blue dashed lines indicate the time of the shear peaks and a red solid line indicates the time of the axial tension peak which is over 50 kips. The main shear peaks, i.e. two positive and one negative shear peaks, appeared between 7.8 and 8.2 sec of each test, as shown in Section 4.4.1. First, the cross-section at h=10″ did not experience any residual curvature in SP1 but it did in SP2 with the amount of approximately -0.25×10^{-3} in^{-1} at the end of the 2nd X+Z test. Second, the curvature at h=60″ increased as the 125%-scale runs were repeated with the residual curvature approaching zero, from -0.31×10^{-3} in^{-1} (run 1-9) to -0.14×10^{-3} in^{-1} (run 1-10) to -0.08×10^{-3} in^{-1} (run 1-11). Also, the peak-to-peak amplitudes in SP1 increased significantly as the 125%-scale runs were repeated, but they did not in SP2; refer to Table 5.1 and Fig. 5.2. Similar to smaller scale runs, the column was in double curvature during the strong motion part of the excitation between 7.5 and 8.5 sec, and large curvature peaks occurred at the shear peaks. However, after 9.5 sec, the column experienced complex curvature pattern due to the large curvature peaks and concentration of damage at h=60″ unlike the small scale runs. In general, the curvature at the top cross-section of the column was at least three times higher than that at the bottom cross-section at shear peaks when tensile strain occurred at the top.

Fig. 5.2 presents the change of the maximum peak-to-peak amplitude (Table 5.1). It increased until the 125%-scale '1st X+Z' test. The increase of the maximum peak-to-peak amplitude at h=60″ was most significant between 70% and 95%-scale tests.

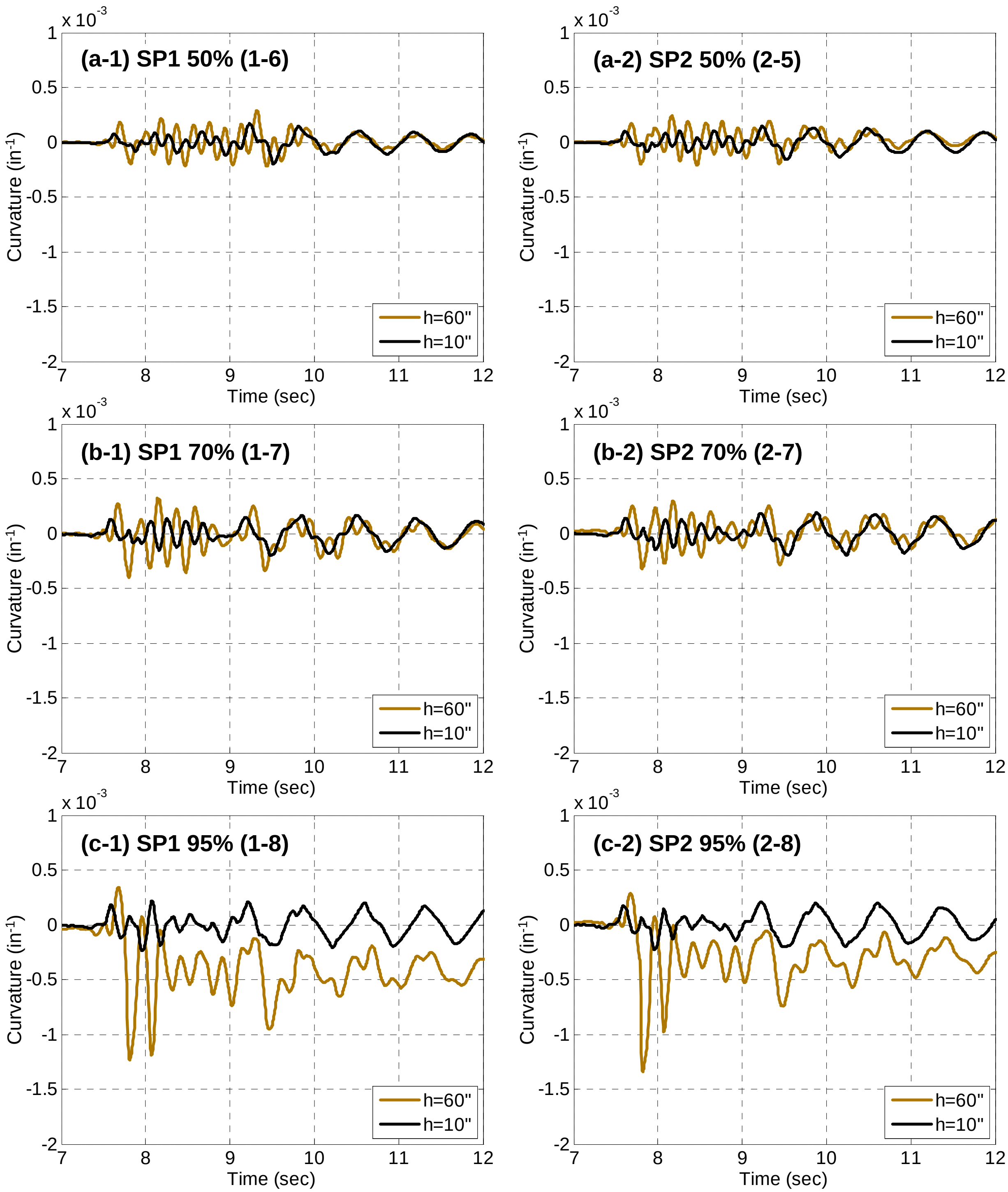

Fig. 5.1 Comparison of curvature histories at *h*=10″ and 60″

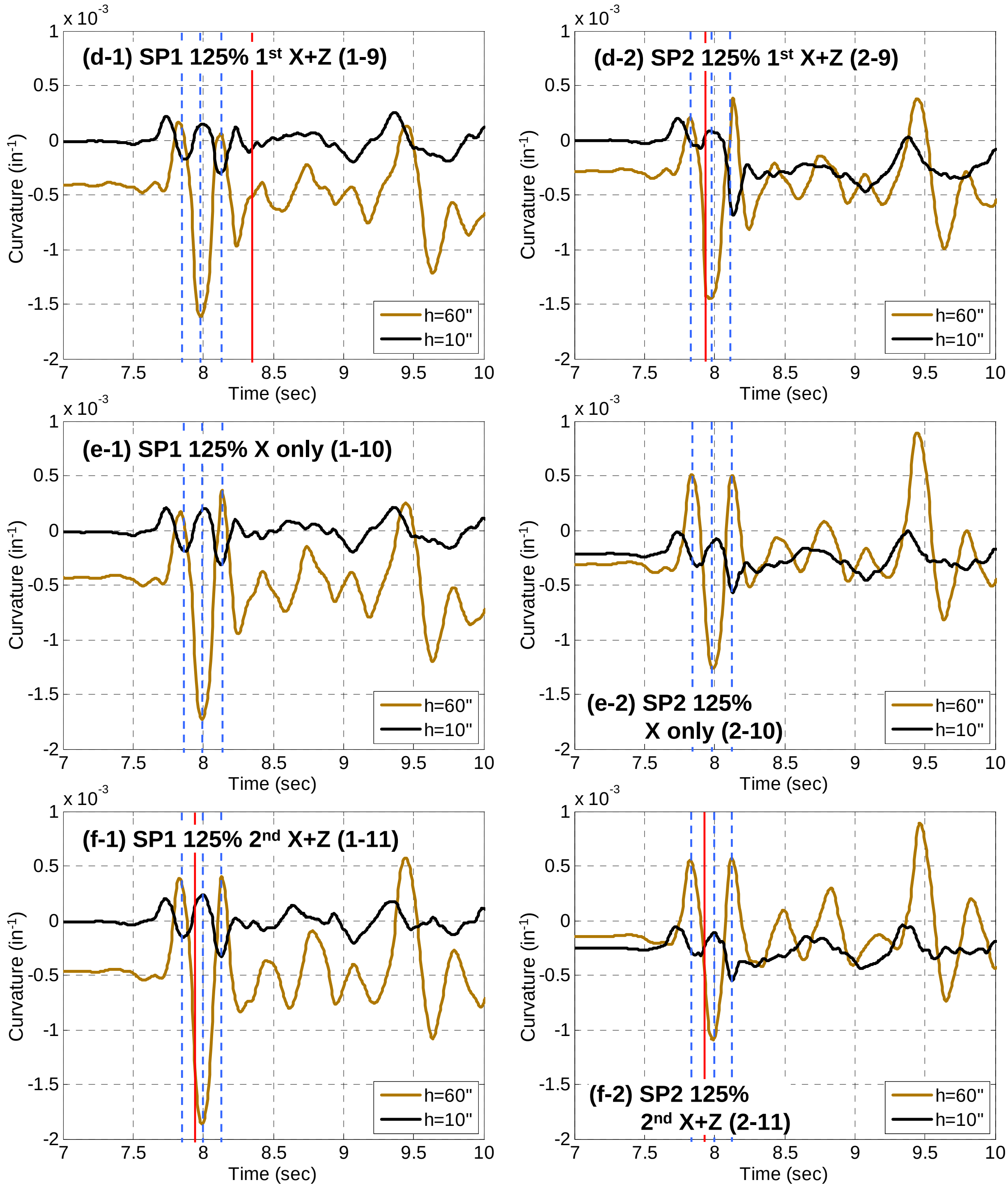

Fig. 5.1 Comparison of curvature histories at h=10″ and 60″ (continued)

Table 5.1 Peak curvatures

SP	Run	Negative and positive peaks		Peak to peak	
		(a) h=10″ [10^{-3} in^{-1}]	(b) h=60″ [10^{-3} in^{-1}]	(c) h=10″ [10^{-3} in^{-1}]	(d) h=60″ [10^{-3} in^{-1}]
1	50% (1-6)	-0.20, 0.17	-0.22, 0.29	0.37	0.51
	70% (1-7)	-0.20, 0.17	-0.41, 0.32	0.37	0.73
	95% (1-8)	-0.24, 0.22	-1.23, 0.34	0.45	1.57
	125% ‘1st X+Z’ (1-9)	-0.30, 0.26	-1.62, 0.16	0.56	1.78
	125% ‘X only’ (1-10)	-0.32, 0.21	-1.73, 0.37	0.53	2.10
	125% ‘2nd X+Z’ (1-11)	-0.33, 0.57	-1.86, 0.58	0.57	2.44
2	50% (2-5)	-0.16, 0.14	-0.21, 0.24	0.30	0.45
	70% (2-7)	-0.20, 0.19	-0.32, 0.29	0.39	0.61
	95% (2-8)	-0.22, 0.21	-1.34, 0.29	0.43	1.63
	125% ‘1st X+Z’ (2-9)	-0.69, 0.20	-1.45, 0.39	0.89	1.83
	125% ‘X only’ (2-10)	-0.57, -0.01	-1.26, 0.89	0.56	2.15
	125% ‘2nd X+Z’ (2-11)	-0.55, -0.04	-1.09, 0.89	0.51	1.98

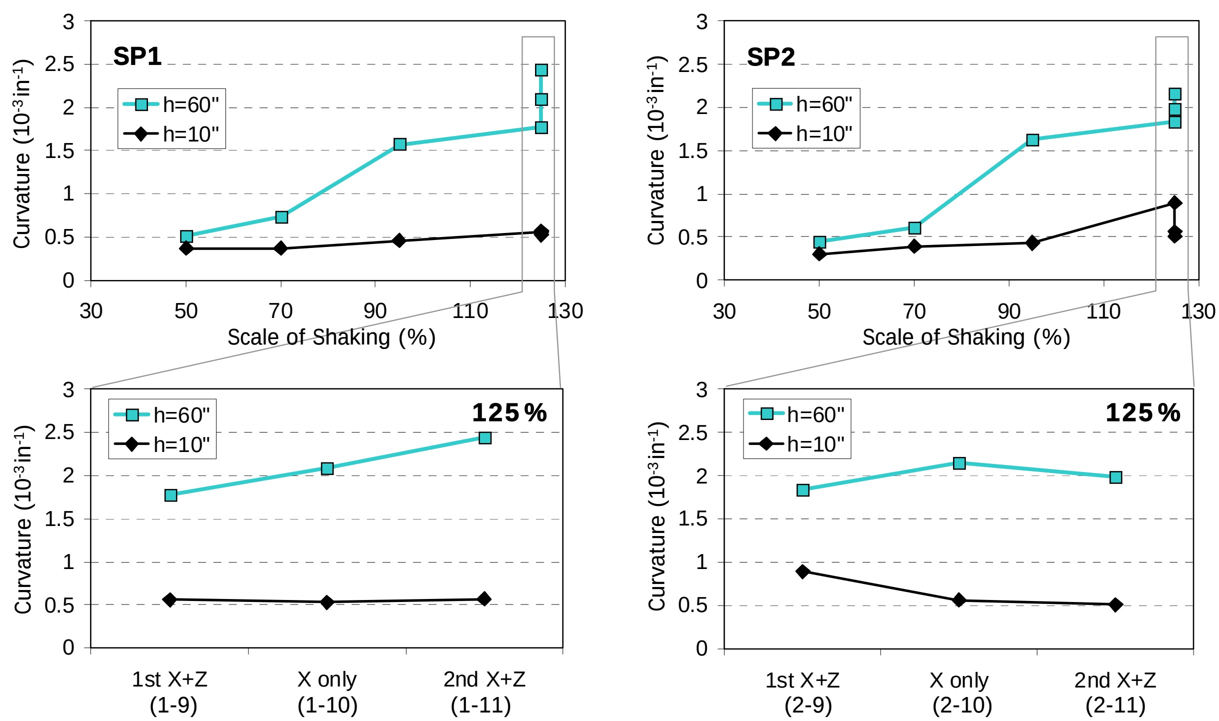

Fig. 5.2 Peak-to-peak curvatures of the specimens

5.3 Moment-Curvature Relationships

In Fig. 5.3, the moment-curvature relationships under 50%-, 70%-, 95%-, and 125%-scale motions are presented. These relationships at *h*=10″ and 60″ are compared to each other. As discussed in Section 4.4.2, bending moment at the top was larger than that at the base. This was consistent in all the tests and the moment peaks at 60″ were larger than the peaks at 10″ by up to 90%.

In 50%- and 70%-scale tests, each specimen had almost linear moment-curvature relationship. Under 95%-scale motion, it was no longer linear at *h*=60″. The curvature at the top cross-section of the column shifted to the negative $0.3\sim0.4\times10^{-5}$ in^{-1} and continued to oscillate around it. However, the moment-curvature relationship remained linear at *h*=10″ and the maximum values were similar to those in the smaller intensity level tests. In addition, the tangent of the moment-curvature relationship at *h*=60″ started to degrade and became different from that at *h*=10″ for both specimens during the 95%-scale test.

In 125%-scale tests, the two specimens had different moment-curvature relationships. First, due to different residual curvature, the relationships at the same height, *h*=10″ or *h*=60″ did not have the same origin. For example, the residual curvature of SP1 cross-section at *h*=10″ remained zero for all tests, but that of SP2 became roughly -3.0×10^{-5} in^{-1} after the 125%-scale '1st X+Z' test, i.e. SP2 was more damaged at *h*=10″ than SP1. Second, at *h*=60″, the area of the hysteresis loops (indicative of the dissipated energy due to material damage) of SP1 was larger than that of SP2. SP1 with hoops with closer spacing was able to dissipate more energy in flexure, while SP2 with larger spaced hoops dissipated less energy in flexure due to the existence of brittle shear damage. Moreover, the hysteresis loops of each specimen became flatter (less stiff) due to larger curvature beyond that corresponding to the maximum bending moment. The initial tangent of the moment-curvature relationship at *h*=60″ of both specimens, as shown by the superposed straight lines in Fig. 5.3(d), (e) and (f), decreased by about 17% in 'X only' test compared to '1st X+Z' test (4800 kip-in^2 to 4000 kip-in^2), but remained almost the same in the '2nd X+Z test'. Finally, due to less damage of the column bottom cross-section compared to that of the column top cross-section, the reduction of the initial tangent at *h*=10″ was not noticeable compared to that at *h*=60″.

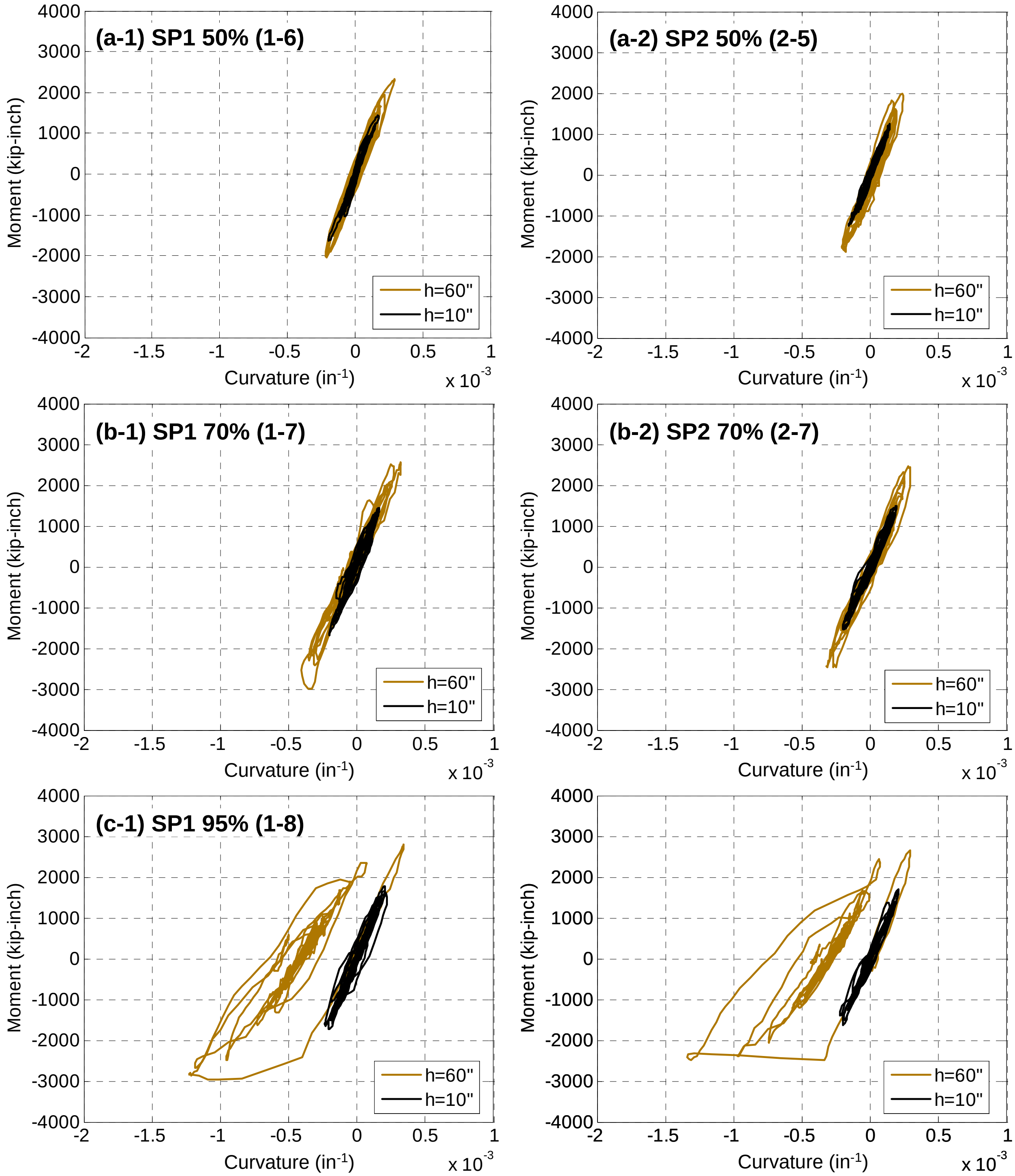

Fig. 5.3 Moment-curvature relationships at h=10″ and 60″

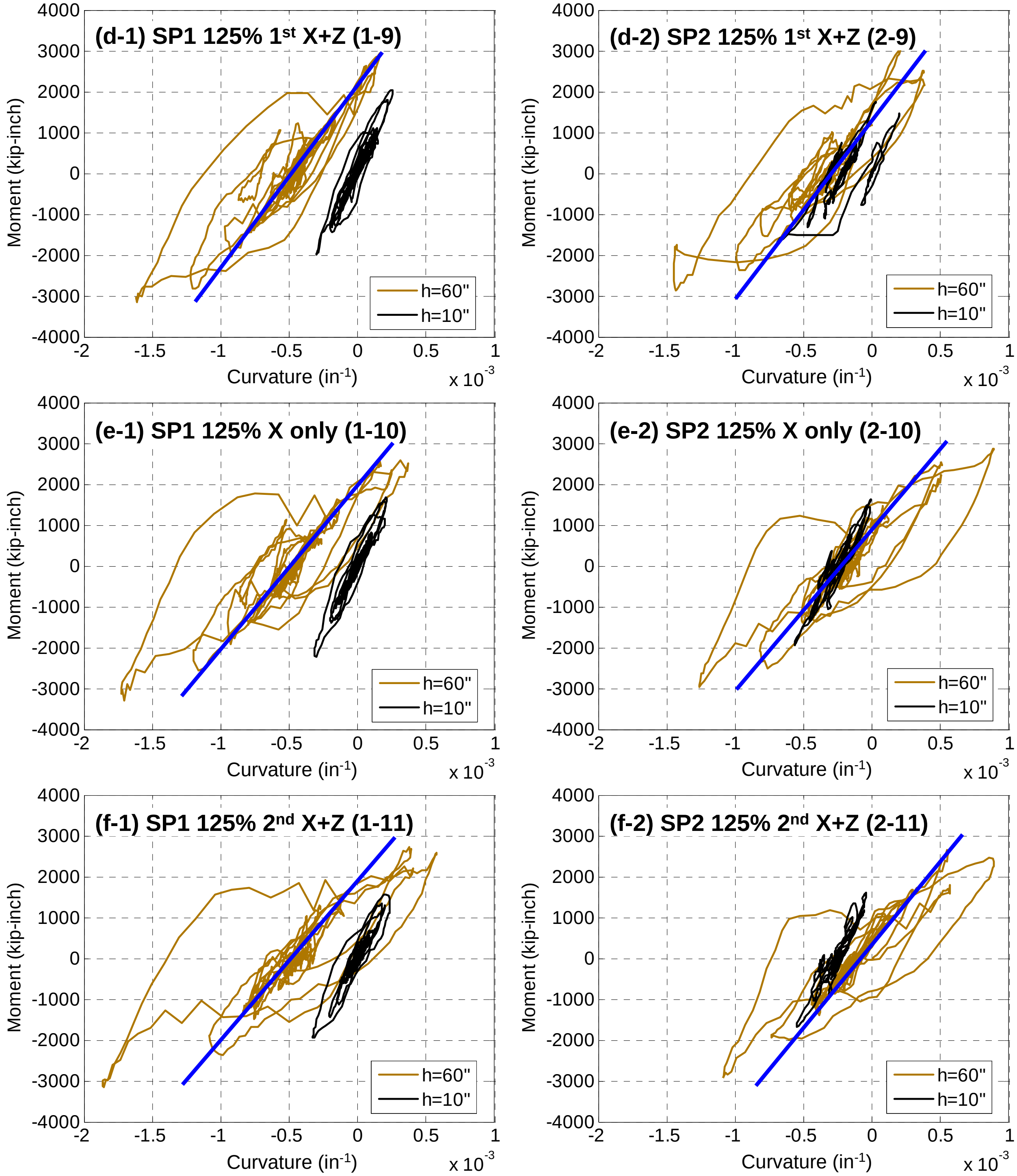

Fig. 5.3 Moment-curvature relationships at *h*=10″ and 60″ (continued)

5.4 Longitudinal Strains

5.4.1 Longitudinal Strains on the North and South (X direction)

In this section, the longitudinal strains of the two specimens during the three 125%-scale tests are compared to each other. In Fig. 5.4, the strain history of longitudinal reinforcing bars on the north and south sides of SP1 is shown. Similarly, that of SP2 is shown in Fig. 5.5. In these two figures, NL and SL indicate measurements on the north and south sides, respectively. Each of these designations is followed by a number pointing to the height where the strain gages are located according to the shown key in the figures. For example, 'NL3' stands for the longitudinal strain at h=30″ on the north side. Since there are six gages on each bar on the north and south sides, the responses at six cross-sections were acquired. Note that positive strain indicates shortening (compression) and negative strain indicates elongation (tension). To observe the response at the times of the axial tension and shear peaks, one solid line (for axial tension) and three dashed lines (for shear) are superposed on the time histories.

Fig. 5.4(a) shows the strains under 125%-scale '1st X+Z' motion for SP1 where the tension peak took place after the shear peaks. The following remarks can be made:

- There was a remarkable difference in the strain history along the height. For example, NL1 was shortened at the first shear peak, but the strain became tensile as the height increased and NL6 showed a tensile strain peak at that point. This behavior was observed at other shear peaks and on the south side as well. This behavior implies that the test specimen was in double-curvature as evidenced by the bending moments and curvatures discussed in previous sections.
- A strain peak was noticeable at the tension peak after the main shear peaks. This was particularly the case at h=60″ on the north side (NL6) and at h=10″ on the south side (SL1).
- The south side (SL6) was about 6 times more elongated than the north side (NL6) due to the large negative moment peak measured at around 8 sec.

For SP1, the 125%-scale 'X only' motion was applied (Fig. 5.4(b)) after the '1st X+Z' run. The response was very similar to the previous case except for the tension peak effect and the strain measurements at NL6, which showed larger tensile strain peaks. The maximum tensile strain was almost three times larger than that of the '1st X+Z' and it occurred at the 3rd shear peak. Also, the tensile strain due to rocking of the mass blocks after the shear peaks was almost 2.5 times larger than that of the '1st X+Z' run. However, SL6 was similar to that of the '1st X+Z' run. This implies that the damage at the column top propagated from the south side to the north side. It is expected, because the horizontal acceleration is not symmetric. It leans toward the positive side (Fig. 4.8) and the shear force also does (Fig. 4.14). This causes large tension on the south side first, i.e. damaging the south side first.

Fig. 5.4(c) shows the response when 125%-scale '2nd X+Z' motion was applied to SP1. It was observed that strains on the north side, NL1 to NL3, changed abruptly from the compression side (positive) to the tension side (negative) at the tension peak. Other gages had similar results compared to '1st X+Z' and 'X only', but NL6 and SL6 did not. First, as tests were repeated, their residual strain increased. Second, the difference between the 1st and 3rd shear peaks also increased. However, the longitudinal strain on the south side was larger than that on the north side. As mentioned in Section 5.2, the specimen was in double-curvature at the shear peaks.

In Fig. 5.5, the strain history plots on the north and south sides of SP2 under the 125%-scale runs are shown. The response was similar to SP1, but the peak values were larger. It should be noted that SL1 had 3 to 4 times larger tensile strain values than those of SP1. This was particularly the case for the elongation under the '1st X+Z' run, Fig. 5.5(a). Moreover, NL6 for SP2, obtained from the '1st X+Z' run, had larger strain than that of SP1. This resulted from the damage at the top of SP2, which was more severe than that of SP1 for the different runs.

Fig. 5.6 and Fig. 5.7 present the peak-to-peak amplitude and the maximum (in an absolute sense) tensile strain on the north and south sides. Note that the tensile strain is negative but the absolute values are used in these plots. Since the strain can stay negative from the beginning to the end of a run, it is possible that the maximum tensile strain is larger than the corresponding peak-to-peak amplitude. For example, the maximum tensile peak of SL6 of SP1 was larger than the corresponding peak-to-peak amplitude for the same run. The following remarks can be summarized:

- The longitudinal strain near the top had the largest tensile value in most runs. The only exception was NL6 of SP1, especially in the '1st X+Z' test run. There was no significant difference between NL6 and NL1 or NL3 in this particular test.
- In SP1, the elongation measured by SL6 was the largest and increased as the runs were repeated. Compared to SL1, the strains from SL6 were about 5 times larger in peak-to-peak amplitude and 7 times larger in the maximum tensile strain. NL6 of SP1 also increased with repeated runs and it was 4 times larger than other locations for the '2nd X+Z' test. NL1 was slightly larger than NL3 in most cases, but the difference was not significant compared to NL6.
- In case of SP2, NL6 and SL6 remained the largest on each side, but they did not increase with repeated runs. The decrease of SL6 in the X only test compared to the '1st X+Z' run was remarkable where the peak-to-peak amplitude and the maximum tensile strain decreased by 26% and 9.3%, respectively. In the '2nd X+Z' run, these values remained almost the same, with slight decrease by 3.6% and slight increase by 0.8%, respectively. SL1 showed a similar trend and it was slightly less than half of SL6 but its maximum tensile value for SP2 was about twice as large as that of SP1. Finally, NL1 and NL3 remained less than 25% of NL6.

Fig. 5.8 shows schematics of the deflected shapes of the test specimens. As discussed above, the strain responses near the top and the base were different at each shear peak and the observed anti-phase during the main excitation. This is expected because the bending moment histories at the top and the base also show anti-phase (Fig. 4.16). This implies double curvature ignoring the residual elongation due to tension at the top. At the 1st shear peak, the top on the north side elongated and the base on the north side shortened. On the other hand, the top on the south side shortened and the base on the south side elongated. These directions (signs) of the straining actions were reversed at the 2nd peak but where the same at the 3rd shear peak.

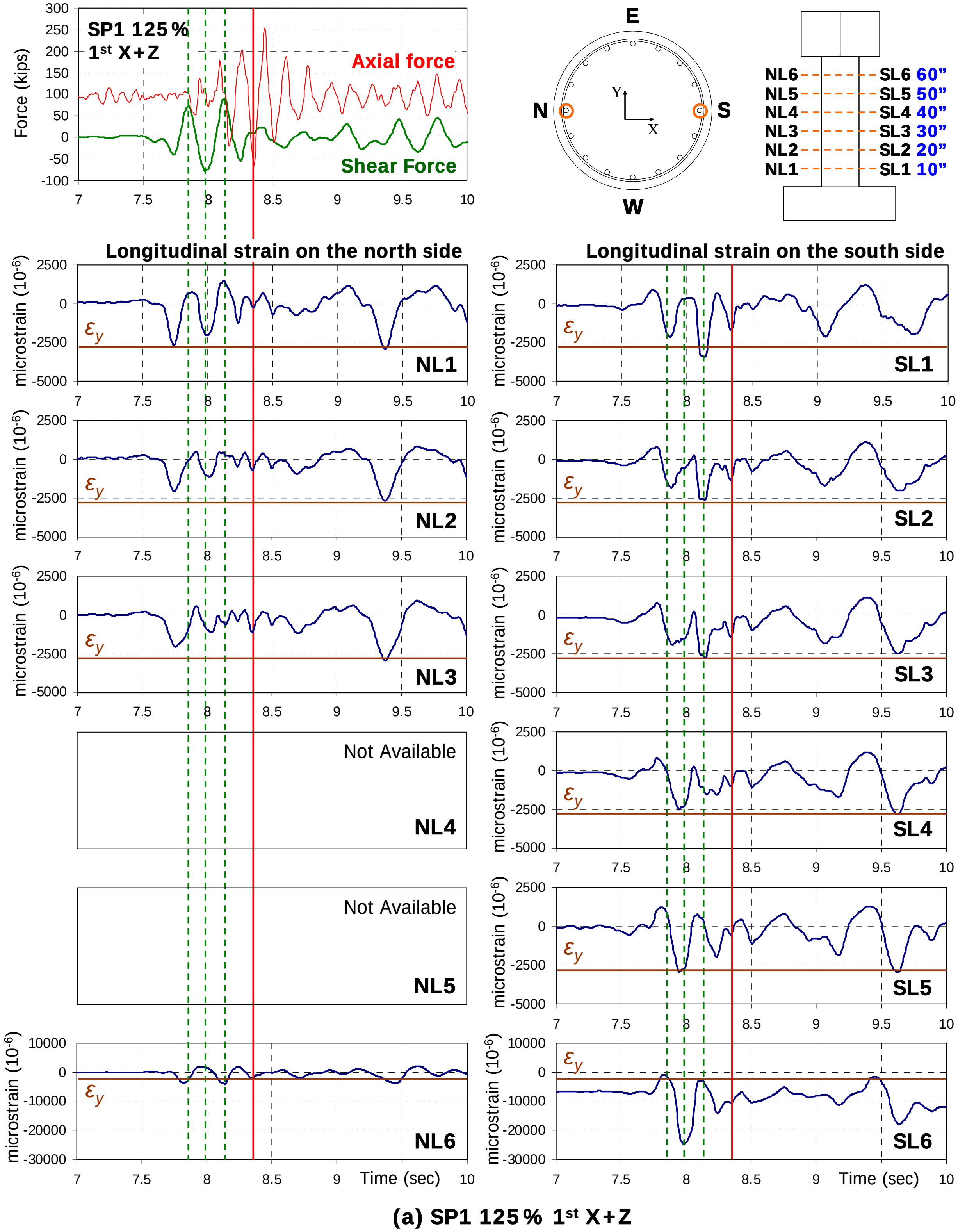

Fig. 5.4 Longitudinal strains on the north and south sides of SP1 in the 125%-scale runs

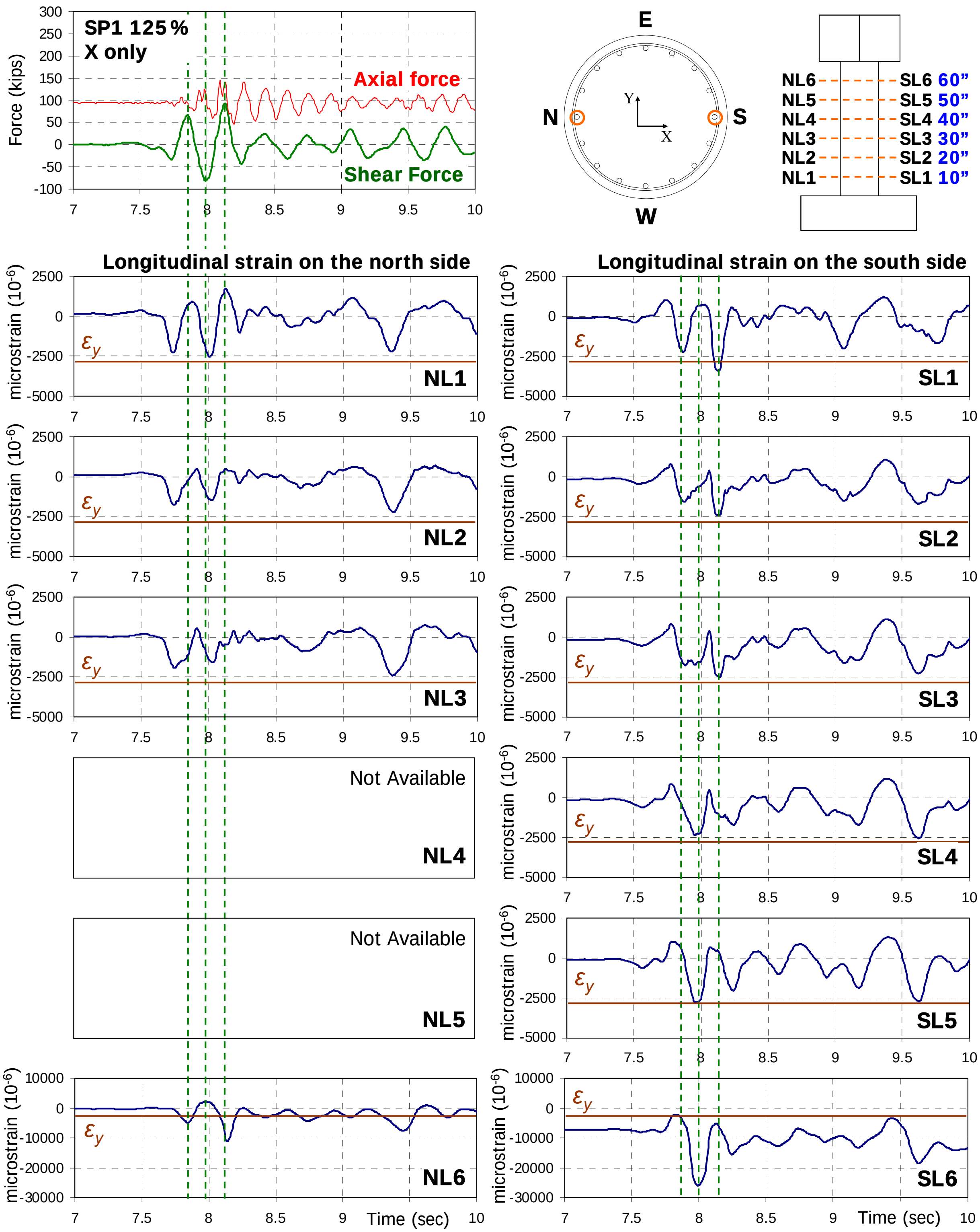

(b) SP1 125% X only

Fig. 5.4 Longitudinal strains on the north and south sides of SP1 in the 125%-scale runs (continued)

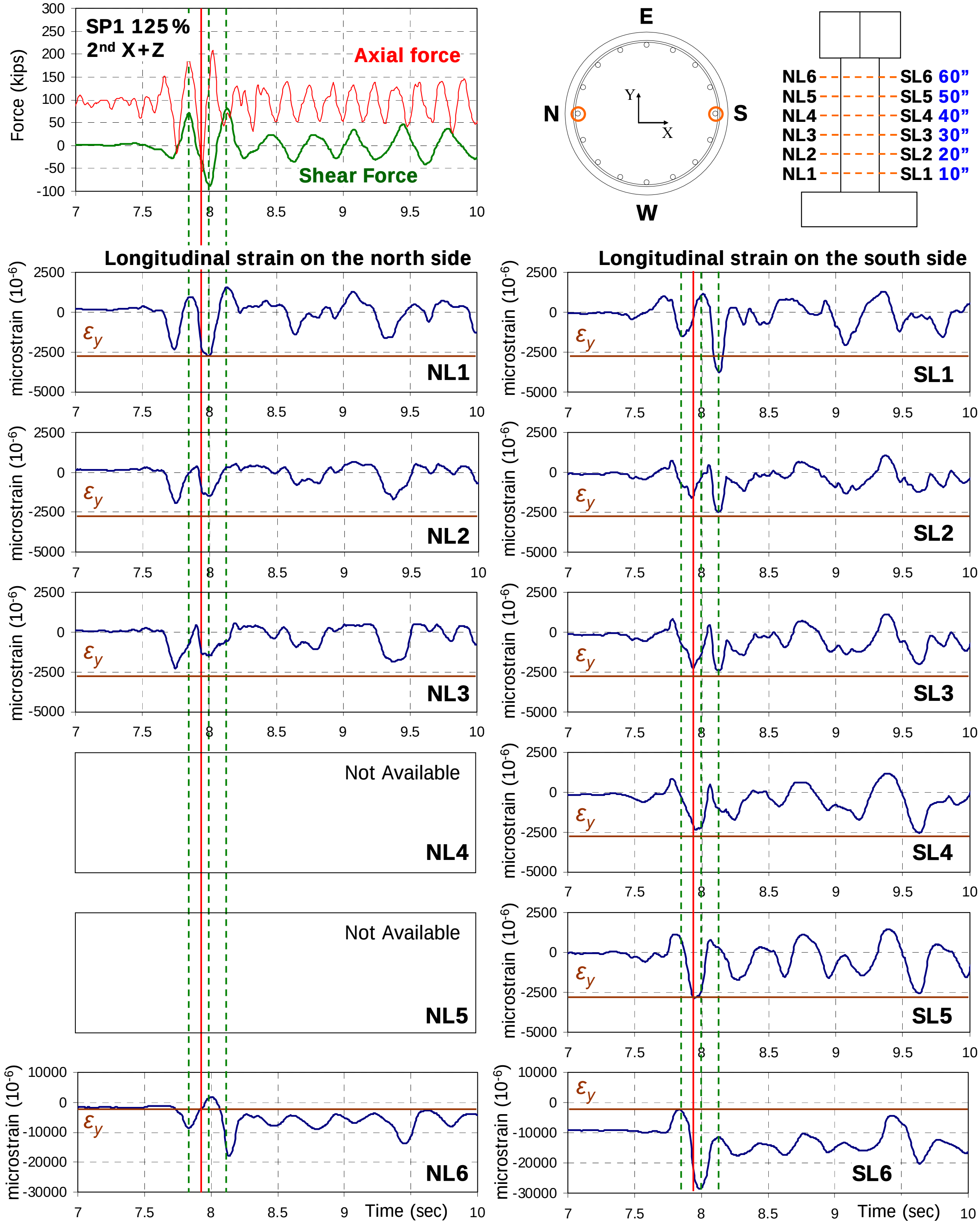

(c) SP1 125% 2nd X+Z

Fig. 5.4 Longitudinal strains on the north and south sides of SP1 in the 125%-scale runs (continued)

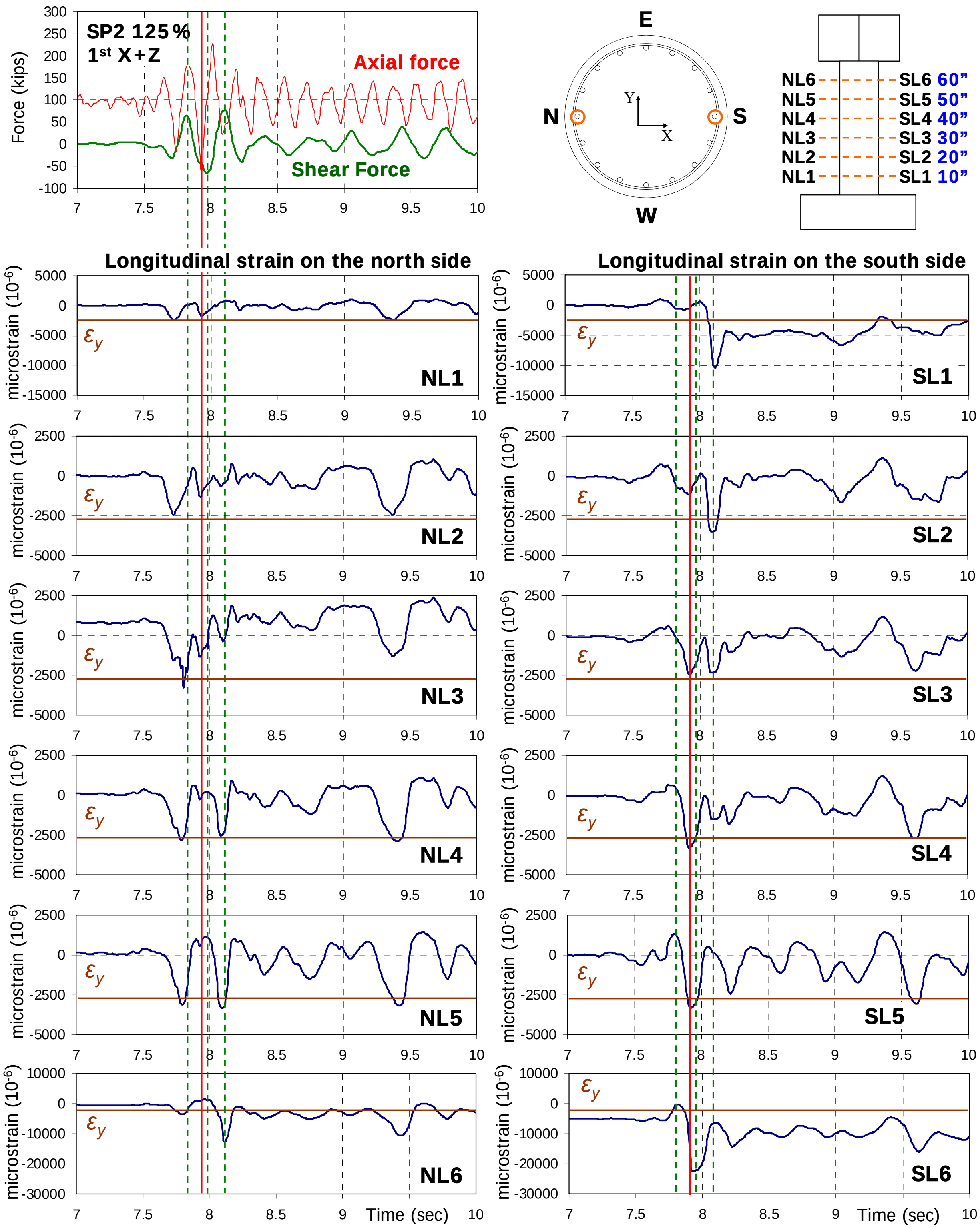

(a) SP2 125% 1st X+Z

Fig. 5.5 Longitudinal strains on the north and south sides of SP2 in the 125%-scale runs

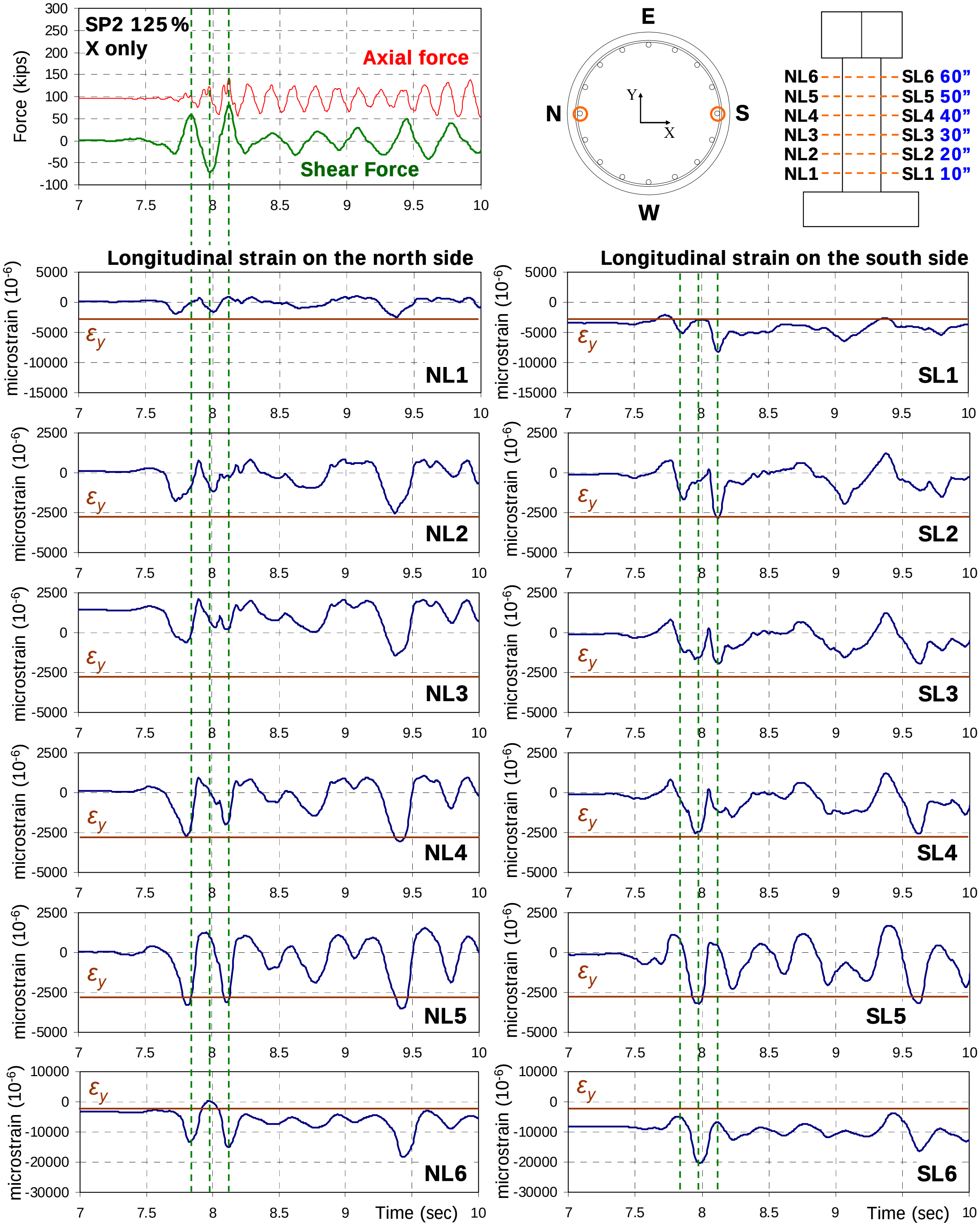

(b) SP2 125% X only

Fig. 5.5 Longitudinal strains on the north and south sides of SP2 in the 125%-scale runs (continued)

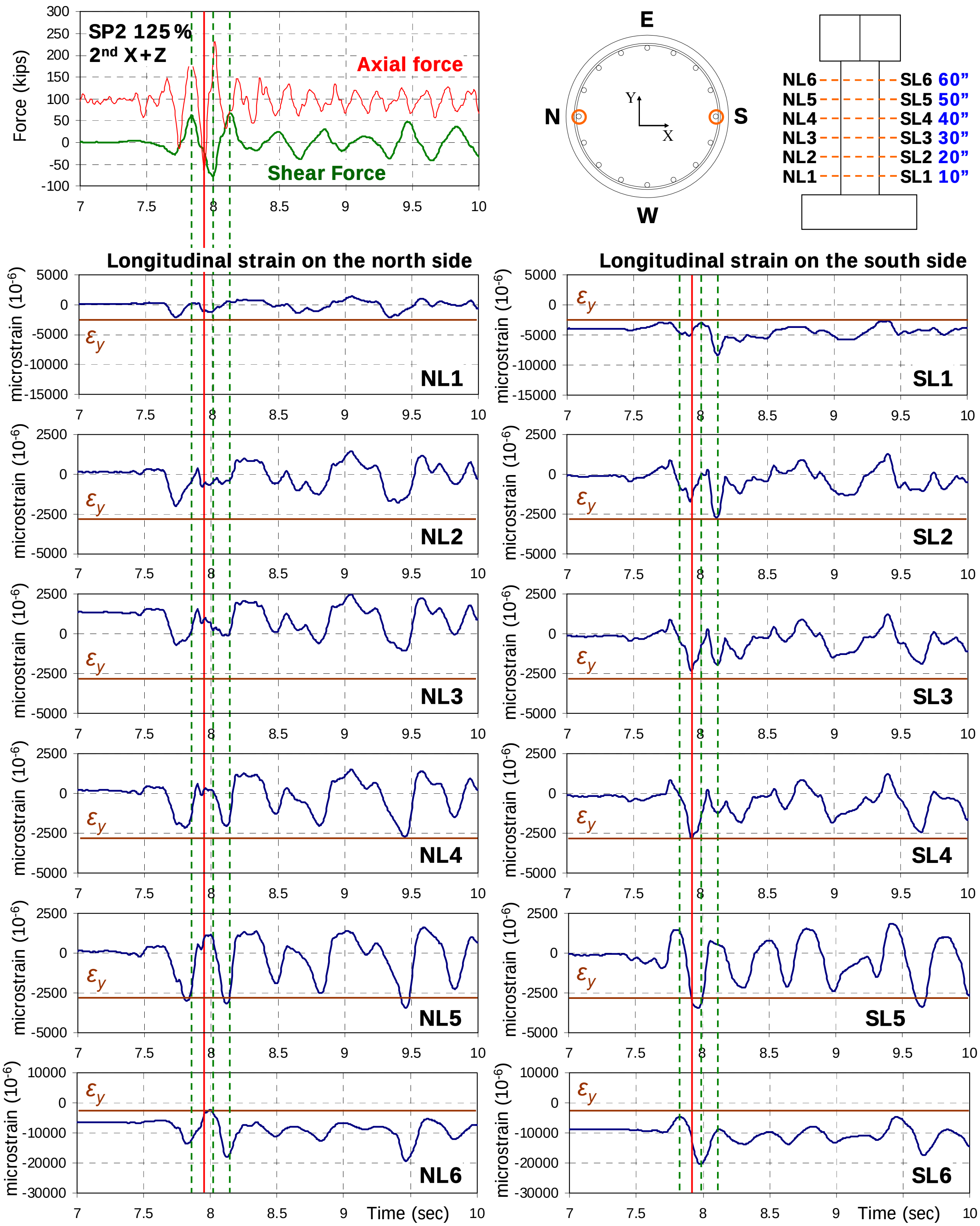

(c) SP2 125% 2nd X+Z

Fig. 5.5 Longitudinal strains on the north and south sides of SP2 in the 125%-scale runs (continued)

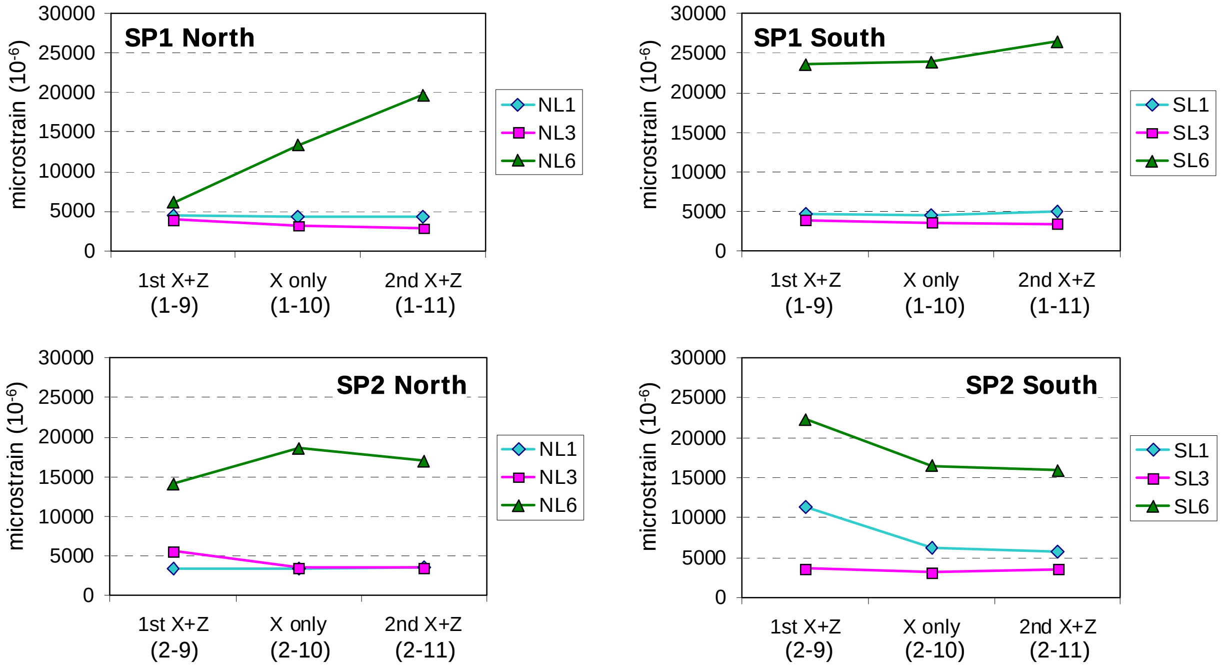

Fig. 5.6 Peak-to-peak strain amplitudes of NL and SL in the 125%-scale runs

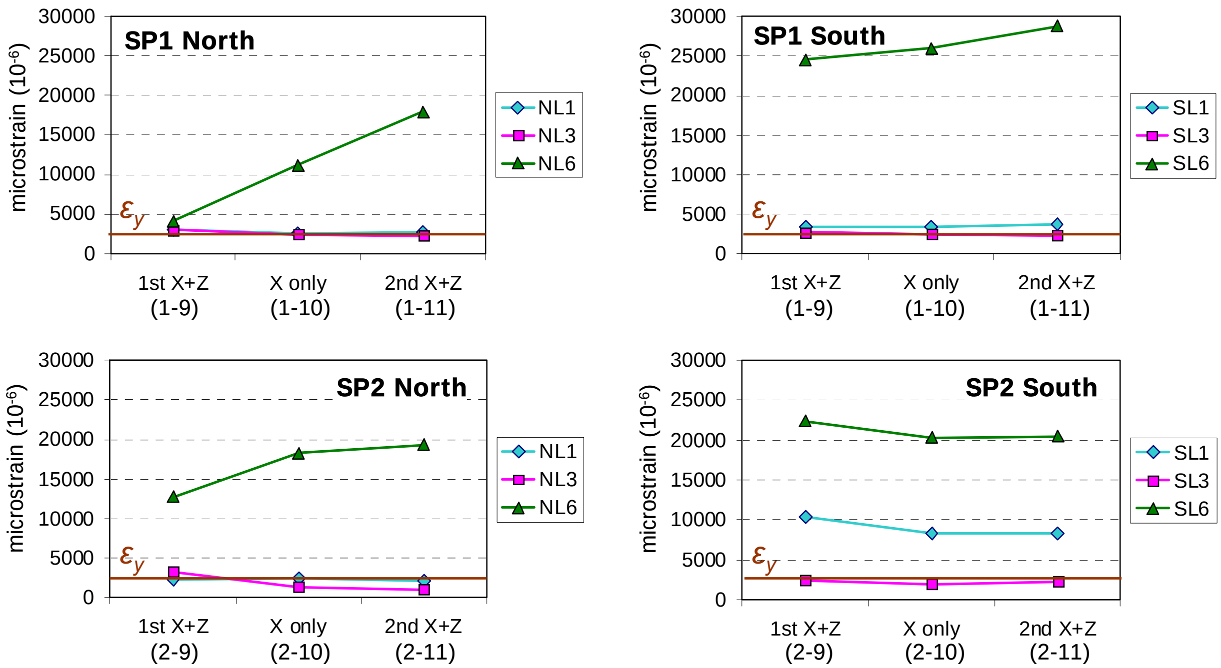

Fig. 5.7 Peak tensile strains of NL and SL in the 125%-scale runs

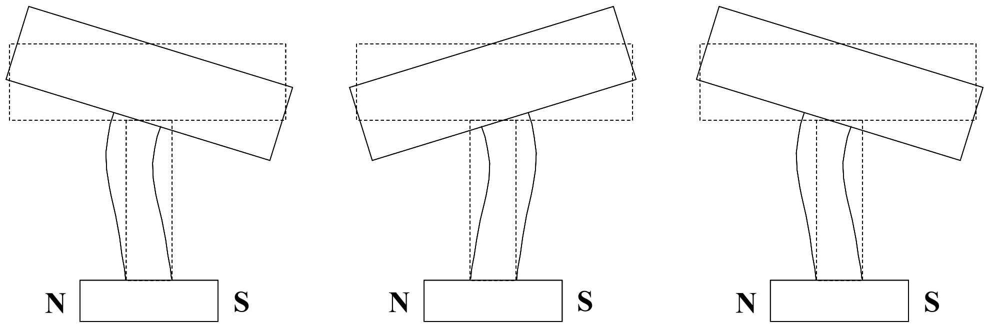

(a) 1st shear peak **(b) 2nd shear peak** **(c) 3rd shear peak**

Fig. 5.8 Schematic deflected shapes of the test specimens at shear peaks

5.4.2 Longitudinal Strains on the East and West (Y direction)

Similar to the X direction, Fig. 5.9 presents the longitudinal strains on the east and west (Y direction) sides of SP1 and Fig. 5.10 presents those of SP2. Since three gages were installed on each bar on the east and west sides, only the response at these three sections were obtained.

In Fig. 5.9(a), the strain at each section of SP1 under 125%-scale '1st X+Z' motion is shown. 'EL' and 'WL' designations imply the longitudinal strain on the east and west sides, respectively. Similar to the north and south sides, the number following these designations indicates the section height. For example, 'EL1' indicates the longitudinal strain at the first instrumented section, i.e. h=20″, on the east side. The following remarks can be made:

- All the strain values were less than those on the north and south sides. Maximum tensile strain at WL1 was less than 80% of that at NL2, both of which were at the same height.
- The strain at h=35″ was less affected by the shear peaks than that at h=20″ or 50″. Moreover, the west side was very slightly affected by the tension peak.
- The strain remained negative, i.e. tensile, in most locations and runs except at EL3 partly due to the initial strain of EL3. This implies that the force distribution was not uniform on the east and west sides suggesting the presence of biaxial bending with a small component in the transverse direction. This was confirmed by the difference between EL and WL at the same height where WL was more elongated than EL. Similar to the north and south sides, the strains below h=35″ (EL1 and WL1) had distinct peaks before the three main shear peaks.

Fig. 5.9(b) shows the strain under 'X only' run. In this case, EL1 and WL1 were more comparable than the previous run. In addition, the strain values decreased slightly in most runs. The strain results from the '2nd X+Z' run for SP1 are shown in Fig. 5.9(c). The following remarks can be made:

- WL1 showed larger tensile strain than EL1, especially at the tension peak and the 3rd shear peak.
- The tension peak occurred between the 1st and 2nd shear peaks and the strain peak which was once observed at the 2nd shear peak was not obvious in this run.
- The strain peak at the tension peak was clear in all runs.

- Compared to the strains at the 1st and 2nd shear peaks, that at the 3rd shear peak increases more in the '2nd X+Z' run. In the '1st X+Z' and 'X only' runs, the strain at the 3rd peak was similar to them, but larger tensile strain is observed. In particular, the increase in EL3 and WL3 is significant. The only difference is the presence of the tension peak between the 1st and the 2nd shear peaks. In the '1st X+Z' also had the tensile peak over 50 kips, but it occurred after the 3rd shear peak. This implies that the tension and the arrival time interval may affect the tensile strain in the upper part of the column.

In Fig. 5.10(a), the strain at each section of SP2 under 125%-scale '1st X+Z' motion is shown. The following remarks can be made:

- Similar to the '2nd X+Z' run of SP1, the tension peak was observed between the 1st and 2nd shear peaks and corresponded to a strain peak at the tension peak rather than at the 2nd shear peak. In case of SP1, the 3rd shear peak had the largest strain peak at almost all gages, but this was not the case for SP2.
- EL2 and EL3 had the largest strain peaks at the tension peak and this was observed in the '2nd X+Z' run.

For the 'X only' run (Fig. 5.10(b)), EL2 and EL3 had their peak strains at the 2nd shear peak. In Fig. 5.10(c), WL2 and WL3 were not significantly affected at the 2nd shear peak. Clearly, the top mass rocking between the east and west sides affected the strain of the upper part of the column. The following are observations on the peak-to-peak amplitude (Fig. 5.11) and the maximum tensile strain (Fig. 5.12) on the east and west sides of SP2:

- The variation in Fig. 5.11 is wider than that of SP1. For example, the peak-to-peak amplitude of WL3 (in micro-strains) changed for the three 125%-scale runs as follows: from 2172 to 1996 to 2639 for SP1 and 3994 to 3841 to 4186 for SP2. The amplitude decreased in the 2nd run and increased in the 3rd run and in most locations. The only exception was WL2 of SP2, which increased gradually, but the difference between the 1st and the 2nd runs was about 10%, i.e. significantly smaller than that between the 2nd and 3rd runs, which was 33%.
- The maximum tensile strain for SP2 had a similar trend (Fig. 5.12) as that of SP1. Another interesting feature of the strain peak was that the measured strain location made a certain order in the amplitude value and it was found to be consistent in most runs. On the west side, WL3 was the largest, WL1 was the second largest, and WL2 was the smallest (i.e. WL3 > WL1 > WL2). On the east side, the same trend (i.e. EL3 > EL1 > EL2) was observed except for the maximum tensile strain of SP2. It should be noted that the variation of EL1 was not as remarkable as those of the other gages.

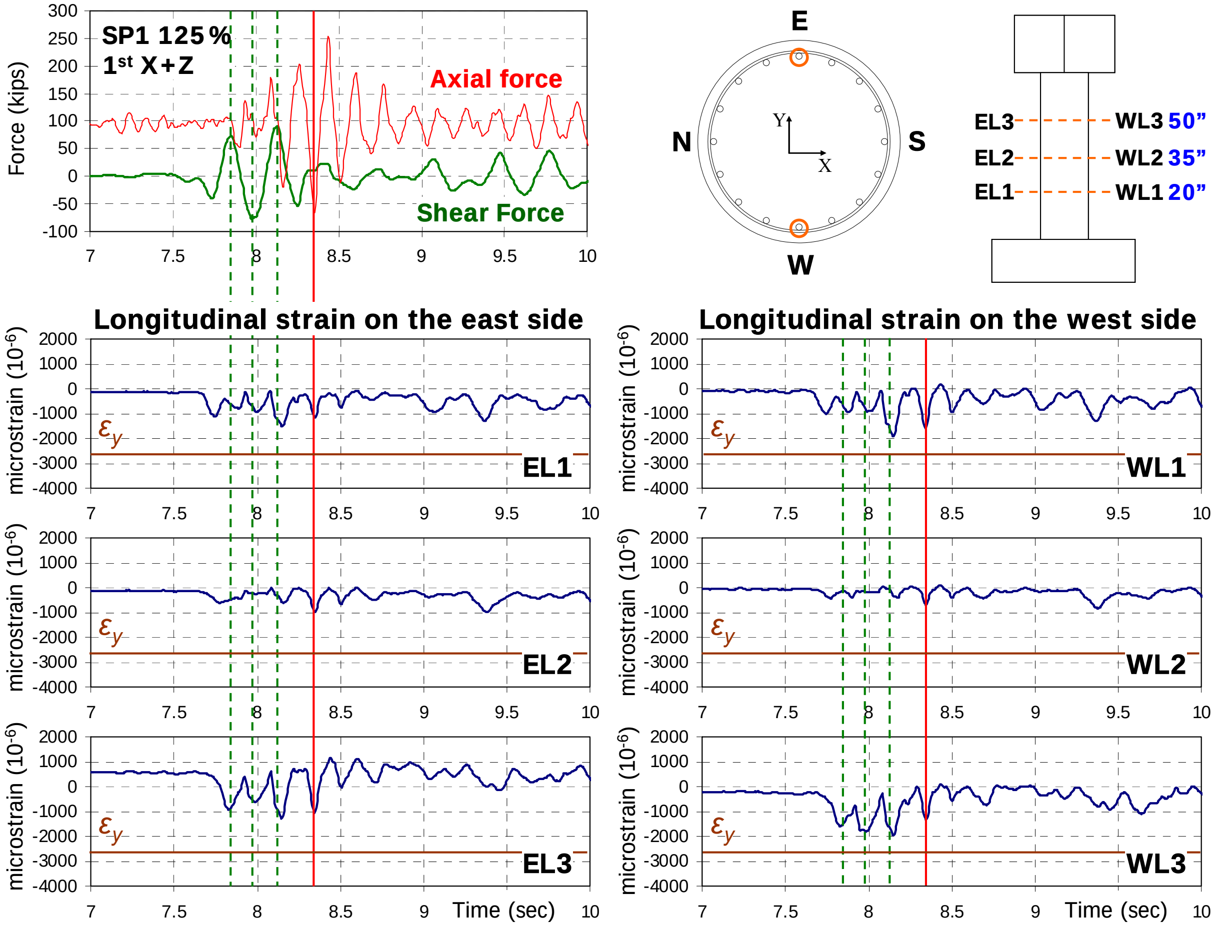

(a) SP1 125% 1st X+Z

Fig. 5.9 Longitudinal strains on the east and west sides of SP1 in the 125%-scale runs

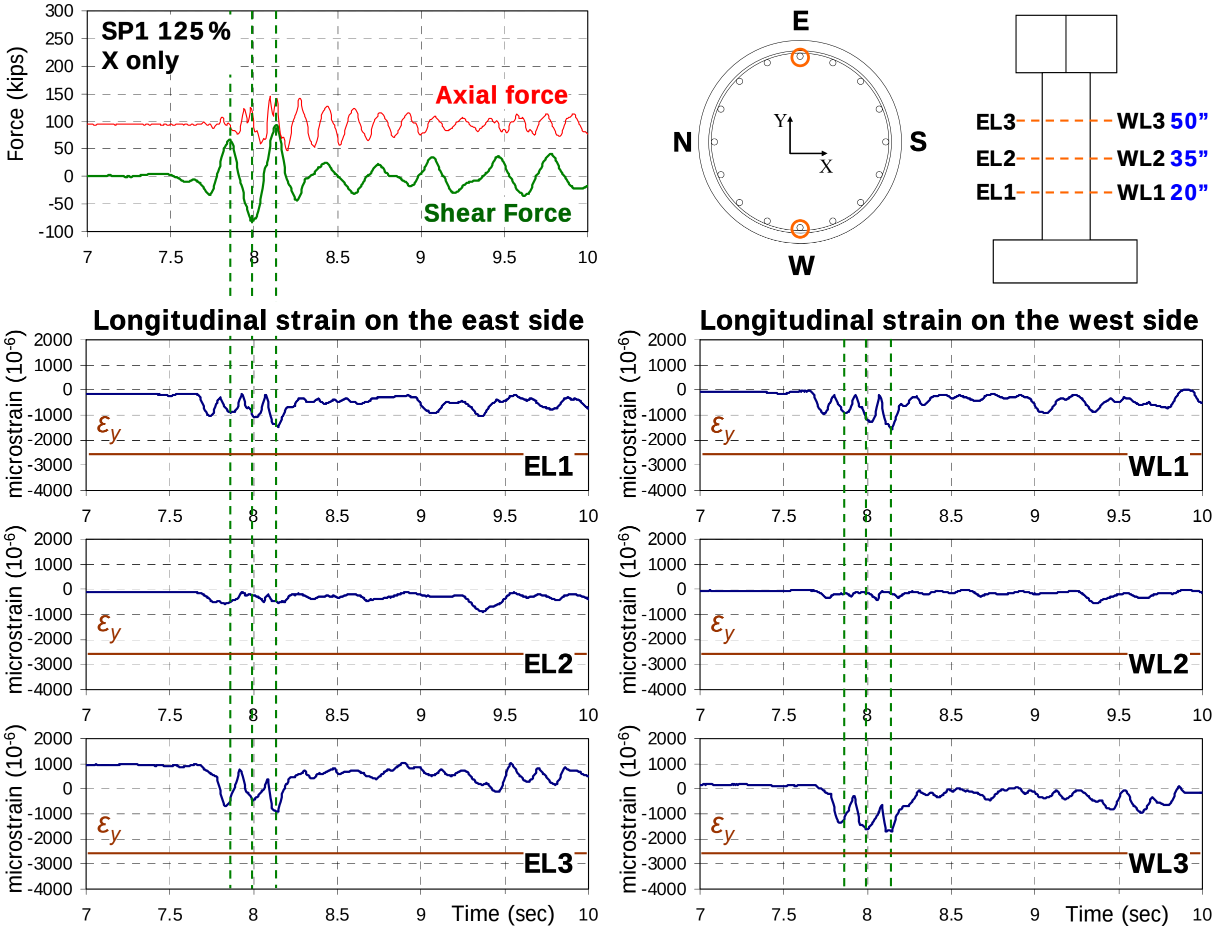

(b) SP1 125% X only

Fig. 5.9 Longitudinal strains on the east and west sides of SP1 in the 125%-scale runs (continued)

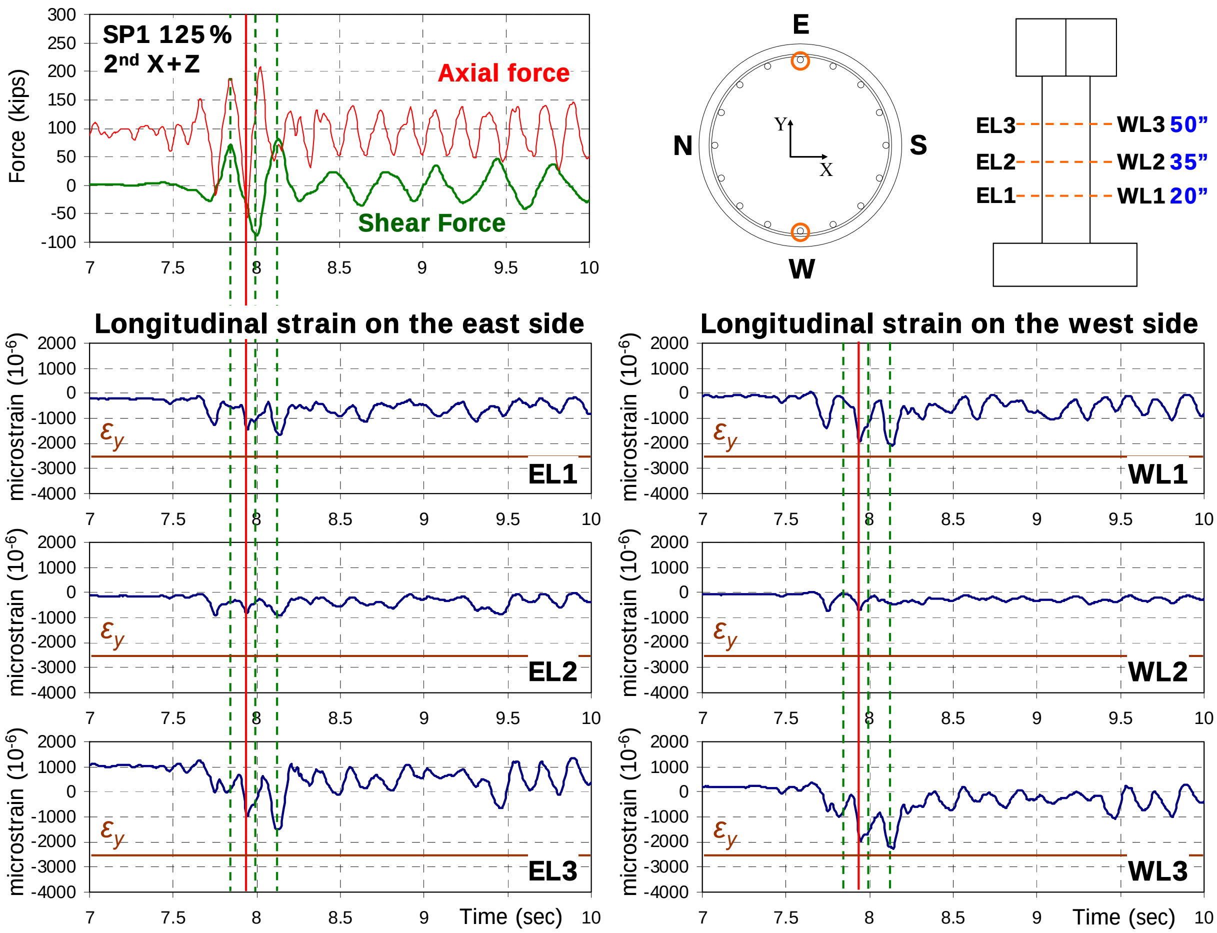

(c) SP1 125 % 2nd X+Z

Fig. 5.9 Longitudinal strains on the east and west sides of SP1 in the 125%-scale runs (continued)

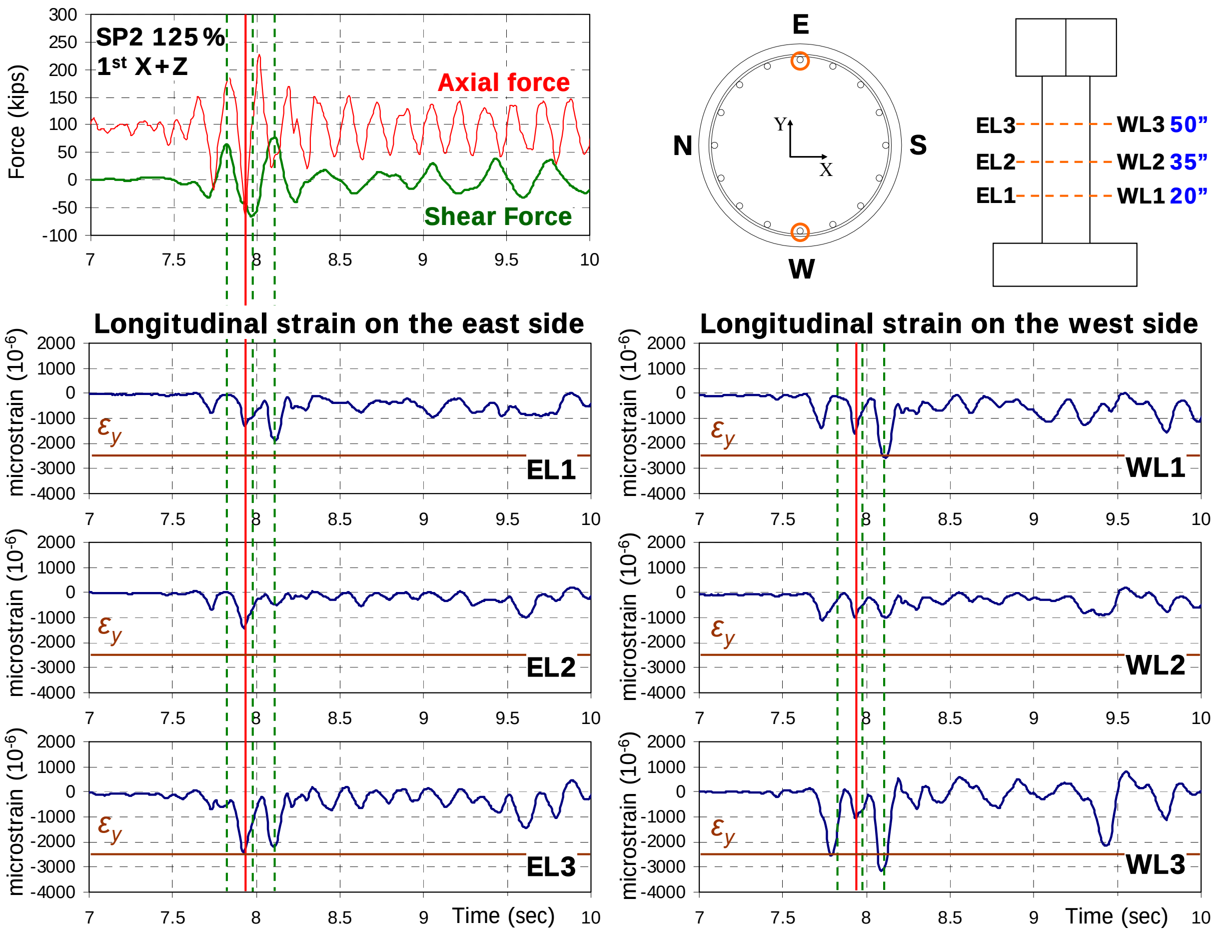

(a) SP2 125% 1st X+Z

Fig. 5.10 Longitudinal strains on the east and west sides of SP2 in the 125%-scale runs

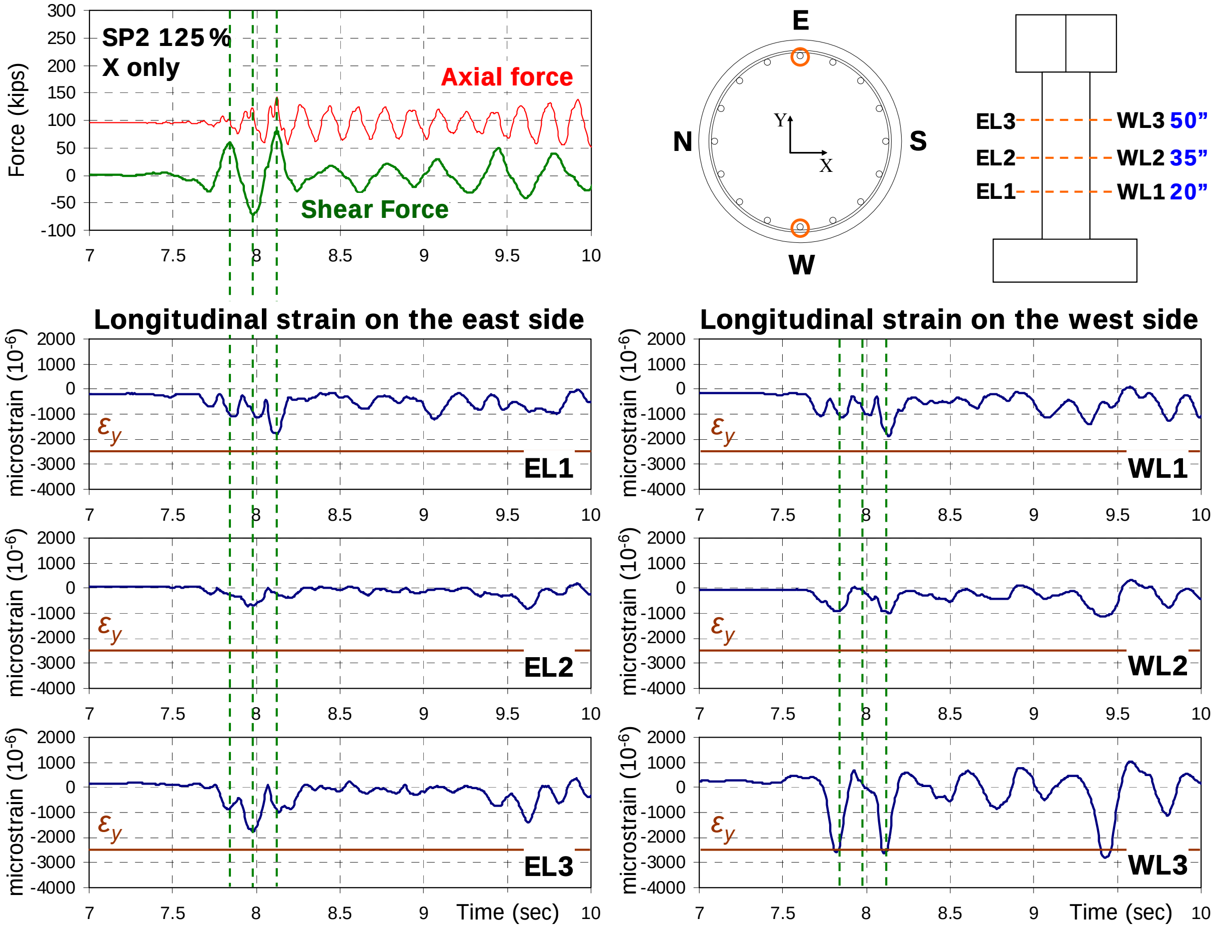

(b) SP2 125% X only

Fig. 5.10 Longitudinal strains on the east and west sides of SP2 in the 125%-scale runs (continued)

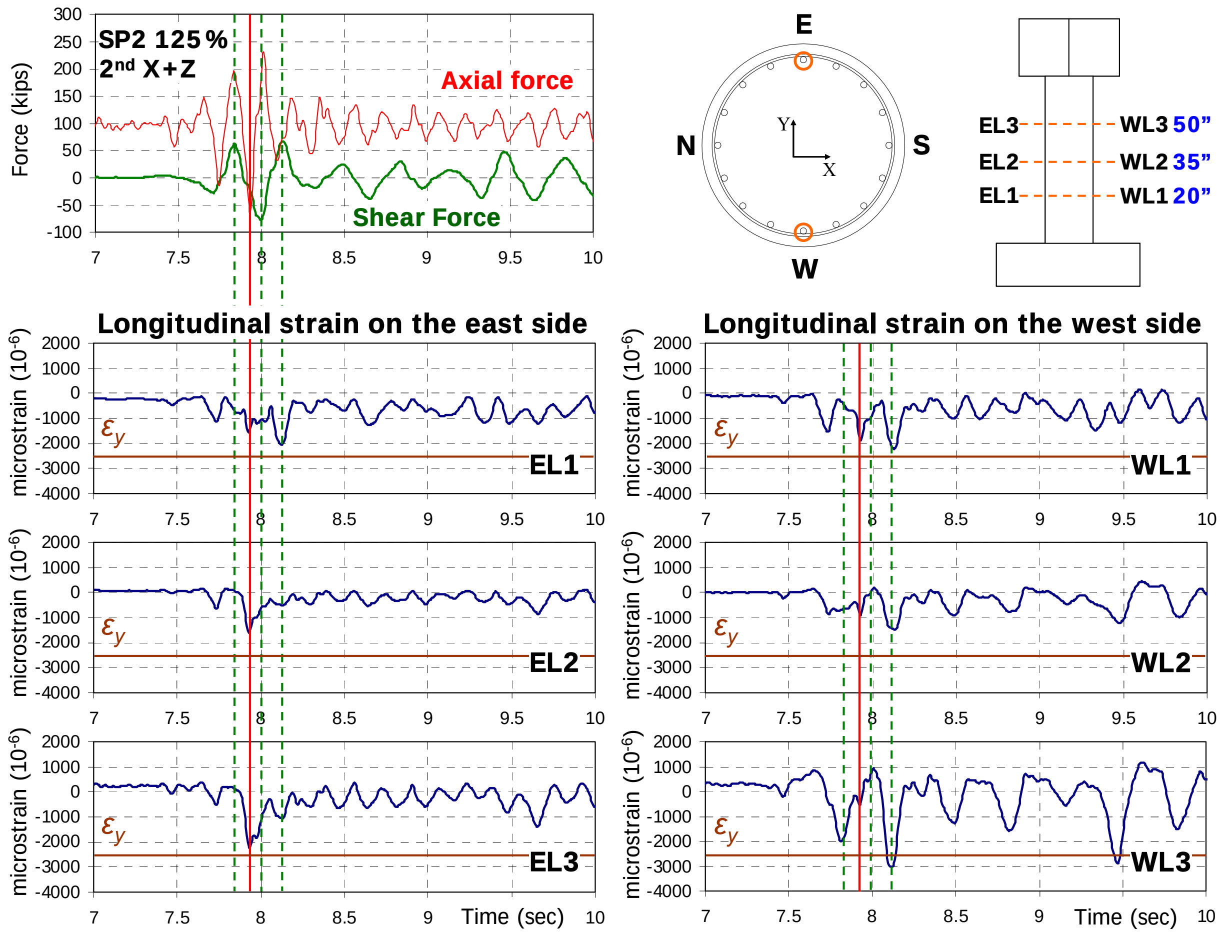

(c) SP2 125% 2nd X+Z

Fig. 5.10 Longitudinal strains on the east and west sides of SP2 in the 125%-scale runs (continued)

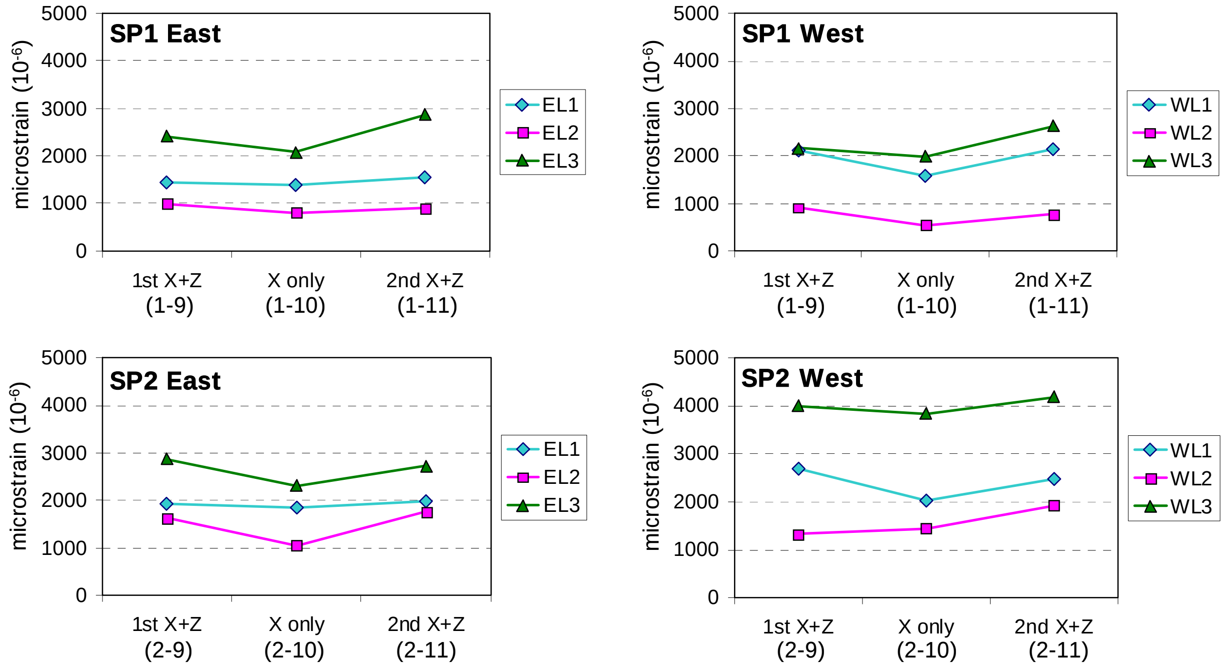

Fig. 5.11 Peak-to-peak strain amplitudes of EL and WL in the 125%-scale runs

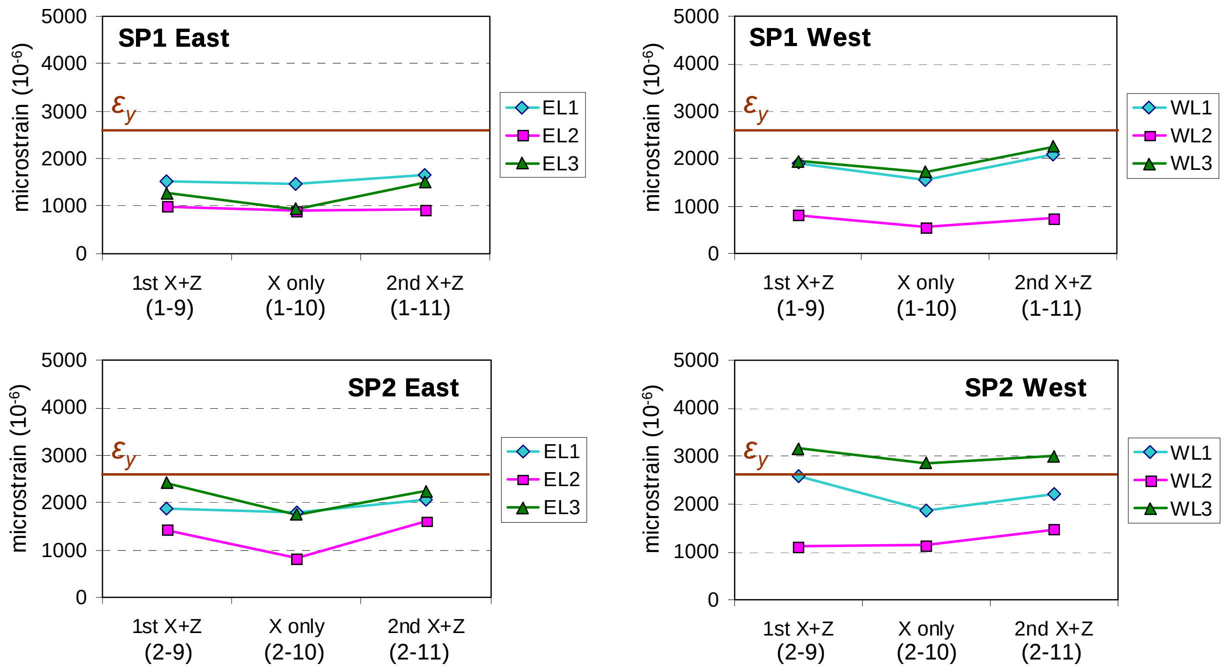

Fig. 5.12 Peak tensile strains of EL and WL in the 125%-scale runs

5.5 Transverse Strains

5.5.1 Transverse Strains on the North and South (X direction)

Total of 14 strain gages were installed on the hoops on the north and south sides of the columns. Each side had 7 gages with six gages were uniformly distributed with spacing of 10″ and one gage at *h*=35″, i.e. at the middle of the column. Fig. 5.13 shows the results of the hoop strains of SP1 and Fig. 5.14 shows the results from strain gages of SP2. Similar to the previous designations, "NH" and "SH" stand for the hoop strains on the north and south, respectively. The following number (ranging from 1 to 7) following these designations indicates the height of section where the gage is installed, corresponding to h=10″, 20″, 30″, 35″ (mid-height), 40″, 50″, and 60″, respectively.

In Fig. 5.13(a), the hoop strain at each section of SP1 under 125%-scale '1st X+Z' motion is shown. The observations are as follows:

- Similar to the longitudinal strain, the transverse strain had peaks at the shear peaks and the tension peak.
- The lower and upper parts of the column were different in terms of the strain peak amplitudes. For example, NH2 and NH3 were smaller than NH4, NH5, and NH6. On the south side, SH1, SH3, SH4, and SH5 were relatively small. This implies confinement variation as the section location was higher and the corresponding hoop tensile strain increased near the column top (i.e. at NH5, NH6, SH6, and SH7). This was expected since the compressive uniaxial stresses and accordingly the lateral strains and stresses were larger at the top due to the presence of larger bending moments.
- SH2 had the largest tensile peak at the 1st and 3rd shear peaks and the tension peak and there was no significant peak at the maximum tension in any of the other strain gages.
- Some gages, such as NH2, SH1, and SH4, measured larger tensile strain at the 2nd shear peak rather than the 1st and 3rd shear peaks. These peaks were small because of the tension-compression reversal caused by the double-curvature behavior.

Under 'X only' run (Fig. 5.13(b)), the response was very similar to the '1st X+Z' run, but the hoop strain increased. NH3 had the largest peak at the 2nd shear peak compared to NH2, SH1, and SH4. Note that SH4 remained almost the same and relatively small. In Fig. 5.13(c), the vertical component was added and it had a tension peak between the 1st and 2nd shear peaks. The hoop strain continued to increase in this run which is clearly shown in Fig. 5.15 and Fig. 5.16

Fig. 5.14(a) shows the hoop strain of SP2 subjected to the '1st X+Z' run. The following remarks can be inferred:

- Most gages on the south side had no noticeable peak before the 3rd shear peak and this was also observed in NH1. However, the tensile peak of SH7 increased gradually at every shear peak.
- Different from the south side, the north side gages had two tensile peaks at the 1st and 3rd shear peaks except for NH2 and NH7, where the peak tensile strain occurred at the 3rd shear peak and it increased as the height increased.

- Even without vertical component (Fig. 5.14(b)), the overall strain increased similar to the SP1 specimen. The strain peaks at the 1st and 2nd shear peaks were noticeable. However, the 3rd peak was still the largest in most runs and strain gage locations.

The results from the '2nd X+Z' run are shown in Fig. 5.14(c). In this run, it was observed that the hoop strain continued to increase. It was noticeable that NH6 had a relatively large and sharp peak at the 2nd shear peak.

The peak-to-peak amplitude (Fig. 5.15) and the maximum tensile strain (Fig. 5.16) at h=10″, 40″, and 60″ in each run provided the following remarks:

- In SP1, three different sections had similar peak-to-peak amplitude and tension peak values on the north side, but they differed on the south side. In particular, SH6 was about three times larger than SH1 and SH4.
- In every run, the hoop strain peak increased as the runs progressed, except for NH1 and NH4 among the six shown in Fig. 5.16.
- In SP2, five gages among the six (except for NH1) had larger values than those of SP1.
- The strain increased as the location of the hoop got higher. The only exception was NH4 where its tensile strain peak decreased by 19.6% in the '2nd X+Z' test. Other than that, the strain increased as runs progressed.

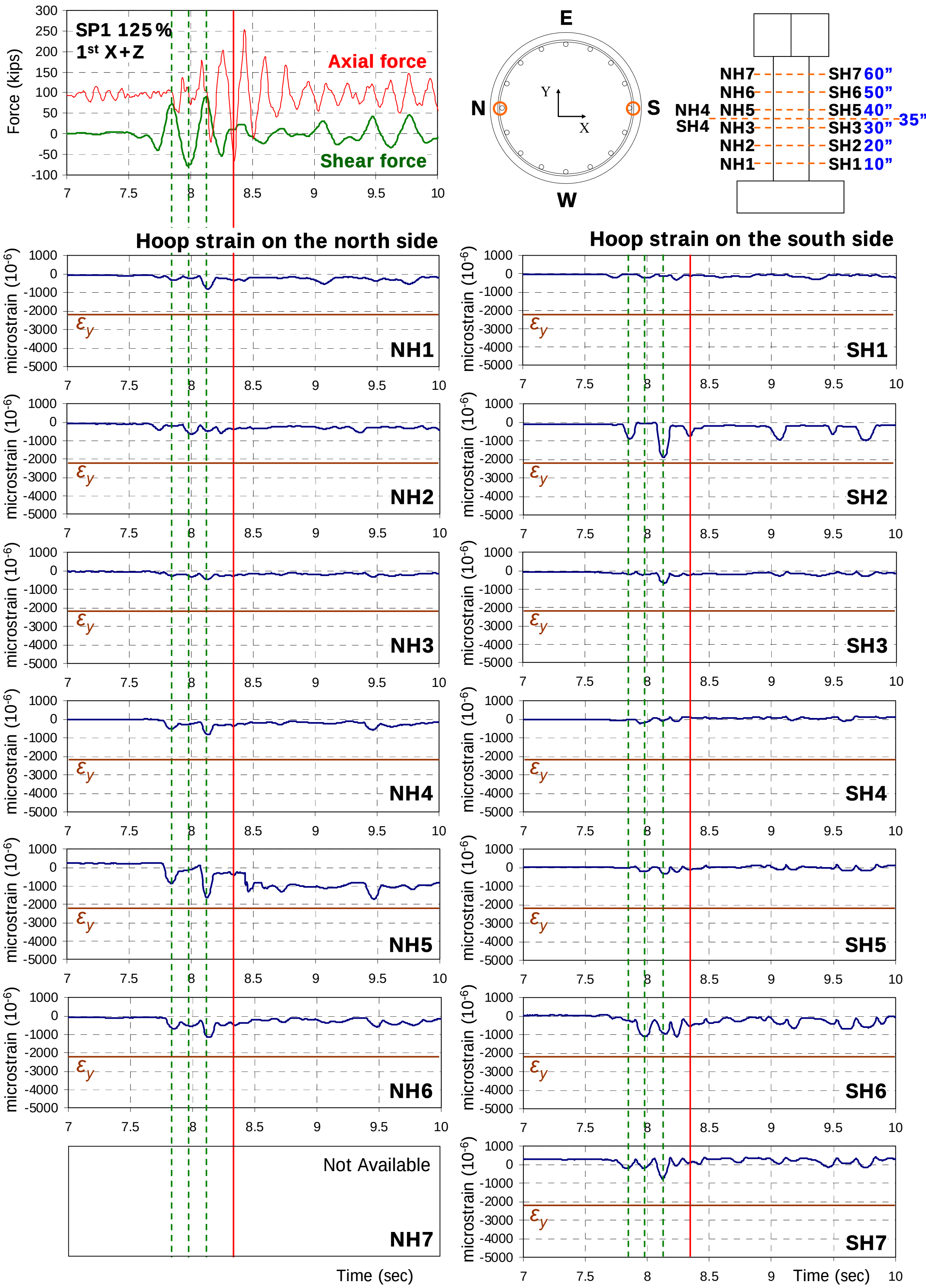

(a) SP1 125% 1st X+Z

Fig. 5.13 Hoop strains on the north and south sides of SP1 in the 125%-scale runs

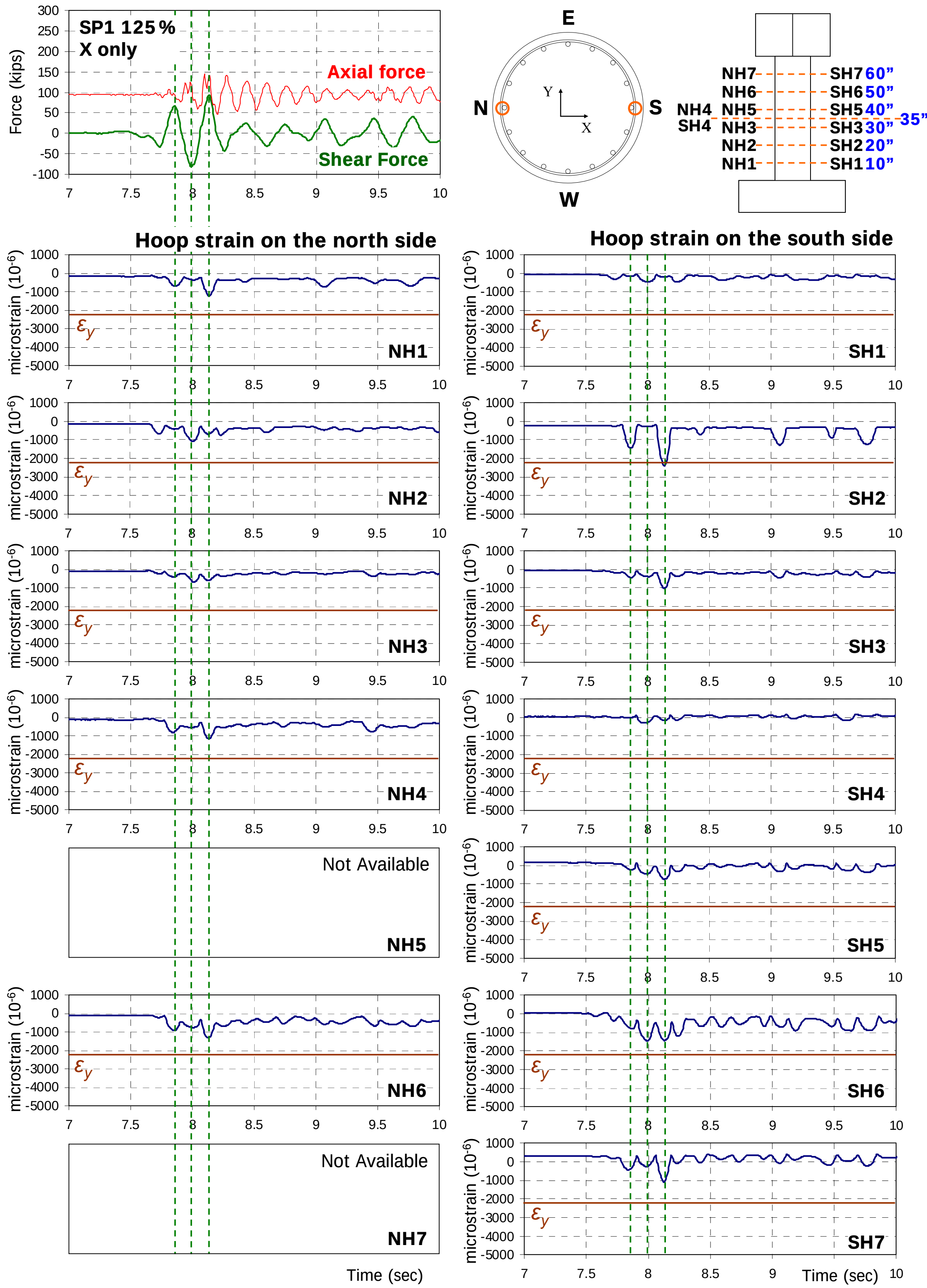

(b) SP1 125% X only

Fig. 5.13 Hoop strains on the north and south sides of SP1 in the 125%-scale runs (continued)

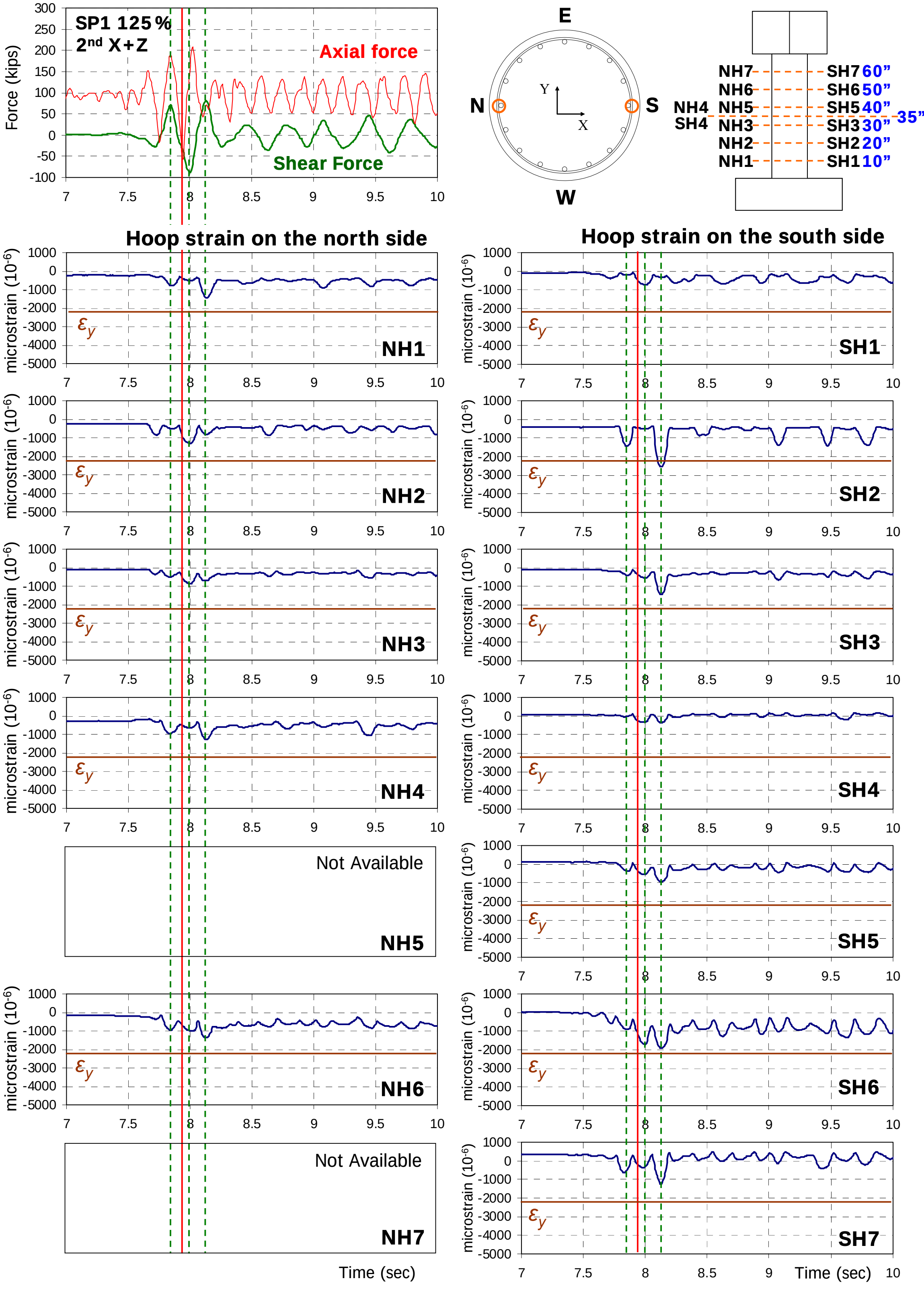

(c) SP1 125% 2nd X+Z

Fig. 5.13 Hoop strains on the north and south sides of SP1 in the 125%-scale runs (continued)

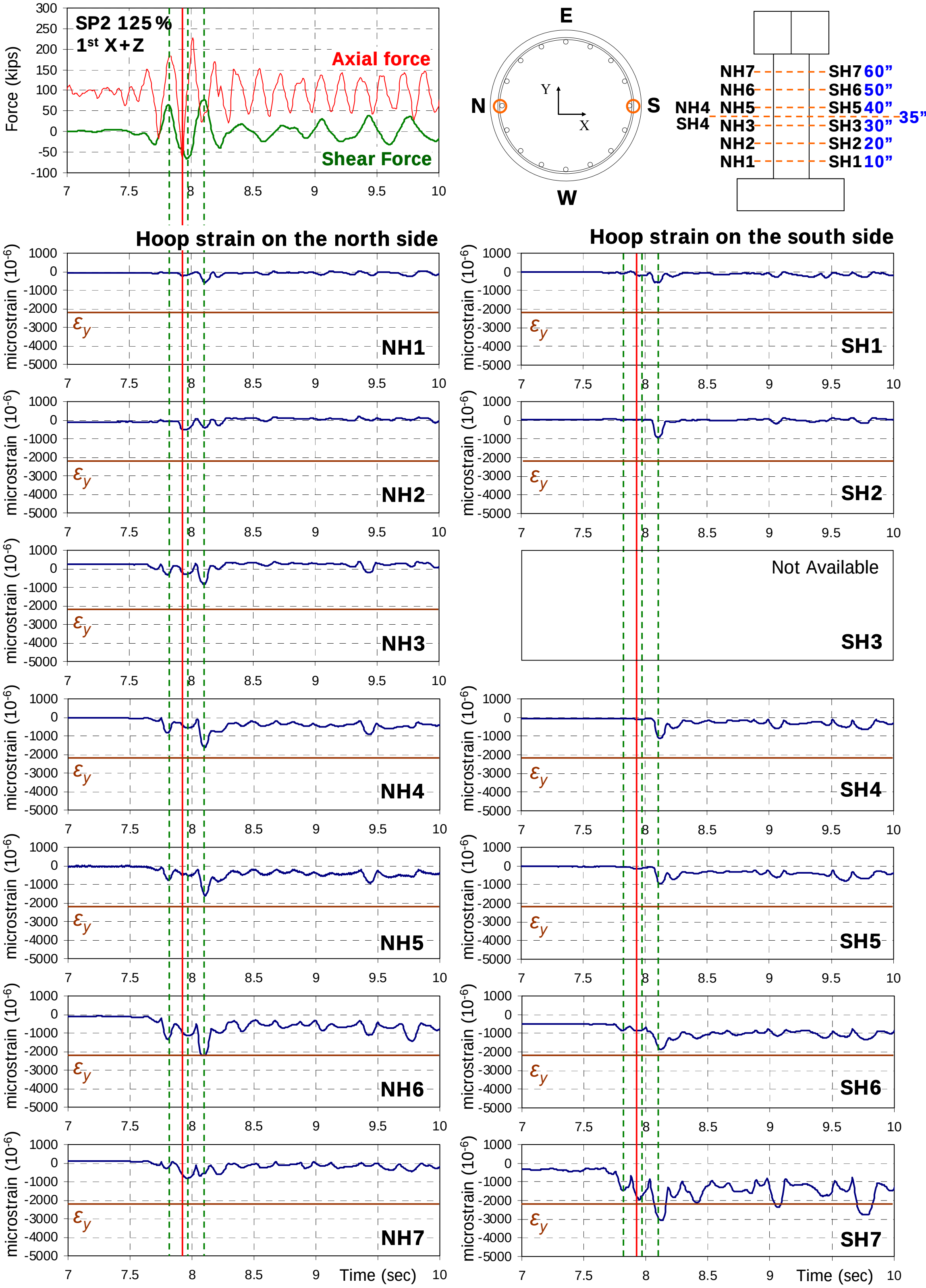

(a) SP2 125% 1st X+Z

Fig. 5.14 Hoop strains on the north and south sides of SP2 in the 125%-scale runs

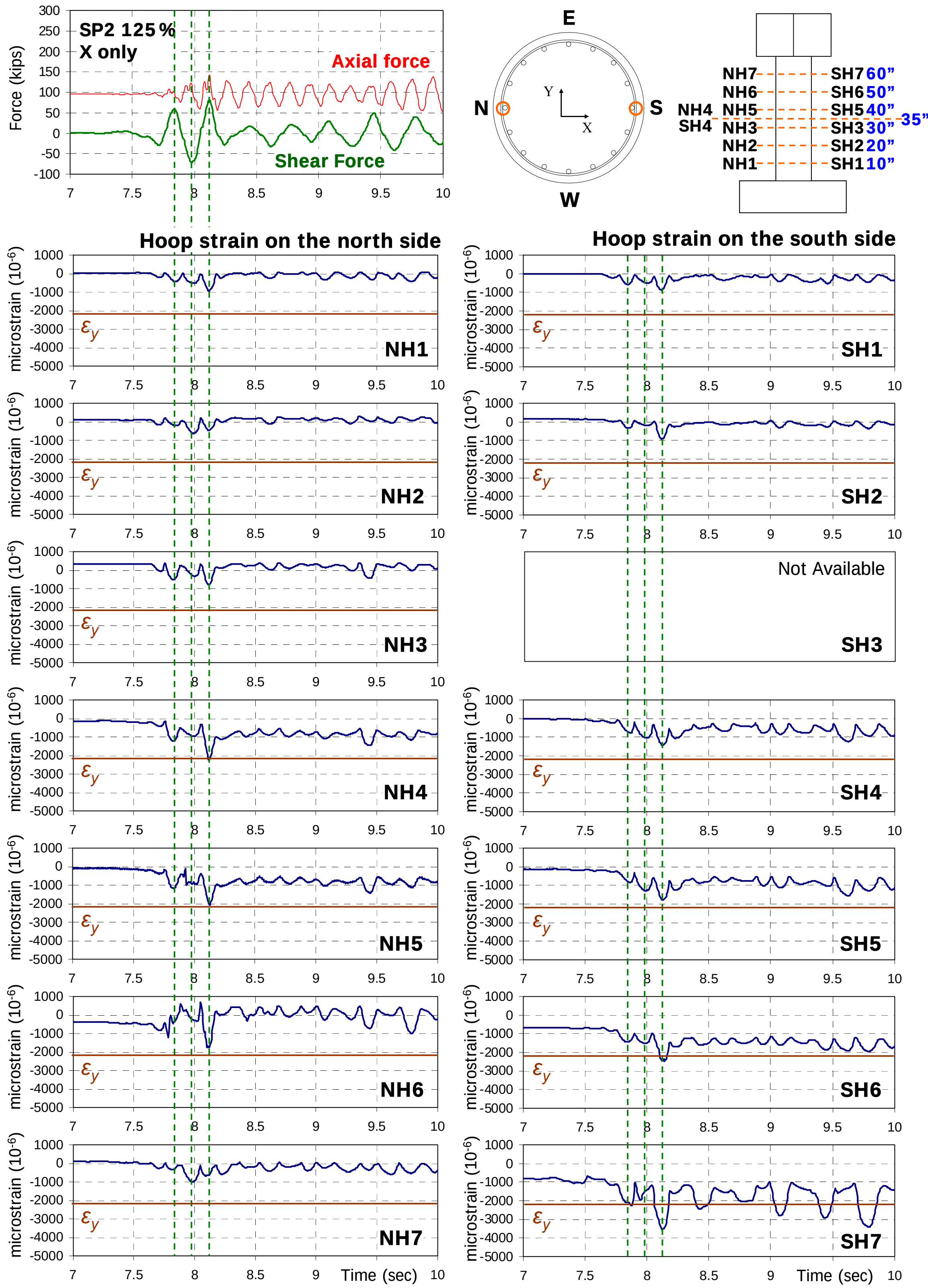

(b) SP2 125% X only

Fig. 5.14 Hoop strains on the north and south sides of SP2 in the 125%-scale runs (continued)

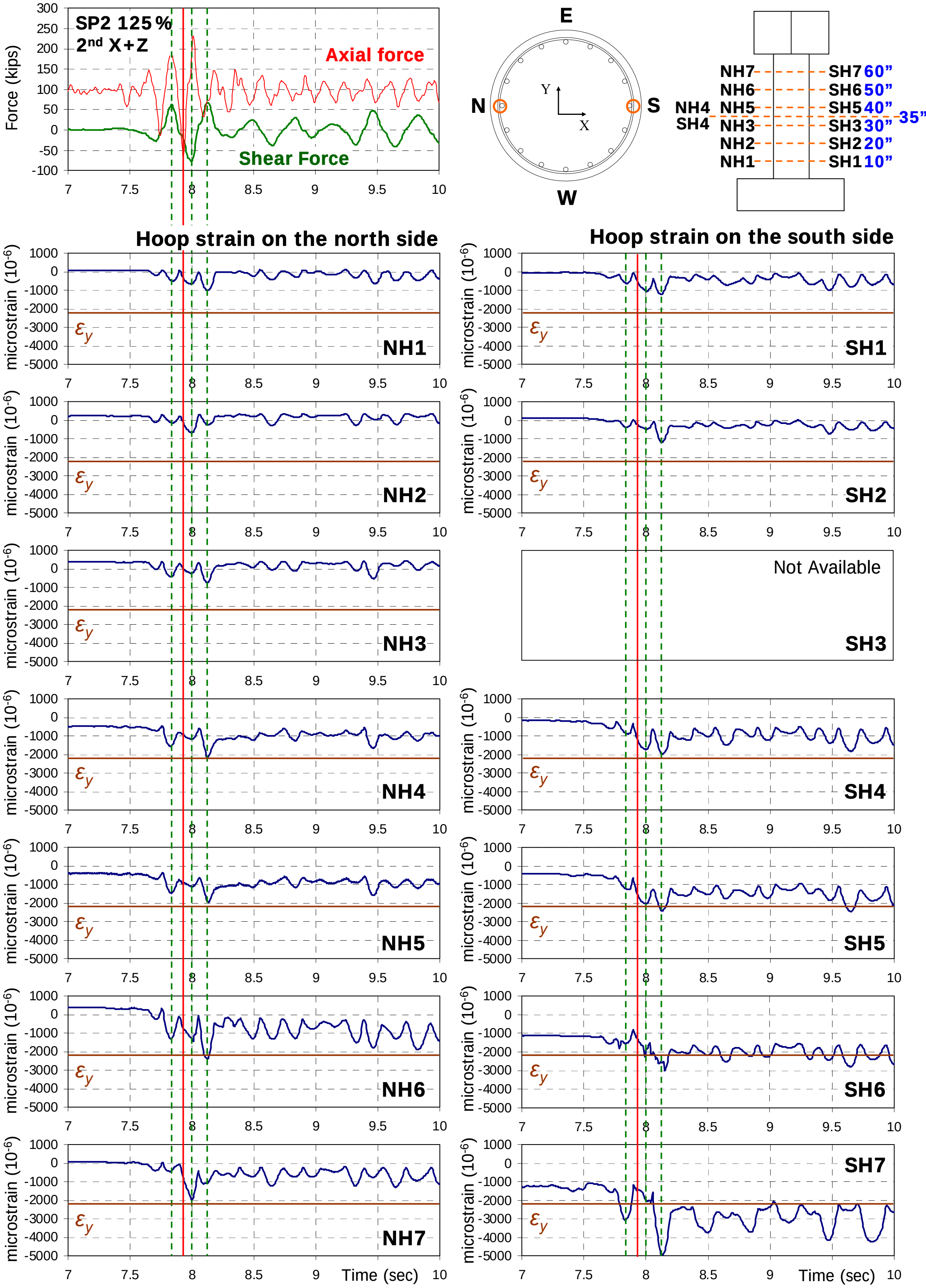

(c) SP2 125% 2nd X+Z

Fig. 5.14 Hoop strains on the north and south sides of SP2 in the 125%-scale runs (continued)

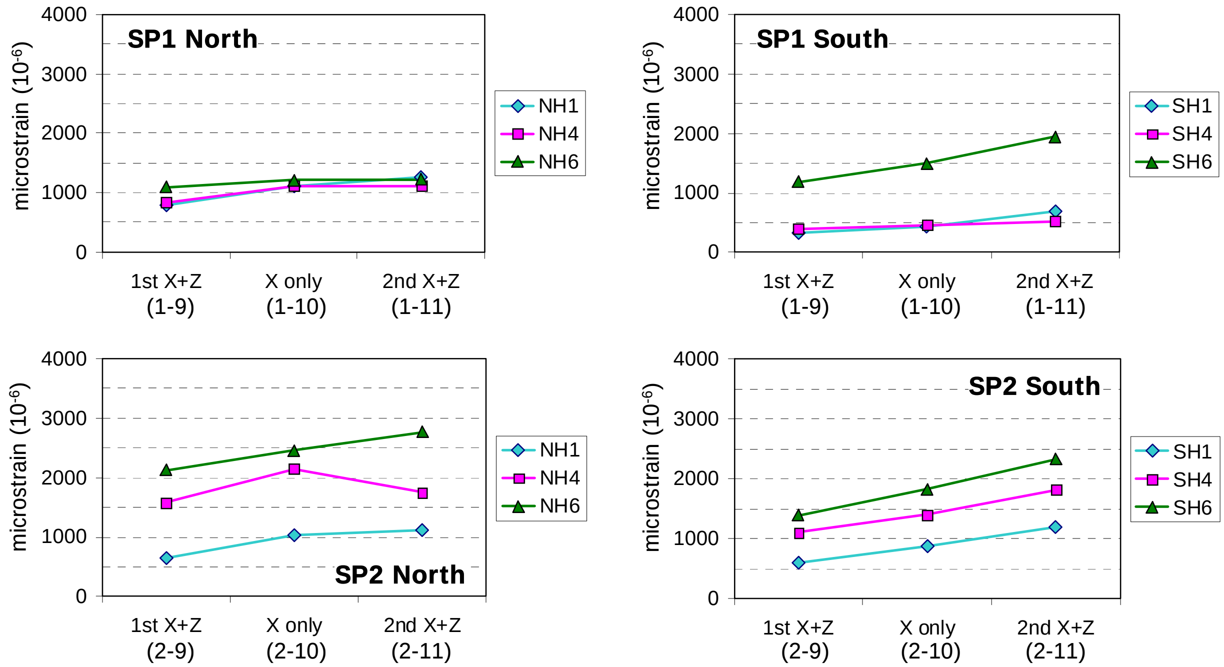

Fig. 5.15 Peak-to-peak amplitudes of NH and SH in the 125%-scale runs

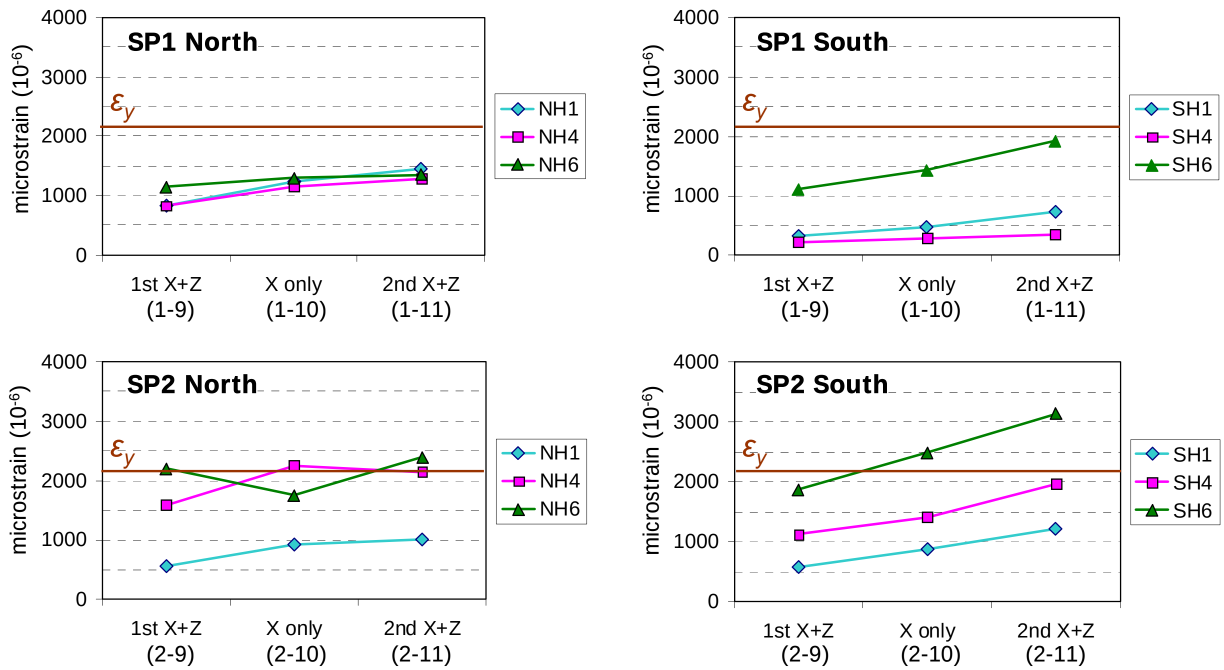

Fig. 5.16 Peak tensile strains of NH and SH in the 125%-scale runs

5.5.2 Transverse Strains at *h*=10″ and 35″

Total of 10 gages were attached to two hoops to capture transverse strain in different directions along the hoop circumference. For the hoop at *h*=10″, six gages were used and the central angle between two adjacent gages was 60°. Among the six gages, two gages, NH1 and SH1, were already discussed in Section 5.5.1, but they are compared to other gages on the same hoop in this section. For the hoop at *h*=35″, four gages were installed and the central angle between two adjacent gages was 90°. The hoop strains around these two cross-sections of SP1 are shown in Fig. 5.17 and those of SP2 are shown in Fig. 5.18.

Fig. 5.17(a) presents the strain response when '1st X+Z' was applied to SP1. The following remarks can be made:

- At *h*=10″, most gages had the maximum tensile strain at the 3rd shear peak. Among the used 6 gages, NEH1 and NWH1 had noticeable peak and residual strains.
- At *h*=35″, the response measured by NH4 was the largest and it had the maximum tensile peak at the 3rd shear peak. Other than for the gages on the north side, the hoop strain at *h*=10″ was larger than that at *h*=35″.

Fig. 5.17(b) presents the strain response when 'X only' motion was applied to SP1. The following remarks can be made:

- All the peak values at *h*=10″ increased by at least 20% compared with those in the '1st X+Z' test. The trend of the increase was also detected in the peak-to-peak amplitude. Due to residual strain after the '1st X+Z' run, the peak-to-peak amplitude of NWH1 did not significantly grow (5%), but the maximum tensile peak increased by almost 30%.
- The hoop strain on the south side had the maximum tensile peak at the 2nd shear peak even though it was relatively small.

Fig. 5.17(c) presents the strain response when '2nd X+Z' motion was applied to SP1. The following remarks can be made:

- The peaks were larger than the previous runs, except for the peak-to-peak amplitude of NEH1 and WH4. The strain of WH4 at *h*=35″ was more on the compression side, as runs progressed.
- The peak-to-peak amplitude at *h*=10″ on the south side increased by 30% or more and this was larger than that on the north side.
- The maximum tensile peak on the south side occurred at the 2nd shear peak and it became more distinct than the run of 'X only' motion.

For SP2 (Fig. 5.18), the following observations are made:

- Under the '1st X+Z' motion (Fig. 5.18(a)), most gages had large peaks at the 3rd shear peak, but EH4 and WH4 had their peaks at the tensile peak. The elongation was larger than SP1 in most runs and gage locations. In particular, the tensile strain at *h*=35″ was more than 188% of that measured from SP1. However, the decrease in the amplitude was detected at NWH1 and NH1, where NWH1 was almost 2/3 of that measured in SP1. This trend was consistent in the peak-to-peak amplitude and the maximum tensile strain values.
- The peak at the 1st shear peak observed in SP1 was not that clear in SP2. Larger hoop strain in SP2 compared to SP1 at *h*=35″, where the effect of bending moment was not

significant, was the due to the greater shear damage in SP2, whereas smaller strain in SP2 than SP1 at *h*=10″, where the effect of bending moment was considerable, was due to the smaller moments and corresponding smaller axial compressive stresses and lateral pressure in SP2.

- The response under 'X only' motion (Fig. 5.18(b)) was similar to that of SP1. The strain peak increased by 15% or more, compared to the previous run. In addition, the strain peaks at the 1st shear peak were observed.
- Under the '2nd X+Z' run (Fig. 5.18(c)), the peaks increased and this trend was significant on the south side regardless of the cross-section location. Except for SWH1, EH4, and WH4, the maximum strain peaks appeared at the 3rd shear peak. It should be noted that the strains from WH4 of SP2 were very different from those of SP2. They had the smallest peak in SP1, but they were comparable to SH4 in SP2.

Fig. 5.19 and Fig. 5.20 present the peak-to-peak amplitudes and the maximum tensile strains of the hoop at *h*=10″. Similarly, those for *h*=35″ are shown in Fig. 5.21. From these plots, one can observe the followings:

- The north and south difference at *h*=10″ was noticeable in SP1.
- The gages which were not along the X axis (N-S) of each cross-section had larger values than those on the NH or SH located along the X axis. In case of the cross-section at *h*=35″, the discrepancy between the north and other directions was observed and it was more remarkable in SP1 than SP2.
- Most strain peaks increased as runs progressed.

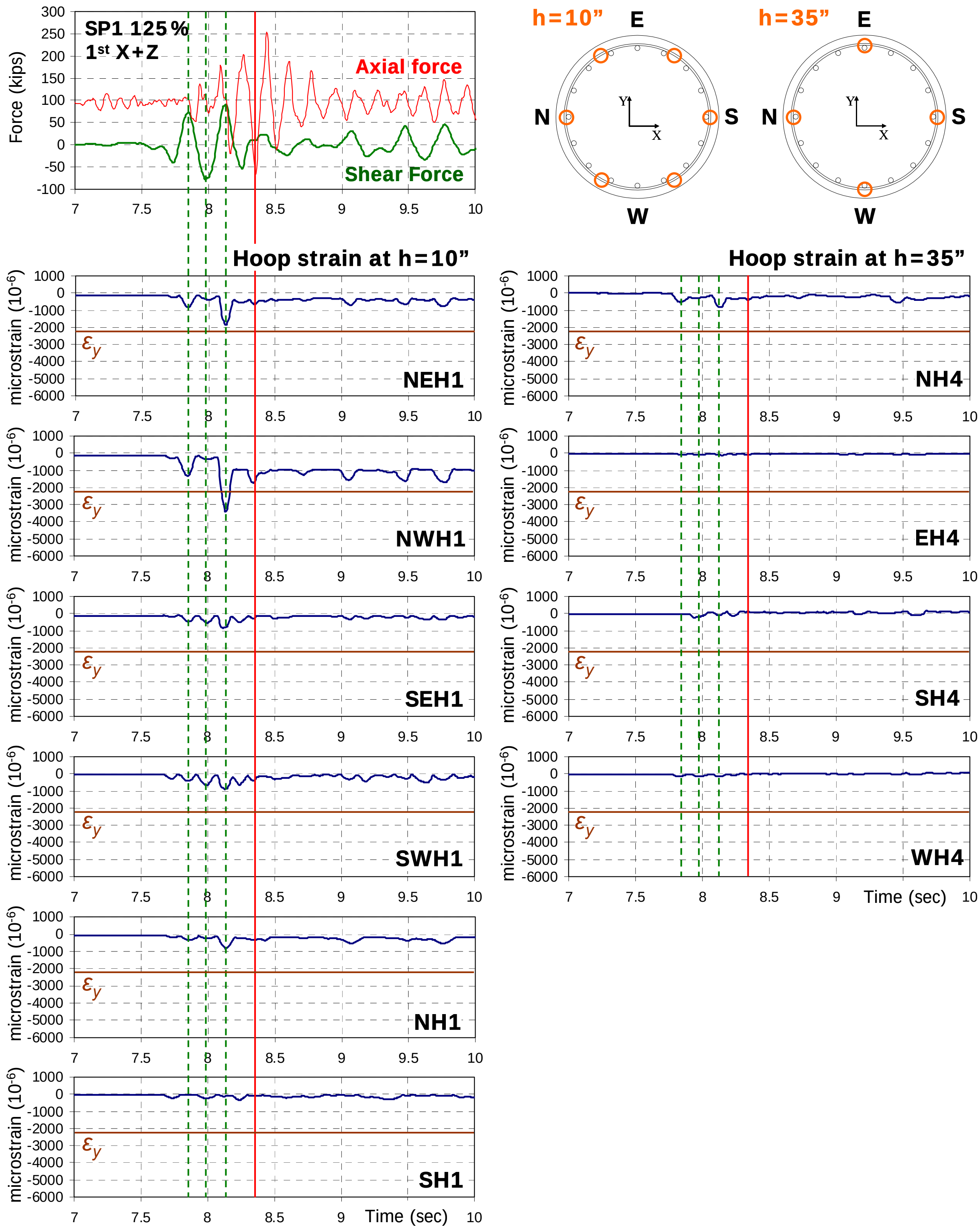

(a) SP1 125% 1st X+Z

Fig. 5.17 Hoop strains at two cross-sections of SP1 in the 125%-scale runs

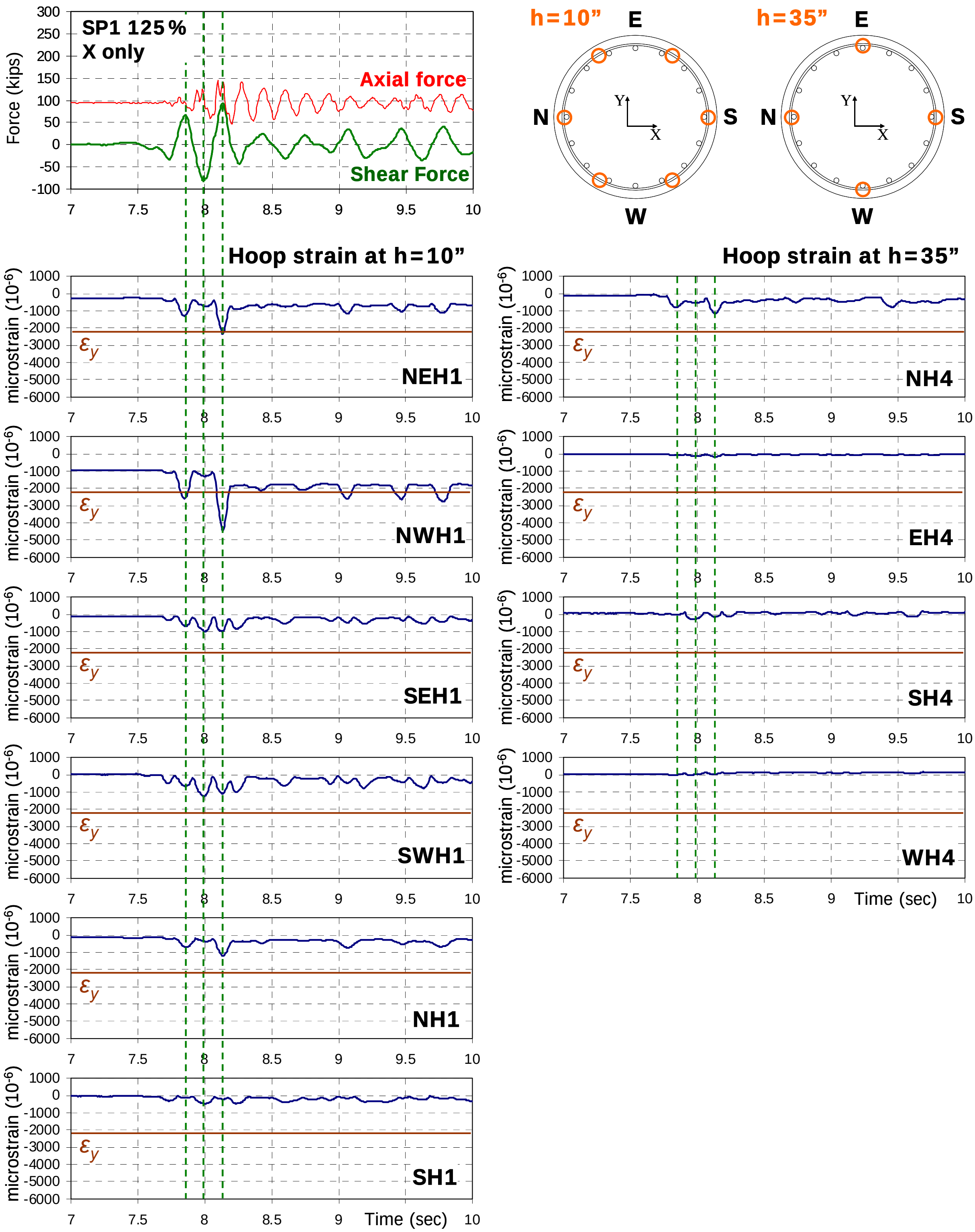

(b) SP1 125% X only

Fig. 5.17 Hoop strains at two cross-sections of SP1 in the 125%-scale runs (continued)

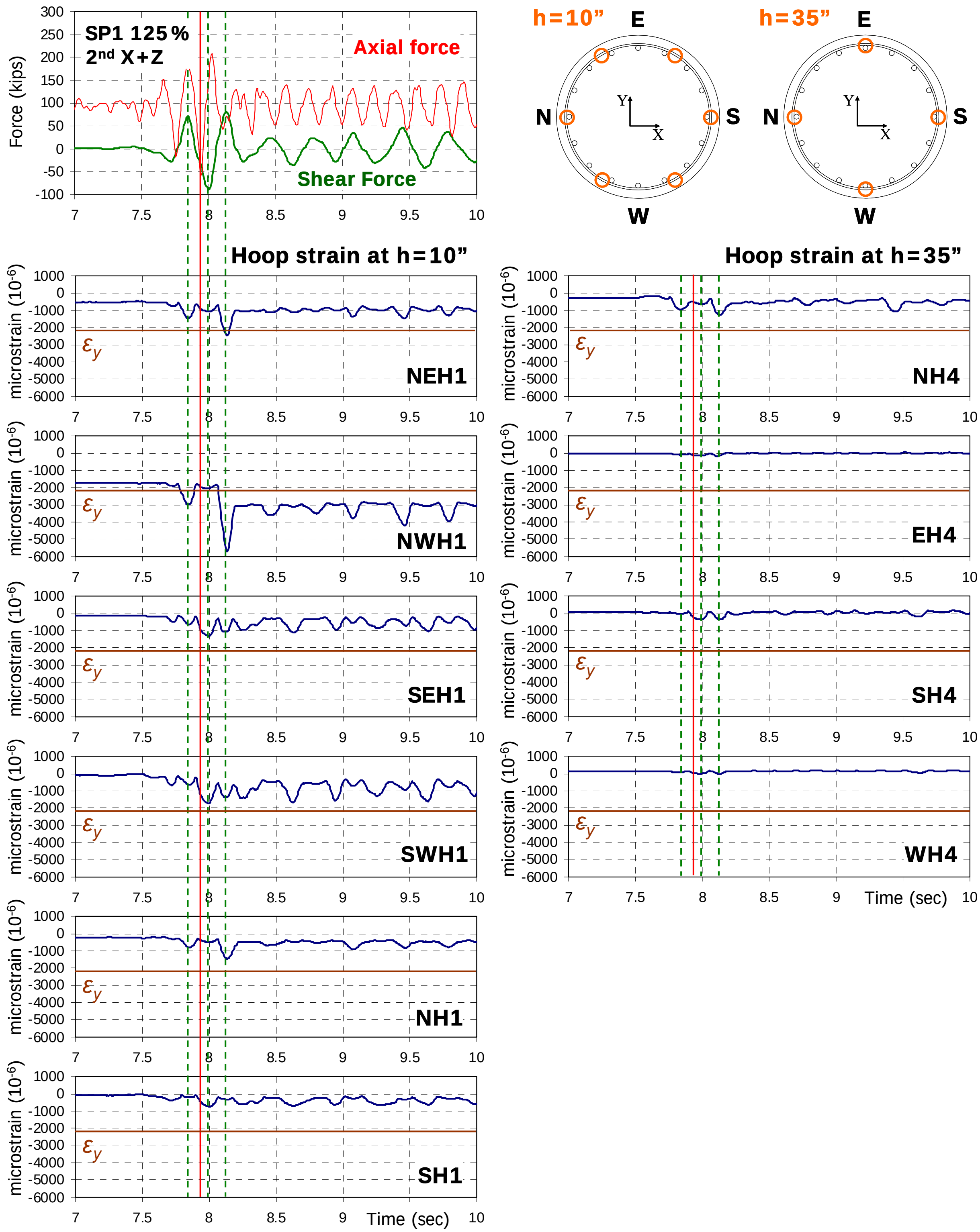

(c) SP1 125% 2nd X+Z

Fig. 5.17 Hoop strains at two cross-sections of SP1 in the 125%-scale runs (continued)

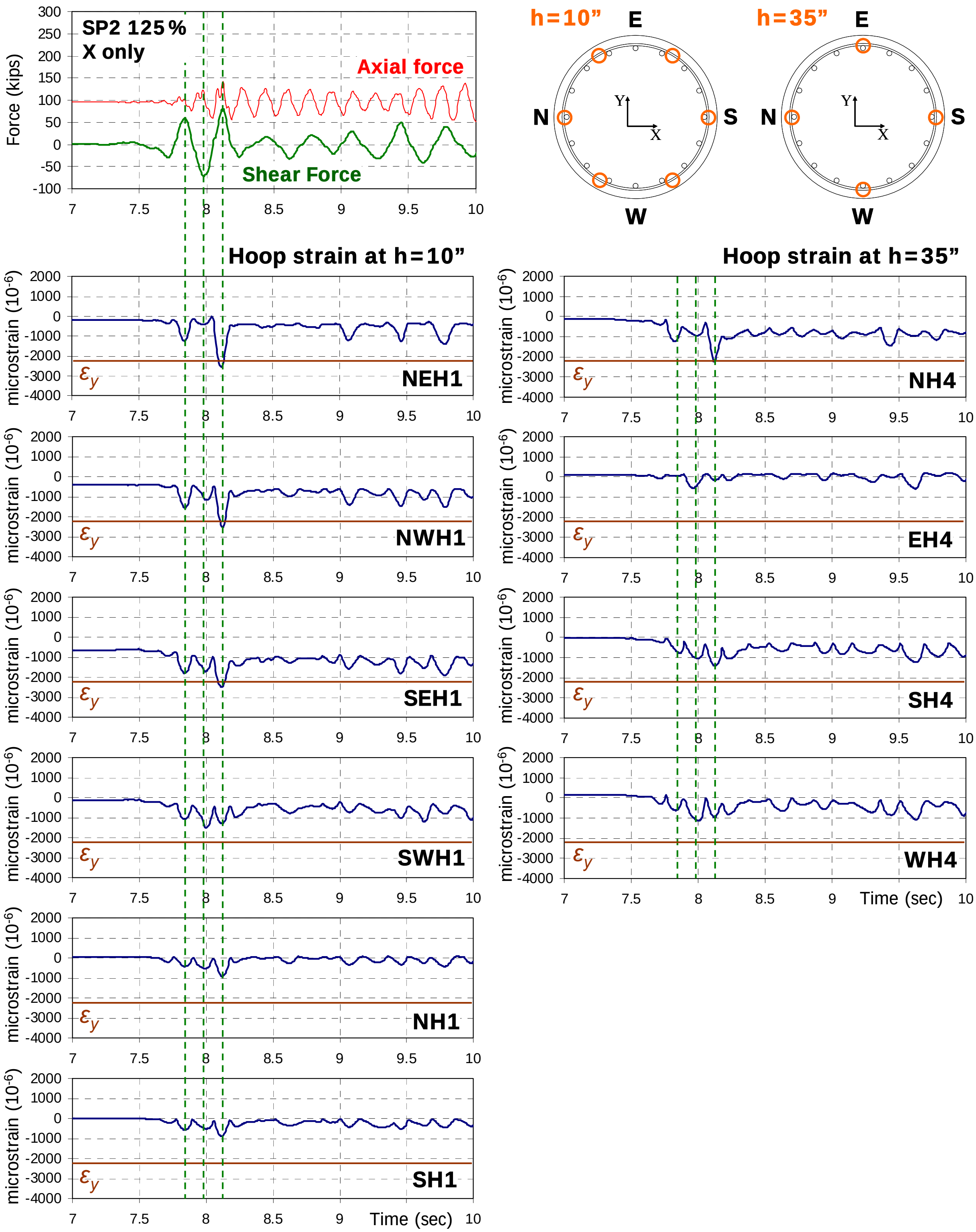

(b) SP2 125% X only

Fig. 5.18 Hoop strains at two cross-sections of SP2 in the 125%-scale runs

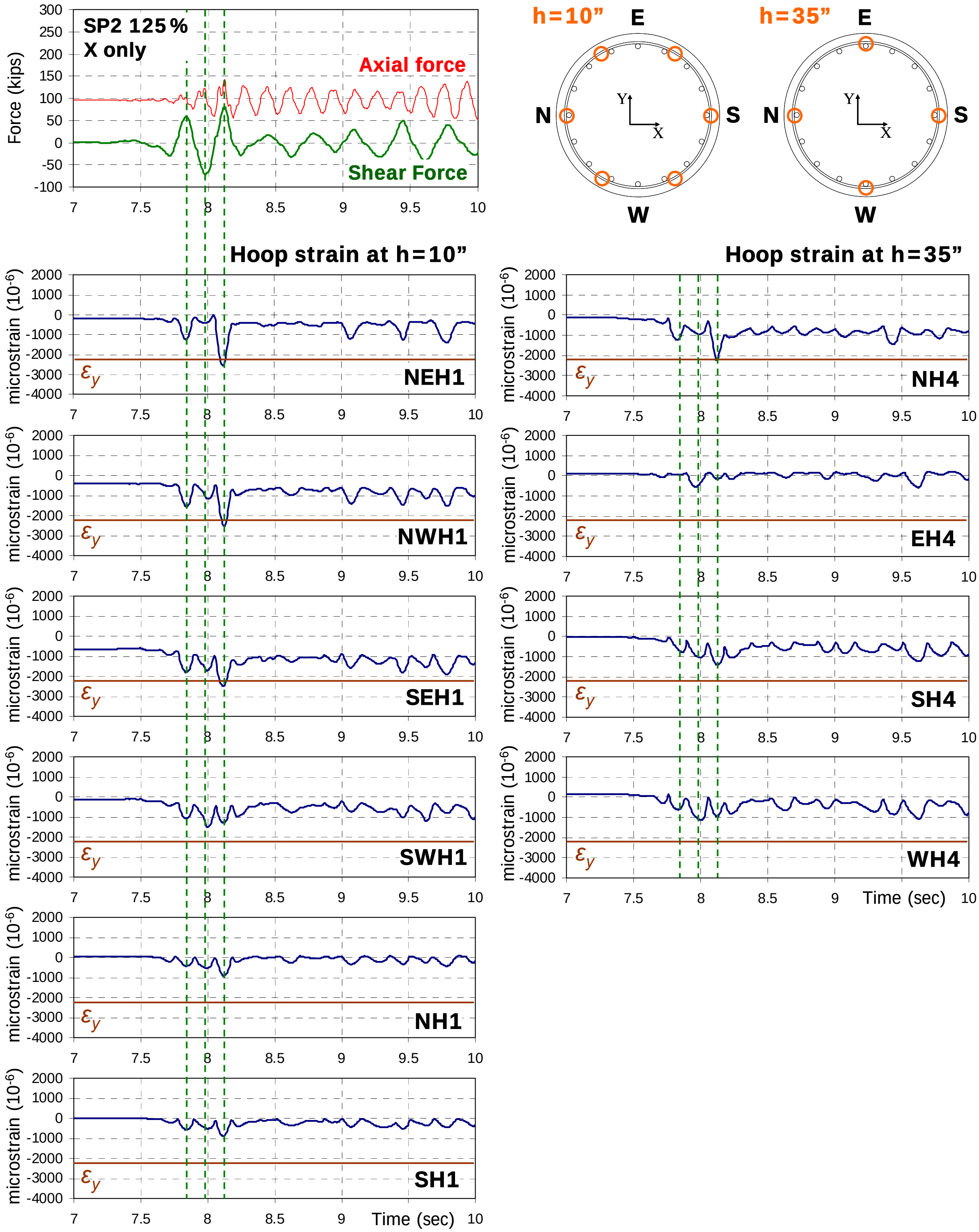

(b) SP2 125% X only

Fig. 5.18 Hoop strains at two cross-sections of SP2 in the 125%-scale runs (continued)

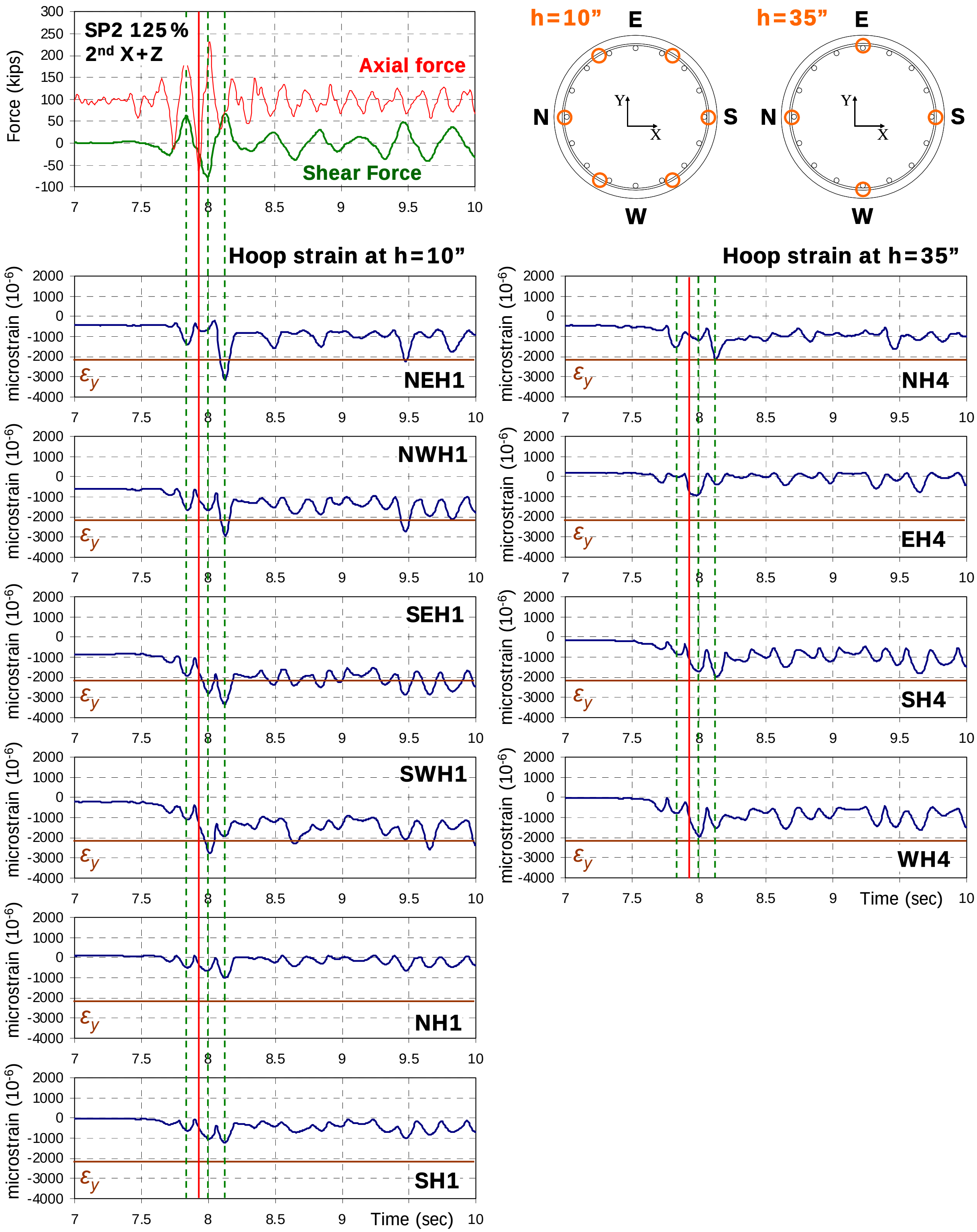

(c) SP2 125% 2nd X+Z

Fig. 5.18 Hoop strains at two cross-sections of SP2 in the 125%-scale runs (continued)

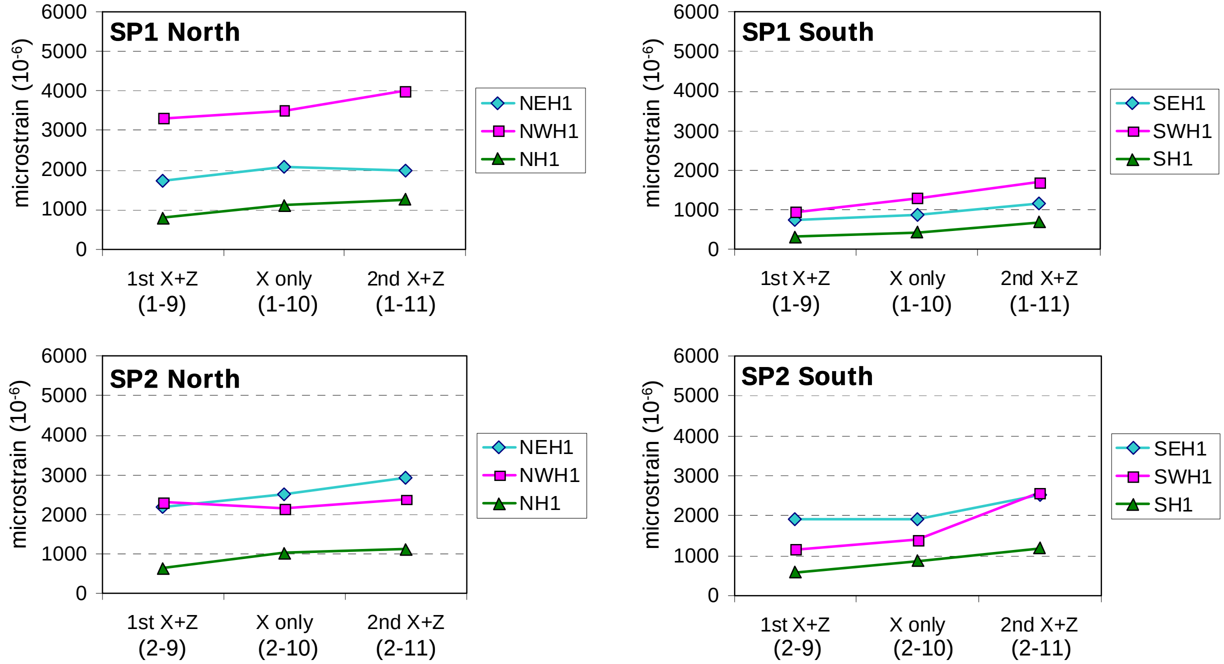

Fig. 5.19 Peak-to-peak amplitudes of hoop strain at h=10″ in the 125%-scale runs

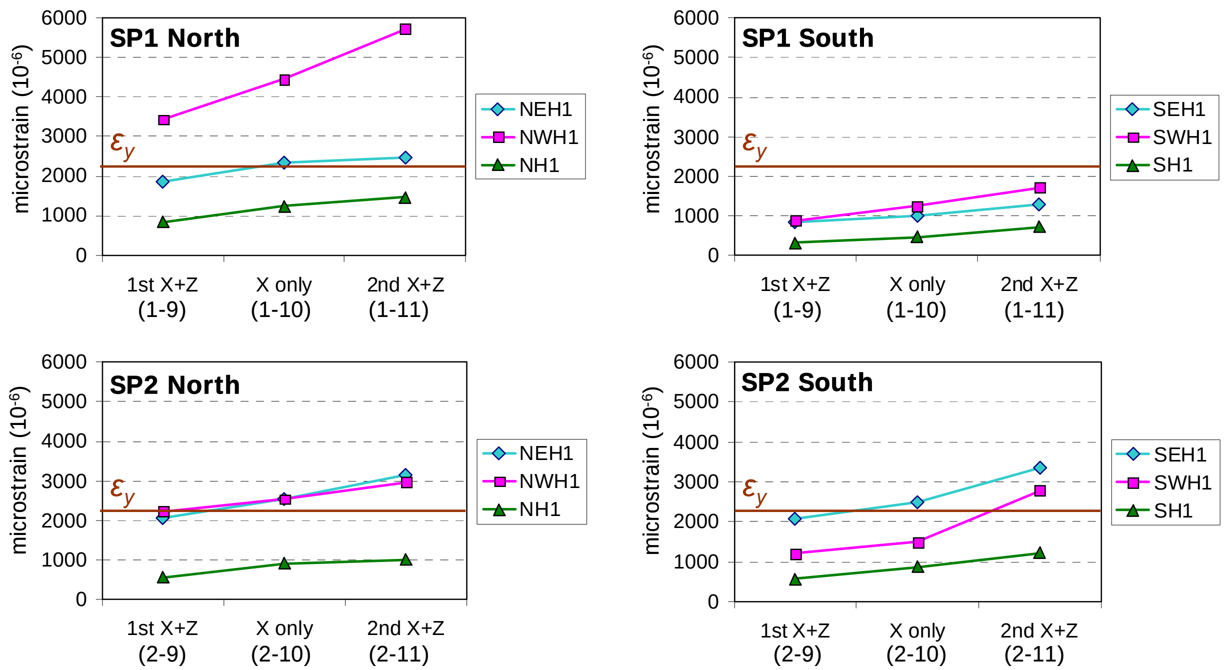

Fig. 5.20 Peak tensile strains of the hoop at h=10″ in the 125%-scale runs

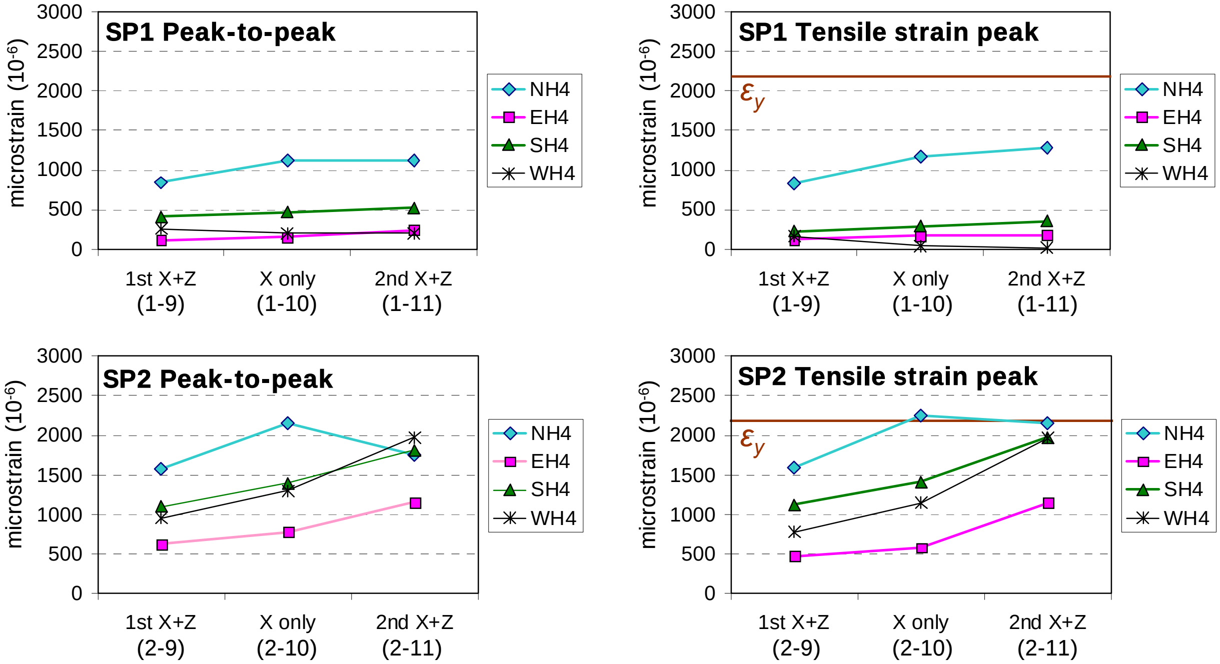

Fig. 5.21 Peak-to-peak amplitudes and peak tensile strains at h=35″ in the 125%-scale runs

5.6 Summary

The local responses were presented and discussed in this chapter. The curvature histories were calculated from the longitudinal strains on the north and south sides. The closest cross-sections to the base and the top were at h=10″ and 60″, respectively. The comparison suggests that the column was in double-curvature during the main excitation. The peak curvature at h=60″ was up to 5 times larger than that at h=10″. The initial tangent in moment-curvature relationship (M-φ) decreased as the intensity increased, especially at h=60″. On the contrary, the initial tangent at h=10″ did not change significantly.

The longitudinal strain response was measured at the 4 reinforcing bars on the north, south, east, and west sides. Total of 6 cross-sections were instrumented for the north and south direction, and 3 cross-sections were instrumented for the east and west direction. As observed in the curvature responses, double-curvature was confirmed by the longitudinal strain on the north and south sides, since the phase angle between the time histories of the strain measurements was shifted along the height during the main excitation. The largest longitudinal strain was detected near the top of the column. This was followed by the value near the base and finally the middle had the smallest strain value. The effect of the 125%-scale 'X only' motion was not remarkably different from that of the '1st X+Z' or '2nd X+Z' runs. For the east and west sides, an abrupt change in tensile strain due to axial tension was remarkable. It was more significant than that not he north and south sides. The axial force significantly affected the strain histories on the east and west, and one of the peaks in each history appeared at the tension peak. The maximum tensile strain under 125%-scale motion decreased when the vertical (Z) component was not applied. A phase angle shift was also detected on the east and west sides.

The transverse strains on the north and south were measured at 7 cross-sections. Moreover, two cross-sections at columns heights from the base of h=10″ and 35″ had 6 and 4 gages around the hoop, respectively. The maximum transverse strain increased with repeated runs for most gages. It is concluded that the effect of vertical excitation on transverse strains was not significant. Effect of shear was dominant on the strains at h=35″, whereas bending moment induced axial stresses and corresponding lateral stresses affected the strains more at h=10″.

Chapter 6

Development and Evaluation of Computational Models

6.1 Introduction

This chapter presents the computational models developed in order to predict the response of the tested bridge columns. In addition to the conventional modeling of RC columns, a new shear spring is developed and implemented in the utilized computational platform, OpenSees [28], in order to incorporate shear strength estimation based on ACI [2] or Caltrans SDC [13] equations. Various response quantities obtained from the different models are compared with the test results to evaluate the developed computational models.

6.2 Development of OpenSees Elements

OpenSees, a software framework for developing applications to simulate the performance of structural systems [28], provides a considerable number of material models. However, none of the existing models can be directly employed to model the variation of the shear capacity as a function of the axial force or the ductility as implied by the code equations such as ACI or Caltrans SDC . In this section, existing material models are discussed and a new material model for SDC or ACI-based shear springs is proposed.

6.2.1 Existing Material and Element Objects in OpenSees

6.2.1.1 Flexure-Shear Interaction Displacement-Based Beam-Column Element

Massone et al. [41] proposed and developed a beam-column element model that includes flexure and shear interaction in OpenSees. They modified the displacement-based element which already included linear curvature and constant axial strain distributions to include shear deformation. Element formulation (fiber element), sectional analysis and fiber modeling were modified.

Based on linear interpolation of the curvature and constant axial strain, a third strain component was included to account for shear flexibility. The fiber discretization leads no longer to just uniaxial behavior, but rather a bidirectional response by incorporating a membrane material model based on simple uniaxial stress-strain relationships for concrete and steel. Although the material models can be cyclic, the element model formulation has been implemented and verified initially for monotonic static analysis. Details of the formulation can be found in [41]. The compatibility equations to relate nodal displacements and internal strains are defined only in 2D. Therefore, 3D analysis is not possible using this element. In addition, only a specific geometric transformation called "LinearInt", which is based on the traditional geometric linear transformation, can be used.

The proposed modeling approach in [41] involves incorporating RC panel behavior into a macroscopic fiber-based model. Results obtained with the analytical model were compared to test results for a slender wall and four short wall specimens [41]. A reasonably good lateral load-displacement response prediction is obtained for the slender wall. The model underestimates the inelastic shear deformations experienced by the wall. However, shear yielding and coupled nonlinear shear-flexure behavior are successfully represented in the analysis results. Unfortunately, the above mentioned code equations (ACI or Caltrans SDC) cannot be represented with this element since it does not consider the effect of axial force in the shear strength estimation.

6.2.1.2 Limit State Uniaxial Material

Elwood and Moehle [42] developed Limit State material models based on the existing Hysteretic material in OpenSees. Each Limit State material model can be interpreted as a spring in series with the nonlinear beam-column element. It captures the additional deformations, either shear or axial, that takes place after detection of failure. The Limit State material uses a drift capacity model to determine the point of shear or axial failure for a column (Fig. 6.1) and subsequently controls the post-failure response of the element resulting in strength degradation. In this Limit State material, empirical drift capacity models at shear failure are proposed (Eqs. (6.1) and (6.2)), where the influence of axial load (P) on the drift ratio is taken into consideration only for columns with transverse reinforcement ratio, ρ_S.

$$\frac{\Delta_S}{L}=\frac{1}{30}+5\rho_S-\frac{4}{1000}\frac{\nu}{\sqrt{f_c^{'}}}\geq\frac{1}{100}\quad \text{(psi)}$$
$$\frac{\Delta_S}{L}=\frac{1}{30}+5\rho_S-\frac{1}{3010}\frac{\nu}{\sqrt{f_c^{'}}}\geq\frac{1}{100}\quad \text{(MPa)}\qquad \text{for } \rho_S>0.4\% \tag{6.1}$$

Incorporating the influence of axial load on the drift ratio,

$$\frac{\Delta_S}{L}=\frac{3}{100}+4\rho_S-\frac{1}{500}\frac{\nu}{\sqrt{f_c^{'}}}-\frac{1}{40}\frac{P}{A_g f_c^{'}}\geq\frac{1}{100}\quad \text{(psi)}$$
$$\frac{\Delta_S}{L}=\frac{3}{100}+4\rho_S-\frac{1}{6020}\frac{\nu}{\sqrt{f_c^{'}}}-\frac{1}{40}\frac{P}{A_g f_c^{'}}\geq\frac{1}{100}\quad \text{(MPa)}\qquad \text{for } \rho_S<0.4\% \tag{6.2}$$

where Δ_S/L is the drift ratio of the column at shear failure, f_c' is the concrete compressive strength, ν is the maximum experienced shear stress, P is the axial load and A_g is the gross cross-sectional area. It should be noted that P is positive for compression.

It should be noted that the equations presented above (Eqs. (6.1) and (6.2)) were proposed to be used in modeling shear-critical columns only, i.e. if the shear capacity defined by an appropriate shear strength model is exceeded by the shear demand calculated according to accepted analytical procedures. The axial failure model was also derived, and it determines how much axial load must be transferred to neighboring elements after a column shear failure and to aid in quantifying the ability of a structural system to resist collapse. However, results of this collapse analysis are beyond the scope of this research. Moreover, the data used for calibration of the shear and axial limit curve equations are derived from column experiments conducted mostly under compressive axial loads and none under tensile loads, which occurred in the test specimens. For an interested reader in the topic of progressive collapse analysis, refer to Talaat and Mosalam [43].

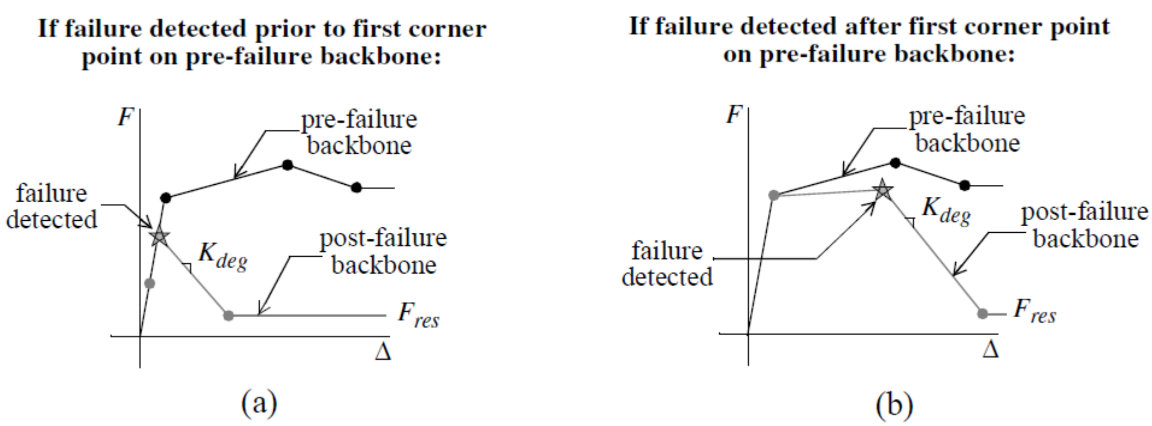

Fig. 6.1 Post-failure backbone curves using the Limit State uniaxial material [42]

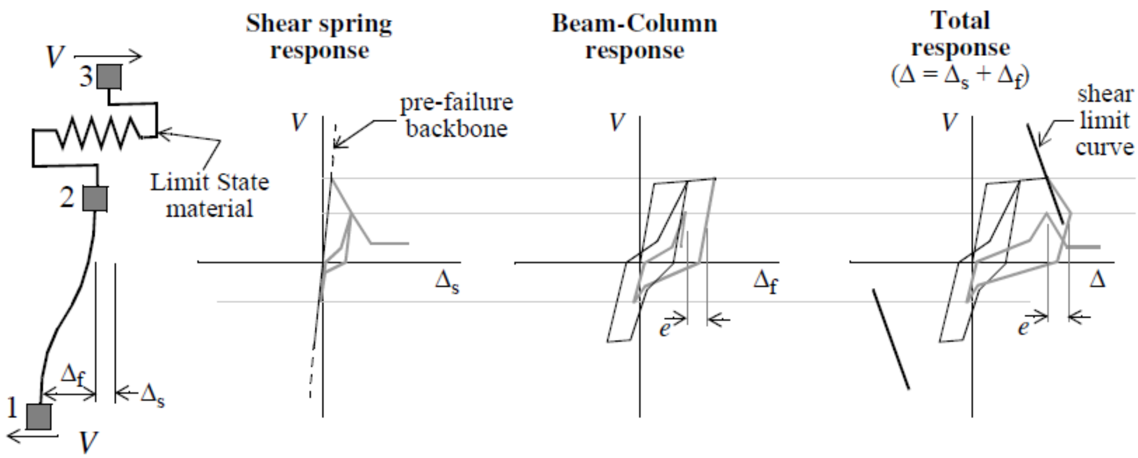

Fig. 6.2 Shear spring model in series using the Limit State uniaxial material [42]

The proposed drift capacity model defined with Eqs. (6.1) and (6.2) (and schematically demonstrated with Fig. 6.1 and Fig. 6.2 represents the shear failure modeling and estimation in an alternative approach compared to the code equations, in the sense of defining a drift ratio corresponding to the shear failure rather than defining the shear failure in terms of shear strength and reducing the shear strength as a function of ductility or axial tensile force. The use of this drift capacity model is not applicable in this study since Eq. (6.2) is derived from a database of tests with only axial compression and therefore does not represent the investigated axial tension effects caused by including the vertical acceleration component of the ground motion.

6.2.2 Proposed Shear Spring Model

Incorporation of ACI and SDC code equations for shear capacity into OpenSees is achieved by proposing a new material and implementing it into the source code of OpenSees. Although, a common and intended use of this new material is within a zero-length element connected to a beam-column element, it can be directly employed within a beam column element by aggregating the material into a section. The former approach is followed in the analyses conducted within this study. Considered cases are designated as 'ACI shear spring' and 'SDC shear spring' in order to represent ACI and SDC equations, respectively. The force-displacement relationship of the proposed spring material model is demonstrated in Fig. 3.1. This relationship is based on a bilinear envelope (for simplicity) which is defined by the initial stiffness ($K_{elastic}$), the yield force (V_y), and the hardening ratio for post-yield stiffness (r). Initial stiffness is the shear stiffness calculated as GA/L, where G is the shear modulus, A is shear area and L is the length of the column. Before yielding, the yield force is updated at each integration time step with Eqs. (1.1) to (1.6) for ACI shear spring using the axial force at that time step in Eqs. (1.5) and (1.6) and with Eqs (1.32) to (1.38) for Caltrans SDC shear spring using the displacement ductility and axial force at that time step in Eqs. (1.34) to (1.37). The displacement ductility is calculated as the displacement at a specified node (the node at the top of the column in the analyses presented here) normalized by the yield displacement, both of which (the node number and the yield displacement) are input parameters to the new material model in OpenSees.

At the time step where the demand reaches the capacity, yielding takes place and the force-displacement relationship follows the post-yield behavior. The yield force is not updated and kept constant afterwards unless the column is subjected to any value of axial tension for the case of Caltrans SDC spring and a predetermined value of tension (specified as an input parameter) for the case of ACI spring. The yield force is kept constant after this final modification. The basis of this second modification is the significant change of the yield force as a result of axial tension. For the case of ACI spring, if the predetermined tension value takes place before any yielding, the yield force is not updated after reaching this predefined tension value. This option permits the investigation of the yielding situations in the close vicinity of the maximum axial tension. For example, if the maximum axial tension, which produces significant reduction in shear strength, takes place before a shear peak with a small time interval in between, and the demand do not reach the capacity, a potential yielding may not be captured unless the yield force is kept constant in this small interval. The yielding would take place if the axial and shear peaks were closer. In addition, as mentioned in the previous chapter, it was observed that the shear strength degradation was due to the existence of previous tensile peaks during the tests. Such an option was not required for the SDC shear spring since the shear force is explicitly kept constant in the SDC equation in the mentioned small interval due to the fact that the contribution of concrete to the shear strength is zero under any value of tension.

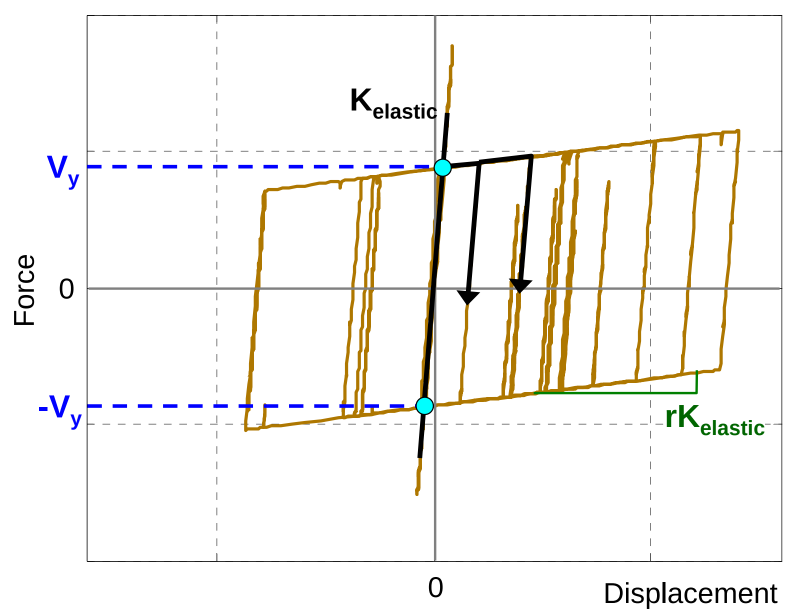

Fig. 6.3 Hysteresis of the proposed shear spring material model

6.3 Computational Modeling

In this section, the analytical modeling of the test specimens is discussed. First, the structural model including a column, a footing, mass, and springs for the load cells is discussed and the force-based beam-column elements used in the modeling, namely 'Beam With Hinges' and 'Nonlinear Beam Column' elements are described. Second, the material models for concrete and reinforcing bars are presented. Third, the fiber section modeling to capture the nonlinear behavior is presented. Finally, the obtained computational results are compared with the test results in the following section.

6.3.1 Modeling of the Single Reinforced Concrete Column

The specimen consists of a footing, a column, and a top block. Steel beams and mass blocks are placed on top of the test specimen and four load cells connect the specimen to the table below the footing. These features are expected to affect the dynamic and nonlinear responses of the test column. Hence, the whole setup above the table is modeled in this computational investigation.

6.3.1.1 Models Using "Beam With Hinges" Elements: A-1 and A-2

A 'Beam With Hinges' (BWH) element is a commonly used force-based element to examine the nonlinear response of frame structures. Fig. 6.4 shows the composition of a BWH element. It has localized plasticity at the ends, i.e. hinges, and the remaining part is kept linear elastic. The length of each hinge is defined by the user.

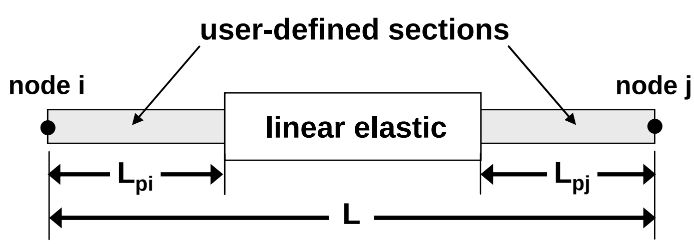

Fig. 6.4 "Beam With Hinges" element [28]

To reduce computational cost, a modified Gauss-Radau integration [44] is implemented in 'Beam With Hinges 1' instead of the conventional integration method which uses two integration points per hinge. Scott and Fenves [44] developed the modified Gauss-Radau integration to evaluate the integration over a length of $4L_p$ instead of L_p. As a result, the integration points are at 0, $8L_{pi}/3$, $L-8L_{pj}/3$, and L as shown in Fig. 6.5. Nonlinear behavior is confined to the integration points at the ends and the largest bending moment at the ends are captured.

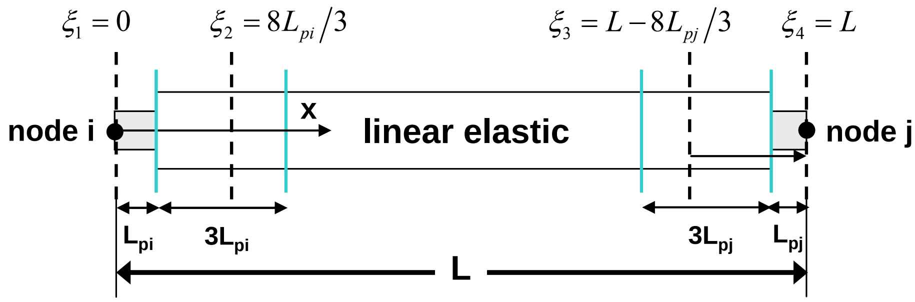

Fig. 6.5 Modified Gauss-Radau integration [28]

Since the 2nd and 3rd sections are in the linear elastic part, they are not applicable to record strain and stress histories which are necessary for comparison to the test data. A 'Beam With Hinges 2' element is an alternative, because it adopts the original Gauss-Radau integration with integration points at 0, $2L_{pi}/3$, $L-2L_{pj}/3$, and L, where all four sections are in the plastic hinge zones. Therefore, instead of 'Beam With Hinges 1', a 'Beam With Hinges 2' element can be utilized for more refined local responses.

Fig. 6.6(a) presents the test specimen models using BWH elements to represent the column. Two rigid elements at the top and the base are used for the top block and the footing, respectively. The nodal mass above the top rigid element has three translational and three rotational degrees of freedom, associated with the mass and mass moment of inertia of the mass assembly consisting of the top block, steel beams, lead blocks, and additional concrete blocks. A rotational spring is added below the rigid element at the base, because the specimen was placed on four load cells which were connected to the shaking table and they are not perfectly rigid. As shown in Fig. 6.6(a), the difference between Models A-1 and A-2 is the existence of a shear spring in Model A-2. Comparison of the results from these two models leads to the investigation of the effect of the code-based shear spring on the response. ACI and SDC code equations are implemented in the spring as discussed in Section 6.2.2 and they are designated as Model A-2-ACI and Model A-2-SDC, respectively. It should be noted that the hardening ratio in the shear springs is set as $r = 0.01$.

The hinge length is defined by Caltrans SDC 7.6.2. It is based on Paulay and Priestly [45] and specifies the plastic hinge length of RC columns as follows:

$$L_p = \begin{cases} 0.08L + 0.15 f_{ye} d_{bl} \geq 0.3 f_{ye} d_{bl} & (\text{in, ksi}) \\ 0.08L + 0.022 f_{ye} d_{bl} \geq 0.044 f_{ye} d_{bl} & (\text{mm, MPa}) \end{cases} \tag{6.3}$$

where f_{ye} and d_{bl} are respectively the expected yield stress and the nominal bar diameter of the column longitudinal reinforcing bars. Since the column with diameter D was in double-curvature and had damage due to flexure at the base and the top, the same hinge length was assumed at both ends, i.e. $L_{pi} = L_{pj} = L_p$. The calculated L_p based on SDC is 14.5″ (368 mm) which corresponds to 0.725D, where D is the diameter of the column.

6.3.1.2 Models Using "Nonlinear Beam Column" Elements: B-1 and B-2

Unlike BWH elements, 'Nonlinear Beam Column' (NLBC) elements in OpenSees consider the spread of plasticity along the element. The user should define the number of integration points. Fig. 6.6(b) shows the specimen model with four NLBC elements. Elements at the ends are 15″ in length and 7 integration points are employed in each element. Elements in the middle are 20″ in length and 5 integration points are used. Other components of the NLBC model are identical to those of the BWH Models A. Similar to Models A, the shear spring makes a distinction between Models B-1 and B-2. ACI and SDC shear springs are included and models are designated as Model B-2-ACI and Model B-2-SDC, respectively. Similar to A-2-ACI and A-2-SDC, the hardening ratio is specified as $r = 0.01$ in the shear springs.

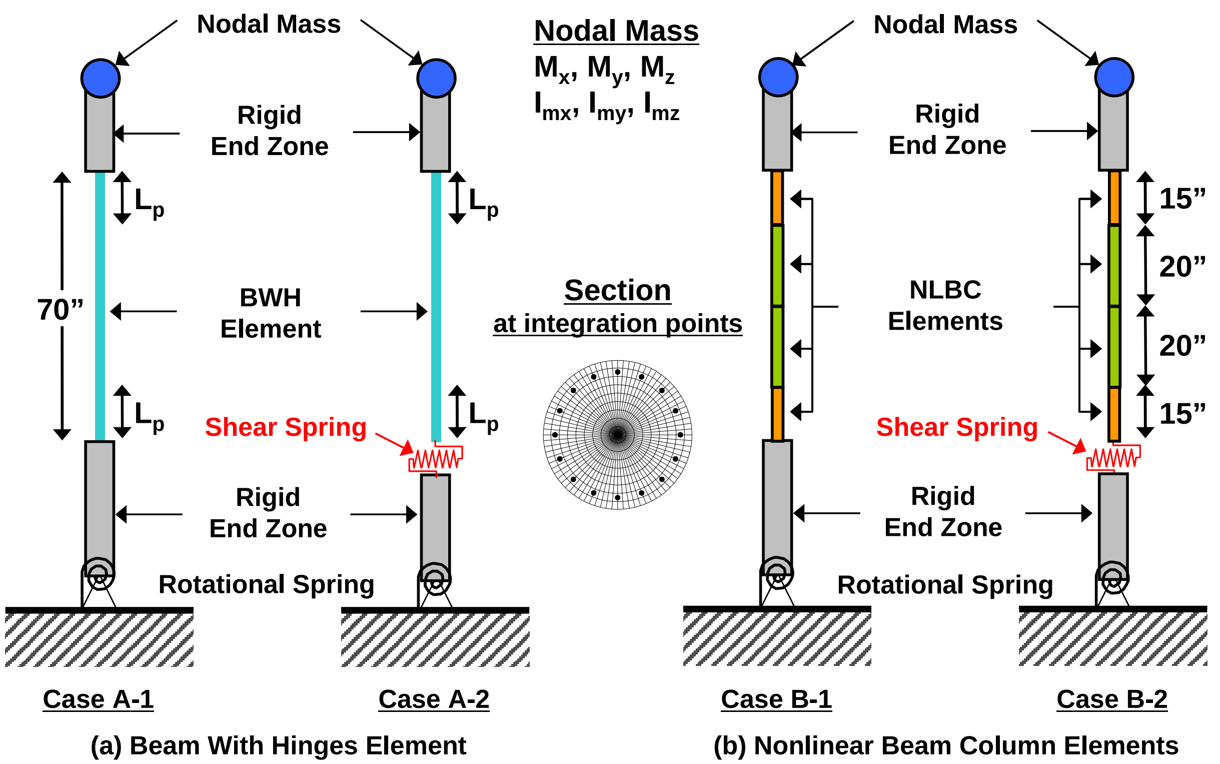

Fig. 6.6 Specimen modeling

6.3.2 Material Modeling

6.3.2.1 Concrete Modeling

For the core and cover concrete, 'Concrete02' model is utilized. It is a uniaxial concrete material model with tensile strength and linear tension softening. The parameters which define this model are as follows:

- \$fpc: compressive strength
- \$epsc0: strain at compressive strength

- $fpcu: crushing strength
- $epsu: strain at crushing strength
- $ft: tensile strength
- $Ets: absolute value of tension softening stiffness
- $lambda: ratio between unloading slope at $epsu and initial slope. The initial slope for this model is 2$fpc/$epsc0.

Fig. 6.7 presents the stress-strain relationship of 'Concrete02' material, where negative and positive stresses (and strains) represent compression and tension, respectively. Table 3.1 summarizes the parameters utilized for this concrete model in this study. Cover concrete properties are based on the material tests presented in Chapter 3. For core concrete of Model A, compressive strength and strain properties are calculated based on Mander's model [29] using the confinement provided by the hoops which have 2″(SP1) or 3″(SP2) spacing. For core concrete of Model B which has NLBC elements, compressive strength is the same as that of Model A. However, the strain corresponding to the compressive strength ($epsc0) is modified to match the initial stiffness calculated as 2$fpc/$epsc0 to the tangent modulus of elasticity obtained from the material tests. This modification was necessary for Model B since the stiffness of the column is obtained by integration of the response of the sections along the column height whereas this is not significant for Model A where the initial stiffness of the column is mostly dominated by the middle elastic part where the elastic modulus is specified separately.

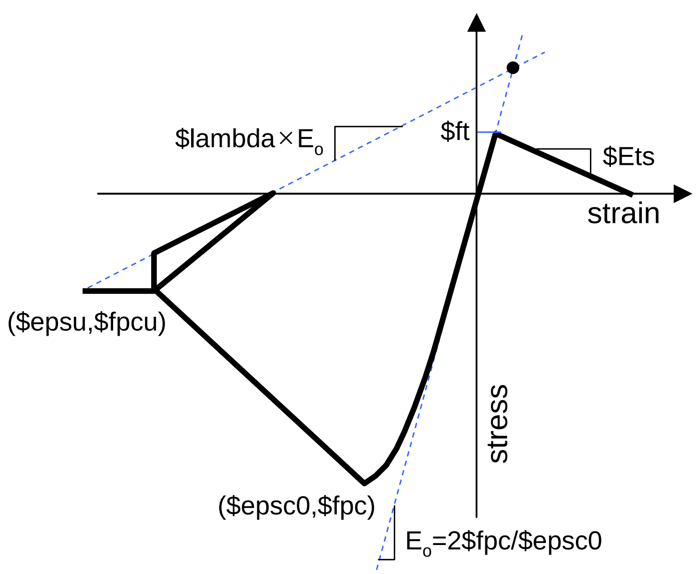

Fig. 6.7 Concrete02 model: material parameters [28]

Table 6.1 Concrete model parameters for computational models

Parameter	Units	Cover concrete	Core concrete	
			Hoops @ 2″	Hoops @ 3″
\$fpc	[ksi] (MPa)	-4.1 (-28.0)	-5.12 (-35.3)	-4.77 (-32.9)
\$epsc0 (A)	N/A	-0.003	-0.0069	-0.0056
\$epsc0 (B)	N/A	-0.003	-0.0085	-0.0094
\$fpcu	[ksi] (MPa)	-0.41 (-2.80)	-2.28 (-15.7)	-0.0 (-0.0)
\$epsu	N/A	-0.006	-0.0126	-0.0097
\$ft	[ksi] (MPa)	0.41 (2.80)		
\$lambda	N/A	0.8		

6.3.2.2 Steel Modeling

For reinforcing bars, ‘Steel02’ model is used which is a uniaxial Giuffre-Menegotto-Pinto [46] steel material with isotropic strain hardening. The model accounts for the Bauschinger effect, which contributes to the gradual stiffness degradation of the reinforced concrete members under cyclic response. This model has an isotropic hardening option for tension and compression portions of the hysteresis. Despite its simplicity, this bilinear model predicts the basic material responses accurately over most of the strain range, but it does not account for the initial yield plateau of the reinforcing steel or the degradation of the steel strength. For this model, the following parameters need to be defined:

- \$F$_y$: yield strength
- \$E: initial elastic tangent modulus
- \$b: strain-hardening ratio (ratio between post-yield tangent and initial elastic tangent)
- \$R0, \$cR1, \$cR2: parameters that control the transition from elastic to plastic branches
- \$a1, \$a2, \$a3, \$a4: isotropic hardening parameters

Table 6.2 summarizes the parameters utilized for this steel model in this study. Longitudinal and transverse reinforcing steel bars have properties specified in columns (a) and (b) of Table 6.2, respectively. Fig. 6.8 presents the stress-strain relationship of ‘Steel02’ material. It should be noted that E_p is defined by multiplying two parameters, \$E and \$b. Based on the properties in Table 6.2, E_p for longitudinal and transverse reinforcement are 455.42 ksi (3140 MPa) and 580.15 ksi (4000 MPa), respectively.

Table 6.2 Steel model parameters for computational models

Parameter	Units	(a) Longitudinal	(b) Transverse
\$F$_y$	[ksi] (MPa)	77.5 (534.3)	63.0 (435.3)
\$E	[ksi] (MPa)	29007.5 (200000)	
\$b	N/A	0.0157	0.0200
\$R0, \$cR1, \$cR2	N/A	Default	
\$a1, \$a2, \$a3, \$a4	N/A	Default (no isotropic hardening)	

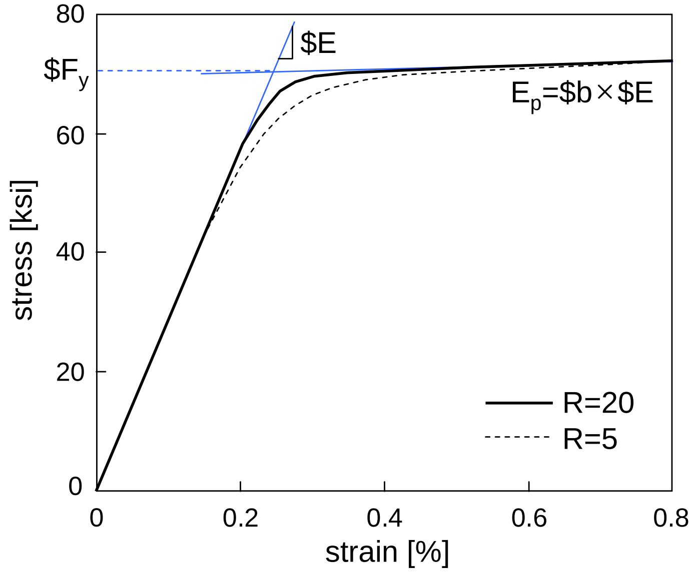

Fig. 6.8 Steel02 model: material parameters [28]

6.3.3 Fiber Section Modeling

Fiber section modeling, which consists of subdividing a cross-section into discretized fibers with a finite area and uniaxial force-deformation relationship of the material associated with the fiber, is capable of representing the flexural behavior and its interaction with the axial force in beam-column elements. Therefore, this type of modeling is widely used in structural analysis applications. There are various commands in OpenSees to divide a section into regular fibers. Amongst these commands, 'Circular Patch' command is useful to define the fibers of a circular cross-section. For the sections of the analyzed columns, the core which is confined by hoops consists of 80 subdivisions in the circumferential direction and 80 subdivisions in the radial direction, as shown in Fig. 6.9. The cover is similarly divided by the same command has 80 and 10 subdivisions in the circumferential and radial directions, respectively. Moreover, 'Circular Layer' command is utilized to construct a circular layer of reinforcing bars. 16 longitudinal bars are uniformly distributed along the circumference for the considered cross-section as shown in Fig. 6.9.

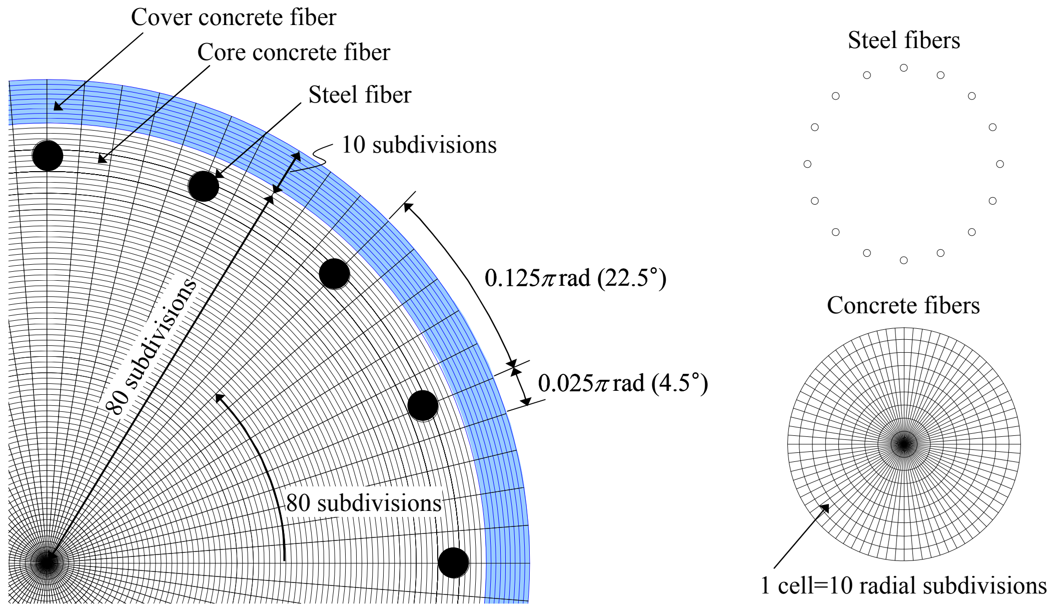

Fig. 6.9 Fiber section modeling

6.3.4 Modeling of Damping

The damping matrix cannot be determined directly from the structural dimensions and the damping properties of the materials. In most of the structural engineering applications, classical damping is utilized which is an adequate idealization if similar damping mechanisms are distributed throughout the structure. The Rayleigh damping matrix, $[C]$, one of the common types of classical damping, is computed as a linear combination of the mass and stiffness matrices, $[M]$ and $[K]$, respectively. It is considered as a practical method because it provides a banded damping matrix even for large systems.

For the analysis of the tested columns, mass-and-tangential stiffness proportional Rayleigh damping is used with constants calculated based on the 1st mode (translation in X) frequency (ω_i) of the computational model and the vertical (translation in Z) frequency of the specimen ($\omega_{vertical}$). The reason of not choosing vertical frequency of the computational model is discussed in Section 6.3.5. As a result, the coefficients for Rayleigh damping (assuming a damping ratio ζ) are calculated as follows,

$$a_0 = \zeta \frac{2\omega_i \omega_{vertical}}{\omega_i + \omega_{vertical}} \quad a_1 = \zeta \frac{2}{\omega_i + \omega_{vertical}} \qquad \text{where } i = 1 \tag{6.4}$$

$$[C] = a_0 [M] + a_1 [K] \tag{6.5}$$

Damping in RC structures, which does not include the hysteretic damping due to yielding and damage, varies based on the level of cracking and some other internal mechanisms of the concrete material. Accordingly, the conducted tests are classified into three groups (Table 6.3), where each group is assigned a different damping ratio (ζ) based on the measured data. The damping ratio for the dynamic tests is calculated from the FFT of the horizontal acceleration measured on the top of the mass blocks using the half-power bandwidth method [40]. Two scale levels of tests are used for this purpose as shown in Table 6.3. On the other hand, the damping ratio in the free vibration tests is estimated from the absolute lateral displacement history in the X-direction. Since the calculated damping ratios of SP1 and SP2 are similar, same damping values are used in analysis of both of the specimens as listed in Table 6.3.

Table 6.3 Damping ratio

Test	Damping ratio, ζ [%]
Free Vibration	2.0
5%-scale or 12.5%-scale	2.5
25%-scale or above	4.0

6.3.5 Model Adjustment due to Shaking Table Effect

As mentioned in Section 4.2.3, the shaking table is not perfectly rigid. Its flexibility affects the response of the test specimen, especially in the vertical direction. Given that the vertical natural period of the column is much shorter than that of the shaking table and the vertical period of the shaking table is dominant in the whole system (combined test specimen and shaking table as one system), this situation is similar to the case of a stiff structure supported on a soft foundation. If the shaking table effect is ignored and the vertical acceleration recorded on the shaking table is directly used as the input to the analytical model, acceleration history with higher frequencies is obtained at the top of the column. However, these high frequencies are not present in the test data (Fig. 6.10) because of the dominance of the shaking table period in the vertical response of the system.

In order to demonstrate the shaking table effect on the vertical response, elastic dynamic analysis is conducted for the 2 DOF system presented in Fig. 6.11(b) where $\mathbf{u_1}$ and $\mathbf{u_2}$ represent the vertical displacements of the shaking table and the test specimen, respectively, and $\ddot{\mathbf{u}}_\mathbf{g}$ represents the input target acceleration denoted as 'target' in Chapter 4. Since the effective mass and stiffness of the shaking table ($\mathbf{m_t}$ and $\mathbf{k_t}$ in Fig. 6.11(b)) are not known accurately, they are varied as input parameters to match the vertical periods identified from the FFT plots of the measured acceleration. Based on the results of the analysis conducted with the ground motion in Fig. 4.1, it is observed from Fig. 6.11 that the acceleration histories at the shaking table level and at the top of the column are very similar and this is in agreement with the test data. It can be stated that the flexibility of the shaking table not only results in the modification of the target accelerations (i.e. difference between input to the shaking table and its output in terms of accelerations) but also governs the test specimen response in the vertical Z-direction.

Based on the findings discussed in the previous paragraph, it can be concluded that not only the test specimen but the whole system including the shaking table should be modeled and the target input should be used as the input to the analytical model instead of the measured accelerations on the shaking table. However, this approach is not feasible since the shaking table effective stiffness varies from test to test and even within a test. Considering that one of the main goals of the investigation in this study is the evaluation of the effect of axial tension (caused by the vertical acceleration of the ground shaking) on the shear capacity and the development of the corresponding analytical modeling, imposing the measured forces directly in the analytical model agrees more with these goals rather than modeling a complex table response with several sources of uncertainties and gross assumptions. Therefore, the recorded axial force history (from the load cells installed underneath the test specimen footing and above the shaking table) is directly applied to the column as an external force excitation in the conducted analyses. Therefore, in order to equate the restoring forces to the external forces, model mass in the vertical direction is set to almost zero, which corresponds to 2.5×10^{-4} of the original mass.

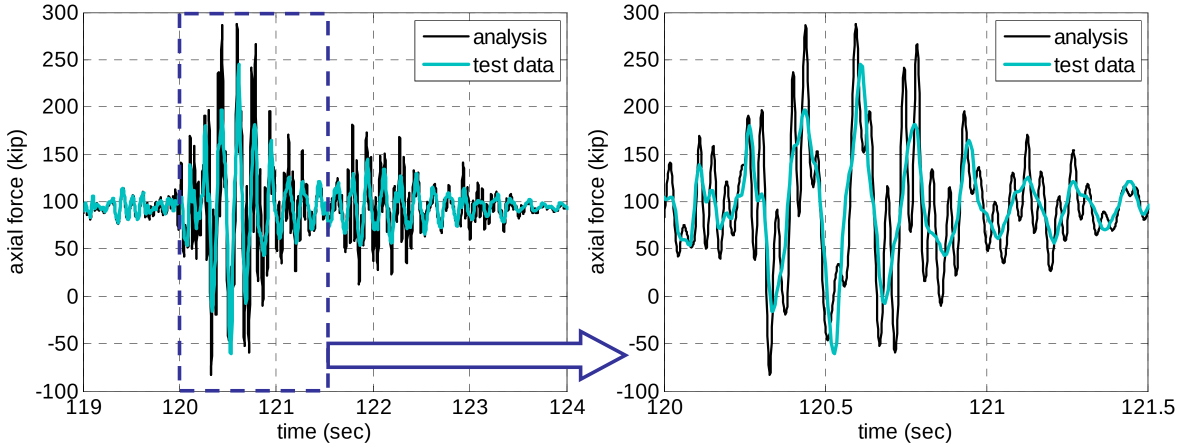

(a) Axial force at the base of SP1 125%-scale '1st X+Z'

(b) Zoomed in (a) for frequency comparison

Fig. 6.10 Axial force difference between the analytical result and test data measured at the base of SP1 under the 125%-scale '1st X+Z' motion

6.3.6 Input Acceleration

Average of the accelerations recorded near the four load cells on the base plate underneath the test specimen is used as an input motion in the X and Y directions. The recorded accelerations are low-pass filtered with a cutoff frequency of 40 Hz. In the vertical direction, the recorded axial force time history filtered with a cutoff frequency of 30 Hz is used as external force excitation as discussed above. In order to be able to capture the correct accumulation of nonlinearity, such as the residual displacements, input for the different scale tests are combined into a single long acceleration record.

6.3.7 Other Parameters for Dynamic Analysis

Damping ratio of 4% as explained in a previous section and as specified in Table 6.3 is used in these analyses. Considering that the test specimen experienced some undetermined shrinkage cracking even before any shaking, 63.8% of E_c obtained from the cylinder tests is used to match the natural periods in the 50%-scale test, which were 0.63 sec for SP1 and 0.65 sec for SP2. Newmark integration with integration parameters γ = 0.5 and β = 0.25 is used for time integration using a time step of 0.0012 sec, which corresponds to only 4% of the vertical period of SP1 and SP2, which was determined as 0.03 sec as previously discussed. This small time step is chosen for accuracy. Also, Newton-Raphson method with line search is used as the nonlinear solution algorithm.

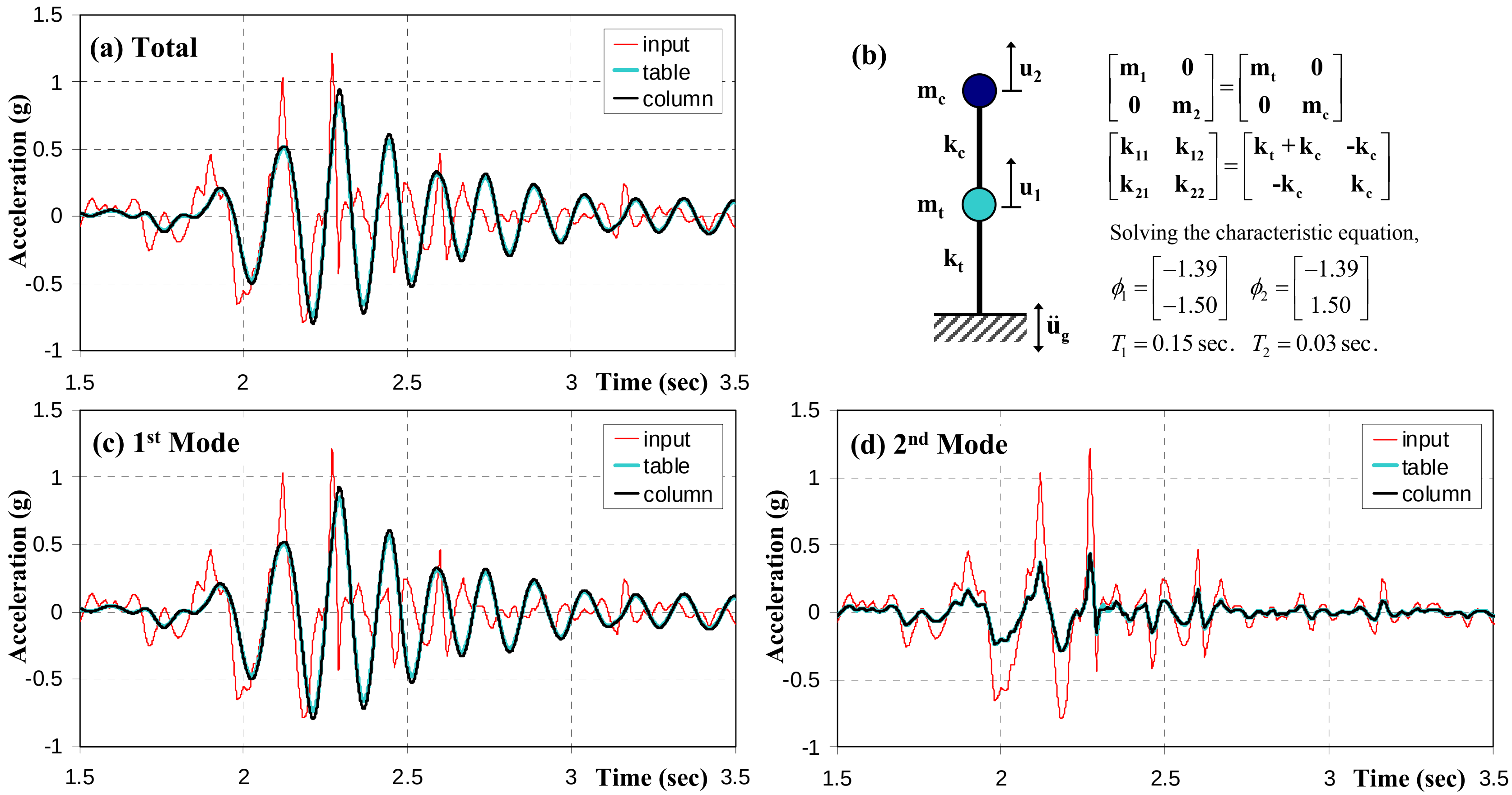

Fig. 6.11 2-DOF analysis for the shaking table and test specimen responses

6.4 Comparison of Computational and Experimental Results

6.4.1 Stiffness and Free Vibration Tests

The stiffness and free vibration test results are simulated with sufficient accuracy by the analytical model described above. For this purpose, the stiffness of each model is first matched to that obtained in the stiffness test. Thereafter, the lateral displacement history from the analysis is compared to the test results. Fig. 6.12 shows the lateral displacement of both specimens from the free vibration tests. Absolute displacement histories are compared since the analytical model involves a rotational spring at the base representing the shaking table flexibility.

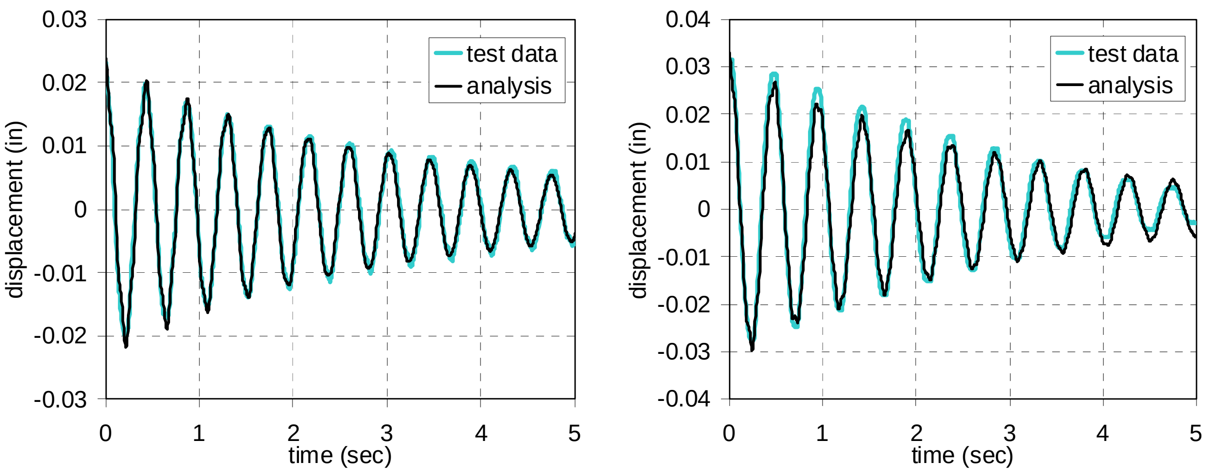

(a) SP1: Absolute displacement 1st trial **(b) SP2: Absolute displacement 2nd trial**

Fig. 6.12 Comparison of the free vibration test data and the analysis results using model A-1

6.4.2 Global Responses

As discussed in Chapter 4, the specimens were not significantly damaged in the tests up to 25%-scale intensity level. In addition, the shear spring affects the response only for high-intensity level motions. Therefore, the behavior of the tested specimen is compared with the analytical investigation results for the tests with scales greater than 50% to examine the effect of vertical component of the ground motion.

The global responses of Models A-1, A-2, B-1, and B-2 are compared. As mentioned, 'A' and 'B' designate the use of BWH and NLBC elements, respectively and 1 and 2 represent the cases with and without the shear spring, respectively. Two springs, i.e. ACI and SDC springs are utilized in Models A-2 and B-2. They are designated as A-2-ACI or B-2-ACI and A-2-SDC or B-2-SDC, respectively.

6.4.2.1 Shear Force

Before investigating the computational results, the code-based shear strength estimation is discussed. Fig. 6.13 and Fig. 6.14 compare the shear strength estimation of ACI and SDC equations with the absolute value of the shear force histories obtained from the test results. As already mentioned in Chapter 1, both ACI and SDC equations have terms for the effect of the axial force on the shear capacity. It should be noted that the axial forces and displacements gathered from the test results are used in these shear strength estimations. The two code equations provide similar estimations under compression, but they differ under tension, which is clearly shown in Fig. 6.13(b) for 95%-scale run applied to specimen SP2. Up to 70%-scale, SDC and ACI have similar shear capacity estimation and the shear force is less than the shear capacity. In the 95%-scale run of SP2, the first sudden decrease in shear strength takes place using the SDC estimation due to a small axial tension of 1.4 kips (6.2 kN). SDC and ACI estimations are considerably different under the 125%-scale motions as shown in Fig. 6.14. Since there is significant axial tension in the 1st and 3rd runs (Runs 1-9 and 1-11 for SP1 and Runs 2-9 and 2-11 for SP2), SDC estimation reduces down to V_s (shear strength provided by the hoops) only, i.e. 43.8 kips (194.8 kN) for SP1 and 27.5 kips (122.3 kN) for SP2, which correspond to 57.3% and 66.8% reduction compared to the initial full shear capacity, i.e. V_s+V_c where V_c is the shear strength provided by the concrete with no axial tension. Moreover, there are noticeable decreases in SDC estimation due to large ductility. As a result, SDC equation provides a more conservative estimation than ACI equation due to tension or large ductility. Accordingly, the shear demands of SP1 and SP2 exceed the shear capacity estimated by SDC in all the 125%-scale tests, consistent with the observed shear damage described in Chapter 4. However, although SDC equation predicts the presence of shear damage, it does so in a rather conservative manner as it can be observed from the comparison of the shear strength equation prediction of SDC with the shear force. The SDC shear capacity prediction is sometimes smaller than half of the shear force, as in runs 1-11 and 2-11. Noting that the shear forces are obtained from the test data, they should be bounded by the shear capacity values, signifying the underestimation of the shear strength by the SDC equation.

Similar observations to those mentioned in the previous paragraph can be made by the examination of the computational results. In Fig. 6.15 and Fig. 6.16, the shear force responses obtained from Models A-1, A-2-ACI, A-2-SDC, B-1, B-2-ACI, and B-2-SDC are compared to those from the SP1 tests. Fig. 6.15 presents the shear force histories from Models A-1, B-1, and the test data of SP1 subjected to 50%, 70%, and 95%-scale excitations. Since the shear springs do not yield at these levels, Models A-2 and B-2 with the shear springs produce very similar results to models A-1 and B-1, and therefore, they are not presented. It should be noted that small differences are expected because the additional flexibility introduced by the finite stiffness of the shear spring can cause slight changes in the dynamic response. It can be observed that there is a close resemblance in shear force responses obtained from models A-1 and B-1 and these responses are comparable to the shear force history from the test data. An exception is the presence of high frequency, which is more noticeable in the analysis results. In particular, the high frequency content is notable in the response of A-1 under the 50%-scale motion. It seems that the free vibtation occurs between 12.5 and 14.5 sec.

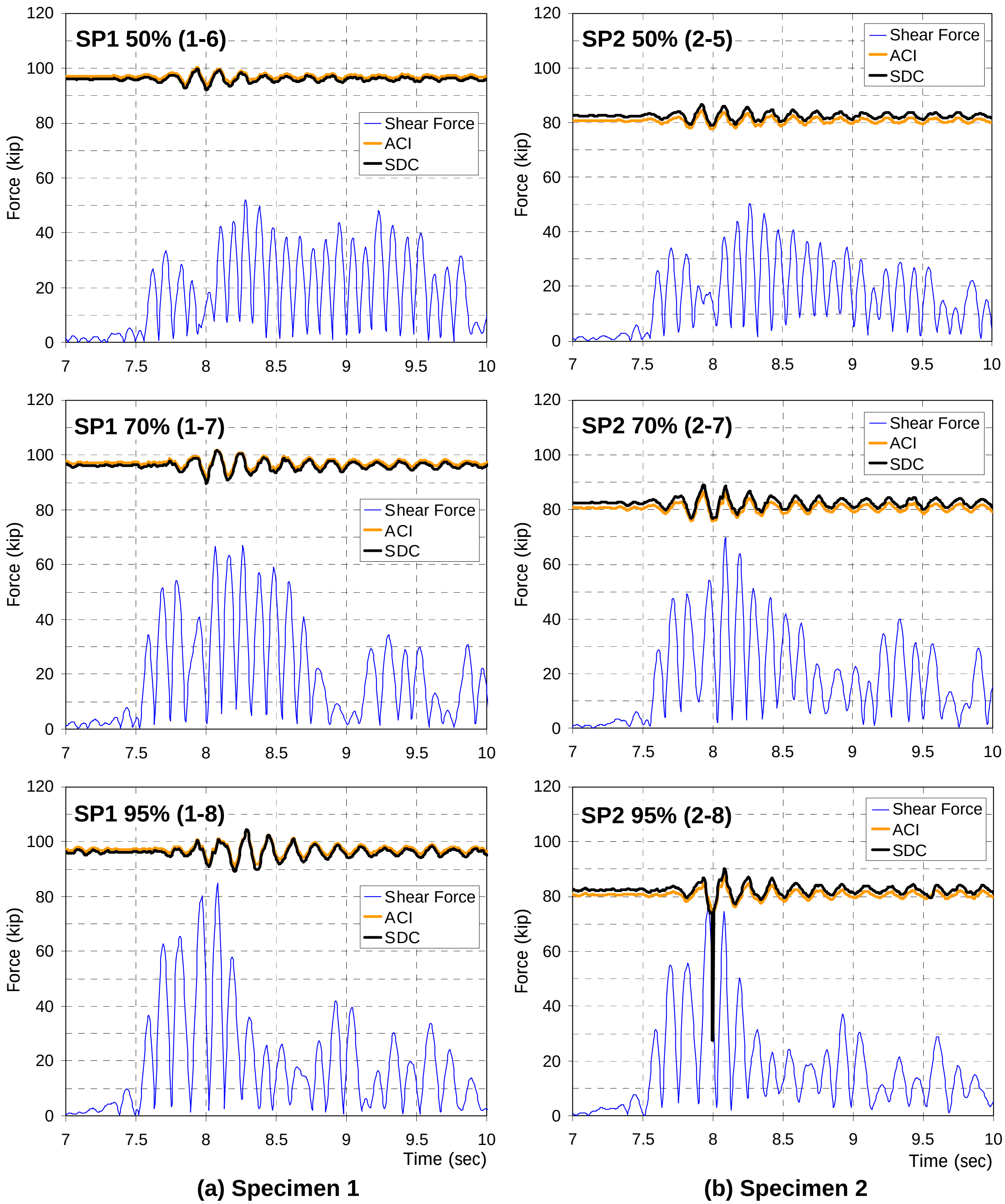

Fig. 6.13 Comparison of shear force and shear strength estimation of ACI and SDC based on the data from 50%, 70%, and 95%-scale runs

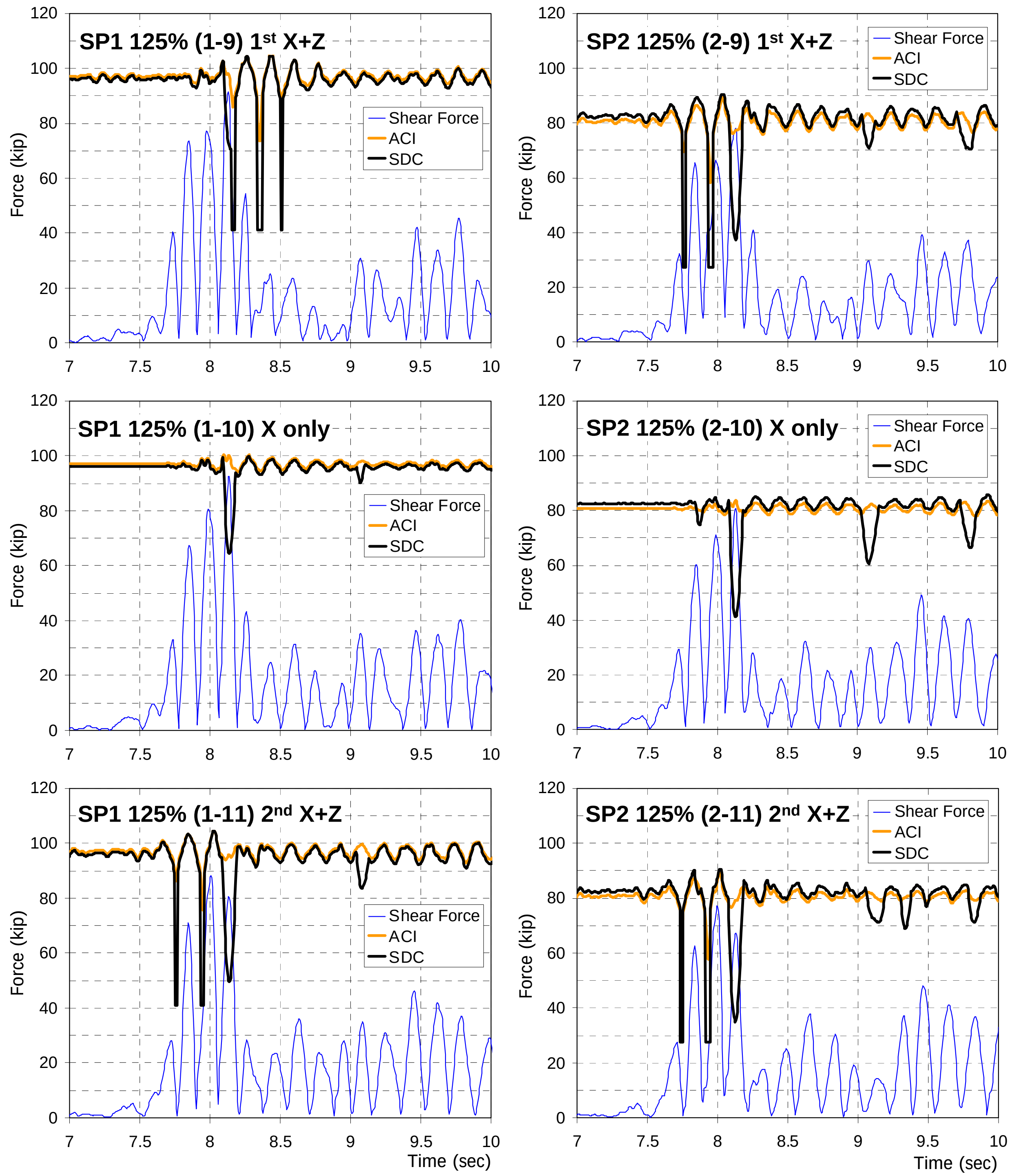

(a) Specimen 1 **(b) Specimen 2**

Fig. 6.14 Comparison of shear force and shear strength estimation of ACI and SDC based on the data from 125%-scale runs

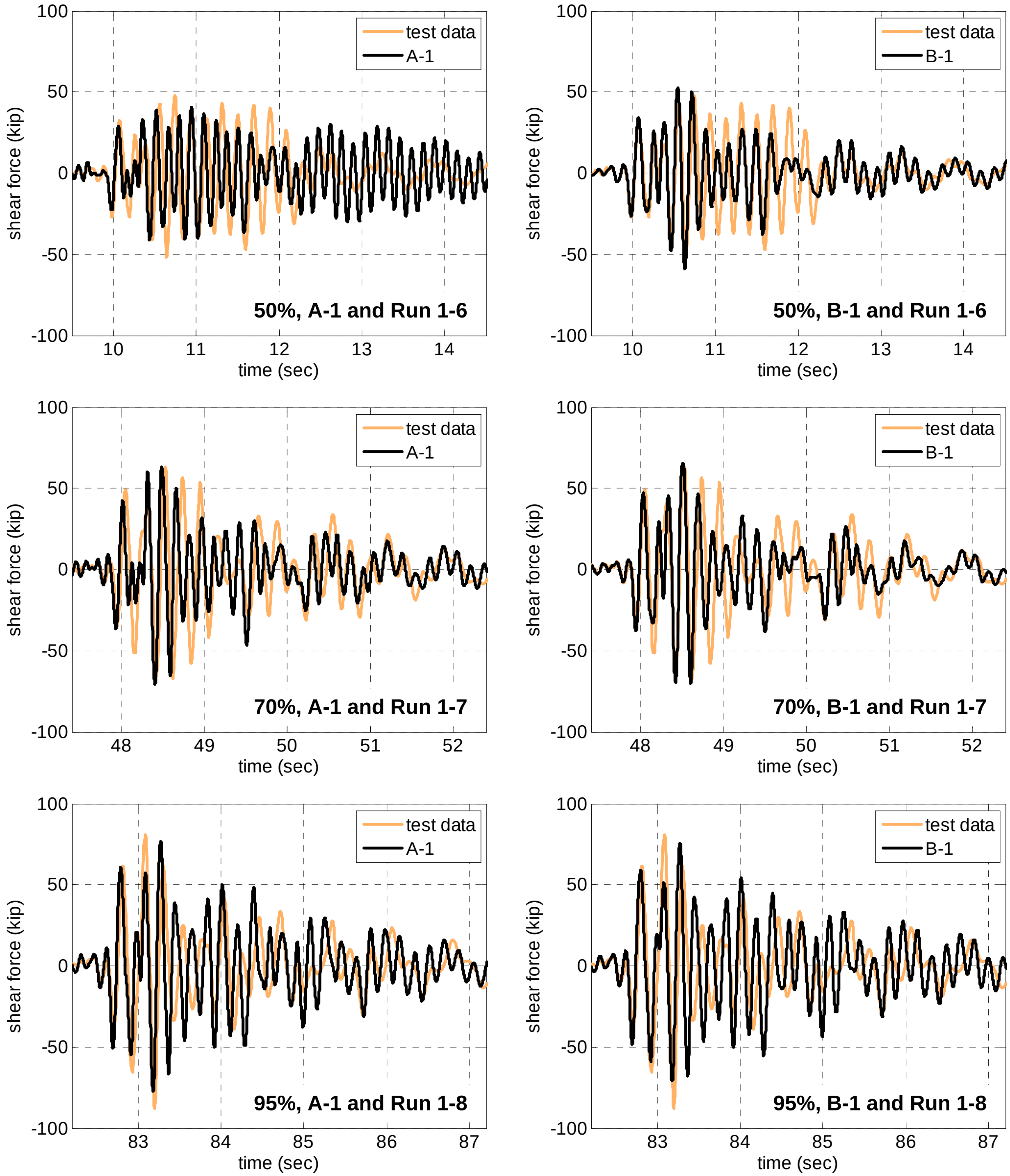

Fig. 6.15 Comparison of shear force histories of SP1 subjected to 50%, 70%, and 95%-scale motions

Fig. 6.16 compares the shear force histories obtained from the analysis of each model and from the 125%-scale runs of SP1. Fig. 6.16(a), (b), and (c) present the comparisons for the '1st X+Z', 'X only', and '2nd X+Z', respectively. In Fig. 6.16(a), it is demonstrated that the six models produce similar results. All of them are successful in matching the maximum shear forces at the peaks designated as 1, 2, and 3. At the 3rd peak (indicated as '3', which corresponds to the time of maximum shear force in test data, shear force of models A-1 and B-1 are equal to 90.6% and 91.3% of the experimental results, respectively. A-2 or B-2 is slightly more successful than A-1 or B-1 to detect the maximum because the period is slightly changed with the presence of the shear spring, which further affects the global responses. However, these differences are not due to the inelastic response (i.e. yielding) in the shear spring. The only remarkable difference regarding the inelastic response of the shear spring is the peak value of A-2-SDC for the peak designated with '4'. Compared to other models, it has smaller shear force, -54.63 kips, which is close to the test response, -58.4 kips. This is caused by the unique features of the SDC estimation because the 4th shear peak appears after tension (8.175 sec in Fig. 6.14, 120.33 sec in Fig. 6.17). Therefore, the shear strength is reduced to only the contribution of the transverse steel reinforcement (hoops) at this time and is kept at this value afterwards. However, this tension does not result in yielding of the ACI shear spring because the shear demand is still smaller than the strength calculated in the spring, and the tension is smaller than the specified limit (note that the tension limit in the analysis is set to be close to the maximum tension, refer to Section 6.2.2 for the use of the tension limit). As a result, the two code springs provide different shear force values at the 4th peak at 120.4 sec as shown in Fig. 6.16(a).

In contrast to the successful prediction of the shear force at the 4th shear peak by A-2-SDC, B-2-SDC does not capture the 4th peak. The reason for this difference can be better understood from the comparison of the spring responses in Fig. 6.17 for Models A-2-SDC and B-2-SDC. Fig. 6.17 (a) presents the axial force applied to the shear spring, whereas Fig. 6.17(b) and (c) plot the deformation and shear force histories recorded at the SDC springs. Dashed vertical lines indicate the start and end points of the axial tension interval. Some observations regarding these figures are as follows:

- The two SDC springs have different deformation and force histories after the 1st tension.
- The significant deformation starts at different times which correspond to the 1st tension for A-2-SDC and the 2nd tension for B-2-SDC suggesting that the two springs yield at different times.
- The two models have the same axial force histories (Fig. 6.17(a) and (d)) but the shear force during the 1st tension is not the same (Fig. 6.17(e)). A-2-SDC model has a slightly larger force, and it exceeds the code-based strength under tension. However, the force in B-2-SDC model is slightly under the limit, V_y, which is equal to V_s due to tension. Therefore, yielding takes place in A-2-SDC, but not in B-2-SDC. This observation is a good example to demonstrate the dependence of the analytical model prediction on slight changes and the corresponding difficulties that can arise during the prediction of the observed response with analytical modeling.

The different yielding patterns of the springs in the two models are observed in the hysteresis plots (e.g. Fig. 6.18(a-2) versus Fig. 6.19(a-2)), where the horizontal axis represents the deformation of the spring. The shear spring in the B-2-SDC model yields at the time corresponding to the 2nd tension and the shear strength decreases by the SDC code equation.

Fig. 6.16(b) shows the shear responses under the 125%-scale ‘X only’ motion. As the previous run, the responses of A-1 and B-1 are still comparable to the test data with peak shear force estimations equal to 93.3% and 91.3% of the test response, respectively. The shear springs in the two SDC models (A-2-SDC and B-2-SDC) have 35.8% or less lower shear peaks compared to the other models because of the yield shear force consisting of only the transverse steel reinforcement (hoops) contribution. Another noticeable observation is the decreased peaks of ACI models. As shown in Fig. 6.18(b-1) and Fig. 6.19(b-1), yielding takes place in the shear springs of the two ACI models. However, except for the 3rd and 4th peaks, the shear force histories remain similar to those of A-1 and B-1 since the shear strength of the ACI spring is larger than that of the SDC spring. Finally, Fig. 6.16(c) presents the shear responses under the 125%-scale ‘2nd X+Z’ motion. The shear force obtained from models A-1 and B-1 are equal to 98.7% and 101.7% of the maximum test response at the 3rd peak. Analysis results are in general comparable to the test data for this run.

The change of the analytical to the experimental response ratios under repeated runs for the 125%-scale is interesting. The ratio of the shear force obtained from the analytical models to the shear force obtained from test results at the 3rd shear peak, denoted as ‘Response ratio’ in the Y-axis, are presented in Fig. 6.20 for the 125%-scale runs. It is observed that the analytical models without the shear spring (A-1 and B-1) tend to improve their predictions with repeated runs. Predictions of the models with the shear springs are comparatively less successful for the ‘X only’ run. Considering that the goal of the shear springs are the accurate consideration of the effect of the axial force on the shear strength, it can be concluded that the ACI shear spring is successful in achieving this goal both for the A and B models. Successful prediction of the shear strength for the ‘2nd X+Z’ motion, which is the strength reduced due to degradation of concrete contribution leads to this conclusion. It can be observed that A-1 and B-1 model predictions for this motion are more accurate. However, the slight conservativeness of the code spring is a desirable result. This is observed more clearly for SP2. Another important observation is that A-1 and B-1 have a deficiency in reflecting the shear degradation even though they are good in predicting the peak values under the ‘2nd X+Z’. The peaks under the ‘1st X+Z’ and ‘2nd X+Z’ did not significantly change (A-1: 84.82→84.10 kips, B-1: 85.47→86.71 kips), but these peaks decreased more in the tests. This explains why A-1 and B-1 become better in their predictions under the ‘2nd X+Z’. If the model provided a better prediction under ‘1st X+Z’, its overestimation under the last motion, i.e. the ‘2nd X+Z’, could be significant. In addition, the increase in ratio from ‘X only’ to ‘2nd X+Z’ is bigger than that from ‘1st X+Z’ to ‘X only’, as clearly shown in Fig. 6.20. This observation implies that the models without the shear springs do not accurately take into account the damage of the column due to the vertical excitation. This is observed more clearly for test specimen SP2, as discussed later. This increase of the ratio between the model prediction and the experimental finding is not the case for the A-2-ACI and B-2-ACI and clearly not the case for A-2-SDC and B-2-SDC, where the SDC spring is more sensitive to the damage accumulation than the ACI spring.

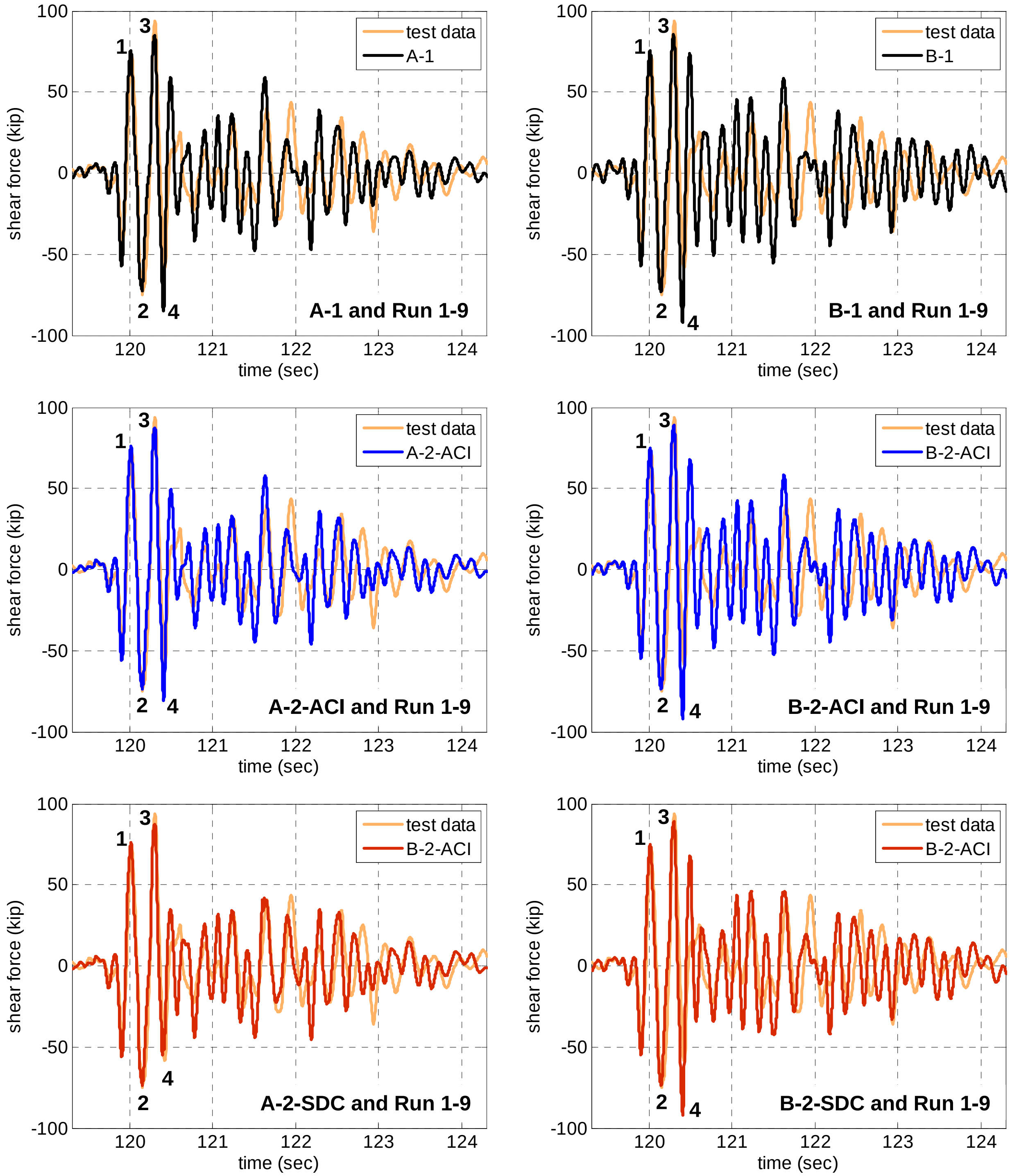

(a) 125% 1st X+Z

Fig. 6.16 Comparison of shear force histories of SP1 subjected to 125%-scale motions

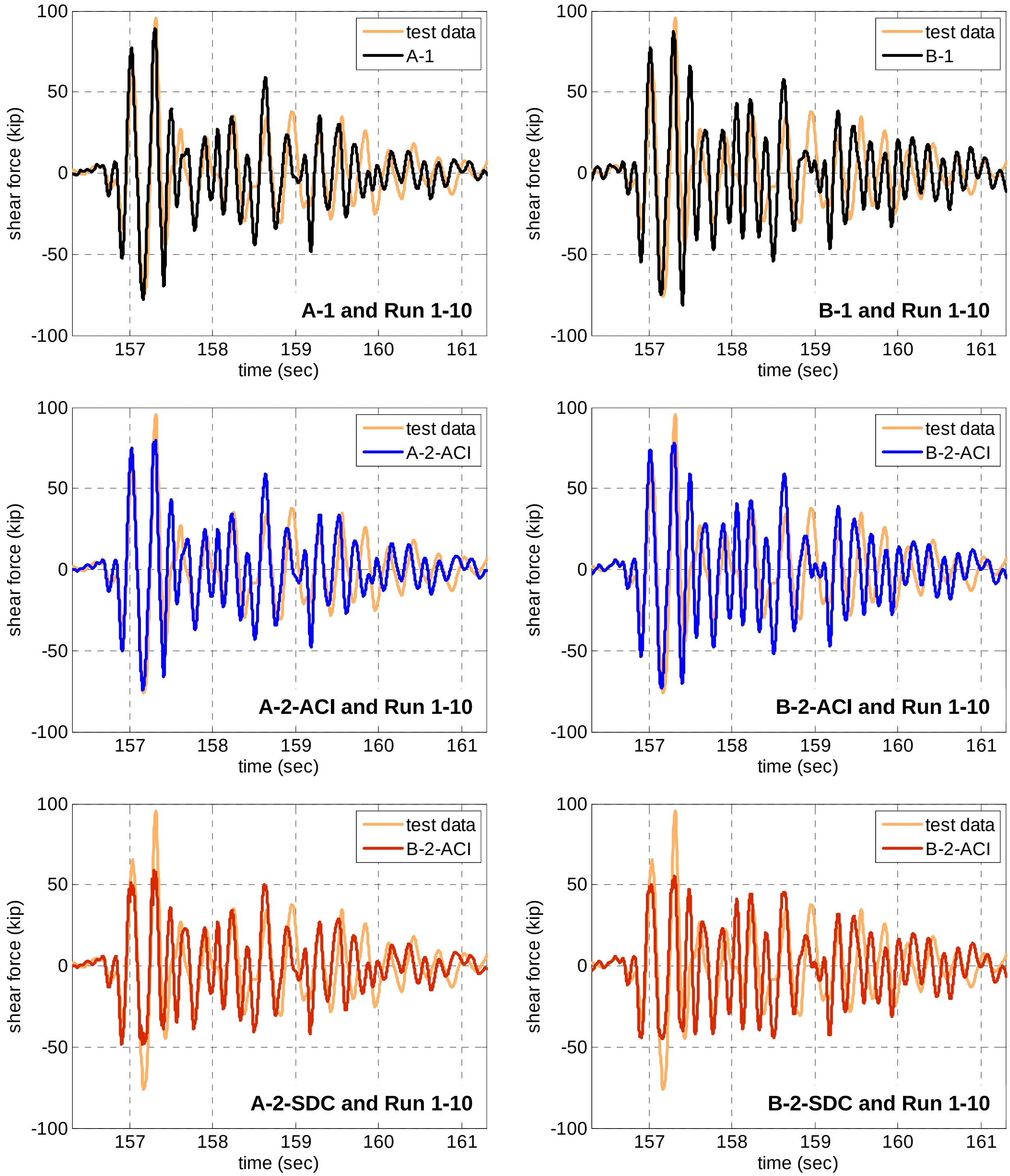

(b) 125% X only

Fig. 6.16 Comparison of shear force histories of SP1 subjected to 125%-scale motions (continued)

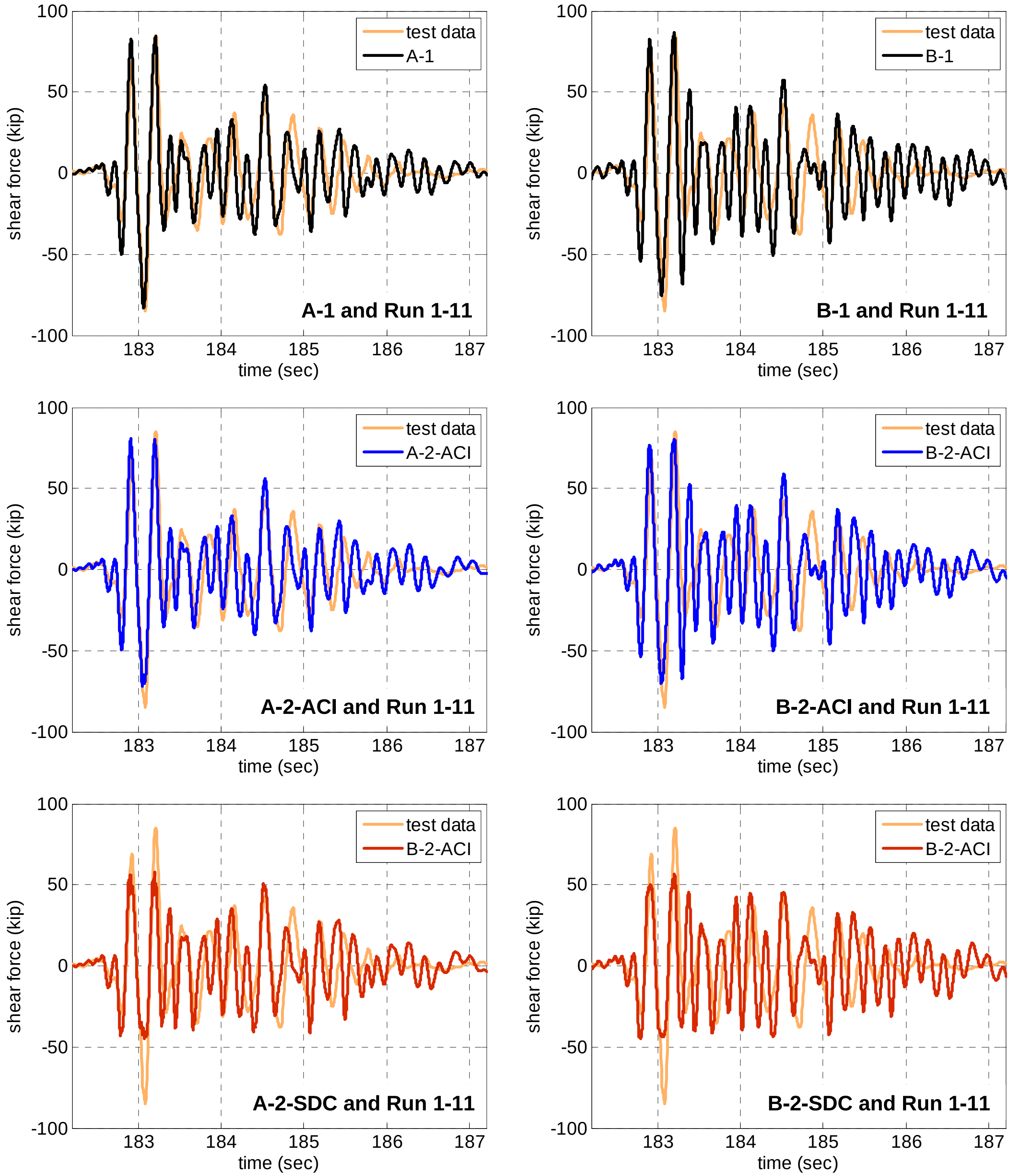

(c) 125% 2nd X+Z

Fig. 6.16 Comparison of shear force histories of SP1 subjected to 125%-scale motions (continued)

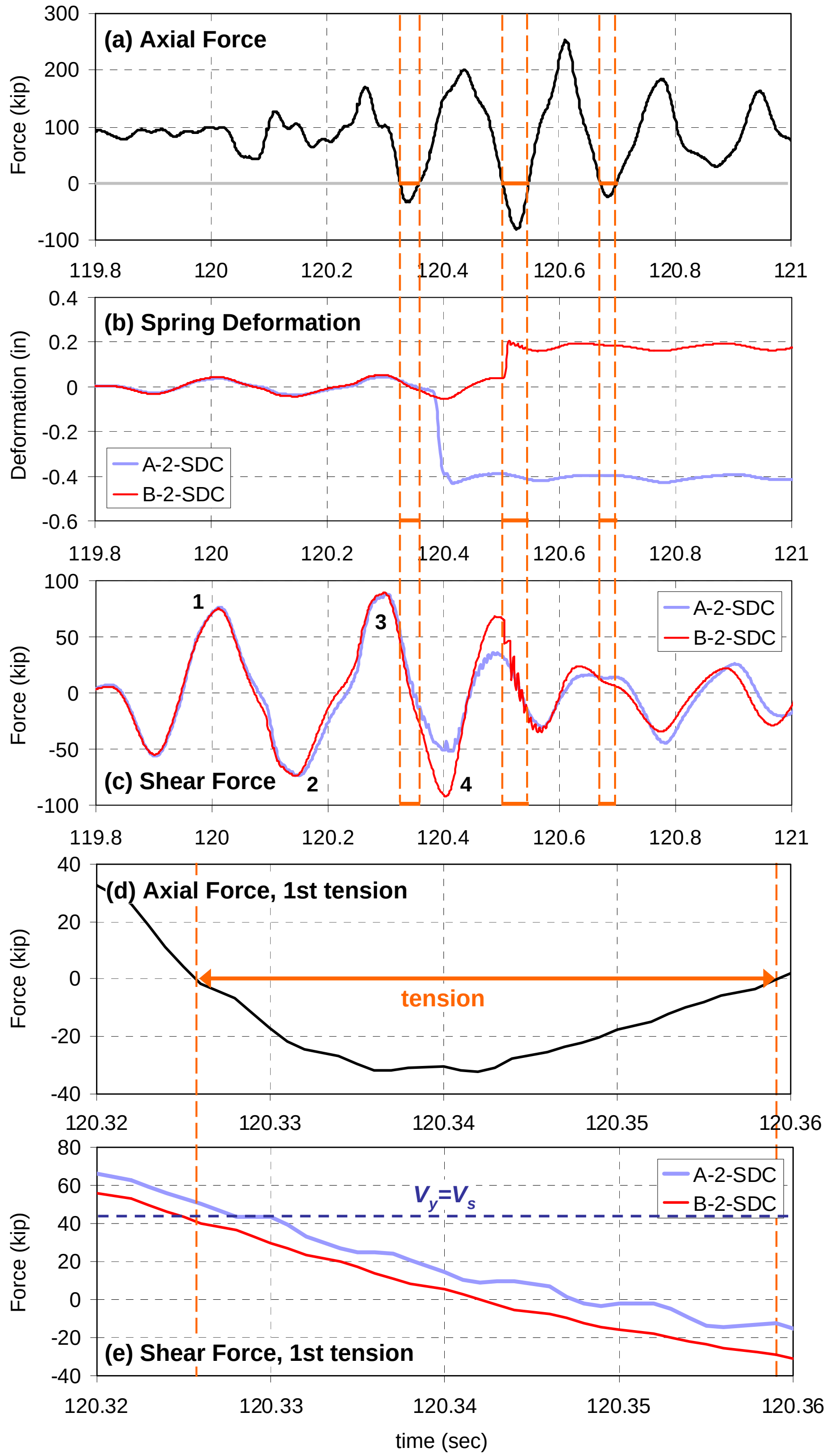

Fig. 6.17 Comparison of the shear spring responses of SP1 A-2-SDC and B-2-SDC models subjected to 125%-scale '1st X+Z' motion

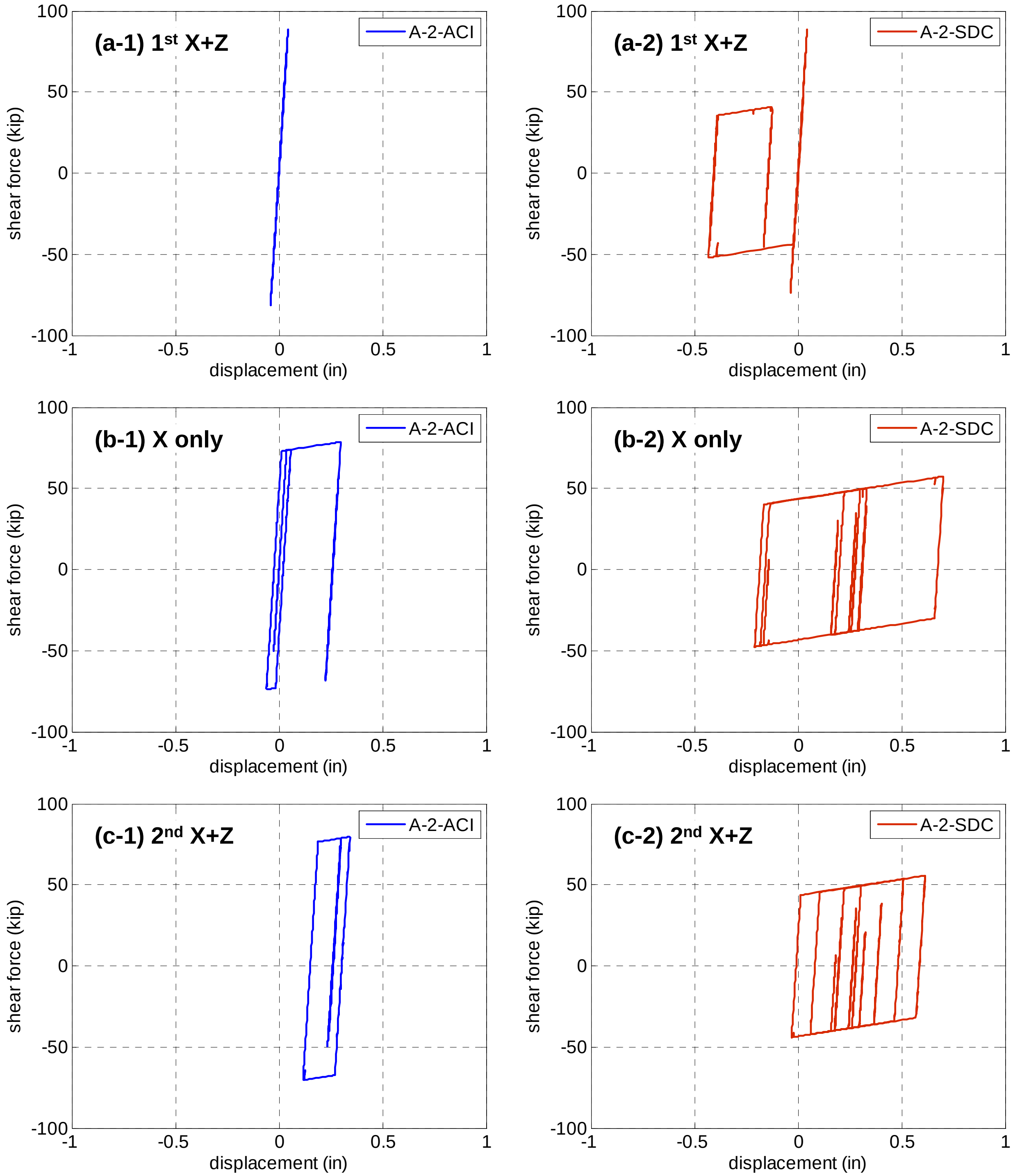

Fig. 6.18 Shear spring hysteresis of SP1 A-2 models subjected to 125%-scale motions

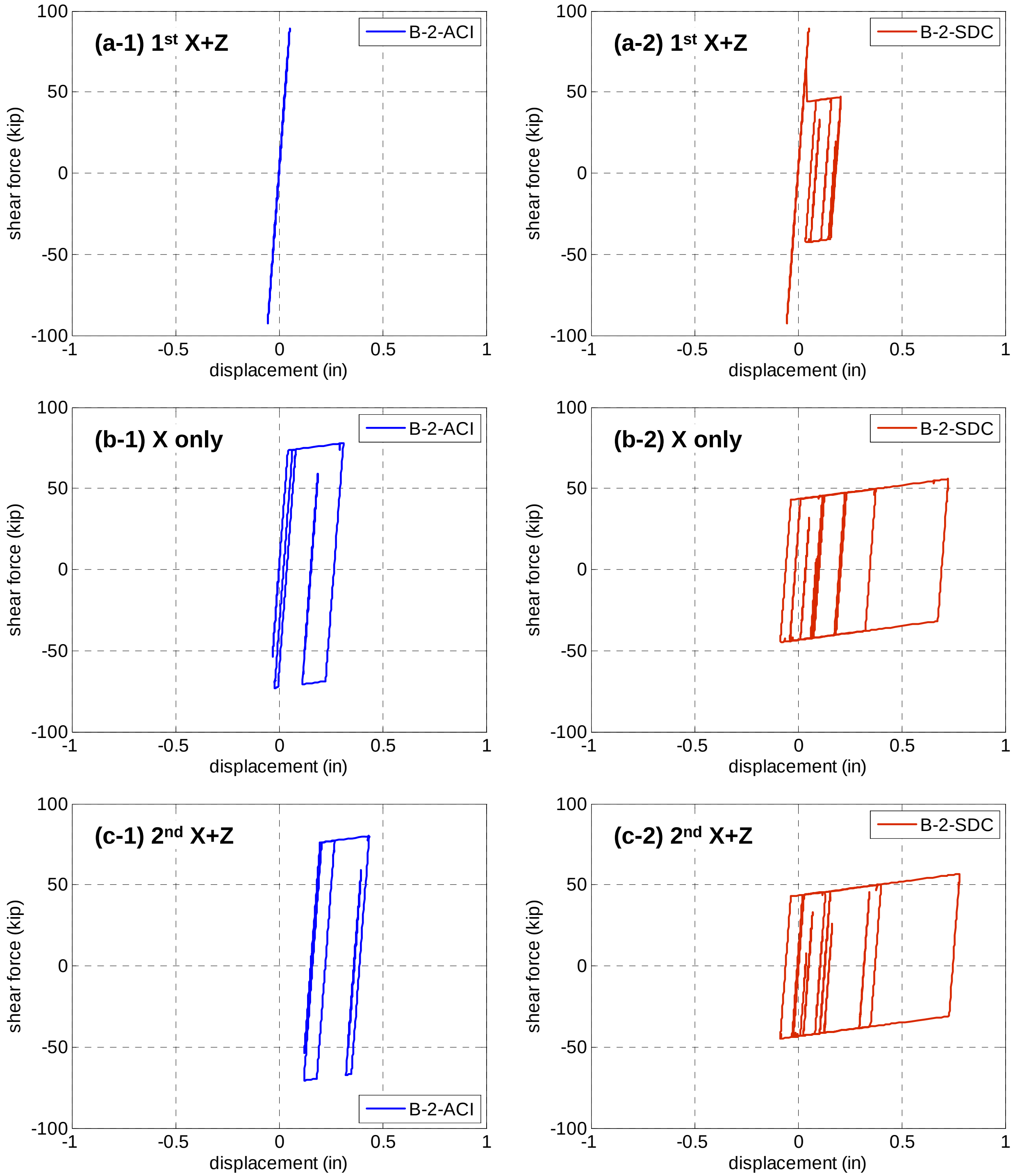

Fig. 6.19 Shear spring hysteresis of SP1 B-2 models subjected to 125%-scale motions

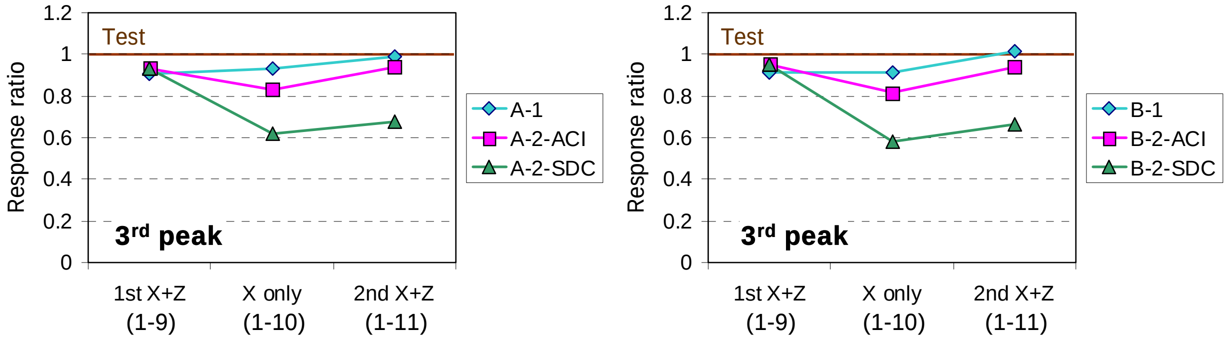

Fig. 6.20 Comparison of the 3rd peak ratios obtained from SP1 A and B models to the test data under the 125%-scale motions

Similar to the previous discussion related to test specimen SP1, the shear force responses under 50% to 125%-scale motions are presented in the following figures for SP2. Fig. 6.21 compares the responses from Models A-1 and B-1 to SP2 test data under 50%, 70%, and 95%-scale motions. A-1 and B-1 provide different shear responses. However, they are comparable to the test data with varying degree of matching at different points in time. Fig. 6.22(a), (b) and (c) present the results under 125%-scale '1st X+Z', 'X only', and '2nd X+Z' motions, respectively. Similar to SP1 results, the maximum value of the test data is observed at the 3rd peak for all of the runs. Both of A-2 and B-2 models have smaller values than the test data at this peak in every run, which is basically dictated by the value of the shear strength and the time at which it takes place. In case of SP1, the shear strength (yield shear, V_y) of the ACI spring was determined by the tension peak which occurred after the main shear peaks under the '1st X+Z' ground motion because of the predefined tension limit and the yielding took place later as it is caused by the demand under the 'X only' motion. However, for SP2, the shear demand reaches V_y of the ACI spring at the instant of the tension peak which occurs between the 1st and 2nd shear peaks during the '1st X+Z' motion. As a result, yielding takes place during this motion and the remaining shear history is affected by this value of V_y. This observation is also confirmed by the examination of the hysteresis relationships in Fig. 6.23 and Fig. 6.24, where it is observed that the yielding initially takes place in the '1st X+Z' motion for both of the models with ACI and SDC springs. In addition, V_y values for both springs in SP2 are smaller than those for the springs of SP1 shown in Fig. 6.18 and Fig. 6.19. For SP2, V_y for ACI and SDC springs are 54.39 kips and 29.01 kips (they are 73.0 kips and 43.8 kips for SP1) which are decreased by 25.5% and 33.8%, respectively. This reduction is due to the lower contribution provided by steel hoops (V_s) caused by the lower transverse reinforcement ratio.

Fig. 6.25 presents the ratios between the computational results and the test data at the 3rd peak. Similar to those of SP1 (Fig. 6.20), A-1 and B-1 are comparable to the test data. But, they overestimate the shear force response of SP2 subjected to the '2nd X+Z' motion. A-1 and B-1 reach 106.3% and 112.5% of the maximum from the test data, respectively. Models with ACI shear springs (A-2-ACI and B-2ACI) are deemed to be successful in the prediction of the '2nd X+Z' motion in the sense that they capture the shear strength degradation accurate enough while being on the desirable conservative (underestimation) side. Conservative estimates of the SDC shear spring for SP2 lack accuracy as in the case of SP1. Similar to SP1 models, A-1 and B-1 have a deficiency in reflecting the shear degradation. The peaks of A-1 and B-1 under the '1st X+Z' and the '2nd X+Z' runs changed as follows: 78.64→81.38 kips (A-1), 84.27→86.13 kips

(B-1). In addition, the increase in these response ratios from 'X only' run to '2nd X+Z' run is bigger than the previous change from '1st X+Z' run to 'X only' run.

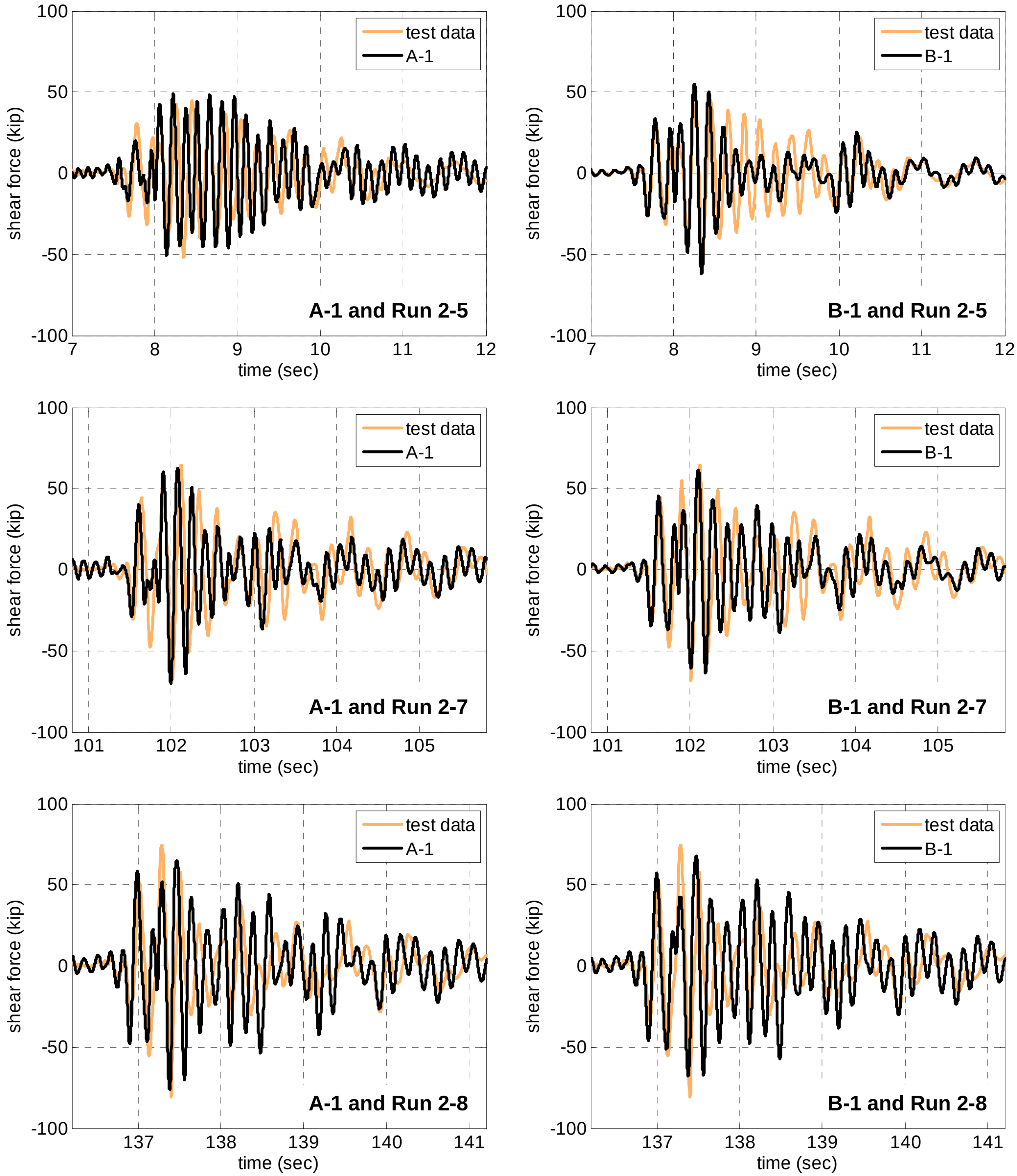

Fig. 6.21 Comparison of shear force histories of SP2 subjected to 50%, 70%, and 95%-scale motions

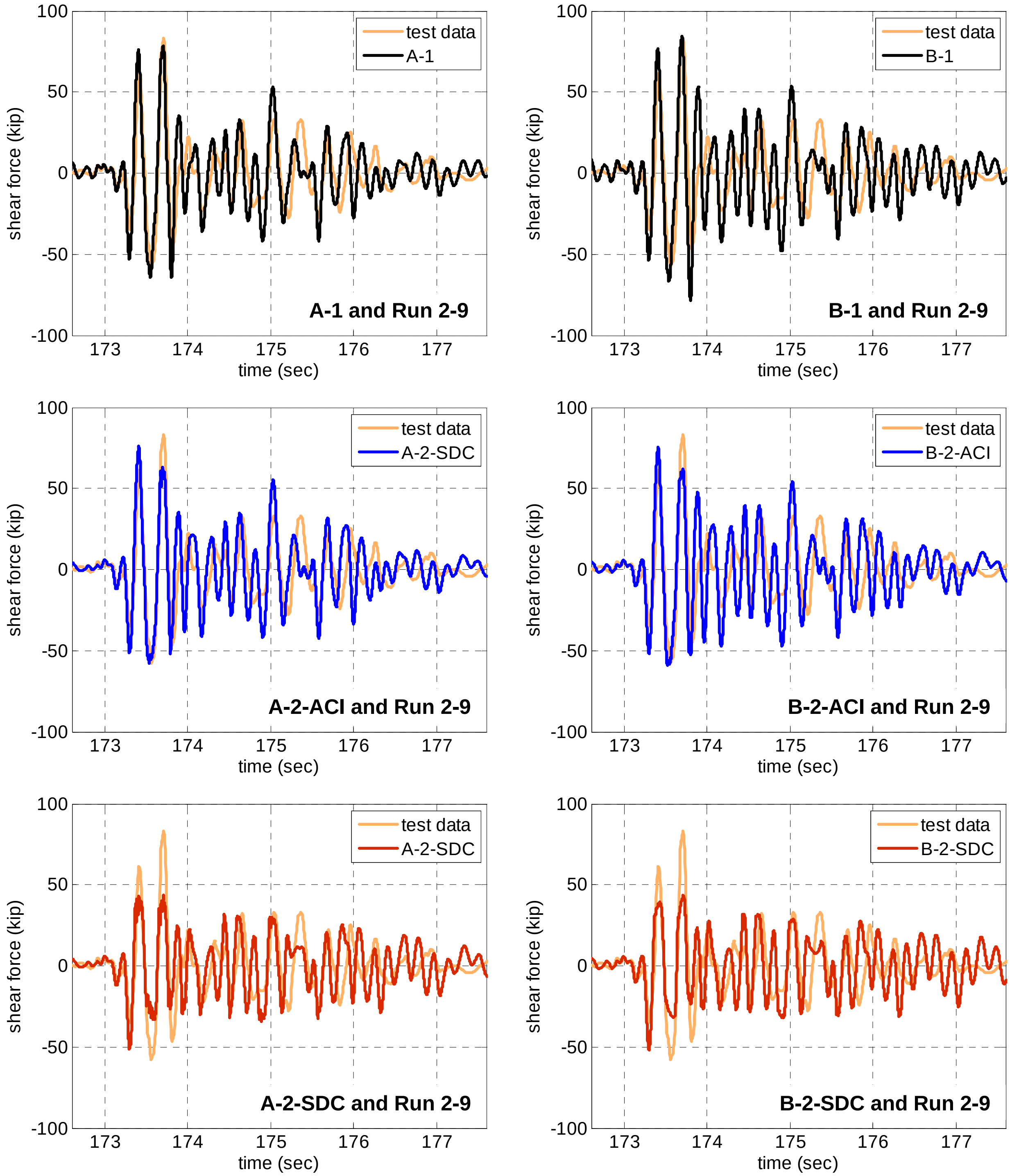

(a) 125% 1st X+Z

Fig. 6.22 Comparison of shear force histories of SP2 subjected to 125%-scale motions

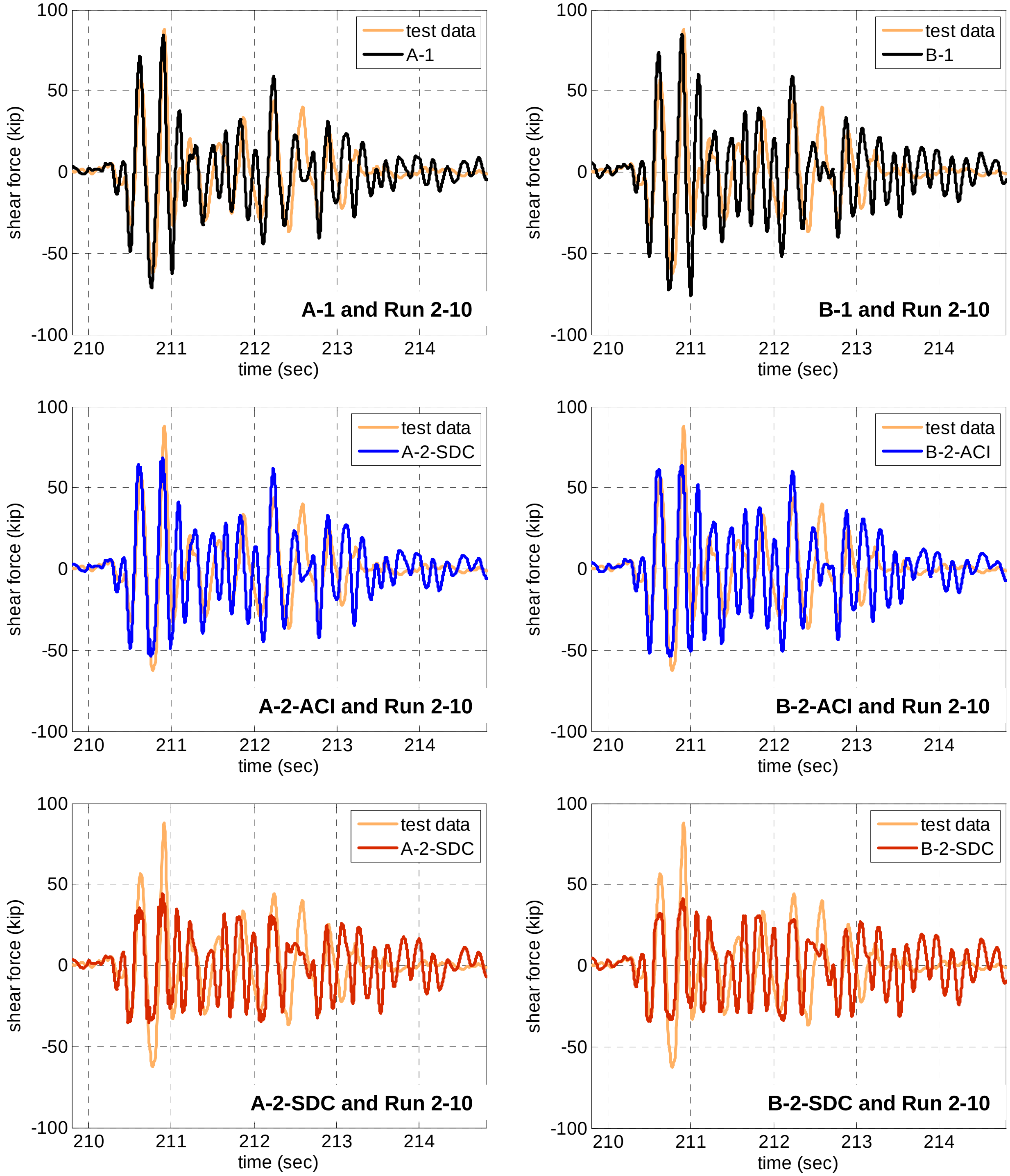

(b) 125% X only

Fig. 6.22 Comparison of shear force histories of SP2 subjected to 125%-scale motions (continued)

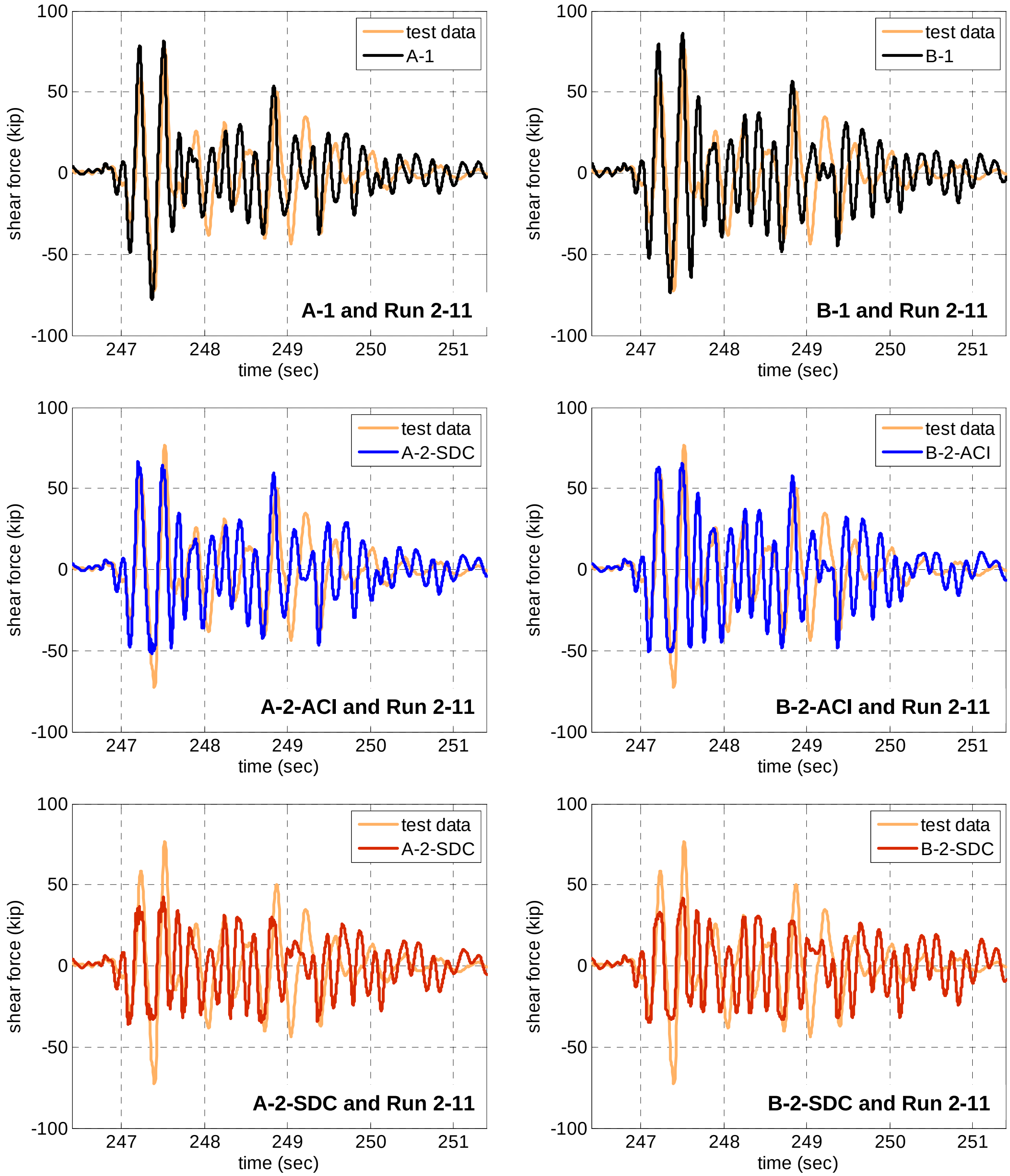

(c) 125% 2nd X+Z

Fig. 6.22 Comparison of shear force histories of SP2 subjected to 125%-scale motions (continued)

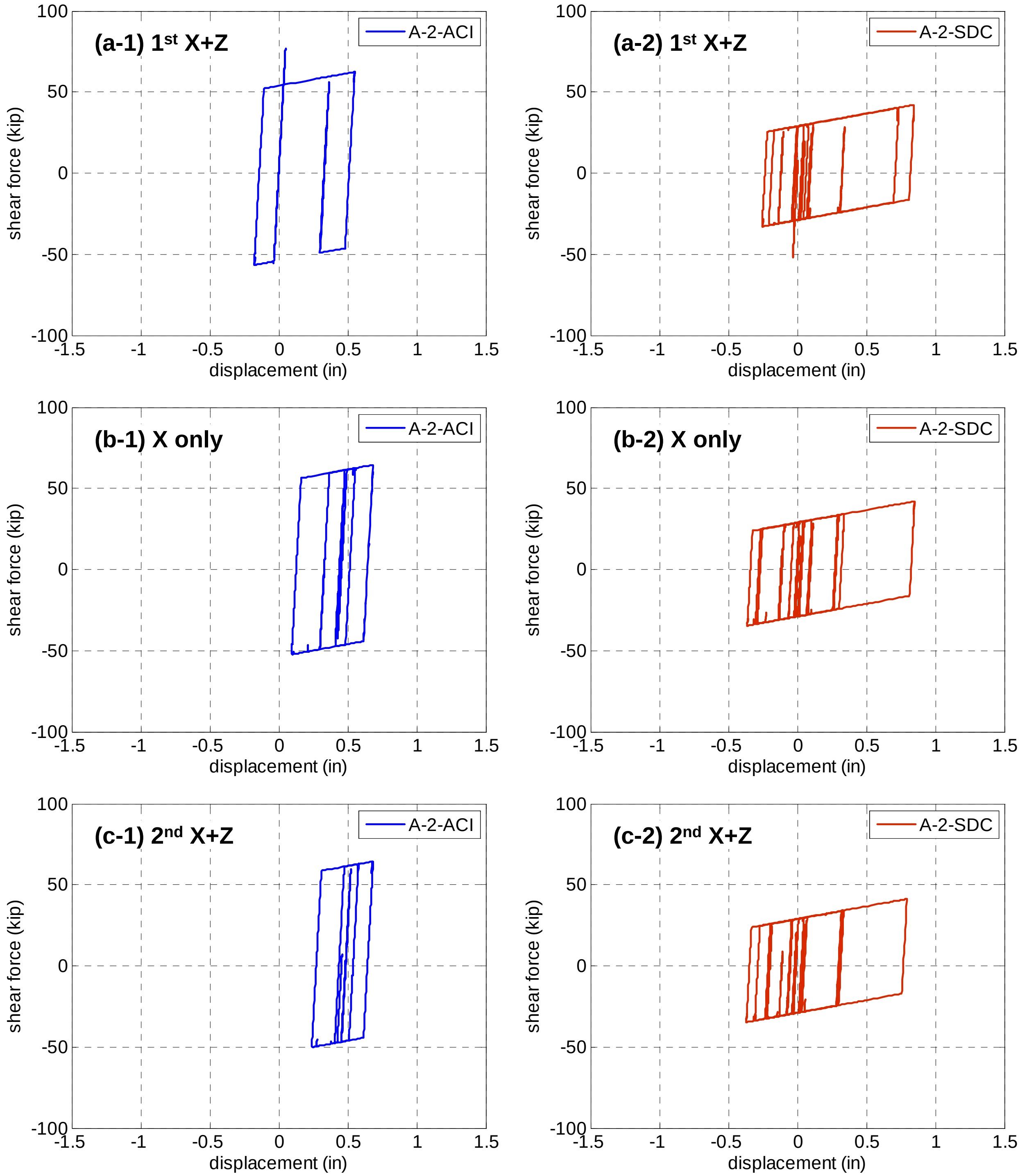

Fig. 6.23 Shear spring hysteresis of SP2 A-2 models subjected to 125%-scale motions

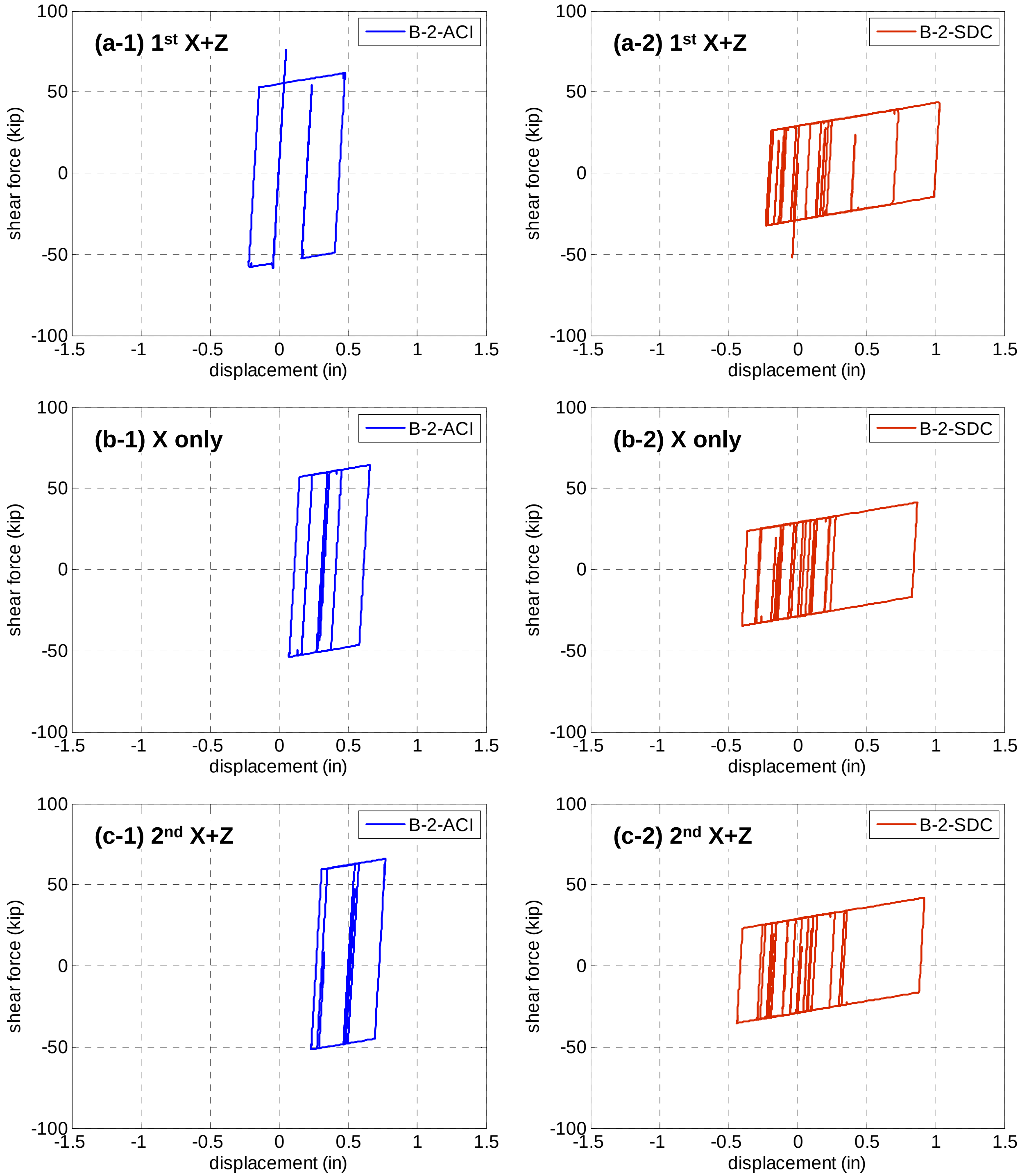

Fig. 6.24 Shear spring hysteresis of SP2 B-2 models subjected to 125%-scale motions

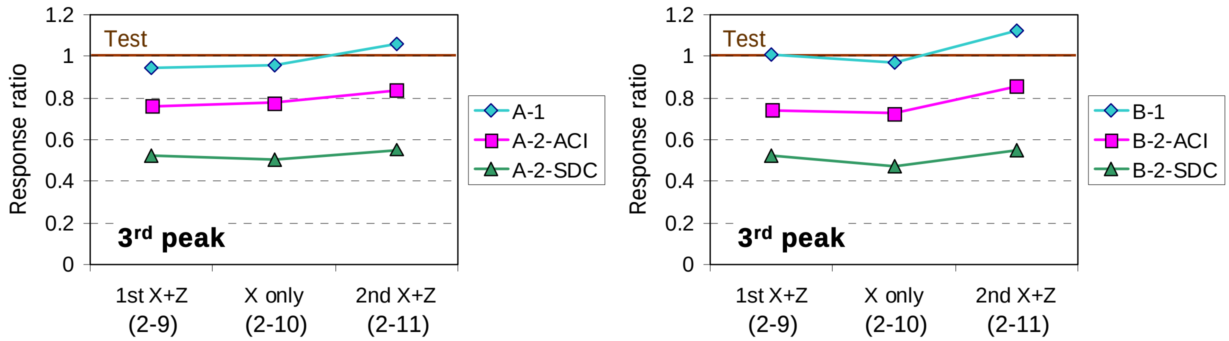

Fig. 6.25 Comparison of the 3rd peak ratios obtained from SP2 A and B models to the test data subjected to 125%-scale motions

6.4.2.2 Bending Moment at the Base

The bending moment at the base of the column are discussed in this section by examining the time histories and maximum values. Fig. 6.26 compares the bending moment histories of SP1 obtained from the computational models, A-1 and B-1, with the test data under 50%, 70%, and 95%-scale motions. It is observed that A-1 and B-1 produce similar responses which are sufficiently close to the test data except for the presence of high frequency contents in the analytical results of the A-2 and B-2 models. The results of A-2 and B-2 models are not presented here as they provide similar responses to the models A-1 and B-1.

Fig. 6.27 presents the comparison of the moment at the base obtained from the analytical models with the test results for the 125%-scale motions. Under the '1st X+Z' motion, all six models provide very similar results. The 4th peak, indicated as '4', has the maximum base moment in all cases. Test results are well matched by the analytical models in this case. The only observed discrepancy is that the frequency of the base moment time history caused by the top mass rotation after 122 sec is not well captured. Considering the fact that these periods are matched under the lower-intensity level motions, it can be concluded that the periods of each model are not elongated to the same extent. This observation is valid for the following two 125%-scale runs as shown in Fig. 6.27(b) and (c). Similar to the shear force time histories, the ACI and SDC springs decrease the amplitude of the main peaks under 'X only' motion which is remarkable especially at the 4th peak. It should be noted that the 4th peak of the base moment coincides with the 3rd peak of the shear force.

Fig. 6.28 and Fig. 6.29 are for the base moment responses of SP2. Similar to the shear force, the ACI spring affects the amplitude of the peaks from the 125%-scale 'X only' motion, but SDC spring initially yields under '1st X+Z' motion. Both models have smaller peaks than those for SP1 which is due to wider hoop spacing, i.e. lower V_y. In addition, SP2 has a greater change in the frequency after the main excitation than SP1 does, which is expected because SP2 was more damaged than SP1 even before the 125%-scale runs.

Fig. 6.30 presents the ratio between the maximum bending moment values from the computational models and the test data under 125%-scale motions at the 4th peak, which corresponds to the maximum of the test data. A-1 and B-1 overestimate the base moment responses in most of the cases, with the overestimation being larger for the runs with vertical excitation compared to the 'X only' case. Similar to the case of maximum shear values, models

A-2 and B-2 with the shear springs are successful in reducing these ratios, with accurate estimations of ACI spring model while the SDC spring produces inaccurate conservative results.

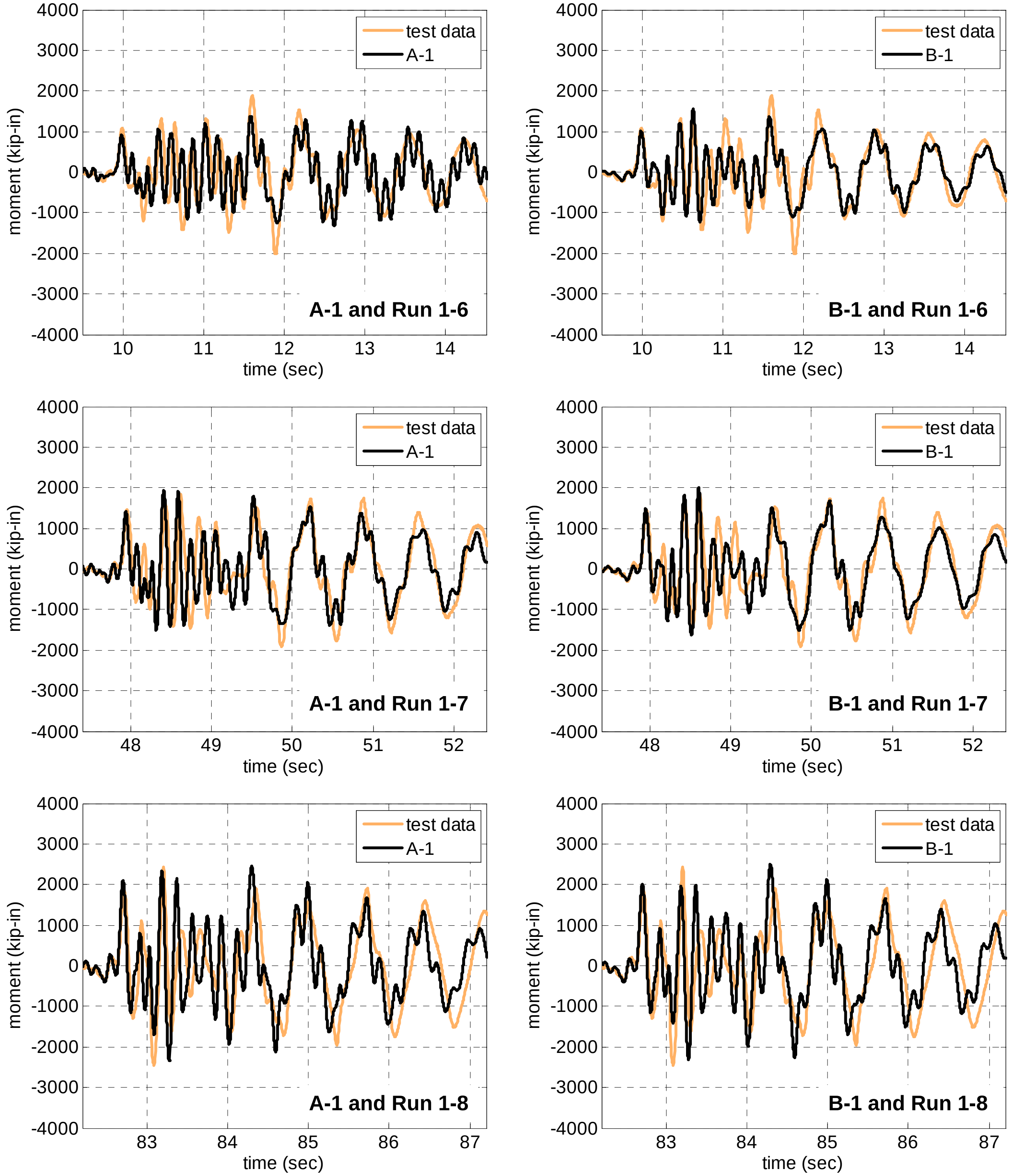

Fig. 6.26 Comparison of bending moment histories at the base of SP1 subjected to 50%, 70%, and 95%-scale motions

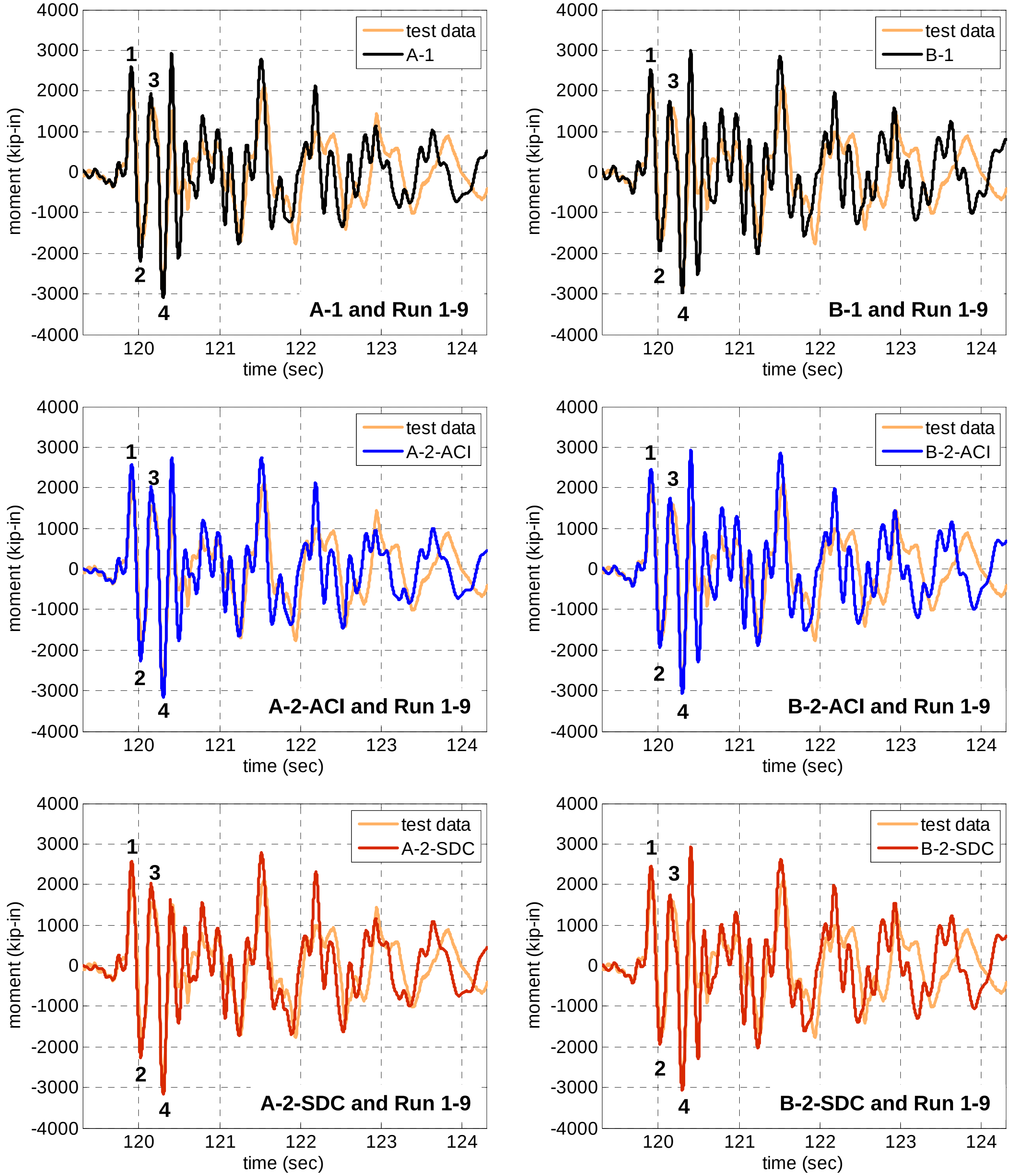

(a) 125% 1st X+Z

Fig. 6.27 Comparison of bending moment histories at the base of SP1 subjected to 125%-scale motions

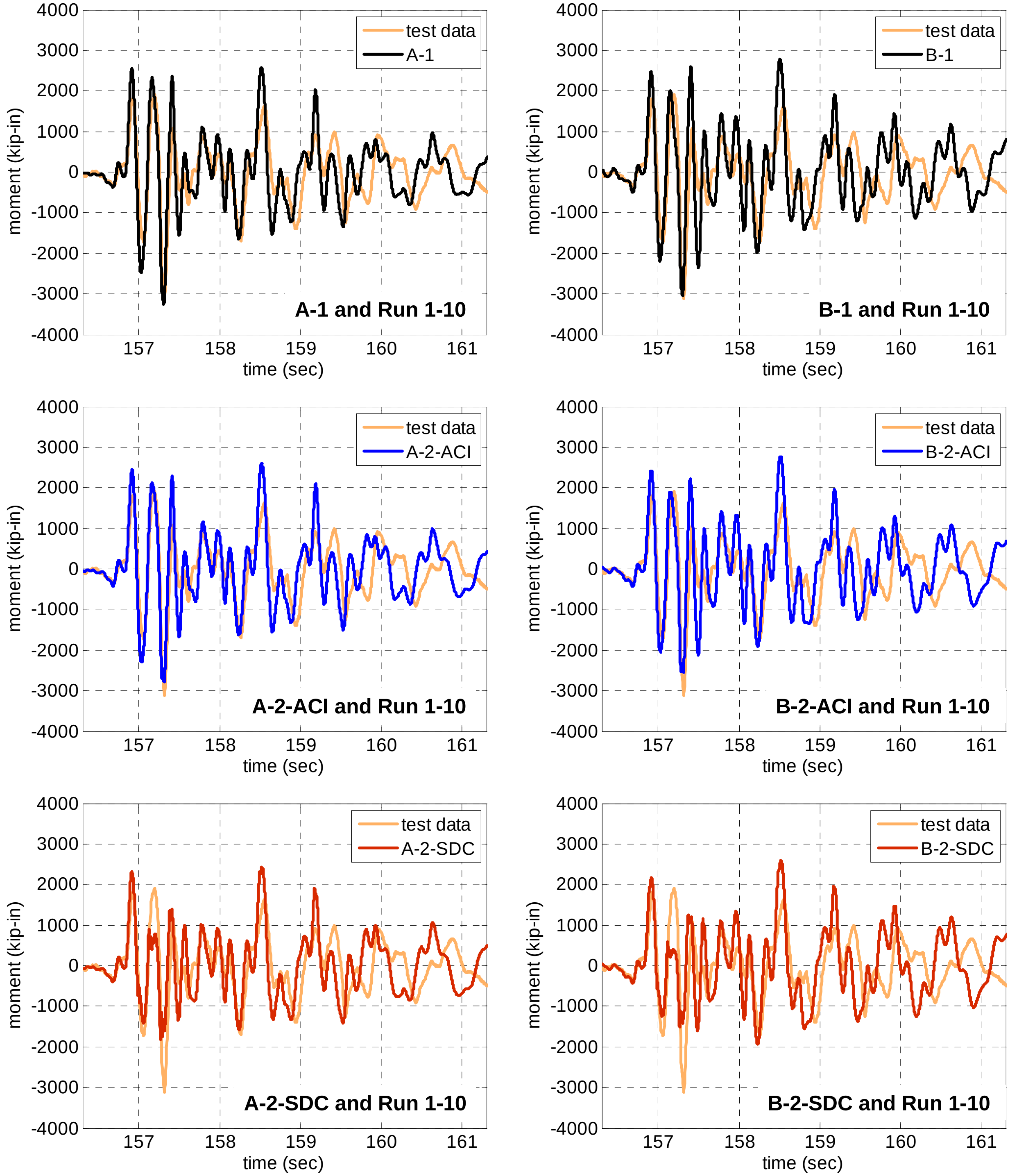

(b) 125% X only

Fig. 6.27 Comparison of bending moment histories at the base of SP1 subjected to 125%-scale motions (continued)

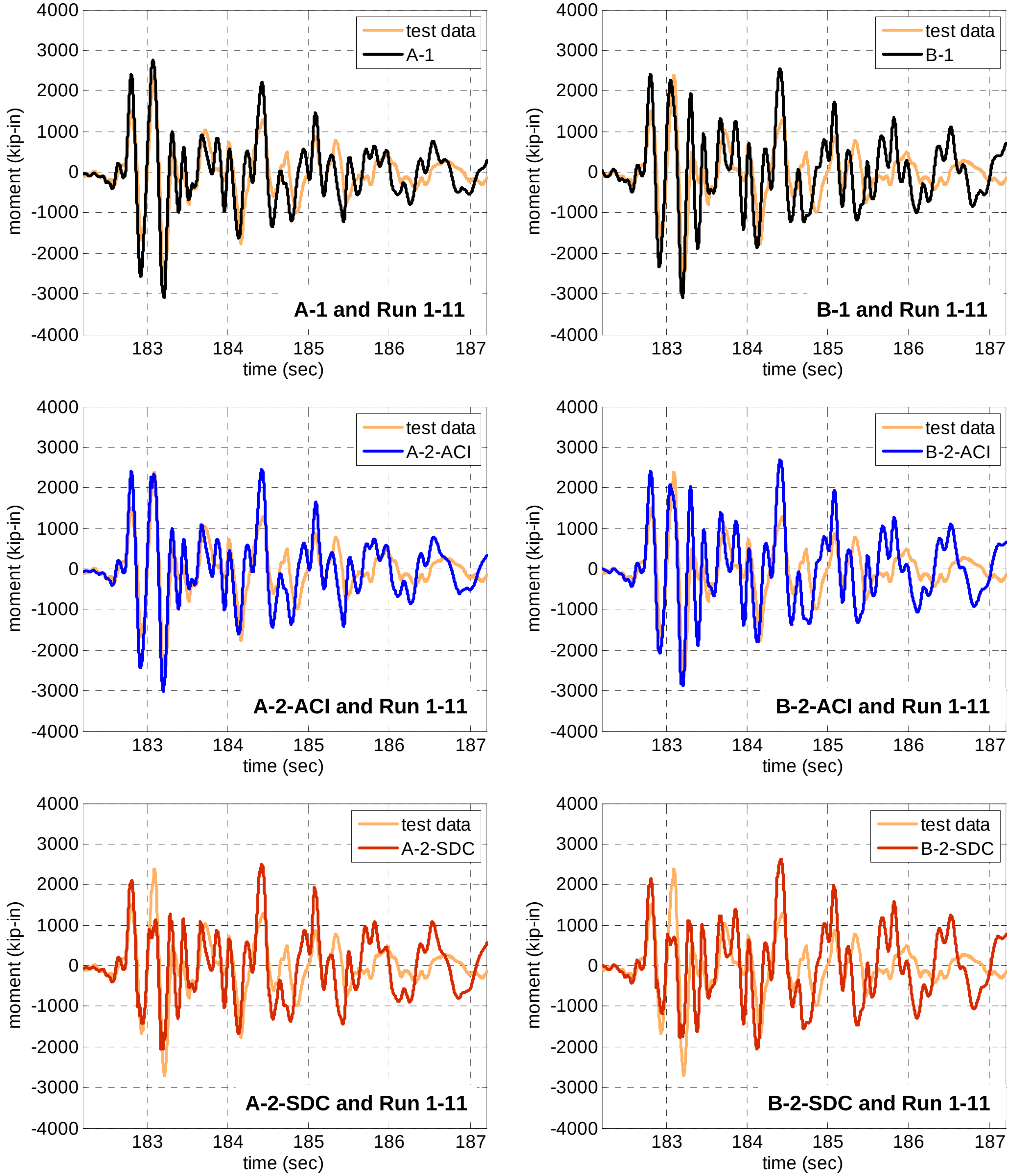

(c) 125% 2nd X+Z

Fig. 6.27 Comparison of bending moment histories at the base of SP1 subjected to 125%-scale motions (continued)

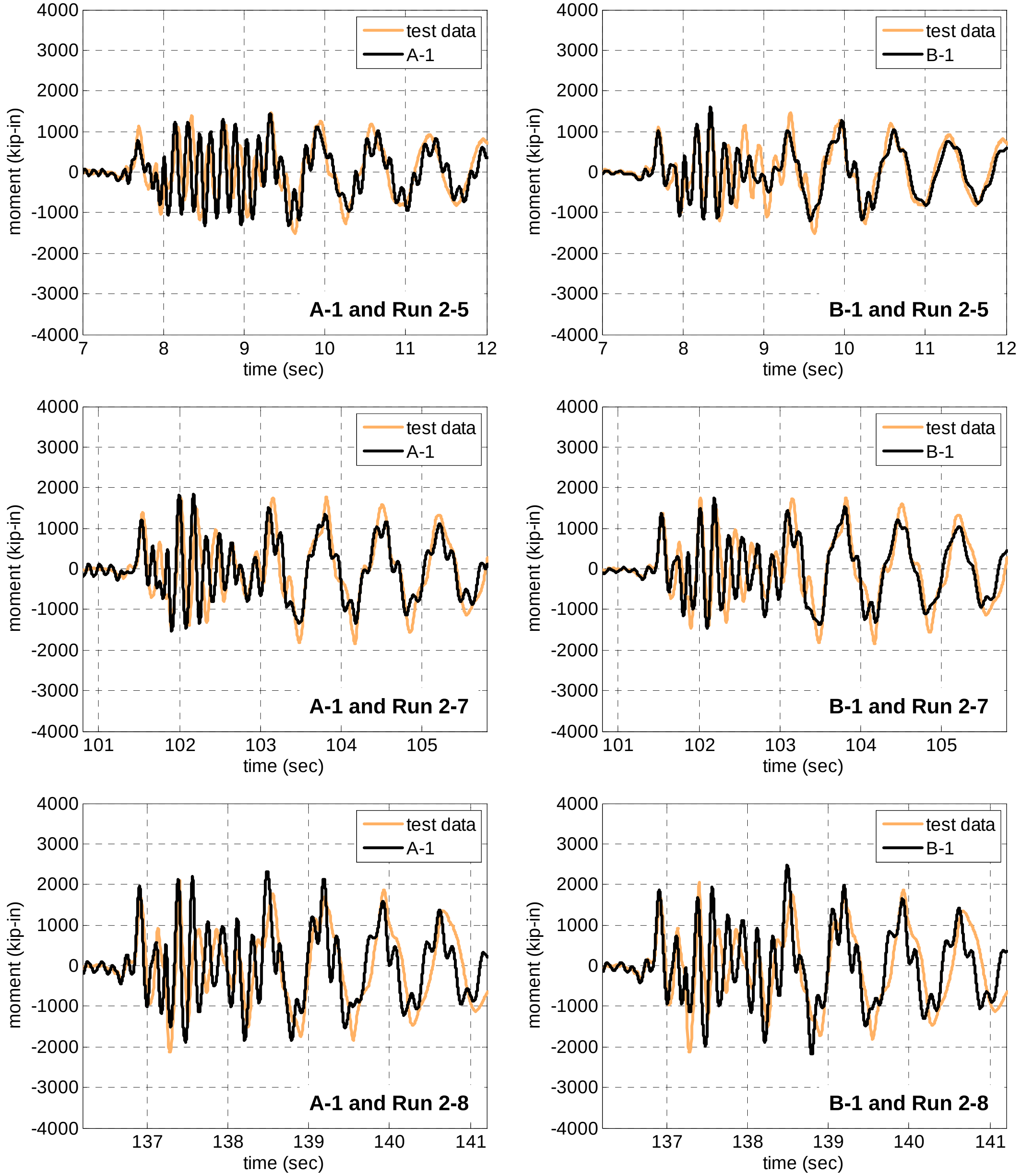

Fig. 6.28 Comparison of bending moment histories at the base of SP2 subjected to 50%, 70%, and 95%-scale motions

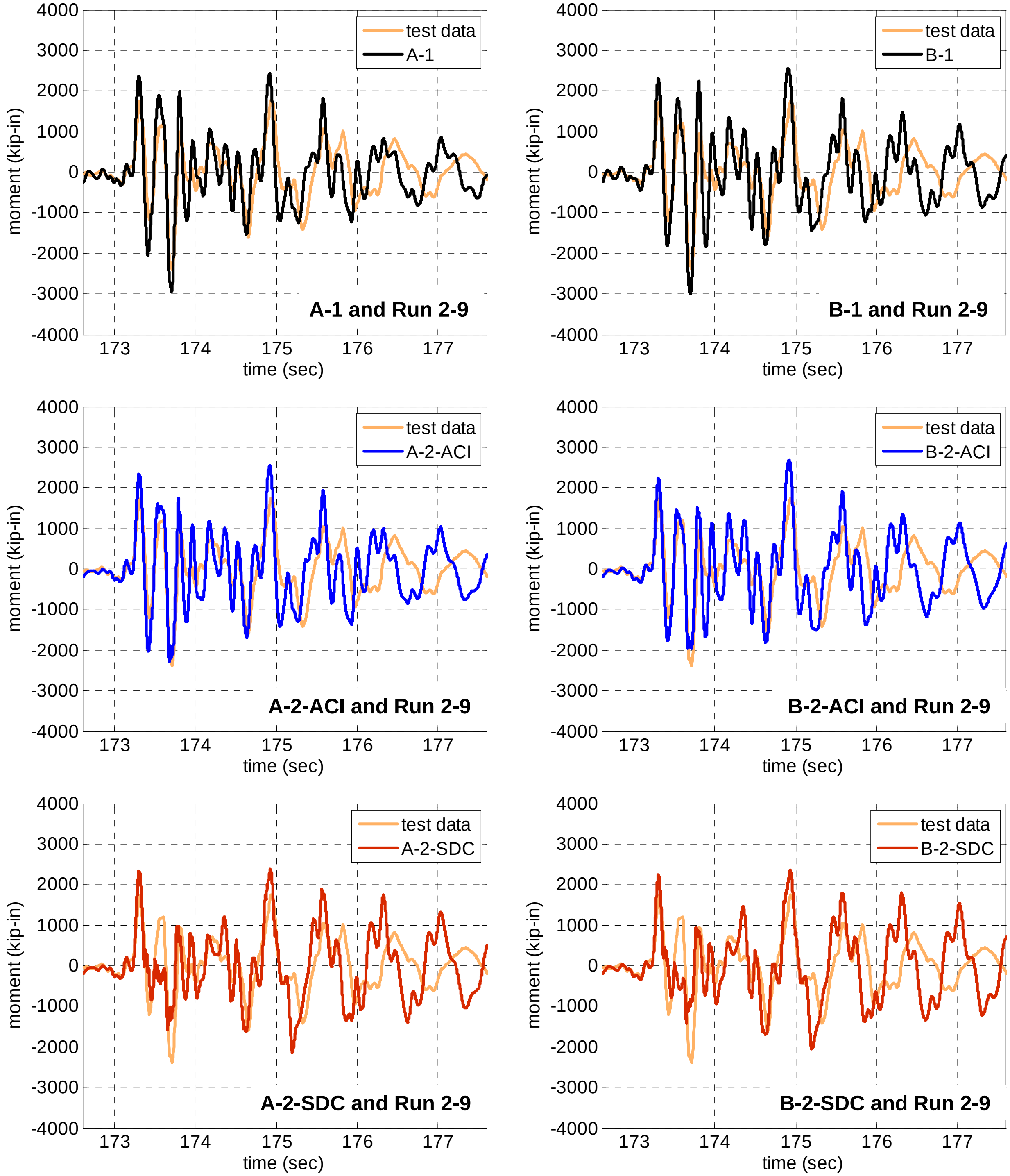

(a) 125% 1st X+Z

Fig. 6.29 Comparison of bending moment histories at the base of SP2 subjected to 125%-scale motions

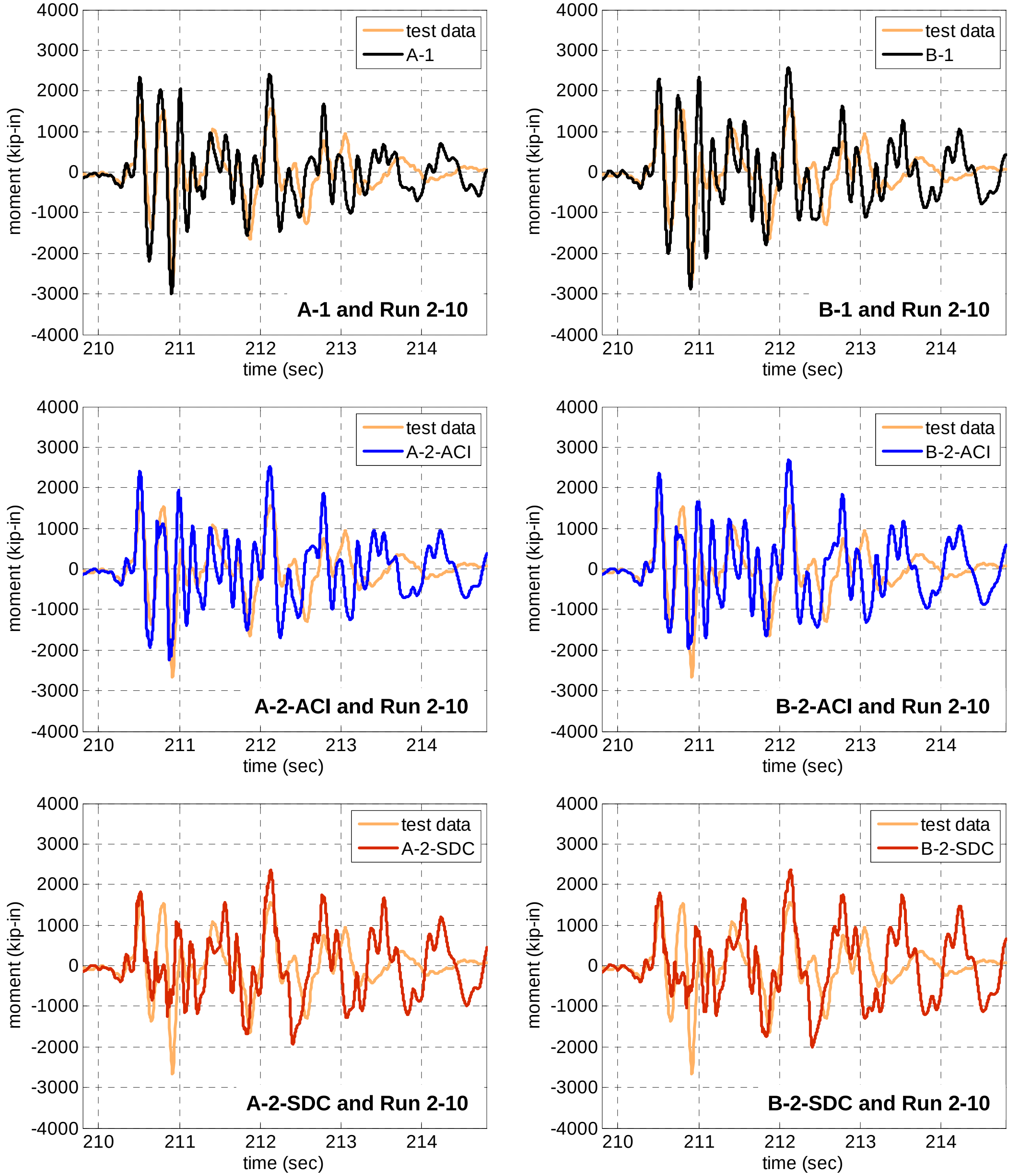

(b) 125% X only

Fig. 6.29 Comparison of bending moment histories at the base of SP2 subjected to 125%-scale motions (continued)

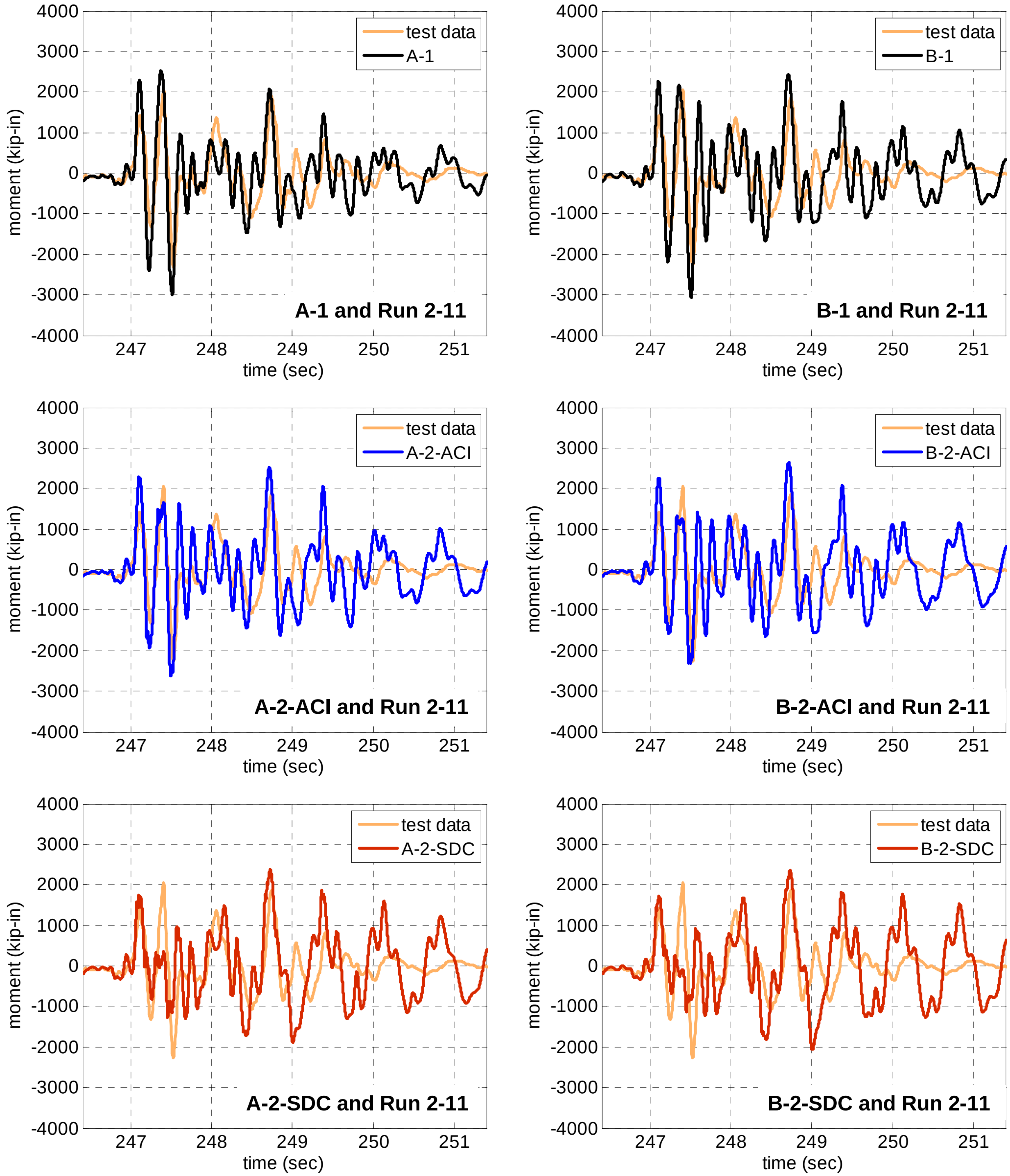

(c) 125% 2nd X+Z

Fig. 6.29 Comparison of bending moment histories at the base of SP2 subjected to 125%-scale motions (continued)

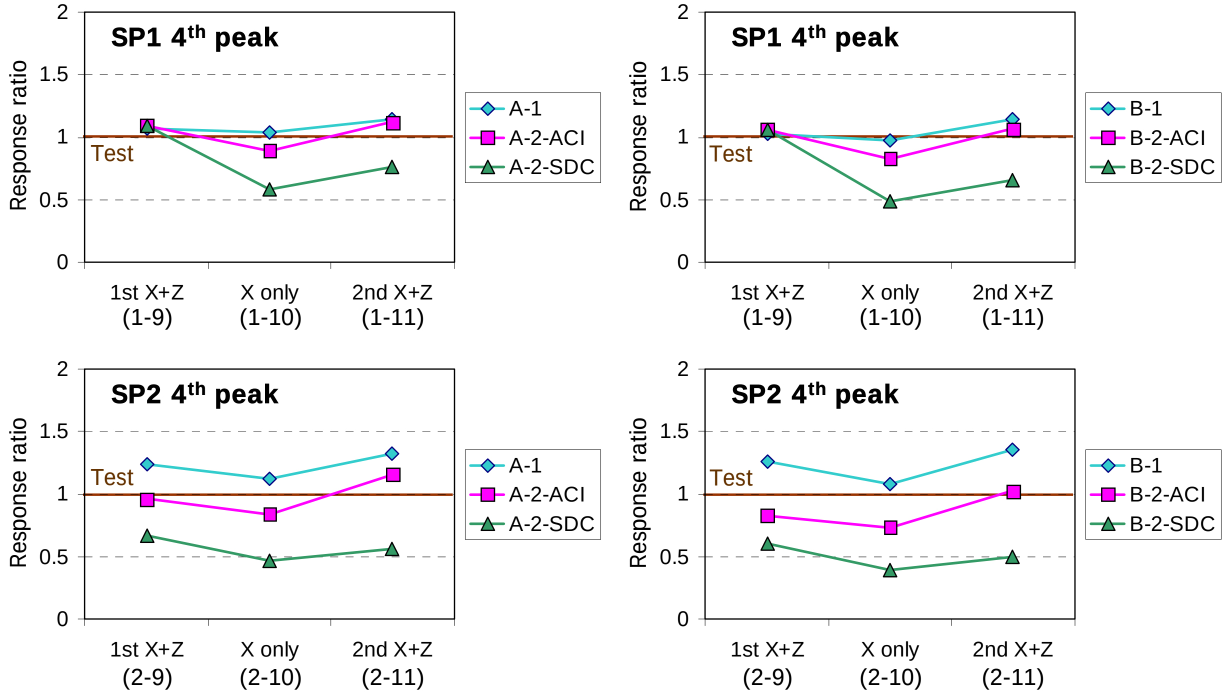

Fig. 6.30 Comparison of base moment ratios between the computational models to the test data at the 4th peak under the 125%-scale motions

6.4.2.3 Bending Moment at the Top

The bending moment at the top of the column is discussed in this section. Fig. 6.31 compares the test results and the top moment responses obtained from Models A-1 and B-1. Compared to the base moment responses, the top moment has noticeable high-frequency content which is due to the effect of the top mass rotational mode of vibration on the bending moment at the top of the column. In general, the analytical models are successful in the incorporation of this effect.

Fig. 6.32 presents the top moment responses of each model subjected to 125%-scale motions. In Fig. 6.32(a), the responses under '1st X+Z' are compared to the test data. The 3rd peak, denoted as '3', is the maximum and it coincides with the time of maximum shear force. Although the models underestimate the bending moment at this peak, they capture the variation of the bending moment with time very well. Fig. 6.35 compares the response ratios of each model to the test data at peak '3'. Similar to the previous cases, the order of these ratios is as follows: A-1 > A-2-ACI > A-2-SDC (or B-1 > B-2-ACI > B-2-SDC) in most cases.

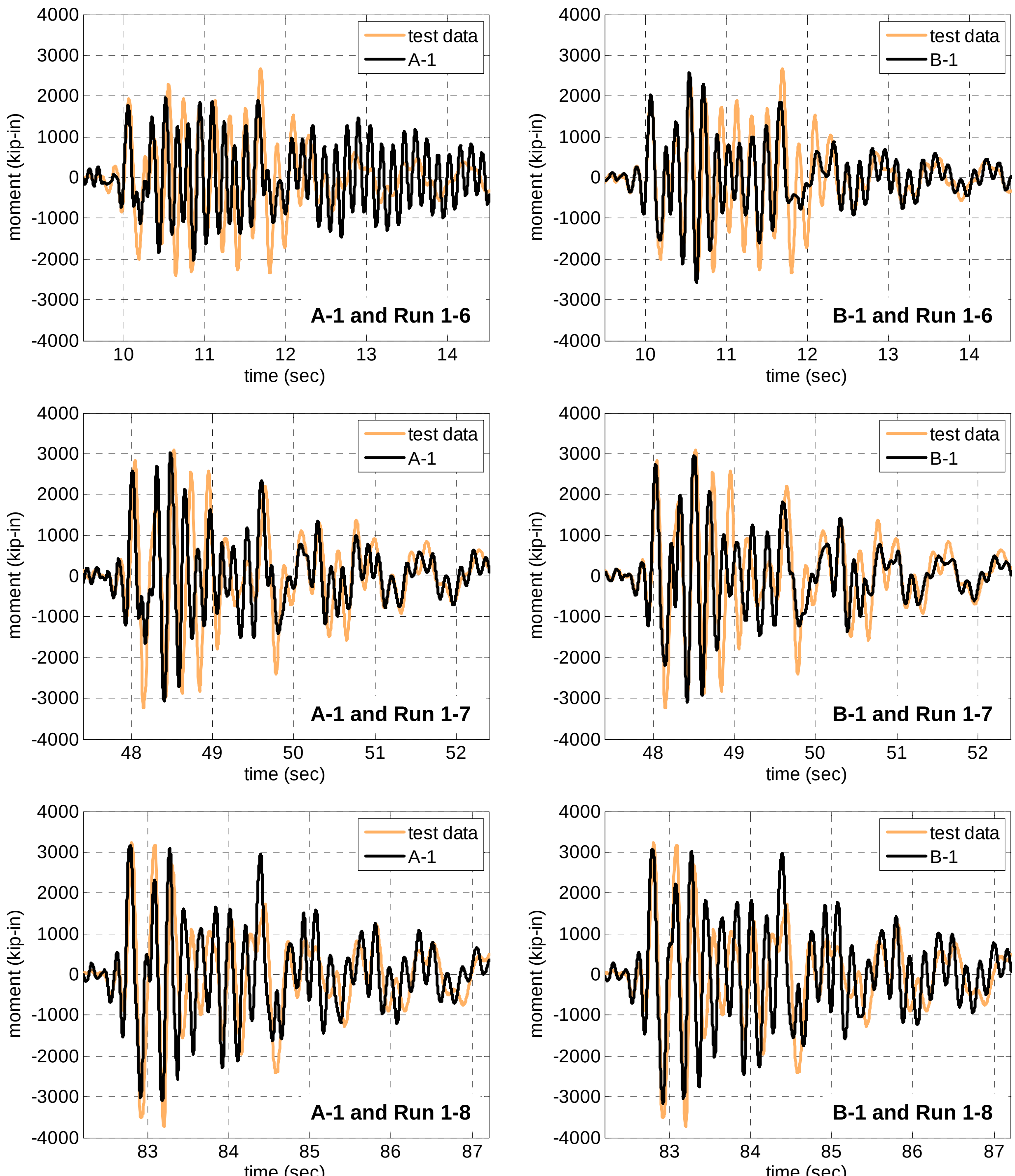

Fig. 6.31 Comparison of bending moment histories at the top of SP1 subjected to 50%, 70%, and 95%-scale motions

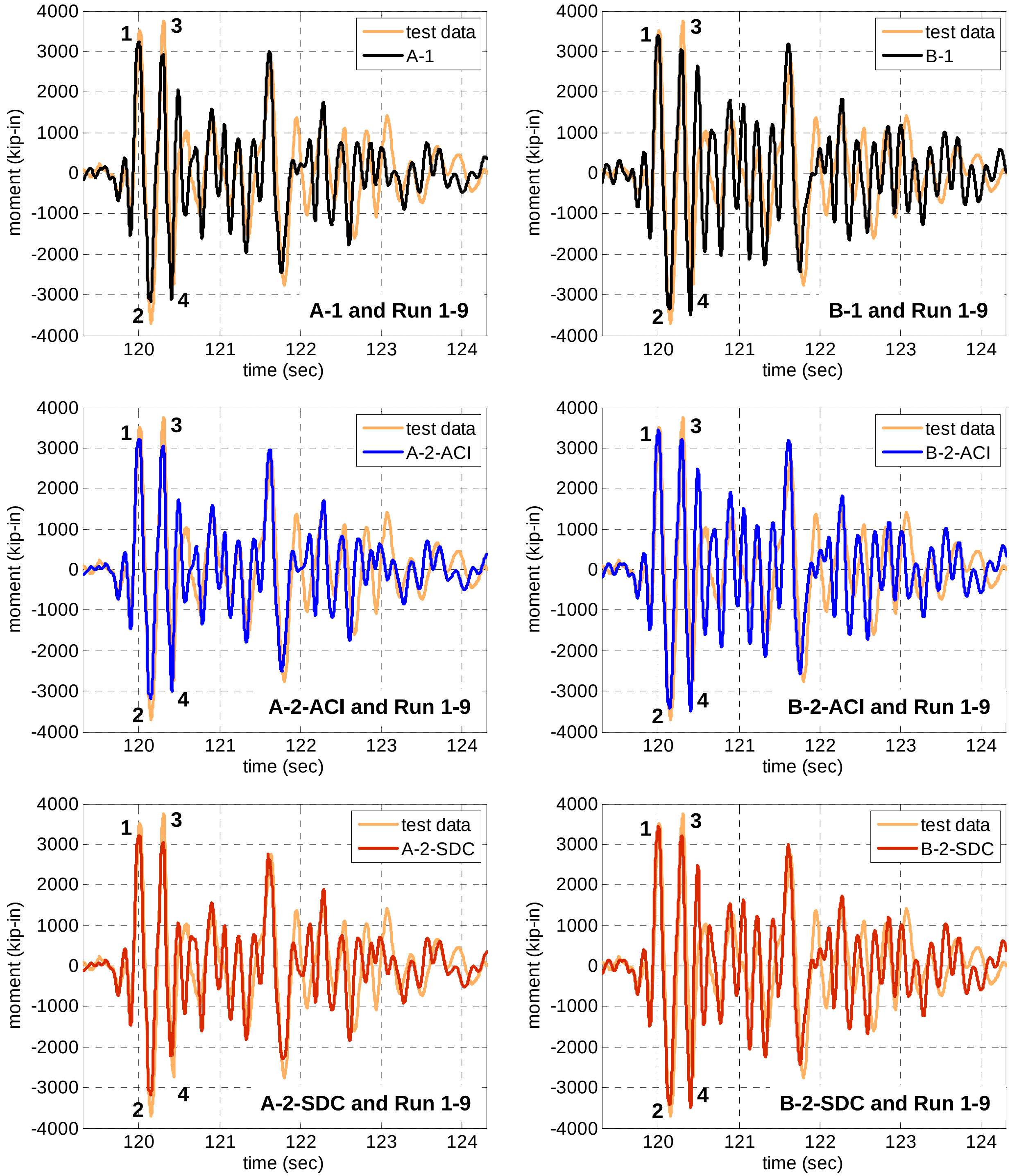

(a) 125% 1st X+Z

Fig. 6.32 Comparison of bending moment histories at the top of SP1 subjected to 125%-scale motions

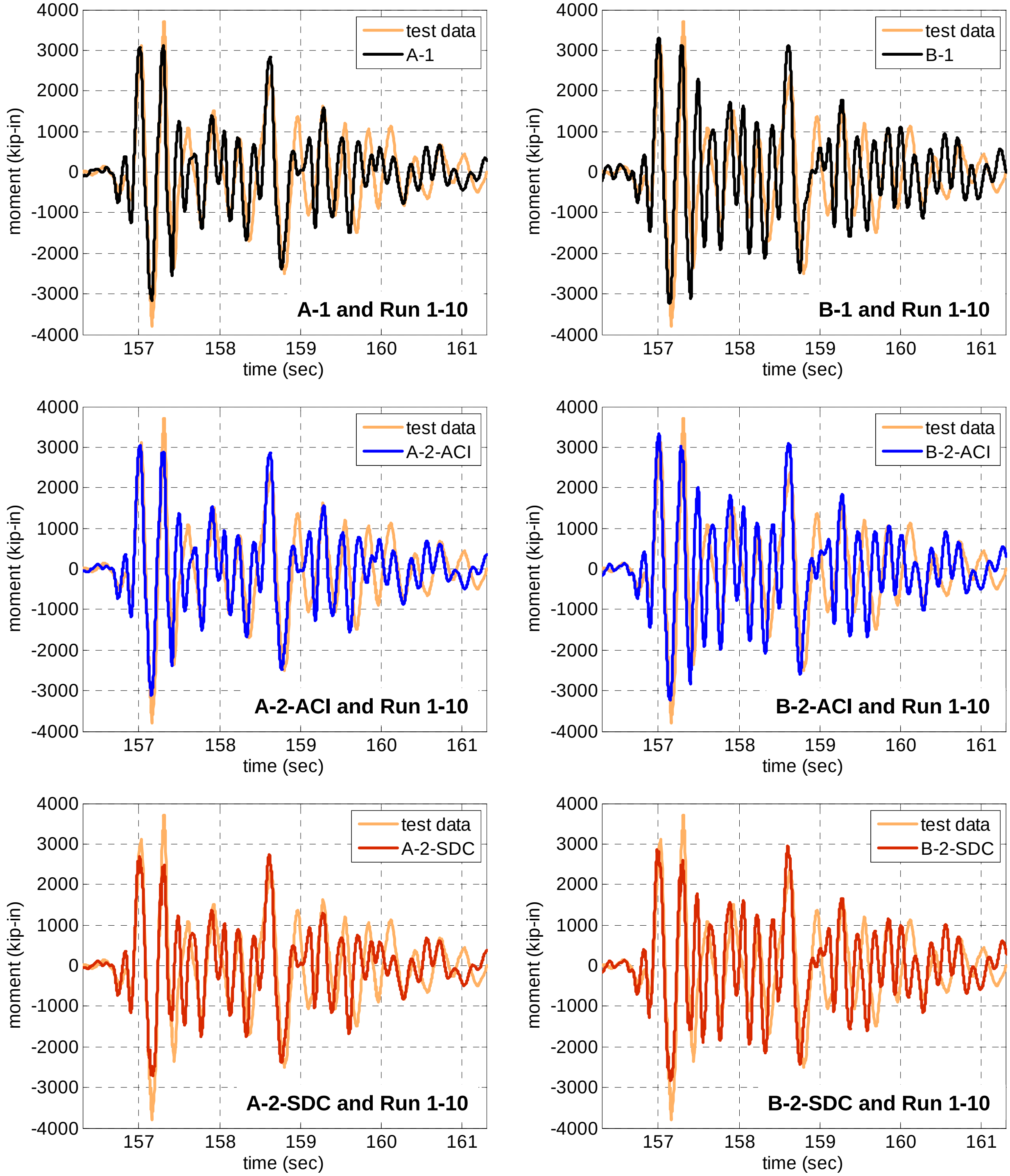

(b) 125% X only

Fig. 6.32 Comparison of bending moment histories at the top of SP1 subjected to 125%-scale motions (continued)

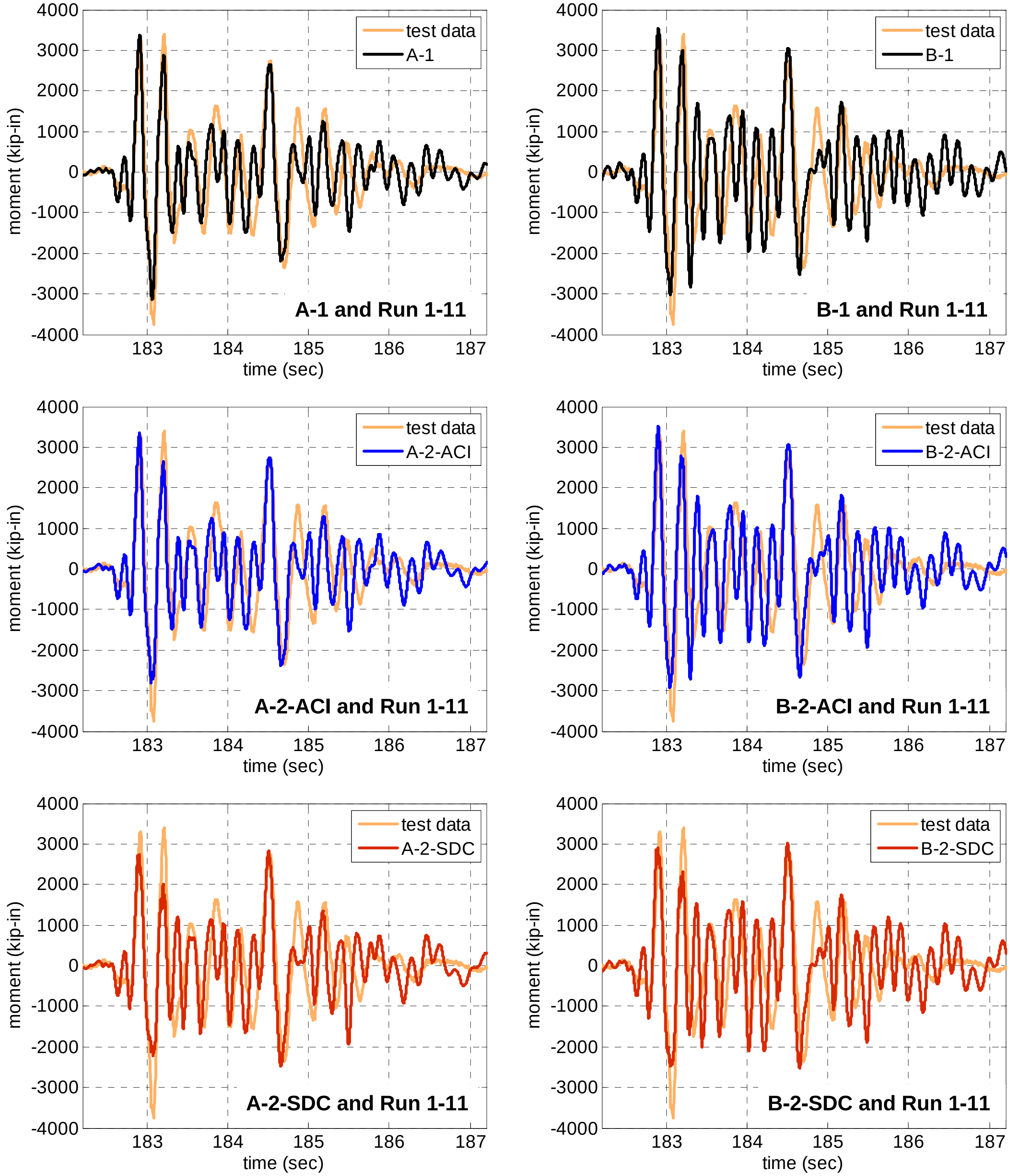

(c) 125% 2nd X+Z

Fig. 6.32 Comparison of bending moment histories at the top of SP1 subjected to 125%-scale motions (continued)

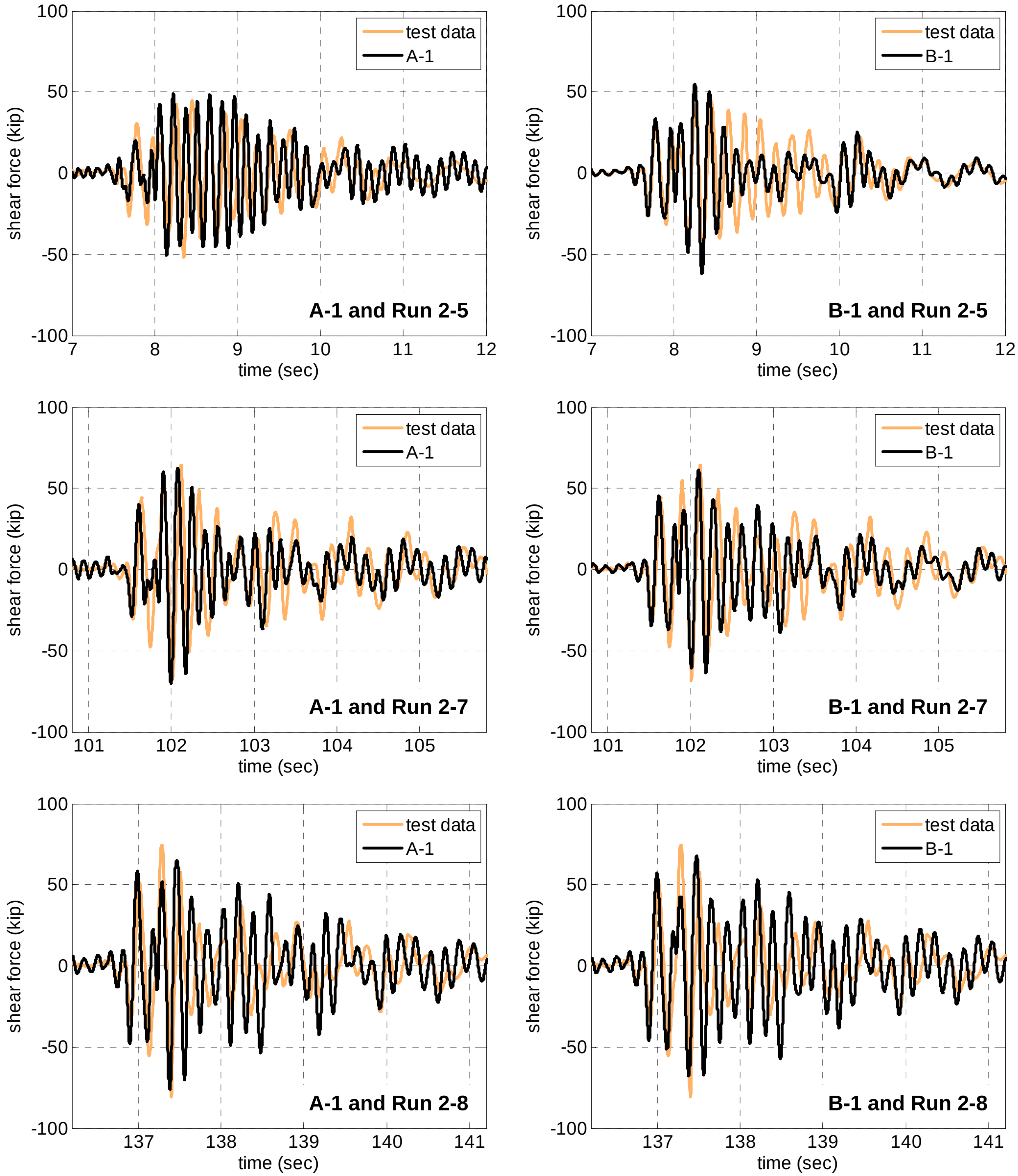

Fig. 6.33 Comparison of bending moment histories at the top of SP2 subjected to 50%, 70%, and 95%-scale motions

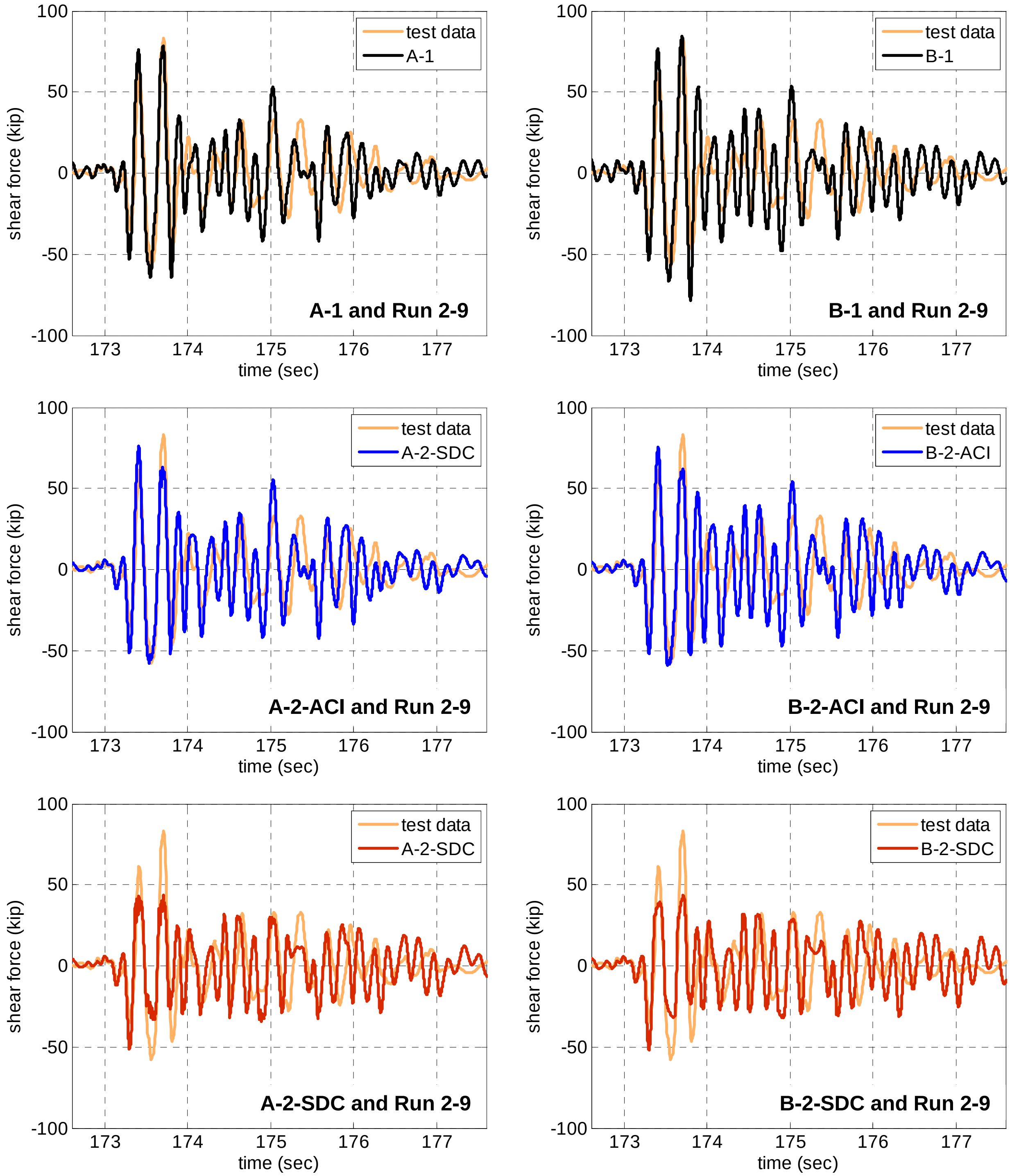

(a) 125% 1st X+Z

Fig. 6.34 Comparison of bending moment histories at the top of SP2 subjected to 125%-scale motions

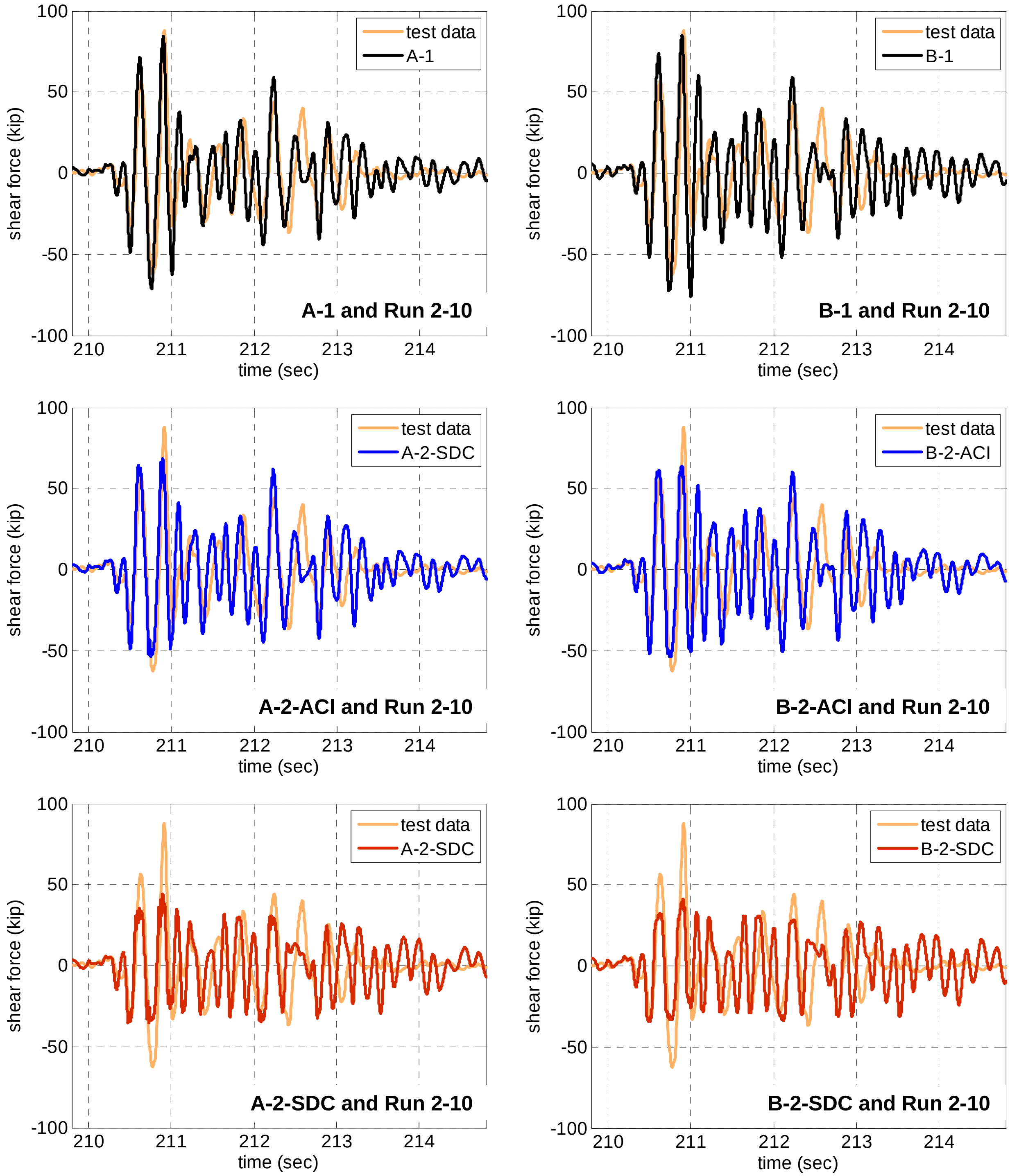

(b) 125% X only

Fig. 6.34 Comparison of bending moment histories at the top of SP2 subjected to 125%-scale motions (continued)

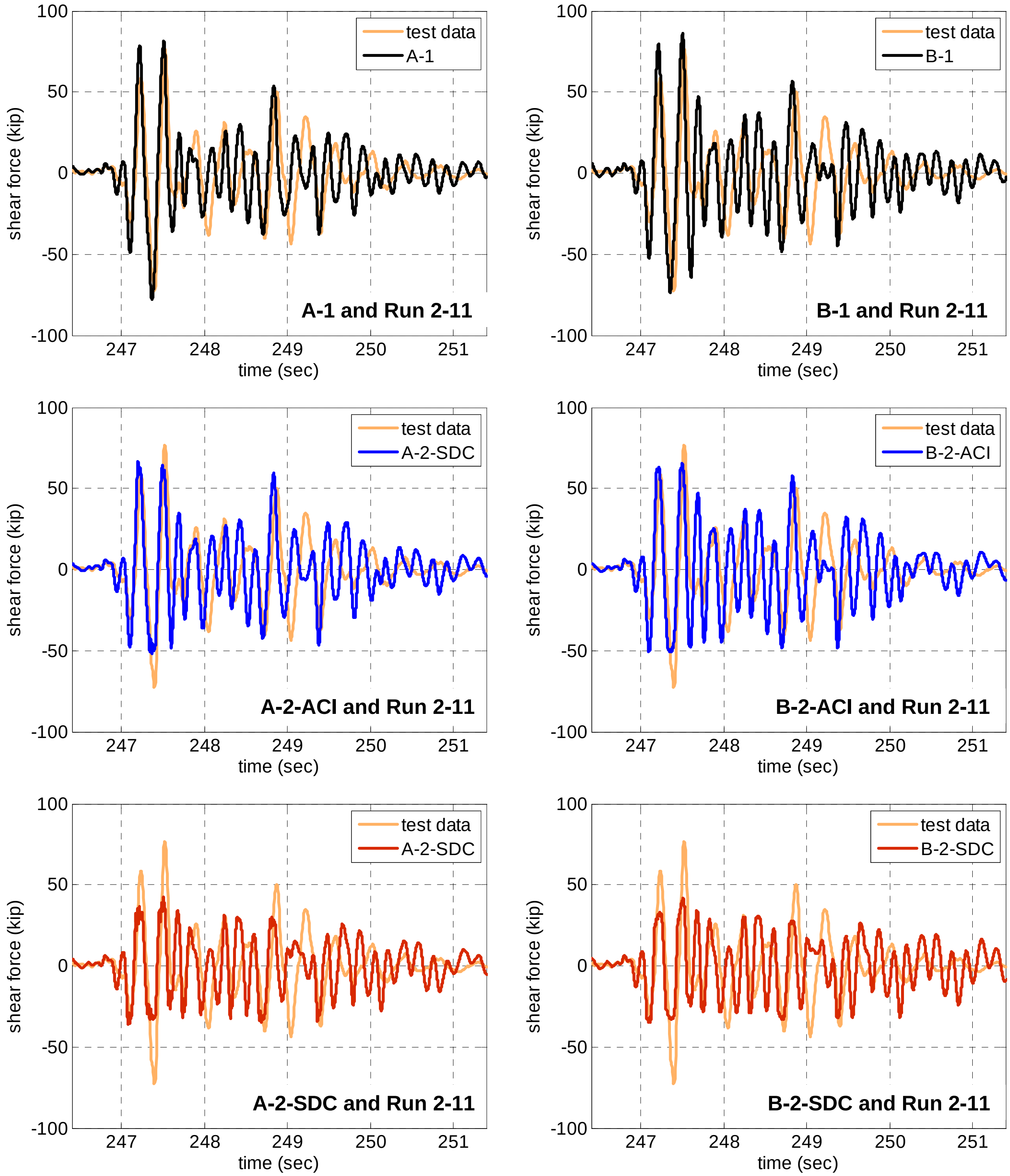

(c) 125% 2nd X+Z

Fig. 6.34 Comparison of bending moment histories at the top of SP2 subjected to 125%-scale motions (continued)

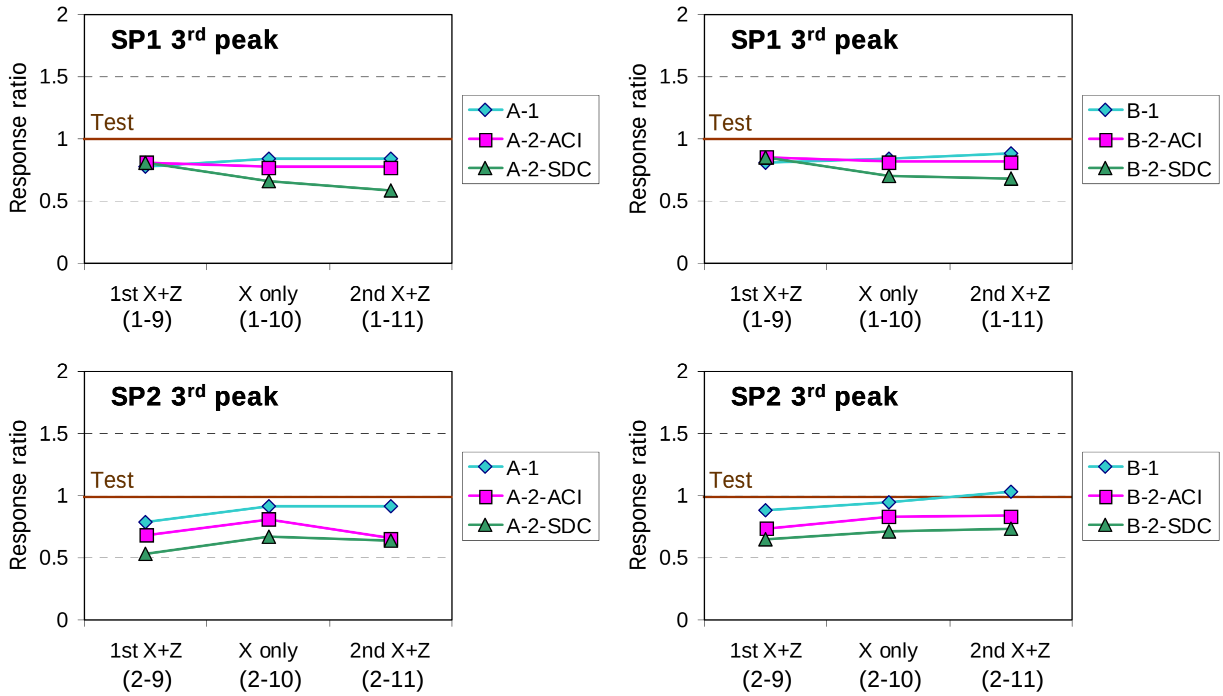

Fig. 6.35 Comparison of top moment ratios between the computational models to the test data at the 3rd peak under the 125%-scale motions

6.4.2.4 Lateral Displacement at the Top

In this section, the top displacement histories in the X direction obtained from the computational models are compared to those measured during the tests. Fig. 6.36 presents the lateral displacement histories of SP1 subjected to 50%, 70%, and 95%-scale motions and Fig. 6.37 presents the displacement histories for the 125%-scale motions. Despite the slight frequency shifts at the second half of motions 1-8 and 1-9 and some difference in the negative peak displacement of motion 1-9, models A-1, B-1, A-2-ACI, and B-2-ACI can be accepted to result in sufficiently accurate displacement estimations. Differences between the test data and A-2-SDC and B-2-SDC models are more significant for motion 1-9. Presence of a shear spring improves the results considerably for motion 1-10. Both of the models with ACI and SDC springs provide displacement histories close to the test data with the A-2-ACI model resulting in the best predictions. A similar observation can be stated for motion 1-11. It should be noted that model A-2-ACI which provides the best predictions for motions 1-10 and 1-11 captures the positive displacements with very good accuracy. However, this model underestimates the negative displacements. Overall, displacement predictions provided by the analytical models can be regarded as sufficiently accurate with the presence of a shear spring resulting in an improvement in the predictions.

Similar to SP1, model predictions of SP2 for the motions 2-5 to 2-9 are accurate as shown in Fig. 6.38 and Fig. 6.39(a). However, for ground motions 2-10 and 2-11, the presence of a shear spring is not sufficient to improve the predictions where the responses obtained from the analytical models are different from the test results, refer to Fig. 6.38(b) and (c).

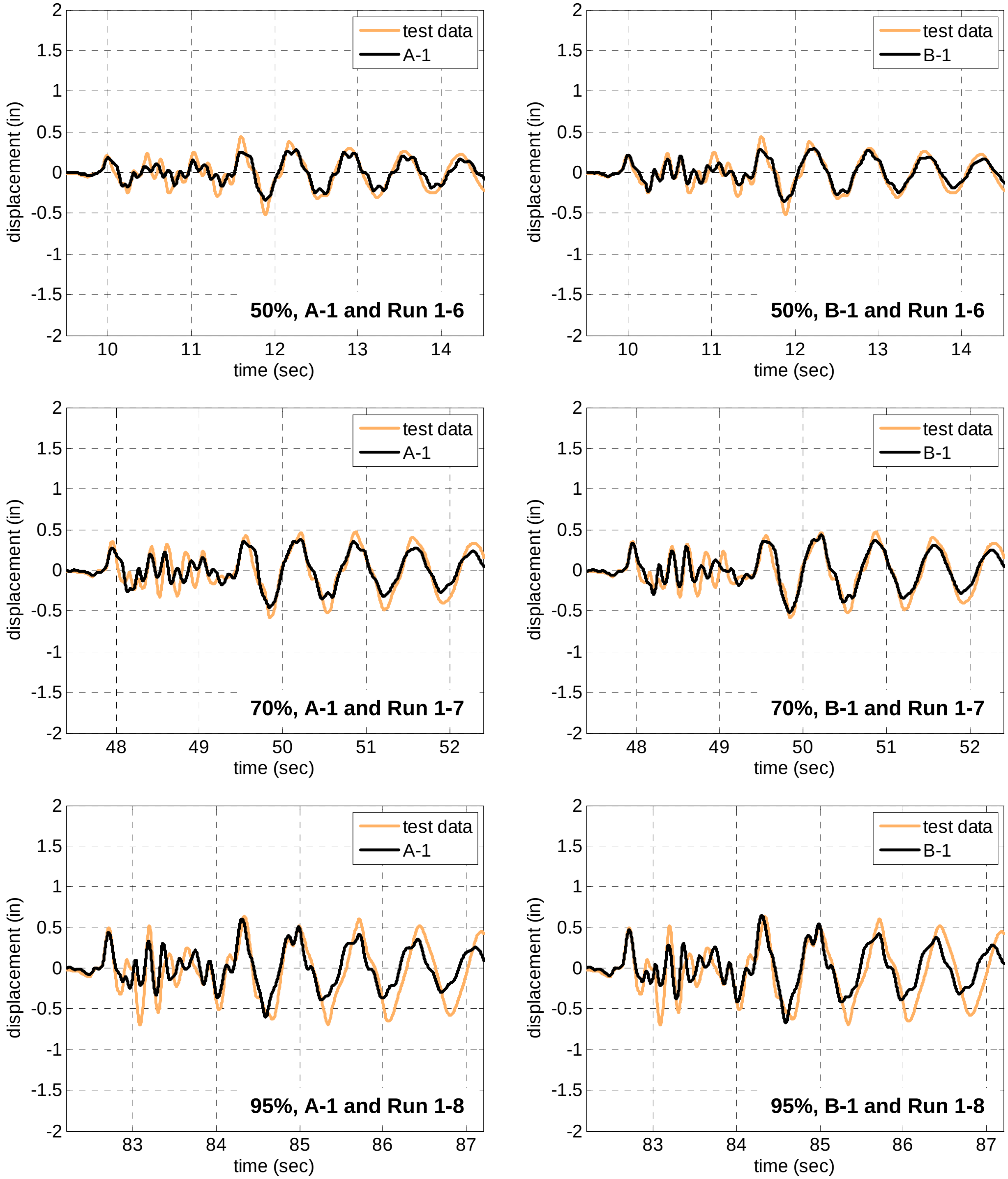

Fig. 6.36 Comparison of lateral displacement histories of SP1 subjected to 50%, 70%, and 95%-scale motions

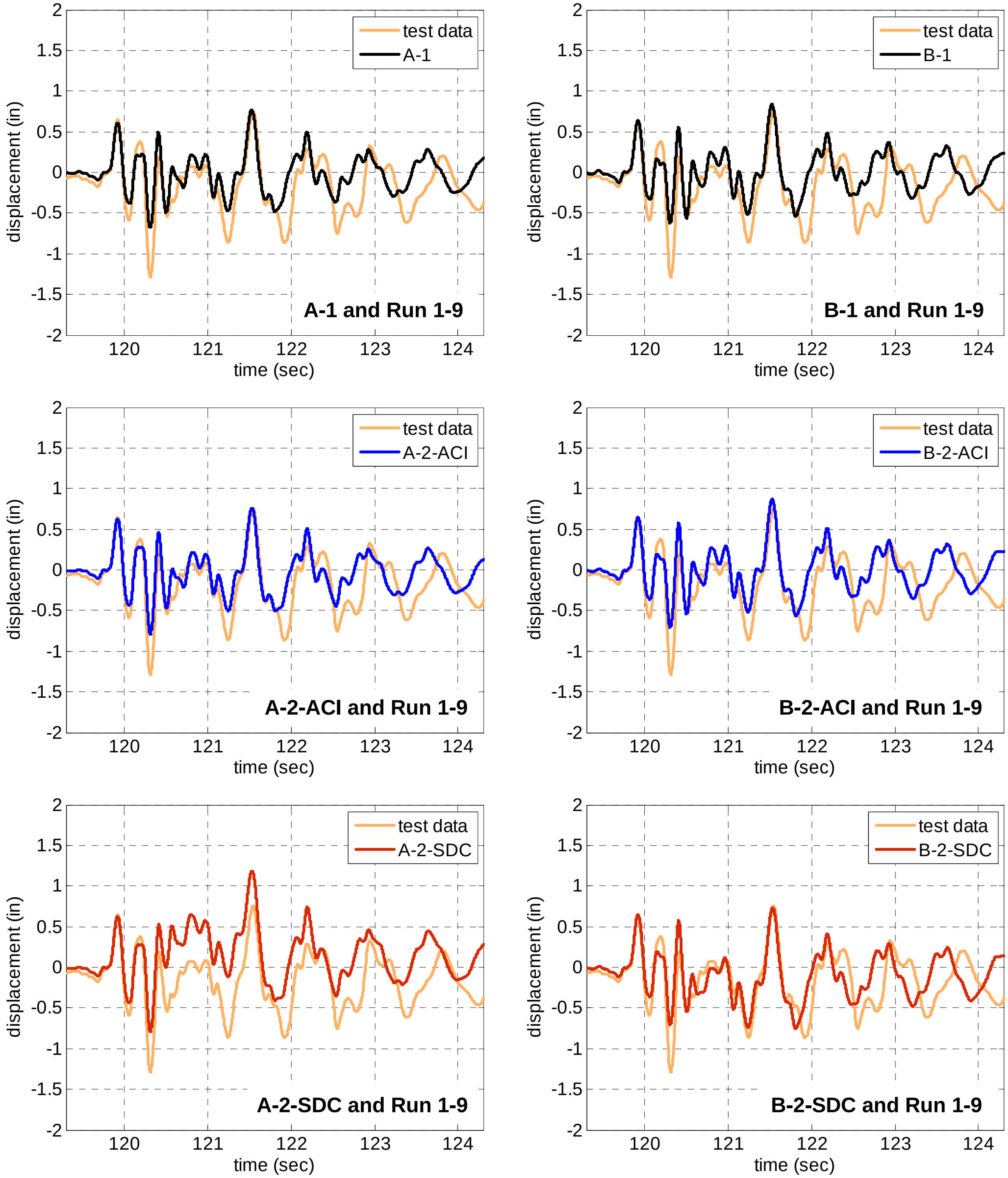

(a) 125% 1st X+Z

Fig. 6.37 Comparison of lateral displacement histories of SP1 subjected to 125%-scale motions

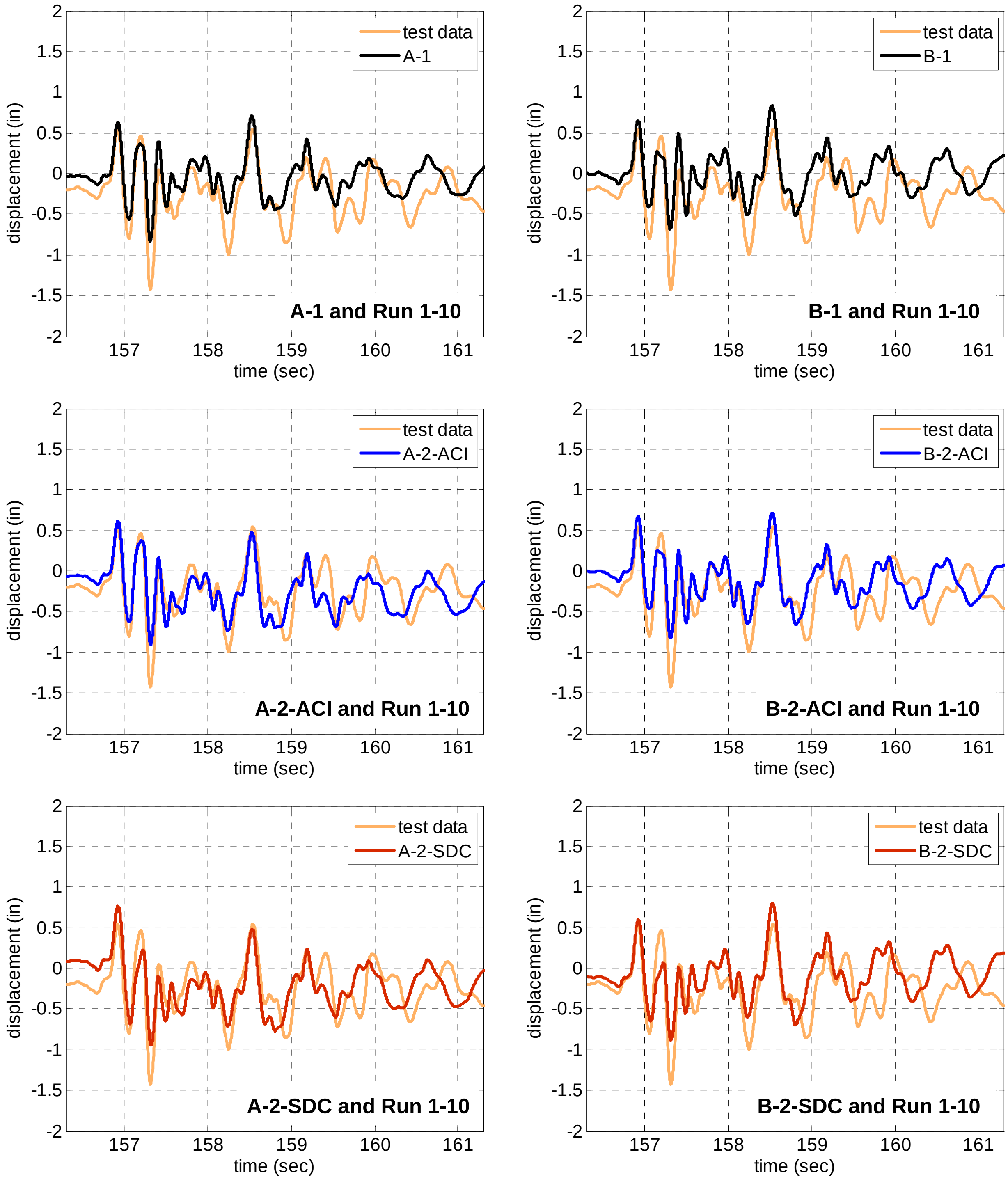

(b) 125% X only

Fig. 6.37 Comparison of lateral displacement histories of SP1 subjected to 125%-scale motions (continued)

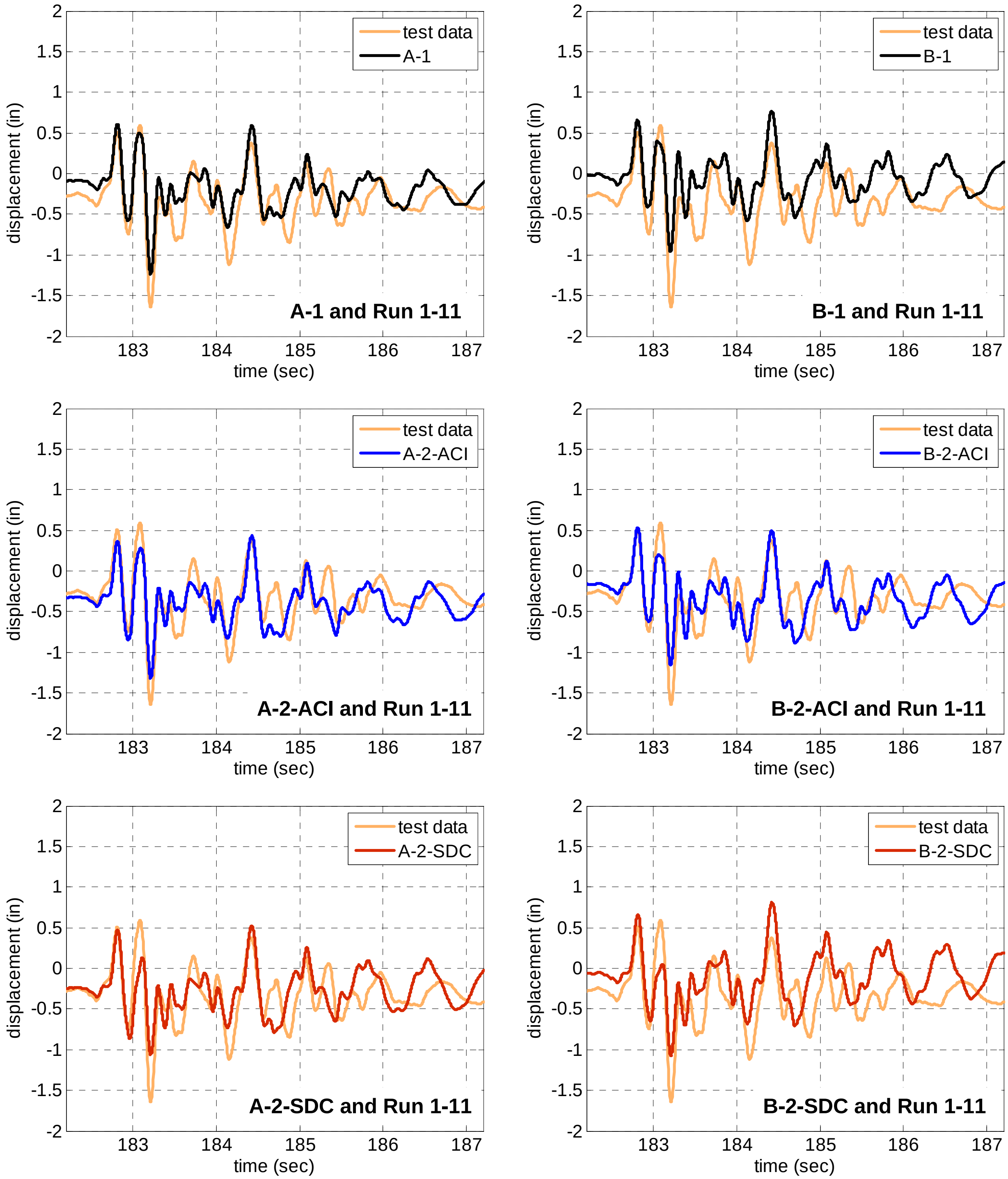

(c) 125% 2nd X+Z

Fig. 6.37 Comparison of lateral displacement histories of SP1 subjected to 125%-scale motions (continued)

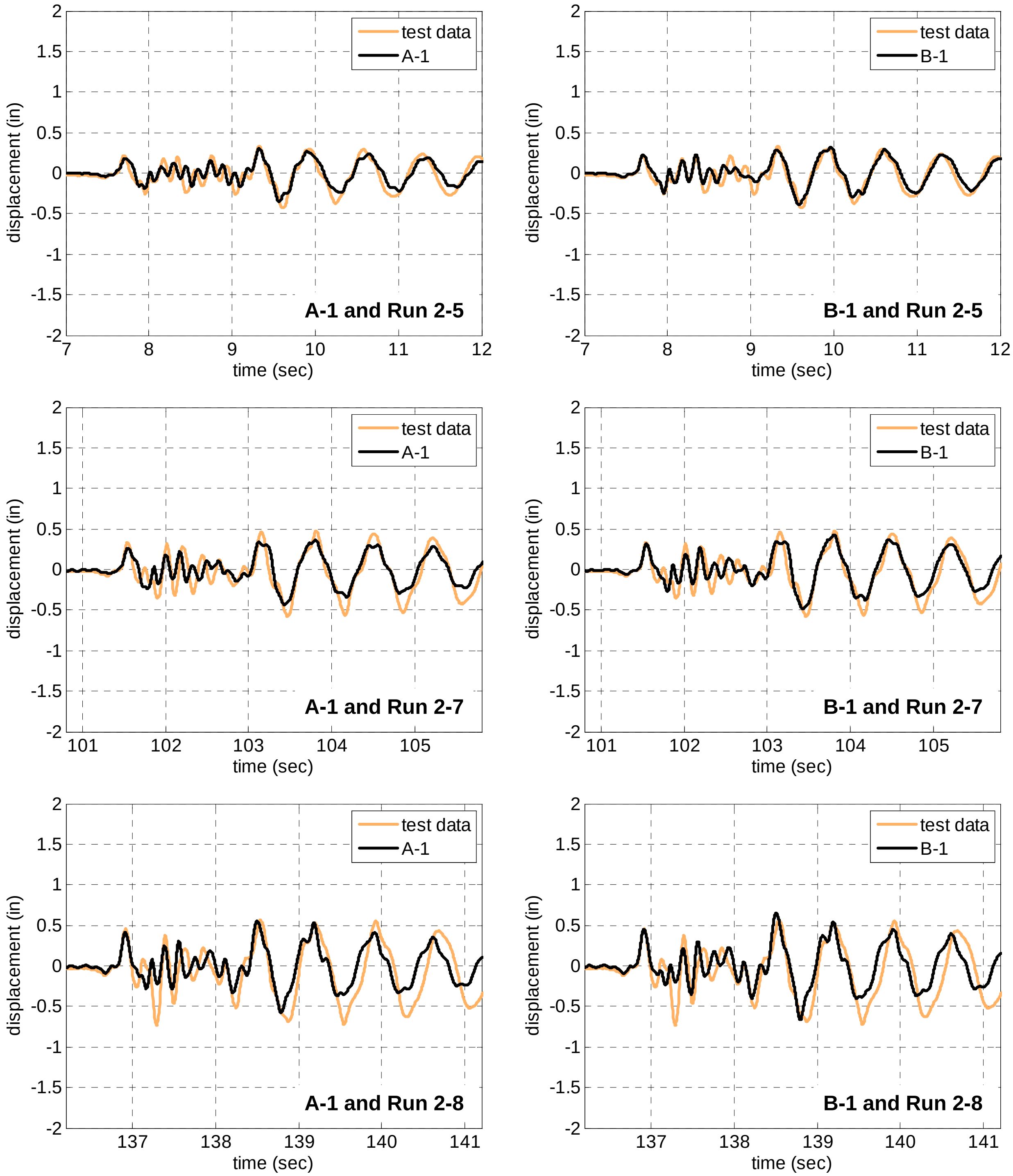

Fig. 6.38 Comparison of lateral displacement histories of SP2 subjected to 50%, 70%, and 95%-scale motions

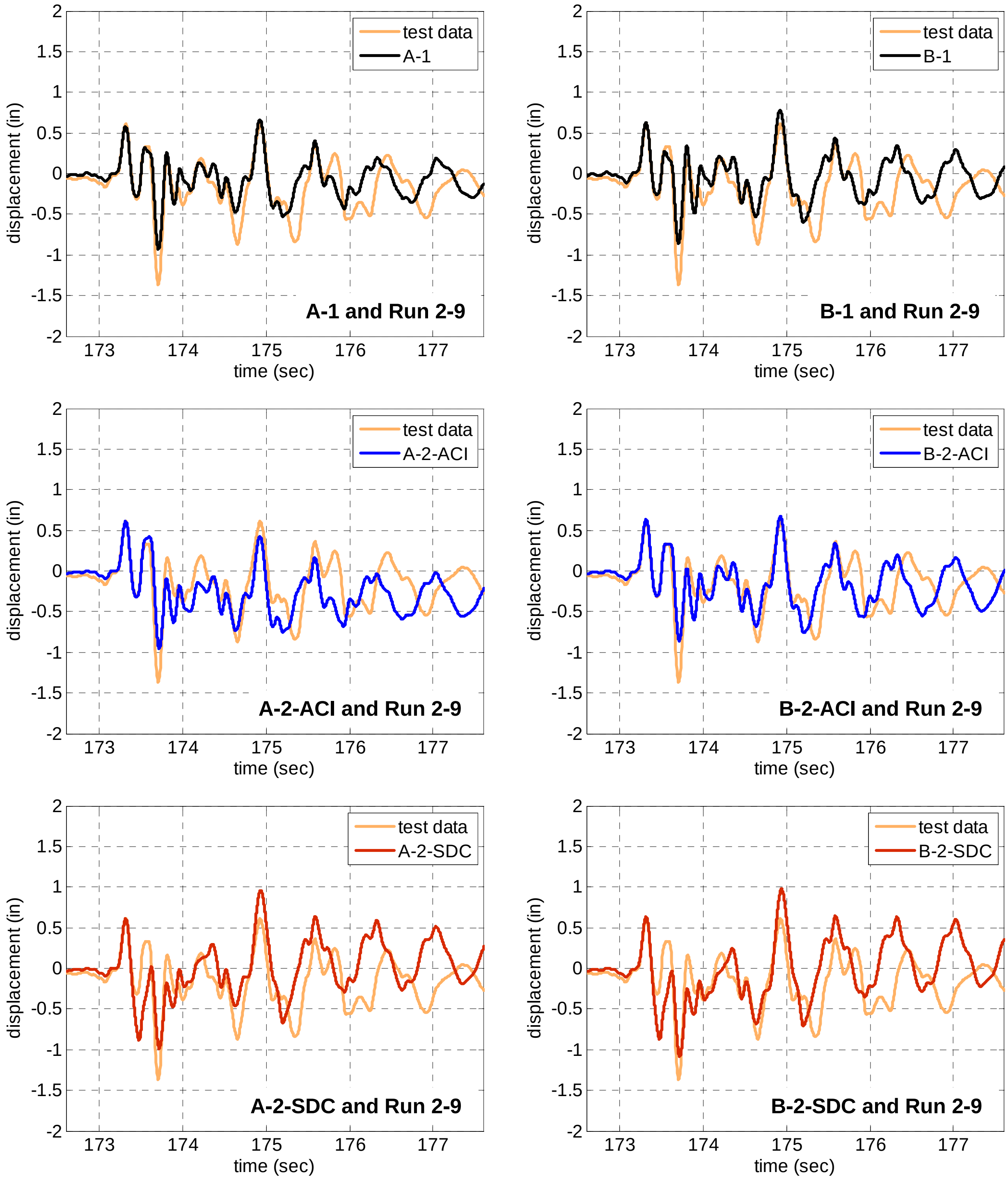

(a) 125% 1st X+Z

Fig. 6.39 Comparison of lateral displacement histories of SP2 subjected to 125%-scale motions

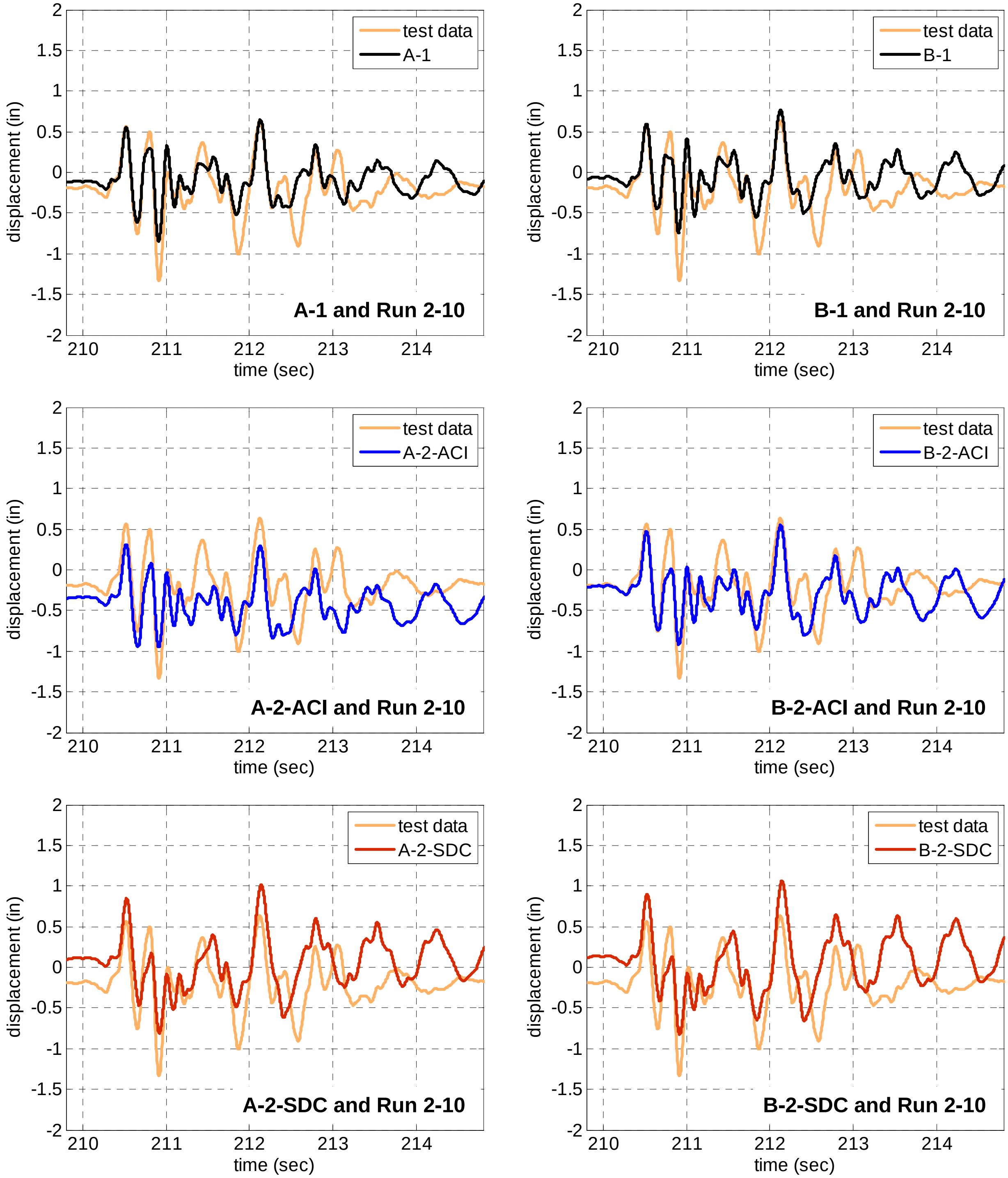

(b) 125% X only

Fig. 6.39 Comparison of lateral displacement histories of SP2 subjected to 125%-scale motions (continued)

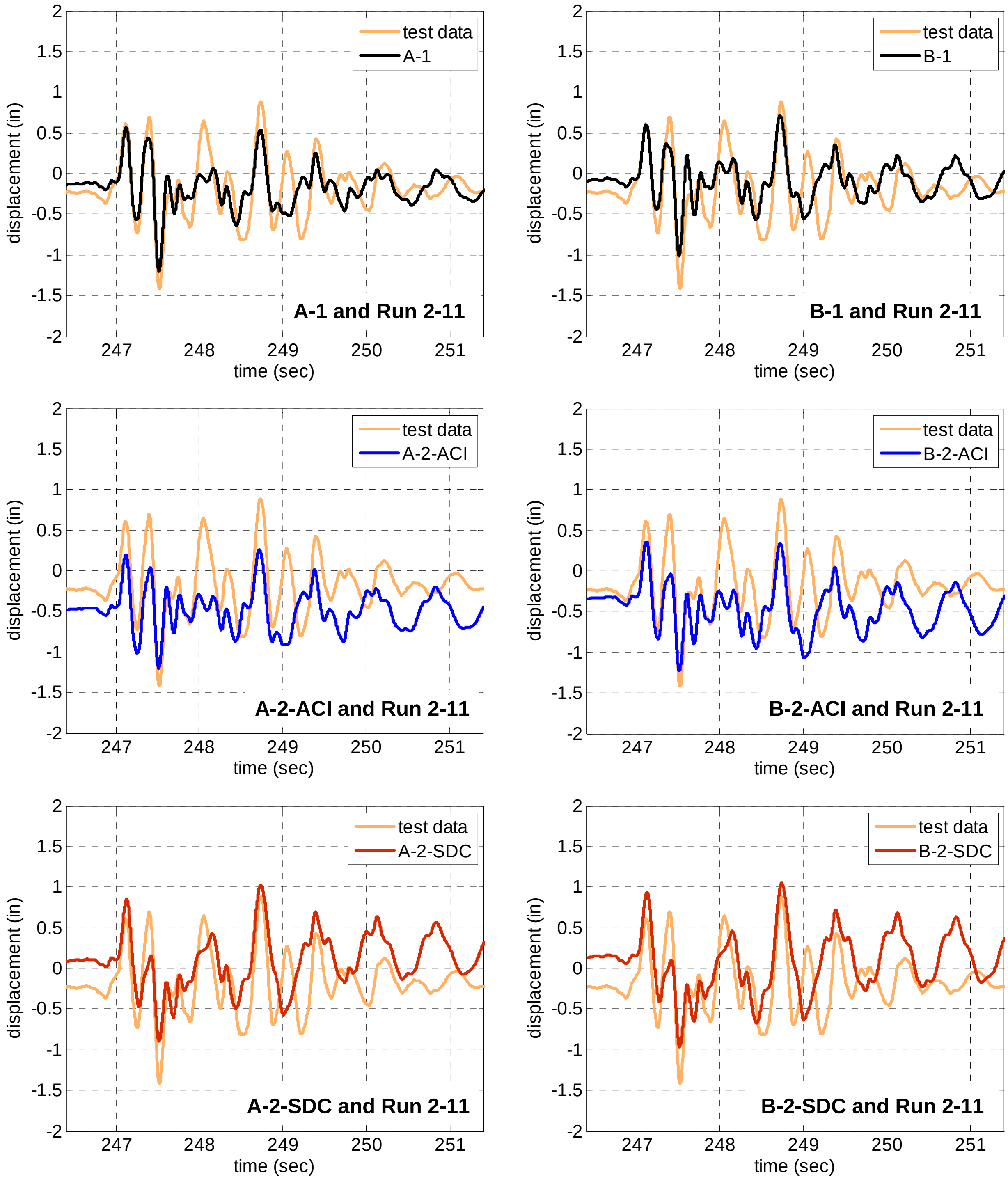

(c) 125% 2nd X+Z

Fig. 6.39 Comparison of lateral displacement histories of SP2 subjected to 125%-scale motions (continued)

6.4.2.5 Vertical Displacement at the Top

The vertical displacement responses from the computational models are compared to the test data in this section. A-1 or B-1 models for SP1 do not provide an estimate close to the vertical displacement measured in the 50%, 70%, and 95%-scale tests (Fig. 6.40), since crack opening (especially the shear cracks on the east and west sides) is not adequately modeled in a fiber section analysis. This trend continues for the higher-intensity tests. Fig. 6.41 shows the computational results for SP1 under the 125%-scale motions. Under '1st X+Z' motion, all six models have similar responses. It is interesting to note that all the analytical models not only predict smaller elongation compared to the test data but also the results indicate shortening for a duration of time which is not observed in the test data. This is mainly due to the lack of explicit consideration of the shear cracks and their openings in the analytical model. These observations are also valid for SP2 as shown in Fig. 6.42 and Fig. 6.43.

Errors in the vertical displacement prediction do not introduce significant problems regarding the main aim of the study which is the investigation of the effect of axial tension on the shear capacity. Therefore, further improvement of the vertical displacement predictions using modifications in the model is not considered since these further modifications would be beyond the scope of fiber modeling and would require more detailed finite element models.

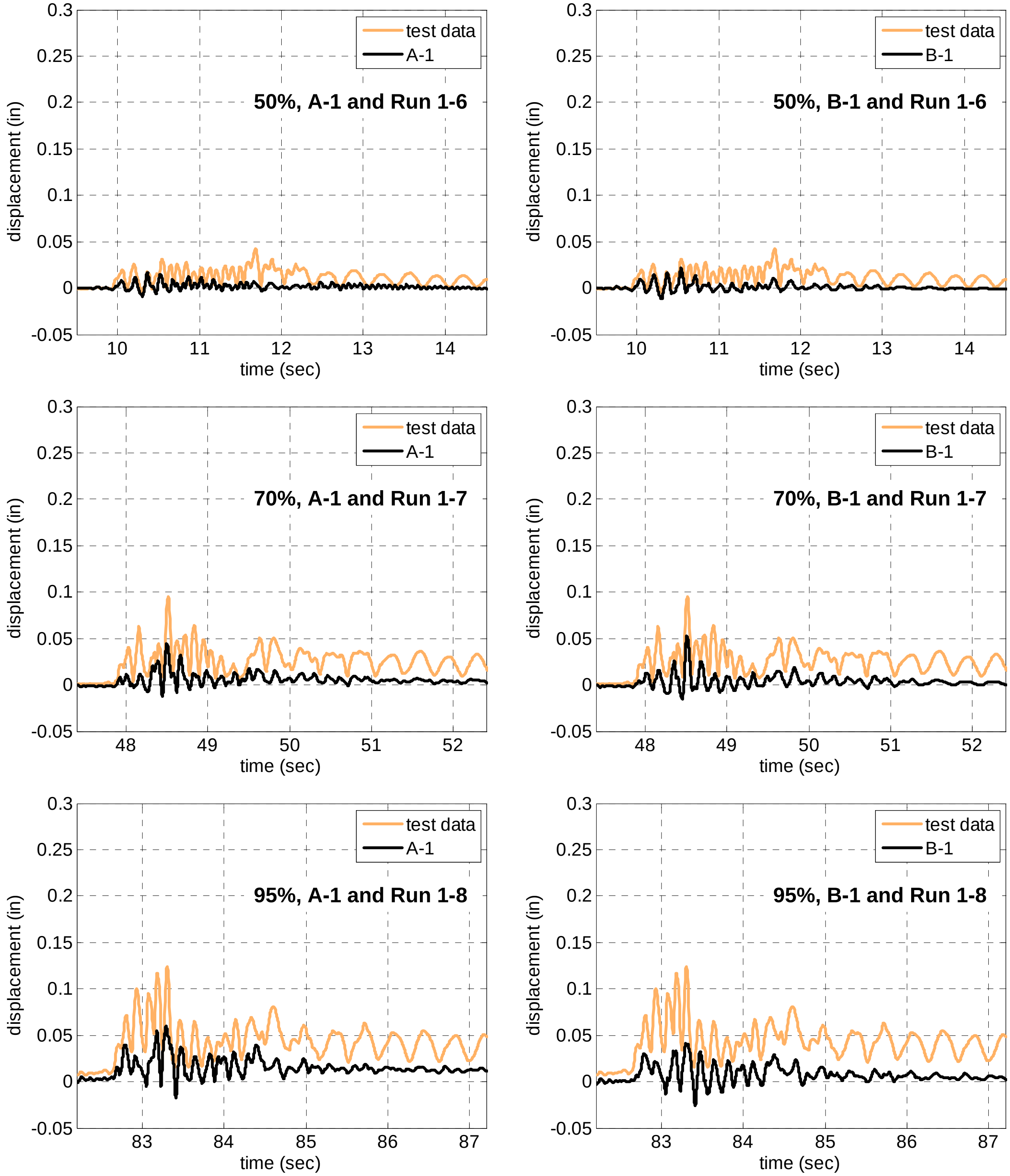

Fig. 6.40 Comparison of vertical displacement histories of SP1 subjected to 50%, 70%, and 95%-scale motions

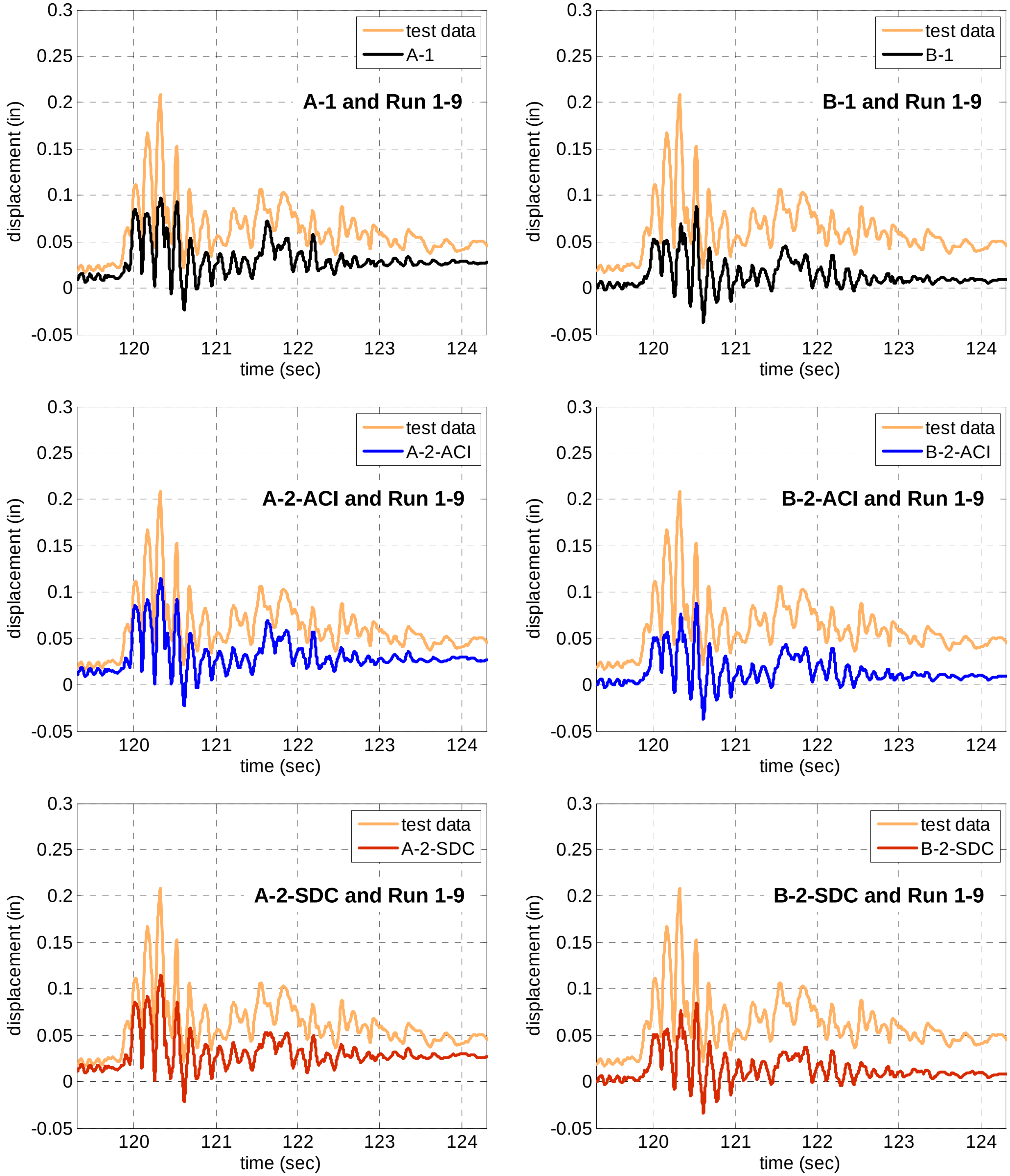

(a) 125% 1st X+Z

Fig. 6.41 Comparison of vertical displacement histories of SP1 subjected to 125%-scale motions

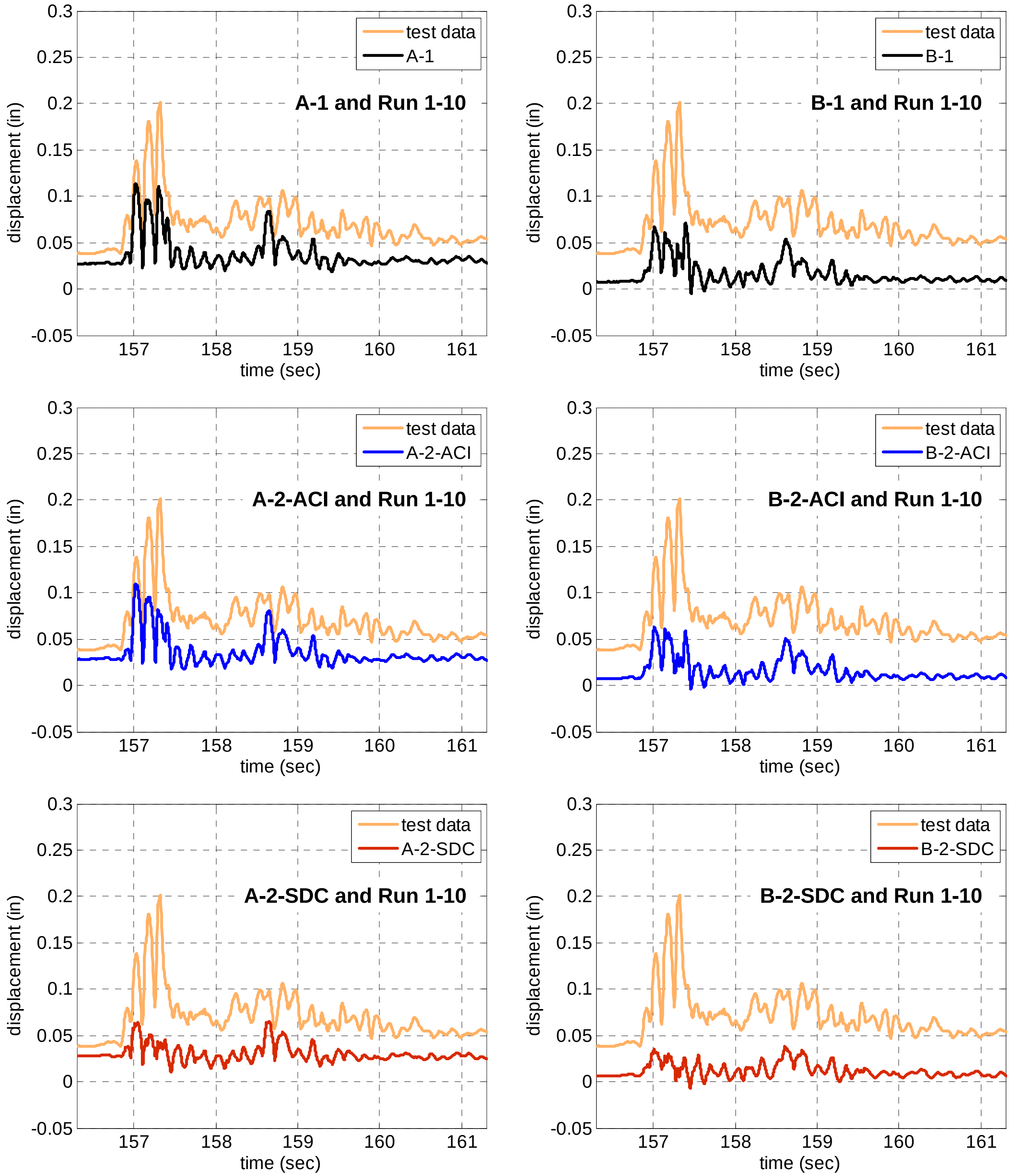

(b) 125% X only

Fig. 6.41 Comparison of vertical displacement histories of SP1 subjected to 125%-scale motions (continued)

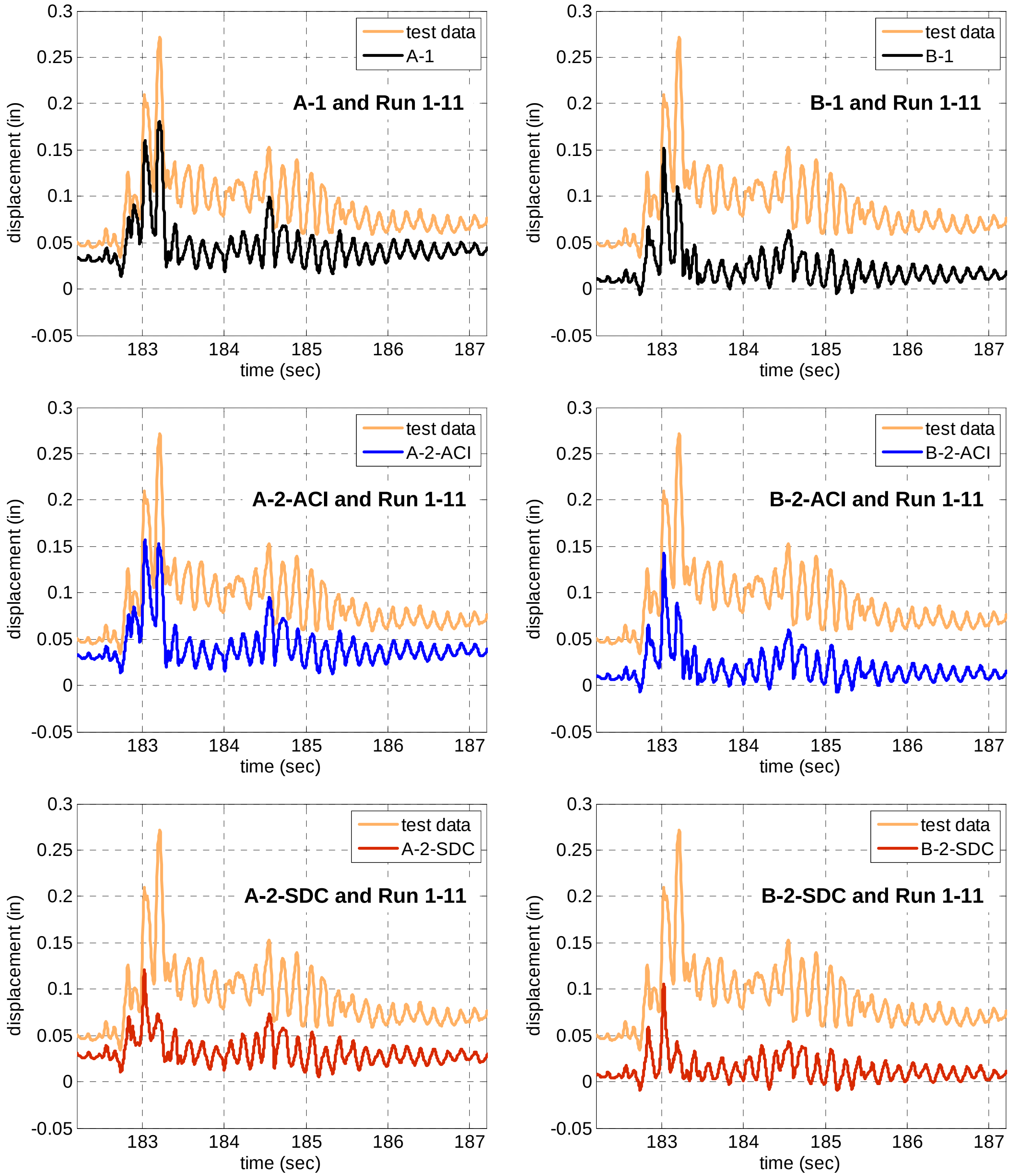

(c) 125% 2nd X+Z

Fig. 6.41 Comparison of vertical displacement histories of SP1 subjected to 125%-scale motions (continued)

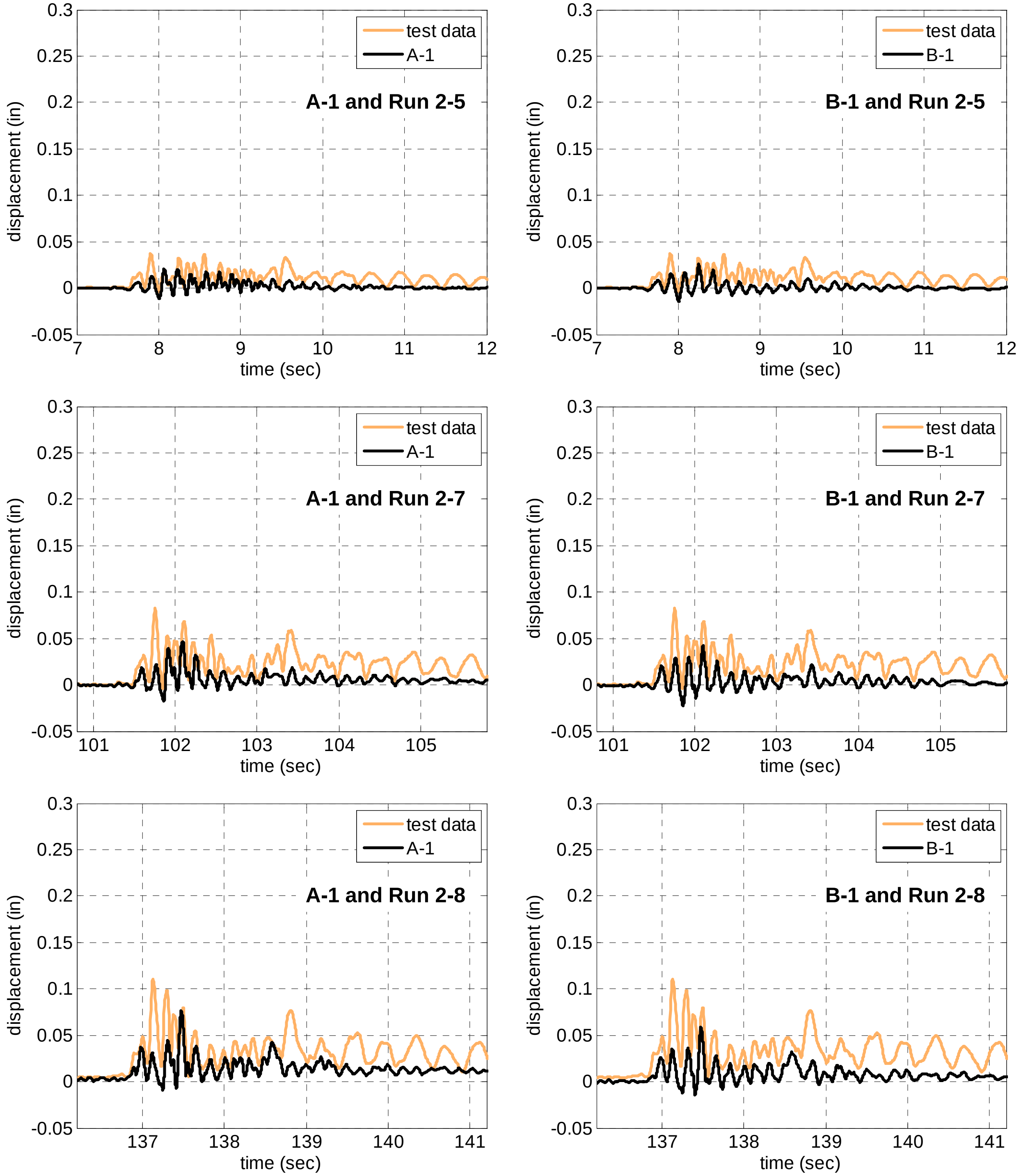

Fig. 6.42 Comparison of vertical displacement histories of SP2 subjected to 50%, 70%, and 95%-scale motions

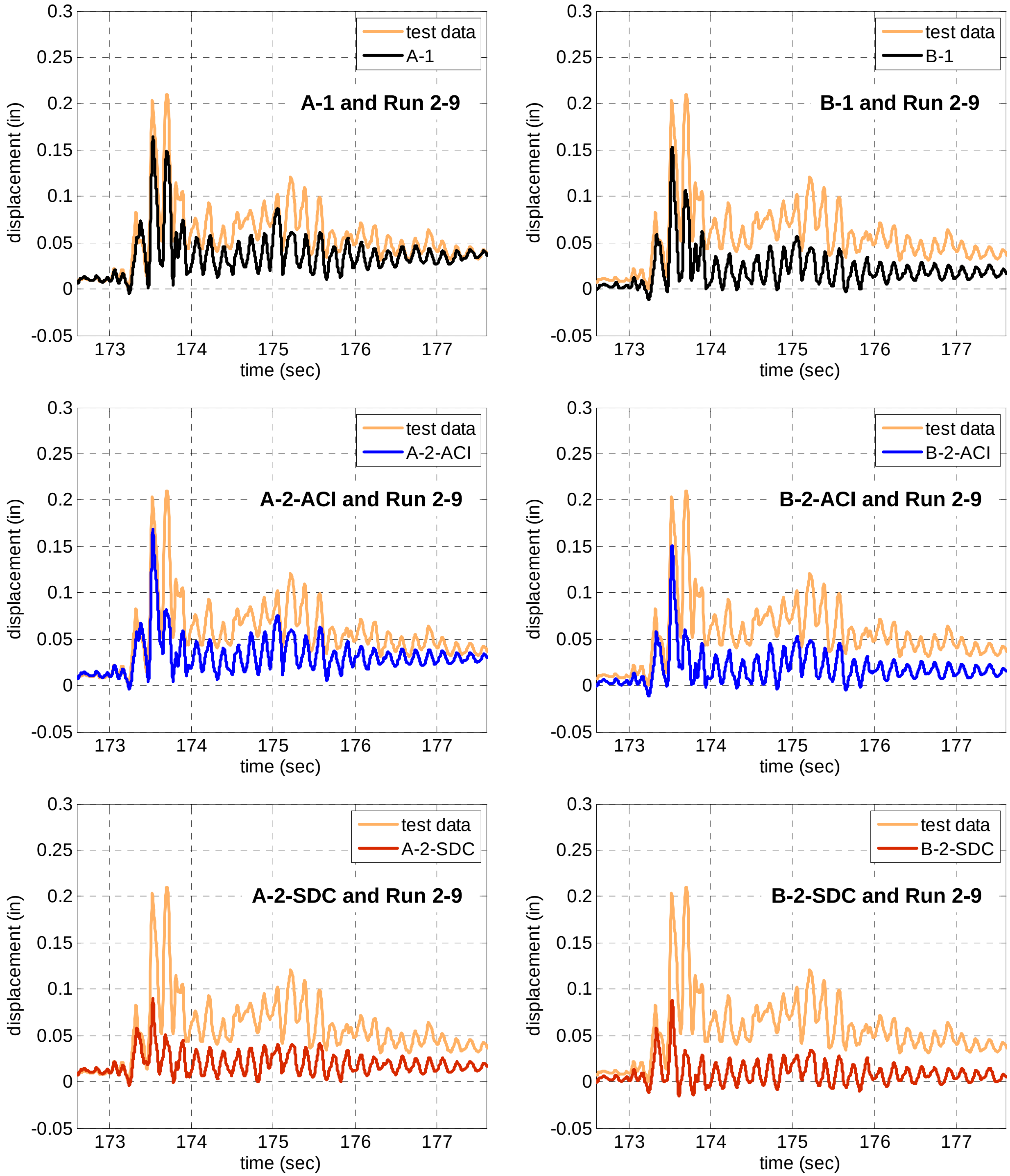

(a) 125% 1st X+Z

Fig. 6.43 Comparison of vertical displacement histories of SP2 subjected to 125%-scale motions

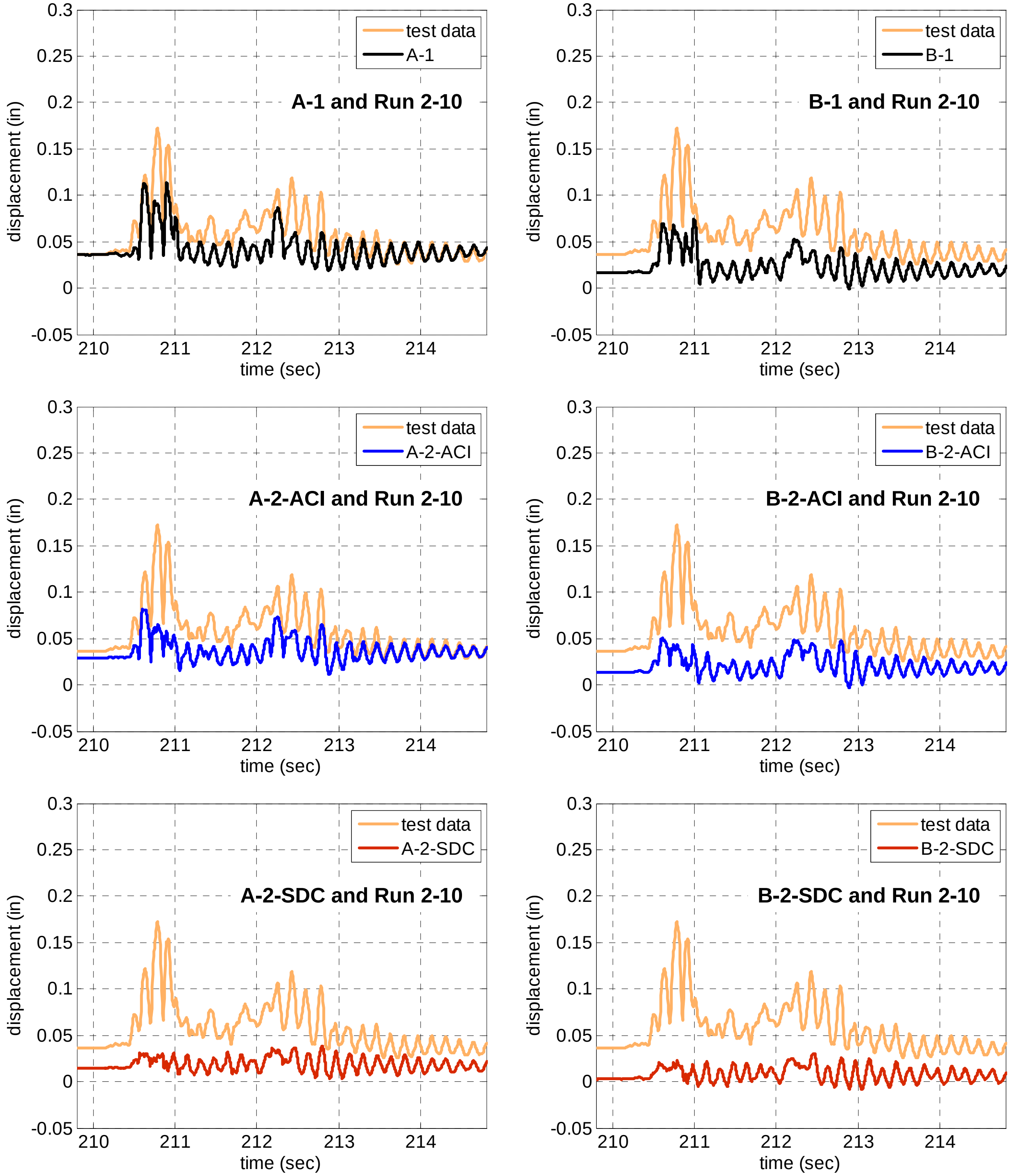

(b) 125% X only

Fig. 6.43 Comparison of vertical displacement histories of SP2 subjected to 125%-scale motions (continued)

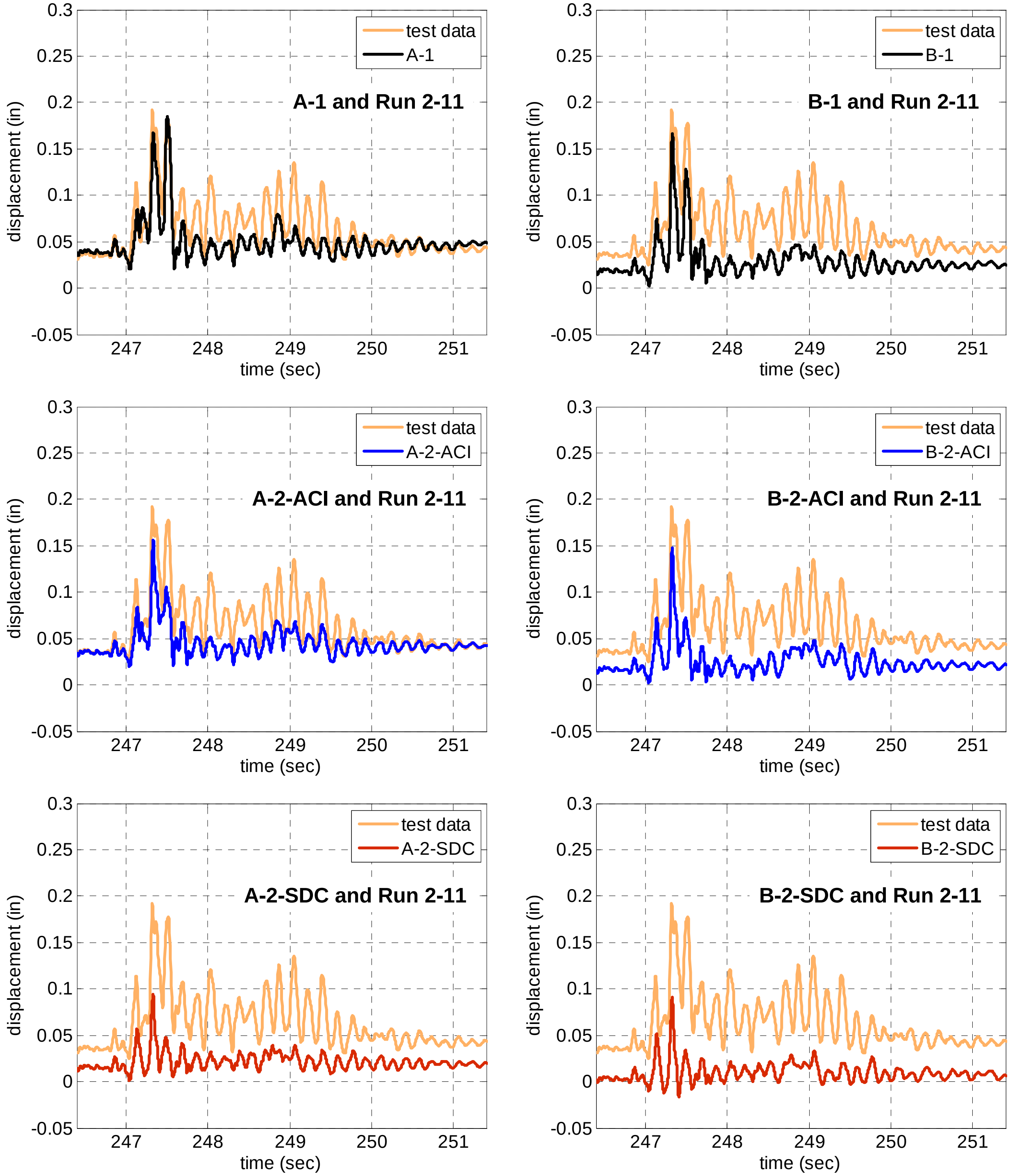

(c) 125% 2nd X+Z

Fig. 6.43 Comparison of vertical displacement histories of SP2 subjected to 125%-scale motions (continued)

6.4.2.6 Force-Displacement Relationships

Fig. 6.44 and Fig. 6.45 present the force-displacement relationship comparisons for SP1 and SP2, respectively, subjected to the 125%-scale motions. Effect of the shear spring in reducing the shear forces is once again observed in these figures. As indicated before, the ACI spring model achieves this reduction in a more accurate manner compared to the SDC spring model with both springs remaining on the conservative side. The flatness of the top and bottom parts of the relationships for the models with springs indicates the presence of more hardening However, since the shear spring dictates the response in the 125%-scale runs, strain hardening in flexural response becomes ineffective in changing this behavior.

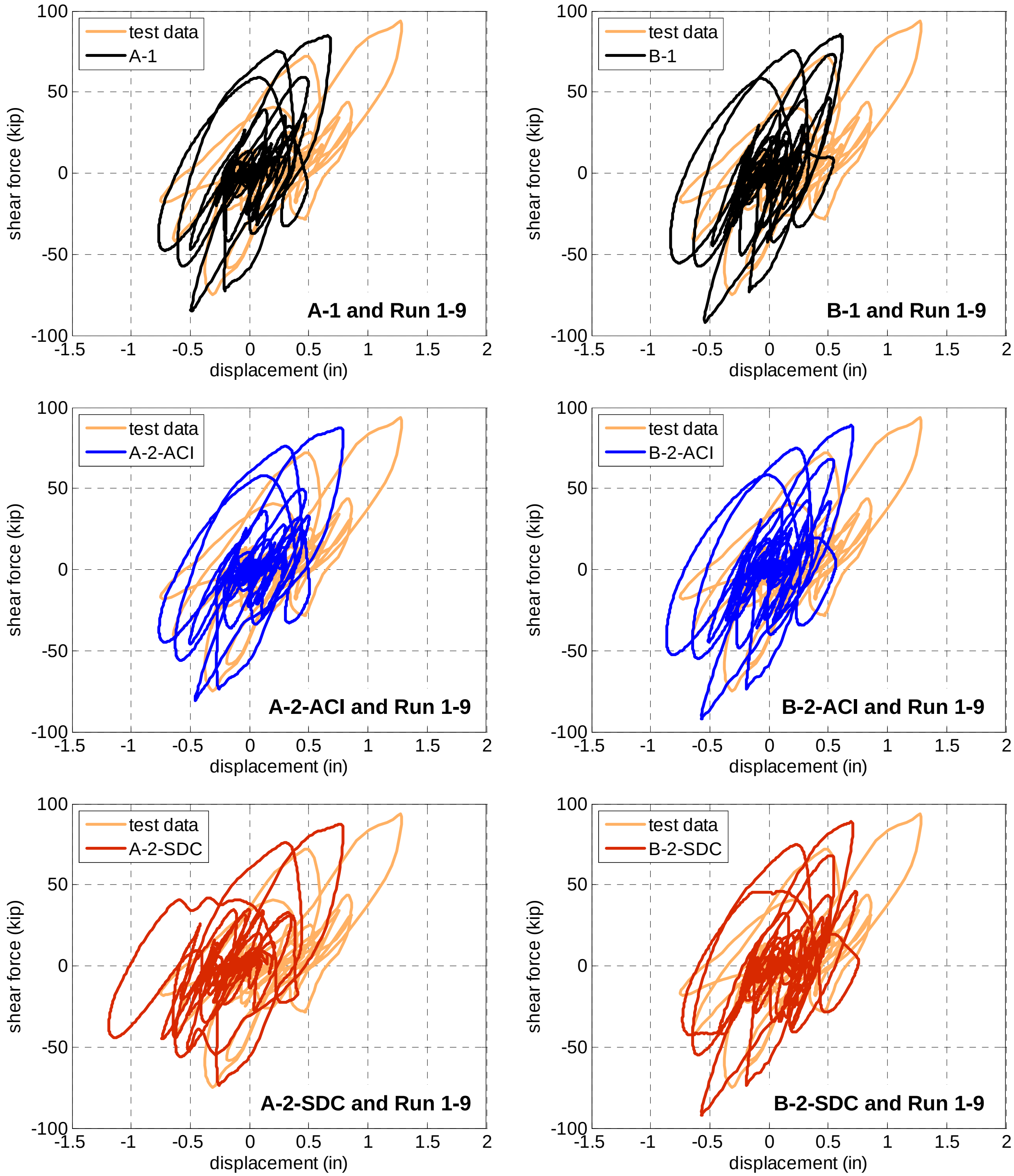

(a) 125% 1st X+Z

Fig. 6.44 Comparison of shear force-lateral displacement relationships of SP1 subjected to 125%-scale motions

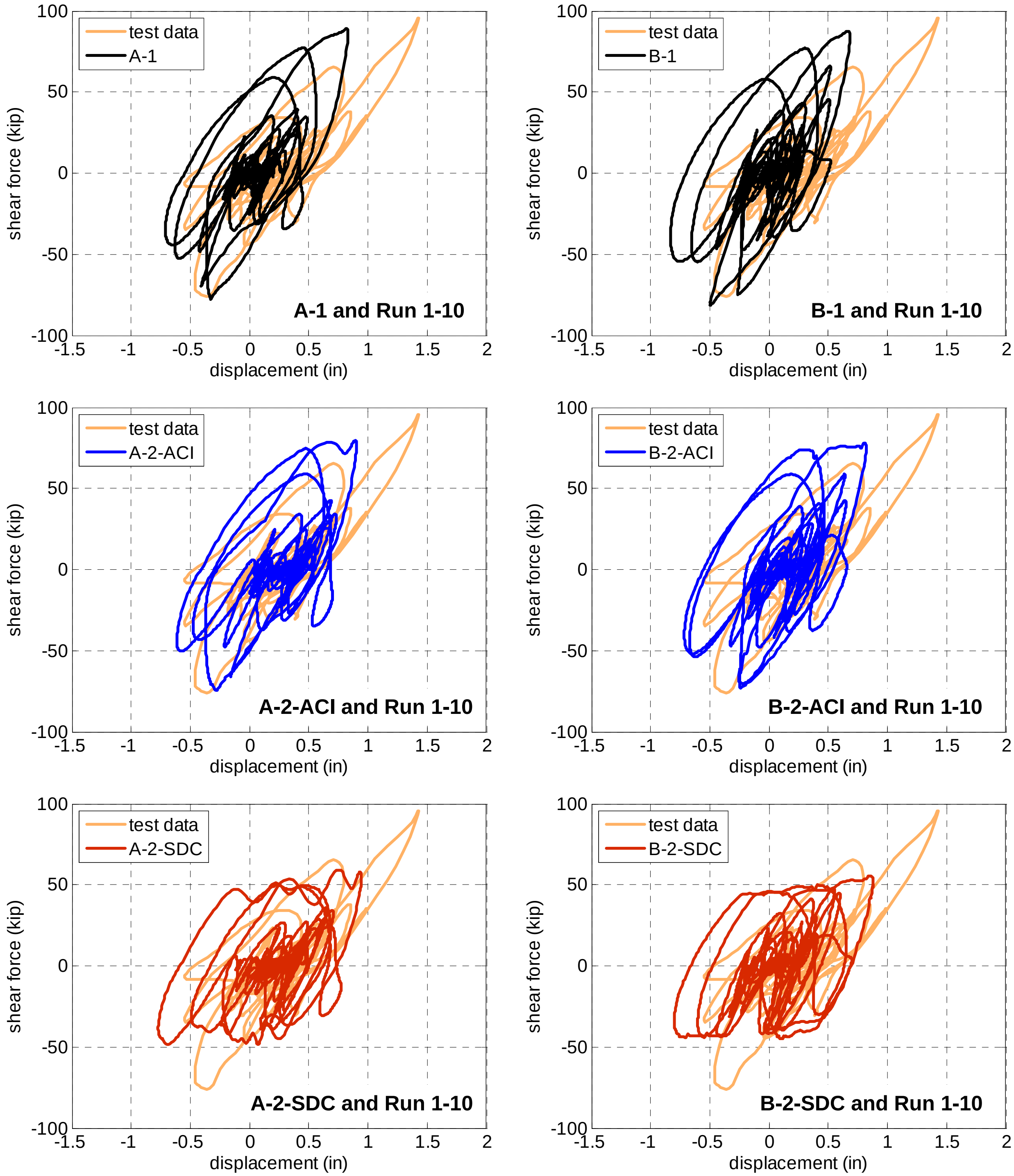

(b) 125% X only

Fig. 6.44 Comparison of shear force-lateral displacement relationships of SP1 subjected to 125%-scale motions (continued)

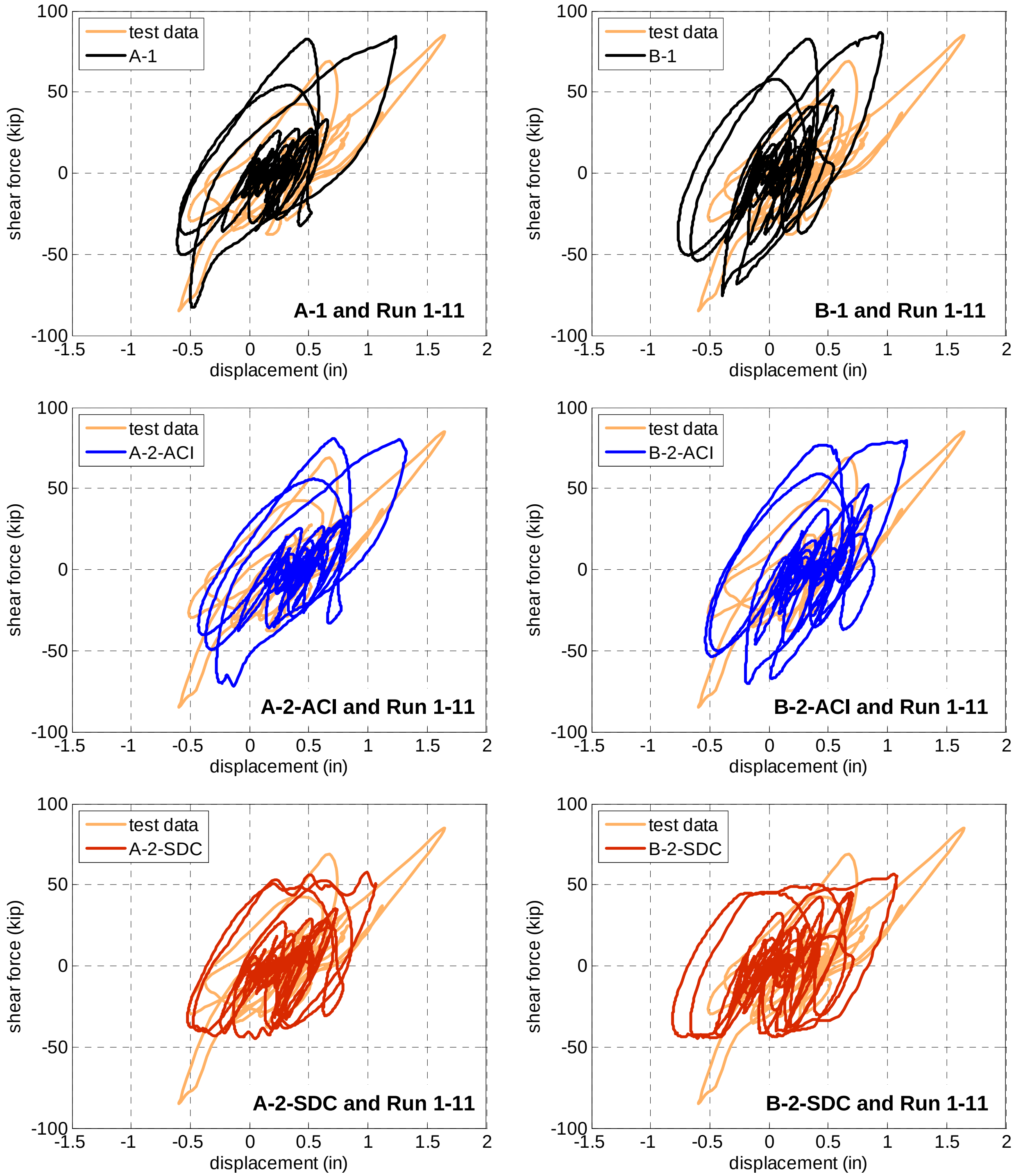

(c) 125% 2nd X+Z

Fig. 6.44 Comparison of shear force-lateral displacement relationships of SP1 subjected to 125%-scale motions (continued)

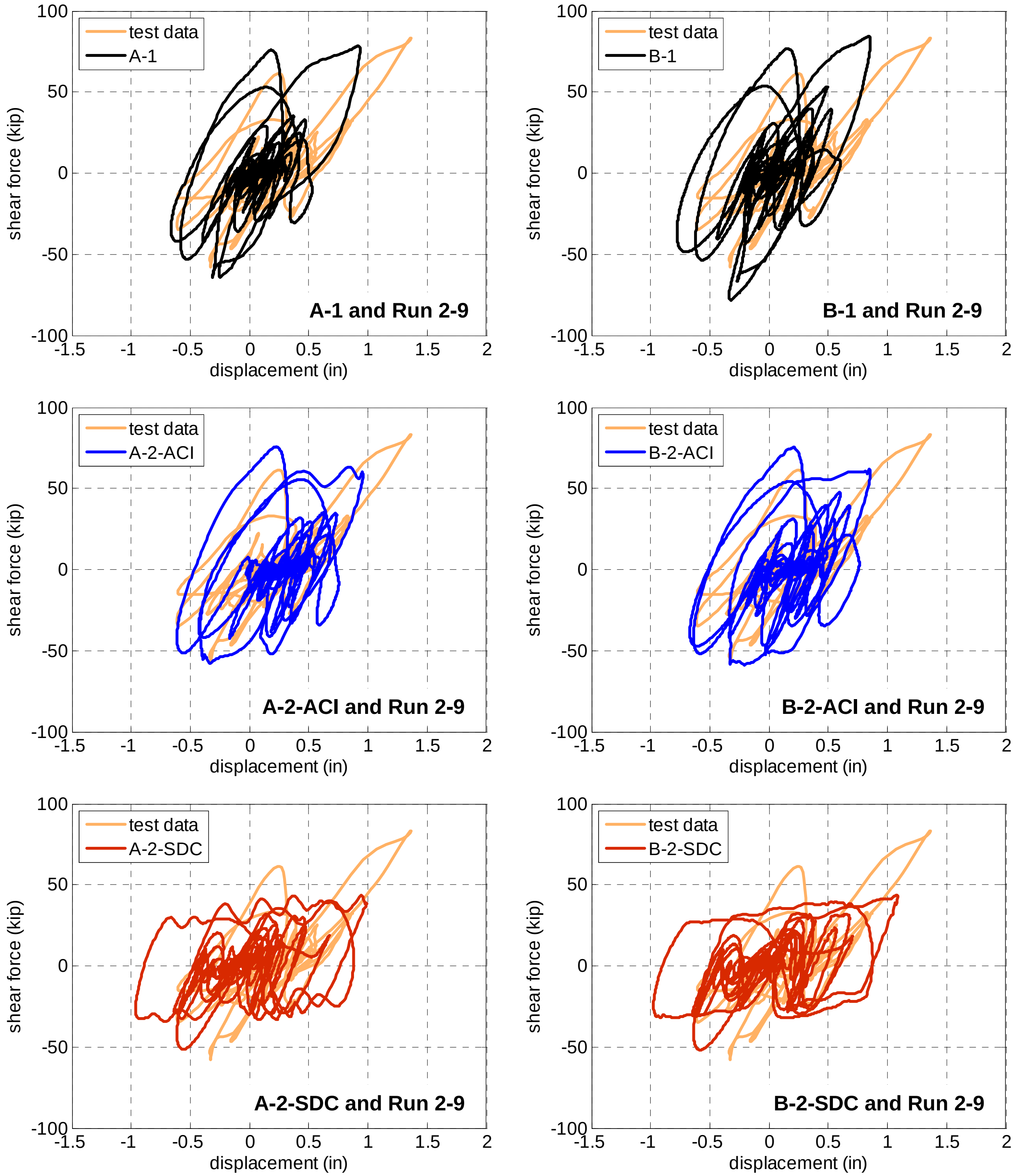

(a) 125% 1st X+Z

Fig. 6.45 Comparison of shear force-lateral displacement relationships of SP2 subjected to 125%-scale motions

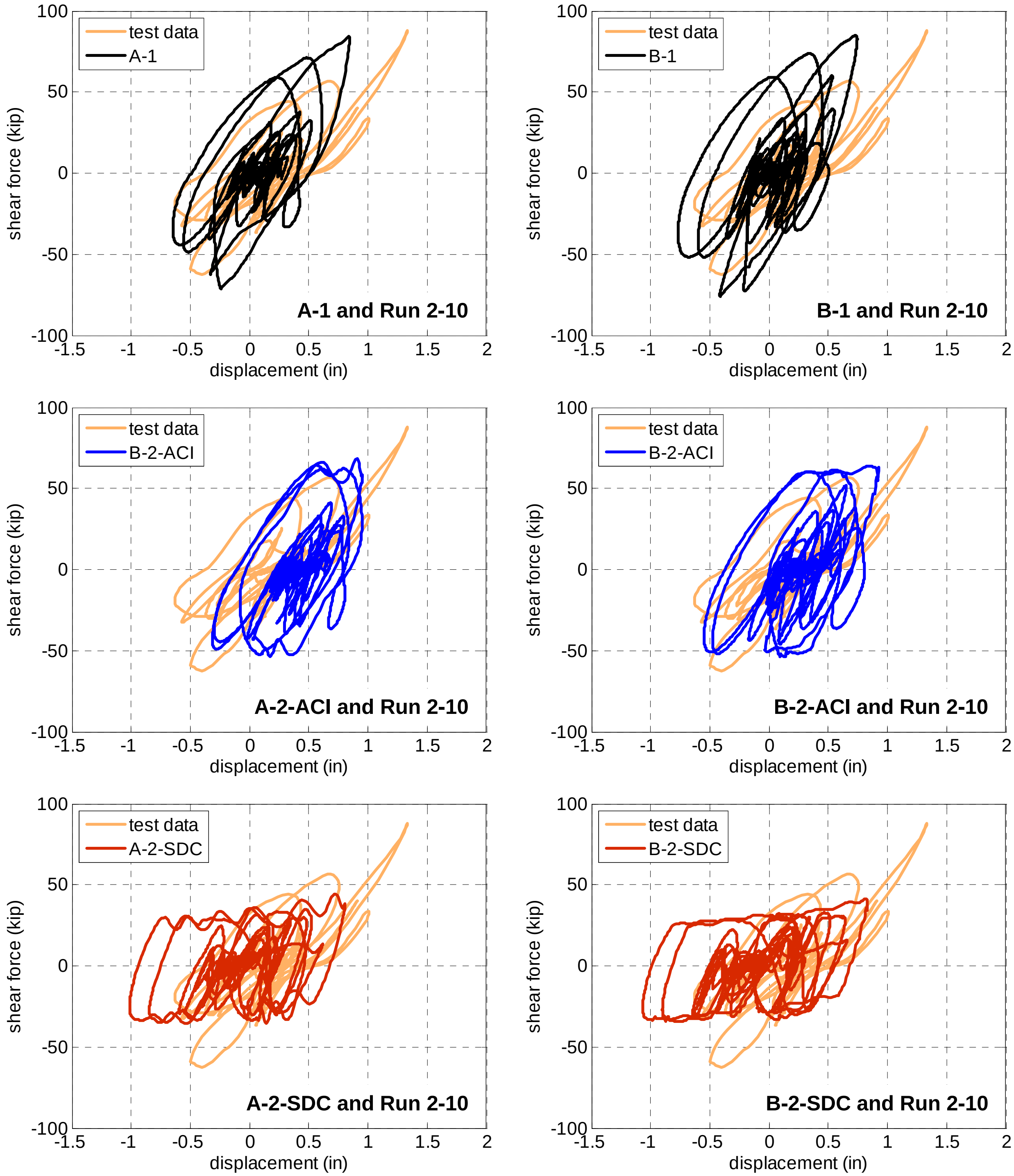

(b) 125% X only

Fig. 6.45 Comparison of shear force-lateral displacement relationships of SP2 subjected to 125%-scale motions (continued)

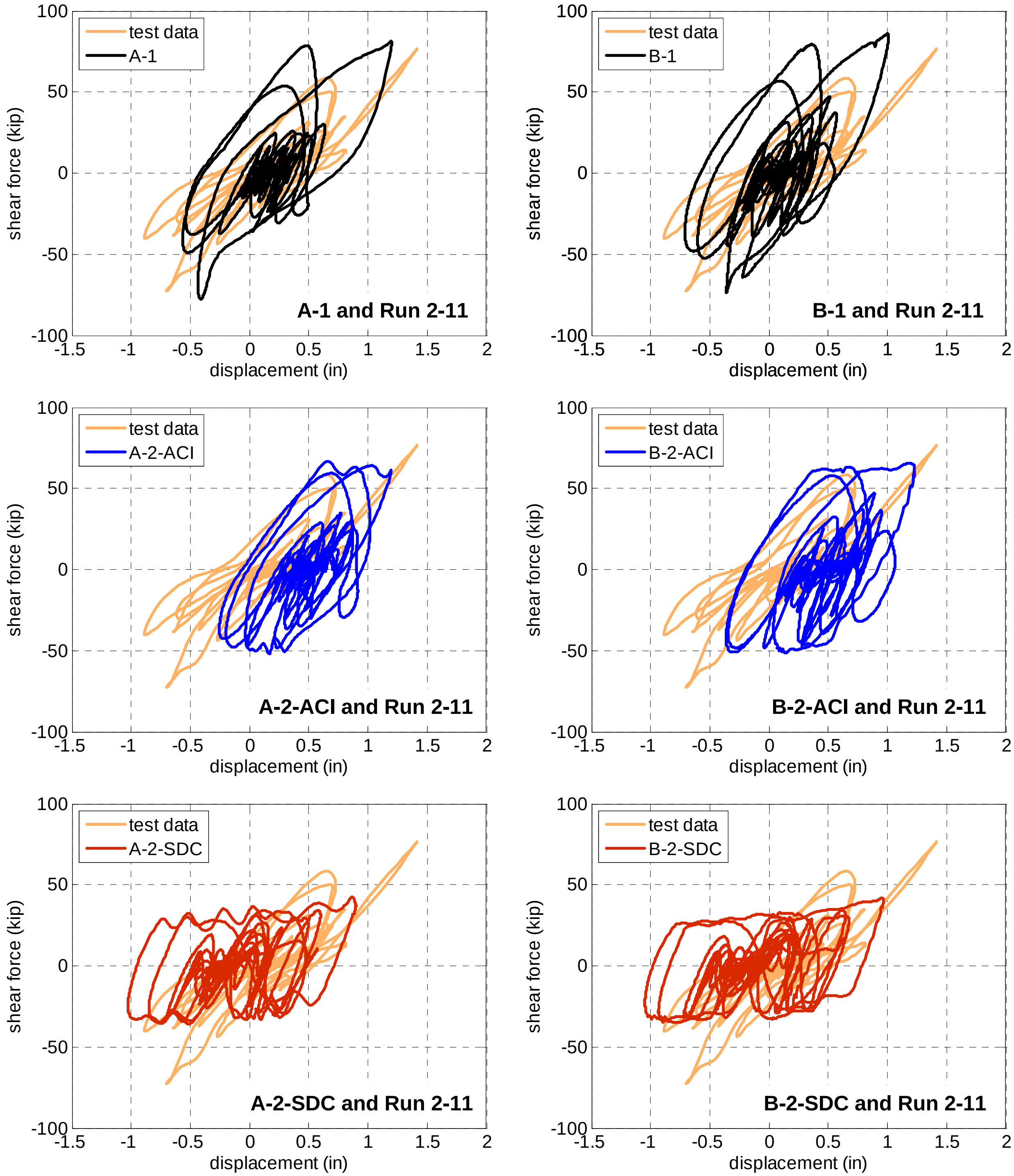

(c) 125% 2nd X+Z

Fig. 6.45 Comparison of shear force-lateral displacement relationships of SP2 subjected to 125%-scale motions (continued)

6.4.3 Local Responses

Local responses are obtained from the predefined sections in Model B with NLBC elements. As mentioned in Section 6.3.1.1, two middle sections in a 'Beam With Hinges 1' element are in the elastic range. Instead, 'Beam With Hinges 2' is utilized for local responses, and they are similar to the results from Model B. A part of the results is compared to the test data in Appendix F. It can be stated that the curvatures and strains close to the column base reasonably match the experimental data. However, errors are particularly significant for the strains close to the column top. As sample results, the bending moment-curvature relationships of SP1 at h=60″ and 10″ are shown in Fig. 6.46. The relationships under 50%- to 125%-scale motions were estimated by B-1, B-2-ACI and B-2-SDC. It is obvious that all the models provide similar moment-curvature relationships at h=10″ or 60″. Also, they are good in estimating the relationships at h=10″, but the results for the section at h=60″ are not close to the test data. Especially, they fail to capture large negative curvatures. In Fig. 6.47, the bending moment-curvature relationships of SP2 at h=60″ and 10″ are presented. Like SP1 cases, the models do not provide a good prediction of large curvature. Since the section at h=10" of SP2 experienced larger curvature than that of SP1, the computational result is not as accurate as that for SP1. But, it is still better than the prediction for the section at h=60″.

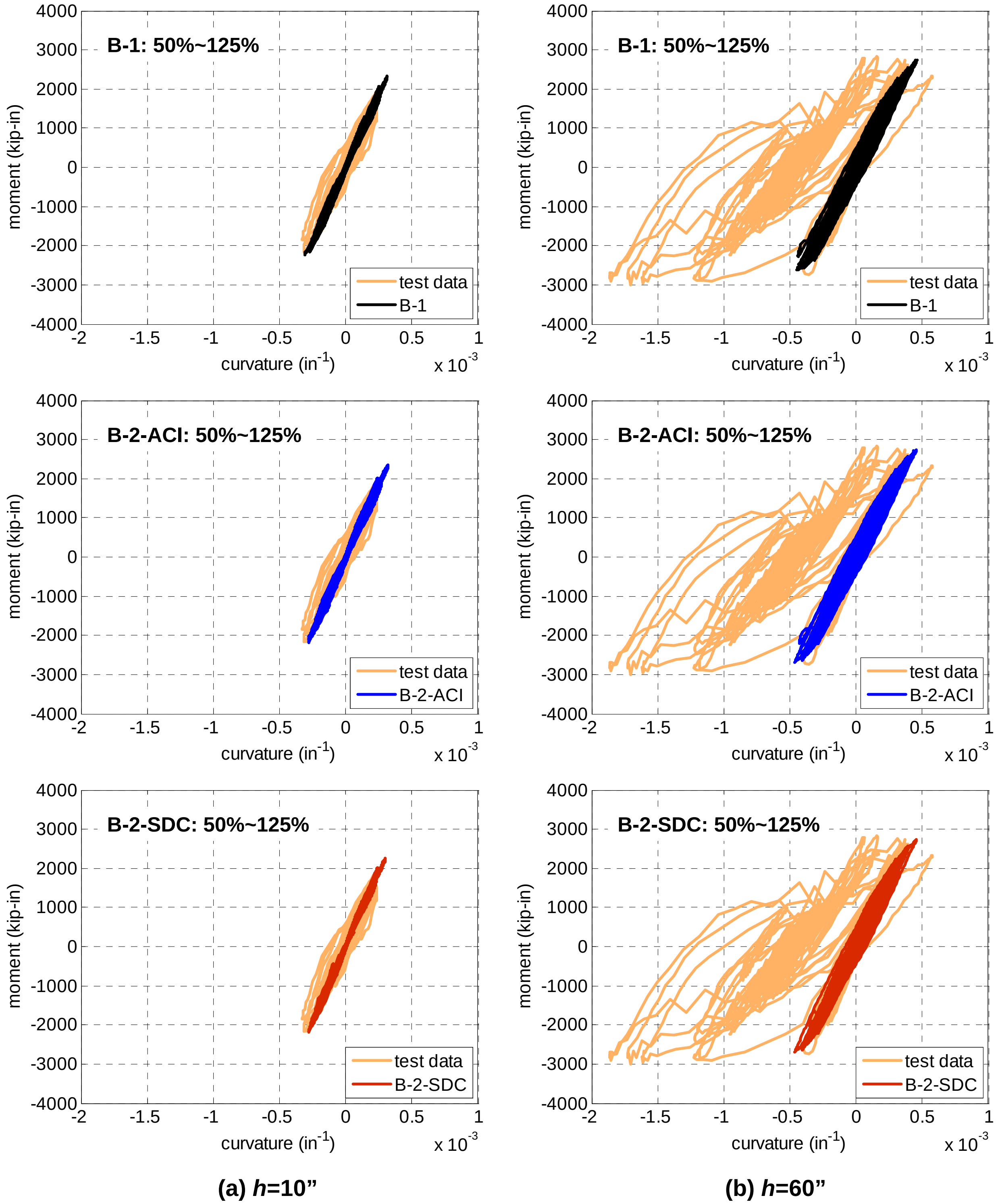

Fig. 6.46 Comparison of bending moment-curvature relationships at h=10″ and 60″ of SP1 under 50%- to 125%-scale motions

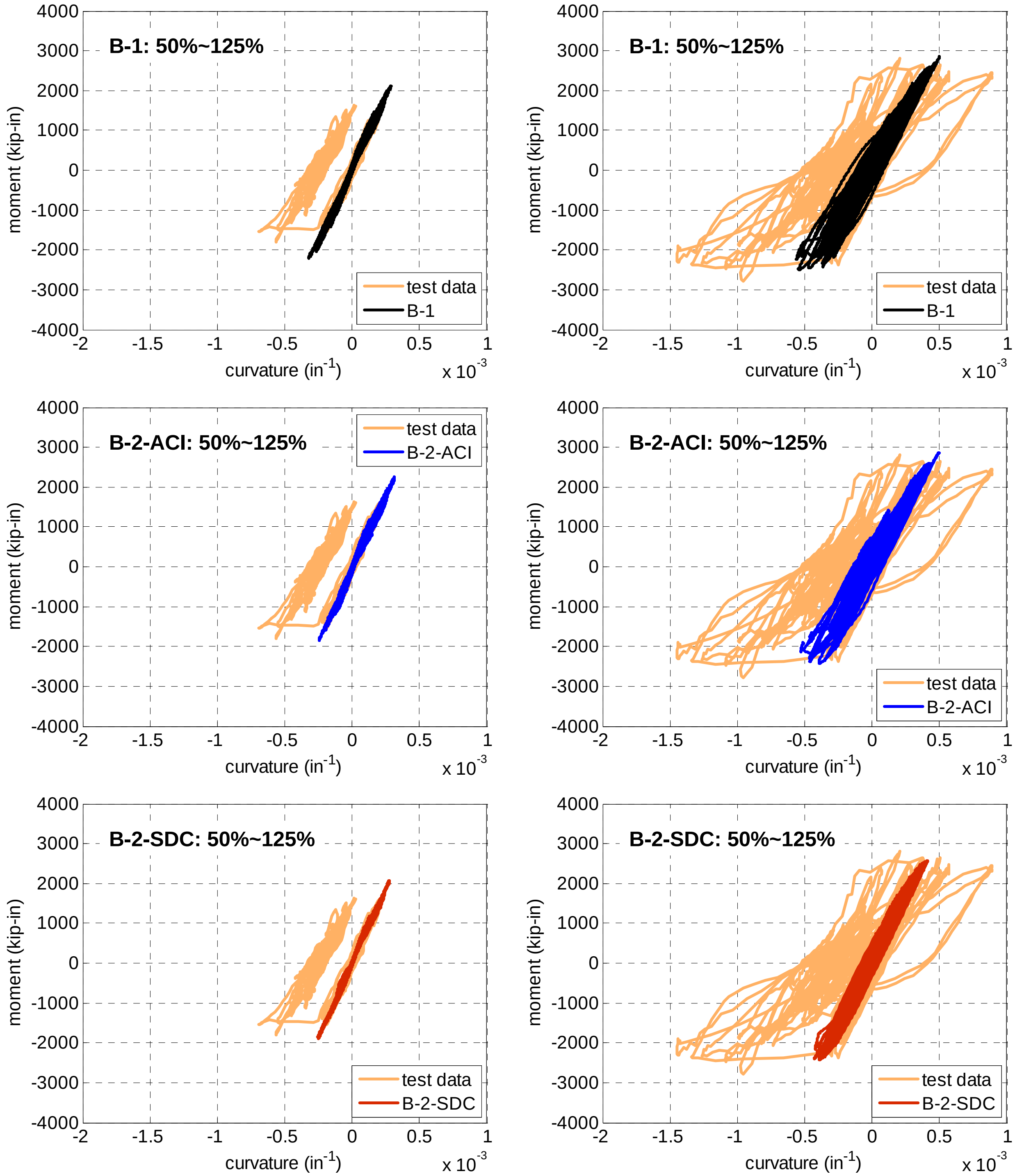

(a) *h*=10” **(b) *h*=60”**

Fig. 6.47 Comparison of bending moment-curvature relationships at h=10″ and 60″ of SP2 under 50%- to 125%-scale motions

6.5 Summary

Since the existing elements in OpenSees are not suitable to incorporate the code-based shear strength estimation, two shear springs, which adopt the shear strength predictions by ACI and SDC equations, are developed. The force-displacement relationship of the proposed springs is based on a bilinear envelope which is defined by the initial stiffness, the yield force, and the hardening ratio for post-yield stiffness. Before yielding, the yield force is updated at each integration time step using the axial force and displacement ductility at that time step. At the time step where the demand reaches the capacity, yielding takes place and the force-displacement relationship follows the post-yield behavior. The yield force is not updated and kept constant afterwards unless the column is subjected to any value of axial tension for the case of Caltrans SDC spring and a predetermined value of tension for the case of ACI spring. The yield force is kept constant after this final modification. Due to some unique features of the SDC equation, its shear strength is estimated as V_s. In other words, the shear resistance of concrete is completely ignored under axial tension.

Two types of computational models are utilized. Model A has a BWH element, and Model B has NLBC elements for the column. Each model has two types, namely without (A-1 and B-1) and with the shear springs. They are designated as A-2-ACI, A-2-SDC, B-2-ACI, and B-2-SDC for the models with shear springs. For the input motion in X and Y directions, the acceleration histories recorded on the shaking table during 50% to 125%-scale tests were used. For the Z direction, the axial force recorded by the load cells (after summation of all four values) is used instead of vertical acceleration, due to flexibility of the shaking table. To maintain the dynamic equilibrium, negligible nodal mass is utilized for the Z direction. The computational results are compared with those obtained from the tests.

The computational models containing BWH and NLBC elements provide similar results and both models are successful in capturing the shear force and lateral displacement history measured during the tests. They capture the rotational mode effect on the moment at the column top accurately. In shear force and bending moment, the amplitude of each response is generally in the following order: A-1>A-2-ACI>A-2-SDC (or B-1>B-2-ACI>B-2-SDC). It is observed that the models without the shear springs do not capture the shear strength degradation accurately, whereas the models including ACI and SDC shear springs capture the shear strength degradation due to axial tension. Both of the springs provide results on the conservative side, where ACI shear spring predictions can be considered as accurate and SDC shear spring predictions as highly conservative. It should be noted that all the models employed in this chapter provide reasonable estimations for the lateral displacement response, but they do not for the vertical displacement response. As a result, local responses obtained from each model are far from the test results.

Chapter 7

Concluding Remarks

7.1 Main Contributions of the Dissertation

Various research projects have been conducted to examine the effect of vertical excitation on reinforced concrete (RC) bridge columns. Field evidence, analytical studies and static or hybrid simulations suggested that excessive axial tension or tensile strain of the column may lead to shear degradation and that vertical excitation can be the cause of shear failure. However, the published literature does not have dynamic experiments to investigate the effect of vertical excitation on the shear strength of RC bridge columns due to the limitation of the test facility. This dissertation provides the experimental and analytical results which confirm that the vertical acceleration can result in shear strength degradation of RC structures.

Two ¼-geometrical scale specimens (SP1 and SP2) were constructed and tested on the UC-Berkeley shaking table at the Richmond Field Station. The two specimens have different transverse reinforcement ratio. Only SP1 satisfies the requirement of Caltrans Bridge Design Specifications. As a result of an extensive analytical investigation and preliminary fidelity tests, 1994 Northridge earthquake acceleration recorded at the Pacoima Dam was selected as an input motion among 3,551 earthquake acceleration records in the PEER NGA database. The chosen ground motion was applied to the test specimens at various levels ranging from 5% to 125%. The specimens were subjected to the combination of a vertical component and a single horizontal component in most of the cases. A single horizontal component was also applied in some of the cases (25%-, 50%-, and 125%-scales) to make a direct evaluation of the effect of the vertical excitation.

As part of the computational modeling, a new shear spring model is developed and implemented in the utilized computational platform, OpenSees [28]. The model was developed in order to incorporate shear strength estimations based on ACI or Caltrans SDC equations addressing the effect of column axial load and displacement ductility on these estimates according to these two codes provisions.

7.2 Main Conclusions

The dissertation conclusions are grouped into two sets. The first deals with findings from the experimental investigations. The second deals with findings from the analytical modeling.

7.2.1 Experimental Results

- The horizontal component of the acceleration on the mass blocks is significantly lower than that at the top of the column. This is a result of the rigid body rotation of the mass blocks due to the rotation at the top of the column. Reduction of the horizontal acceleration increases the bending moment at the top of the column relative to the bending moment at the base.
- The shaking table flexibility has a pronounced effect on the vertical response. The dynamic mode, which is introduced by the shaking table stiffness (in the vertical direction) and its mass, governs the response in the vertical direction. Therefore, the response due to the column's axial mode is reduced compared to the case of a rigid shaking table. However, it should be stated that the flexibility of the shaking table did not affect the conducted investigation since the mode introduced by the shaking table flexibility has a significantly larger period compared to the column's vertical period. As a matter of fact, the effect of the shaking table flexibility is analogous to the effect of the bridge girders in elongating the period of the bridge system compared to the period of a single bridge column.
- Considerable tensile force is induced on the test column due to vertical excitation.
- Tension in the columns results in degradation of shear strength, which is mainly due to the degradation of the concrete contribution to shear strength.
- Reduction in the concrete strength is also evidenced by the comparison of shear cracks in the 125% scale horizontal only and horizontal and vertical tests.
- Flexural damage at the top of the column takes place before the flexural damage at the base since the bending moment at the top is larger. This is a result of the large mass moment of inertia at the top of the column. Reduction of the acceleration on the mass block due to the rotations contributes to this situation as well.
- Flexural damage takes place and propagates both at the top and base of the column as the scale of the ground motion increases.
- As a result of flexural yielding both at the top and base of the column bending in double curvature, shear force reaches the shear capacity which would not take place if yielding happened at the base and the bending moment at the top was smaller than the yielding bending moment. Shear cracks take place as a result of this situation.
- Tensile force due to vertical excitation reduces the shear strength and increases the shear cracks.

7.2.2 Analytical Results

- Developed computational models are successful in capturing the shear force and displacement histories measured during the tests. They capture the rotational mode effect on the bending moment at the column top accurately.
- Investigated computational models, namely “Beam With Hinges” BWH (Model A) and “Nonlinear Beam-Column” NLBC (Model B) provide similar results.
- The dominance of the shaking table flexibility on the vertical response is demonstrated by an elastic dynamic analysis of a 2 degrees-of-freedom (DOF) system which models the column and the shaking table together as a structural system.
- Due to the difficulty in modeling the shaking table stiffness which varies during a test, as well as between different intensity tests, measured axial force is directly applied to the computational models. This approach was accepted to fit well with the main purposes of this investigation, which are the evaluation of the axial tension on the shear capacity and the development of the corresponding computational modeling approach.
- Accurate representation of the vertical displacement response requires a more detailed finite element model where the cracks can be modeled. However, since the vertical displacement is an end result, produced by the axial force, and therefore does not change the interaction of axial and shear response; such a detailed finite element model was not employed in this dissertation.
- Both ACI and SDC equations capture the shear strength degradation due to axial force. Both of the equations provide results on the conservative side, where ACI equation predictions can be considered as accurate and SDC equation predictions as highly conservative. Elimination of the concrete contribution to shear strength under tension is the main reason for the highly conservative predictions of SDC equation. The strength reduction caused by ductility is not as significant as that by tension.
- The developed shear springs which are implemented in OpenSees fulfill the objectives of the computational modeling for simulating the effect of the axial force on the shear strength.

7.3 Suggested Future Extensions

The experimental and computational investigation conducted in this study revealed that considerable axial tension can be induced in bridge columns which result in degradation in the shear strength. Based on the obtained results and gained experience, the following is stated as future extensions.

- Hybrid simulation where the column is tested and the rest of the bridge system is computationally modeled is a viable option for the evaluation of the column axial tension for a full bridge system. This approach has three advantages. First, the elongated vertical period due to presence of the bridge deck can be considered. Second, the elimination of a possible shaking table effect on the vertical response can be achieved. Third, an advantage is introduced by modeling the complicated mass assembly in the computer. The hybrid simulation test can be conducted by using three actuators, where one horizontal actuator is for the lateral degree of freedom and two vertical actuators are for the lateral and rotational degrees of freedom at the top of the column.
- Developed shear springs which adopt the ACI and SDC equations are based on a bilinear hysteresis relationship. It is recommended to modify the hysteresis model to include strength and stiffness degradation as well as pinching.
- The response of the tested and computationally-modeled columns can be investigated with a suite of ground motions, e.g. using the PEER NGA database. It is possible to generate fragility curves based on three cases namely, a) no shear spring, b) ACI-based shear spring, and c) SDC-based shear spring.
- Generalization of the developed shear spring can be conducted where coupling between the fiber discretization and the shear behavior can be addressed on a more fundamental level, e.g. using the modified compression field theory (MCFT) [3].

References

[1] Pristley, M. J. N., Benzoti, G., Ohtaki, T., and Seible, F. (1996), "Seismic Performance of Circular Reinforced Concrete Columns under Varying Axial Load," Report-SSRP-96/04, Division of Structural Engineering, University of California.

[2] ACI Committee 318 (2008), Building Code Requirements for Structural Concrete and Commentary, ACI 318-08, American Concrete Institute, Farmington Hills, MI.

[3] Vecchio, F. J. and Collins, M. P. (1986), "The Modified Compression-Field Theory for Reinforced Concrete Elements Subjected to Shear," *ACI Journal*, 83, No. 2, pp. 219-231.

[4] Walraven, J. C. (1981), "Fundamental Analysis of Aggregate Interlock," *Proceedings*, ASCE, V. 107, ST11, pp.2245-2270.

[5] AASHTO (2005), "LRFD Bridge Design Specifications, 3rd Edition, 2005 Interim Revisions," American Association of State and Highway Transportation Officials, Washington, DC.

[6] AASHTO (2010), "LRFD Bridge Design Specifications, 5th Edition, 2010 Interim Revisions," American Association of State and Highway Transportation Officials, Washington, DC.

[7] CSA Committee A23.3. (2004), Design of Concrete Structures (CSA-A23.3-04), Canadian Standards Association, Rexdale, ON.

[8] Bentz, E. C., Vecchio, F. J., and Collins, M. P. (2006), "Simplified Modified Compression Field Theory for Calculating Shear Strength of Reinforced Concrete Elements," *ACI Structural Journal*, 103, No. 4, pp. 614-624.

[9] Eurocode 2. (2004), "Design of Concrete Structures," Part 1, CEN, European Standard ENV 1992-1-1, Brussels.

[10] Papazoglou, A. J. and Elnashai, A. S. (1996), "Analytical and Field Evidence of the Damaging Effect of Vertical Earthquake Ground Motion," *Earthquake Engineering and Structural Dynamics*, Vol. 25, pp. 1109-1137.

[11] PEER-NGA Database (2011), http://peer.berkeley.edu/nga/

[12] Newmark, N. M., Blume, J. A., and Kapur, K. K. (1973), "Seismic Design Spectra for Nuclear Power Plants," *Journal of Power Division*, ASCE, Vol. 99, pp. 287-303.

[13] California Department of Transportation (Caltrans) (2010), "Seismic Design Criteria," SDC-2010, Sacramento, CA.

[14] Silva, W. (1997), "Characteristics of Vertical Strong Ground Motions for Applications to Engineering Design," *FHWA/NCEER Workshop on the National Representation of Seismic Ground Motion for New and Existing Highway Facilities, Burlingame, CA*, Proceedings, Technical Report NCEER-97-0010, National Center for Earthquake Engineering Research, Buffalo, New York.

[15] Kawase, H. and Aki, K. (1990), "Topography Effect at the Critical SV-wave Incidence: Possible Explanation of Damage Pattern by the Whittier Narrows, California, Earthquake of 1 October 1987," *Bulletin of the Seismological Society of America*, 80, pp.1-30.

[16] Amirbekian, R. V. and Bolt, B. A. (1998), "Spectral Comparison of Vertical and Horizontal Seismic Strong Ground Motions in Alluvial Basins," *Earthquake Spectra*, 14, pp. 573-595.

[17] Elnashai, A. S. (1997), "Seismic Design with Vertical Earthquake Motion," Seismic Design for the Next Generation of Codes, eds. Fajfar, P. and Krawinkler, H. (Balkema, Rotterdam), pp. 91-100.

[18] Elnashai, A. S. and Papazoglou, A. J. (1997), "Procedure and Spectra for Analysis of RC Structures Subjected to Strong Vertical Earthquake Loads," *Journal of Earthquake Engineering*, Vol. 1, No. 1, pp. 121-155.

[19] Collier, C. J. and Elnashai, A. S. (2001), "A Procedure for Combining Vertical and Horizontal Seismic Action Effects," *Journal of Earthquake Engineering*, Vol. 5, No. 4, pp. 521-539.

[20] Elgamal, A. and He, L. (2004), "Vertical Earthquake Ground Motion Records: An Overview," *Journal of Earthquake Engineering*, Vol. 8, No. 5, pp. 663-697.

[21] Bozorgnia, Y. and Campbell K. W. (2004), "The Vertical-to-Horizontal Response Spectral Ratio and Tentative Procedures for Developing Simplified V/H and Vertical Design Spectra," *Journal of Earthquake Engineering*, Vol. 8, No. 2, pp. 175-207.

[22] Kim, S. J. and Elnashai, A. S. (2008), "Seismic Assessment of RC Structures Considering Vertical Ground Motion," MAE Center report, No. 08-03.

[23] Sakai, J. and Unjoh, S. (2007), "Shake Table Experiment on Circular Reinforced Concrete Bridge Column under Multidirectional Seismic Excitation," *Proceedings of the Research Frontiers*, SEI, May.

[24] ACI Committee 318 (2005), Building Code Requirements for Structural Concrete and Commentary, ACI 318-05, American Concrete Institute, Farmington Hills, MI.

[25] Priestley, M. J. N., Verma, R., and Xiao, Y. (1994), "Seismic Shear Strength of Reinforced Concrete Columns," *Journal of Structural Engineering*, ASCE, Vol. 120(8), pp. 2310-2329.

[26] Kawashima, K., Ukon, H., and Kajiwara, K. (2007), "Bridge Seismic Response Experiment Program using E-Defense," *Proceedings of 39th UJNR Panel on Wind and Seismic Effect*, Technical Memorandum, Public Works Research Institute, Tsukuba Science City, Japan, No. 4075, pp. 57-66.

[27] Kunnath, S. K., Abrahamson, N., Chai, Y. H., Erduran, E., and Yilmaz, Z. (2008), "Development of Guidelines for Incorporation of Vertical Ground Motion Effects in Seismic Design of Highway Bridges," A Technical Report Submitted to the California Department of Transportation, May.

[28] OpenSees (2009), http://opensees.berkeley.edu/

[29] Mander, J. B., Priestley, M. J. N., and Park, R., "Theoretical Stress–Strain Model for Confined Concrete," *Journal of the Structural Division,* ASCE*,* Vol. 114, pp. 1804–1826

[30] FEMA-356 (2000). Prestandard and Commentary for the Seismic Rehabilitation of Buildings. Report FEMA-356. Washington (DC): Federal Emergency Management Agency.

[31] Jeong, H., Mahin, S. A., Sasaki, T., and Kawashima, K. (2008), "Progress Report: Large-scale Tests of a US Bridge Column Using the E-Defense Shaking," April 2008.

[32] SAP2000 Manuals (2006). Computers and Engineering, Inc., Version 11, Berkeley, CA.

[33] Newmark, N. M. and Hall, W. J. (1982), "Earthquake Spectra and Design." Earthquake Engineering Research Institute, Berkeley, CA.

[34] Fenves, G. L. and Mojtahedi, S. (1995), "Effect of Contraction Joint Opening on Pacoima Dam in the 1994 Northridge Earthquake," SMIP95 Seminar on Seismological and Engineering Implications of Recent Strong-Motion Data, p. 57 - 68.

[35] Alves, S. W. (2005), "Nonlinear Analysis of Pacoima Dam with Spatially Nonuniform Ground Motion," Doctoral Thesis at California Institute of Technology, Pasadena, California.

[36] ASTM Standard C31/C31M (2010), "Standard Practice for Making and Curing Concrete Test Specimens in the Field," ASTM International, West Conshohocken, PA, 2003

[37] ASTM Standard C172/C172M (2010), "Standard Practice for Sampling Freshly Mixed Concrete," ASTM International, West Conshohocken, PA, 2003

[38] ASTM Standard E8/E8M (2009), "Standard Test Methods for Tension Testing of Metallic Materials", ASTM International, West Conshohocken, PA, 2003

[39] California Department of Transportation (Caltrans) (2010), "California Amendments to the AASHTO LRFD Bridge Design Specifications (Fourth Edition)," Sacramento, CA.

[40] Chopra, A. K. (2006), Dynamics of Structures, Theory and Applications to Earthquake Engineering, Pearson Prentice Hall, 3rd Edition, Upper Saddle River, NJ.

[41] Massone, L. M., Orakcal, K., and Wallace, J.W. (2006), "Shear-Flexure Interaction for Structural Walls," *ACI Special Publication*, 236, pp. 127-150.

[42] Elwood, K. and Moehle, J. (2003), "Shake table tests and analytical studies on the gravity load collapse of reinforced concrete frames," PEER Report 2003/01, Pacific Earthquake Engineering Research Center, University of California, Berkeley, CA.

[43] Talaat, M. M. and Mosalam, K. M. (2008), "Computational Modeling of Progressive Collapse in Reinforced Concrete Frame Structures," PEER Report 2007/10, Pacific Earthquake Engineering Research Center, University of California, Berkeley, CA.

[44] Scott, M.H. and Fenves, G.L. (2006), "Plastic Hinge Integration Methods for Force of Structural Engineering, ASCE, 132(2):244-252.

[45] Paulay, T. and Priestley, M. J. N. (1992), Seismic Design of Reinforced Concrete and Masonry Buildings, John Wiley and Sons, New York.

[46] Menegotto, M., and Pinto, P. (1973). "Method of Analysis for Cyclically Loaded Reinforced Concrete Plane Frames Including Changes in Geometryand Non-elastic Behavior of Elements Under Combined Normal Force and Bending." *Proceedings. IABSE Sympoium on Resistance and Ultimate Deformability of Structures Acted on by Well-Defined Repeated Loads*, Final Report, Lisbon.

Appendix A

Table A.1 presents the list of 61 ground motions selected in Section 2.1. It provides the record sequence number, earthquake ID, earthquake name, record date, station name, and peak acceleration values of the three components of each ground motion.

Table A.1 Selected ground motions

No.	RSN	EQID	Earthquake name	YYYYMMDD	Station name	PGA, unit=g		
						H1	H2	V
1	495	0097	Nahanni, Canada	19851223	Site 1	0.9778	1.0957	2.0865
2	181	0050	Imperial Valley-06	19791015	El Centro Array #6	0.4105	0.4390	1.6550
3	126	0041	Gazli, USSR	19760517	Karakyr	0.6083	0.7175	1.2639
4	1051	0127	Northridge-01	19940117	Pacoima Dam (upper left)	1.5849	1.2852	1.2291
5	779	0118	Loma Prieta	19891018	LGPC	0.9663	0.5872	0.8860
6	319	0073	Westmorland	19810426	Westmorland Fire Sta	0.3682	0.4963	0.8380
7	1063	0127	Northridge-01	19940117	Rinaldi Receiving Sta	0.8252	0.4865	0.8343
8	982	0127	Northridge-01	19940117	Jensen Filter Plant	0.5706	1.0239	0.8249
9	879	0125	Landers	19920628	Lucerne	0.7268	0.7892	0.8185
10	825	0123	Cape Mendocino	19920425	Cape Mendocino	1.4973	1.0395	0.7536
11	585	0110	Baja California	19870207	Cerro Prieto	1.3883	0.8904	0.5896
12	3474	0175	Chi-Chi, Taiwan-06	19990925	TCU079	0.6224	0.7743	0.5807
13	407	0080	Coalinga-05	19830722	Oil City	0.8663	0.4471	0.5683
14	949	0127	Northridge-01	19940117	Arleta - Nordhoff Fire Sta	0.3440	0.3081	0.5523
15	752	0118	Loma Prieta	19891018	Capitola	0.5285	0.4433	0.5411
16	1633	0144	Manjil, Iran	19900620	Abbar	0.5146	0.4964	0.5378
17	706	0113	Whittier Narrows-01	19871001	Whittier Narrows Dam upstream	0.2294	0.3160	0.5050
18	959	0127	Northridge-01	19940117	Canoga Park - Topanga Can	0.3558	0.4203	0.4888
19	3475	0175	Chi-Chi, Taiwan-06	19990925	TCU080	0.5376	0.4688	0.4800
20	540	0101	N. Palm Springs	19860708	Whitewater Trout Farm	0.4922	0.6121	0.4712
21	1507	0137	Chi-Chi, Taiwan	19990920	TCU071	0.5669	0.6548	0.4487
22	459	0090	Morgan Hill	19840424	Gilroy Array #6	0.2222	0.2920	0.4050
23	802	0118	Loma Prieta	19891018	Saratoga - Aloha Ave	0.5125	0.3242	0.3893
24	230	0056	Mammoth Lakes-01	19800525	Convict Creek	0.4165	0.4416	0.3881
25	149	0048	Coyote Lake	19790806	Gilroy Array #4	0.2481	0.2710	0.3873
26	189	0050	Imperial Valley-06	19791015	SAHOP Casa Flores	0.2874	0.5060	0.3793
27	95	0031	Managua, Nicaragua-01	19721223	Managua, ESSO	0.4213	0.3373	0.3766
28	1085	0127	Northridge-01	19940117	Sylmar - Converter Sta East	0.8283	0.4930	0.3765
29	810	0118	Loma Prieta	19891018	UCSC Lick Observatory	0.4502	0.3946	0.3673
30	619	0113	Whittier Narrows-01	19871001	Garvey Res. - Control Bldg	0.3836	0.4568	0.3619
31	418	0082	Coalinga-07	19830725	Coalinga-14th & Elm (Old CHP)	0.4311	0.7325	0.3324

32	412	0080	Coalinga-05	19830722	Pleasant Valley P.P. - yard	0.6020	0.3268	0.3165
33	952	0127	Northridge-01	19940117	Beverly Hills - 12520 Mulhol	0.6169	0.4444	0.3142
34	265	0064	Victoria, Mexico	19800609	Cerro Prieto	0.6212	0.5873	0.3043
35	1042	0127	Northridge-01	19940117	N Hollywood - Coldwater Can	0.2982	0.2707	0.2894
36	1006	0127	Northridge-01	19940117	LA - UCLA Grounds	0.2779	0.4738	0.2650
37	235	0057	Mammoth Lakes-02	19800525	Mammoth Lakes H. S.	0.4407	0.3895	0.2644
38	1620	0138	Duzce, Turkey	19991112	Sakarya	0.0160	0.3764	0.2590
39	232	0056	Mammoth Lakes-01	19800525	Mammoth Lakes H. S.	0.3211	0.2392	0.2527
40	372	0077	Coalinga-02	19830509	Anticline Ridge Free-Field	0.5763	0.6733	0.2496
41	1645	0145	Sierra Madre	19910628	Mt Wilson - CIT Seis Sta	0.2760	0.2001	0.2372
42	185	0050	Imperial Valley-06	19791015	Holtville Post Office	0.2526	0.2208	0.2301
43	1642	0145	Sierra Madre	19910628	Cogswell Dam - Right Abutment	0.3020	0.2641	0.2275
44	809	0118	Loma Prieta	19891018	UCSC	0.3112	0.3862	0.2266
45	1520	0137	Chi-Chi, Taiwan	19990920	TCU088	0.5223	0.5084	0.2224
46	398	0079	Coalinga-04	19830709	Oil City	0.3868	0.3705	0.2103
47	1617	0138	Duzce, Turkey	19991112	Lamont 375	0.9701	0.5137	0.1934
48	589	0113	Whittier Narrows-01	19871001	Alhambra - Fremont School	0.3327	0.4137	0.1899
49	248	0061	Mammoth Lakes-06	19800527	Convict Creek	0.2658	0.3156	0.1884
50	264	0063	Mammoth Lakes-08	19800531	USC McGee Creek Inn	0.5316	0.1840	0.1795
51	1623	0139	Stone Canyon	19720904	Melendy Ranch	0.4798	0.5153	0.1734
52	71	0030	San Fernando	19710209	Lake Hughes #12	0.3658	0.2828	0.1673
53	1009	0127	Northridge-01	19940117	LA - Wadsworth VA Hospital North	0.2526	0.2536	0.1630
54	2622	0172	Chi-Chi, Taiwan-03	19990920	TCU071	0.3803	0.1945	0.1425
55	395	0079	Coalinga-04	19830709	Anticline Ridge Pad	0.3775	0.2611	0.1370
56	708	0114	Whittier Narrows-02	19871004	Altadena - Eaton Canyon	0.2644	0.1990	0.1217
57	394	0079	Coalinga-04	19830709	Anticline Ridge Free-Field	0.3300	0.2746	0.1146
58	683	0113	Whittier Narrows-01	19871001	Pasadena - Old House Rd	0.2314	0.2576	0.1019
59	2942	0174	Chi-Chi, Taiwan-05	19990922	CHY024	0.2626	0.2391	0.1003
60	714	0114	Whittier Narrows-02	19871004	LA - Obregon Park	0.3741	0.2606	0.0985
61	380	0077	Coalinga-02	19830509	Oil Fields - Skunk Hollow	0.3129	0.3428	0.0822

Appendix B

B.1 Construction Procedures

Two specimens were constructed from July 8 to July 28, 2010 at the Richmond Field Station. Table B.1 summarizes the sequence of construction. The photographs taken at each step are shown from Fig. B.1 to Fig. B.4.

First, forms for footings were made (Fig. B.1(a)) and the steel cages were woven. Mainly, top, bottom, and transverse reinforcement formed the cage (Fig. B.1(b)). Since the longitudinal reinforcing bars and hoops of the column were embedded into the footing, they were also included in the construction of the cages (Fig. B.1(c) and (d)). Eighteen strain gages per specimen were installed on the longitudinal reinforcing bars prior to making the cages. Second, the formwork for footings was completed (Fig. B.2(a)) and the concrete mix specified in Section 3.4.3.1 was placed into the forms (Fig. B.2(b)). After leveling the footing surface (Fig. B.2(c)), the footings were watered and covered by plastic. Third, hoops were placed around the column longitudinal reinforcing bars. SP1 had 2-in spacing and SP2 had 3-in spacing. It should be noted that the strain gages on the longitudinal reinforcing bars were attached inward to avoid damage due to placing the hoops. Subsequently, gages for transverse strain were installed on the hoops (Fig. B.3(a)).

Table B.1 Construction process

Date	Items
July 8~10	Strain gages on longitudinal reinforcing bars installed
July 15~16	Footing reinforcing bars completed
July 20	Footing concrete mix placed
July 21	Hoops in-place
July 21~22	Strain gages on hoops installed
July 23	Sonotube, top block forms in-place
July 27	Top block rebars completed
July 28	Column concrete mix placed

(a) Bottom reinforcement

(b) Top and transverse reinforcement

(c) Column hoops

(d) Longitudinal reinforcement of the column

Fig. B.1 Footing Construction: Reinforcement

(a) Finishing formwork

(b) Placing concrete mix

(c) Leveling footing surface

(d) Finished footing surface

Fig. B.2 Footing construction: Placing concrete

(a) Strain gages on column reinforcement

(b) Formwork for top block

(c) Top block form

(d) Top block reinforcement

Fig. B.3 Column and top block construction: Reinforcement

(a) Placing concrete mix

(b) Leveling top block surface

(c) Finished top block surface

(d) Test cylinders

Fig. B.4 Column and top block construction: Placing concrete

B.2 Setup Procedures

To hold the test specimen and the mass blocks on the shaking table, a base plate and four steel beams were added to the test setup. The specimen cannot be held at the center of the shaking table with the existing system unless the footing size is increased. If the specimen is off the center, an erroneous result is expected with high probability. If the footing size is increased, it causes overweight on the shaking table and lowers the maximum applicable intensity of an input motion. A thick steel plate is an alternative to put the specimen at the center without adding significant weight on the table. Fig. B.5(a) shows the base plate fixed to the shaking table. Four load cells were attached to the plate and the specimen was supported on them (Fig. B.5(b)). Loadcells between the plate and the specimen capture the force below the specimen. The steel beams shown in Fig. B.5(c) and (d) were connected to the specimen by prestressing rods. They supported the concrete blocks and lead blocks.

In Fig. B.6, the procedure of hanging the lead blocks and putting the concrete blocks on the specimen is presented. As shown in Fig. B.6, total of three bundles of lead blocks were hung from each beam. Each bundle had different numbers of lead blocks as discussed in Section 3.5.1.4. The closest bundle to the specimen has 4, the middle one had 6, and the farthest has 8 blocks. Each bundle was assembled outside of the shaking table and moved by the overhead crane. Finally, it was hung by four prestressing rods at the tip of 6×4 tubes. After hanging the lead blocks, two concrete blocks were placed on the specimen. The prestressing rods through the beams and the concrete blocks provided fixation of these concrete blocks during the test. To ensure integration and avoid the damage of the concrete blocks, grout was applied between the beams and the bottom concrete block, and between the concrete blocks themselves (Fig. B.6(c)). Finally, another concrete block was added as shown in Fig. B.6(d), and the prestressing rods were tightened.

(a) Connecting base plate to the table

(b) Installing loadcells and the specimen on the base plate

(c) Connecting the beams to the specimen by prestressing rods

(d) Elevation of the setup before adding mass blocks

Fig. B.5 Test setup before adding mass blocks

(a) Hanging lead blocks

(b) Installing the first concrete block on the specimen

(c) Grouting between the beam and the concrete block

(d) Installing the second concrete block

Fig. B.6 Adding mass blocks to the test setup

Appendix C

C.1 Specimen Drawings

Drawings for the test setup and specimens are presented in this section. In Fig. C.1, the schematic drawing of the test setup is shown. The setup height is about 13 ft, from the base plate to the concrete blocks. The specimen height is 9 ft 4 in, including its footing and top block. As shown in Fig. C.2, two specimens were identical except for the hoop spacing. The top block is 45° off compared to the footing and the steel beams in Fig. C.6 are connected to this top block by prestressing rods. Fig. C.3 and Fig. C.4 present the details of the reinforcement for the top block and footing.

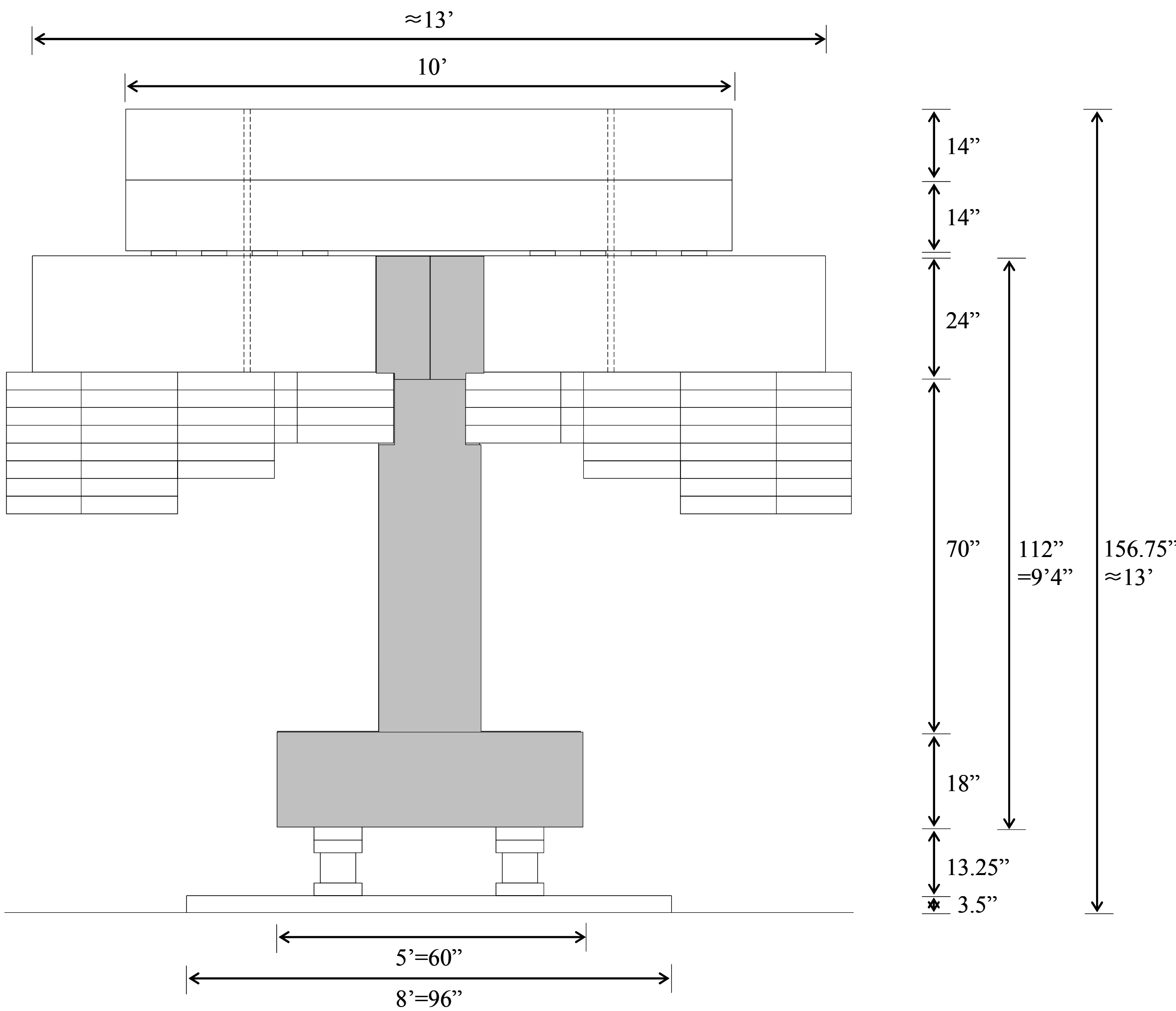

Fig. C.1 Schematic drawing of test setup

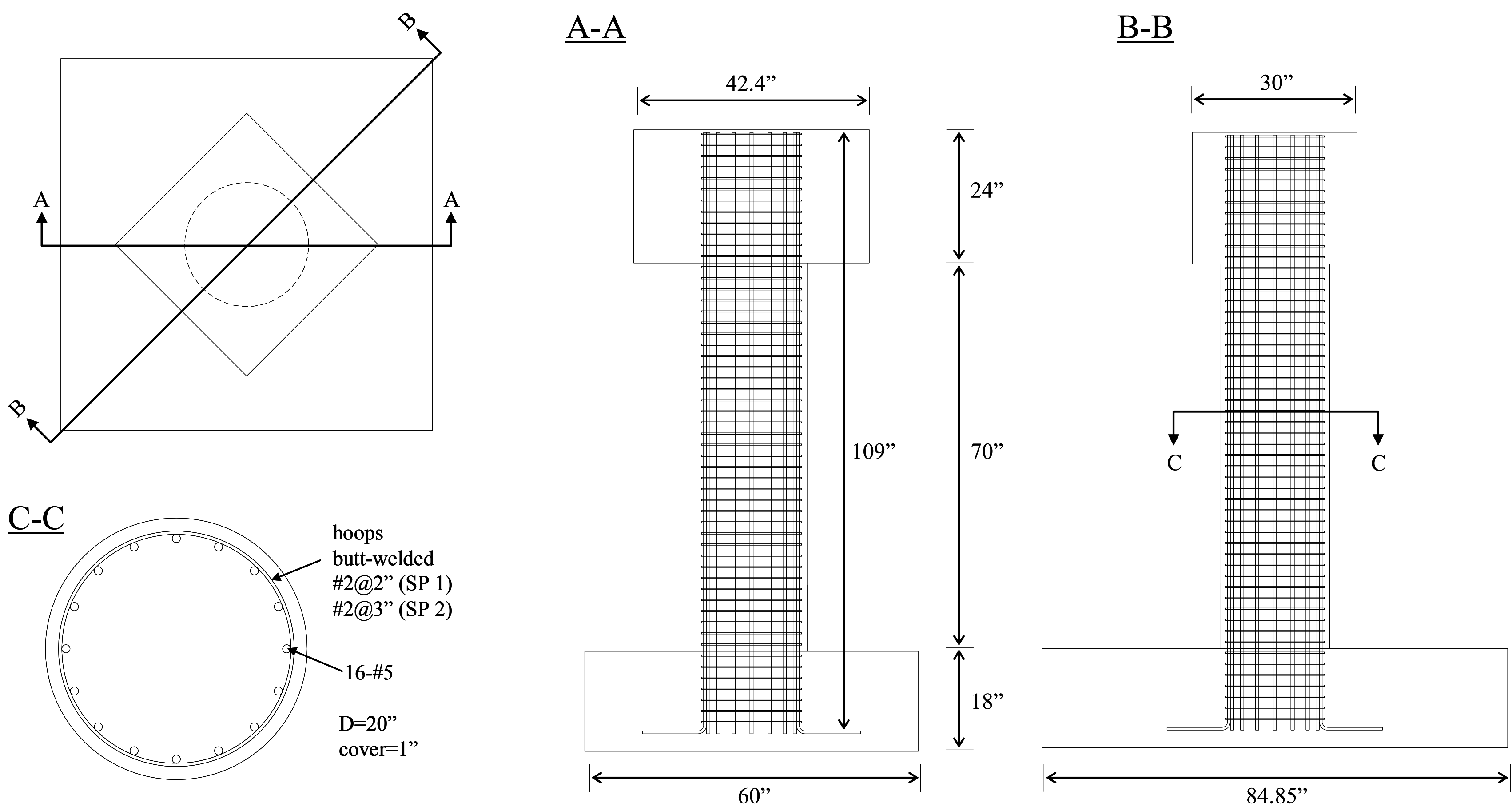

Fig. C.2 Column cross-section and reinforcement

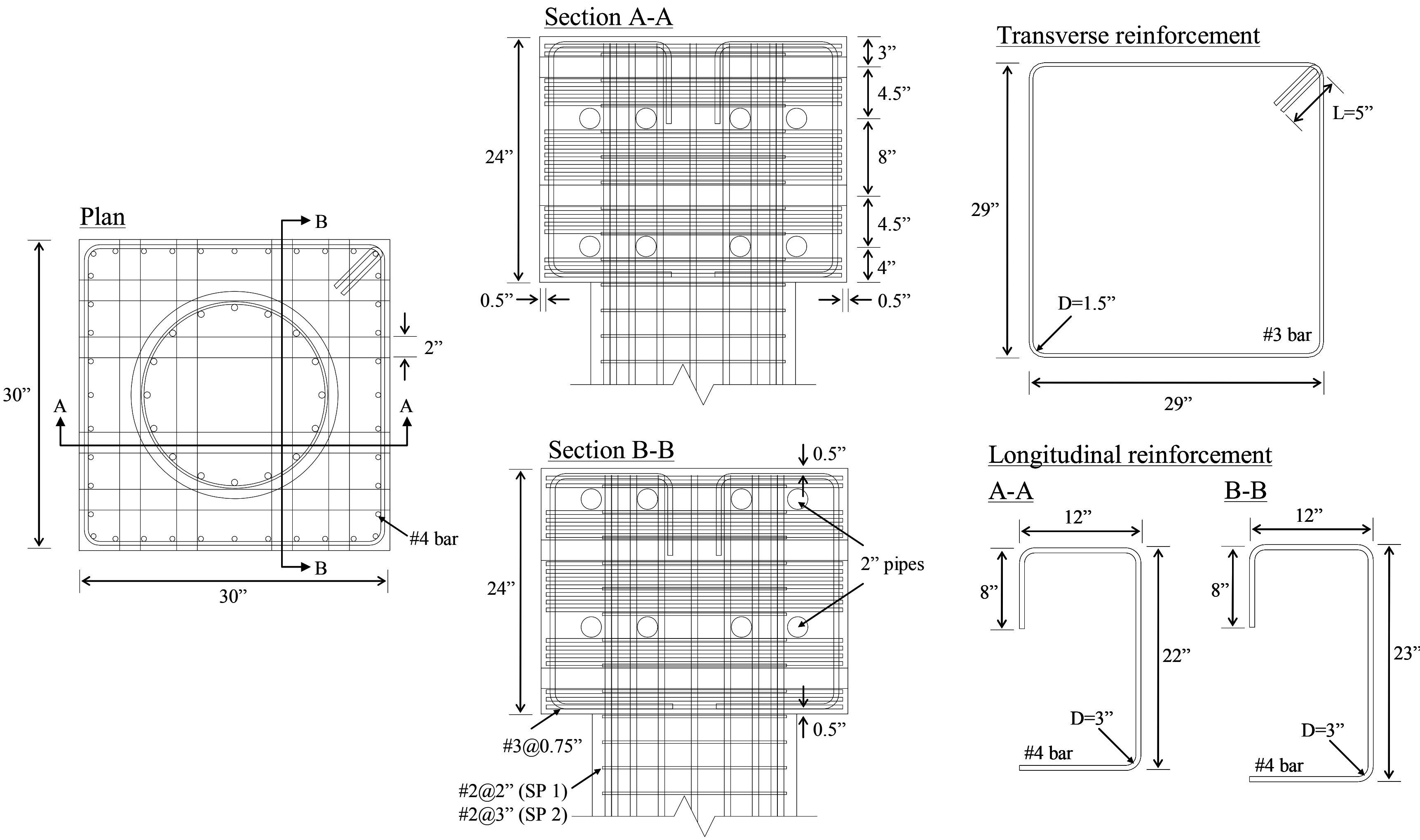

Fig. C.3 Top block plan, cross-sections and reinforcement

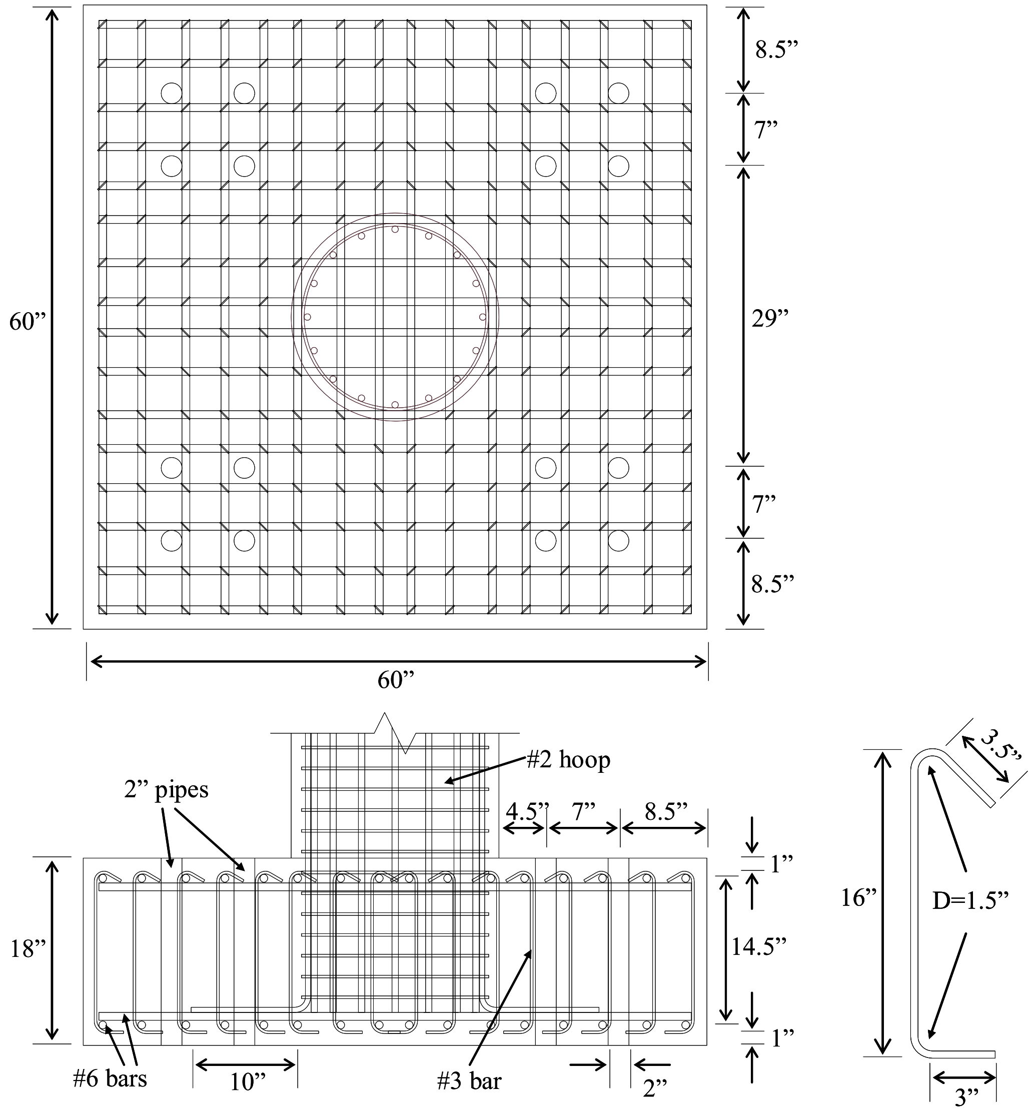

Fig. C.4 Footing plan, cross-section and reinforcement

C.2 Design of the Base Plate and Top Steel Beams

A base plate was designed to place the test specimen at the center of the shaking table. 9-2.5″ holes and 16-7/8″ tap holes were drilled on an 8′×8′×3.35″ steel plate made of ASTM A36. Fig. C.5 specifies the location of these holes. 9-2.5″ holes connect the plate to the shaking table and 16-7/8″ tab holes connect the load cells to the plate. As a result, the test specimen could be at the center of the shaking table.

Total of 4 steel beams were designed to support the concrete blocks and to hang the lead blocks as shown in Fig. C.6. Six hangers, HSS6×4×1/2 tubes, were welded to the beam, a HSS12×20×1/2 tube. Four thick plates were welded to the hangers to fill the gap between concrete blocks and hangers. The beam length is 8 ft. and its depth is about 27 in from the top plate to the bottom of the HSS12×20. In the middle of the big tube, there is a 3″-hole for prestressing rod which holds the concrete blocks during excitation. Since the beams were connected by horizontal steel rods through the top block of the test specimen, the beams in the opposite sides should have the holes at the same location. For this reason, NE and SW beams were the same and NW and SE beams were also identical. The weight per one beam was about 2.36 kips.

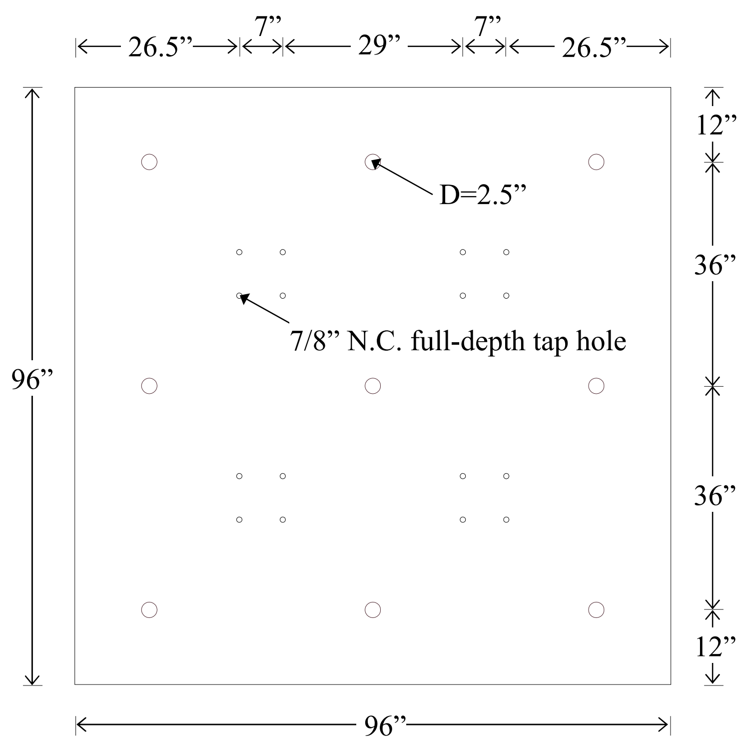

Fig. C.5 Base plate plan

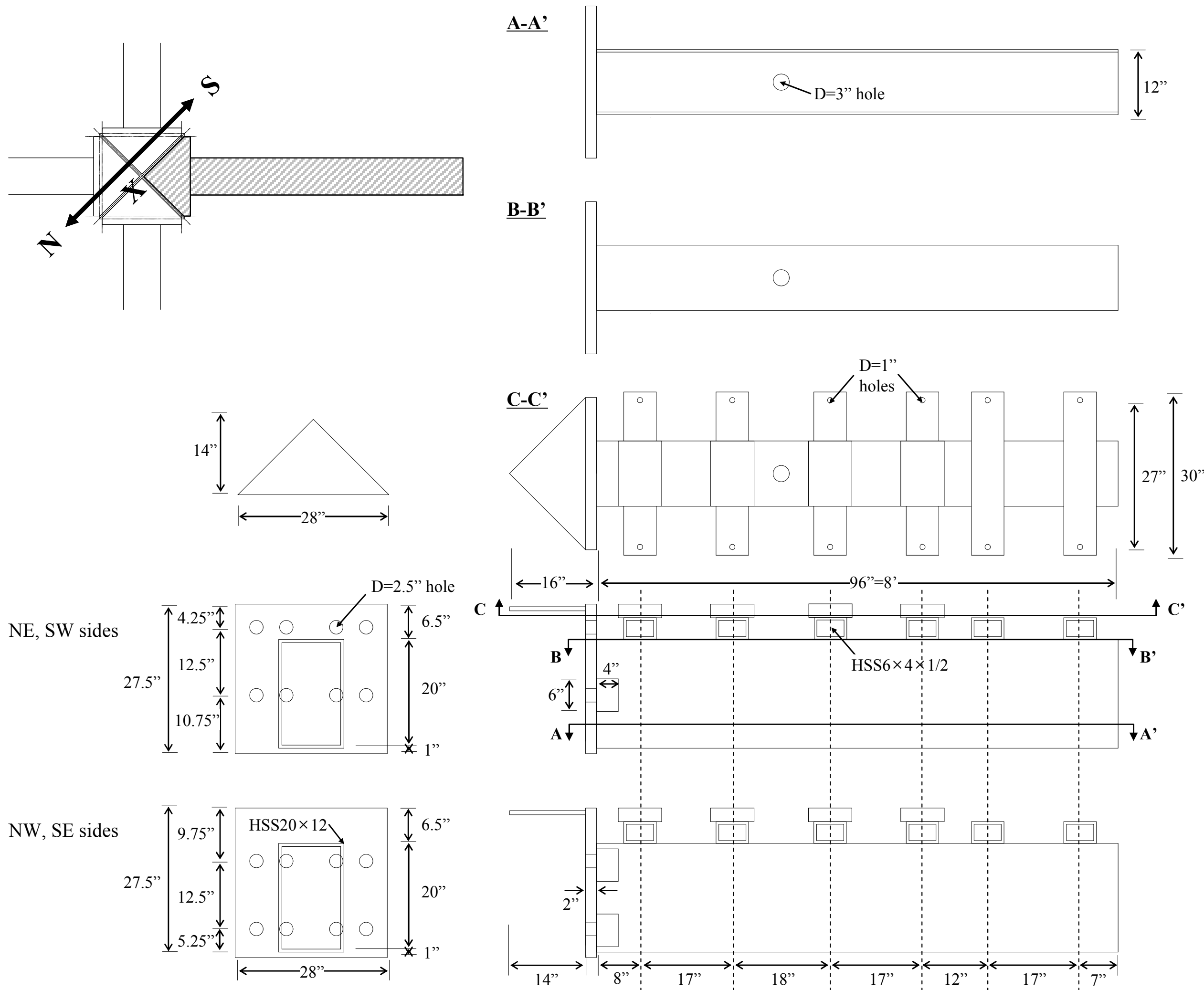

Fig. C.6 Top steel beam plan, elevations and cross-sections

Appendix D

This section describes the channels and measuring instruments used in a series of tests. They are also discussed in Section 3.5.2. Total of 137 channels were used and they included 16 default channels for the actuators under the shaking table. Other channels were used to obtain strains, forces, accelerations, and displacements over the specimen and setup. Section D.1 provides the list of all channels and it specifies the channel name, type of measurement, location … etc. Section D.2 presents the removed channels during the tests. Section D.3 provides drawings which present the location of each measuring instrument.

D.1 Channel List

The channels used in the tests are summarized in Table D.1.

Table D.1 Channel description

No.	Name	Type	Location	Note
1	H1O	Default measurement below the table (displacement)	South side actuator	displacement (Y-dir)
2	H2O		East side actuator	displacement (X-dir)
3	H3O		North side actuator	displacement (Y-dir)
4	H4O		West side actuator	displacement (X-dir)
5	V1O		SE corner actuator	displacement (Z-dir)
6	V2O		NE corner actuator	
7	V3O		NW corner actuator	
8	V4O		SW corner actuator	
9	H1-2	Default measurement below the table (acceleration)	East side actuator	acceleration (Y-dir)
10	H3-4		West side actuator	acceleration (X-dir)
11	H4-1		South side actuator	acceleration (Y-dir)
12	H2-3		North side actuator	acceleration (X-dir)
13	V1ACC		SE corner actuator	acceleration (Z-dir)
14	V2ACC		NE corner actuator	
15	V3ACC		NW corner actuator	
16	V4ACC		SW corner actuator	
17	SE LC1SX	Loadcell	SE corner below the footing	shear force (X-dir)
18	SE LC1SY			shear force (Y-dir)
19	SE LC1Ax			axial force (Z-dir)
20	NE LC2SX		NE corner below the footing	shear force (X-dir)
21	NE LC2SY			shear force (Y-dir)
22	NE LC2Ax			axial force (Z-dir)
23	NW LC3SX		NW corner below the footing	shear force (X-dir)
24	NW LC3SY			shear force (Y-dir)
25	NW LC3Ax			axial force (Z-dir)

26	SW LC4SX		SW corner below the footing	shear force (X-dir)
27	SW LC4SY			shear force (Y-dir)
28	SW LC4Ax			axial force (Z-dir)
29	Accel1X	3D Accelerometer	SE corner on the base plate	acceleration (X-dir)
30	Accel1Y			acceleration (Y-dir)
31	Accel1Z			acceleration (Z-dir)
32	Accel2X		NE corner on the base plate	acceleration (X-dir)
33	Accel2Y			acceleration (Y-dir)
34	Accel2Z			acceleration (Z-dir)
35	Accel3X		NW corner on the base plate	acceleration (X-dir)
36	Accel3Y			acceleration (Y-dir)
37	Accel3Z			acceleration (Z-dir)
38	Accel4X		SW corner on the base plate	acceleration (X-dir)
39	Accel4Y			acceleration (Y-dir)
40	Accel4Z			acceleration (Z-dir)
41	Accel5X		SE corner on the mass blocks	acceleration (X-dir)
42	Accel5Y			acceleration (Y-dir)
43	Accel5Z			acceleration (Z-dir)
44	Accel6X		NE corner on the mass blocks	acceleration (X-dir)
45	Accel6Y			acceleration (Y-dir)
46	Accel6Z			acceleration (Z-dir)
47	Accel7X		NW corner on the mass blocks	acceleration (X-dir)
48	Accel7Y			acceleration (Y-dir)
49	Accel7Z			acceleration (Z-dir)
50	Accel8X		SW corner on the mass blocks	acceleration (X-dir)
51	Accel8Y			acceleration (Y-dir)
52	Accel8Z			acceleration (Z-dir)
53	Accel9Z	1D Accelerometer	North side, *h* =0″	acceleration (Z-dir)
54	Accel10Z		North side, *h* =5″	
55	Accel11Z		North side, *h* =15″	
56	Accel12Z		North side, *h* =25"	
57	Accel13Z		Center on the mass blocks	
58	Accel14Z		North side, *h* =45″	
59	Accel15Z		North side, *h* =55″	
60	Accel16Z		North side, *h* =65″	
61	NovoT1	Novotechnik	North side, *h* =0~5″	displacement (Z-dir)
62	NovoT2		North side, *h* =5~15″	
63	NovoT3		North side, *h* =15~25″	
64	NovoT4		North side, *h* =25~35″	
65	NovoT5		North side, *h* =35~55″	
66	NovoT6		North side, *h* =55~65″	
67	NovoT7		North side, *h* =65~70″	
68	NovoT8		South side, *h* =0~5″	
69	NovoT9		South side, *h* =5~15″	
70	NovoT10		South side, *h* =15~25″	
71	NovoT11		South side, *h* =25~35″	

72	NovoT12		South side, *h* =55~65″	
73	NovoT13		South side, *h* =65~70″	
74~ 111	SG1~38	Strain gage	Longitudinal re-bars and hoops	
112	NovoT14	Novotechnik	South side, *h*=35~55″	displacement (Z-dir)
113	W Vrt.DCDT	DCDT	West side, *h*=70″	displacement (Z-dir)
114	WP1	Wire potentiometer	North, below the mass blocks	displacement (Z-dir)
115	WP2		South, below the mass blocks	
116	WP3		East, below the mass blocks	
117	WP4		West, below the mass blocks	
118	WP5		South, footing, *h*=0″	displacement (X-dir)
119	WP6		South, footing, *h*=0″	
120	WP7		South, column, *h*=15″	
121	WP8		South, column, *h*=35″	
122	WP9		South, column, *h*=55″	displacement (X-dir)
123	WP10		South, column, *h*=70″	
124	WP11		South, mass block	
125	WP12		South, mass block	
126	WP13		Northwest, column, *h*=35″	displacement (diagonal)
127	WP14		Northwest, column, *h*=70″	
128	WP15		Southwest, column, *h*=35″	
129	WP16		Southwest, column, *h*=70″	
130	WP17		West, footing, *h*=0″	displacement (Y-dir)
131	WP18		West, mass block	
132	WP19		West, mass block	
133	Accel17X	3D Accelerometer	East side, *h* =70″	acceleration (X-dir)
134	Accel17Y			acceleration (Y-dir)
135	Accel17Z			acceleration (Z-dir)
136	E Vrt.DCDT	DCDT	East side, *h* =70″	displacement (Z-dir)
137	Accel18Z	1D Accelerometer	North side, *h* =70″	acceleration (Z-dir)

D.2 Data Reduction

Not all data are appropriate to be used in the data analysis due to misreading. In particular, strain gages are vulnerable to damage. During a series of tests, only several channels for strain gages had erroneous readings. The followings in Table D.2 are the channels removed in each test.

Table D.2 Removed channels

SP	Channel name	Location
1	NL4	Longitudinal rebar on the north side, *h*=40″
	NL5	Longitudinal rebar on the north side, *h*=50″
	NH5	Hoop on the north side, *h*=40″
	NH7	Hoop on the north side, *h*=60″
2	SH3	Hoop on the south side, *h*=30″

D.3 Instrumentation Drawings

Fig. D.1 presents the location of strain gages in each cross-section. Small rectangles represent the gages on the hoop and the longitudinal reinforcing bars at each cross-section. The location of each cross-section was discussed in Section 3.5.2.1. Fig. D.1(a) is for *h*=30″, 40″, and 60″, Fig. D.1(b) is for *h*=10″, Fig. D.1(c) is for *h*=20″ and 50″, and Fig. D.1(d) for *h*=35″.

Fig. D.2 and Fig. D.3 present elevations and plans of the setup with external measuring instruments, respectively. The locations of the Novotechniks, wire potentiometers and accelerometers are indicated. Six threaded rods go through the column at *h*=5″, 15″, 25″, 35″, 55″, and 65″ in the X direction. They are unbonded from the surrounding concrete except near the center of the column. The length of the bonded part is roughly 14 in. Total of fourteen Novotechniks are mounted on the north and south sides (Fig. D.2(a) and (b)). Each Novotechnik's location is specified in Table D.1. For example, 'NovoT1' is attached to the rod at *h*=5″ and measures the Z directional displacement between *h*=0″ and 5″ on the north side of the column. 'NovoT8' is at the same position on the opposite side. As a result, the curvature at *h*=2.5″ can be obtained with these measurements. Similarly, the curvature histories at *h*=10″, 20″, 30″, 45″, 60″ and 67.5″ are obtained. They are more clearly shown in Fig. D.4. The curvature history from the Novotechniks can be compared to that from the strain gages on the longitudinal reinforcing bars at *h*=10″, 20″, 30″, and 60″.

Wire potentiometers are connected to the south and west sides of the setup (Fig. D.2(b) and (c)). On the south side (Fig. D.2(b)), two wire potentiometers are connected to the footing (*h*=0″) and the average of both measurements is used to calculate relative displacement of the column. Four wire potentiometers are connected to the column at *h*=15″, 35″, 55″ and 70″ and two wire potentiometers are connected to the top concrete block. On the west side, one perpendicular wire potentiometer is for the footing, and four diagonal wire potentiometers are connected to the column (Fig. D.3(b)), i.e. two at *h*=35″ and two at *h*=70″. Two wire potentiometers on the concrete blocks capture the Y directional displacement. Four wire potentiometers are connected to the bottom of the concrete block as shown in Fig. D.3(d) and they measure vertical displacement of the block from the base plate.

Two DCDTs measure the vertical displacement of the column on the east and west sides. The average of the DCDTs is considered as a more reliable measurement rather than the average of two wire potentiometers on the east and west sides. This is due to fluctuations of the concrete blocks. These two different measurements are compared in Fig. 4.20.

Nine 3D accelerometers are attached to the setup. Four at the corners of the base plate (Fig. D.3(a)), four at the corners of the top concrete block (Fig. D.3(c)) and one below the top block capture the acceleration in X, Y and Z directions. Nine 1D accelerometers are used on the north side of the column and their locations are specified in Table D.1.

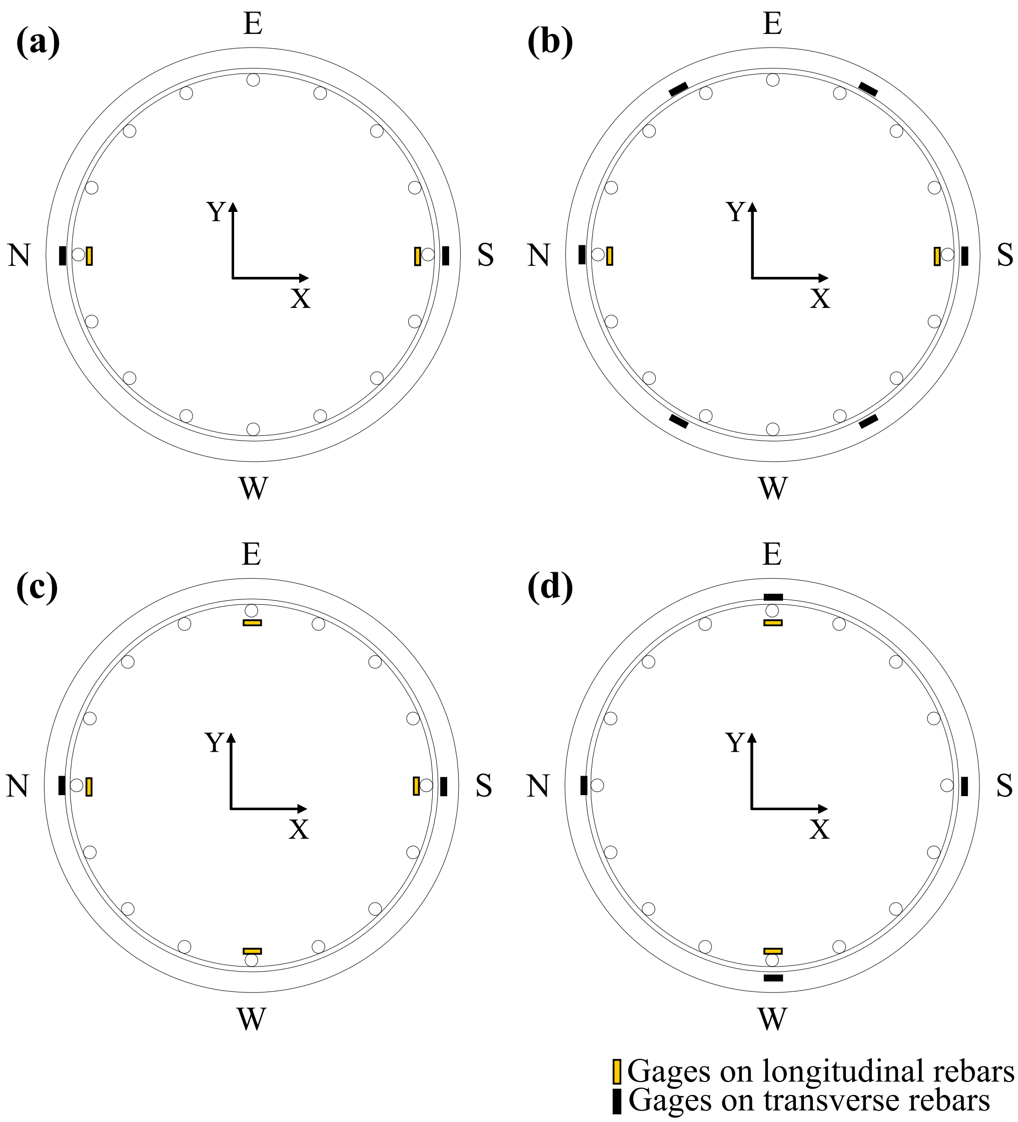

Fig. D.1 Strain gages

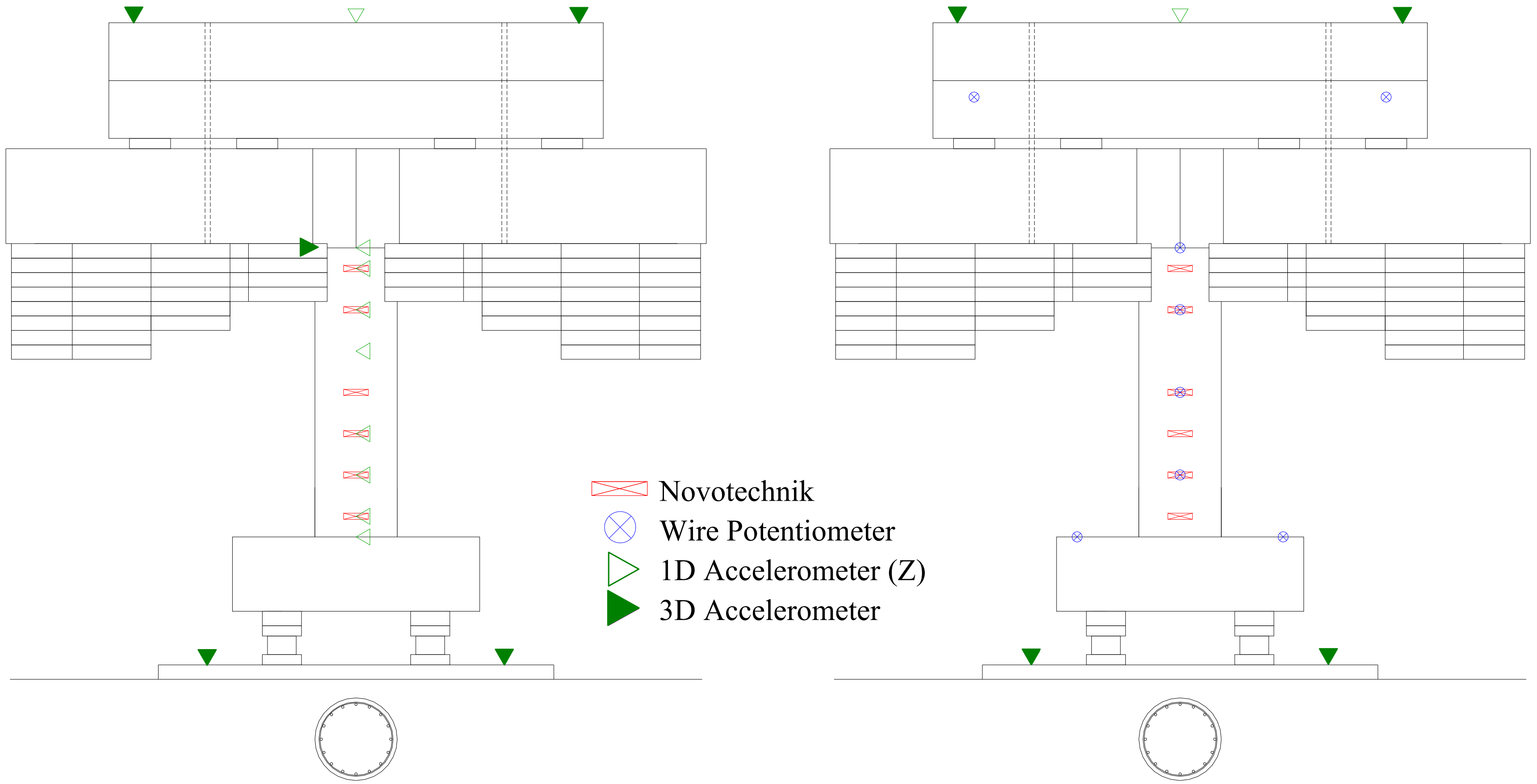

(a) North **(b) South**

Fig. D.2 External measurement: Elevation

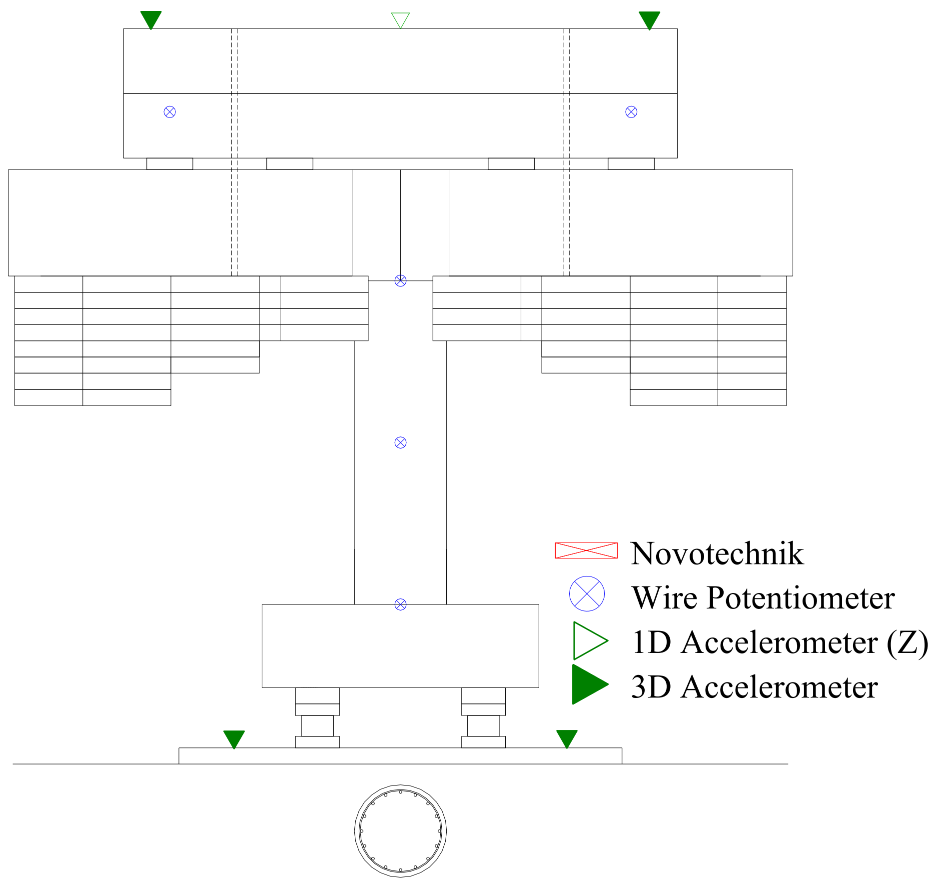

(c) West

Fig. D.2 External measurement: Elevation (continued)

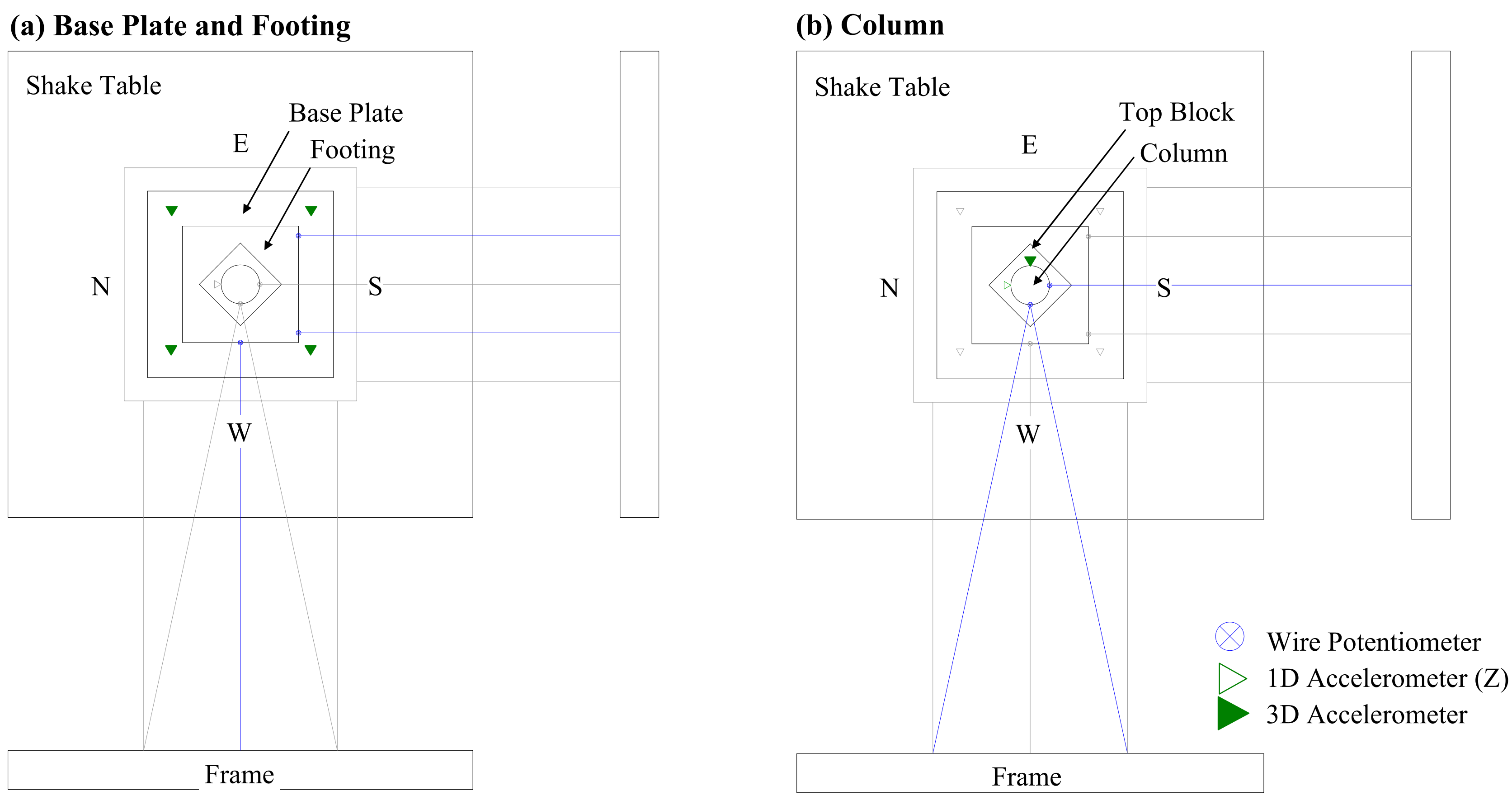

Fig. D.3 External measurement: Plan

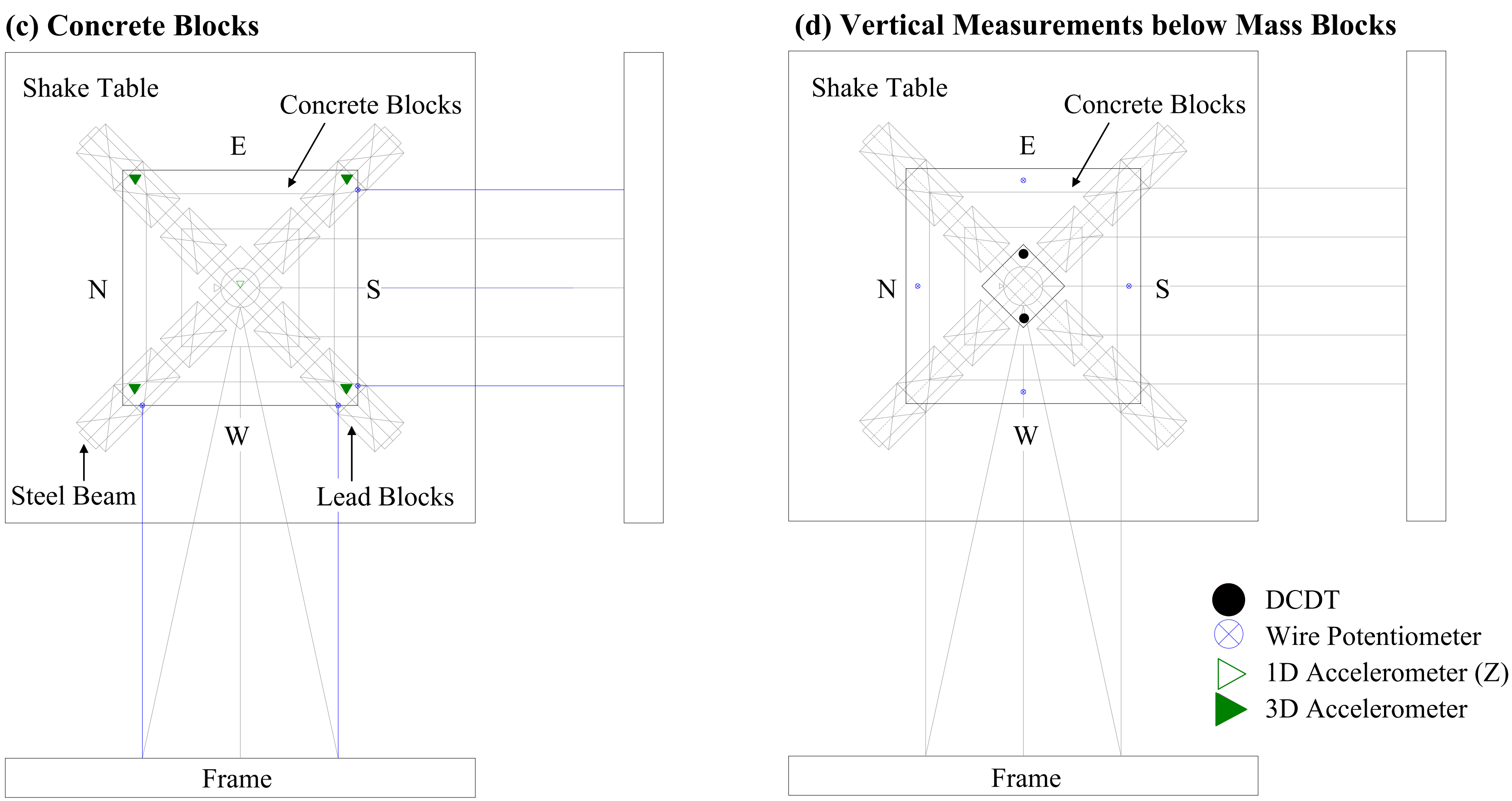

Fig. D.3 External measurement: Plan (continued)

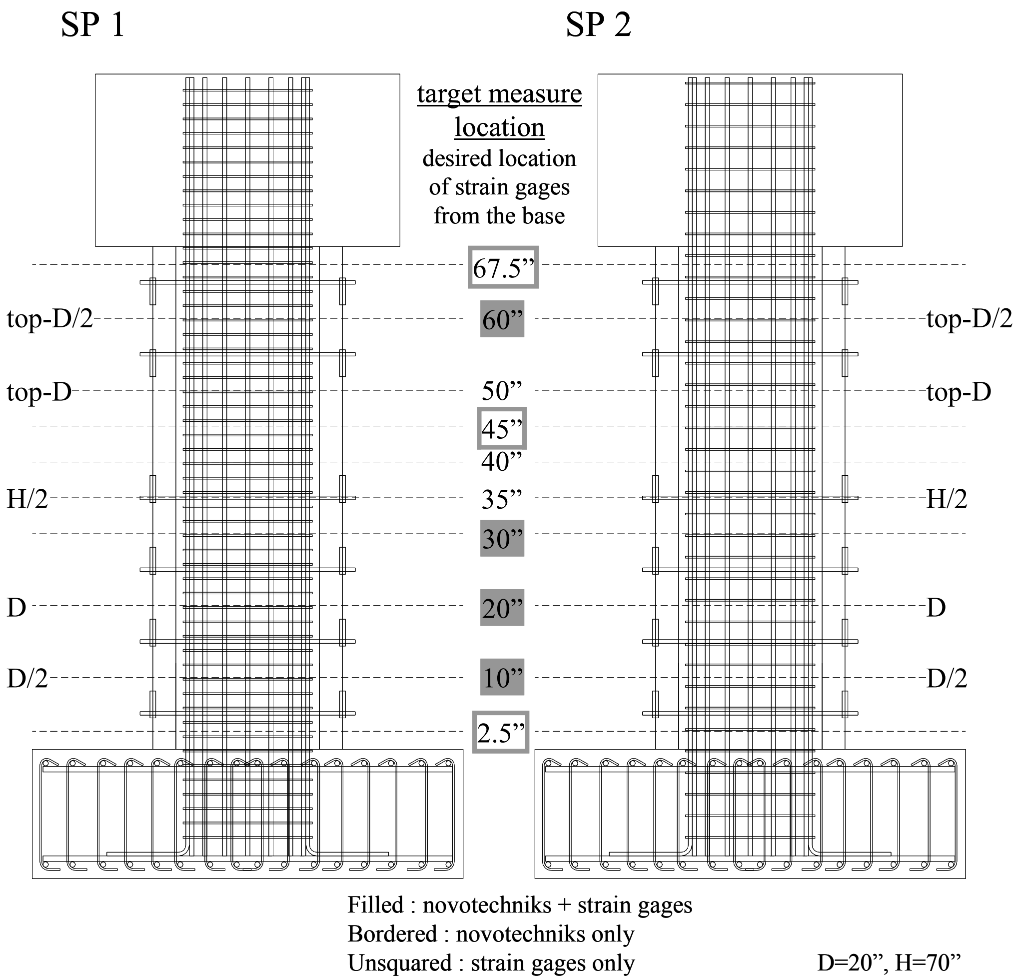

Fig. D.4 Target measure location of the Novotechniks and strain gages

Appendix E

The photographs of test specimens were taken on the north, west, south and east sides of the specimen. Fig. E.1 shows damage at the top and the base of both specimens after a series of tests, i.e. the 3rd 125%-scale test. The photographs of SP1 after 70%, 95% and the 3rd 125%-scale runs are presented in Fig. E.2, Fig. E.3, and Fig. E.4. Those of SP2 are shown in Fig. E.5, Fig. E.6 and Fig. E.7. For clear crack patterns, refer to Fig. 4.25 and Fig. 4.26 in Section 4.7.


(a) SP1 top on the north (b) SP1 base on the north


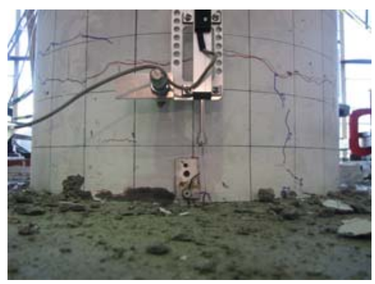

(c) SP1 top on the south (d) SP1 base on the south


(d) SP2 top on the north (e) SP2 base on the north

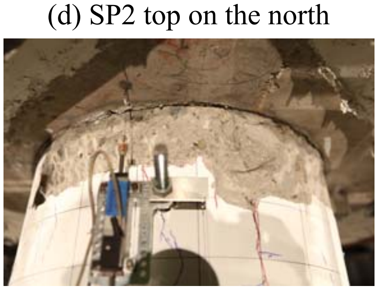
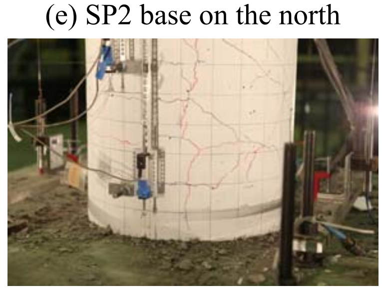

(f) SP2 top on the south (g) SP2 base on the south

Fig. E.1 Test photographs of the top and base, after 125%-scale runs (runs 1-11, 2-11)

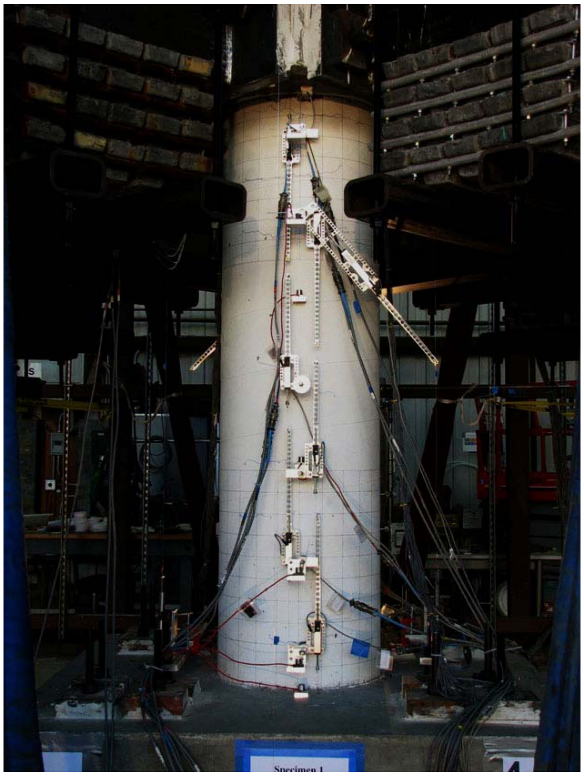

(a) North

(b) West

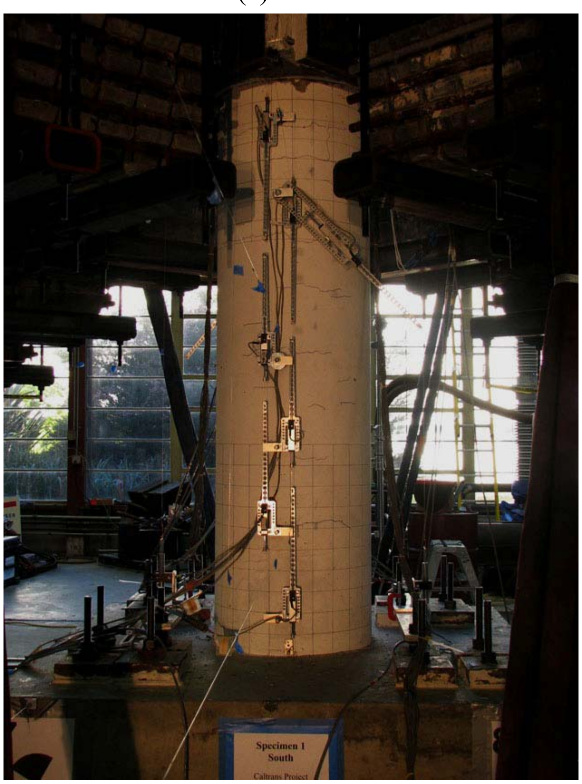

(c) South

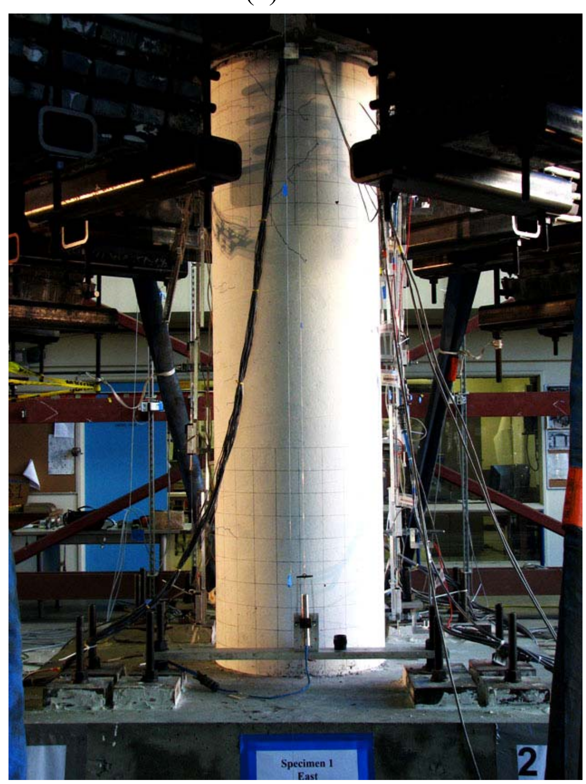

(d) East

Fig. E.2 Test photographs of SP1, after the 70%-scale run (run 1-7)

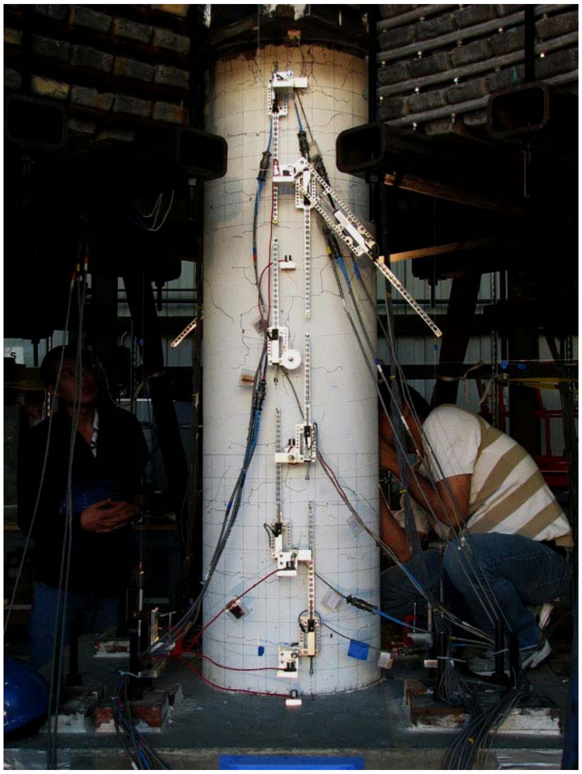

(a) North

(b) West

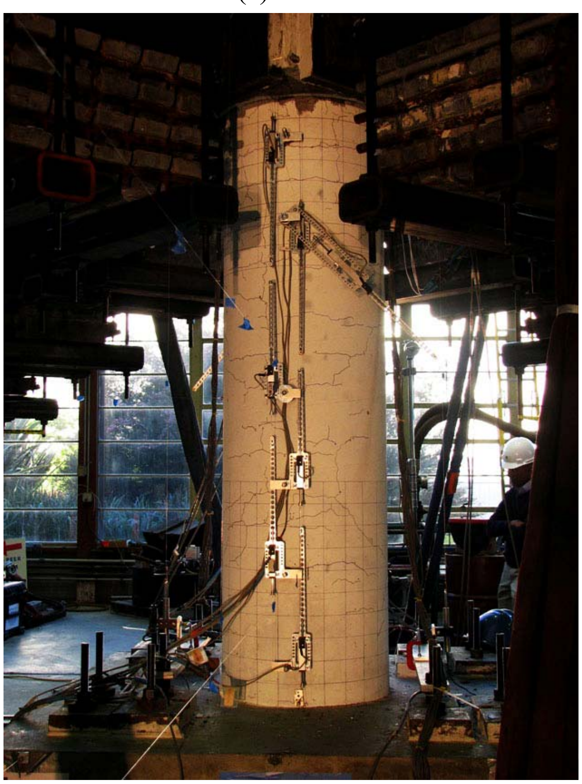

(c) South

(d) East

Fig. E.3 Test photographs of SP1, after the 95%-scale run (run 1-8)

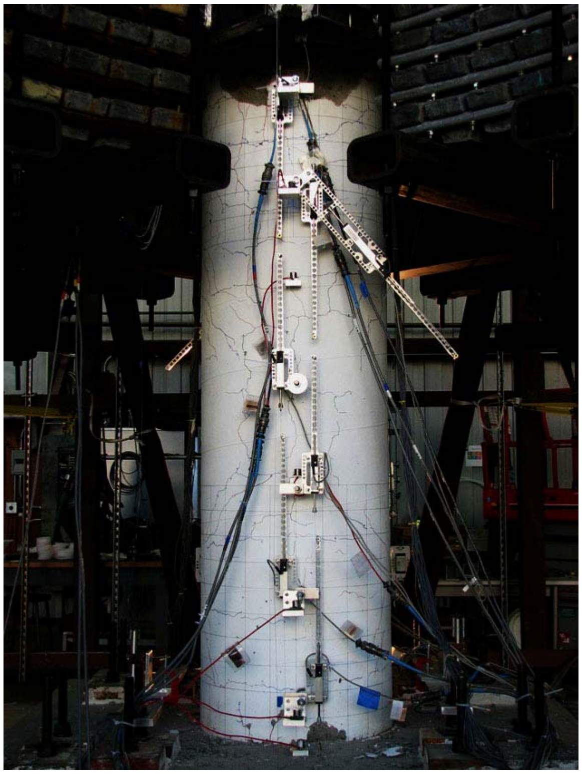

(a) North

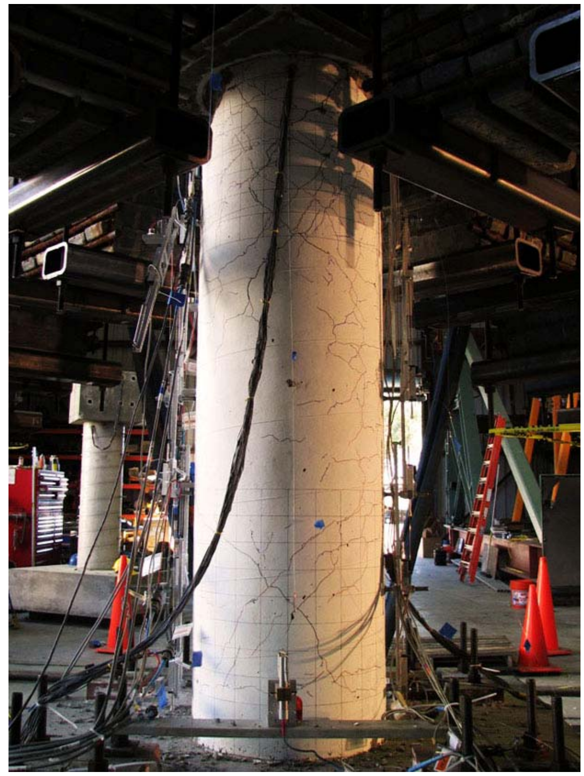

(b) West

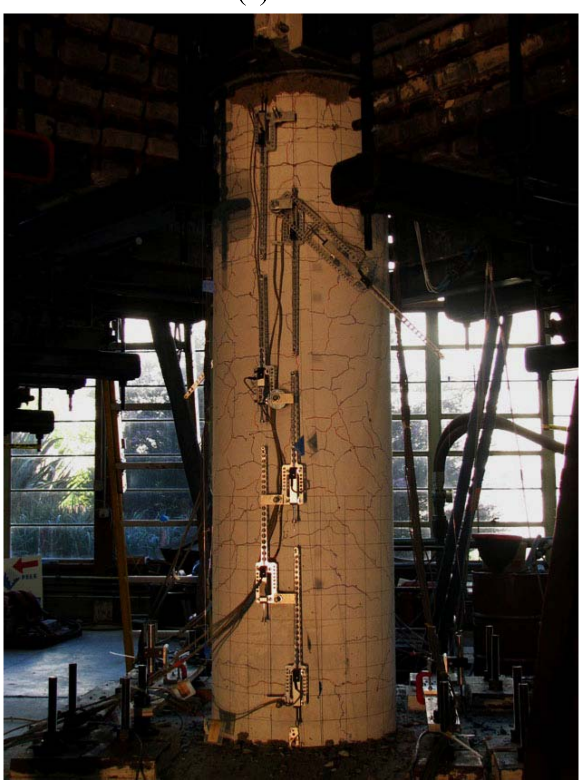

(c) South

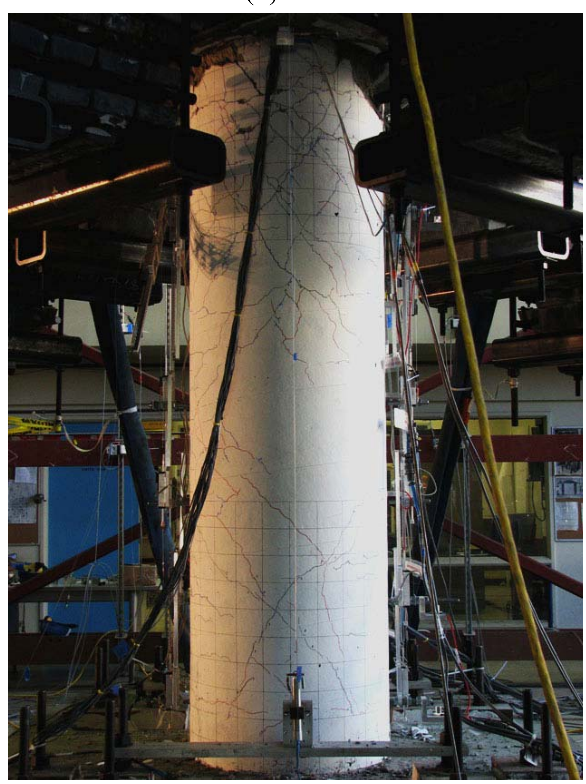

(d) East

Fig. E.4 Test photographs of SP1, after the 125%-scale run (run 1-11)

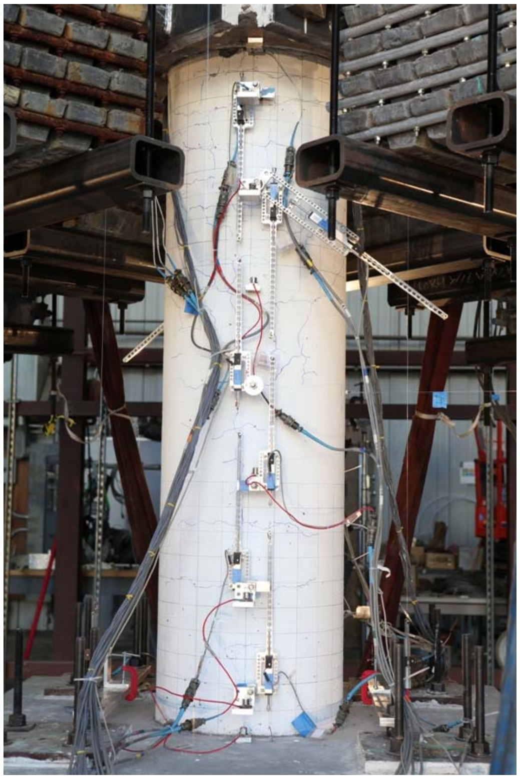

(a) North

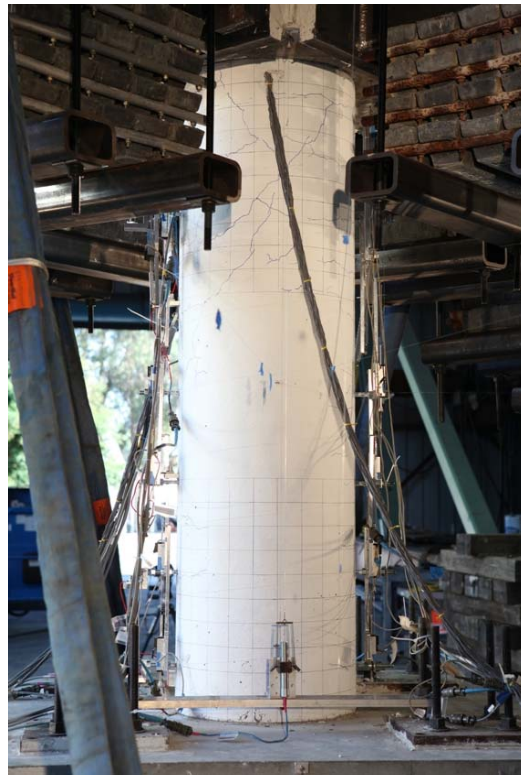

(b) West

(c) South

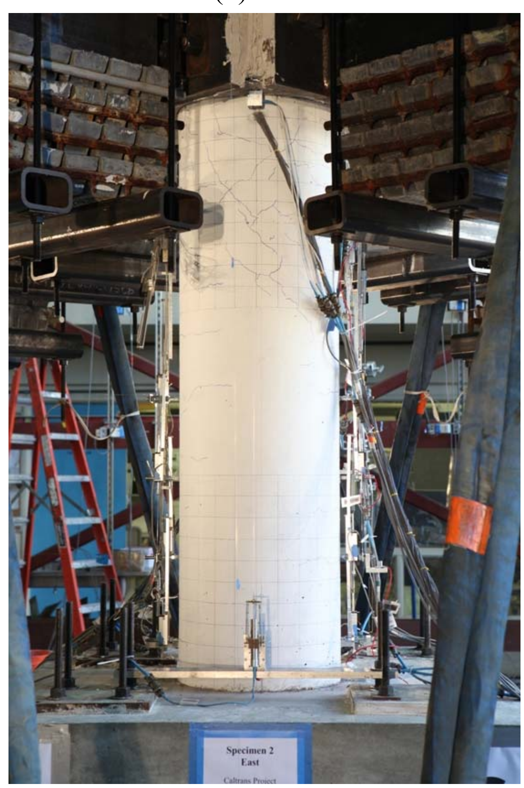

(d) East

Fig. E.5 Test photographs of SP2, after the 70%-scale run (run 2-7)

(a) North

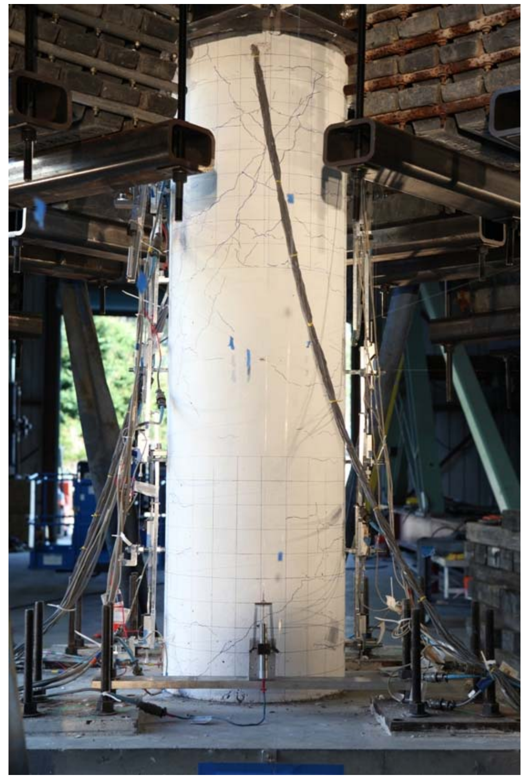

(b) West

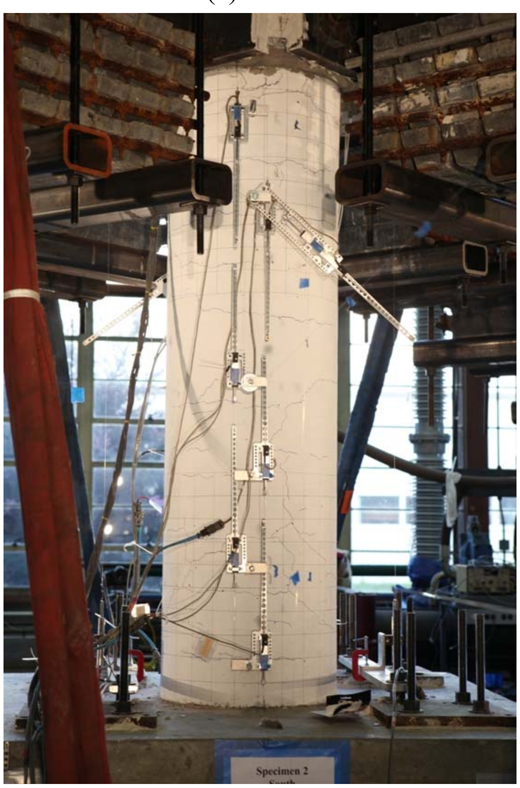

(c) South

(d) East

Fig. E.6 Test photographs of SP2, after the 95%-scale run (run 2-8)

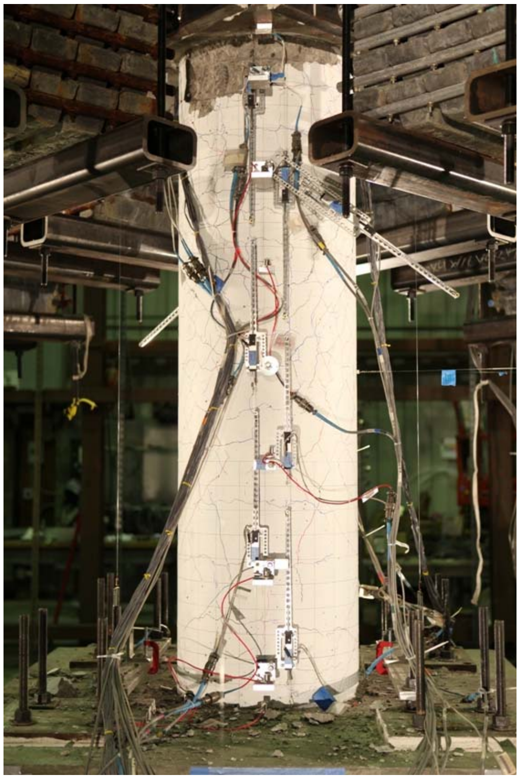
(a) North

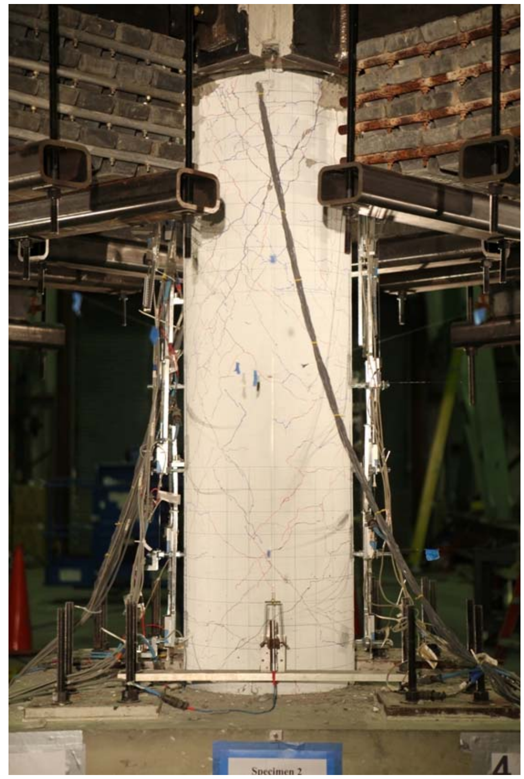
(b) West

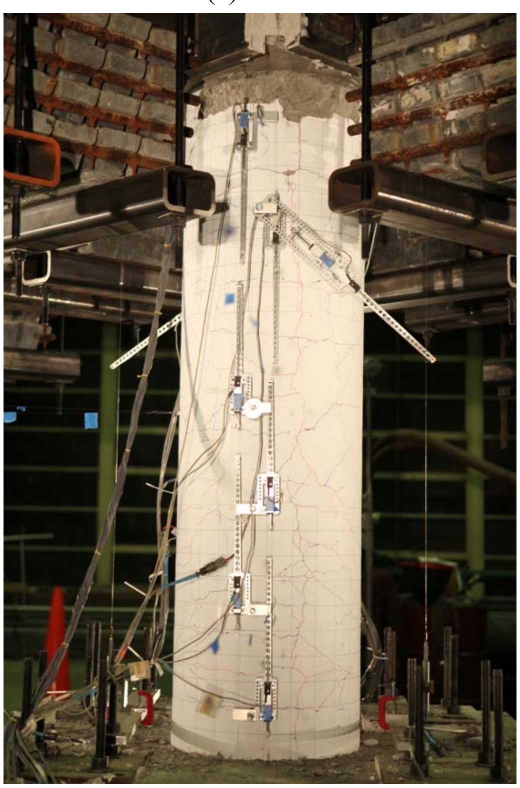
(c) South

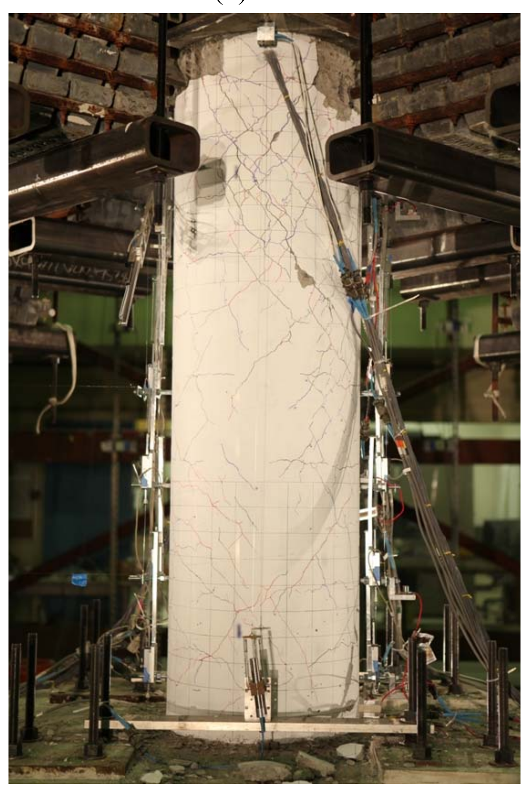
(d) East

Fig. E.7 Test photographs of SP2, after the 125%-scale run (run 2-11)

Appendix F

In this section, the local responses of the computational model B-1 are discussed. Only the results from B-1 are presented, since B-1, B-2-ACI and B-2-SDC provide similar local responses and those of A-1, A-2-ACI and A-2-SDC with a BWH2 element are also similar.

F.1 Curvatures

Fig. F.1 and Fig. F.2 compare curvature histories from the computational model, B-1, to the test data of SP1. Both B-1 and SP1 have the steel reinforcing bars on the north and south sides, and the curvatures in the X direction (N-S) were calculated from those longitudinal strains at *h*=10” and 60”. The following are observations on the curvature histories of SP1:

- The curvature history at *h*=60″ is larger than that at *h*=10″. The results from B-1 agree with this trend qualitatively.
- B-1 is accurate in predicting the curvature history at *h*=10″, and it is between -3.1×10^{-4} and 3.1×10^{-4} in^{-1}.
- B-1 is also accurate in predicting the curvature history at *h*=60″ subjected to 50% and 70%-scale motions. The minimum and maximum values from B-1 are -3.2×10^{-4} and 3.6×10^{-4} in^{-1}, respectively.
- From 95%-scale, the difference between the curvatures of B-1 and SP1 increases significant. In particular, B-1 does not capture the negative peaks and negative residual curvatures. Comparing the minimum values under each motion, B-1 reaches 32.1%, 27.6%, 25.2%, and 23.6% of the test data subjected to 95% and the three 125%-scale motions. Even in the peak-to-peak amplitude, i.e. fluctuation, the results from B-1 are not comparable to the test data.

The trend in the difference between curvatures from the computational model and the test specimen, which is discussed above, is still valid for SP2 qualitatively. It should be noted that the section of SP2 at 10″ had large curvature history, but B-1 does not capture its peaks after 95%-scale motion, refer to Fig. F.3 and Fig. F.4.

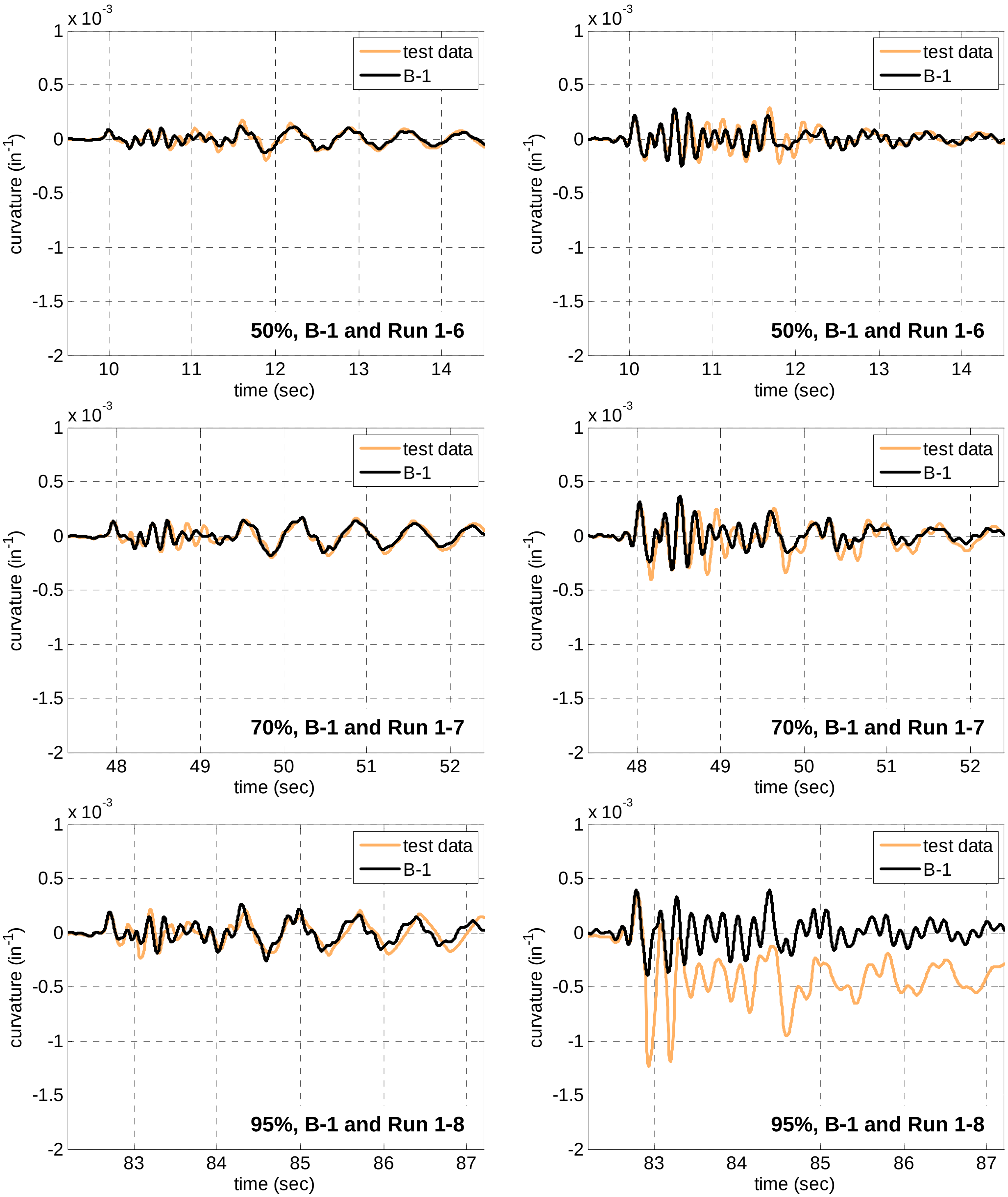

(a) *h*=10” **(b) *h*=60”**

Fig. F.1 Comparison of curvature histories at *h*=10″ and 60″ of SP1 subjected to 50%, 70%, and 95%-scale motions

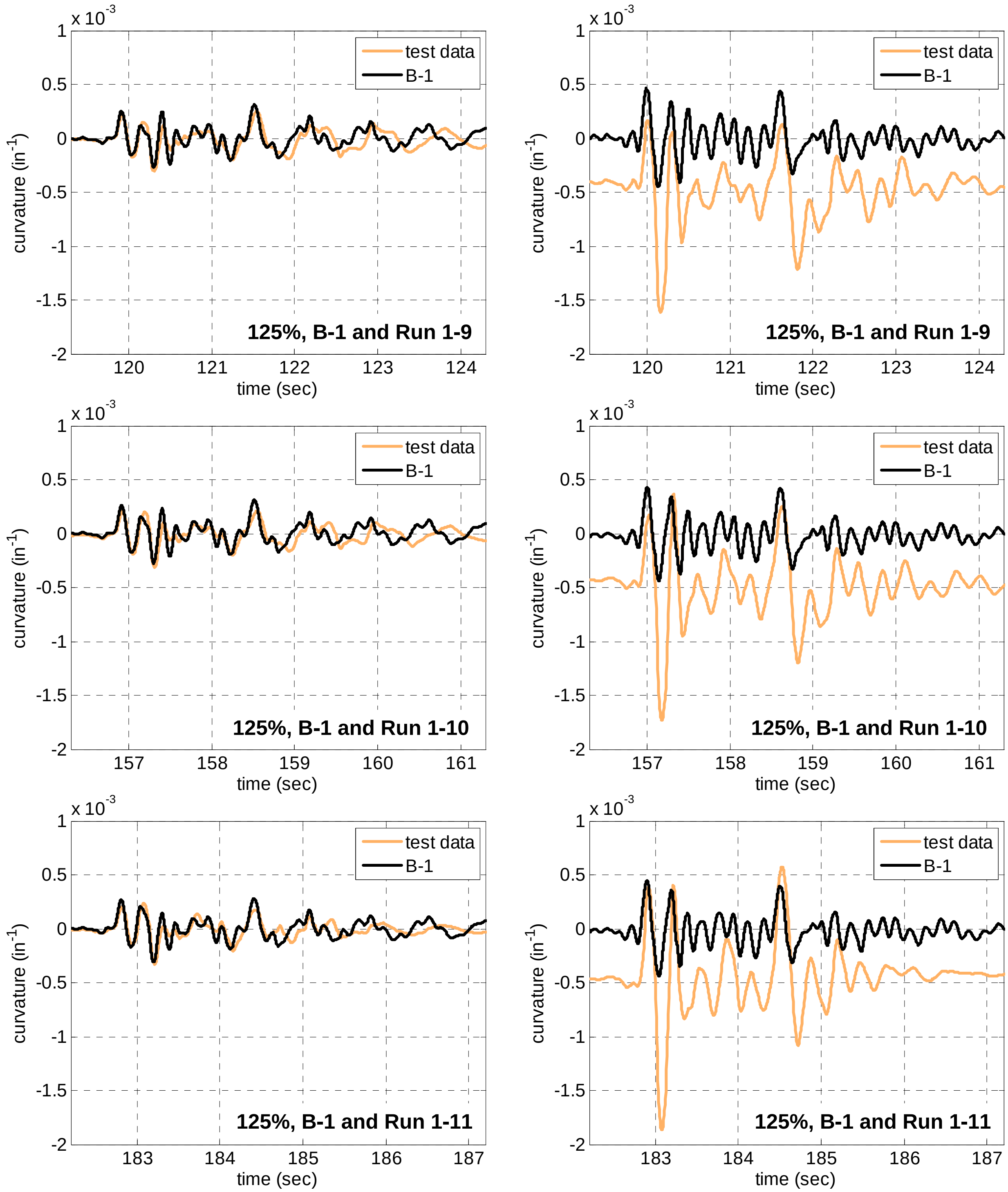

(a) *h*=10” **(b) *h*=60”**

Fig. F.2 Comparison of curvature histories at h=10″ and 60″ of SP1 subjected to 125%-scale motions

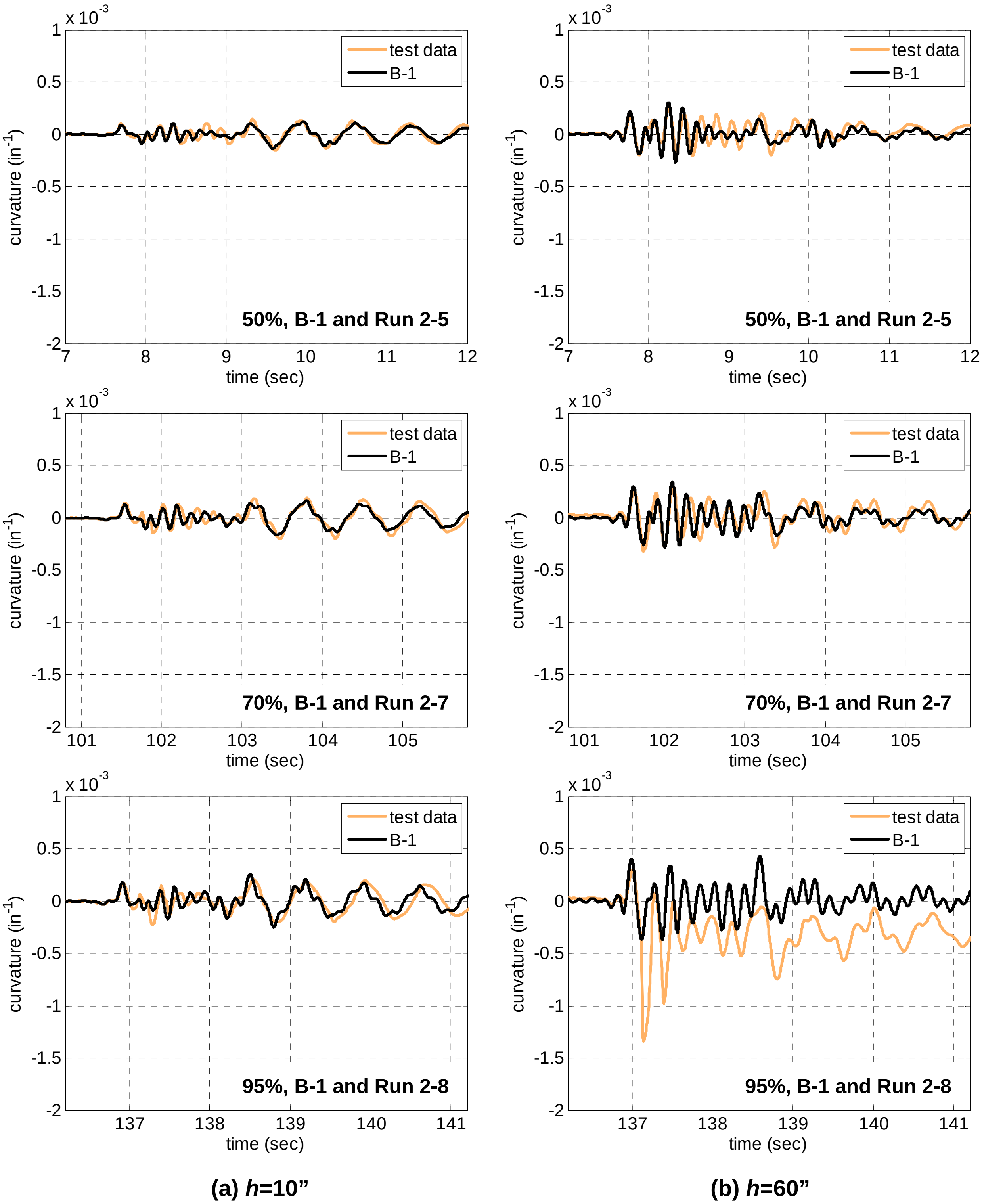

Fig. F.3 Comparison of curvature histories at h=10″ and 60″ of SP2 subjected to 50%, 70%, and 95%-scale motions

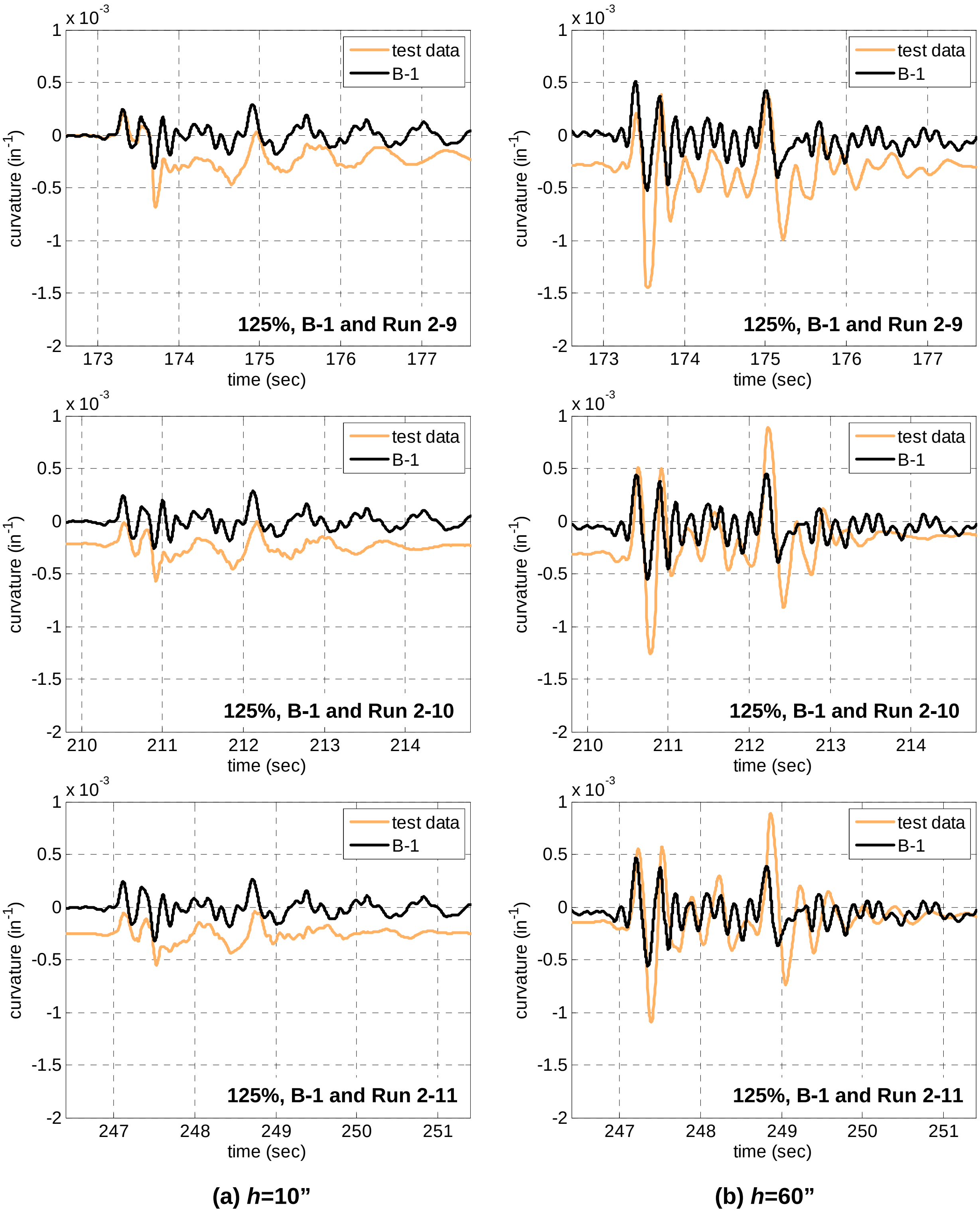

Fig. F.4 Comparison of curvature histories at h=10″ and 60″ of SP2 subjected to 125%-scale motions

F.2 Moment-Curvature Relationships

The bending moment-curvature relationships obtained from the sections at *h*=10″ and 60″ are compared to the test data in Fig. F.5. The results are obtained from B-1. As mentioned in Section F.1, B-1 does not capture the amplitude of the curvature, especially at *h*=60″ under 125%-scale motions.

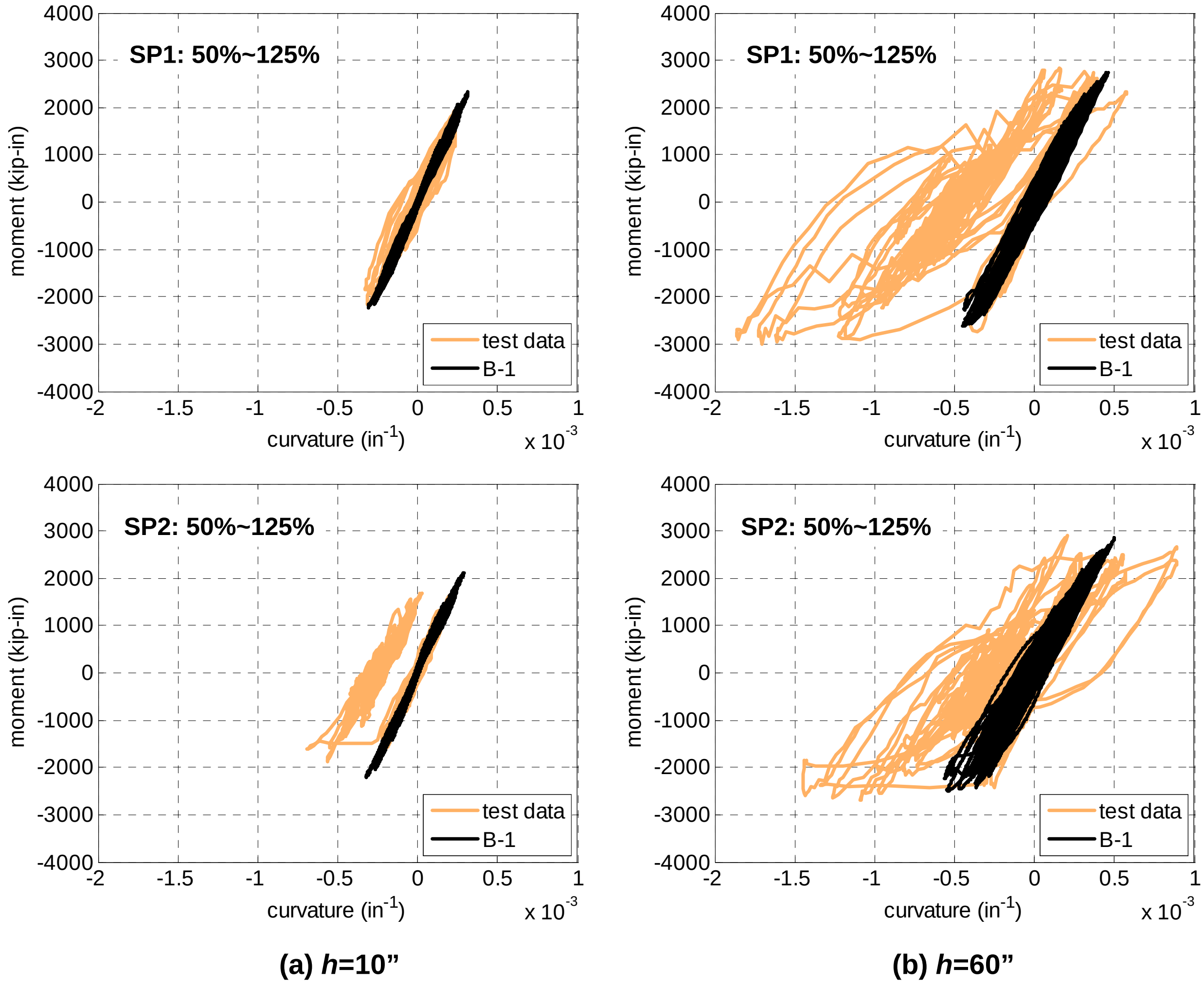

Fig. F.5 Comparison of bending moment-curvature relationships at *h*=10″ and 60″ of SP1 and SP2 under 50% to 125%-scale motions

F.3 Longitudinal Strains

Since the curvatures were calculated based on the longitudinal strains on the north and south, the difference between computational and experimental data resulted from the strain histories obtained from B-1. The figures, from Fig. F.6 to Fig. F.11, compare the longitudinal strain histories on the north, south, east, and west of B-1 to the test data obtained from SP1. Fig. F.6 and Fig. F.7 show the longitudinal strain histories on the north and south sides at h=10″ from 50%-scale motion. Fig. F.8 and Fig. F.9 present those on the north and south sides at h=60″ from 50%-scale motion. The strains on the east and west sides at h=35″ subjected to the same motions are shown in Fig. F.10 and Fig. F.11. The observations on the longitudinal strains of SP1 are as follows:

- The longitudinal strains on the north and south at h=10″ obtained from B-1 are comparable to the test data, even though the peak values are somewhat different.
- B-1 is not accurate in predicting the longitudinal strains on the north and south at h=60″. It provides good estimation for the strains on the north before 125%-scale 'X only' motion, and for the strains on the south before 95%-scale motion. It does not capture the significant difference in longitudinal strain between north and south sides.
- B-1 captures the peak strains on the east and west sides at h=35″ with accuracy, except for the response under 125%-scale 'X only' motion. It underestimates the tensile strain. In addition, positive strain, i.e. shortening, caused by fluctuation of axial force is detected in all computational results from B-1, but it was not observed in the tests.

Similar to the curvatures, analogues observations to SP1 could be made for the computational results of SP2. To avoid repetition, only the results for SP1 are shown in this appendix.

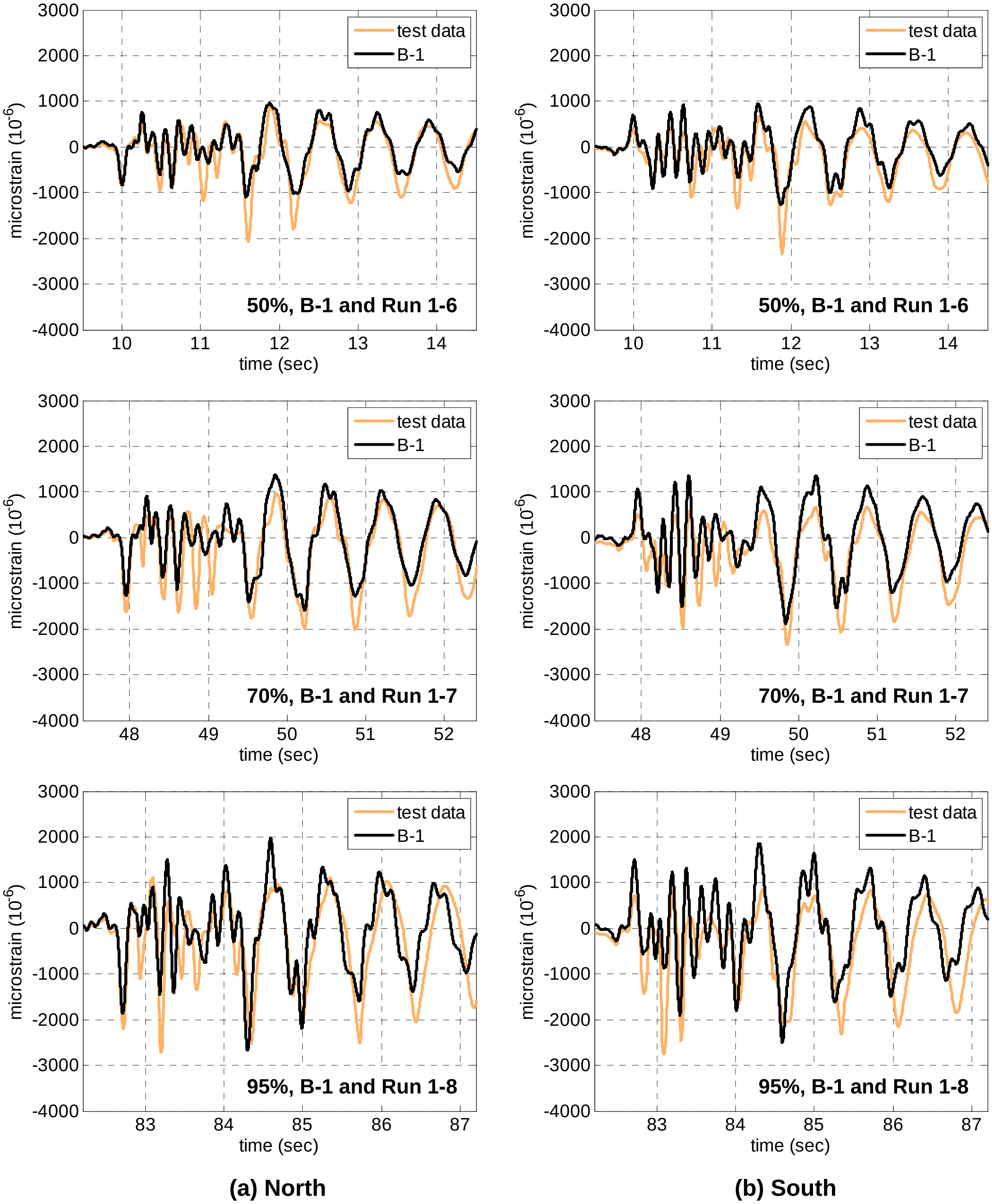

Fig. F.6 Comparison of longitudinal strain histories at h=10″ on the north and south of SP1 subjected to 50%, 70%, and 95%-scale motions

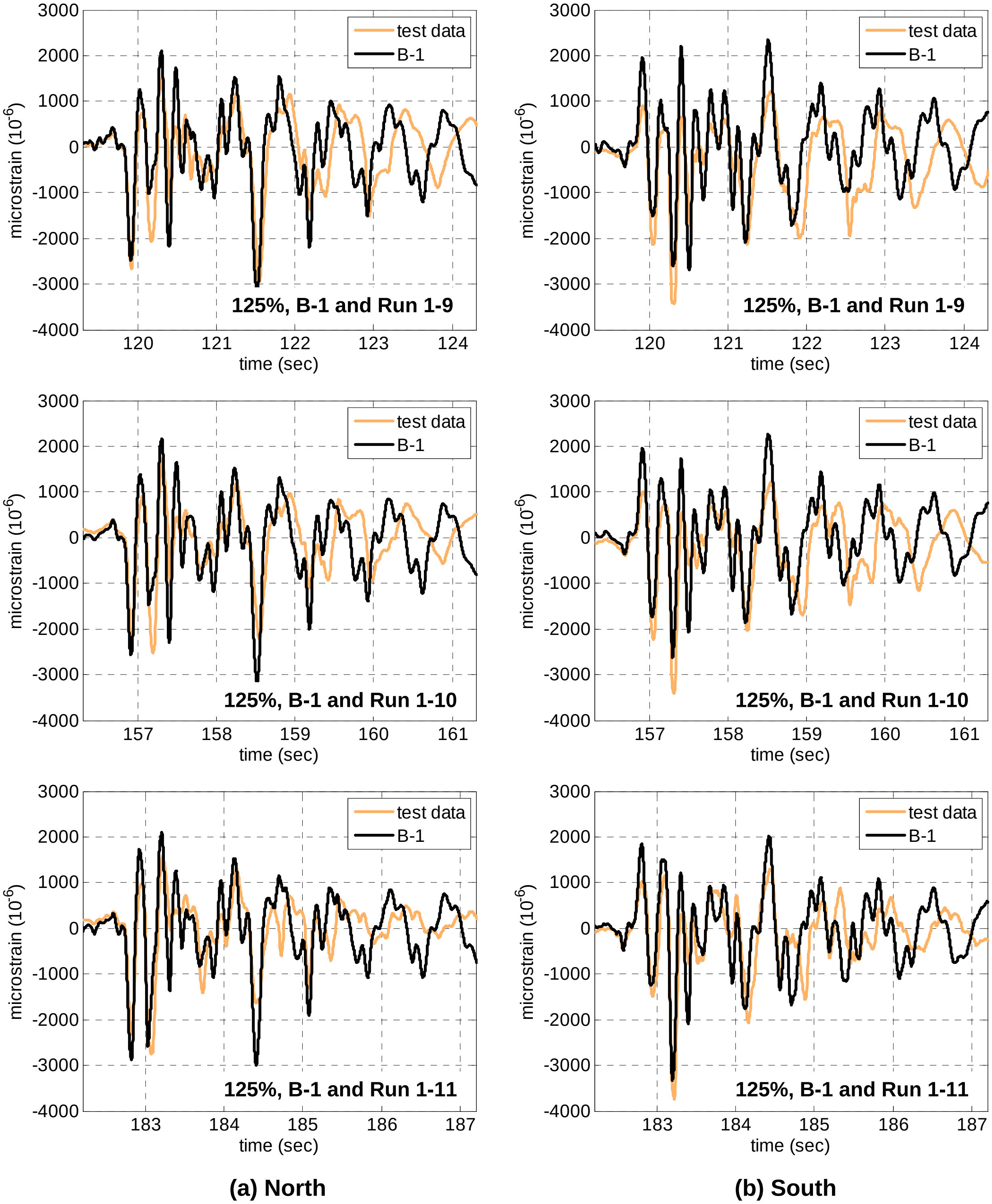

Fig. F.7 Comparison of longitudinal strain histories at *h*=10″ on the north and south of SP1 subjected to 125%-scale motions

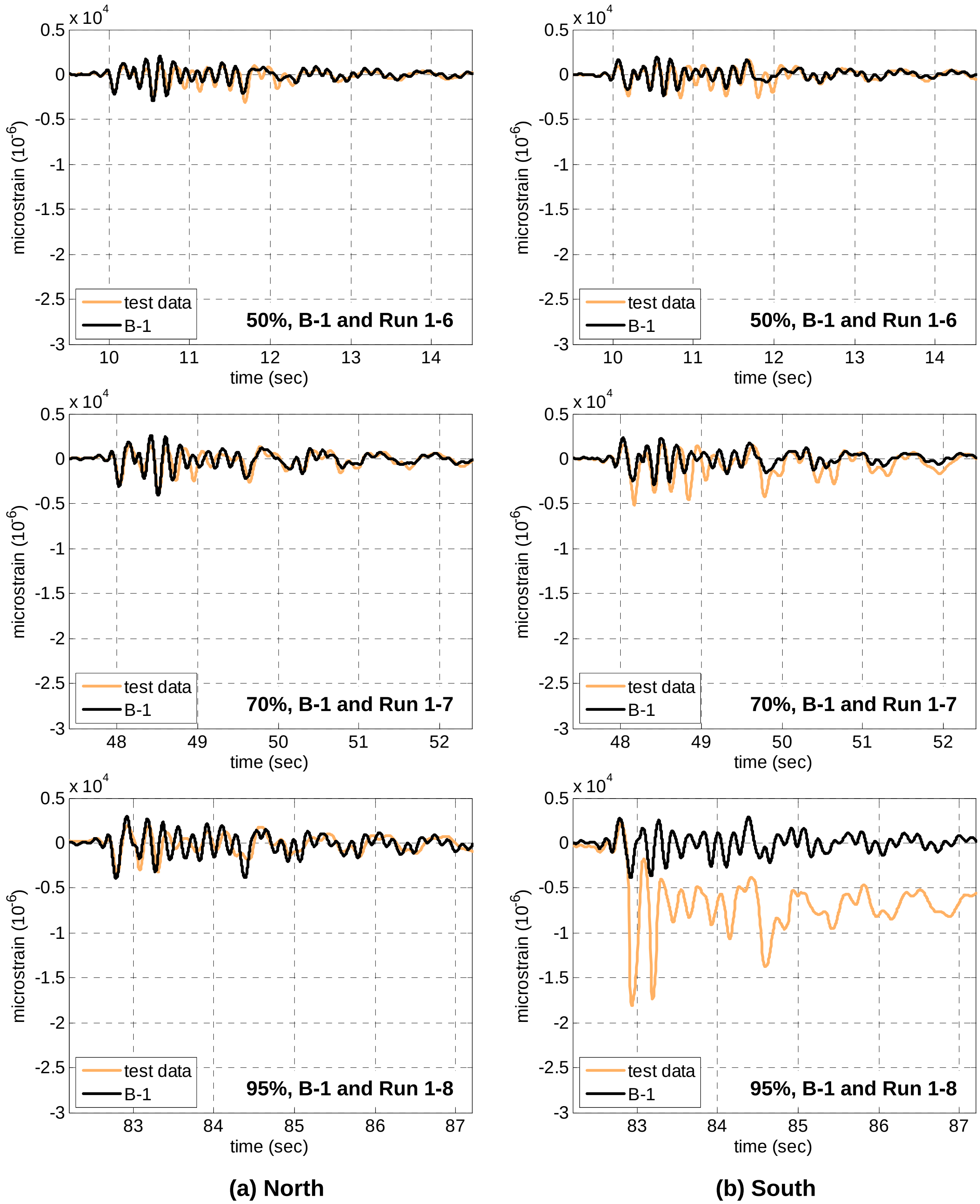

Fig. F.8 Comparison of longitudinal strain histories at h=60″ on the north and south of SP1 subjected to 50%, 70%, and 95%-scale motions

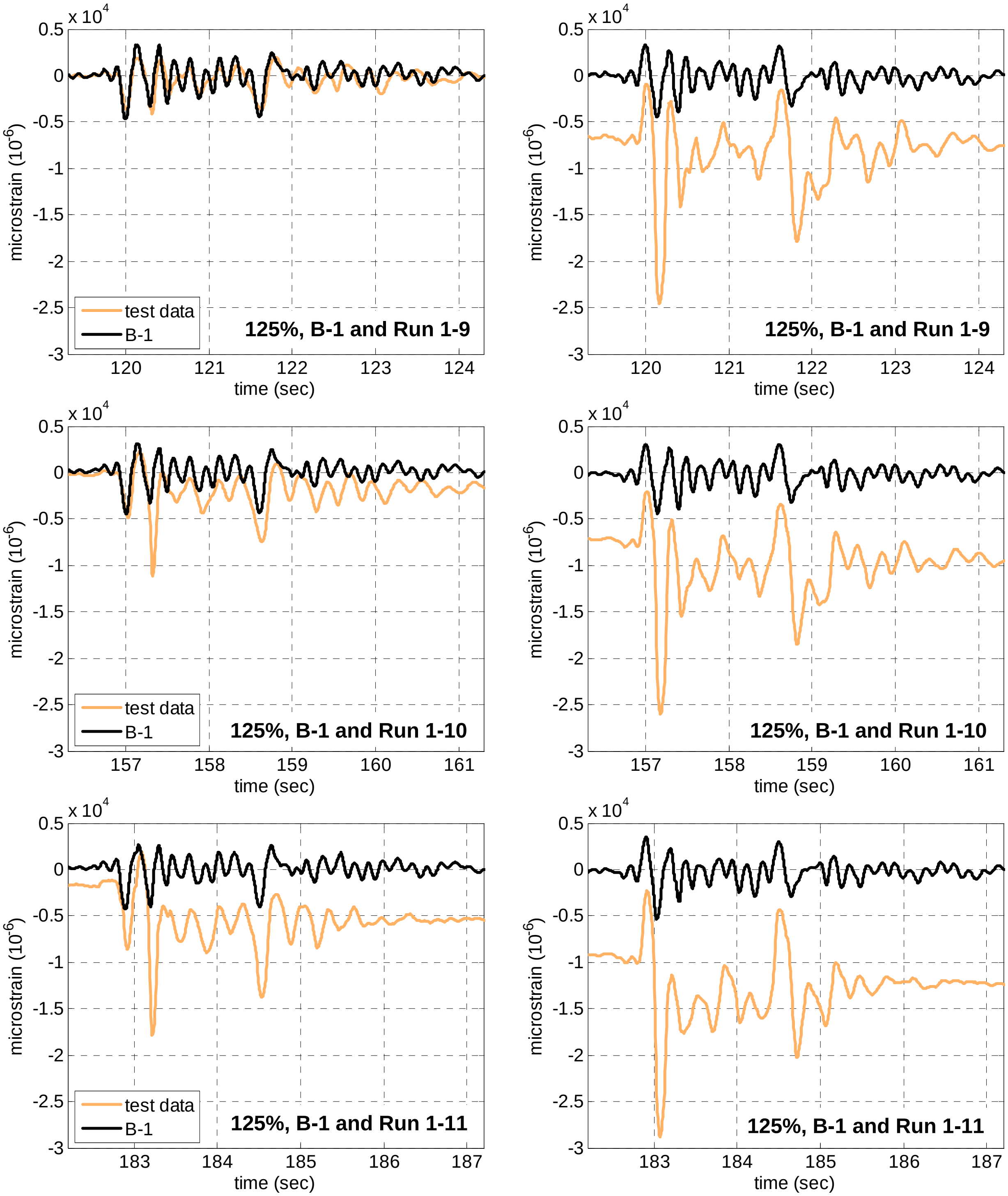

(a) North **(b) South**

Fig. F.9 Comparison of longitudinal strain histories at h=60″ on the north and south of SP1 subjected to 125%-scale motions

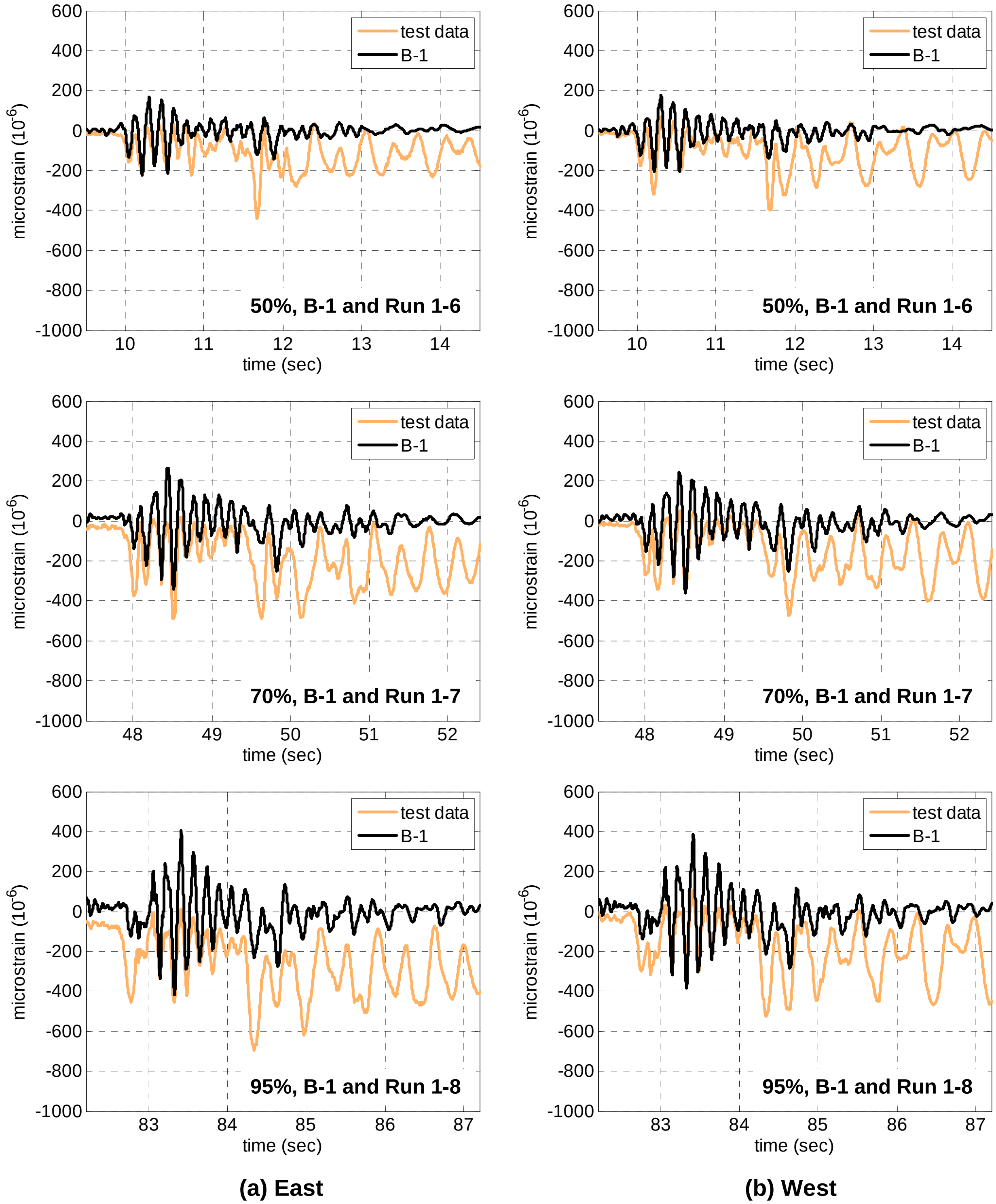

Fig. F.10 Comparison of longitudinal strain histories at h=35″ on the east and west of SP1 subjected to 50%, 70%, and 95%-scale motions

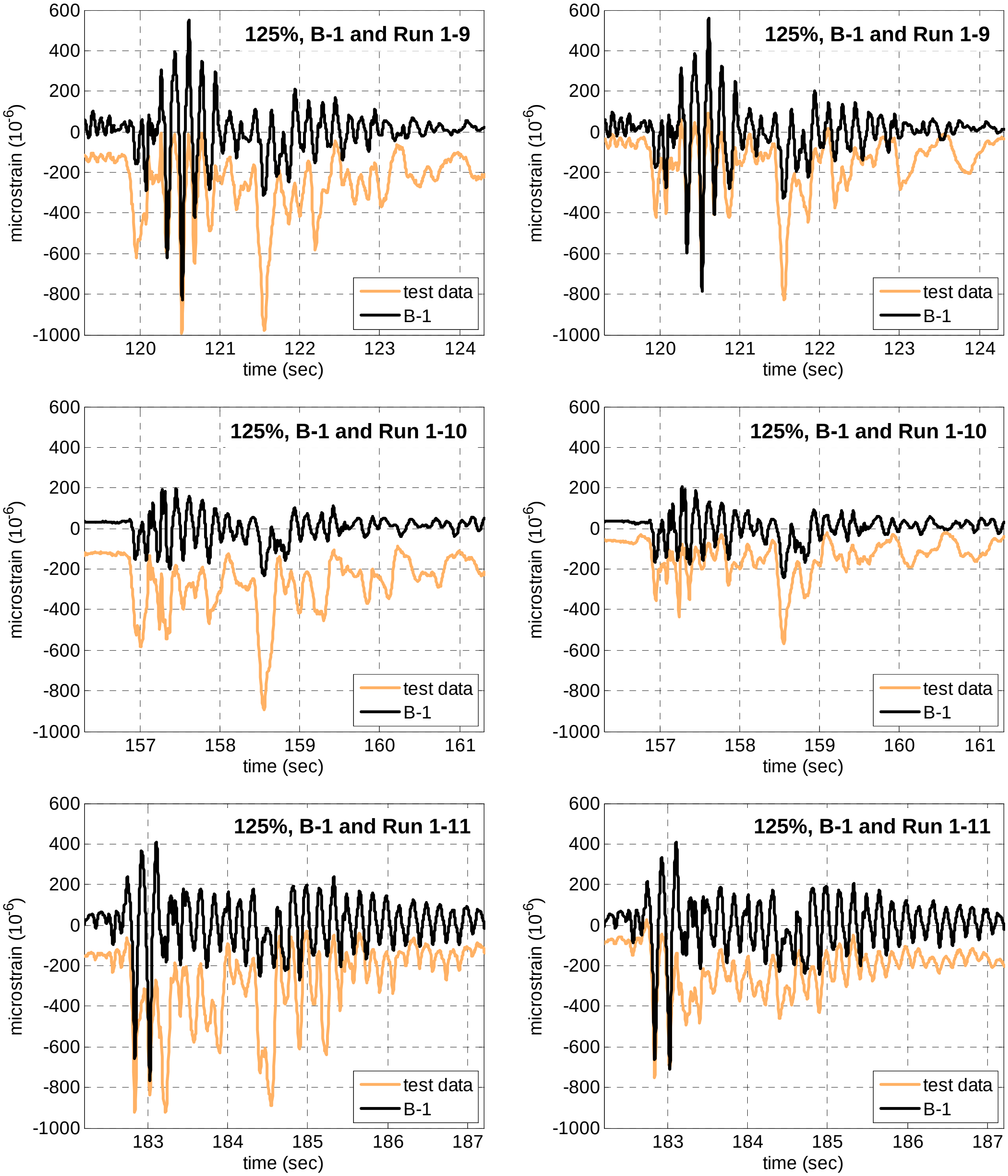

(a) East **(b) West**

Fig. F.11 Comparison of longitudinal strain histories at *h*=35″ on the east and west of SP1 subjected to 125%-scale motions